frontiers | Research Topics

Monitoring, early warning and mitigation of natural and engineered slopes, volume III

Edited by
Wen Nie, Haijun Qiu and Afshin Asadi

Published in
Frontiers in Earth Science
Frontiers in Ecology and Evolution
Frontiers in Environmental Science

ISSN 1664-8714
ISBN 978-2-8325-5321-3
DOI 10.3389/978-2-8325-5321-3

About Frontiers

Frontiers is more than just an open access publisher of scholarly articles: it is a pioneering approach to the world of academia, radically improving the way scholarly research is managed. The grand vision of Frontiers is a world where all people have an equal opportunity to seek, share and generate knowledge. Frontiers provides immediate and permanent online open access to all its publications, but this alone is not enough to realize our grand goals.

Frontiers journal series

The Frontiers journal series is a multi-tier and interdisciplinary set of open-access, online journals, promising a paradigm shift from the current review, selection and dissemination processes in academic publishing. All Frontiers journals are driven by researchers for researchers; therefore, they constitute a service to the scholarly community. At the same time, the *Frontiers journal series* operates on a revolutionary invention, the tiered publishing system, initially addressing specific communities of scholars, and gradually climbing up to broader public understanding, thus serving the interests of the lay society, too.

Dedication to quality

Each Frontiers article is a landmark of the highest quality, thanks to genuinely collaborative interactions between authors and review editors, who include some of the world's best academicians. Research must be certified by peers before entering a stream of knowledge that may eventually reach the public - and shape society; therefore, Frontiers only applies the most rigorous and unbiased reviews. Frontiers revolutionizes research publishing by freely delivering the most outstanding research, evaluated with no bias from both the academic and social point of view. By applying the most advanced information technologies, Frontiers is catapulting scholarly publishing into a new generation.

What are Frontiers Research Topics?

Frontiers Research Topics are very popular trademarks of the *Frontiers journals series*: they are collections of at least ten articles, all centered on a particular subject. With their unique mix of varied contributions from Original Research to Review Articles, Frontiers Research Topics unify the most influential researchers, the latest key findings and historical advances in a hot research area.

Find out more on how to host your own Frontiers Research Topic or contribute to one as an author by contacting the Frontiers editorial office: frontiersin.org/about/contact

Monitoring, early warning and mitigation of natural and engineered slopes, volume III

Topic editors

Wen Nie — Jiangxi University of Science and Technology, China

Haijun Qiu — Northwest University, China

Afshin Asadi — EnvoGéotechnique, New Zealand

Citation

Nie, W., Qiu, H., Asadi, A., eds. (2024). *Monitoring, early warning and mitigation of natural and engineered slopes, volume III*. Lausanne: Frontiers Media SA.

doi: 10.3389/978-2-8325-5321-3

Table of contents

frontiers | Frontiers in Earth Science

TYPE Editorial
PUBLISHED 05 August 2024
DOI 10.3389/feart.2024.1465911

OPEN ACCESS

EDITED AND REVIEWED BY
Gordon Woo,
Risk Management Solutions, United Kingdom

*CORRESPONDENCE
Wen Nie,
wen.nie@vip.tom.com

RECEIVED 17 July 2024
ACCEPTED 22 July 2024
PUBLISHED 05 August 2024

CITATION
Qiu H, Nie W and Asadi A (2024), Editorial: Monitoring, early warning and mitigation ofnatural and engineered slopes–volume III. *Front. Earth Sci.* 12:1465911. doi: 10.3389/feart.2024.1465911

Editorial: Monitoring, early warning and mitigation of natural and engineered slopes–volume III

Haijun Qiu[1], Wen Nie[2]* and Afshin Asadi[3]

[1]College of Urban and Environmental Sciences, Northwest University, Xi'an, China, [2]College of Resource and Environmental Sciences, Jiangxi University of Science and Technology, Ganzhou, China, [3]International College of Auckland (ICA), Auckland, New Zealand

KEYWORDS

natural and engineering slope, slope failure mechanism, slope monitoring, risk assessment, ecology and land use

Editorial on the Research Topic
Monitoring, early warning and mitigation of natural and engineered slopes–volume III

Introduction

Natural and engineered slopes are geological bodies with lateral free surfaces formed naturally or artificially on the surface of the earth, which are widely distributed around the world (Zhou et al., 2022; Qiu et al., 2024). Due to climate change and intensified human activities, mountains, highways, mining areas, and reservoir slopes have become increasingly unstable, and even gradually evolved into landslide disasters, posing a serious threat to people's lives, property safety and infrastructure construction (Qiu et al., 2022; Yang et al., 2023). Recently, with the progress of slope control technology and the development of interdisciplinary theory, new development space has been provided for the dynamic monitoring and early warning of unstable slopes (Zhu et al., 2021; Wei et al., 2024; Ye et al., 2024). However, large-scale and long-term monitoring, precise risk assessment, and low-cost disaster recovery are still worth considering (Wang et al., 2022; Liu et al., 2024). Volume II of this Research Topic received 16 manuscripts (Qiu et al., 2023). Now, Volume III also gathered 16 papers aimed at further introducing the latest research progress and methods on monitoring, early warning, and mitigation of natural and engineered slopes.

Slope hazards reduction technology and mechanism

Seven of the 16 articles in the Research Topic explored research on slope displacement profile evaluation, landslide deformation monitoring, and the use of multiple models to quantitatively evaluate disaster risks, aiming at providing scientific support for slope treatment and disaster prevention. Li et al. proposed a three-dimensional nested Newmark method (3D-NNM) within the framework of kinematic theorems in limit analysis. Compared with

the original nested Newmark method, the results showed that the proposed 3D-NNM can effectively evaluate the permanent displacement profile of slopes under seismic action. Bai et al. proposed a rapid evaluation method for the spatial distribution of road traffic sections under earthquake and landslide damage based on the MDT model. Liu et al. applied the time series InSAR method to determine the time series deformation of the main landslide source area of Baihetan Reservoir after water storage and conducted a refined analysis of the deformation monitoring results of typical source areas. Jiang et al. inverted the depth of the active zone of the expansive soil slope in the middle route of the South to North Water Diversion Project using the InSAR method, and analyzed its distribution pattern and dynamic characteristics, providing a basis for designing slope protection measures and ensuring the safety of water channels. Zheng et al. used FLAC^{3D} numerical simulation experimental method to study the effect of coupling between the surface shape of loess slopes and the structure of coal seam cover on slope movement and deformation. Shen et al. took Meilonggou in Danba County, Sichuan Province as an example to study the factors and triggering mechanisms of the formation of debris flow disaster chains in the area, which can provide guidance for strengthening the construction of monitoring and early warning systems in the local area. Furthermore, Zhang et al. applied the RAMMS model to numerically simulate the movement process of debris flows in the Xigou area of the Three Gorges Reservoir Area, and conducted a risk assessment on debris flows with different recurrence intervals when multiple debris flows erupt simultaneously.

Natural disasters in different regions

Due to different geographical and tectonic environments, different regions face different types of disaster risks. Four different studies have revealed this issue. To evaluate the research focus and development direction of glacier lake disaster identification in plateau areas, Liu et al. collected literature related to glacier lake disaster identification from the Web of Science core Research Topic database from 1991 to 2023 and conducted a comprehensive bibliometric analysis. Huang et al. used SBAS-InSAR technology to monitor subsidence disasters in complex karst areas of mining areas. The author believed that deformation is influenced by various factors such as elevation, slope, precipitation, and vegetation. Li et al. discussed the spatiotemporal drought characteristics of winter wheat and summer maize growing seasons in the North China Plain based on the standardized precipitation evapotranspiration index (SPEI). Results indicated the spatial pattern of winter wheat and summer maize growth seasons is consistent with the distribution of drought and humid conditions. Wang et al. (2022) carried out a hydrological simulation of mountain torrents in small basins caused by rainstorms. The results indicated that the flood process in small watersheds has strong spatial heterogeneity, and there exists intensity changes between flood flow and rainfall.

Ecological and environmental security

The impact of environmental factors on ecologically sustainable development has received widespread attention from scholars. In this issue, five studies focused on the distribution of biological communities affected by environmental factors, the evolution of vegetation spatiotemporal patterns, and the estimation of biomass. Xu et al. analyzed the trend and periodicity of the evolution characteristics of secondary suspended rivers in the lower Yellow River from 1960 to 2021 and quantitatively explored the factors affecting their development. Mai et al. studied the abundance of eukaryotic plankton in the Danjiangkou Reservoir and its relationship with environmental factors. The results showed significant differences in the vertical distribution of eukaryotic plankton community diversity, which were influenced by factors such as pH, water temperature and other factors. Chen et al. used a comprehensive KNDVI dataset and trend analysis to evaluate vegetation restoration activities and changes in vegetation spatiotemporal patterns in mining areas. The results indicated the overall KNDVI of vegetation shows a clear positive trend, with further improvement compared to the years 2000–2010, which is of great significance for the ecological restoration of vegetation in the mining area. He et al. explored the practicality of various remote sensing inversion models for estimating grassland biomass, analyzed the changes in national grassland biomass of the Three Rivers Source on the Tibetan Plateau from 2015 to 2020, predicted future biomass trends, and explored the potential impact of climate change on grassland biomass. Hao et al. analyzed the efficiency of ecotourism in the Yellow River Basin from 2015 to 2019 using a method based on super-slacks-based measurement. The results showed that the four regional development factors of innovation, green, openness, and sharing have a positive impact on the efficiency of ecotourism in the Yellow River Basin. This study is of great significance in managing ecological constraints and improving the quality of sustainable development of regional ecotourism.

Perspectives

The Research Topic is dedicated to applying modern remote sensing techniques, machine learning and numerical simulation models, integrated multidisciplinary theories to monitor natural and engineered slopes and to warn and mitigate associated disaster risks. However, in the context of global climate change and intensified human activities, the in-depth study of slope failure needs further consideration. On this basis, it provides a reference for disaster mitigation from the following aspects. 1) Multi-scale and multidisciplinary integration to analyze the physical mechanism and dynamic process inside the slope; 2) Monitoring and analysis of slope instability based on remote sensing and numerical physical model; 3) Innovative green, efficient and sustainable ecological restoration projects.

Author contributions

HQ: Writing–original draft. WN: Writing–original draft. AA: Writing–review and editing.

Funding

The author(s) declare that financial support was received for the research, authorship, and/or publication of this article. This work

was supported by Jiangxi Provincial Natural ScienceFoundation (No. 20212ACB214005).

Conflict of interest

The authors declare that the research was conducted in the absence of any commercial or financial relationships that could be construed as a potential conflict of interest.

Publisher's note

All claims expressed in this article are solely those of the authors and do not necessarily represent those of their affiliated organizations, or those of the publisher, the editors and the reviewers. Any product that may be evaluated in this article, or claim that may be made by its manufacturer, is not guaranteed or endorsed by the publisher.

References

Liu, Y., Qiu, H., Kamp, U., Wang, N., Wang, J., Huang, C., et al. (2024). Higher temperature sensitivity of retrogressive thaw slump activity in the Arctic compared to the Third Pole. *Sci. Total Environ.* 914, 170007. doi:10.1016/j.scitotenv.2024.170007

Qiu, H., Nie, W., and Asadi, A. (2023). Editorial: monitoring, early warning, and mitigation of natural and engineered slopes — Volume II. *Front. Earth Sci.* 11, 1200777. doi:10.3389/feart.2023.1200777

Qiu, H., Su, L., Tang, B., Yang, D., Ullah, M., Zhu, Y., et al. (2024). The effect of location and geometric properties of landslides caused by rainstorms and earthquakes. *Earth Surf. Process. Landf.* 49, 2067–2079. doi:10.1002/esp.5816

Qiu, H., Zhu, Y., Zhou, W., Sun, H., He, J., and Liu, Z. (2022). Influence of DEM resolution on landslide simulation performance based on the Scoops3D model. *Geomatics, Nat. Hazards Risk* 13 (1), 1663–1681. doi:10.1080/19475705.2022.2097451

Wang, L., Qiu, H., Zhou, W., Zhu, Y., Liu, Z., Ma, S., et al. (2022). The post-failure spatiotemporal deformation of certain translational landslides may follow the pre-failure pattern. *Remote Sens.* 14, 2333. doi:10.3390/rs14102333

Wei, Y., Qiu, H., Liu, Z., Huangfu, W., Zhu, Y., Liu, Y., et al. (2024). Refined and dynamic susceptibility assessment of landslides using InSAR and machine learning models. *Geosci. Front.* 15 (6), 101890. doi:10.1016/j.gsf.2024.101890

Yang, D., Qiu, H., Ye, B., Liu, Y., Zhang, J., and Zhu, Y. (2023). Distribution and recurrence of warming-induced retrogressive thaw slumps on the central qinghai-tibet plateau. *J. Geophys. Res. Earth Surf.* 128 (8), e2022JF007047. doi:10.1029/2022jf007047

Ye, B., Qiu, H., Tang, B., Liu, Y., Liu, Z., Jiang, X., et al. (2024). Creep deformation monitoring of landslides in a reservoir area. *J. Hydrol.* 632, 130905. doi:10.1016/j.jhydrol.2024.130905

Zhou, W., Qiu, H., Wang, L., Pei, Y., Tang, B., Ma, S., et al. (2022). Combining rainfall-induced shallow landslides and subsequent debris flows for hazard chain prediction. *CATENA* 213, 106199. doi:10.1016/j.catena.2022.106199

Zhu, Y., Qiu, H., Yang, D., Liu, Z., Ma, S., Pei, Y., et al. (2021). Pre- and post-failure spatiotemporal evolution of loess landslides: a case study of the jiangou landslide in ledu, China. *Landslides* 18 (10), 3475–3484. doi:10.1007/s10346-021-01714-5

frontiers | Frontiers in Earth Science

TYPE Methods
PUBLISHED 10 August 2023
DOI 10.3389/feart.2023.1253272

OPEN ACCESS

EDITED BY
Haijun Qiu,
Northwest University, China

REVIEWED BY
Chao Chen,
Suzhou University of Science and Technology, China
Pan Cao,
University of Hertfordshire, United Kingdom

*CORRESPONDENCE
Zhiquan Yang,
yzq1983816@kust.edu.cn
Wenfei Xi,
xiwenfei911@163.com

RECEIVED 05 July 2023
ACCEPTED 01 August 2023
PUBLISHED 10 August 2023

CITATION
Liu M, Yang Z, Xi W, Guo J and Yang H (2023), InSAR-based method for deformation monitoring of landslide source area in Baihetan reservoir, China. *Front. Earth Sci.* 11:1253272. doi: 10.3389/feart.2023.1253272

InSAR-based method for deformation monitoring of landslide source area in Baihetan reservoir, China

Meishan Liu[1], Zhiquan Yang[1,2,3]*, Wenfei Xi[2,3,4,5]*, Junqi Guo[4] and Hong Yang[4]

[1]Faculty of Public Safety and Emergency Management, Kunming University of Science and Technology, Kunming, China, [2]Key Laboratory of Geological Disaster Risk Prevention and Control and Emergency Disaster Reduction of Ministry of Emergency Management of the People's Republic of China, Kunming University of Science and Technology, Kunming, China, [3]Key Laboratory of Early Rapid Identification, Prevention and Control of Geological Diseases in Traffic Corridor of High Intensity Earthquake Mountainous Area of Yunnan Province, Kunming, China, [4]Faculty of Geography, Yunnan Normal University, Kunming, China, [5]Yunnan Key Laboratory of Plateau Geographic Processes and Environmental Change, Kunming, China

As a cascading disaster, the surge caused by the reservoir bank landslide seriously affects the stability of the reservoir bank and the dam body. In addition, large-scale hydropower projects are usually built in mountain and canyon areas with active geological structure movement, which provides rich material sources for the occurrence of landslides, so it is of great significance to monitor the deformation in the landslide source area of the reservoir. As science and technology have been leaping forward, a wide variety of high and novel technologies have been proposed, which can be adopted to monitor landslide deformation. It is noteworthy that InSAR is capable of monitoring target monitoring areas all time under all weathers without the need to install any equipment. In this study, the time series deformation of the main landslide source area of the Baihetan reservoir after water storage was determined based on the time series InSAR method. The average annual deformation rate of the landslide source area of the Baihetan reservoir from April 2021 to January 2023 was determined by combining the Sentinel-1 SAR data of 55 ascending tracks and 46 descending tracks. Moreover, the vegetation cover variations from April 2021 to January 2023 in the study area were determined by combining the remote sensing data of Landsat8-9. A total of four typical source areas were selected based on the field investigation to analyze the deformation monitoring results and the vegetation cover variations. As indicated by the results: 1) After water storage, the slope deformation in all source areas was larger in the short term, and the deformation rate of the lower part turned out to be more significant, and the deformation rate exceeded 334.583 mm/year. 2) On the steep slope, the effect of different types of vegetation on restraining deformation was different. The optimal effect was reported in shrubs, followed by grasslands, and the worst effect was reported in woodlands. The results of this study can provide scientific support for the prevention and control of regional geological disasters.

KEYWORDS

SBAS-InSAR, landslide source area, deformation monitoring, vegetation coverage, surface deformation

1 Introduction

In general, large-scale hydropower projects are built in high mountain canyons with developed water systems, which are affected by significant geological tectonic activities. The topography varies violently, and the damage degree of rock mass turns out to be serious (Guo, 2022; Yang et al., 2023a; Yang et al., 2023b), such that abundant material sources are provided for the occurrence of landslide. Moreover, the deformation of the reservoir bank and slope instability will easily occur under the large rise and fall of water level arising from reservoir water regulation (Jiang et al., 2019), as well as the occasional rainstorm (Liu et al., 2023; Yang et al., 2023c), earthquake (Ahmed et al., 2023), and human engineering activities (Hu, 2017). As a cascading disaster, the impact of landslides may be not limited to the landslide while resulting in more serious secondary disasters and further triggering greater losses (Zhu et al., 2021), especially in the reservoir area. When considerable landslide slides into the reservoir, the surge generated by it seriously affects the stability of the bank slope and the dam (Dong et al., 2021). In 1963, a large landslide on the bank of the Vajont dam in Italy caused a surge that destroyed surrounding buildings, flooded the dam, and killed over 2,000 people downstream (Bosa and Petti, 2011). In 2003, the Qianjiangping landslide on the bank of the Three Gorges Reservoir in China created a huge surge and blocked the river to form a barrier lake, killing 14 people and leaving 10 missing (Wen et al., 2008). Accordingly, researching the deformation monitoring of the reservoir landslide source area takes on critical significance.

Deformation monitoring has been confirmed as the most direct and effective method in the process of identifying and quantitatively monitoring landslide disasters (Qiu et al., 2022). It is capable of evaluating the stability of the slope by monitoring the deformation of the slope and indicating its motion state (Li et al., 2021). As revealed by this method, the monitoring methods primarily cover GPS, distributed optical fiber sensing technology, InSAR, and so forth. The GPS monitoring method is capable of providing high-accuracy 3D deformation data for users, whereas the landslide should be investigated in detail, and the monitoring network should be arranged following its integral or local deformation characteristics. Moreover, the GPS monitoring signal exhibits low anti-interference ability in complex environments with high densities, such that the measuring station should be opened (Ren et al., 2020; Wang et al., 2023). The distributed optical fiber sensing technology is capable of achieving real-time automatic remote monitoring, and it exhibits several advantages (e.g., corrosion resistance, electromagnetic resistance, high sensitivity, and high precision). However, it is difficult to ensure that the optical fiber can run normally in the laying and working processes for a long time since it can be easily damaged by shear (Cheng et al., 2022). Compared with the two previously proposed monitoring methods, the InSAR monitoring method can be adopted to conduct all-weather and all-time monitoring of the surface without the need to install any equipment in the target monitoring area, the monitoring coverage is wide, and the monitoring accuracy is as high as the centimeter level to the millimeter scale (Karaca et al., 2021; Yang et al., 2022a; Wang et al., 2022; Ma et al., 2023).

The multitemporal InSAR technology conforms to the conventional D-InSAR technology. The conventional D-InSAR technique refers to a technique employing two SAR images in an identical area at different times to examine ground deformation. However, due to the effect of atmospheric, topographic, temporal, and spatial decorrelation, deformation monitoring achieves a highly limited accuracy when the conventional D-InSAR technology is adopted for long-term micro-deformation monitoring. Thus, the conventional D-InSAR technology can only achieve the deformation monitoring capability of the centimeter scale (Yun et al., 2020). To monitor the slow deformation landslide for a long time and increase the accuracy of deformation monitoring to the millimeter scale, SBAS-InSAR technology has been developed using multiple SAR images in the identical area to acquire interference image pairs with short space-time baselines and then generate interference maps (Emil et al., 2021; Dong et al., 2022). SBAS-InSAR technology was proposed by Berardino et al. (Berardino et al., 2002) and has been investigated for over two decades. The main application of SBAS-InSAR technology is long-term monitoring of slow surface deformation, but if this technology is applied in alpine and canyon areas, geometric distortion will be caused by terrain (Dai et al., 2020). Therefore, it is often necessary to employ different SAR data or combine other techniques to reduce the impact of geometric distortion on the results. SBAS-InSAR technology has been employed in several studies to monitor landslides in the Baihetan reservoir area. Before the reservoir was impounded, Dai, K.R. et al. (Dai et al., 2022) combined the multitemporal InSAR technology and UAV aerial survey to identify hidden trouble points in the reservoir area. Dun, J.W. et al. (Dun et al., 2023) identified active landslides on both banks of the river from Hulukou to Xiangbi Ling section in the Baihetan reservoir area before water storage using the SBAS-InSAR technology and SAR data. Based on the SBAS-InSAR technology, Yang, Z.R. et al. (Yang et al., 2022b) analyzed the effect of water storage factors on the deformation trend of potential landslide in the Baihetan reservoir area using the field survey of unmanned aerial vehicles and the Sentinel-1 SAR data set of ascending and descending tracks.

As the second largest hydropower station in China (Dai et al., 2023), the Baihetan Hydropower Station is located at the junction of Ningnan County in Sichuan Province and Qiaojia County in Yunnan Province. It is situated in the Hengduan Mountain area on the eastern edge of the Qinghai-Tibet Plateau. Since the Baihetan Hydropower Station exhibits a complex geological structure and strong tectonic movement, the rock mass in this area is fractured, the soil is loose (Yang et al., 2023d; Zhao et al., 2023), and the geological disasters occur frequently in this area (Li et al., 2020). The hydropower station will store water in April 2021, and the water level ranges from 765 to 825 m. The stability of the bank slope is destroyed under the effect of large periodic fluctuations of reservoir water and rainfall, such that the safety of the reservoir can be seriously affected (Yang, 2021). Accordingly, based on the SBAS-InSAR technology, the deformation monitoring was performed in the landslide source area of the Baihetan reservoir using Sentinel-1A SAR data of ascending and descending tracks from April 2021 to January 2023. The temporal information of vegetation coverage analyzed by Landsat8-9 remote sensing data and rainfall in the corresponding period was concluded to analyze the deformation of the research area, and technical support can be provided for the relevant departments for disaster prevention and mitigation work.

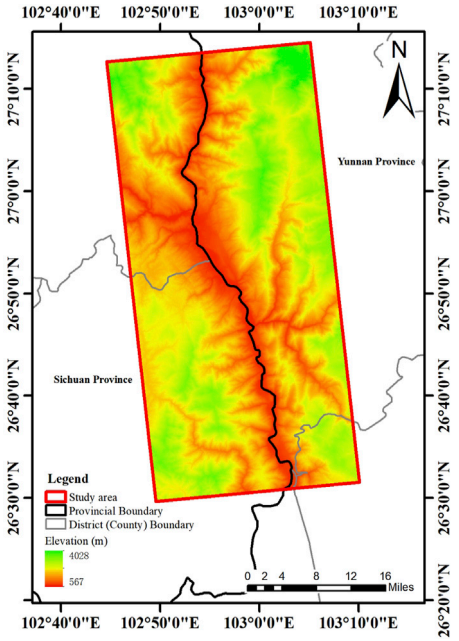

FIGURE 1
Location of the study area.

2 Overview of the study area

In this study, the Baihetan hydropower station reservoir area is selected as the research area. The entire study area exhibits a length of nearly 89.84 km, a width of about 38.30km, and a total area of approximately 3440.87 km^2 (Figure 1). The area is located in the southeast margin of the Qinghai-Tibet Plateau, belonging to the mountain canyon landform. The terrain of the area is high in the northwest and low in the southeast, with the developing geological fault and strong tectonic movement. Due to the effect of climate and topography, this area pertains to a typical dry and hot valley. Furthermore, rainfall is largely concentrated in June-October, which is small in the valley and heavy on both sides of the river, thus triggering considerable hidden hazards (e.g., landslides and other geological hazards in this area) (Zhou, 2018; Dun, 2021).

3 Technical principles

3.1 SBAS-InSAR technology

The basic principle of the SBAS-InSAR technique refers to the generation of high coherence differential interferogram by the image of short space-time baselines. Following the relation between the phase and observation time of highly coherent pixels, the deformation rate of the ground surface and its time series in the study area were determined through singular value decomposition (SVD) (Guo et al., 2019; Feng et al., 2020). The above-mentioned method is capable of reducing the incoherence phenomenon arising from long spatial and temporal baselines to a certain extent and increasing the time sampling rate of deformation monitoring (Bai, 2020). The basic process is expressed as follows:

It was assumed that $N+1$ SAR images in the study area were acquired in chronological order $(t_0, \cdots, t_n)$, one image was selected as the main image, and the other SAR images were registered to this image. The interference pair were combined by an appropriate space-time baseline threshold to generate a M amplitude differential interferogram, where M satisfies the following conditions:

$$\frac{N+1}{2} \le M \le \frac{N(N+1)}{2} \tag{1}$$

For the jth differential interferogram generated from the SAR image generated from the time of the image t_A and the main image t_B ($t_A < t_B$), the interference phase of the pixels having the azimuth coordinate x and the distance coordinate r can be written as:

$$\begin{aligned}\delta\varphi_j(x,r) &= \varphi_B(x,r) - \varphi_A(x,r) \\ &\approx \frac{4\pi}{\lambda}[d(t_B,x,r) - d(t_A,x,r)] + \Delta\varphi_j^{topo}(x,r) \\ &+\Delta\varphi_j^{atm}(t_B,t_A,x,r) + \Delta\varphi_j^{noise}(x,r)\end{aligned} \tag{2}$$

Where $j \in (1, \cdots, M)$; λ denotes radar wavelength; $d(t_B,x,r)$ and $d(t_A,x,r)$ represent the cumulated variables of the radar line-of-sight direction relative to $d(t_0,x,r)=0$ at times t_B and t_A; $\Delta\varphi_j^{topo}(x,r)$ expresses the residual terrain phase in the differential interferogram; $\Delta\varphi_j^{atm}(t_B,t_A,x,r)$ represents atmospheric delay phase; $\Delta\varphi_j^{noise}(x,r)$ denotes decoherence noise.

When the residual terrain phase, atmospheric delay phase, and noise phase were ignored, Eq. 2 was simplified as:

$$\delta\varphi_j(x,r) = \varphi_B(x,r) - \varphi_A(x,r) \approx \frac{4\pi}{\lambda}[d(t_B,x,r) - d(t_A,x,r) \tag{3}$$

To obtain a settlement sequence of physical significance, the phase in Eq. 3 is expressed as the product of the average phase velocity and time between the two acquisition times:

$$v_j = \frac{\varphi_j - \varphi_{j-1}}{t_j - t_{j-1}} \tag{4}$$

The phase value of the jth interferogram is written as:

$$\sum_{k=t_{A,j+1}}^{t_{B,j}} (t_k - t_{k-1})v_k = \delta\varphi_j \tag{5}$$

where the integral of the velocity of the respective period on the time interval of the primary and the slave images, which is written in a matrix form:

$$Bv = \delta\varphi \tag{6}$$

Equation 6 is a matrix. When the matrix B is a full rank or rank deficit, the minimum norm solution of velocity vector can be determined using the SVD method, and the corresponding cumulative topographic variables can be obtained following the integral of velocity in the respective period (Mehrabi, 2020; Xu et al., 2021; Gong et al., 2022).

3.2 Calculation of vegetation coverage

In general, vegetation coverage is obtained by remote sensing or field investigation. Despite the accuracy of the field survey, it is time-consuming and laborious, and it does not apply to obtaining vegetation coverage on a large scale. In contrast, remote sensing

TABLE 1 Sentinel-1A data parameters.

Orbital direction	Imaging mode	Polarization mode	Band	Wavelength/cm	Revisiting Period/d	Time span
ascending	IW	VV	C	5.6	12	2021.04.09-2023.01.29
descending	IW	VV	C	5.6	12	2021.04.11-2023.01.07

TABLE 2 Landsat8-9 data parameters.

Data source	Launch time	Path and row number	Revisiting Period/d	Time span
Landsat 8	2013.02.11	129/40 129/41	16	2021.04.10-2023.01.26
Landsat 9	2021.09.27	129/40 129/41	16	2021.11.18-2023.01.18

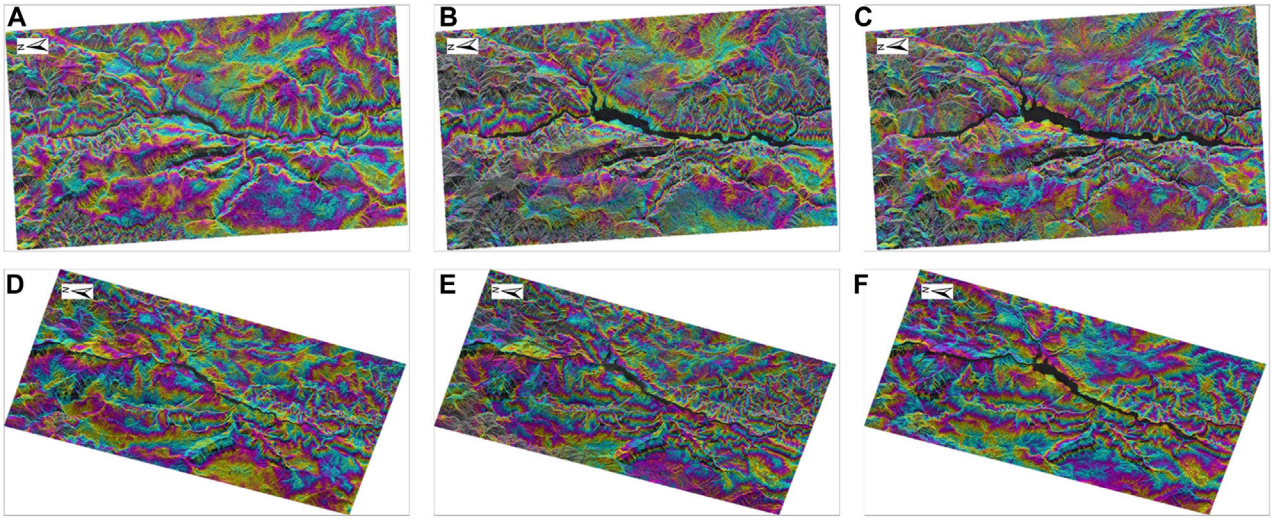

FIGURE 2
Interferogram of study area. **(A)**, **(B)**, and **(C)** are interferograms generated using the ascending track data, and their time spans are 2021.04.21-2021.04.09, 2022.02.15-2022.02.03, and 2022.12.24-2022.11.18, respectively. **(D)**, **(E)**, and **(F)** are interferograms generated using the descending track data, and their time spans are 2021.04.11-2021.04.23, 2022.02.15-2022.02.03, and 2022.12.24-2022.11.18, respectively.

data exhibit high resolution and wide range, applying to the collection of a wide range of vegetation cover information. Besides, it can be employed for large-scale environmental monitoring and assessment. The estimation of vegetation coverage by remote sensing was primarily based on the normalized vegetation index (NDVI) using the pixel binary model. The vegetation index was obtained by processing multi-spectral image data obtained by the remote sensing sensor. Its basic principle is to indicate the growth and coverage of vegetation by the changes in plant chlorophyll absorption and reflectance spectrum. To be specific, NDVI has been confirmed as the most common and classic vegetation index in the remote sensing estimation method of vegetation coverage, which is largely calculated by the ratio of the infrared reflection band to the visible band, as expressed by Equation 12. The basic principles of the pixel binary model are illustrated as follows:

Assuming that all the information of the remote sensing sensor can fall into two parts, i.e., the vegetation information S_v and the vegetation cover information S_s. All information S can be expressed as:

$$S = S_v + S_s \tag{7}$$

It was assumed that the information of vegetation in the pixel (i.e., vegetation coverage) is expressed as FVC, such that the information of no vegetation coverage can be expressed as $1 - FVC$. If S_{veg} represents the maximum vegetation cover area in the pixel, the information S_v presented by the hybrid pixel vegetation section may be expressed as:

$$S_v = FVC \cdot S_{veg} \tag{8}$$

Likewise, if S_{soil} represents the maximum non-vegetated area in the pixel, the remote sensing information S_s determined from the non-vegetated part of the hybrid pixel is expressed as:

$$S_s = (1 - FVC) \cdot S_{soil} \tag{9}$$

Vegetation coverage can be obtained according to the above equation:

$$FVC = (S - S_{veg}) / (S + S_{soil}) \tag{10}$$

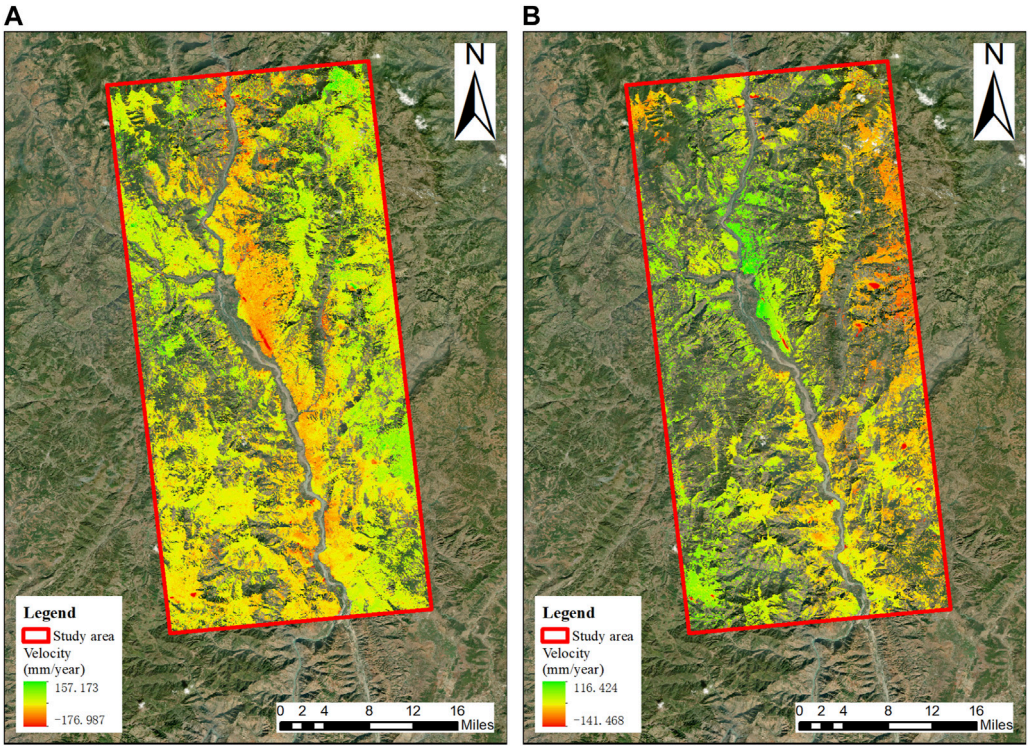

FIGURE 3
Results of LOS direction deformation rate in study area. **(A)** InSAR deformation rate map with ascending Sentinel-1A images from April 2021 to January 2023. **(B)** InSAR deformation rate map with descending Sentinel-1A images from April 2021 to January 2023.

Substitute $NDVI$ to:

$$FVC = (NDVI - NDVI_{veg}) / (NDVI + NDVI_{soil}) \quad (11)$$

$NDVI$ Value Calculation:

$$NDVI = (NIR - R) / (NIR + R) \quad (12)$$

where NIR denotes the reflectance in the near-infrared band; R represents the reflectance in the infrared band (Chen and Lin, 2019; Feng et al., 2023).

4 Experimental data and processing

4.1 Data sources

To conduct a more precise analysis of the deformation trends in the study area after impoundment, we gathered Single Look Complex (SLC) images from the European Space Agency (ESA) spanning from April 2021 to January 2023. The data set includes 55 ascending track and 46 descending track data, as indicated in Table 1. The entire data set covers the time period from the onset of water storage at Baihetan Hydropower Station (April 2021) to the beginning of the study (January 2023). It provides us with the most comprehensive deformation data to enhance the accuracy of InSAR results. To further improve the orbit accuracy of the satellite and remove the effect of the topographic phase, the corresponding Copernicus Sentinel Precise Orbit Ephemerides Data (POD) issued by ESA and the Digital Elevation Model (DEM) with the spatial resolution of ALOS World 3D-30 m issued by Japan Aerospace Exploration Agency (JAXA) were introduced.

Optical image data are obtained from the United States Geological Survey (USGS) free download of 54 views of Landsat 8 and 34 views of Landsat 9. To be specific, Landsat 8 and Landsat 9 achieved an 8-day offset. The data parameters are shown in Table 2.

4.2 Data processing under SBAS-InSAR technology

The image data was processed by SBAS-InSAR technology, the data was imported and cut, the maximum percentage of critical baseline was 5%, and the maximum time baseline was 36 days, and the interference image pairs of ascending track 156 pairs and descending track 122 pairs co-existed. To suppress the speckle noise, the interference workflow was processed by the Minimum Cost Flow deconvolution method and the Goldstein filtering method. After adjusting and eliminating the unideal image pair, the interference graph of the research area was generated, and some ideal interference graph is shown in Figure 2.

The orbit was refined and re-flattened, and the deformation rate and residual topography were estimated through the first inversion. Based on the second inversion, the atmospheric phase was estimated and removed to obtain the final displacement result in a purer time series. Finally, after the sequence

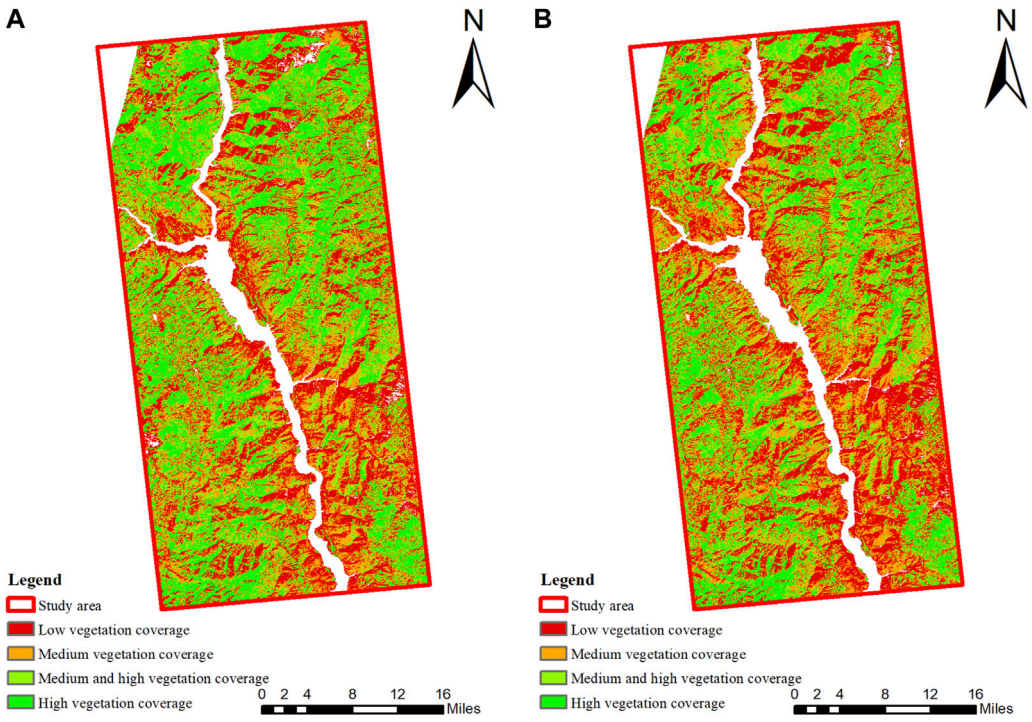

FIGURE 4
Vegetation coverage map of study area. **(A)** is the vegetation coverage in 2021.12.14, and the data is from Landsat 9. **(B)** is the vegetation coverage in 2023.01.10, and the data is from Landsat 8.

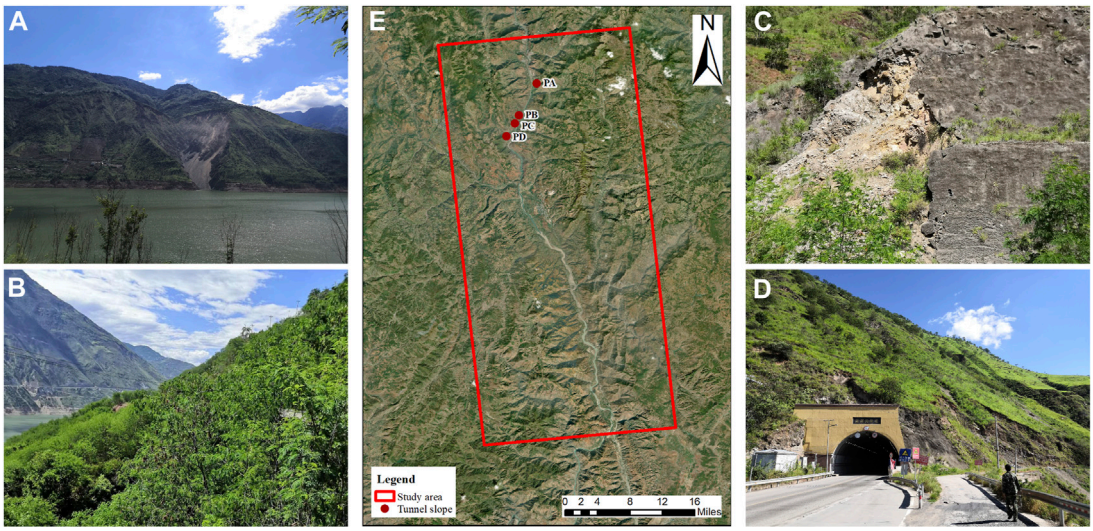

FIGURE 5
Location of typical source areas and results of field investigation. **(A)** is the field investigation of Sunjialiang Tunnel slope. **(B)** is the field investigation of Jiefangcun Tunnel slope. **(C)** is the field investigation of Yingdiliangzi Tunnel slope. **(D)** is the field investigation of Qiluogou Tunnel slope. In **(E)**, PA is the location of Sunjialiang tunnel slope; PB is the location of Jiefangcun tunnel slope; PC is the location of Yingdiliangzi tunnel slope; PD is the location of Qiluogou tunnel slope.

information was geocoded, the result of the deformation of the ascending and descending tracks in the LOS direction from 9 April 2021 to 29 January 2023 in the study area was obtained (Figure 3).

Compared with Figures 3A,B, the deformation information detected by the ascending track data was more abundant and largely concentrated on the east bank of Jinsha River. Its whole deformation rate ranged from −176.987 mm/year to 157.173 mm/

TABLE 3 Basic information of study objects.

Number	Study object	Overview of surface	Substrate vegetation
PA	Sunjialiang Tunnel Slope	soil	sparse grass
PB	Jiefangcun Tunnel Slope	soil	wood
PC	Yingdiliangzi Tunnel Slope	soil	shrub
PD	Qiluogou Tunnel Slope	gravel soil	grass

TABLE 4 Selection results.

Number	Study object	Slope orientation	Satellite local incidence Angle/°	Select results
PA	Sunjialiang Tunnel Slope	west	38.466	descending
PB	Jiefangcun Tunnel Slope	east	38.397	descending
PC	Yingdiliangzi Tunnel Slope	southeast	43.408	ascending
PD	Qiluogou Tunnel Slope	northeast	38.377	descending

year. However, the deformation information detected by the descending track data was less, and the whole deformation rate ranged from −141.468 mm/year to 116.424 mm/year. Since the satellite flies from south to north while collecting the ascending track data, and the opposite is true when collecting the descending track data, the radar line of sight of both was located on the right side, and the research area was located in the high mountain gorge. The high mountain position on both sides of the satellite resulted in serious geometric distortion phenomena (e.g., shadow, overlay and perspective contraction) in the deformation monitoring process of the ground surface using InSAR technology. Therefore, it is necessary to combine the ascending and descending data for analysis in a complementary manner.

4.3 Data processing of vegetation coverage

The data downloaded in this study were corrected by the atmosphere and then calibrated through radiation. The image can be directly mosaic and cut, and NDVI and FVC were calculated. Because the study area is often obscured by clouds, some data that are too heavily obscured by clouds to be useable have been eliminated. The vegetation coverage of the study area is shown in Figure 4. Following the actual situation in the study area, the vegetation coverage in the area fell into four grades, i.e., low vegetation coverage (45%), medium vegetation coverage (45%–60%), medium and high vegetation coverage (60%–75%), as well as high vegetation coverage (75%) (Huang et al., 2023).

5 Results and analysis

5.1 Study object selection

The tunnel slopes located in four typical source areas were selected as the research objects, i.e., Sunjialiang Tunnel Slope, Jiefangcun Tunnel Slope, Yingdiliangzi Tunnel Slope, and Qiluogou Tunnel Slope (Figure 5) through field investigation following the actual situation of the reservoir area of Baihetan Hydropower Station.

Except Qiluogou Tunnel slope is composed of gravel soil landslide, other research objects are soil landslide, and their vegetation conditions are also different. Table 3 lists the basic information of the research objects:

When the satellite was collecting data, if the satellite's local incident angle was smaller than the residual angle of the slope angle, the resolution was further improved, and deformation monitoring was optimal in this area (Zhu et al., 2022). To reduce the geometrical distortion in the scanning and imaging process of the Sentinel satellite and acquire more accurate deformation information of the radar line of sight, different data were selected to analyze the deformation characteristics of the slope according to the different slope orientations of each side, the relationship between the slope and the local incidence angle of the sentinel satellite, and the difference in the flight direction of the satellites collecting the ascending and descending tracks data. The selection results are shown in Table 4.

5.2 Sunjialiang Tunnel

Sunjialiang Tunnel is 2096 m long, and the deformation rate of the side slope is presented in Figure 6A, and the whole deformation rate ranged from −96.755 mm/year to 30.471 mm/year. The optical remote sensing image was observed, and three characteristic points (i.e., PA1, PA2, and PA3) in the range of heart-shaped landslides were selected. To be specific, PA1 was located in the upper part of the slope, i.e., the area with the maximum deformation rate of the landslide. Its average deformation rate was −82.622 mm/year. PA2 was positioned in the middle of the slope, and the average deformation rate reached 4.886 mm/year. PA3 was located in the lower part of the slope with an average deformation rate of 16.583 mm/year. When rainfall varied significantly, the vegetation coverage on the landslide fluctuated less, usually between 0.15 and 0.25 (Figure 6C).

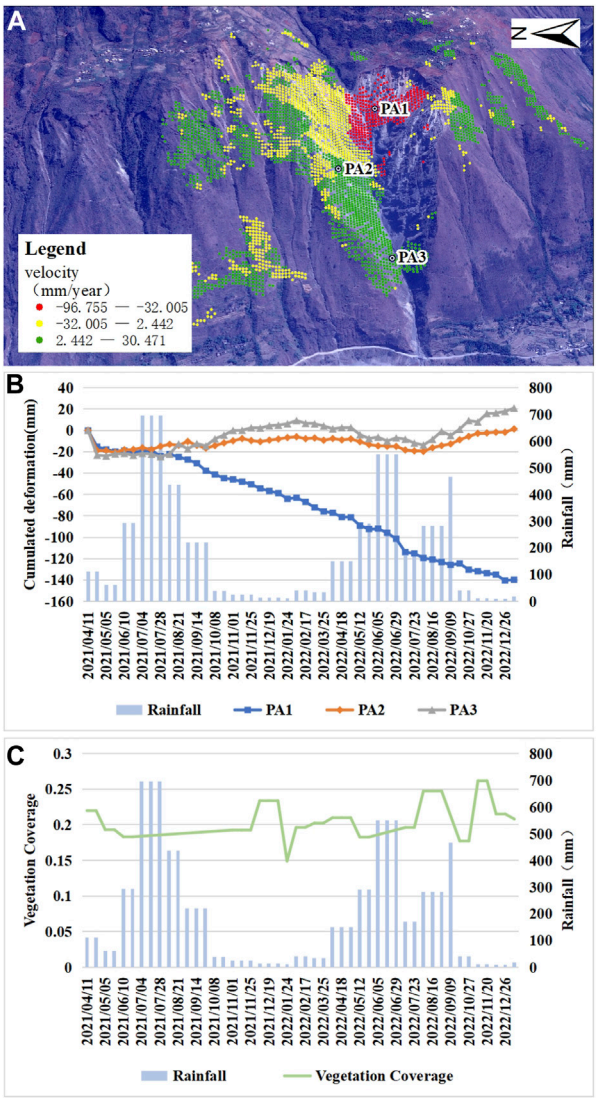

FIGURE 6
Deformation result and vegetation coverage of Sunjialiang tunnel slope. **(A)** is the annual average deformation of Sunjialiang tunnel slope using the descending track data. **(B)** is the time series deformation of selected feature points on Sunjialiang tunnel slope and rainfall from April 2021 to January 2023. **(C)** is the variation of vegetation coverage and rainfall in Sunjialiang tunnel slope from April 2021 to January 2023.

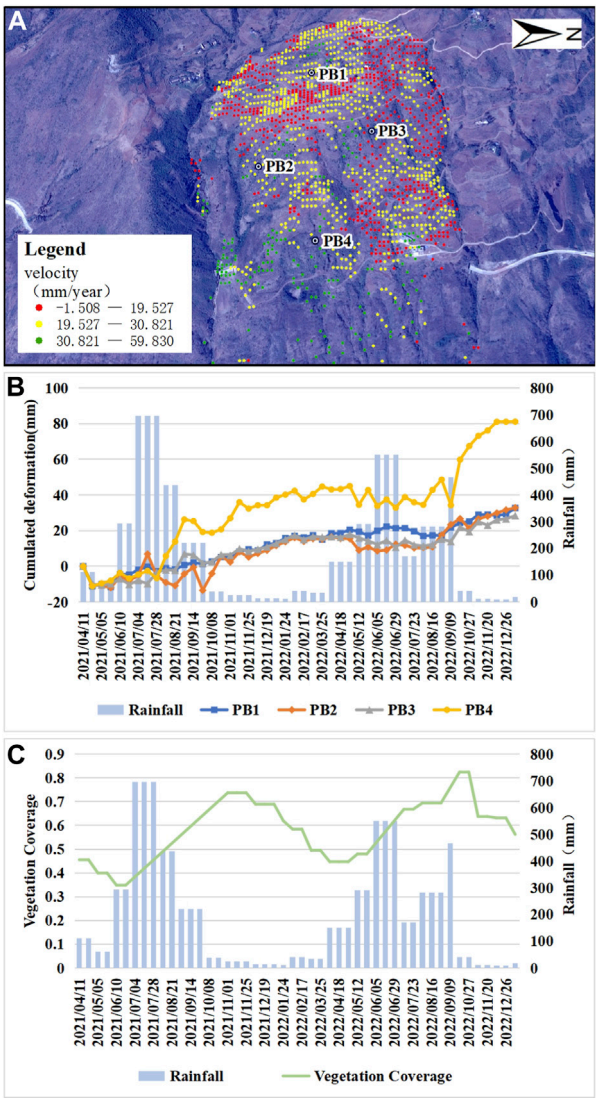

FIGURE 7
Deformation result and vegetation coverage of Jiefangcun tunnel slope. **(A)** is the annual average deformation of Jiefangcun tunnel slope using the descending track data. **(B)** is the time series deformation of selected feature points on Jiefangcun tunnel slope and rainfall from April 2021 to January 2023. **(C)** is the variation of vegetation coverage and rainfall in Jiefangcun tunnel slope from April 2021 to January 2023.

Under the effect of the water impoundment, the three characteristic points all declined significantly in the direction of LOS in April 2021, and then stabilized. Subsequently, under the effect of a rainstorm in July of the same year, PA1 displayed a downward trend in the direction of LOS, while PA2 and PA3 tended to be increased. From February to August 2022, the upper part of the landslide slipped and deposited into the soil mass in the middle and lower part of the landslide, which continued to slip under the action of rainfall and its gravity, and points PA2 and PA3 showed a downward trend in this period. However, because the upper part of the slope was in an unstable sliding state, considerable soil accumulated in the middle and lower part of the slope.

5.3 Jiefangcun Tunnel

Jiefangcun Tunnel is 766 m long, the deformation rate of the side slope is presented in Figure 7A, and the whole deformation rate ranges from −1.508 mm/year to 59.830 mm/year. The area was divided into four parts along the topographic direction, and feature point PB1 was selected from the upper part, feature point PB2 was selected from the middle south, feature point PB3 was selected from the middle north and feature point PB4 was selected from the lower part. As depicted in Figure 7B, the trends of PB1, PB2, and PB3 were consistent, and PB4 point shape variable was the most obvious among the four characteristic points, up to

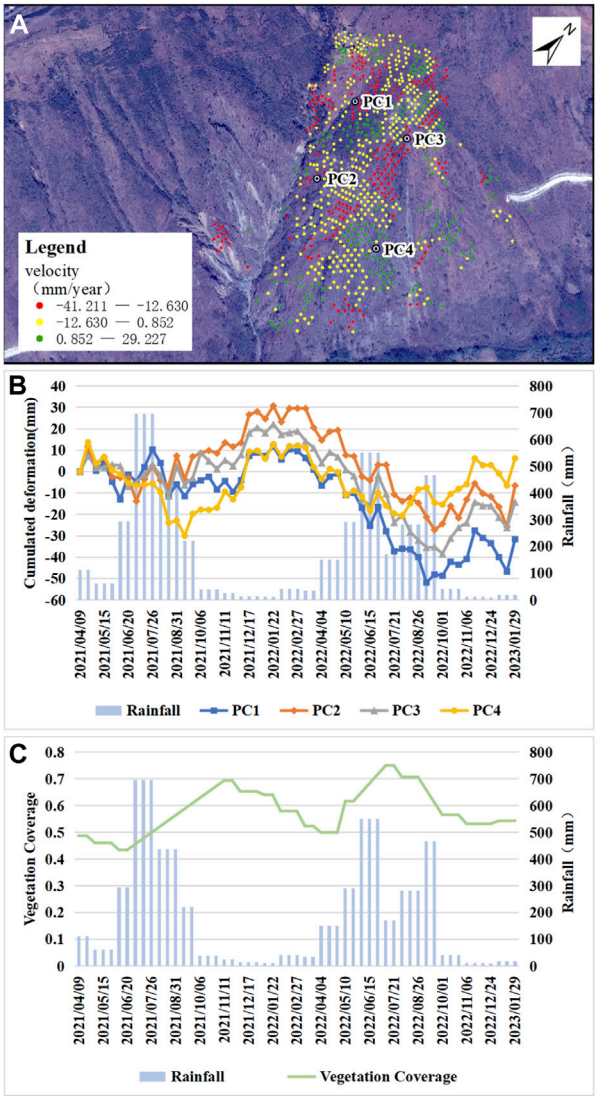

FIGURE 8
Deformation result and vegetation coverage of Yingdiliangzi tunnel slope. **(A)** is the annual average deformation of Yingdiliangzi tunnel slope using the descending track data. **(B)** is the time series deformation of selected feature points on Yingdiliangzi tunnel slope and rainfall from April 2021 to January 2023. **(C)** is the variation of vegetation coverage and rainfall in Yingdiliangzi tunnel slope from April 2021 to January 2023.

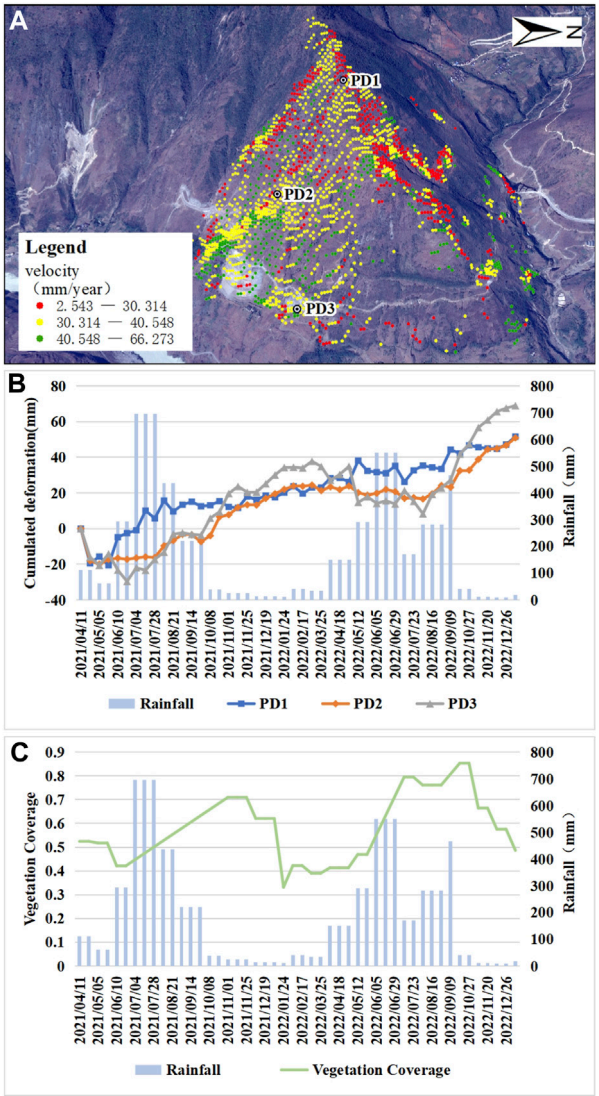

FIGURE 9
Deformation result and vegetation coverage of Qiluogou tunnel slope. **(A)** is the annual average deformation of Qiluogou tunnel slope using the descending track data. **(B)** is the time series deformation of selected feature points on Qiluogou tunnel slope and rainfall from April 2021 to January 2023. **(C)** is the variation of vegetation coverage and rainfall in Qiluogou tunnel slope from April 2021 to January 2023.

81.142 mm. As depicted in Figure 7C, the change of vegetation cover in this area was positively correlated with rainfall.

Field investigation suggested that the slope of the upper part of the slope was slow, covered with dense woodland, and the vegetation coverage was relatively high, such that it can effectively intercept rainwater and reduce the impact of rainfall on the slope, thus effectively inhibiting the deformation of the slope. In addition, the root system of the woodland was well developed, which can effectively fix soil and further enhance the stability of slope. In contrast, although the woodland has a certain deformation-inhibiting effect, the slope of the lower slope was steep, and the vegetation coverage was high, which resulted in the lower dead weight, and the slope deformation turned out to be more obvious.

5.4 Yingdiliangzi Tunnel

Yingdiliangzi tunnel is 1144 m in length, and the deformation rate of the side slope is shown in Figure 8A, and the whole deformation rate ranges from −41.211 mm/year to 29.227 mm/year. The deformation information of the northeast side slope in this area is too little, and most of the deformation information is mainly concentrated on the south side slope. The southward slope in this area was further subdivided into southwest slope and southeast slope, the characteristic point PC1 was selected from the upper part of the southwest slope, and the characteristic point PC2 was selected from the lower part. The characteristic point PC3 was selected from the upper part of

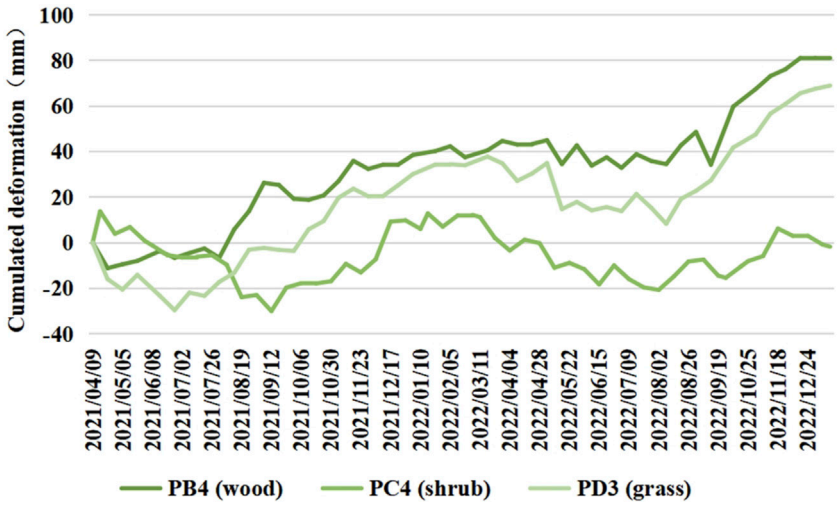

FIGURE 10
Time series deformation of lower slope under different vegetation coverage from April 2021 to January 2023. PB4 is located in the lower part of the Jiefangcun tunnel slope, which is covered by woodland. PC4 is located in the lower part of the Yingdiliangzi tunnel slope, which is covered by shrubs. PD4 is located in the lower part of the Qiluogou tunnel slope, which is covered by grassland.

the southeast slope, and the characteristic point PC4 was selected from the lower part. To be specific, the average deformation rates of the characteristic points PC1, PC2, PC3, and PC4 reached −27.881 mm/year, −12.399 mm/year, −18.371 mm/year, and −0.632 mm/year, respectively. There is a positive correlation between vegetation coverage and rainfall in this region (Figure 8C).

As indicated by the time series deformation of characteristic points, the variation trend of the above-mentioned four points was nearly identical, and the variation of shape variable showed a correlation with the variation of rainfall. During the rainy season, because of the increase in rainfall, the soil was loosened and flowing due to water infiltration, thus the deformation of the slope displayed a downward trend. On the contrary, during the dry season, the moisture was absent, and the deformation of the slope displayed an upward trend. Moreover, the upper deformation variable of the two-way slope was larger, and the whole slope was in a sliding state. Furthermore, as indicated by the result of the field investigation, PC2 point was in the area of the landslide trace, and the soil body near PC1 point and its upper part was accumulated at the upper edge of the landslide trace.

5.5 Qiluogou Tunnel

The total length of Qiluogou tunnel is 1582m, and the deformation rate of the side slope is shown in Figure 9A, and the whole deformation rate ranges from 2.543 mm/year to 66.273 mm/year. The area is divided into southeast side slope, east side slope and north side slope according to the slope direction. Since the slope of the east side slope is steep, the deformation information on the east side slope was less, while the north side slope is far from the Jinsha River. Therefore, the characteristic point PD1 was selected on the ridge of this area, the characteristic point is PD2 in the middle of the southeast slope and PD3 in the lower part of the southeast slope. The average deformation rates of PD1 and PD2 approximately reached 32.859 mm/year and 34.634 mm/year, respectively. Figure 9C shows that there was a positive correlation between vegetation coverage and rainfall.

As indicated by the time series deformation of characteristic points, the deformation trend of PD1, PD2 and PD3 points was consistent, and the whole trend of uplift arose after settling due to water storage. However, the deformation of the respective point is different. The closer it is to the lower characteristic point, the more susceptible the deformation will be to the rainy season. When rainfall was increased, the lower part displayed a downward trend compared with the middle and upper parts. When rainfall declined, the lower part showed a rising trend compared with the middle and upper parts. In addition, the area was covered by grassland. Although the vegetation coverage was high, slope deformation cannot be effectively restrained due to steep slope and underdeveloped root system, such that the slope deformation turned out to be more significant.

6 Discussion

SBAS-InSAR technology has been proved to be a valuable method for monitoring landslide deformation (Yang et al., 2022a; Dai et al., 2022; Dun et al., 2023; Guo et al., 2023), which can effectively monitor surface deformation and reveal the spatial distribution of landslide source area. The comparison with several papers (Yang et al., 2022b; Guo et al., 2023) shows that the deformation trend in the reservoir area of Baihetan Hydropower Station is consistent in the same time period and within the same research scope, which effectively supplements the deformation monitoring in the reservoir area of Baihetan Hydropower Station. In addition, the influence of rainfall and vegetation on slope stability is discussed by combining the

rainfall and vegetation coverage and the deformation trend of four typical landslide source areas.

Rainfall is one of the important factors affecting the stability of bank slope. When the rainy season comes, considerable rain will penetrate the soil, increasing the saturation degree of the soil, such that the internal pressure of the soil is increased. If the saturation degree of the soil exceeds a certain degree, it will cause the liquefaction or flow of the soil, which will lead to the destruction of the bank slope. In addition, rainfall may also cause surface erosion and erosion of the bank slope of the reservoir, and aggravate the stability of the slope.

The effect of different vegetation on restraining slope deformation is different. To explore this difference, we selected the time series deformation data of B4 points at the lower part of the Jiefangcun tunnel slope, C4 points at the lower part of the Yingdiliangzi tunnel slope, and D4 points at the lower part of the Qiluogou tunnel slope for comparative analysis (Figure 10). It can be seen from Figure 10 that C4 has the smallest deformation and B4 has the largest deformation. This indicates that shrub vegetation has the best effect on restraining slope deformation, followed by grassland, while woodland has the worst effect and may even promote slope deformation. The root system of the shrub is more developed than that of grassland, which can effectively restrain the deformation of slope. Although the root system of forest land is developed, its own weight is larger, which increases the own weight of slope, but promotes the occurrence of slope deformation.

7 Conclusion

In this study, the deformation results of the study area from 9 April 2021 to 29 January 2023 were obtained using SBAS-InSAR technology and Sentinel-1 SAR data of the ascending and descending tracks. The vegetation coverage in the study area was extracted using Landsat8-9 remote sensing data. The deformation characteristics of four typical source areas were analyzed by combining rainfall data. The following conclusions were obtained.

(1) The deformation rate of four typical source areas in the LOS direction ranged from −96.755 mm/year to 66.273 mm/year. Since the reservoir began to fill in April 2021, the slope of the respective source area had a large deformation in a short period, especially the lower part of the slope turned out to be more significant, and the deformation rate exceeded 334.583 mm/year.

(2) Except for the slope of the Sunjialiang tunnel, the change trend of vegetation coverage in the other three typical source areas was similar, and all showed a positive correlation with rainfall. The lower slope of these three typical source areas was steep. As indicated by the result of the comparative analysis, the restraining effect of different types of vegetation on slope deformation was different. Compared with grassland, the root system of shrubs was developed, such that the inhibition effect on the slope deformation was optimal. Although the woodland has a developed root system and good rainfall interception effect, it exerts the worst inhibition effect on slope deformation for its relatively large dead weight.

Data availability statement

The raw data supporting the conclusion of this article will be made available by the authors, without undue reservation.

Author contributions

ZY and WX developed the idea for the manuscript. HY processed optical remote sensing data. ML processed the SBASInSAR data and wrote the manuscript. WX, JG, and ML surveyed the area. All authors contributed to the article and approved the submitted version.

Funding

This research was funded by the National Natural Science Foundation of China (Grant No. 41861134008), Muhammad Asif Khan academician workstation of Yunnan Province (Grant No. 202105AF150076), Key R&D Program of Yunnan Province (Grant No. 202003APC100002), General Program of basic research plan of Yunnan Province (Grant No. 202001AT070059), Major scientific and technological projects of Yunnan Province:Research on Key Technologies of ecological environment monitoring and intelligent management of natural resources in Yunnan (No: 202202AD080010), and “Study on High-Level Hidden Landslide Identification Based on Multi-Source Data” of Key Laboratory of Early Rapid Identification, Prevention and Control of Geological Diseases in Traffic Corridor of High Intensity Earthquake Mountainous Area of Yunnan Province (KLGDTC-2021-02).

Acknowledgments

We would like to thank Japan Aerospace Exploration Agency (JAXA), European Space Agency (ESA) and United States Geological Survey (USGS) for providing the ALOS World 3D-30m DEM, Sentinel-1A datasets, orbit ephemerides data and optical image data, respectively.

Conflict of interest

The authors declare that the research was conducted in the absence of any commercial or financial relationships that could be construed as a potential conflict of interest.

Publisher’s note

References

Ahmed, M. F., Sher, F., and Mehmood, E. (2023). Evaluation of landslide hazards potential at Dasu dam site and its reservoir area. *Environ. Earth Sci.* 82 (7), 183. doi:10.1007/s12665-023-10789-3

Bai, Y. P. (2020).Analysis of surface deformation feature and early identification of potential landslides in the middle reaches of Bailong River based on SBAS-InSAR technology M. D. thesis. Lanzhou, China: Lanzhou University. doi:10.27204/d.cnki.glzhu.2020.000212

Berardino, P., Fornaro, G., Lanari, R., and Sansosti, E. (2002). A new algorithm for surface deformation monitoring based on small baseline differential SAR interferograms. *IEEE Trans. Geoscience Remote Sens.* 40 (11), 2375–2383. doi:10.1109/TGRS.2002.803792

Bosa, S., and Petti, M. (2011). Shallow water numerical model of the wave generated by the Vajont landslide. *Environ. Model. Softw.* 26 (4), 406–418. doi:10.1016/j.envsoft.2010.10.001

Chen, C. Y., and Lin, C. L. (2019). Applications of UAS-obtained thermal images for vegetation coverage ratio monitoring of mudstone areas. *IOP Conf. Ser. Mater. Sci. Eng.* 652, 012062. doi:10.1088/1757-899X/652/1/012062

Cheng, G., Wang, Z. X., Zhu, H. H., Li, D. Y., and Ma, Q. (2022). Research review of rock and soil deformation monitoring based on distributed fiber optic sensing. *Laser & Optoelectron. Prog.* 59 (19), 51–70. doi:10.3788/LOP202259.1900004

Dai, K. R., Tie, Y. B., Xu, Q., Feng, Y., Zhuo, G. C., Shi, X. L., et al. (2020). Early identification of potential landslide Geohazards in alpine-canyon terrain based on SAR interferometry-a case study of the middle section of yalong river. *J. Radars* 9 (3), 554–568. doi:10.12000/JR20012

Dai, K. R., Shen, Y., Wu, M. T., Feng, W. K., Dong, X. J., Zhuo, G. C., et al. (2022). Identification of potential landslides in Baihetan Dam area before the impoundment by combining InSAR and UAV survey. *Acta Geodetica Cartogr. Sinica* 51 (10), 2069–2082. doi:10.11947/j.AGCS.2022.20220305

Dai, K. R., Wu, M. T., Zhuo, G. C., Ju, A. H., Wen, N. L., Feng, W. K., et al. (2023). Review on InSAR early Identification and monitoring of reservoirandslides for large hydropower engineering projects in southwest mountainous area of China. *J. Earth Sci. Environ.* 45 (3), 559–577. doi:10.19814/j.jese.2022.12080

Dong, J. J., Mei, Y., Li, X., Liu, S. Y., and Yan, B. (2022). SBAS-InSAR monitoring of slope safety and stability of high altitude dumps. *China Saf. Sci. J.* 32 (1), 92–101. doi:10.16265/j.cnki.issn1003-3033.2022.01.013

Dong, K., Li, Z. F., Lu, X., Chen, C., Sheng, J. B., Chen, J. K., et al. (2021). Analysis of dam overtopping failure risks caused by landslide-induced surges considering spatial variability of material parameters. *Front. Earth Sci.* 9. doi:10.3389/FEART.2021.675900

Dun, J. W. (2021).Early identification and deformation monitoring of active landslides before water storage in Baihetan reservoir area by InSAR M. D. thesis. Chengdu, China: Chengdu University of Technology. doi:10.26986/d.cnki.gcdlc.2021.000718

Dun, J. W., Feng, W. K., Yi, X. Y., Zhang, G. Q., and Wu, M. T. (2023). Early InSAR identification of active landslide before impoundment in baihetan reservoir area—A case study of Hulukou town xiangbiling section. *J. Eng. Geol.* 31 (2), 479–492. doi:10.13544/j.cnki.jeg.2022-0016

Emil, M. K., Sultan, M., Alakhras, K., Sataer, G., Gozi, S., AlMarri, M., et al. (2021). Countrywide monitoring of ground deformation using InSAR time series: a case study from Qatar. *Remote Sens.* 13 (4), 702. doi:10.3390/rs13040702

Feng, P. F., Jia, F. X., and Chen, M. (2023). Analysis of correlation between vegetation coverage and topographic factors based on Landsat remote sensing image in Weichang county. *Water Resour. Plan. Des.* 233 (3), 111–116. doi:10.3969/j.issn.1672-2469.2023.03.023

Feng, W. K., Dun, J. W., Yi, X. Y., and Zhang, G. Q. (2020). Deformation analysis of Woda village old landslide in Jinsha river basin using SBAS-InSAR technology. *J. Eng. Geol.* 28 (2), 384–393. doi:10.13544/j.cnki.jeg.2019-411

Gong, Y. F., Wang, H., Wu, X. H., Zhang, J., and Liu, J. (2022). Identification of potential landslide hazards using time-series InSAR in xiji county of ningxia. *Saf. Environ. Eng.* 29 (6), 114–121. doi:10.13578/j.cnki.issn.1671-1556.20211490

Guo, J. Q., Xi, W. F., Shi, Z. T., Yang, Z. Q., and Yang, Z. R. (2023). Study on deformation monitoring of typical tunnel slope in baihetan reservoir area under SBAS-InSAR technology. *J. Guizhou Univ.* 40 (4), 48–55. doi:10.15958/j.cnki.gdxbzrb.2023.04.07

Guo, J. (2022).Research on formation and transformation mechanism of landslide-induced debris flow disaster chain Ph. D. thesis. Xian, China: Chang'an University. doi:10.26976/d.cnki.gchau.2022.000934

Guo, R., Li, S. M., Chen, Y. N., and Yuan, L. W. (2019). A method based on SBASInSAR for comprehensive identification of potential goaf landslide. *J. Geo-Information Sci.* 21 (7), 1109–1120. doi:10.12082/dqxxkx.2019.180630

Hu, Y. P. (2017).Study on the influence of bank collapse on qiaomeng highway in the area of baihetan reservoir M. D. thesis. Chengdu University of Technology. Chengdu, China.

Huang, L. Y., Yang, Y. L., Gao, P., Yan, X. R., You, J. Y., Zhang, H., et al. (2023). Temporal and spatial variation of vegetation coverage and its topographical differentiation in the upstream of minjiang river with Landsat remote sensing image. *J. North-East For. Univ.* 51 (1), 54–60. doi:10.13759/j.cnki.dlxb.2023.01.005

Jiang, Q. Q., Jiao, Y. Y., Song, L., Wang, H., and Xie, B. T. (2019). Experimental study on reservoir landslide under rainfall and water-level fluctuation. *Rock Soil Mech.* 40 (11), 4361–4370. doi:10.16285/j.rsm.2018.1617

Karaca, S. O., Abir, I. A., Khan, S. D., Ozsayın, E., and Qureshi, K. A. (2021). Neotectonics of the western suleiman fold belt, Pakistan: evidence for bookshelf faulting. *Remote Sens.* 13 (18), 3593. doi:10.3390/rs13183593

Li, B., Zhang, Q., Wang, W. P., Zhao, Q. S., Wang, C. H., He, K., et al. (2020). Geohazard monitoring and risk management of high-steep slope in the Wudongde dam area. *J. Geomechanics* 26 (4), 556–564. doi:10.12090/j.issn.1006-6616.2020.26.04.048

Li, X. A., Zhou, L., Su, F. Z., Wu, W. Z., et al. (2021). Application of InSAR technology in landslide hazard:Progress and prospects. *J. Remote Sens.* 25 (2), 614–629. doi:10.11834/jrs.20209297

Liu, Z. Q., Yang, Z. Q., Chen, M., Xu, H. H., Yang, Y., Zhang, J., et al. (2023). Research hotspots and Frontiers of mountain flood disaster: bibliometric and visual analysis. *Water* 15 (4), 673. doi:10.3390/w15040673

Ma, S. Y., Qiu, H. J., Zhu, Y. R., Yang, D. D., Tang, B. Z., Wang, D. Z., et al. (2023). Topographic changes, surface deformation and movement process before, during and after a rotational landslide. *Remote Sens.* 15 (3), 662. doi:10.3390/rs15030662

Mehrabi, A. (2020). Monitoring the Iran Pol-e-Dokhtar flood extent and detecting its induced ground displacement using sentinel 1 imagery techniques. *Nat. Hazards* 105 (3), 2603–2617. doi:10.1007/s11069-020-04414-w

Qiu, H. J., Zhu, Y. R., Zhou, W. Q., Sun, H. S., He, J. Y., and Liu, Z. J. (2022). Influence of DEM resolution on landslide simulation performance based on the Scoops3D model. *Nat. Hazards Risk* 13 (1), 1663–1681. doi:10.1080/19475705.2022.2097451

Ren, K. Y., Yao, X., Zhao, X. M., and Li, L. J. (2020). Study of landslide failure prediction based on TS-InSAR, GPS and image offset monitoring. *Chin. J. Rock Mech. Eng.* 39 (S2), 3421–3431. doi:10.13722/j.cnki.jrme.2019.1095

Wang, L., Xu, H., Shu, B., Li, X. R., Tian, Y. Q., You, J., et al. (2023). The pattern of alternative splicing and DNA methylation alteration and their interaction in linseed (Linum usitatissimum L) response to repeated drought stresses. *Navigation Position. Timing* 10 (1), 12–26. doi:10.1186/s40659-023-00424-7

Wang, L. Y., Qiu, H. J., Zhou, W. Q., Zhu, Y. R., Liu, Z. J., Ma, S. Y., et al. (2022). The post-failure spatiotemporal deformation of certain translational landslides may follow the pre-failure pattern. *Remote Sens.* 14 (10), 2333. doi:10.3390/rs14102333

Wen, B. P., Shen, J., and Tan, J. M. (2008). The influence of water on the occurrence of Qianjiangping landslide. *Hydrogeology Eng. Geol.* 35 (3), 12–18. doi:10.16030/j.cnki.issn.1000-3665.2008.03.016

Xu, Q., Pu, C. H., Zhao, K. Y., He, P., Zhang, H. Y., and Liu, J. L. (2021). Time series InSAR monitoring and analysis of spatiotemporal evolution characteristics of land subsidence in yanan new district. *Geomatics Inf. Sci. Wuhan Univ.* 46 (07), 957–969. doi:10.13203/j.whugis20200146

Yang, J. (2021).Study on the stability of gravel-soil bank slope of Xiaojiang Bridge in Baihetan Reservoir Area under reservoir water fluctuation M. D. thesis. Chengdu University of Technology. Chengdu, China. doi:10.26986/d.cnki.gcdlc.2021.001033

Yang, Z. Q., Chen, M., Zhang, J., Ding, P., He, N., and Yang, Y. (2023a). Effect of initial water content on soil failure mechanism of loess mudflow disasters. *Front. Ecol. Evol.* 11, 1141155. doi:10.3389/fevo.2023.1141155

Yang, Z. Q., Wei, L., Liu, Y. Q., He, N., Zhang, J., and Xu, H. H. (2023b). Discussion on the relationship between debris flow provenance particle characteristics, gully slope, and debris flow types along the karakoram highway. *Sustainability* 15, 5998. doi:10.3390/su15075998

Yang, Z. Q., Xiong, J. F., Zhao, X. G., Meng, X. R., Wang, S. B., Li, R., et al. (2023c). Column-hemispherical penetration grouting mechanism for Newtonian fluid considering the tortuosity of porous media. *Processes* 11 (6), 1737. doi:10.3390/pr11061737

Yang, Z. Q., Zhao, X. G., Chen, M., Zhang, J., Yang, Y., Chen, W. T., et al. (2023d). Characteristics, dynamic analyses and hazard assessment of debris flows in

niumiangou valley of wenchuan county. *Appl. Sci.* 13 (2), 1161. doi:10.3390/app13021161

Yang, Z. R., Xi, W. F., Shi, Z. T., Xiao, B., and Zhou, D. Y. (2022a). Deformation analysis in the bank slopes in the reservoir area of Baihetan Hydropower Station based on SBAS-InSAR technology. *Chin. J. Geol. Hazard Control* 33 (05), 83–92. doi:10.16031/j.cnki.issn.1003-8035.202202056

Yang, Z. R., Xi, W. F., Yang, Z. Q., Shi, Z. T., and Qian, T. H. (2022b). Monitoring and prediction of glacier deformation in the meili snow mountain based on InSAR technology and GA-BP neural network algorithm. *Sensors* 22 (21), 8350. doi:10.3390/s22218350

Yun, Y., Lu, X. L., Fu, X. K., and Xue, F. Y. (2020). Application of spaceborne interferometric synthetic aperture radar to geohazard monitoring. *J. Radars* 9 (01), 73–85. doi:10.12000/JR20007

Zhao, X. G., Yang, Z., Meng, X. R., Wang, S. B., Li, R., Xu, H. H., et al. (2023). Study on mechanism and verification of columnar penetration grouting of time-varying Newtonian fluids. *Processes* 11 (4), 1151. doi:10.3390/pr11041151

Zhou, Z. K. (2018).Study of geo-hazards investigation for baihetan reservoir bank by InSAR technology M. D. thesis. Beijing, China: Chinese Academy of Geological Sciences. doi:10.27744/d.cnki.gzgdk.2018.000006

Zhu, J. J., Hu, J., Li, Z. W., Sun, Q., and Zheng, W. J. (2022). Recent progress in landslide monitoring with InSAR. *Acta Geodetica Cartogr. Sinica* 51 (10), 2001–2019. doi:10.11947/j.agcs.2022.20220294

Zhu, Y., Peng, M., Cai, S., and Zhang, L. M. (2021). Risk-based warning decision making of cascade breaching of the tangjiashan landslide dam and two smaller downstream landslide dams. *Front. Earth Sci.* 9. doi:10.3389/FEART.2021.648919

frontiers | Frontiers in Ecology and Evolution

TYPE Original Research
PUBLISHED 23 August 2023
DOI 10.3389/fevo.2023.1264936

OPEN ACCESS

EDITED BY
Haijun Qiu,
Northwest University, China

REVIEWED BY
Kang Liao,
China University of Geosciences Wuhan, China
Zongxing Zou,
China University of Geosciences Wuhan, China

*CORRESPONDENCE
Zhenwei Dai
daizhenwei@mail.cgs.gov.cn

RECEIVED 21 July 2023
ACCEPTED 04 August 2023
PUBLISHED 23 August 2023

CITATION
Zhang A, Dai Z, Qin W, Fu X, Gao J, Guo L, Liu L, Jiang X and Wang H (2023) Risk assessment of the Xigou debris flow in the Three Gorges Reservoir Area. *Front. Ecol. Evol.* 11:1264936. doi: 10.3389/fevo.2023.1264936

Risk assessment of the Xigou debris flow in the Three Gorges Reservoir Area

Anle Zhang[1,2], Zhenwei Dai[1]*, Weibing Qin[3], Xiaolin Fu[1], Jingxuan Gao[4,5], Lianjun Guo[6], Liang Liu[6,7], Xiannian Jiang[8] and Heng Wang[8]

[1]Wuhan Center, China Geological Survey (Geosciences Innovation Center of Central South China), Wuhan, Hubei, China, [2]College of Civil Engineering & Architecture, China Three Gorges University, Yichang, Hubei, China, [3]River Basin Hub Operation Management Center, China Three Gorges Corporation, Yichang, Hubei, China, [4]College of Geological Engineering and Geomatics, Chang'an University, Xi'an, China, [5]China Institute of Geological Environment Monitoring, Beijing, China, [6]The Eighth Geological Brigade, Hebei Bureau of Geology and Mineral Resources Exploration, Qinhuangdao, China, [7]School of Earth Sciences and Engineering, Nanjing university, Nanjing, China, [8]No. 208 Hydrogeology and Engineering Geology Team of Chongqing Bureau of Geology and Minerals Exploration, Chongqing, China

On June 18, 2018, under the influence of heavy rainfall, a debris flow disaster broke out in Xigou village of the Three Gorges Reservoir Area in Chongqing, causing some residential houses to be buried along with great economic losses. The on-site investigation found many loose solid material sources in the debris flow gully. Under the conditions of heavy rainfall, debris flows are prone to occur again, which would seriously threaten the lives and property of nearby residents. In this paper, taking the Xigou debris flow as a research case, numerical simulation by rapid mass movements simulation (RAMMS) is used to invert the movement process of the 2018 debris flow event; the dynamic calculation parameters of the Xigou debris flow event are obtained; a quantitative hazard prediction of debris flows with different recurrence intervals (30, 50, and 100 years) is carried out in the study area; and risk assessment is conducted based on the vulnerability characteristics of the disaster-bearing bodies in the study area. The results show that the maximum accumulation thickness of debris flow in the 30-year, 50-year, and 100-year recurrence intervals is 6.54 m, 10.18 m, and 10.00 m, respectively, and the debris flow in the 100-year recurrence interval has the widest influence range and greatest hazard. The low-, medium-, and high-risk areas account for 75%, 23%, and 2%, respectively. The high-risk area mainly includes some buildings near the #1 and #2 gullies. This study provides support for the prevention and control of potential debris flow disasters in Xigou village and a scientific basis for disaster prevention and mitigation in the Three Gorges Reservoir area.

KEYWORDS

Three Gorges Reservoir Area, debris flow, RAMMS, analysis of movement characteristics, risk assessment

1 Introduction

Debris flow is a common geological disaster in the mountainous areas of Southwest China. Characterized by high speed, suddenness, and high energy, it often causes serious economic losses and casualties (Yu et al., 2010; Tang et al., 2012; Zou et al., 2020; Qin et al., 2022; Dai et al., 2023a; Dai et al., 2023b). The Three Gorges Reservoir area has large undulating topography, complex strata and lithology, intense geological tectonic activities, frequent extreme rainfall events, and intense human activities (engineering constructions) (Yin et al., 2020; Zou et al., 2023), which have created favorable conditions for debris flows in the area. The population of the Three Gorges Reservoir area has grown more concentrated after the area's resettlement project. After a debris flow occurs in a resettlement area, it could cause huge losses of life and property (Wang et al., 2018; Zhang et al., 2019; Guo et al., 2020; Zhang et al., 2021; Qiu et al., 2022; Zhang et al., 2022; Dai et al., 2023c; Pei et al., 2023). Many mountain towns in China are located on the joint alluvial fans of multiple and adjacent past debris flows (Cui et al., 2013). During heavy rainfall, multiple debris flows can easily break out at the same time, leading to disasters of various forms. In addition to direct dynamic impact destruction, debris accumulation, and subsequent damage induced by lifeline destruction and chain-reaction disasters that occur due to river blockages. Therefore, it is urgent to clarify the movement process of debris flows and evaluate the hazard and risk areas for the prevention of debris flow disasters in the Three Gorges Reservoir area.

Debris flow disaster risk refers to the likelihood of loss of human life, property, economic activities, etc., due to a debris flow disasters within a certain area within a certain time (Liu et al., 2012). The core of risk assessment is hazard and vulnerability assessments of debris flows. As computer technology and numerical calculation methods have advanced, numerical calculations can not only reflect the velocity variation characteristics of debris flows but also yield intuitive information such as the influence range of debris flows, and are an effective method for the quantitative debris flow hazard assessment.

In recent years, scholars have performed much research on the hazards and risk assessment of debris flows (Ouyang et al., 2019; Lai et al., 2021; Wang et al., 2022; Dai et al., 2023c), and proposed various methods and models to carry out risk assessments of single-gully debris flows. Zhang et al. (2014) applied FLO-2D to simulate three debris-flow gullies in Qingshuigou, Zuizizigou, and Duanheba, and achieved good results. Gentile et al. (2008) assessed the hazard degrees of four types of debris flow by analyzing the hazards of debris flows in southern Italy. Calvo and Savi (2009) proposed a method for risk analysis of debris flow-prone areas, applied Monte Carlo procedures to debris flows in Valtellina in the Alps, and explored the impact of different vulnerability functions on risk.

Many scholars have carried out debris flow simulations and achieved valuable results, but most of the research has focused on the risk assessment of a single-gully debris flow and have rarely considered the harm caused by the simultaneous eruption of multiple debris flows. Although the method of hazard and vulnerability has been widely used in the risk assessment of single natural disasters, there are still many challenges for the risk assessment of complex disasters.

In this paper, taking the Xigou debris flows in the Three Gorges Reservoir area as a research case, numerical simulation by RAMMS is used for the inversion of the movement process of the 2018 debris flow event. The dynamic calculation parameters of the debris flow in Xigou are obtained; a quantitative hazard prediction of debris flows with different recurrence intervals (30, 50, and 100 years) in the study area when debris flows simultaneously break out in multiple gullies is carried out; and risk assessment is conducted based on the vulnerability characteristics of the disaster-bearing body in the study area. This study can provide empirical and theoretical support for the prevention and control of debris flow disasters in Xigou village and can serve as a reference for the prevention and control of debris flow disasters in the Three Gorges Reservoir area.

2 Geological background of the study area

The Xigou debris flow is located in Wushan County, Chongqing (31°09′16″ N, 109°58′34″ E). The terrain of the study area is high in the north and low in the south, with an altitude of 265-1890 m. The terrain is steep at the top and gentle at the bottom. The upper part of the valley has steep slopes (30° to 50°), and the lower part has gentle slopes (10° to 20°). There are three debris-flow gullies in this area. The basins of the #1, #2, and #3 debris-flow gullies are all rectangular in shape. The valley trend is 10° southeast, the cross-section has a V shape, the channel is straight, and the overall basin area is approximately 0.479 km² (Figure 1). The topographic information of the debris flow basin is shown in Table 1.

The study area is located in the southeast flank of the Qiyaoshan anticline, with a monoclinic output. The strata occurrence is 160-180°∠45-58°. No faults are developed. The strata distributed in this area are the Quaternary artificial filling soil (Q_4^{ml}), Quaternary Holocene landslide accumulation layer (Q_4^{del}), Quaternary colluvial soil layer (Q_4^{col+dl}), and Quaternary Pleistocene alluvial-diluvial layer (Q_4^{al+pl}). The exposed bedrock is mainly Triassic Badong Formation (T_2b) mudstone, fractured marl, and Lower Triassic Jialingjiang Formation (T_1j^4) limestone. Some weak interlayers and loose accumulation layers are distributed in each channel, providing good material source conditions for the formation of debris flows.

The study area has a subtropical monsoon humid climate, with an annual average temperature of 18.4 °C, an annual average rainfall of 1066.22 mm, a maximum annual rainfall of 1509.9 mm, a maximum monthly rainfall of 445.9 mm (September), and a maximum daily rainfall of 384.6 mm (August 31, 2014), and 68.8% of the rainfall occurs in the rainy season (May-September). From January to August in 2018, the cumulative rainfall was 824.8 mm, and the cumulative rainfall in June reached 194.2 mm, far exceeding the historical average rainfall of June (Figure 2), which provided external triggering conditions for the debris flow.

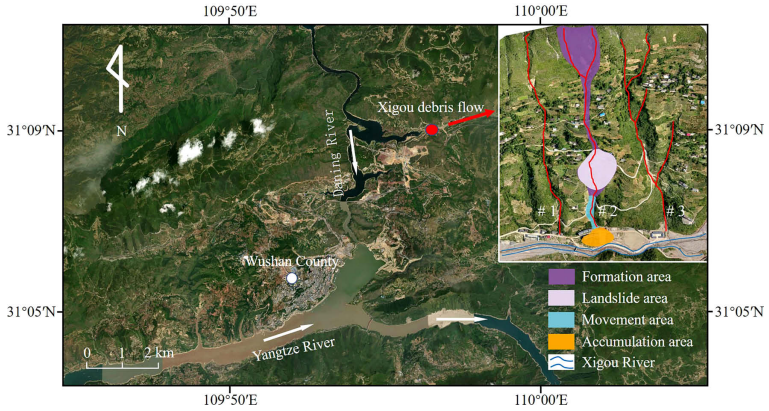

FIGURE 1
Geographic location and movement zones of the Xigou debris flow.

On June 18, 2018, Wushan County suffered continuous heavy rainfall adding up to 174.3 mm. Due to the rainfall, many small landslides occurred on the rear edge of the slope and accumulated in the ditch to mix with the rainwater in the ditch, resulting in debris flow disasters. According to the movement characteristics of the debris flow in gully #2, there are three areas: formation area, movement area, and accumulation area. There is a landslide area in the formation area (Figure 1).

In the formation area, the elevation is mainly 310-560 m, the slope is approximately 30°, and the overall area is approximately 0.448 km^2. The overburden layer on the slope surface is mainly gravel soil of avalanche deposits, the thickness of the soil layer is approximately 20 m, and the strongly weathered bedrock is exposed locally. The phenomenon of collapses and shallow landslides in this area is relatively serious, providing much loose solid for debris flows.

The movement area stretches 135 m long, mainly located between the elevation of 310 m and the debris flow channel outlet. The channel is generally narrow and straight, which is conducive to the rapid flow of debris. Many deposits can be seen along the valley in this area, resulting in a significant narrowing of the channel and obvious signs of erosion on the sidewall and bottom of the channel.

The accumulation area is located near the debris flow channel outlet. With flat terrain and an open space, it is shaped like a fan and spans approximately 6,643 m^2. This area is where residential houses and infrastructure are concentrated.

Geographically, gullies #1, #2, and #3 are located from west to east. Since the three debris-flow gullies are adjacent and are located

TABLE 1 Topographic information of #1, #2, and #3 debris-flow gullies.

Name	Basin area (km^2)	Length (km)	Elevation difference (m)	Average slope (°)	Vegetation cover (%)
#1	0.111	0.76	260	27	75
#2	0.159	0.81	280	29	70
#3	0.209	0.87	255	26	80

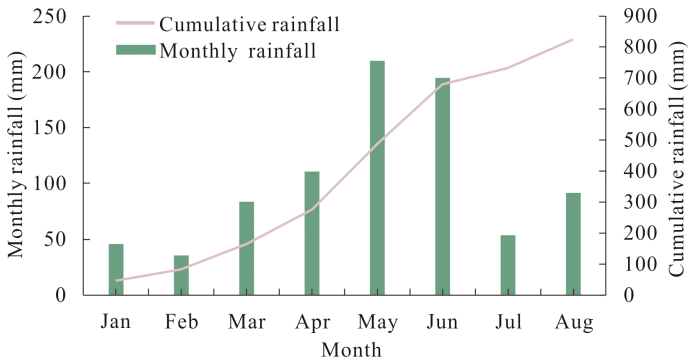

FIGURE 2
Monthly and cumulative rainfall in the study area in 2018. Modified according to reference Dai et al., 2023c.

on the same slope, their valley characteristics and topography are relatively similar. In short, the debris flow channel is narrow and straight, the elevation difference is nearly 300 m, the slope is steep, and the rock mass is severely weathered. There are serious collapses and shallow landslides in the upper reaches of the gully, and much loose soil remains in the gully, which provides a rich solid material source for the formation of debris flows. Seasonal rainfall varies widely in this area, with abundant rainfall in summer, accounting for approximately 65% of the annual rainfall, when the area is prone to landslides, debris flows, and other disasters. The topography, provenance, water source, and other conditions of the study area are conducive to the formation of debris flows. Therefore, the study area has the conditions for the eruption of debris flows. Affected by extreme rainfall and human activities (engineering constructions) in recent years, slope erosion and soil erosion have intensified, and the amount of loose solid material sources has increased greatly, resulting in a possible decrease in the critical rainfall intensity that will trigger debris flows and an increase in the frequency of debris flows.

At present, some villagers in Xigou village live on slopes and at the debris flow channel outlet. Once debris flows erupt, many people's lives and property can be lost. Therefore, it is very important to carry out disaster risk assessments of debris flows in Xigou village.

3 Numerical simulation and inversion of the Xigou debris flow

On June 18, 2018, a debris flow disaster occurred in gully #2 in the study area. In this section, we reproduce the 2018 debris flow event by numerical simulation, and reasonable calculation parameters and calculation models are obtained by inversion. Finally, the validated parameters and model are used to predict the scope of the influence of debris flows with different recurrence intervals and risk assessments.

3.1 Introduction to RAMMS

The RAMMS software was developed by the Swiss Federal Institute for Snow and Avalanche Research. It is mainly used to simulate the whole process of avalanches, collapses, debris flows, and shallow landslides from initial failure to movement and accumulation on 3D terrain. The DEBRIS-FLOW module (that is, the debris flow module) in the software can predict the spatial distribution of data, such as debris flow movement paths, flow velocities, flow depths, and pressure, allowing for better numerical simulation of the movement of debris flows (Christen et al., 2010).

In the RAMMS model, debris flow is regarded as a fluid with rheological properties. The Voellmy–Salm rheological continuum model is used to address rheological problems, the laws of material energy and motion transformation are used to address the movement and accumulation process of debris flow, and the random kinetic energy (RKE) model is used to make additional adjustments. In this study, the dynamic characteristics of the parameters are analyzed to obtain the desired simulation results.

3.1.1 Voellmy–Salm rheological model

The movement characteristics of debris flows are determined by two main parameters: the debris flow depth H (x, y, t) and the flow velocity U (x, y, t). The flow depth is expressed as follows:

$$\partial_t H + \partial_x (HU_x) + \partial_y (HU_y) = Q(x, y, t) \tag{1}$$

where H represents the fluid height (m) and $Q(x, y, t)$ is the mass source [kg/(m^2·s)]; $Q = 0$ means no material deposition.

The flow velocity is expressed as follows:

$$\| U \| = \sqrt{U_x^2 + U_y^2} \tag{2}$$

where $\| U \|$ means the absolute average velocity U, so as to make sure that U is a strictly positive velocity in the vector space. The direction of fluid velocity is:

$$n_U = \frac{1}{\| U \| (U_x, U_y)} \tag{3}$$

The frictional resistance of the Voellmy–Salm rheological model is determined by the following Equations:

$$S_f = (S_{fx} + S_{fy}) \tag{4}$$

$$S_{fx} = nU_x[\mu g_z H + \frac{g \| U \|^2}{\xi}] \tag{5}$$

$$S_{fx} = nU_y[\frac{\mu g_z H + g \| U \|^2}{\xi}] \tag{6}$$

In each Equation, x, y, and z are the coordinates in the Cartesian coordinate system, with x, y being the surface coordinates and z being the elevation; U is the average velocity of the debris flow; S_f is the frictional resistance; μ is the Coulomb friction coefficient; ξ is the turbulent flow friction coefficient; t is the movement time of the debris flow; and g is the acceleration due to gravity.

3.1.2 RKE model

The RKE model can make real-time adjustments to correct the debris flow simulation process. Due to the chaotic change in the fluid velocity and direction, the RKE model divides the flow velocity U into the average velocity and the instantaneous velocity. The flow velocity in the x and y directions is the vector sum of the average velocity and instantaneous velocity, and the average velocity in the z direction is set to 0 to better represent the real-time movement characteristics of the debris flow (Christen et al., 2010). In the RKE model, the friction coefficient μ and turbulence coefficient ξ play important roles.

The friction coefficient μ equals:

$$\mu(R) = \mu_0 exp(-\frac{R}{R_0}) \tag{7}$$

The turbulence coefficient ξ equals:

$$\xi(R) = \xi_0 exp(\frac{R}{R_0}) \quad (8)$$

where μ_0 is the static dry Coulomb, ξ_0 is the turbulence friction coefficients, R_0 is a constant (defined as the exponential growth rate of friction representing a random kinetic energy density function), and R is the depth-averaged random kinetic energy.

3.2 Numerical simulation of debris-flow gully #2

Based on unmanned aerial vehicle (UAV) aerial imagery data, a digital elevation model (DEM) with a resolution of 0.98 m was established. After importing the digital elevation model into RAMMS software, the grid size was set to 2 m, and the basin range and material source area were delineated. According to the actual situation, a value is assigned to the material source thickness, the simulation parameters are adjusted, and the three-point method is used to generate a flow curve (detailed parameters in Table 2).

According to the on-site investigation, debris flowed out from the side of the residential building and accumulated in a fan shape at the debris flow channel outlet (Figures 3A, B). Figure 3B shows the damage to the residential building when the debris flows occurred in 2018. The residential building was hit by the debris flows from the front. Doors, windows, and walls were severely damaged, and one wall was partially damaged. The first floor was buried. The debris flows accumulated behind the residential building with a thickness up to 2 stories high.

The thickness of the simulated debris flow in Figure 3C is 5.74 m, and the simulated debris flow is located near the northeast corner of the residential building, which is basically consistent with the actual accumulation range and thickness of the 2018 debris flow. Therefore, the 2018 debris flow event as reproduced using the current calculation model and parameters has good accuracy and reliability.

For the 2018 debris flow event, the debris flow depths at t=0 s, 80 s, 160 s, 240 s, 320 s, and 400 s are shown in Figure 4. Initially, the debris flow does not move, and the depth of the debris flow at t=0 represents the thickness of the unstable material source in the gully. In the landslide area at the end of the formation area, the phenomena of collapse and shallow landslides are more serious, and there are many loose solid material sources, so the material source in the landslide area is relatively thick. At t=80 s, the head of the debris flow passes through the movement area to the channel outlet, and the debris flow entrains many loose solids in the landslide area to flow downstream and accumulate in the narrow movement area. At t=160 s, the head of the debris flow rushes out of the channel outlet and hits nearby residential buildings, damaging some residential buildings. At t=240 s, with the continuous movement of the debris flow, the head of the debris flow, after

TABLE 2 Inversion parameters of the 2018 debris flow event.

Density ρ (g/cm^3)	Gravity g (m/s^2)	Average slope ψ (°)	Friction coefficient μ	Turbulence coefficient ξ
1.61	9.8	29	0.25	300

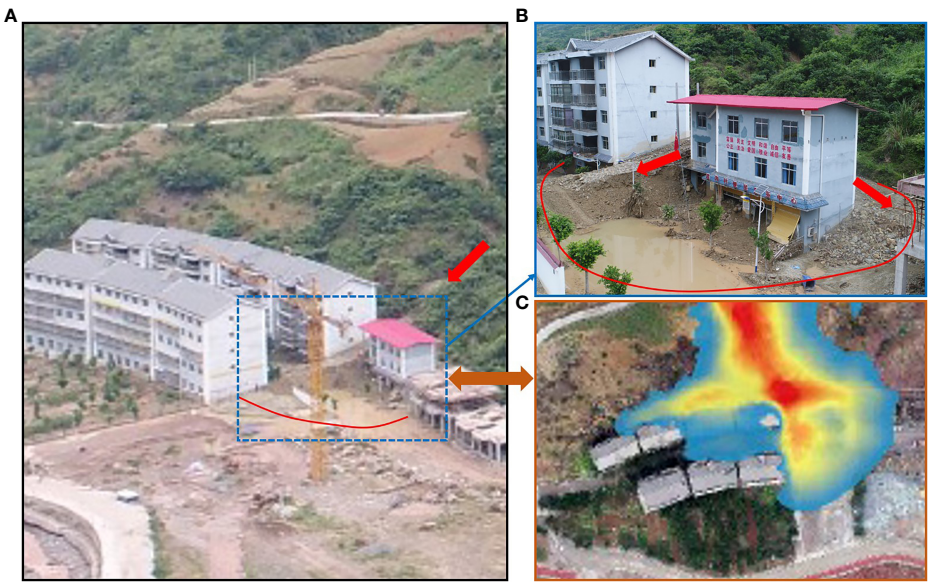

FIGURE 3
Photographs of the 2018 Xigou debris flow event. **(A)** Actual accumulation pattern. **(B)** Damage to residential buildings. **(C)** Simulated accumulation pattern.

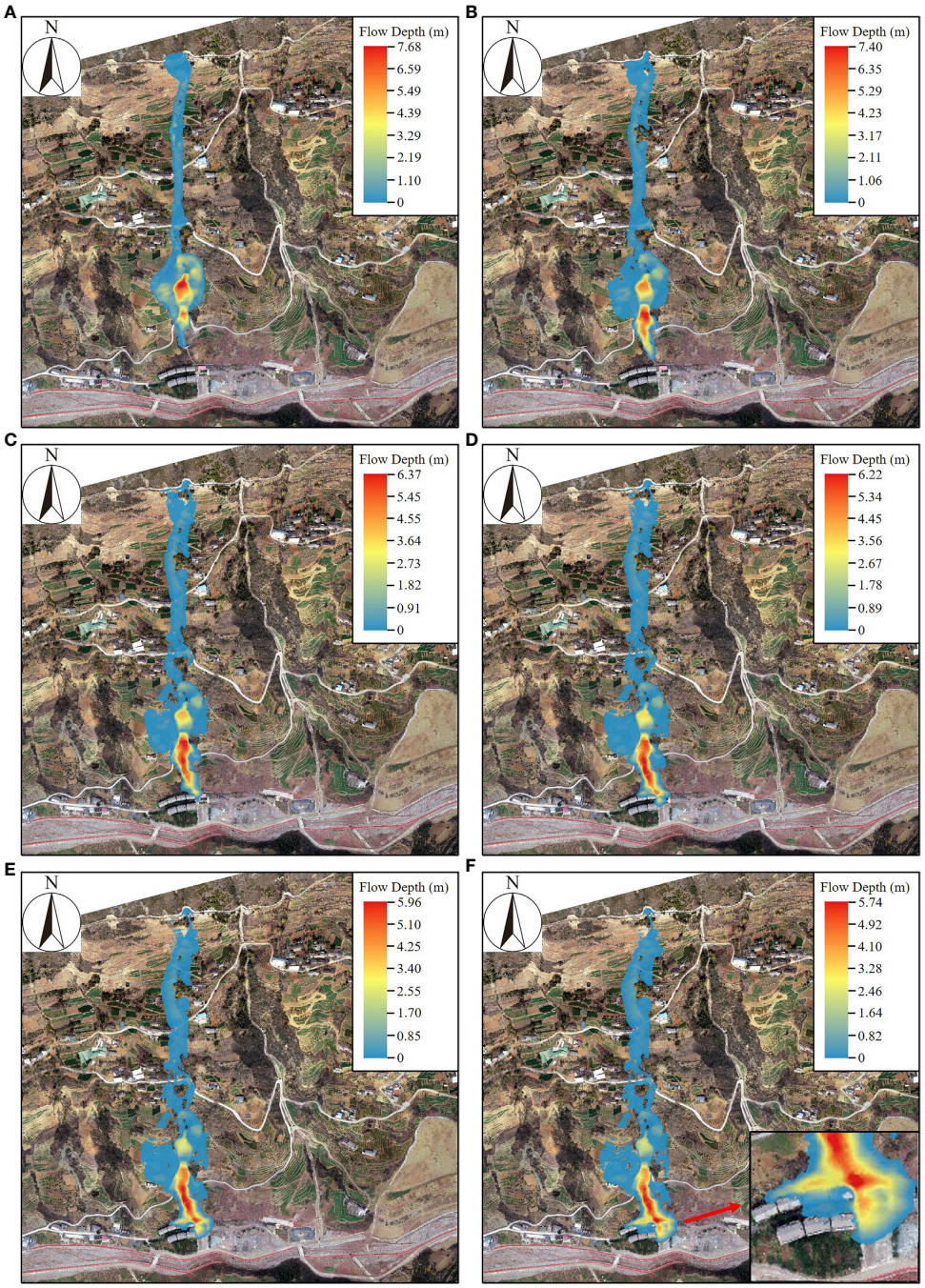

FIGURE 4
State of the Xigou debris flow at different times. **(A)** t=0 s, **(B)** t=80 s, **(C)** t=160 s, **(D)** t=240 s, **(E)** t=320 s, **(F)** t=400 s.

being blocked by the residential building, flows in two directions on the rear and the east side of the residential building. At t=320 s, the debris flow reaches the flat area and gradually accumulates in the rear and east of the residential building. At t=400 s, the debris flow stops moving. At this time, the debris flow depth is the accumulation thickness, and the debris flow forms a fan-shaped accumulation area at the channel outlet. The maximum accumulation thickness is 5.74 m, which happens near the northeast corner of the residential building.

4 Prediction and analysis of debris flow in the study area

In this paper, the rain-flood method is used to calculate the peak flow of debris flow. If debris flow and heavy rain occur at the same frequency and synchronously, the peak storm water flow in the sub-basin at different frequencies of the section is first calculated according to the hydrological method, and then the blockage

factor is chosen to calculate the debris flow according to the following Equation:

$$Q_c = (1 + \varnothing)Q_p D_c \quad (9)$$

where Q_c is the peak flow of debris flow with frequency P (m^3/s); $\varnothing$ is the sediment correction coefficient of debris flow; Q_p is the design flow for a rainstorm flood with frequency P (m^3/s); and D_c is the debris flow blockage coefficient.

$$\varnothing = (\gamma_c - \gamma_w)/(\gamma_H - \gamma_c) \quad (10)$$

where γ_c is the bulk density of the debris flow (kg/m^3); γ_w is the bulk density of clean water (kg/m^3), with γ_w =1.0 kg/m^3; and γ_H is the bulk density of solid matter in the debris flow (kg/m^3), with γ_H =2.65 kg/m^3.

Flood peak flow can be calculated by empirical formulas widely used by urban construction and water conservancy departments in the study area:

$$Q_p(1\,\%) = 11.2F^{0.84} \quad (11)$$

where $Q_p(1\,\%)$ is the design flow for storm floods with a 100-year recurrence interval (m^3/s), and F is the basin area (km^2). For the Three Gorges Reservoir area, the peak flood flow with different frequencies has the following empirical distribution: $Q_p(2\,\%)$ =0.8 $Q_p(1\,\%)$, $Q_p(3.3\,\%)$ =0.6 $Q_p(1\,\%)$, of which $Q_p(2\,\%)$, $Q_p(3.3\,\%)$ indicates the design flow (m^3/s) of the storm flood with a 50-year recurrence interval and a 30-year recurrence interval, respectively.

The calculation results are shown in Table 3.

The key to numerical simulation of debris flow is the determination of μ and ξ. Based on the inversion of the 2018 debris flow event, the specific μ and ξ are obtained. Corresponding models and related parameters are used to analyze and predict the potential impact range of debris flows in different return periods.

Figures 5A–C shows the accumulation thickness and influence range of the debris flow at different return periods. The common feature of the three return periods is that the debris flow hazards occur at gullies #1, #2, and #3 simultaneously, the differences being mainly the accumulation thickness of debris flow and the scope of the hazard area. For the debris flow with a 30-year recurrence interval, the maximum accumulation thickness in gully #1 is 4 m, and its head touches the houses and other buildings at the channel outlet, which poses a certain threat to the residents at the channel outlet. After the debris flow occurred in ditch #2 in 2018, some debris flow material sources remained in the gully. Therefore, under this condition, the potential hazard area of debris flow in gully #2 is slightly larger than it was in 2018. The maximum accumulation thickness is 6.54 m, which is located near the northeast corner of the residential buildings. The debris flow in the middle of gully #3 is thick and can reach approximately 5 m. The debris flow stops moving after it reaches the downstream part of the gully and never reaches the channel outlet, so it cannot affect the residents directly.

For the debris flow with a 50-year recurrence interval, in gully #1, the debris flows through the residential area at the channel outlet and arrives near the Xigou River, with the maximum accumulation thickness of approximately 6 m, so the debris flow can bury some houses in the residential area. The scope of the debris flow hazard area in gully #2 expands further and spreads to the farmland in front of the channel outlet. With an accumulation thickness of 10.18 m, the debris flow seriously threatens the lives and property of the residents in gully #2. The accumulation thickness of the debris flow in gully #3 is mostly between 6 and 9 m, and its head rushes out of the channel outlet, which gradually threatens the factory buildings.

For the debris flow with a 100-year recurrence interval, due to the proximity of the Xigou River to gully #1, the debris flows into the Xigou River, accumulates in large quantities and blocks the river, forming a barrier dam. Many debris flow in gully #2 accumulate on the farmland in front of the residential buildings, the accumulation thickness is as high as 8 m, and a small amount of debris flows into the Xigou River. The debris flow in gully #3 flows out from the channel outlet, forming a fan-shaped accumulation area with a thickness of 5 m, burying the factory buildings in front of the channel outlet.

The numerical simulation results show that in these three cases, the places near the outlet of #1, #2, and #3 gullies are the most vulnerable to debris-flow damage, while slopes and places away from the channel outlet are relatively safe. The maximum accumulation thickness of the debris flow in the 30-year recurrence interval is 6.54 m, which occurs at the outlet of gully #2 and the middle reaches of gully #3 and has a great impact on the residential buildings at the outlet of gully #2. The maximum accumulation thickness of the debris flow in the 50-year recurrence interval is 10.18 m, the accumulation thicknesses at gully #2 and the middle and lower reaches of gully #3 are high, and the buildings at each gully are greatly threatened. The debris flow in the 100-year recurrence interval has the widest influence range, the maximum accumulation thickness is 10.00 m, and the debris flow is mainly concentrated downstream of gullies #2 and #3. In this case, the buildings at the channel outlet are all impacted or even buried. The outgoing debris flow can block the river and may cause more serious disasters.

TABLE 3 Simulation parameters of the debris flow in the study area.

Basin area F (km^2)	Frequency P (%)	Bulk density γ_c (kg/m^3)	Blockage factor D_c	Sediment correction coefficient $\varnothing$	Peak flood flow Q_p(m^3/s)	Peak debris flow Q_c(m^3/s)
0.479	3.3	1.61	1.6	0.587	9.279	23.554
	2	1.61	1.7	0.587	10.034	27.063
	1	1.61	1.8	0.587	11.353	32.421

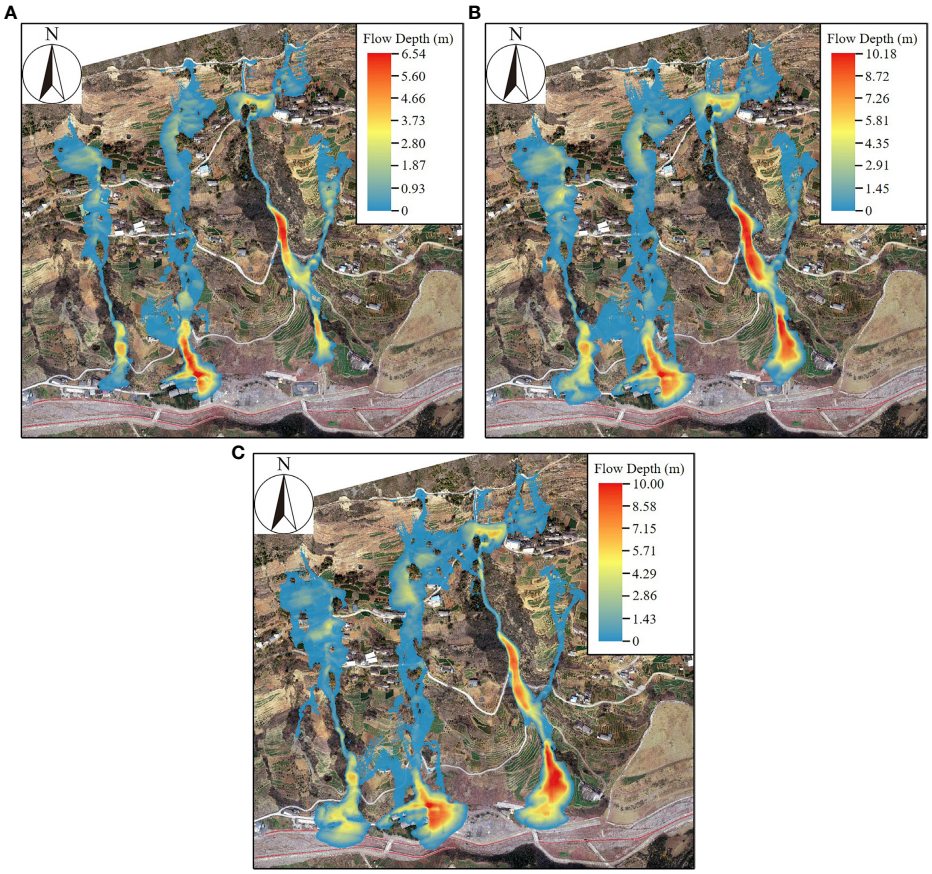

FIGURE 5
The debris flow accumulation thickness for different recurrence intervals. **(A)** 30-year recurrence interval **(B)** 50-year recurrence interval **(C)** 100-year recurrence interval.

5 Discussion

5.1 Hazard zones

In this paper, referring to Swiss and Austrian standards (Fiebiger, 1997; Garcia et al., 2004), combined with the intensity and probability of debris flow, the hazard of debris flow is divided into three levels: low, medium, and high. Debris flow intensity is defined as the combination of the maximum debris flow depth (H) multiplied by the maximum flow velocity (V) (Chang et al., 2017). The classification of debris flow intensity based on H and V is shown in Table 4. According to the classification criteria in Table 4, the classification results of debris flow intensity in different recurrence intervals are obtained (Figures 6A–C).

TABLE 4 Debris flow intensity classification.

Debris flow intensity	Maximum depth H (m)	Relation	Maximum depth (H) multiplied by maximum velocity (V) (m^2/s)
High	H>2.5	or	VH>2.5
Medium	0.5<H<2.5	and	0.5<VH<2.5
Low	0<H<0.5	and	VH<0.5

The annual probability of debris flow can be calculated by the following Equation:

$$P_m = 1 - \left(1 - \frac{1}{T}\right)^m \tag{12}$$

where P_m is the probability of debris flow occurring over m years and T is the recurrence interval of debris flow. The Taiwan Debris Flow Risk Classification (Lin et al., 2011) divides debris flows into high probability (greater than 10%), medium probability (between 10% and 1%), and low probability (between 1% and 0.2%). We specify m=1.

By combining the intensity level with the occurrence probability, the hazard of debris flow is classified, as shown in Figure 7. Based on this classification system, the map of hazard zones of the Xigou debris flow is drawn (Figure 8). The high-hazard area covers an area of 37378 m^2, accounting for 21% of the affected area, and is mainly located inside debris-flow gullies #1, #2, and #3. The medium-hazard area covers an area of 67108 m^2, accounting for 37% of the affected area, and is mainly located near gullies #1 and #2 and the landslide area. The low-hazard area covers an area of 758,559 m^2, accounting for 42% of

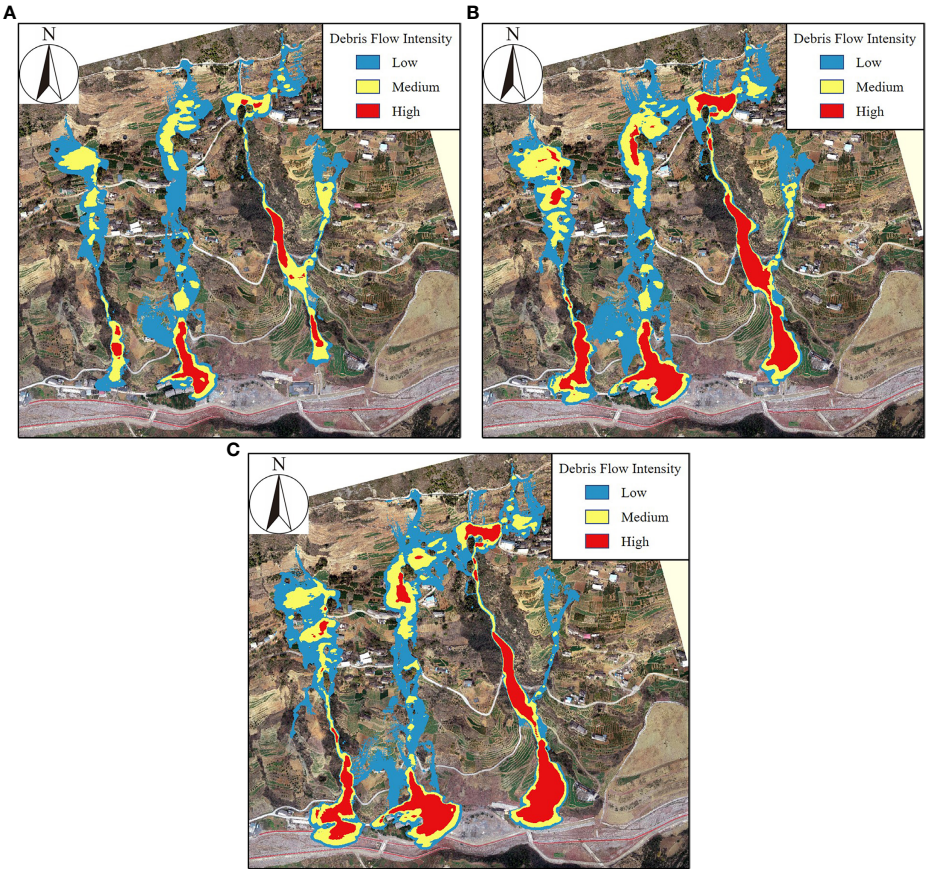

FIGURE 6
Zones of debris flow intensity for different recurrence intervals. **(A)** 30-year recurrence interval, **(B)** 50-year recurrence interval, **(C)** 100-year recurrence interval.

the affected area, and is mainly located at the upstream and channels outlet of debris flow.

5.2 Vulnerability zones

Vulnerability mainly reflects the disaster-bearing capacity of the disaster-bearing body. Cui et al. (2013) defined vulnerability according to economic loss, which is related to the economic value and degree of damage of disaster-affected objects.

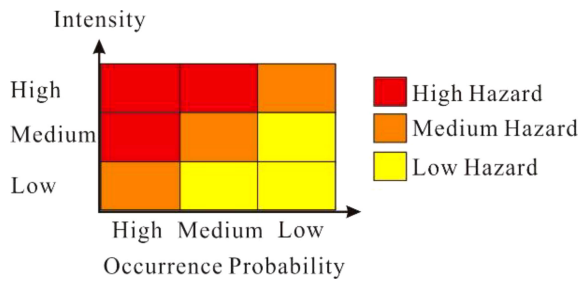

FIGURE 7
Hazard classification by debris flow intensity and occurrence probability.

$$V = V(u) \times C \tag{13}$$

where V is the degree of vulnerability; $V(u)$ is an economic index with a value range of 0 to 1; and C is an index to measure the degree of damage to disaster-affected objects, with a range of 0 to 1. $V(u)$ is the unit price $P(/\mathrm{m}^2)$ of the disaster-affected object multiplied by its area $N(\mathrm{m}^2)$:

$$V(u) = P \times N \tag{14}$$

According to the difference in function and value, the disaster-bearing objects of the Xigou debris flow are divided into three categories: houses, farmland (including open space), and rivers. The area N and the number of disaster-affected objects are determined according to field surveys and UAV images, and the unit price P of each disaster-affected object is determined according to the reference price provided by the government of Chongqing. C represents the degree of damage to the disaster-affected object by the impact of debris flow, and its value ranges from 0 to 1: The larger the C is, the more vulnerable the disaster-affected object is. The C of disaster-affected objects of different structural types is different. Cui et al. (2013) conducted a detailed investigation of debris flow disasters in the central and western regions of China and proposed a vulnerability index standard for different buildings or structures (Table 5). The value of C refers to Table 5. A C value of 1

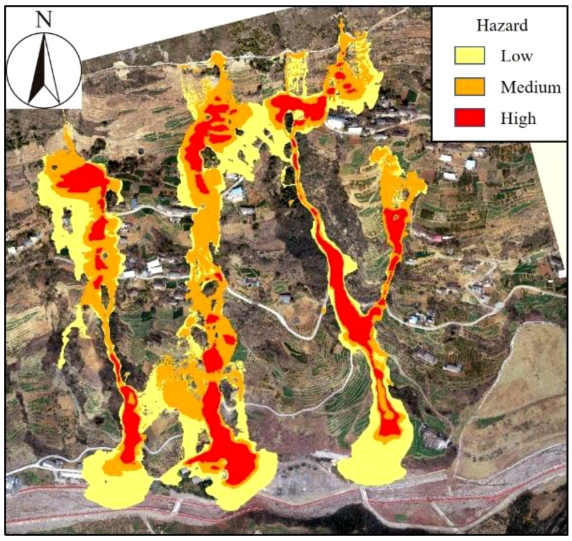

FIGURE 8
Hazard zones of the Xigou debris flow.

for agricultural land means that it can be completely damaged by a debris flow.

Finally, the vulnerability based on economic loss is calculated by Equation (14). The economic value of the vulnerability of each disaster-bearing body is superimposed on ArcGIS to obtain a map of vulnerability zones (Figure 9). Figure 9 shows that the high-vulnerability area covers an area of 9416 m^2, accounting for 6% of the affected area, and its disaster-affected objects are mainly residential buildings. The medium-vulnerability area covers an area of 3945 m^2, accounting for 3% of the affected area, and its disaster-affected objects are mainly the Xigou River. The low-vulnerability area covers an area of 140,850 m^2, accounting for 91% of the affected area, and its disaster-affected objects are mainly farmland.

5.3 Debris-flow risk zones

We adopt the expression of the risk of natural disasters such as debris flows proposed by the United Nations Department of Humanitarian Affairs in 1992:

$$R = H \times V \tag{16}$$

where R is the risk level, H is the hazard level, and V is the vulnerability level.

The map of risk zones of Xigou debris flows are obtained by a raster operation on the hazard and vulnerability results of debris flows on the ArcGIS platform (Figure 10). As shown in Figure 10, the areas affected by debris flows are divided into three risk levels: low, medium, and high. Table 6 summarizes the areas and proportions for different hazard, vulnerability, and risk levels. Among them, the high-risk area is the smallest, accounting for 2% of the total risk area, and mainly includes some houses and buildings near the #1 and #2 gullies. This area has the highest risk of debris flow in the future, and the protection of this area should be strengthened. The medium risk area covers an area of 40,531 m^2, and is mainly located inside the #1, #2, #3 debris-flow gullies. The low-risk area is the largest, accounting for 75% of the total risk area (136,025 m^2), and mainly covers large tracts of farmland and some river channels where the debris flows through. Figure 10 can provide a reference for debris flow prevention and control in the future.

6 Conclusion

In this paper, taking the debris flow in Xigou, Chongqing, China, as the research object, the RAMMS numerical simulation software and ArcGIS software are both used to simulate and analyze the 2018 debris flow event and carry out the risk assessment of debris flows with different recurrence interval when debris flows simultaneously break out in multiple gullies. We draw the following conclusions.

(1) Using RAMMS software, the Voellmy–Salm rheological model and the RKE model are used to simulate the 2018 debris flow event, whose movement and influence range are analyzed. The simulation shows that the debris flows for 400 s and the maximum accumulation thickness is 5.74 m, which happens near the northeast corner of the residential buildings.

TABLE 5 Vulnerability index of buildings or structures.

Types of structures	Vulnerability grades	Vulnerability values	Characteristics
Adobe construction	V	0.9-1.0	Small-scale debris flows can entirely destroy this type of structure.
Timber structure	IV	0.8-0.9	Small-scale or medium-scale debris flows can seriously damage this type of structure.
Brick-wood structure	III	0.5-0.8	Small-scale or medium-scale debris flows can partially destroy this type of structure.
Brick-concrete structure	II	0.2-0.5	Small-scale or medium-scale debris flows do not generally affect this type of structure, but it can be partially destroyed by large-scale debris flow.
Steel reinforced concrete structure	I	0.1-0.2	This type of structure is not generally affected in small-scale or medium-scale debris flows, but it can be partially destroyed by a devastating debris flow of huge magnitude.

*The Specification of Geological Investigation for Debris Flow Stabilization (DZ/T 0220-2006) grades debris-flow magnitude on the basis of the total runoff: the total runoff of a small-scale debris flow is less than 1×10^4 m^3, that of a medium-scale debris flow is between 1×10^4 m^3 and 10×10^4 m^3, that of a large-scale debris flow is between 10×10^4 m^3 and 100×10^4 m^3, and that of a mega debris flow is over 100×10^4 m^3.

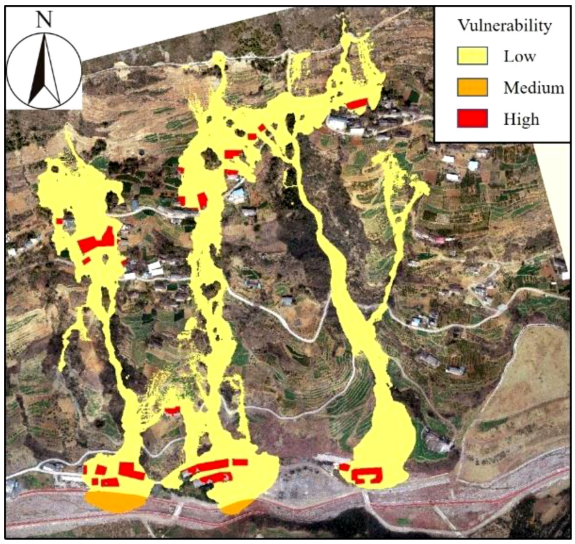

FIGURE 9
Vulnerability zones based on economic loss.

(2) The verified models and parameters are used to simulate and predict the debris flow in gullies #1, #2, and #3 in the study area and determine the potential hazard areas of debris flow in different recurrence intervals. The area around the channel outlet is most vulnerable to the hazards of debris flow, while places on the slope and away from the channel outlet are relatively safe. The maximum accumulation thicknesses of debris flow in the 30-year, 50-year, and 100-year recurrence intervals are 6.54 m, 10.18 m, and 10.00 m, respectively. The 100-year recurrence interval has the greatest influence and hazard.

(3) In this paper, referring to the disaster classification standards of Switzerland and Austria, combined with the intensity and occurrence probability of debris flow, a classification model of debris flow hazard zones with low, medium, and high-risk levels is established, and a map of hazard zones is drawn based on this classification system. From field surveys and UAV images, an economic vulnerability analysis of the disaster-bearing bodies in the study area is carried out, and a map of vulnerability zones is drawn. Finally, the hazard and vulnerability results are rasterized on the ArcGIS platform to generate a map of risk zones. The low-risk area is relatively large, accounting for 75% of the impact area of the debris flow,

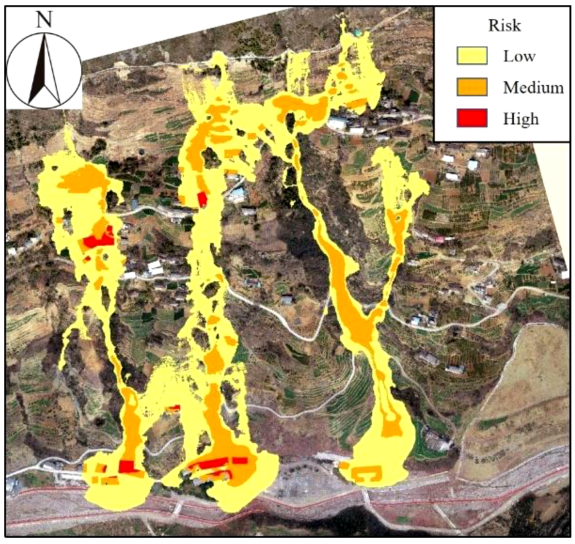

FIGURE 10
Risk zones for the Xigou debris flow.

TABLE 6 Summary of hazard, vulnerability and risk zones.

	Low	Medium	High	Total area
Hazard	75,859 m^2 (42%)	67,108 m^2 (37%)	37,378 m^2 (21%)	180,345 m^2
Vulnerability	164,114 m^2 (91%)	5410 m^2 (3%)	10,821 m^2 (6%)	
Risk	136,025 m^2 (75%)	40531 m^2 (23%)	3789 m^2 (2%)	

while the medium-risk area and high-risk area only account for 23% and 2%, respectively. The high-risk disaster-bearing bodies are mainly the buildings near the #1 and #2 gullies. The middle- and low-risk areas mainly include debris-flow gullies and nearby farmland. The high-risk area has the highest risk of damage in the event of future debris flows, so the protection of this area should be strengthened.

Data availability statement

The original contributions presented in the study are included in the article/supplementary material. Further inquiries can be directed to the corresponding author.

Author contributions

ZD: Project administration, Supervision, Writing – review & editing. AZ: Writing – original draft. WQ: Conceptualization, Writing – review and editing. XF: Formal Analysis, Writing – review and editing. JG: Software, Writing – review and editing. LG: Supervision, Writing – review and editing. LL: Visualization, Writing – review and editing. XJ: Data curation, Writing – review and editing. HW: Investigation, Writing – review and editing, Investigation, Writing – review and editing.

Funding

This study was supported by the follow-up of the Geological Disaster Prevention and Control Project in the Three Gorges area (000121 2023C C60 001 and 000121 2021C C60 001), Qianlong Plan Top Talent Project of Wuhan Center of China Geological Survey (QL2022-06).

Conflict of interest

Author WQ was employed by River Basin Hub Operation Management Center, China Three Gorges Corporation.

The remaining authors declare that the research was conducted in the absence of any commercial or financial relationships that could be construed as a potential conflict of interest.

Publisher's note

References

Calvo, B., and Savi, F. (2009). A real-world application of Monte Carlo procedure for debris flow risk assessment. *Comput. Geosciences.* 35, 967–977. doi: 10.1016/j.cageo.2008.04.002

Chang, M., Tang, C., Van Asch, T. W. J., and Cai, F. (2017). Hazard assessment of debris flows in the Wenchuan earthquake-stricken area, South West China. *Landslides* 14 (5), 1783–1792. doi: 10.1007/s10346-017-0824-9

Christen, M., Kowalski, J., and Bartelt, P. (2010). RAMMS: Numerical simulation of dense snow avalanches in three-dimensional terrain. *Cold Regions Sci. Technology.* 63 (1-2), 1–14. doi: 10.1016/j.coldregions.2010.04.005

Cui, P., Zou, Q., Xiang, L. Z., and Zeng, C. (2013). Risk assessment of simultaneous debris flows in mountain townships. *Prog. Phys. Geography.* 37 (4), 516–542. doi: 10.1177/0309133313491445

Dai, Z. W., Wang, L. Q., Fu, X. L., Huang, B. L., Zhang, S. L., Gao, X. C., et al. (2023a). Degradation of typical reverse sand-mudstone interbedded bank slope based on multi-source field experiments. *Int. J. Environ. Res. Public Health.* 20 (3), 2591. doi: 10.3390/ijerph20032591

Dai, Z. W., Yang, L., Zhang, N., Zhang, C. Y., Zhang, Z. H., and Wang, H. (2023b). Deformation characteristics and reactivation mechanism of an old landslide induced by combined action of excavation and heavy rainfall. *Front. Earth Sci.* doi: 10.3389/feart.2022.1009855

Dai, Z. W., Zhang, A. L., Wang, S. F., Fu, X. L., Yang, L. W., Jang, X. N., et al. (2023c). The development characteristics and mechanisms of the Xigou debris flow in the Three Gorges Reservoir Region. *Front. Earth Sci.* doi: 10.3389/feart.2023.1122562

Fiebiger, G. (1997). Hazard mapping in Austria. *J. Torrent Avalanche Landslide Rockfall Engineering.* 134 (61), 93–104.

Garcia, R., Rodriguez, J. J., and Brien, J. S. (2004). Hazard zone delineation for urbanized alluvial fans. *2004 ASCE World Water & Environmental Resources Congress — Arid Lands Symposium*, Salt Lake City, Utah, 2004. doi: 10.1061/40737(2004)11

Gentile, F., Bisantino, T., and Liuzzi, G. T. (2008). Debris flow risk analysis in South Gargano watersheds (Southern-Italy). *Natural Hazards.* 44, 1–17. doi: 10.1007/s11069-007-9139-9

Guo, J., Zhang, P., Zhang, Q., Huang, B. L., and Qin, Z. (2020). Study on landslide hazard identification tech-nology based on multispectral remote sensing images in wu gorge. *Geology Mineral Resour. South China* 36 (2), 38–45. doi: 10.3969/j.issn.1007-3701.2020.01.005

Lai, B., Liu, J., and Wu, S. T. (2021). Division of geological hazard inspection units based on arcGIS–– A case study of zhuhai city. *South China Geology* 37 (1), 75–82. doi: 10.3969/j.issn.2097-0013.2021.01.006

Liu, G. X., Dai, E. F., Wu, S. H., and Wu, W. X. (2012). A Study on theory and method in debris flow risk assessment. *Prog. Geography.* 31 (3), 383–391. doi: 10.11820/dlkxjz.2012.03.015

Ouyang, C. J., Wang, Z. W., An, H. C., Liu, X. R., and Wang, D. P. (2019). An example of a hazard and risk assessment for debris flows-A case study of Niwan Gully, Wudu, China. *Eng. Geology.* 263, 105351. doi: 10.1016/j.enggeo.2019.105351

Pei, Y. Q., Qiu, H. J., Yang, D. D., Liu, Z. J., Ma, S. Y., Li, J. Y., et al. (2023). Increasing landslide activity in the Taxkorgan River Basin (eastern Pamirs Plateau, China) driven by climate change. *Catena* 223, 106911. doi: 10.1016/J.CATENA.2023.106911

Qin, P. P., Huang, B. L., Li, B., Chen, X. T., and Jiang, X. N. (2022). Hazard analysis of landslide blocking a river in Guang'an Village, Wuxi County, Chongqing, China. *Landslides* 19 (11), 2775–2790. doi: 10.1007/s10346-022-01943-2

Qiu, H. J., Zhu, Y. R., Zhou, W. Q., Sun, H. S., He, J. Y., and Liu, Z. J. (2022). Influence of DEM resolution on landslide simulation performance based on the Scoops3D model. *Geomatics Natural Hazards Risk* 13 (1), 1663–1681. doi: 10.1080/19475705.2022.2097451

Tang, C., van Asch, T. W. J., Chang, M., Chen, G. Q., Zhao, X. H., and Huang, X. C. (2012). Catastrophic debris flows on 13 August 2010 in the Qingping area, southwestern China: The combined effects of a strong earthquake and subsequent rainstorms. *Geomorphology.* 139, 559–576. doi: 10.1016/j.geomorph.2011.12.021

Wang, J., Huang, B. L., Zhao, Y. B., Zhang, Z. H., and Hu, M. J. (2018). Study on deformation and failure mechanism of Huangnanbeixi dangerous rock in Three Gorges Reservoir Area. *Geology Mineral Resour. South China* 34 (4), 339–346. doi: 10.3969/j.issn.1007-3701.2018.04.009

Wang, L. Y., Qiu, H. J., Zhou, W. Q., Zhu, Y. R., Liu, Z. J., Ma, S. Y., et al. (2022). The post-failure spatiotemporal deformation of certain translational landslides may follow the pre-failure pattern. *Remote Sensing.* 14, 2333. doi: 10.3390/rs14102333

Yin, Y. P., Huang, B. L., Zhang, Q., Yan, G. Q., and Dai, Z. W. (2020). Research on recently occurred reservoir-induced Kamenziwan rockslide in Three Gorges Reservoir, China. *Landslides* 17 (8), 1–15. doi: 10.1007/s10346-020-01394-7

Yu, B., Yang, Y. H., Su, Y. C., Huang, W. J., and Wang, G. F. (2010). Research on the giant debris flow hazards in Zhouqu county, Gansu province on August 7, 2010. *J. Eng. Geology.* 18 (4), 437–444. doi: 10.3724/SP.J.1011.2010.01138

Zhang, Q., Huang, B. L., Chen, X. T., and Wang, J. (2019). Research on deformation mechanism transformation of jurassic consequent bank slope based on thickness variation of deposition layer. *Geology Mineral Resour. South China* 35 (3), 354–360. doi: 10.3969/j.issn.1007-3701.2019.03.009

Zhang, P., Ma, J. Z., Shu, H. P., and Wang, G. (2014). Numerical simulation of erosion and deposition debris flow based on FLO-2D model. *J. Lanzhou Univ. (Natural Sciences)* 50 (3), 363–368 + 375. doi: 10.1039/f19787400211

Zhang, C. Y., Yin, Y. P., Yan, H., Li, H. X., Dai, Z. W., and Zhang, N. (2021). Reactivation characteristics and hydrological inducing factors of a massive ancient landslide in the three Gorges Reservoir, China. *Eng. Geol.* 292, 106273. doi: 10.1016/j.enggeo.2021.106273

Zhang, A. L., Zhang, P., Dai, Z. W., Huang, B. L., Zhang, C. Y., Wang, L. Q., et al. (2022). Failure mechanism of the Simiqiao landslide under rainfall and slope cutting. *Arabian J. Geosciences* 15, 1432. doi: 10.1007/s12517-022-10698-y

Zou, Z. X., Luo, T., Zhang, S., Duan, H. J., Li, S. W., Wang, J. E., et al. (2023). A novel method to evaluate the time-dependent stability of reservoir landslides: exemplified by Outang landslide in the Three Gorges Reservoir. *Landslides* 20, 1731–1746. doi: 10.1007/S10346-023-02056-0

Zou, Z. X., Yan, J. B., Tang, H. M., Wang, S., Xiong, C. R., and Hu, X. L. (2020). A shear constitutive model for describing the full process of the deformation and failure of slip zone soil. *Eng. Geology* 276, 105766. doi: 10.1016/j.enggeo.2020.105766

frontiers | Frontiers in Earth Science

TYPE Original Research
PUBLISHED 05 September 2023
DOI 10.3389/feart.2023.1273389

OPEN ACCESS

EDITED BY
Haijun Qiu,
Northwest University, China

REVIEWED BY
Shiliang Liu,
Shandong University, China
Qingbiao Guo,
Anhui University, China

*CORRESPONDENCE
Shijie Song,
kkkbff@163.com

RECEIVED 06 August 2023
ACCEPTED 24 August 2023
PUBLISHED 05 September 2023

CITATION
Zheng B, Song S, Cheng X, Niu R, Cheng X, Ruan H and Li G (2023), The influence of coal mining subsidence on the movement and deformation of loess slope in the loess gully area of Northern Shaanxi.
Front. Earth Sci. 11:1273389.
doi: 10.3389/feart.2023.1273389

The influence of coal mining subsidence on the movement and deformation of loess slope in the loess gully area of Northern Shaanxi

Beibei Zheng[1,2,3], Shijie Song[1,2,3]*, Xia Cheng[4], Ruilin Niu[1,2,3], Xing Cheng[1,2,3], Hao Ruan[1,2,3] and Guodong Li[5]

[1]Xi'an University of Science and Technology, College of Geology and Environment, Xi'an, China, [2]Research Institute of Coal Green Mining Geology, Xi'an University of Science and Technology, Xi'an, China, [3]Key Laboratory of Geological Guarantee for Coal Green Development of Shaanxi Province, Xi'an, China, [4]Ningxia Survey and Monitor Institute of Land and Resources, Xi'an, China, [5]Shanxi Water Group Construction Investment Co., Ltd., Shanxi, China

Introduction: How to solve the contradiction between coal mining and soil and water conservation is a key scientific problem to realize ecological environment protection and high-quality development in the middle reaches of the Yellow River.

Methods: Using FLAC^{3D} numerical simulation experiment method, the influence of loess slope surface shape and coal seam overburden structure coupling on slope movement and deformation is studied.

Results: Under any surface slope shape, the average slope subsidence coefficient ($q_{slope\ average}$) increases with the increase of sand layer coefficient after coal mining subsidence. When the sand layer coefficient is less than 0.71, the $q_{slope\ average}$ increases rapidly, with an increase of more than 2.86%, and when the sand layer coefficient is greater than 0.71, the $q_{slope\ average}$ tends to be stable. Under any surface slope shape, the $q_{slope\ average}$ decreases with the increase of sand-mud ratio. When the overburden structure characteristics of any coal seam and the natural slope of the surface slope are less than or equal to 5°, the $q_{slope\ average}$ of the convex slope is the largest, and the $q_{slope\ average}$ of the four slope types is ranked as follows: convex slope > straight slope ≈ composite slope > concave slope; When the structural characteristics of overlying strata in any coal seam and the natural slope of surface slope are more than 5°, the $q_{slope\ average}$ of concave slope is the largest, and the $q_{slope\ average}$ of four slope types is in the order of concave slope > straight slope ≈ composite slope > convex slope. With the increase of the natural slope of the surface slope, the $q_{slope\ average}$ first decreases and then increases, and the inflection point is 15°. The influence law of loess slope surface morphology and coal seam overburden structure on the average horizontal movement of slope surface is similar to that of average subsidence of slope surface.

Discussion: The results can provide scientific basis for surface movement and deformation and soil and water conservation in the mining subsidence area of northern Shaanxi in the middle reaches of the Yellow River Basin in China.

KEYWORDS

coal mining subsidence, loess slope, moving deformation, overburden rock structure, China Northern Shaanxi coal mining area

1 Introduction

As an important disposable energy source in China, coal plays a leading role in the energy structure of China. Based on the energy structure characteristics of China, which is "short of oil, short of gas and relatively rich in coal", coal resources, as the ballast stone of China's energy security, will not change in the short term (Wang et al., 2021; Song et al., 2023a; Song et al., 2023c). Even by 2050, the proportion of coal in China's primary energy consumption will not be less than 40% (Qiu et al., 2022). With the development of coal resources in eastern China, the western region has become the main producing area of coal development (Liu F. et al., 2022; Qiu et al., 2022; Song et al., 2023d), and the middle reaches of the Yellow River have become the center of coal strategic westward movement (Fang et al., 2016; Zhang et al., 2019; Shen et al., 2022). However, the soil erosion in the middle reaches of the Yellow River Basin is serious, and the natural ecology is very fragile. Especially, the mining area in northern Shaanxi and the national key control area of soil erosion with heavy sand and coarse sand in the Yellow River are highly overlapped in space (Song et al., 2022), so that the mining damage problems such as surface deformation, water resources destruction and soil quality degradation caused by coal mining continue to aggravate regional soil erosion (Song et al., 2018; Li, 2019; Li et al., 2019). This is contrary to the important instruction on ecological environment protection in the middle reaches of the Yellow River (Song et al., 2023b) and the requirement of "paying special attention to soil and water conservation in the middle reaches of the Yellow River" in the Outline of Ecological Protection and High-quality Development Plan of the Yellow River Basin. Therefore, how to solve the sharp contradiction between coal mining and soil and water conservation has become a key scientific issue to realize ecological environment protection and high-quality development in the middle reaches of the Yellow River Basin in China.

Scholars at home and abroad have been paying attention to the influence of loess layer on the development characteristics and evolution law of coal mining subsidence, and have obtained a lot of valuable research results from the properties of loess layer such as thickness, vertical joints, collapsibility and physical and mechanical properties. For example, Song et al. (2011) studied the influence of the rock-soil ratio of overlying strata on mining subsidence in the elm bay mining area in northern Shaanxi, and found that the extremely thick loess layer over 100 m has the effect of reducing subsidence coefficient. Tang (2011) thought that the surface subsidence in the loess-covered area in the west is caused by the load of loess layer and the uneven settlement of bedrock, and a two-layer medium prediction model of coal mining subsidence considering the effect of the thick loess layer is established through numerical simulation test. Tang F. Q. et al. (2019) studied the quantitative relationship between the equivalent load of loess layer and equivalent mining width, depth and bedrock subsidence, and established a two-medium model to simulate the interaction between loess layers based on random medium theory. The natural form (slope) of loess layer on the surface, as a direct embodiment of the complex topography in the loess gully region, is not only an important geological factor affecting the coal mining subsidence, but also an important topographic basis for shaping the final form of the surface after subsidence, so that there is obvious mutual feedback effect between "the shape and deformation of loess slope" and "the characteristics and laws of coal mining subsidence". However, it is not enough to study and reveal the influence of coal mining subsidence on the surface loess slope shape from the perspective of feedback. As a typical sedimentary mineral, the overburden structure of coal is not only a very significant and important geological condition, but also a carrier for the upward spread of underground mining activities (Song et al., 2011). The sand layer coefficient of coal seam overburden reflects the quantitative characteristics of rock strata in overburden, and the sand-mud ratio of coal seam overburden reflects the overall lithologic characteristics of overburden. The characteristics of strata in the overlying strata structure of coal measures determine the overall shape and panorama of the surface subsidence basin, and mining subsidence will show completely different basic characteristics and laws under different overlying strata structure conditions.

In view of this, taking the loess gully region in Northern China as the research area, this paper studies and reveals the influence of coal mining subsidence on the surface loess slope shape (slope and slope length) under the coupling effect of "the structure of coal seam overburden and the natural shape of surface loess slope" by using the numerical simulation experiment method, with a view to enriching and deepening the research on the law of soil erosion in the coal mining subsidence area and providing scientific basis for soil and water conservation in northern Shaanxi coal mining area in the middle reaches of the Yellow River Basin in China.

2 Overview of the research area

Located in the north of Shaanxi Province, China, the coal mining area in northern Shaanxi Province generally refers to Yushenfu mining area, including two relatively large mining areas, Yushen and Shenfu mining area, so it is also collectively referred to as the northern Shaanxi coal mining area (see Figure 1). The length of northern Shaanxi coal mining area is about 84 km in the east-west direction and 85 km in the North-South direction, and the whole coal mining area is about 7,139.7 km^2 (Liu et al., 2021; Song et al., 2021; Shang et al., 2022). The overall terrain is high in the northwest and low in the southeast, and the altitude is within the range of 1,200–1300 m (Wang, 2020; Pei et al., 2023). According to the genesis and morphological characteristics of the landform in the mining area, it can be divided into three types: wind-blown sand landform, loess landform and valley landform, among which the loess landform can be divided into loess ridge landform, sand cover loess ridge landform and loess hilly landform. It is cold in winter in this area, with low humidity and temperature. The annual average temperature ranges from 6.2°C to 8.5°C, and there is little precipitation, mainly from July to September (Song et al., 2023e;

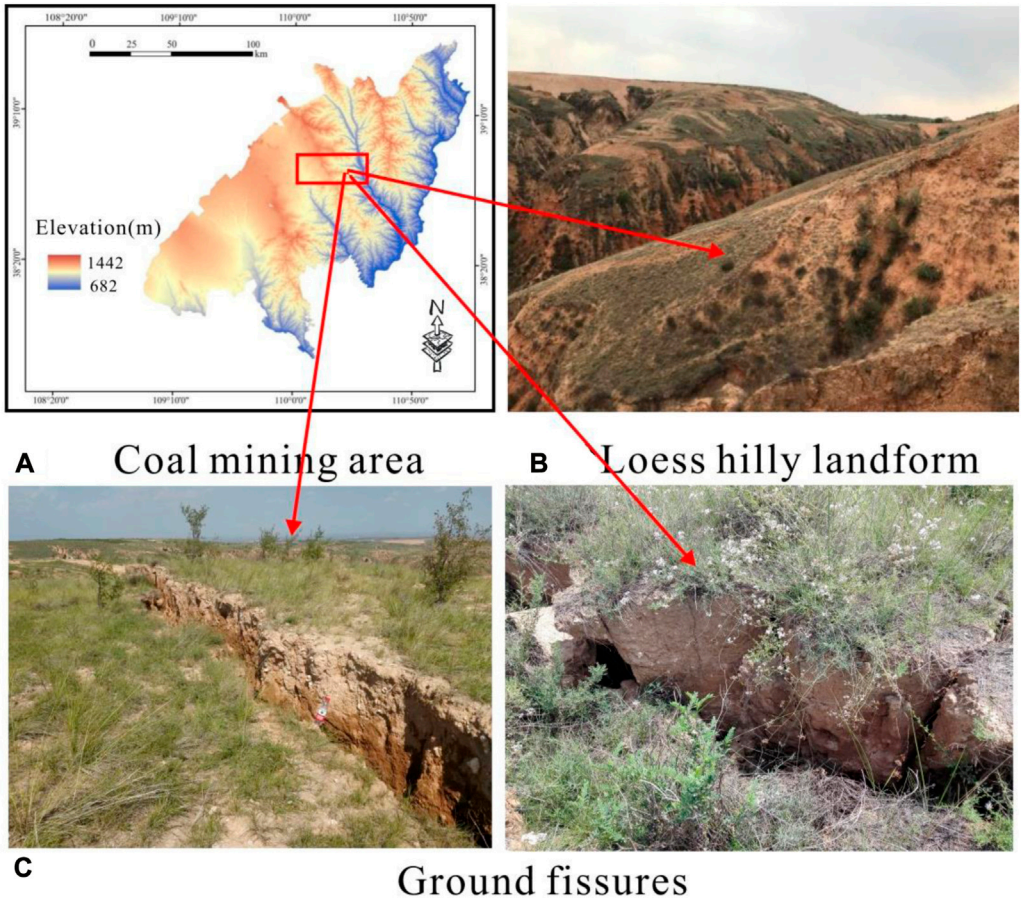

FIGURE 1
Geographical location map of mining area [see figures **(A–C)** for mining area, loess hilly landform and ground fissures].

Ma et al., 2023), and the annual rainfall ranges from 194.7 to 531.6 mm. The vegetation types in the study area are single, mainly including Salix psammophila, Artemisia selengensis, Sabina vulgaris and Caragana korshinskii. The geological structure in the area is simple, 2^{-2} coal is the main coal seam, and the thickness of coal seams is above 2 m, with the maximum thickness of 12.5 m. The overall characteristics of coal seams are shallow burial, large thickness and thin overlying bedrock, which has good mining conditions. The mining method in the mining area is mainly longwall fully mechanized mining, which is easy to cause environmental geological problems. Coal mining and roadway excavation will produce a large area of mined-out area underground, and the collapse of mined-out area will lead to the caving and bending subsidence of overlying strata, and cracks and surface subsidence will appear in different degrees all over the mining area (Shao et al., 2015). The ecological environment of mining areas in Northern Shaanxi is fragile, with drought and little rainfall all the year round and large evaporation. It is the key control area of soil erosion in Shaanxi Province, China, with serious soil erosion for many years, with soil erosion modulus exceeding 5,000 t/(km^2a) (Song et al., 2021). Secondly, the surface damage and soil erosion caused by coal mining in this area are very representative, so the northern Shaanxi mining area in China is chosen as the research area.

3 Model construction and numerical simulation experiment

3.1 Model construction

Based on the overlying strata structure and loess slope shape of coal seam in northern Shaanxi coal mining area, a numerical model framework is designed.

3.1.1 Frame selection

According to the survey data, the type of floor-coal seam-bedrock-loess layer in the actual geological occurrence structure of 2^{-2} main coal seam in the study area accounts for more than 60% (Wang et al., 2010), so it is used as the basic framework of the model.

3.1.2 Structural design of loess layer

Firstly, the topography of the mining area in northern Shaanxi is complex. In order to more accurately express the slope shape of the surface loess layer, we divide the loess layer into two sections. Secondly, the mining area in Northern Shaanxi is covered by loess, and the loess layer is thick. From the point of view of numerical model construction, it is necessary to maintain the consistency and integrity of the overlying geotechnical structure of coal seams on both sides of the model, so the loess layer is divided

into two sections. In addition, Song et al. (2016) found that the mining depth will have an important influence on the deformation of the surface slope during coal mining. In order to eliminate the influence of mining depth on mining subsidence as much as possible, we divide the loess layer into two sections, the upper section is a slope section and the lower section is a horizontal section.

3.1.3 Surface slope shape design

According to the results of detailed geological survey carried out by predecessors in the study area, the slope of loess slope in northern Shaanxi mining area is mainly between 6° and 40°, and according to China's Soil Erosion Classification and Classification Standard (SL190-2007), the slope is set to 5 slopes, which are 5°, 15°, 25°, 35°, and 45° in turn. The external morphology of loess slope is set to four types: straight slope, concave slope, convex slope and compound slope. The design of slope and slope shape covers all types of surface slope morphology in the study area.

3.1.4 Design of overlying strata structure

According to the detailed geological survey results carried out by predecessors in the study area, the overlying bedrock of 2^{-2} coal seam in the whole area is mainly composed of sandstone and mudstone, and the number of sandstone layers is generally 5–15, with a maximum of 35. The thickness ratio of sandstone and mudstone in bedrock is between 60% and 80%, so the sand-mud ratio (reflecting the overall lithologic characteristics of overlying strata) is selected as 6:4 and 8:2. The sand coefficient (reflecting the quantitative characteristics of strata in overlying strata) is 0.67, 0.71, and 0.75.

3.1.5 Geometric parameter design of numerical model frame

Set all models to be 1,000 m long in the X direction, 300 m wide in the Y direction, 295 m high at the top of the slope in the Z direction and 235 m high at the bottom of the slope. Set the floor thickness to be 10 m, the coal seam thickness to be 5 m, the overlying bedrock thickness to be 210 m, the maximum thickness of loess layer to be 70 m, and the lower section thickness to be 10 m.

According to the above variables, 120 different models are constructed.

3.2 Numerical simulation experiment process

In the study area, the thickness of coal seam is 5 m, and in the simulation process, the mining height is cut at one time. In the process of model excavation, the working face is gradually advanced from left to right, and the excavation is once every 50 m, and the ground surface begins to sink and move horizontally until the operation is stopped due to full mining. Take 25° compound slope with sand-mud ratio of 8:2 and sand layer coefficient of 0.75 as an example, and its three-dimensional numerical model is shown in Figure 2.

3.2.1 Setting of physical and mechanical parameters

According to the representative geological drilling and geotechnical test data, the physical and mechanical parameters of each geotechnical layer in the model are assigned, and the results are shown in Table 1.

3.2.2 Boundary condition setting

Mohr Coulomb model is selected in FLAC^{3D} numerical simulation software, and the constraint conditions of the model are set according to the actual excavation situation of the model. Firstly, the front, back, left, right and lower boundaries of the model are defined as fully constrained boundaries, and the upper part of the model is loess layer, which will move in both horizontal and vertical directions after full mining, and is defined as free boundary.

3.2.3 Data extraction and calculation

Through the simulation experiment, the surface subsidence and horizontal movement of each model on the slope are extracted by Fish language, and the extracted data are converted into coordinates to represent the shape of the slope after subsidence. Irregular slope gradient and slope length are replaced by uniform slope under the same conditions (Song et al., 2011). The average slope length of the typical loess slope in the coal mining subsidence area of northern Shaanxi is 50 m. The upper 10 m of the subsidence slope is divided into the top, the middle 30 m is divided into the middle and the lower 10 m is divided into the toe. A monitoring point is arranged every 2 m on the loess slope, and a total of 25 monitoring points are evenly arranged, including 5 monitoring points at the top of the slope, 15 monitoring points at the middle of the slope and 5 monitoring points at the foot of the slope. The subsidence coefficient q_{slope} at the toe of the slope (the maximum subsidence and mining height ratio at the toe of the slope) and the average subsidence coefficient $q_{slope\ average}$ (the weighted average of subsidence and mining height ratio at the top, middle and toe of the slope, in which the weights of monitoring points at the top, middle and toe of the slope are 1/5, 3/5 and 1/5 respectively) are adopted to analyze the overlying strata structure of coal seam. According to the extracted monitoring point data, the horizontal movement of each model is calculated (the translation momentum of all monitoring points on the slope is averaged). Because the moving direction of the model slope is consistent with the advancing direction of the working face, it is a positive value, which is represented by the $u_{slope\ average}$.

4 Results and analysis

4.1 Influence of coal mining subsidence on average subsidence of slope surface

According to the extracted monitoring point data, the subsidence coefficient at the toe of different models and the average subsidence coefficient of the whole slope are calculated, and the calculation results are shown in Table 2. It can be seen from Table 2 that when the subsidence coefficient q_{slope} at the foot of the model is used to analyze the loess slope movement law, the difference of subsidence coefficient among the models is too small, and there is no obvious law. However, when the subsidence coefficient $q_{slope\ average}$ is used to analyze the loess slope movement law, the $q_{slope\ average}$ can represent the

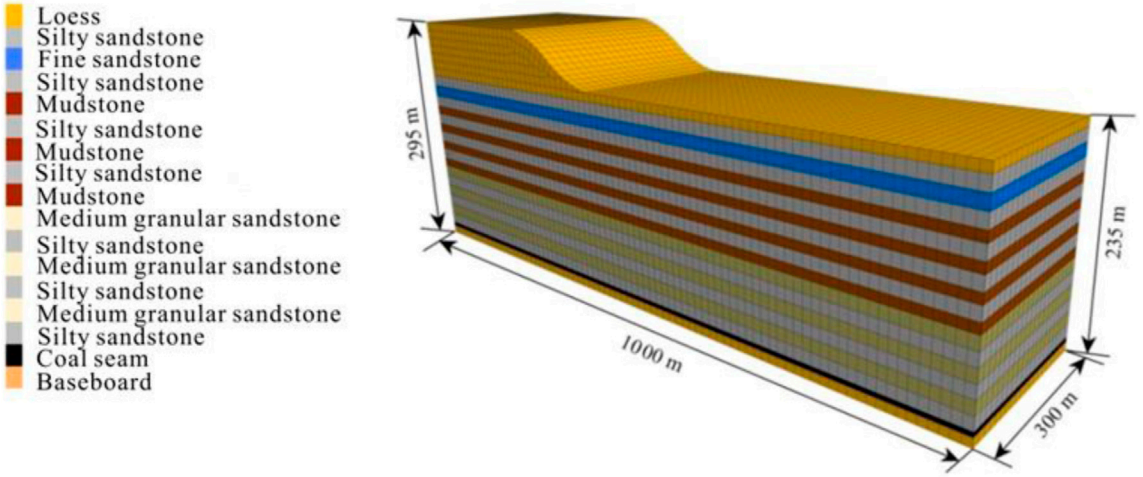

FIGURE 2
Three-dimensional numerical model diagram of 25° compound slope.

TABLE 1 Physical and mechanical parameters of rock and soil layers.

Rock character	Modulus of elasticity/MPa	Tensile strength/MPa	Serious/ kN·m^{-3}	Internal friction angle/(°)	Poisson's ratio	Cohesive strength/MPa
Loess layer	235	0.20	18.70	36.2	0.31	0.50
Fine sandstone	3,310	1.38	24.31	41.0	0.29	2.15
mudstone	3,510	1.23	24.37	39.0	0.35	1.25
Medium grained sandstone	4,705	1.29	25.14	39.0	0.37	4.03
Silty sandstone	4,315	1.31	24.38	43.0	0.40	3.27
coal seam	2,560	0.24	13.56	39.5	0.39	0.69
baseboard	4,730	18.8	23.88	38.7	0.35	3.58

movement and deformation of the whole slope. Under the coupling effect of different loess slope shapes and coal seam overburden structure, the subsidence coefficients among the models are also obviously different, so the $q_{slope\ average}$ is used to analyze the loess slope movement and deformation.

4.1.1 Influence of overlying strata structure on average subsidence coefficient of slope surface

4.1.1.1 Influence of sand layer coefficient on average subsidence coefficient of slope surface

According to the data in Table 2 and Figure 3 is drawn, as shown in the figure below.

From Table 1 and Figure 3, it can be seen that under any coupling type of loess slope surface shape and sand-mud ratio of coal seam overburden, the $q_{slope\ average}$ will show an increasing trend with the increase of sand layer coefficient. Specifically:

Under the coupling effect of "sand-mud ratio of coal seam overburden is 6:4+arbitrary slope shape and natural slope ≤45°", with the sand bed coefficient increasing from 0.67 to 0.71, the increase range of straight slope's $q_{slope\ average}$ is 2.86%–5.80%, the increase range of concave slope's $q_{slope\ average}$ is 4.48%–7.14%, the increase range of convex slope's $q_{slope\ average}$ is 4.23%–7.25%, and that of compound slope is 4.35%–5.80%. Under the coupling effect of "sand-mud ratio of coal seam overburden is 8: 2+arbitrary slope shape and natural slope ≤45°", with the sand layer coefficient increasing from 0.67 to 0.71, the increase range of straight slope's $q_{slope\ average}$ is 3.17%–5.88%, the increase range of concave slope's $q_{slope\ average}$ is 3.08%–7.14%, the increase range of convex slope's $q_{slope\ average}$ is 4.84%–7.94%, and that of compound slope is 4.62%–6.35%. However, under the coupling effect of "sand-mud ratio of overlying strata in any coal seam+arbitrary slope shape of surface and natural slope ≤45°", with the increase of sand bed coefficient from 0.71 to 0.75, the $q_{slope\ average}$ has no obvious change and gradually tends to be stable. Therefore, it can be seen that the $q_{slope\ average}$ is obvious when the sand layer coefficient of coal seam overburden is ≤0.71, but the $q_{slope\ average}$ is stable after the sand layer coefficient is >0.71.

Under the coupling effect of "sand-mud ratio of coal seam overburden is 6:4+arbitrary slope shape and natural slope ≤45°", with the sand bed coefficient increasing from 0.67 to 0.71, the

TABLE 2 Average subsidence coefficient and average displacement of loess slope after full mining.

Slope	Slope shape	The ratio of sand to mud is 6:4.									The ratio of sand to mud is 8:2.								
		Sand layer coefficient is 0.67			Sand layer coefficient is 0.71			Sand layer coefficient is 0.75			Sand layer coefficient is 0.67			Sand layer coefficient is 0.71			Sand layer coefficient is 0.75		
		$q_{slope}/q_{slope\ average}/u_{slope\ average}$(m)			$q_{slope}/q_{slope\ average}/u_{slope\ average}$(m)			$q_{slope}/q_{slope\ average}/u_{slope\ average}$(m)			$q_{slope}/q_{slope\ average}/u_{slope\ average}$(m)			$q_{slope}/q_{slope\ average}/u_{slope\ average}$(m)			$q_{slope}/q_{slope\ average}/u_{slope\ average}$(m)		
5°	Straight slope	0.81	0.70	0.43	0.85	0.72	0.52	0.87	0.72	0.59	0.76	0.64	0.41	0.81	0.67	0.47	0.82	0.69	0.51
	Concave slope	0.79	0.67	0.46	0.84	0.70	0.58	0.86	0.71	0.68	0.75	0.62	0.43	0.80	0.65	0.49	0.82	0.66	0.53
	Convex slope	0.82	0.71	0.42	0.86	0.74	0.46	0.88	0.74	0.48	0.77	0.65	0.40	0.82	0.69	0.45	0.84	0.70	0.46
	Compound slope	0.80	0.69	0.43	0.85	0.72	0.55	0.86	0.72	0.63	0.75	0.63	0.42	0.81	0.67	0.48	0.83	0.68	0.51
15°	Straight slope	0.77	0.59	0.92	0.80	0.61	0.96	0.83	0.62	1.01	0.72	0.55	0.88	0.76	0.58	0.94	0.77	0.59	0.98
	Concave slope	0.78	0.60	0.92	0.81	0.63	0.99	0.84	0.65	1.04	0.73	0.56	0.88	0.77	0.60	0.95	0.78	0.62	1.01
	Convex slope	0.75	0.54	0.87	0.79	0.57	0.92	0.80	0.58	0.97	0.70	0.51	0.86	0.74	0.54	0.89	0.76	0.55	0.92
	Compound slope	0.77	0.58	0.91	0.80	0.60	0.96	0.83	0.63	0.99	0.72	0.55	0.82	0.75	0.58	0.89	0.75	0.61	0.91
25°	Straight slope	0.77	0.65	1.40	0.81	0.68	1.48	0.82	0.69	1.53	0.72	0.63	1.30	0.76	0.65	1.45	0.78	0.66	1.50
	Concave slope	0.78	0.68	1.45	0.82	0.71	1.53	0.84	0.73	1.57	0.73	0.65	1.35	0.77	0.67	1.48	0.79	0.68	1.51
	Convex slope	0.75	0.61	1.37	0.80	0.65	1.48	0.81	0.66	1.53	0.70	0.56	1.25	0.75	0.60	1.41	0.76	0.62	1.48
	Compound slope	0.77	0.65	1.38	0.81	0.68	1.50	0.82	0.69	1.51	0.72	0.63	1.30	0.76	0.66	1.41	0.77	0.66	1.49
35°	Straight slope	0.76	0.69	1.61	0.80	0.73	1.73	0.83	0.75	1.78	0.71	0.66	1.57	0.75	0.69	1.65	0.78	0.70	1.71
	Concave slope	0.78	0.70	1.50	0.82	0.75	1.65	0.84	0.77	1.70	0.73	0.67	1.40	0.77	0.70	1.62	0.79	0.72	1.68
	Convex slope	0.75	0.64	1.72	0.79	0.68	1.86	0.80	0.68	1.90	0.70	0.62	1.71	0.74	0.65	1.82	0.76	0.66	1.88
	Compound slope	0.77	0.69	1.74	0.81	0.73	1.84	0.83	0.74	1.85	0.72	0.65	1.70	0.76	0.68	1.78	0.78	0.68	1.83
45°	Straight slope	0.77	0.72	1.70	0.80	0.76	1.92	0.82	0.78	2.06	0.72	0.68	1.68	0.76	0.72	1.90	0.78	0.72	1.92
	Concave slope	0.78	0.74	1.63	0.81	0.78	1.88	0.84	0.80	1.94	0.73	0.71	1.61	0.77	0.75	1.88	0.79	0.76	1.90
	Convex slope	0.75	0.69	1.89	0.79	0.74	2.06	0.81	0.75	2.14	0.70	0.63	1.85	0.74	0.68	2.02	0.76	0.69	2.07
	Compound slope	0.76	0.71	1.80	0.80	0.75	1.98	0.82	0.77	2.11	0.71	0.68	1.74	0.75	0.72	1.94	0.77	0.73	1.97

10.3389/feart.2023.1273389

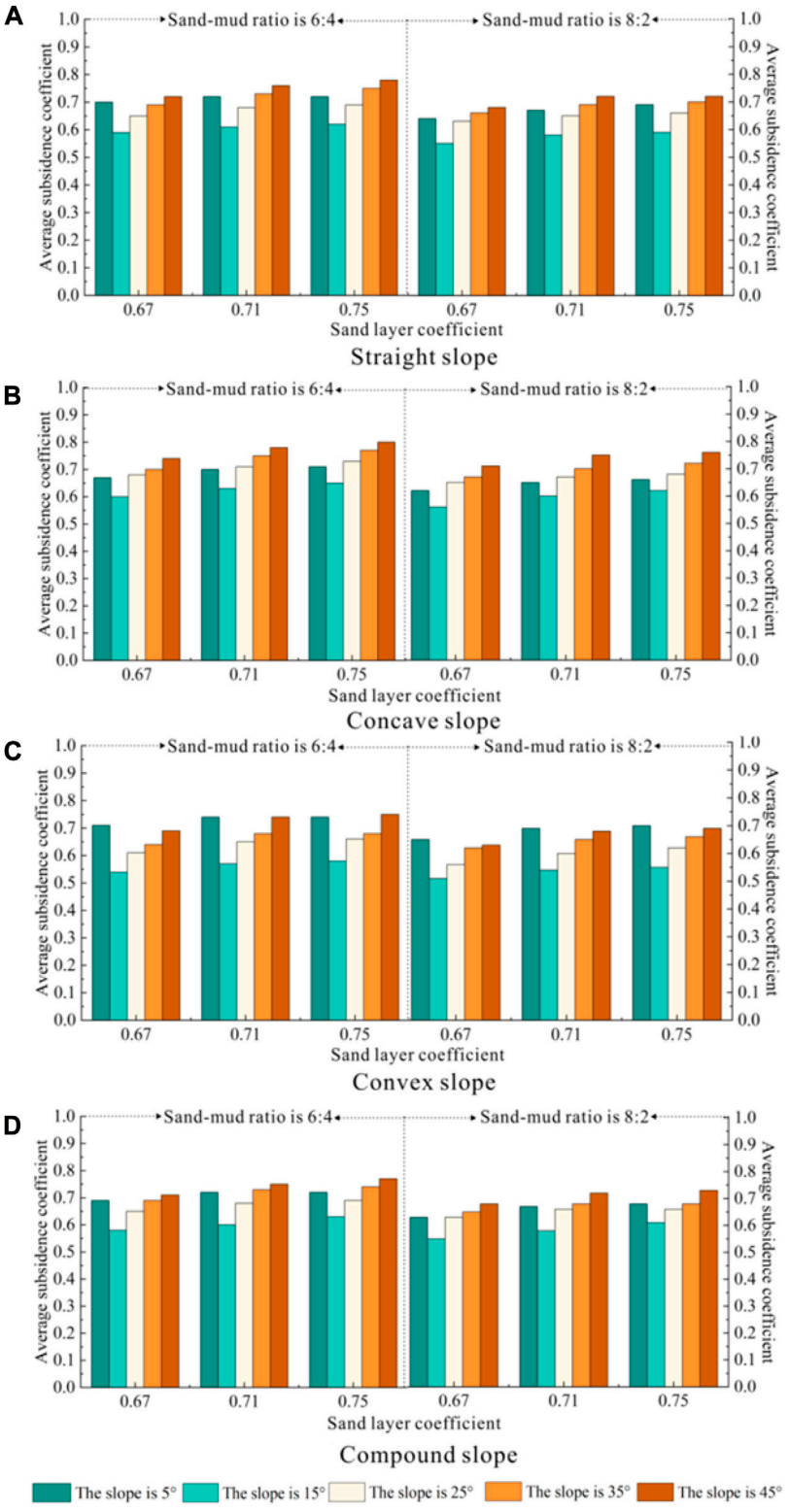

FIGURE 3
Comparison of average subsidence coefficient changes of slopes with different slopes under the coupling effect of loess slope shape and sand-mud ratio of coal seam overlying strata [see Figures **(A–D)** for straight slopes, concave slopes, convex slopes and composite slopes].

increase speed of straight slope's $q_{slope\ average}$ is 0.5–1, the increase speed of concave slope's $q_{slope\ average}$ is 0.75–1.25, the increase speed of convex slope's $q_{slope\ average}$ is 0.75–1.25 and that of composite slope is 0.5–1. Under the coupling effect of "sand-mud ratio of coal seam overburden is 8:2+arbitrary slope shape and natural slope ≤45°", with the sand bed coefficient increasing from 0.67 to

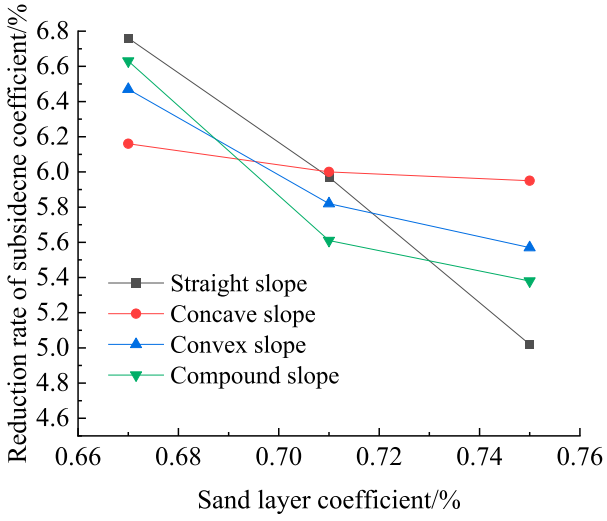

FIGURE 4
Comparison chart of decline rate of the $q_{slope\ average}$ with sand-mud ratio of 8:2 to 6:4.

0.71, the increase speed of straight slope's $q_{slope\ average}$ is 0.5–1, the increase speed of concave slope's $q_{slope\ average}$ is 0.5–1, the increase speed of convex slope's $q_{slope\ average}$ is 0.75–1.25 and that of composite slope is 0.75–1. However, under the coupling effect of "sand-mud ratio of overlying strata in any coal seam+arbitrary slope shape and natural slope ≤45°", with the increase of sand bed coefficient from 0.71 to 0.75, the increase speed of the $q_{slope\ average}$ has no obvious change and gradually tends to be stable. Therefore, it can be seen that the influence of the overburden sand coefficient of the coal seam on the $q_{slope\ average}$ is mainly manifested in two stages: when the overburden sand coefficient of the coal seam is ≤0.71, the increase speed of the $q_{slope\ average}$ is obvious, and it is sensitive to the change of the sand coefficient; When the overburden sand coefficient is >0.71, the increase speed of the $q_{slope\ average}$ does not change obviously, and the influence of the sand coefficient on the $q_{slope\ average}$ is weakened.

4.1.1.2 Influence of sand-mud ratio on average subsidence coefficient of slope surface

According to the data in Table 2, the comparison chart of the decline rate of the $q_{slope\ average}$ when the sand-mud ratio is 8:2 compared with the sand-mud ratio is 6:4 is drawn, as shown in Figure 4 below.

As can be seen from Table 2 and Figure 4, with the increase of overburden sand coefficient of the coal seam, the decline rate of the $q_{slope\ average}$ with sand-mud ratio of 8:2 is gradually reduced compared with that of the $q_{slope\ average}$ with sand-mud ratio of 6:4. Specifically, when the sand layer coefficient is 0.67, the corresponding decline rate of the $q_{slope\ average}$ is the largest, and the decline rates of straight slope, concave slope, convex slope and composite slope are 6.76%, 6.16%, 6.47%, and 6.63% in turn. When the sand coefficient is 0.71, the decline rates of the $q_{slope\ average}$ corresponding to the four slope shapes are 5.98%, 6.00%, 5.82%, and 5.61% in turn. When the sand layer coefficient is 0.75, the decline rate of the corresponding $q_{slope\ average}$ is the smallest, and the decline rates of the four slope shapes are 5.03%, 5.95%, 5.57%, and 5.38% respectively. It can be seen that the decline rate of the $q_{slope\ average}$ decreases with the increase of sand layer coefficient, and the greater the sand layer coefficient, the weaker the influence of sand-mud ratio on the $q_{slope\ average}$.

4.1.2 Influence of loess slope surface morphology on average subsidence coefficient of slope surface

4.1.2.1 Influence of slope gradient on average subsidence coefficient of slope surface

According to the data in Table 2, the average contrast map of the $q_{slope\ average}$ under the coupling effect of different coal seam overburden structure and loess slope shape is drawn, as shown in Figure 5 below. From Table 2 and Figure 5, it can be seen that under the coupling effect of loess slope gradient and coal seam overburden structure, the $q_{slope\ average}$ first decreases and then increases with the increase of loess slope gradient, specifically:

Under the coupling effect of "overburden sand coefficient of any coal seam and sand-mud ratio 6:4+arbitrary slope shape and natural slope ≤15°", with the natural slope increasing from 5° to 15°, the decline rate of the straight slope's $q_{slope\ average}$ is 13.89%–15.71%, the decline rate of the concave slope's $q_{slope\ average}$ is 8.45%–10.45%, the decline rate of the convex slope's $q_{slope\ average}$ is 21.62%–23.94%, and that of the compound slope is 12.50%–15.94%. Under the coupling effect of "overburden sand coefficient of any coal seam and sand-mud ratio 8:2+arbitrary slope shape and natural slope ≤15°", with the natural slope increasing from 5° to 15°, the decline rate of the straight slope's $q_{slope\ average}$ is 13.43%–14.49%, the decline rate of the concave slope's $q_{slope\ average}$ is 6.06%–9.68%, the decline rate of the convex slope's $q_{slope\ average}$ is 21.43%–21.74%, and that of the compound slope is 10.29%–13.43%. It can be seen that when the natural slope is ≤15°, the $q_{slope\ average}$ decreases with the increase of slope, and reaches the minimum when the slope is 15°.

Under the coupling effect of "overburden sand coefficient of any coal seam and sand-mud ratio 6:4+arbitrary slope shape of the surface and 15° < natural slope ≤45°", with the increase of natural slope from 15° to 45°, the increase rate of straight slope's $q_{slope\ average}$ is 10.77%–13.04%, the increase rate of concave slope's $q_{slope\ average}$ is 8.82%–9.86%, and the increase rate of convex slope's $q_{slope\ average}$ is 13.11%–13.85%, and that of compound slope is 9.23%–11.59%. Under the coupling effect of "overburden sand coefficient of arbitrary coal seam and sand-mud ratio of 8:2+arbitrary slope shape of surface and 15° < natural slope ≤45°", with the increase of natural slope from 15° to 45°, the increase rate of straight slope's $q_{slope\ average}$ is 7.94%–10.77%, the increase rate of concave slope's $q_{slope\ average}$ is 9.23%–11.94%, and the increase rate of convex slope's $q_{slope\ average}$ is 11.29%–13.33%, and that of compound slope is 7.94%–10.61%. It can be seen that the $q_{slope\ average}$ increases with the increase of slope when "15° < natural slope ≤45°", and reaches the maximum when the slope is 45°.

4.1.2.2 Influence of slope shape on average subsidence coefficient of slope surface

According to the data in Table 2, the average contrast map of the $q_{slope\ average}$ under the coupling effect of different coal seam

10.3389/feart.2023.1273389

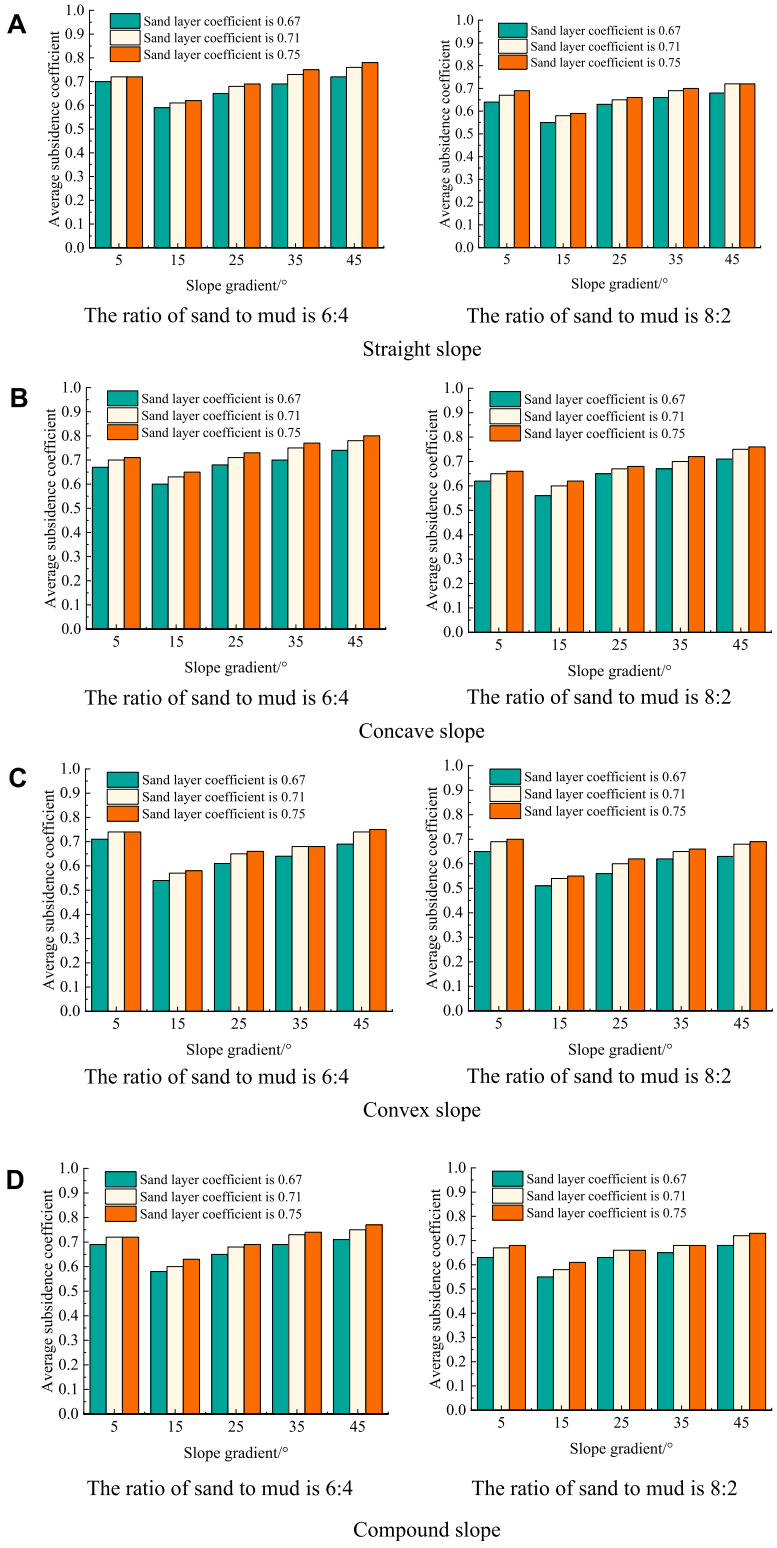

FIGURE 5
Comparison chart of average subsidence coefficient changes under the coupling effect of overburden structure of coal seam (sand-mud ratio of 6:4 is shown on the left and sand-mud ratio of 8:2 is shown on the right) and loess slope surface [straight slope, concave slope, convex slope and composite slope are shown in Figures **(A–D)**].

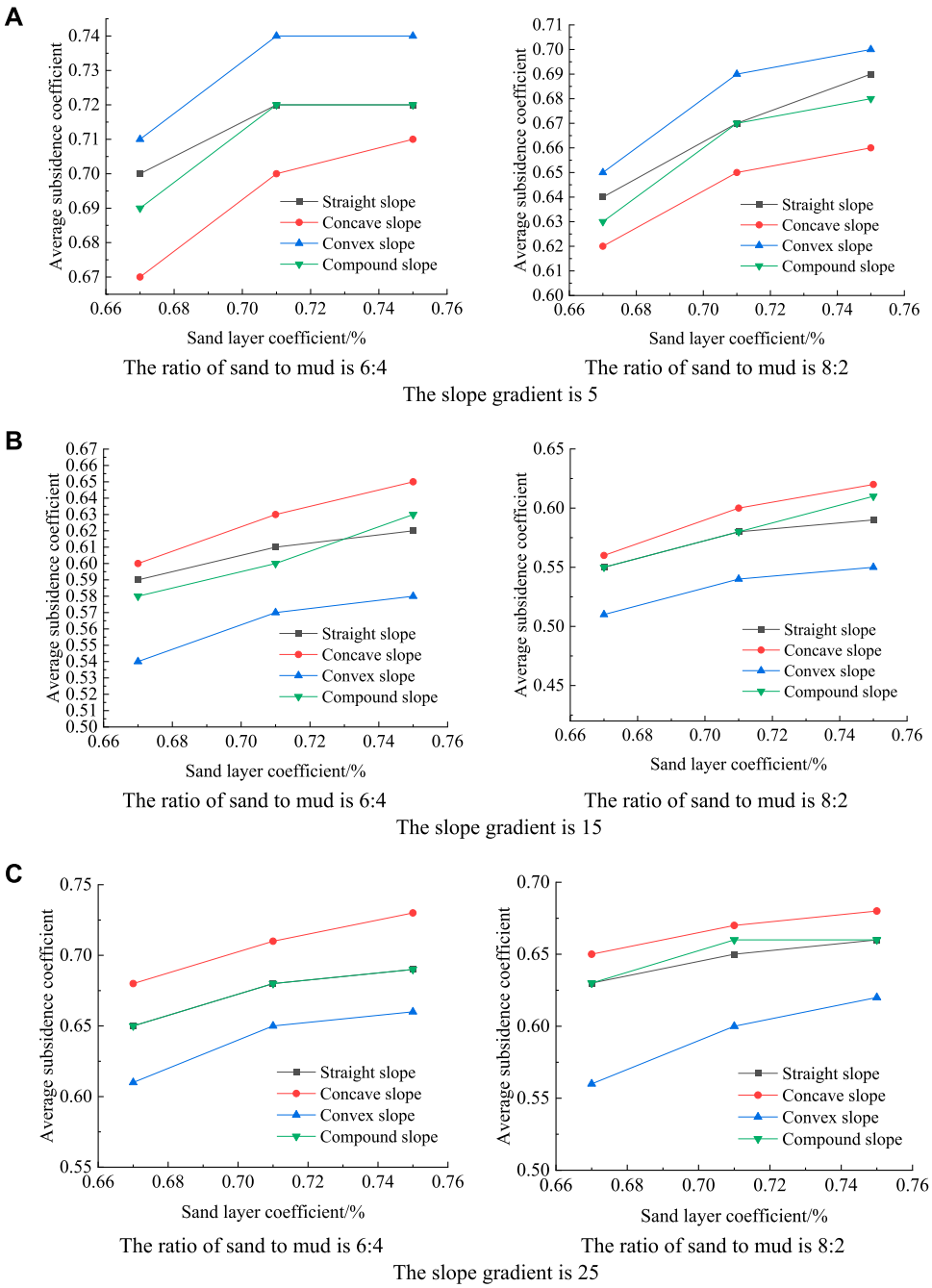

FIGURE 6
(Continued)

overburden structure and loess slope surface gradient is drawn, as shown in Figure 6.

From Table 2 and Figure 6, it can be seen that under the coupling effect of loess slope shape and coal seam overburden structure, the change law of the $q_{slope\ average}$ is different, specifically:

Under the coupling effect of "overburden sand coefficient of any coal seam and sand-mud ratio of 6:4+arbitrary slope shape and natural slope of 5°", with the sand coefficient increasing from 0.67 to 0.71, the $q_{slope\ average}$ of straight slope is 0.7, 0.72 and 0.72, the $q_{slope\ average}$ of concave slope is 0.67, 0.70 and 0.71, and the $q_{slope\ average}$ of convex slope is 0.71, 0.74,0.74, the $q_{slope\ average}$ of compound slope is 0.69, 0.72 and 0.72. Under the coupling effect of "overburden sand coefficient of any coal seam and sand-mud ratio of 8:2+arbitrary slope shape and natural slope of 5°", with the sand coefficient increasing from 0.67 to 0.71, the $q_{slope\ average}$ of straight slope is 0.64, 0.67 and 0.69, the $q_{slope\ average}$ of concave slope is 0.62, 0.65 and 0.66, and the $q_{slope\ average}$ of convex slope is 0.65, 0.69,0.70, the $q_{slope\ average}$ of compound slope is 0.63, 0.67 and 0.68. It can be seen that when the natural slope is ≤5°, the $q_{slope\ average}$ of convex slope is the largest, while that of concave slope is the smallest, and the q_{slope}

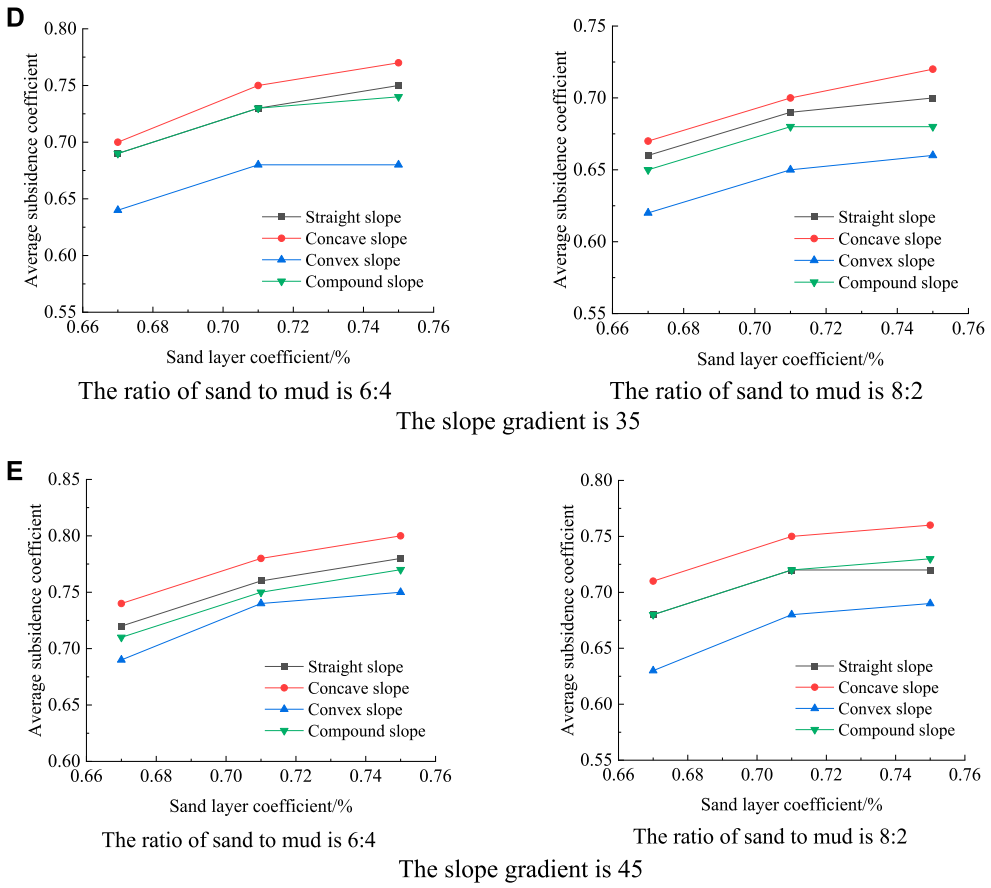

FIGURE 6
Comparison of the changes of the average subsidence coefficient of the slope under the coupling effect of the overburden structure of coal seam (sand-mud ratio of 6:4 is shown on the left, and sand-mud ratio of 8:2 is shown on the right) and the slope of loess slope [natural slopes are 5°, 15°, 25°, 35° and 45°, as shown in Figures **(A–E)** respectively].

$_{average}$ between straight slope and compound slope is not big, which has obvious homogeneity. The $q_{slope\ average}$ of four slopes is convex slope > straight slope ≈ compound slope > concave slope.

Under the coupling effect of "overburden sand coefficient of arbitrary coal seam and sand-mud ratio 6:4+arbitrary slope shape of surface and 5° < natural slope ≤45°", with the sand coefficient increasing from 0.67 to 0.71, the $q_{slope\ average}$ of straight slope is 0.66, 0.70 and 0.71, and the $q_{slope\ average}$ of concave slope is 0.68, 0.72, 0.74, the $q_{slope\ average}$ of convex slope is 0.62, 0.66, 0.67 and the $q_{slope\ average}$ of compound slope is 0.66, 0.69, 0.71. Under the coupling effect of "overburden sand coefficient of arbitrary coal seam and sand-mud ratio of 8:2+arbitrary slope shape of surface and 5° < natural slope ≤45°", with the sand coefficient increasing from 0.67 to 0.71, the $q_{slope\ average}$ of straight slope is 0.63, 0.66 and 0.67, and the $q_{slope\ average}$ of concave slope is 0.65, 0.68, 0.70 and the $q_{slope\ average}$ of convex slope is 0.58, 0.62, 0.63, and the $q_{slope\ average}$ of compound slope is 0.63, 0.66, 0.67. Therefore, when "5° < natural slope ≤45°", the $q_{slope\ average}$ of concave slope is the largest, the $q_{slope\ average}$ of convex slope is the smallest, and the $q_{slope\ average}$ between straight slope and compound slope is not big, which has obvious homogeneity. The $q_{slope\ average}$ of four slope types is as follows: concave slope > straight slope ≈ compound slope > convex slope.

4.1.3 Prediction model of influence of overlying strata structure and surface slope shape on average subsidence coefficient

Using multivariate nonlinear fitting method, the prediction model of average subsidence coefficient of slope under the coupling effect of overburden structure and slope shape under four kinds of slope shapes is constructed, as shown in Formulas (1)–(4).

$$\text{Straight slope: } q_{slope\ average} = -7.541 + 4.581\alpha + 8.831\beta - 0.01S - 0.834\alpha^2 - 5.938\beta^2 - 0.01\alpha\beta + 0.006\beta S \quad (1)$$

$$R^2 = 0.717$$

$$\text{Concave slope: } q_{slope\ average} = -7.554 + 4.586\alpha + 8.613\beta - 0.006S - 0.832\alpha^2 - 5.625\beta^2 - 0.04\alpha\beta + 0.004\beta S \quad (2)$$

$$R^2 = 0.846$$

$$\text{Convex slope: } q_{slope\ average} = -7.953 + 3.539\alpha + 13.249\beta - 0.014S - 0.65\alpha^2 - 9.063\beta^2 + 0.03\alpha\beta + 0.005\beta S \quad (3)$$

$$R^2 = 0.697$$

Compound slope: $$q_{slope\ average} = -7.927 + 4.55\alpha + 9.862\beta - 0.007S - 0.829\alpha^2 - 6.563\beta^2 - 0.01\alpha\beta + 0.002\beta S \quad (4)$$

R^2=0.726

Where: α: sand-mud ratio; β: sand layer coefficient, %; S: natural slope of loess slope, °.

The mining area in northern Shaanxi, China is mainly hilly and gully landform of the Loess Plateau, with complex topography, obvious surface undulation and complex slope morphology. Under this complex terrain condition, the influence of terrain factors on mining subsidence can not be ignored. However, at this stage, scholars at home and abroad have not fully considered and studied this issue. Therefore, we take into account the complex terrain factors in the mining area of northern Shaanxi, China, and construct a prediction equation for the influence of the coupling effect of underground overburden structure and the shape of the upper slope on the average subsidence coefficient of the surface slope. This can provide a new idea and method for surface movement prediction under complex terrain factors in northern Shaanxi mining area.

4.2 Influence of coal mining subsidence on average horizontal movement of slope surface

4.2.1 Influence of overlying strata structure on average horizontal movement of slope surface

According to the data in Table 2, the influence of the overlying strata structure of coal seam on the horizontal movement of slope surface is the same as that on the subsidence of slope surface, and the main laws are as follows:

Under the coupling effect of "sand-mud ratio of coal seam overburden is 6:4+arbitrary slope shape and natural slope ≤45°", with the sand layer coefficient increasing from 0.67 to 0.71, the $u_{slope\ average}$ of straight slope increases by 5.27%–22.50%, the $u_{slope\ average}$ of concave slope increases by 5.38%–26.18%, and the $u_{slope\ average}$ of convex slope increases by 5.38%–10.76%, the $u_{slope\ average}$ of compound slope increases by 5.94%–27.41%. Under the coupling effect of "sand-mud ratio of overlying strata in coal seam is 8:2+arbitrary slope shape and natural slope ≤45°", with the sand layer coefficient increasing from 0.67 to 0.71, the $u_{slope\ average}$ of straight slope increases by 4.58%–14.72%, the $u_{slope\ average}$ of concave slope increases by 8.05%–16.70%, and the $u_{slope\ average}$ of convex slope increases by 3.78%–13.15%, the $u_{slope\ average}$ of compound slope increases by 5.04%–13.03%. However, under the coupling effect of "sand-mud ratio of overlying strata in any coal seam+arbitrary slope shape of the surface and natural slope ≤45°", with the increase of sand bed coefficient from 0.71 to 0.75, the increase rate of $u_{slope\ average}$ no longer changes obviously and tends to be stable gradually. It can be seen from this that when the sand layer coefficient of coal seam overburden is ≤0.71, the $u_{slope\ average}$ increases obviously, but when the sand layer coefficient is >0.71, the $u_{slope\ average}$ does not change obviously and tends to be stable.

The main influence law of sand-mud ratio of coal seam overlying strata is: the $u_{slope\ average}$ shows a decreasing trend with the increase of sand-mud ratio of coal seam overlying strata, which is the same as the influence law of sand-mud ratio of coal seam overlying strata on the $q_{slope\ average}$.

4.2.2 Influence of surface slope morphology on average horizontal movement of slope

According to the data in Table 2, it can be seen that the influence of the loess slope surface shape on slope horizontal movement mainly has the following main laws:

Under the coupling effect of "overburden sand coefficient of arbitrary coal seam and sand-mud ratio of 6:4+arbitrary slope shape of surface and natural slope ≤45°", with the natural slope increasing from 5° to 45°, the $u_{slope\ average}$ of straight slope at 45° is increased by 1.06–1.16 times compared with the $u_{slope\ average}$ of straight slope at 5°–35°, and that of concave slope at 45° is increased by 1.08–1.14 times compared with the slope at 5°–35°. The $u_{slope\ average}$ of convex slope with gradient of 45° is increased by 1.09–1.13 times compared with that of 5°–35°, and the $u_{slope\ average}$ of composite slope with gradient of 45° is increased by 1.03–1.14 times compared with that of 5°–35°. Under the coupling effect of "overburden sand coefficient of any coal seam and sand-mud ratio of 8:2+arbitrary slope shape of the surface and natural slope ≤45°", with the natural slope increasing from 5° to 45°, the $u_{slope\ average}$ of straight slope at 45° is increased by 1.07–1.15 times compared with the $u_{slope\ average}$ of straight slope at 5°–35°, and that of concave slope at 45° is increased by 1.13–1.16 times compared with the slope at 5°–35°. The $u_{slope\ average}$ of convex slope with gradient of 45° is increased by 1.08–1.11 times compared with that of 5°–35°, and the $u_{slope\ average}$ of composite slope with gradient of 45° is increased by 1.03–1.09 times compared with that of 5°–35°. Therefore, under the coupling effect of "overburden sand coefficient of any coal seam and sand-mud ratio+arbitrary slope shape of the surface and natural slope ≤45°", the $u_{slope\ average}$ increases with the increase of loess slope surface slope, and reaches the maximum when the slope is 45°.

The main influence law of loess slope shape on the $u_{slope\ average}$ is: when the overlying strata characteristics and natural slope of any coal seam are less than 35°, the concave slope's $u_{slope\ average}$ is the largest after coal mining subsidence, and when the overlying strata characteristics and natural slope of any coal seam are more than or equal to 35°, the convex slope's $u_{slope\ average}$ is the largest after coal mining subsidence, which has obvious influence on the horizontal movement of slope.

5 Discussion

The increase of sandstone layers will directly lead to the increase of the main structural plane of coal seam overlying strata, which will not only lead to the decline of the overall strength of coal seam overlying strata (Liu Z. J. et al., 2022; Wang et al., 2022), but also weaken the anti-interference ability of coal seam overlying strata to underground mining disturbance. Song et al. (2014) found that when the sand layer coefficient of overlying strata of 2^{-2} coal seam in northern Shaanxi mining area is less than 0.7, the surface subsidence coefficient will increase rapidly with the increase of sand layer coefficient, and when the sand layer coefficient is greater than 0.7, the surface subsidence coefficient tends to be stable. Therefore, under the condition of the same thickness of bedrock,

the subsidence coefficient of surface and slope caused by the same underground coal mining disturbance will increase with the increase of sand layer coefficient, and the development degree of surface coal mining subsidence will continue to improve. In addition, the proportional relationship between the thickness of hard rock and soft rock in coal seam overburden, that is, the sand-mud ratio, will also significantly affect the movement and deformation characteristics of the surface and slope. Song et al. (2014) found that when the sand layer coefficient is constant, the greater the sand-mud ratio, the smaller the surface subsidence coefficient. Qian (2008) found that the main key stratum in overlying strata controls the dynamic process of surface subsidence, and the fracture of the main key stratum will lead to the synchronous fracture of all overlying strata and the rapid subsidence of the surface, which will lead to the obvious increase and periodic change of subsidence speed and subsidence influence boundary. Xu et al. (2007) found that when the lithology changes from soft to hard, the plastic expansion zone is less easily compressed and the surface subsidence coefficient decreases accordingly. This is consistent with the results of this study. It can be seen that the smaller the sand-mud ratio of overlying strata, the thinner the total thickness of sandstone in overlying strata, the weaker the anti-disturbance ability of overlying strata as a whole, and the more intense the movement and deformation caused by the same coal mining subsidence. This may be one of the reasons why the smaller the sand-mud ratio of overlying strata is, the greater the surface subsidence coefficient is.

The negative correlation between slope gradient and slope stability has become a recognized fact. Zhu et al. (2020) used three methods to calculate and analyze the stability of 76 loess slope models with different slopes, and found that the stability coefficient of loess slope decreased with the increase of slope, and the change was most obvious when the slope was less than 55°. Based on the shaking table model test of soil slope model, Tang W. M. et al. (2019) found that under the dynamic load, the greater the slope of soil slope, the stronger the amplification effect of slope acceleration, and the more obvious the signs of deformation and failure of slope. Zhang et al. (2007) found that the slope obviously changed the stress distribution of loess slope, which made the safety factor of slope decrease with the increase of slope, showing an obvious logarithmic relationship. Katz et al. (2014) used the numerical two-dimensional discrete element method to find that the increase of slope will lead to the increase of slope movement size, and then increase the risk of slope movement. Qiu et al. (2018) based on the data of 275 loess landslides in Zhidan County, the central part of China Loess Plateau, and found that the slope gradient indirectly affected the size of slope movement through the slope length. Xi et al. (2021) extracted the slope information of coal mining subsidence area through DEM, and found that coal mining subsidence can increase the slope of surface slope. While Huang et al. (2014) found that coal mining subsidence can reduce the slope length of loess slope by using digital terrain analysis and remote sensing image fusion, which is consistent with the results of this study. Therefore, no matter what slope shape the loess slope is, the greater the slope is, the smaller the stability is, and the more intense the movement and deformation will be under the influence of the same coal mining subsidence, which may be one of the important reasons why the loess slope with any slope shape in this study will increase the slope and decrease the slope length after subsidence. More interestingly, the greater the natural slope of loess slope, the greater the slope increment after subsidence, but the smaller the slope length decline. This provides a new proposition for further study on the characteristics and laws of surface loess slope movement and deformation in coal mining subsidence area. The influence of slope shape on slope stability is still controversial. Tang W. M. et al. (2019) found that slope shape has great influence on slope deformation and failure, and concave slope is less prone to instability and failure than straight slope and convex slope, but the upper part of concave slope usually has a large slip phenomenon. Huang (2017) used small-scale shaking table test and FLAC^{3D} numerical simulation research to find that if the first longitudinal crack at the top of the slope is taken as the standard, the stability of convex slope is the worst, followed by straight slope and concave slope is the most stable. Gao (1993) found that concave slopes with medium height and steep slope are more prone to movement and deformation through remote sensing interpretation. However, this study found that under the same influence of coal mining subsidence, when the natural slope is less than 5°, the movement and deformation of convex slope is the largest, while when the natural slope is more than 5°, the movement and deformation of concave slope is the most obvious. It shows that under the special dynamic load of coal mining subsidence, the influence of slope shape on slope stability and movement deformation degree is closely related to slope. This provides a new insight for scientific understanding of the stability, movement and deformation characteristics of surface loess slope in coal mining subsidence area.

6 Conclusion

Under any surface slope shape, the $q_{slope\ average}$ after coal mining subsidence increases with the increase of overlying sand coefficient of coal seam, and it mainly shows two stages. The first stage: when the sand coefficient is ≤0.71, the $q_{slope\ average}$ is obvious, showing a rapid growth trend, and the increase range is between 2.86% and 7.94%; The second stage: after "sand coefficient >0.71", the $q_{slope\ average}$ no longer changes obviously and tends to be stable gradually. Under any surface slope shape, the $q_{slope\ average}$ after coal mining subsidence decreases with the increase of sand-mud ratio of coal seam overlying strata, and the decline rate of the $q_{slope\ average}$ with sand-mud ratio of 8:2 is greater than 5.03% compared with that with sand-mud ratio of 6:4, that is, the smaller the sand-mud ratio of coal seam overlying strata, the more obvious the influence on loess slope subsidence.

When the overburden structure characteristics of any coal seam and the natural slope of the surface slope are less than or equal to 5°, the $q_{slope\ average}$ of the convex slope is the largest after coal mining subsidence, and the $q_{slope\ average}$ of the four slope types is ranked as follows: convex slope > straight slope ≈ compound slope > concave slope; When the overburden structure characteristics of any coal seam and the surface slope are 5° < natural slope ≤45°, the $q_{slope\ average}$ of the concave slope is the largest after coal mining subsidence, and the $q_{slope\ average}$ of the four slopes is in the order of concave slope > straight slope ≈ compound slope > convex slope, that is,

"convex slope with natural slope ≤5° and concave slope with natural slope ≤45°" has great influence on loess slope surface subsidence. With the increase of natural slope after coal mining subsidence, the $q_{slope\ average}$ first decreases and then increases with the increase of natural slope, and the inflection point is 15°. When the natural slope is less than 15°, the $q_{slope\ average}$ decreases with the increase of natural slope, reaches the minimum value when the natural slope is 15°, and when "15° ≤ natural slope ≤45°", the $q_{slope\ average}$ increases with the increase of natural slope, and reaches the maximum value when the natural slope is 45°, and the difference between the maximum value and the minimum value is greater than 22.03%. Based on the basic principle of multivariate nonlinearity, the prediction equation of the $q_{slope\ average}$ with the increase of sand layer coefficient under the coupling effect of loess slope surface shape and coal seam overburden structure is constructed.

The influence of structural characteristics of coal seam overlying strata on the horizontal movement of loess slope is the same as that of subsidence, that is, the horizontal movement of loess slope is stronger after coal mining subsidence under any surface slope shape and when the sand coefficient of coal seam overlying strata is ≤0.71, and the increase rate of $u_{slope\ average}$ is 5.04%–27.41%, and the $u_{slope\ average}$ is no longer obvious after the sand coefficient is >0.71; Under any surface slope shape, the $u_{slope\ average}$ after coal mining subsidence decreases with the increase of sand-mud ratio of overlying strata in coal seam. Under any structural characteristics of coal seam overburden and any slope shape of surface slope, the $u_{slope\ average}$ increases with the increase of natural slope after coal mining subsidence, and reaches the maximum when the natural slope is 45°, which is more than 1.03 times of the natural slope of 5°–35°. When the overlying strata structure characteristics and natural slope of any coal seam are less than 35°, the $u_{slope\ average}$ of concave slope is the largest after coal mining subsidence, and when the overlying strata structure characteristics and natural slope of any coal seam are more than or equal to 35°, the $u_{slope\ average}$ of convex slope is the largest after coal mining subsidence, which has obvious influence on the horizontal movement of slope.

Data availability statement

The datasets presented in this study can be found in online repositories. The names of the repository/repositories and accession number(s) can be found in the article/Supplementary Material.

Author contributions

BZ: Writing–original draft, Conceptualization, Data curation, Investigation, Methodology, Software. SS: Writing–review and editing, Conceptualization, Methodology. XC: Investigation, Writing–review and editing. RN: Investigation, Writing–review and editing. XC: Data curation, Writing–review and editing. HR: Supervision, Writing–review and editing. GL: Validation, Writing–review and editing.

Funding

The author(s) declare financial support was received for the research, authorship, and/or publication of this article. This work was supported by 2022 Special Fund project of Shaanxi Key Laboratory of Geological Support for Coal Green Development (grant no. DZBZ2022Z-03), the Key Research and Development Program of Shaanxi Province (grant no. 2023-YBSF-458).

Acknowledgments

The author greatly appreciated that the constructive comments from the editors and reviewers.

Conflict of interest

GL was employed by the Shanxi Water Group Construction Investment Co., Ltd.

The remaining authors declare that the research was conducted in the absence of any commercial or financial relationships that could be construed as a potential conflict of interest.

Publisher's note

References

Fang, J., Li, Q. S., Du, W. F., and Cao, Z. G. (2016). Water disaster control in overlying thick loose layer on bedrock in Shendong coal mining area. *Coal Geol. Explor.* 44 (4), 94–97. doi:10.3969/j.issn.1001-1986.2016.04.018

Gao, J. (1993). Identification of topographic settings conducive to landsliding from dem in Nelson county, Virginia, U.S.A. *Earth Surf. Process. Landforms* 18, 579–591. doi:10.1002/esp.3290180702

Huang, Y., Wang, Y., Wang, M., Tian, F., and Ao, J. (2014). Effect of mining subsidence on soil erosion in mountainous area of the Loess Plateau. *Trans. Chin. Soc. Agric. Eng.* 30 (1), 228–235. doi:10.3969/j.issn.1002-6819.2014.01.029

Huang, Z. W. (2017). *Stability analysis of concave and convex slopes under earthquake*. Chongqing University.

Katz, O., Morgan, J. K., Aharonov, E., and Dugan, B. (2014). Controls on the size and geometry of landslides: insights from discrete element numerical simulations. *Geomorphology* 220, 104–113. doi:10.1016/j.geomorph.2014.05.021

Li, J. M., Yu, J. H., and Zhang, W. Z. (2019). Spatial distribution and governance of coal-mine subsidence in China. *J. Nat. Resour.* 34 (4), 867. doi:10.31497/zrzyxb.20190415

Li, S. Z. (2019). Control practices and countermeasure analysis on coal subsidence area in China. *Coal Sci. Technol.* 47 (1), 36–43. doi:10.13199/j.cnki.cst.2019.01.005

Liu, Z., Han, L., Wang, D. Y., Liu, Z. H., and Chen, R. (2021). Soil physicochemical properties and quality assessment in the coal mining area of Loess Plateau in Northern Shaanxi Province. *J. China Coal Soc.* 46 (05), 1555–1564. doi:10.13225/j.cnki.jccs.ST21.8216

Liu, F., Guo, L. F., and Zhao, L. Z. (2022a). Research on coal safety range and green low-carbon technology path under the dual-carbon background. *J. China Coal Soc.* 47 (01), 1–15. doi:10.13225/j.cnki.jccs.yg22.0016

Liu, Z. J., Qiu, H. J., Zhu, Y. R., Liu, Y., Yang, D. D., Ma, S. Y., et al. (2022b). Efficient Identification and Monitoring of Landslides by Time-Series InSAR Combining Single- and Multi-Look Phases. *Remote Sens.* 14 (4), 1026. doi:10.3390/rs14041026

Ma, S. Y., Qiu, H. J., Zhu, Y. R., Yang, D. D., Tang, B. Z., Wang, D. Z., et al. (2023). Topographic Changes, Surface Deformation and Movement Process before, during and after a Rotational Landslide. *Remote Sens.* 15 (3), 662. doi:10.3390/rs15030662

Pei, Y. Q., Qiu, H. J., Yang, D. D., Liu, Z. J., Ma, S. Y., Li, J. Y., et al. (2023). Increasing landslide activity in the Taxkorgan River Basin (eastern Pamirs Plateau, China) driven by climate change. *Catena* 223, 106911. doi:10.1016/j.catena.2023.106911

Qian, M. G. (2008). On Scienized Coal Mining. *China coal.* (08), 5–10+20. doi:10.19880/j.cnki.ccm.2008.08.001

Qiu, H. J., Cui, P., Regmi, A. D., Hu, S., Wang, X. G., and Zhang, Y. Z. (2018). The effects of slope length and slope gradient on the size distributions of loess slides: field observations and simulations. *Geomorphology* 300, 69–76. doi:10.1016/j.geomorph.2017.10.020

Qiu, H. J., Zhu, Y. R., Zhou, W. Q., Sun, H. S., He, J. Y., and Liu, Z. J. (2022). Influence of DEM resolution on landslide simulation performance based on the Scoops3D model. *Geomatics Nat. Hazards Risk* 13 (1), 1663–1681. doi:10.1080/19475705.2022.2097451

Shang, J. X., Gao, Y. K., Yang, F., Bi, Y. L., Quan, W. Z., and Ma, S. P. (2022). Landscape planning model design and layout of loess hills in coal mining area of northern Shaanxi:A study of the subsidence area of Ningtioata Coal Mine. *Coal Geol. Explor.* 50 (07), 128–137. doi:10.12363/issn.1001-1986.21.11.0659

Shao, X. P., Li, X. J., Wu, J. T., and Yang, W. H. (2015). Simulation Study of Overlying Strata Movement Laws at Layer Mining in Northern Shaanxi Local Coal Mines Lying Protected Areas. *Coal Technol.* 34 (06), 1–4. doi:10.16865/j.cnki.1000-7555.2021.0217

Shen, Y. J., Yang, B. H., Wang, S. M., Kou, H. B., Chen, X., and Xu, Y. L. (2022). Typical characteristics of geological hazards and ecological environment of coal base in the bends area of the Yellow River. *Coal Geol. Explor.* 50 (6), 104–117. doi:10.12363/issn.1001-1986.21.12.0887

Song, S. J., Zhao, X. G., Xie, J., and Guan, Y. Y. (2011). "Grey Correlation Analysis and Regression Estimation of Mining Subsidence in Yu-Shen-Fu Mining Area," in 3rd International Conference on Environmental Science and Information Application Technology (ESIAT), AMSTERDAM, 1747–1752. doi:10.1016/j.proenv.2011.09.274

Song, S. J., Zhao, X. G., and Wang, S. M. (2014). Influence of Sandsone Layer Coefficient in Coal Overburden on Mining Subsidecne. *Saf. Coal Mines* 45 (11), 60–63. doi:10.2991/isesce-15.2015.31

Song, S. J., Zhao, X. G., Zhang, Y., and Nie, W. J. (2016). Analyzing the Effect of the Mining Depth on the Shape and Erosion of Surface Slope in Coal Mining Area. *Environ. Sci. Technol.* 39 (08), 178–184. doi:10.3969/j.issn.1003-6504.2016.08.029

Song, S. J., Wang, S. M., Zhao, X. G., and Shen, T. (2018). Stratification transfer method of the mining subsidence based on the characteristics of layered structure in coal overburden. *J. China Coal Soc.* 43 (S1), 87–95. doi:10.13225/j.cnki.jccs.2017.3011

Song, S. J., Zhang, Y. L., Wang, S. M., Du, L., and Liu, M. N. (2021). Influence of mining ground fissures on soil microorganism and enzyme activities in Northern Shaanxi coal mining area. *J. China Coal Soc.* 46 (05), 1630–1640. doi:10.13225/j.cnki.jccs.st21.0203

Song, S. J., Du, L., Wang, S. M., and Sun, T. (2022). Variation of soil erodibility on loess slope under various subsidence years in coal mining subsidence area located Northern Shaanxi. *Coal Sci. Technol.* 50 (02), 289–299. doi:10.13199/j.cnki.cst.QNTK21-126

Song, S. J., Feng, Z. X., Sun, T., Zheng, B. B., and Wei, J. B. (2023a). Loess slope deformation and soil erosion effect in coal mining subsidence area of northern Shaanxi. *J. Xi'an Univ. Sci. Technol.* 43 (02), 301–311. doi:10.13800/j.cnki.xakjdxxb.2023.0210

Song, S. J., Peng, R. S., Wang, Y., Cheng, X., Niu, R. L., and Ruan, H. (2023b). Spatial distribution characteristics and risk assessment of soil heavy metal pollution around typical coal gangue hill located in Fengfeng Mining area. *Environ. Geochem. Health* 22. doi:10.1007/s10653-023-01530-x

Song, S. J., Sun, T., Du, L., Feng, Z. X., and Zheng, B. B. (2023c). Effects of Mining Ground Fissures of Different Shapes on Soil Erodibility in Northern Shaanxi Coal Mining Area Influence. *J. China Coal Soc.*, 1–14. 11.2190.td.20230303.1533.003.html.

Song, S. J., Sun, T., Zheng, B. B., Niu, R. L., Ruan, H., and Cheng, X. (2023d). Effect of coal mining subsidence on loess slope morphology and soil erosion in loess gully region of Northern Shaanxi. *Coal Sci. Technol.* 51 (02), 422–435. doi:10.13199/j.cnki.cst.2022-1913

Song, S. J., Zheng, B. B., Sun, T., Du, L., and Wei, J. B. (2023e). Influence of Different Mining Damage Types on Soil Erodibility in Coal Mining Areas of Northern Shaanxi in the Middle Reaches of the Yellow River in China. *Sustainability* 15 (6), 5434. doi:10.3390/su15065434

Tang, F. Q., Lu, J. X., and Li, P. F. (2019a). A prediction model for mining subsidence in loess-covered mountainous areas of western China. *Curr. Sci.* 116 (12), 2036–2043. doi:10.18520/cs/v116/i12/2036-2043

Tang, W. M., Ma, S. Z., Liu, X. L., and Zhao, X. (2019b). The influence of topographic and geomorphological conditions on the dynamic response of slope. *J. Yangtze River Acad. Sci.* 36 (11), 98–103+109. doi:10.11988/ckyyb.20180443

Tang, F. Q. (2011). Mining subsidence predicition model in western thick loess layer mining areas. *J. China Coal Soc.* 36 (S1), 74–78. doi:10.13225/j.cnki.jccs.2011.s1.025

Wang, S. M., Huang, Q. X., Fan, L. M., Yang, Z. Y., and Shen, T. (2010). Study on overburden aquclude and water protection mining regionazation in the ecological fragile mining area. *J. China Coal Soc.* 35 (01), 7–14. doi:10.13225/j.cnki.jccs.2010.01.007

Wang, G. F., Ren, S. H., Pang, Y. H., Qu, S. J., and Zheng, D. Z. (2021). Development achievements of China's coal industry during the 13th Five-Year Plan period and implementation path of "dual carbon" target. *Coal Sci. Technol.* 49 (09), 1–8. doi:10.13199/j.cnki.cst.2021.09.001

Wang, L. Y., Qiu, H. J., Zhou, W. Q., Zhu, Y. R., Liu, Z. J., Ma, S. Y., et al. (2022). The Post-Failure Spatiotemporal Deformation of Certain Translational Landslides May Follow the Pre-Failure Pattern. *Remote Sens.* 14 (10), 2333. doi:10.3390/rs14102333

Wang, F. (2020). *Analysis of the law of surface rock movement of coal mine goaf in northern Shaanxi*. Chang'an University. doi:10.26976/d.cnki.gchau.2020.001362

Xi, B. S., Gao, Y. G., Yang, B., Li, L., and Kong, W. J. (2021). Analysis of terrain change characteristics and disaster-causing points under mining disturbance in a mine in western mountainous area. *Metal. mine* 541 (07), 172–178. doi:10.19614/j.cnki.jsks.202107024

Xu, J. L., Lian, G. M., Zhu, W. B., and Qian, M. G. (2007). Influecne of the key strata in deep mining to mining subsidence. *J. China Coal Soc.* (07), 686–690. doi:10.13225/j.cnki.jccs.2007.07.003

Zhang, M., Sun, C. Y., Xiao, P. X., Wei, X. L., Huang, Y. L., and Lin, L. (2007). Detailed investigation and demonstration of geological disasters in Baota District, Yan 'an City. *Northwest Geol.* (02), 29–55. doi:10.3969/j.issn.1009-6248.2007.02.002

Zhang, B., Peng, S. P., Wang, T., and Song, M. (2019). Strategic Paths and Countermeasures for Constructing a "Great Power of Coal Resources". *Strategic Study CAE* 21 (1), 88–96. doi:10.15302/J-SSCAE-2019.01.013

Zhu, B. L., Wang, Y. S., and Wang, J. Q. (2020). Study on the variation law of loess slope stability coefficient with slope gradient. *Soil Water Conservation China* (08), 42–43. doi:10.14123/j.cnki.swcc.2020.0191

frontiers | Frontiers in Earth Science

TYPE Original Research
PUBLISHED 18 October 2023
DOI 10.3389/feart.2023.1287577

OPEN ACCESS

EDITED BY
Haijun Qiu,
Northwest University, China

REVIEWED BY
Lili Tan,
Yunnan University, China
Wenhua Qi,
China Earthquake Administration, China

*CORRESPONDENCE
Xianfu Bai,
282961394@qq.com
Zhiquan Yang,
yzq1983816@kust.edu.cn

RECEIVED 02 September 2023
ACCEPTED 04 October 2023
PUBLISHED 18 October 2023

CITATION
Bai X, Dai Y, Zhou Q and Yang Z (2023), An MDT-based rapid assessment method for the spatial distribution of trafficable sections of roads hit by earthquake-induced landslides.
Front. Earth Sci. 11:1287577.
doi: 10.3389/feart.2023.1287577

An MDT-based rapid assessment method for the spatial distribution of trafficable sections of roads hit by earthquake-induced landslides

Xianfu Bai[1,2]*, Yuqian Dai[3], Qingyun Zhou[1,2] and Zhiquan Yang[4]*

[1]Kunming Institute of Earthquake Prediction, China Earthquake Administration, Kunming, China, [2]Yunnan Earthquake Agency, Kunming, China, [3]Earthquake and Disaster Reduction Bureau of Xishan District, Kunming, China, [4]Faculty of Public Safety and Emergency Management, Kunming University of Science and Technology, Kunming, China

In mountainous areas, roads are often damaged by earthquake-induced landslides (EL). The degree of road damage and the existing functional state will have a very important impact on the whole earthquake relief work. However, this question has long been plaguing scientists engaged in the risk assessment. Now, an MDT-based rapid assessment method for the spatial distribution of trafficable sections of roads (TSR) hit by EL is proposed. The method mainly consists of three procedures: 1) Demarcate the road sections in the evaluated region; 2) Create the data for earthquake-induced landslide sensitivity level for the evaluated region; 3) Use the sample data to devise the MDT model for the TSR hit by EL and calculate the trafficability of road sections. This method was applied in the study of the 2008 Wenchuan Ms 8.0, the 2014 Ludian Ms 6.5, the 2012 Yiliang Ms 5.6 and Ms 5.7 earthquake-stricken regions. The case of Wenchuan earthquake was adopted to establish the method. The cares of Ludian and Yiliang were used to evaluate whether the method could be transplanted into similar regions. The *p-value* and the *kappa* coefficient were used to test and evaluate the significance and the consistence of the actual situation. Our results suggest: i) The Wenchuan evaluated region had the *p-value* 2.52×10^{-203} and the *kappa* coefficient 0.91. Less than 1% of the road sections that were inferred to be trafficable with the established method were actually interrupted by EL. The interruptions in the road sections that were inferred to be un-trafficable were 12 times of those in the other road sections. ii) The Ludian and Yiliang earthquake-stricken regions had the *p-value* 9.7×10^{-107} and the *kappa* coefficient 0.81. Only 1.31% of the road sections that were trafficable according to the calculation results of the model had been actually interrupted by EL. The interruptions caused by EL in the un-trafficable road sections according to the calculation results were 5.2 times of those in the trafficable road sections. This method could be applied in other similar regions when a certain error was permitted.

KEYWORDS

rapid assessment, road trafficability, earthquake-induced landslides, multivariate decision tree, model

1 Introduction

The spatial distribution of trafficable sections of roads (TSR) significantly affects emergency rescue decision-making, which impacts both the reduction of earthquake disaster losses and the regional planning for mitigating earthquake disasters. For instance, if the roads are damaged during an emergency rescue, the rescue team may be delayed, which can seriously delay the rescue of the injured in a timely manner (Lan et al., 2009; Chang, 2013; Yang et al., 2023a). An important part of earthquake emergency response is drawing up a plan of action for emergency rescue within a short time after the earthquake. Planning can be enhanced if it is supported by the simulation and analysis of seismic disasters including the prediction of expected road blockage caused by earthquake-induced landslides (EL). The Ministry of Emergency Management of the People's Republic of China undertakes rapidly assessing the impact of significant earthquakes occurring on the Chinese mainland before eyewitness reports have come in and informs the government in earthquake-stricken areas (including the transportation department, armies, and other departments) of the potential effects. The government's immediate plan for rescue and evacuation requires information about road blockage in the disaster area and suggestions from the Ministry of Emergency Management of the People's Republic of China about traffic management. Facing the need for information concerning a large area (the Chinese mainland), the assessment of EL disasters implemented by the Ministry of Emergency Management of the People's Republic of China must adopt methods based on correlation analysis and can at present only provide information on EL sensitivity. Recently, Dai achieved good results in rapid assessment of human death by landslide sensitivity information (Dai et al., 2022). This paper aims to add the capability of being able to predict road blockage using the existing earthquake-induced landslide sensitivity (ELS) data. Road trafficability (RT) during an earthquake event depends mainly on two natural factors. One factor is the ground motion, which causes direct damage to bridges, tunnels, and roadbeds. The other factor is the secondary geological disaster resulting from ELS and mud-rock flow, which destroys or buries roads. Substantial progress has been made in the development of techniques for the rapid assessment of roads directly damaged by ground motion. However, few studies have focused on the rapid assessment of TSR according to the secondary effects of earthquakes such as ELS. The C4.5 method based on the maximum information gain in the decision tree was introduced to explore the risk assessment of road interruptions based on the ELS in the high-intensity areas during the Wenchuan earthquake (An et al., 2015). The study revealed that the ELS level could be used to assess the trafficability of roads. In the C4.5 method, the ELS level was based on the intensity as a parameter of ground motion influence. Five levels of intensity corresponded with the values 1–5 in the landslide cell attribute. The study used the 90 m × 90 m raster data. In the study of the high-intensity areas during the Wenchuan earthquake, the influence on the number of cells was however tested only at a single ELS level for each child node in the decision tree. At the same time, the correlation between attributes, which existed extensively in an information system, was ignored, but it led to costly pruning in the decision tree model. The largest shortcoming was the poor universality of the findings in the study because of the absence of focus on low-intensity areas. To overcome the shortcoming wholly or partially, an MDT (Multivariate Decision Tree)-based rapid assessment method is proposed in this paper for the spatial distribution of TSR based on the ELS. In the method used in the study, the seismic intensity envelope of an assessed region is used to calculate and determine the spatial distribution of ELS levels. Subsequently, the number of cells in the raster data for each ELS level is calculated within the 180 m buffer zone on both sides of each road section. The MDT correlation between the number of cells at each landslide sensitivity level within the buffer zones of each road section and the trafficability of the road section is established to infer the spatial distribution of TSR. This method is established to provide a more universal and accurate way for quickly assessing the spatial distribution of TSR hit by EL. It is hoped that this method can meet the urgent need for quantitative information on the spatial distribution of TSR hit by EL while making decisions on emergency aid in an earthquake and for quantitatively assessing earthquake disasters. In some major projects such as the National Earthquake Social Service Engineering Emergency Response Program, the National Support Plan for Science and Technology, and the Earthquake Disaster Scenario Construction in Large and Medium Cities of China, the ELS was studied to generate the data set for the prediction of ELS level according to the influence of seismic intensities (Bai et al., 2015; Bai et al., 2021). The data set was used in the rapid assessment of ELS after an earthquake. It has 90 m × 90 m raster data displayed as cells in the computer. In terms of landslide probability, the landslide sensitivity of cells was categorized into five levels, that is, very low, low, medium, high, and very high, which correspondingly represent the cell attribute values 1, 2, 3, 4, and 5. The data for the prediction of landslide sensitivity had three key features: 1) it was 90 m × 90 m raster data; 2) it was predicted with the intensity as the parameter influencing ground motion; 3) landslide sensitivity was divided into five levels representing the cell attribute values 1–5 correspondingly. When the landslide sensitivity level of a region was higher, that is, there were more cells with high values, it would be more likely that the earthquake would cause landslides on a larger scale.

This paper is divided into six sections. In the second section, we describe the research areas and available data. The third section presents the basic idea of the rapid assessment method for the spatial distribution of TSR hit by the EL, as well as the MDT theoretical model. In the fourth section, the main results obtained with the method are described. The fifth section discusses the change to parameters and scope of applicability of the constructed method. The sixth section draws conclusions about the method and highlights the matters to which special attention should be paid.

2 The study areas and available data

2.1 Study areas

Situated at the southeast edge of the Qinghai–Tibet Plateau, the Sichuan–Yunnan region is affected by the eastward movement of crustal materials in the Tibet Plateau and the wedging Assam peak, causing its complicated crustal activity and intense neotectonic deformation and seismic activity. It is, therefore, the region most noticeably exposed to strong seismic activity in mainland China (Su et al., 2001). At 14:28 (Beijing time) on 12 May 2008, a strong

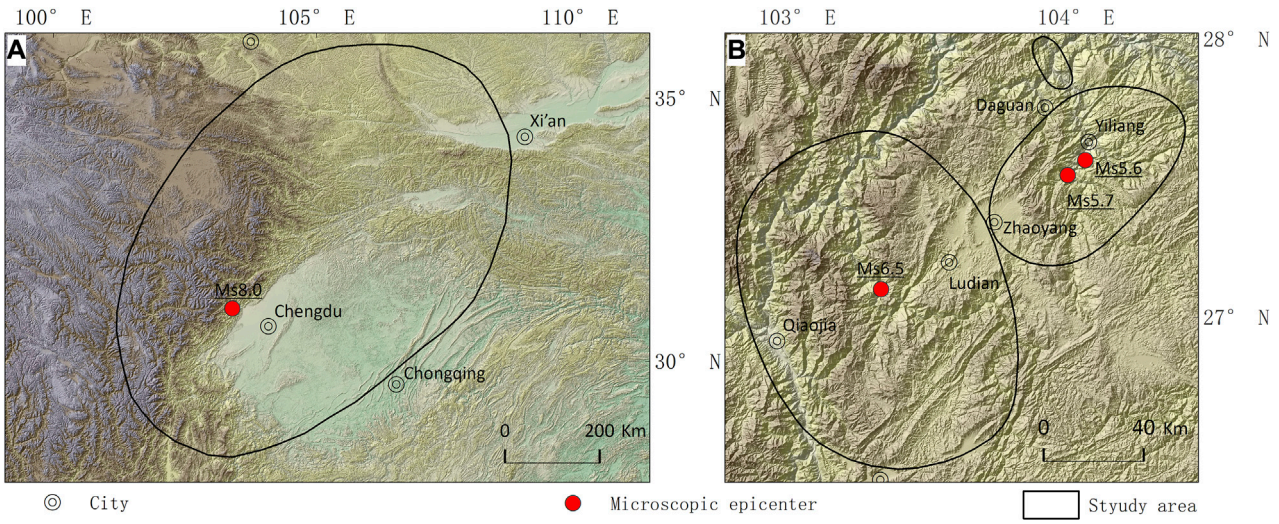

FIGURE 1
Location of the evaluated regions. **(A)** Wenchuan evaluated region; **(B)** Ludian-Yiliang evaluated region.

earthquake of Ms 8.0 occurred in Sichuan, China. The epicenter of the earthquake was located at 31.01 N, 103.42 E in Wenchuan County. The area affected by the Wenchuan earthquake, with intensities up to degree XI, was within the active Longmen Mountain fault zone. This is a zone of active tectonics that separates the Chengdu Plain and Sichuan Basin to the southeast from the Longmen Mountain area and the Tibetan Plateau to the northwest. A significant difference exists between the topography of the two areas, and the major disaster area following the earthquake was in the mountainous area, an area prone to landslides. The earthquake caused severe landslides, and almost all of the roads leading to the worst-hit areas were affected to varying degrees. The road breaks caused by the EL have seriously delayed the rescue progress. Ludian County and Yiliang County, are located in the southwest of Zhaotong City, Yunnan Province, China. On 3 August 2014, an earthquake of Ms6.5 occurred in Ludian, Yunnan, China. The earthquake occurred east of the Xiaojiang fault zone and south of the Lianfeng fault zone. The epicenter was located in the urban area of Longtoushan Town, southwest of Ludian County. A severe landslide occurred at the junction of Huodehong Town and Longtoushan Town on the north bank of the Niulan River. Although the magnitude of the Ludian earthquake was not high, the earthquake intensity in the extreme earthquake area reached IX, the surrounding landforms in the area were complex, the accessibility was extremely poor, and the resource and environmental carrying capacity were fragile. The Ludian earthquake caused the worst landslides in the region's history. Dense landslides have blocked rural roads leading to settlements in the Niulanjiang Valley region, as well as aftershocks and heavy rains in the disaster area, resulting in repeated disruptions to the road. On 7 September 2012, the Ms 5.7 and Ms 5.6 Yiliang earthquakes occurred in Yiliang, Yunnan Province, triggering numerous landslides and causing significant impact on the locals. Many roads around the Luoze River in Yiliang County have been blocked by earthquake landslides.

Identifying the extent and degree of interruption of roads hit by the EL is vital for the development of post-earthquake traffic control strategies in Yunnan and Sichuan (Ouyang, 2013). In this study, a rapid assessment model of the TSR hit by the EL is constructed for the evaluated regions, including the 2008 Wenchuan Ms 8.0 earthquake-stricken region, the 2014 Ludian Ms 6.5 earthquake-stricken region, and the 2012 Yiliang Ms 5.6 and Ms 5.7 earthquakes-stricken region. The earthquake-stricken region is a region with the seismic intensity VI and above based on the post-earthquake field survey (Figure 1). The three earthquake-stricken regions mentioned are typical of the mountainous areas in the Sichuan–Yunnan region and Southwest China, and analyses of these are also applicable in other mountainous areas of China. Among these evaluated regions, the Wenchuan earthquake-stricken region has the most comprehensive set of samples for the interruption of roads hit by the EL. These samples can be used to establish the rapid assessment method for the TSR hit by the EL and thereby evaluate the effectiveness of the method. The Ludian-Yiliang earthquake-stricken region is used to evaluate the extensibility and applicability of the constructed method in similar regions.

2.2 Basic vector data

In this study, the data of roads and seismic intensities were provided by the basic database for earthquake emergency response of Yunnan Province and the basic database for earthquake emergency response of Sichuan Province. The data of the roads in the year immediately preceding the occurrence of an earthquake in a region were taken as the basis for creating the spatial data of the road. The format of road date and intensities date is shapefile. Roads date's feature type is polyline, and the intensities date's feature type is polygon. The analysis of roads took into account only higher levels of classification of roads (including expressways, national highways, and provincial highways) but left out lower levels of roads such as county-level and town-level roads. However, the trafficability of the roads of lower levels is also important in real-life crisis management.

The EL data involved in this study were sourced from the Department of Natural Resources of Yunnan Province (DNRYP).

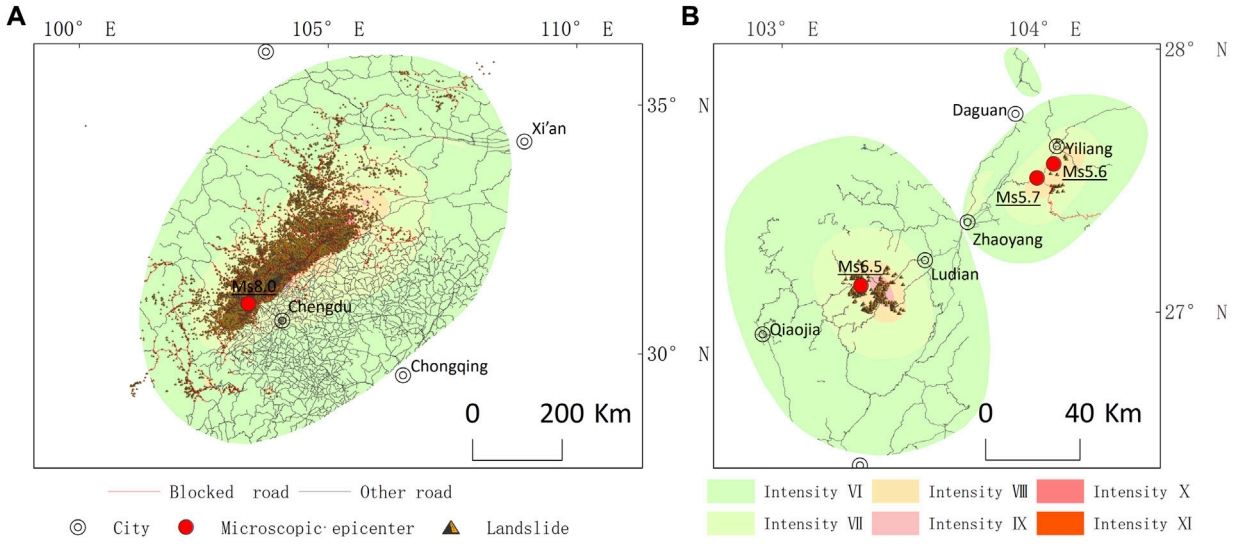

FIGURE 2
Basic vector data of the evaluated regions. **(A)** Wenchuan evaluated region; **(B)** Ludian-Yiliang evaluated region.

After these earthquakes, the DNRYP conducted extensive field investigations and combined remote sensing image interpretation to determine the spatial distribution of EL. The feature type of Yiliang EL date is point, but the others are polygon. Immediately after the Wenchuan earthquake, we carried out a large field investigation in the disaster area to assess the impact of landslides on roads. The field investigation was enhanced by the use of high-resolution images. After the Ludian and Yiliang earthquakes, we also carried out similar work. We used these data to determine which roads in the research area were blocked owing to EL. In this study, the results of the basic vector data we collected are shown in Figure 2.

2.3 Earthquake-induced landslide sensitivity date

The trafficability of roads hit by the EL is closely related to the road condition and the scale of the landslide. Based on the current research findings, the ELS level was selected to represent the influence of landslides on the trafficability of roads in this study. There have been previous studies that focused on the ELS assessment around the world, but the methods developed in these studies that applied to rapid assessment were mainly divided into two categories. One category comprised studies where the methods were based on the Newmark displacement model and its derived models (Capolongo et al., 2002; Havenith et al., 2006; Gaudio et al., 2012; James et al., 2013; Rajabi et al., 2013; Chousianitis et al., 2014), and the other category contained studies that used analysis methods based on landslide sensitivity (Havenith et al., 2006; Kamp et al., 2008; Kamp et al., 2010; Xu et al., 2012a; Xu et al., 2012b; Xu et al., 2012c; Xu et al., 2014). The Newmark models applied to the assessment of smaller regions (Jibson, 2007; Yang et al., 2023b; Pei et al., 2023; Zhao et al., 2023) and not suitable for assessing the potential landslides caused by earthquakes extensively (Qiu et al., 2022; Wang et al., 2022; Yang et al., 2023c; Ma et al., 2023). In the early stage, the studies in China relied on the activity and occurrence conditions of secondary geological disasters in the past earthquakes for the preliminary judgment on the ELS in a specific region, for some time to come (Tang et al., 2001; Liu et al., 2006). The findings in these studies played a significant role in China's land planning and control for a long time, but they could not be easily applied to the rapid assessment of ELS levels during an emergency. After the Wenchuan earthquake occurred, many studies in China explored ELS from the approach of mathematical regression. The methods used in these studies mainly included information quantity (Zhuang et al., 2010), logical regression (Tao et al., 2010; Bai et al., 2015; Xu et al., 2019), analytic hierarchy process (Wang et al., 2012), fuzzy mathematics (Wang et al., 2011), artificial neural network (Xu et al., 2012b), and certainty factor analysis (Xu et al., 2013). A great number of theories, methods, and data have been accumulated in these studies for the research of ELS. In this study, a module was borrowed from a research initiative to rapidly assess the ELS level and formulate the ELS distribution map of the evaluated region. The module was the latest product of the "Research on the analysis methods for ELS" (No. 2016QJGJ09), a special project on earthquake disaster scenario construction in large and medium cities. The method was used to draft the spatial distribution of landslide sensitivity levels on the land of China according to earthquakes of different intensities (Figure 3). It generated the 90 m × 90 m prediction data set of ELS levels with intensity VI–XI. After calculating the probability of EL in each cell for the given intensity, it divided the probability into five levels by natural breaks, that is, very high, high, medium, low, and very low. The cell values for these ELS levels are 5–1, respectively. A higher cell value implies higher ELS (Bai et al., 2021). In Figure 3, each cell value represents the ELS level at the corresponding position. The cell values are highlighted in different colors. When tested with the historical data of EL, the prediction data set of ELS levels is a good indicator for the occurrence of EL (Bai et al., 2021; Zhang et al., 2022).

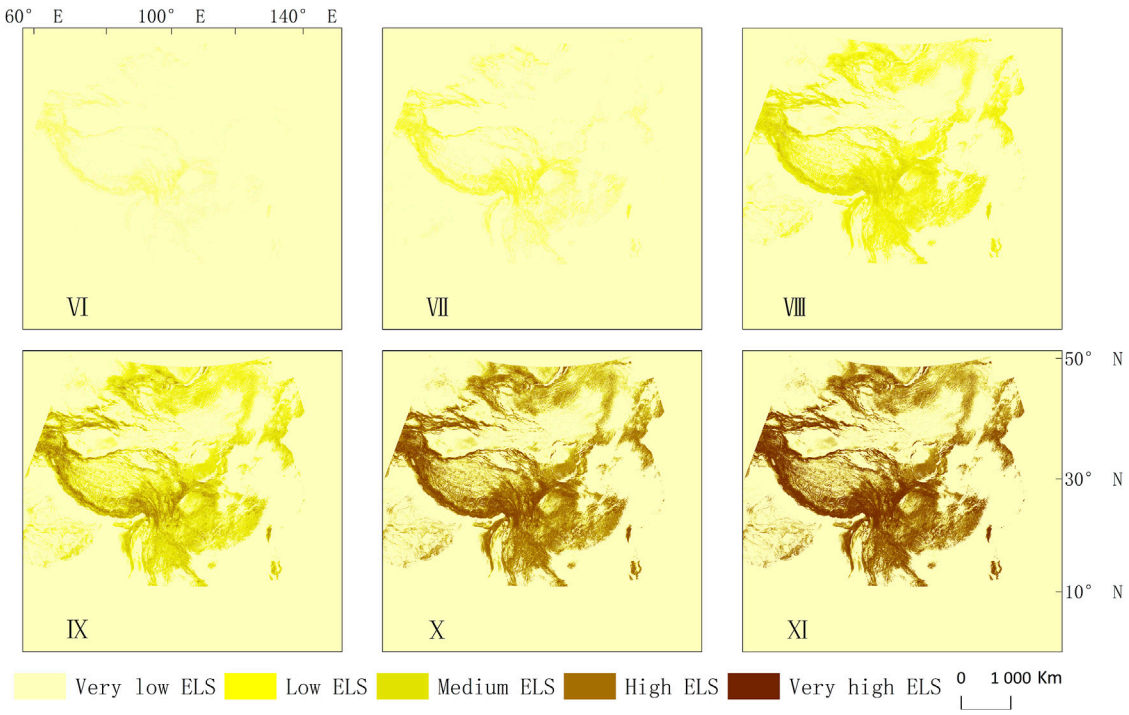

FIGURE 3
Prediction data set of ELS levels with intensity VI–XI (90 m × 90 m raster data).

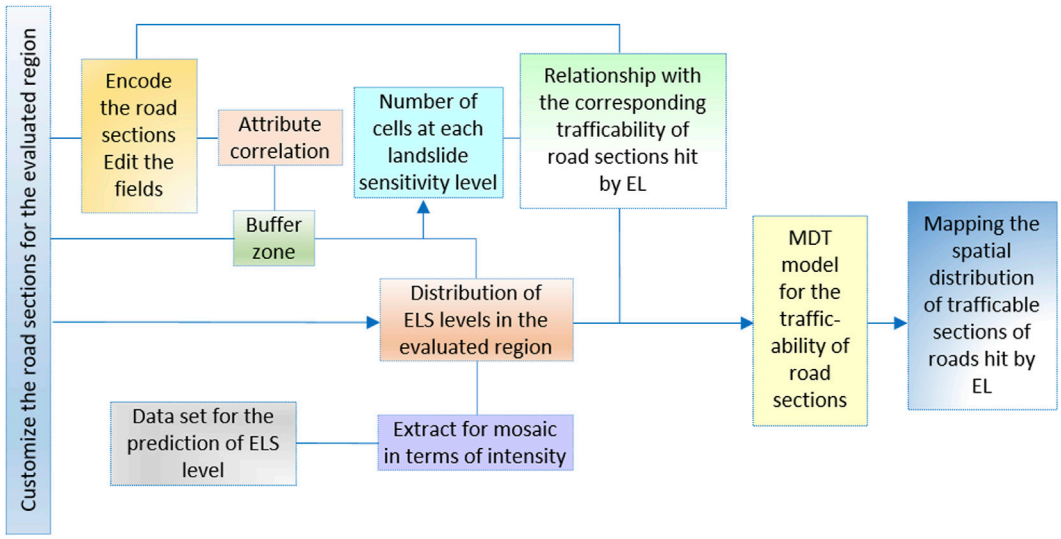

FIGURE 4
Process of the MDT-based rapid assessment for the spatial distribution of TSR hit by the EL.

3 Materials and methods

The MDT-based rapid assessment method for the spatial distribution of TSR hit by the EL is employed to evaluate the road sections, which are then categorized into trafficable and un-trafficable sections. TSR allows vehicles to ply during an earthquake as they are not damaged by EL, while un-trafficable sections are buried or destroyed by EL, making it impossible for vehicles to drive on them. The rapid assessment of the spatial distribution of TSR hit by the EL is meant to classify the TSR by identifying the number of cells at different landslide sensitivity levels within the buffer zones of these sections with the MDT model. The method is implemented in three basic steps (Figure 4): 1) Demarcate the road sections in the evaluated region, that is, partition a road into sections by virtue of the geographic information system (GIS),

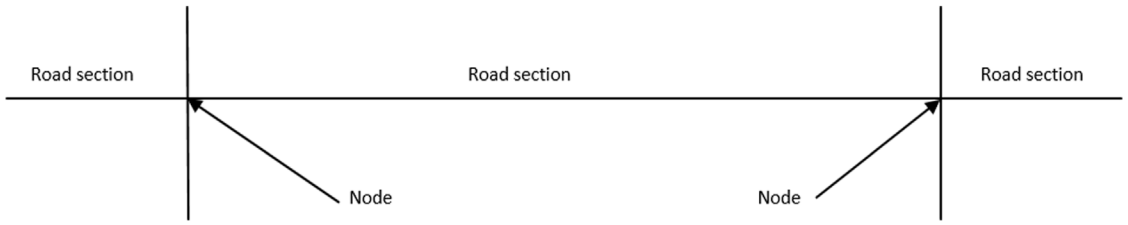

FIGURE 5
A sketch map of road sections.

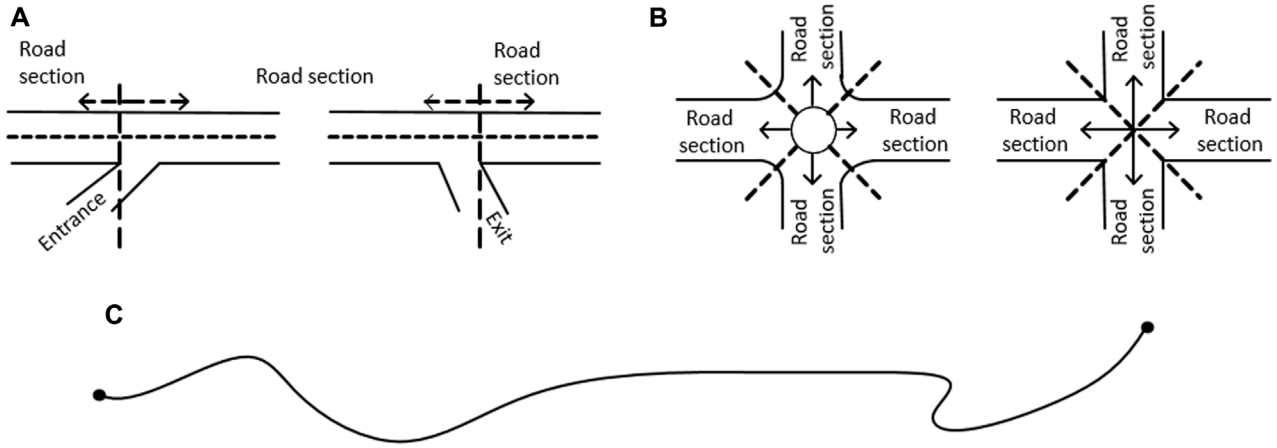

FIGURE 6
A sketch map of some nodes in the traffic network. **(A)** Ramp entrance and exit; **(B)** Roundabout and crossing; **(C)** Road start and end.

and make a 180 m buffer zone on both sides of each road section; 2) Create the data for ELS level for the evaluated region. The data is extracted for the spatial distribution of ELS levels in terms of seismic intensity for the evaluated region. The numbers of cells at different landslide sensitivity levels are recorded within each buffer zone. Seismic intensity is determined in the rapid assessment while we quickly evaluate the spatial distribution of trafficable sections of roads hit by earthquake-induced landslides. The seismic intensity is usually conducted by the model of area attenuation features of earthquake intensity, shakemap, aftershock, and any other methods in the process of rapid assessment after a significant earthquake occurs. A system of seismic intensity rapid assessment technology has been given by Bai et al. (2014) and other researchers. 3) Use the sample data to devise the MDT model for the TSR hit by EL and calculate the trafficability of road sections. The results of the rapid assessment are taken for mapping the spatial distribution of TSR according to conditions of EL in the evaluated region.

3.1 Definition and processing of road section

Road layout normally forms a networked system with some nodes connected by different traffic lines. One or several traffic lines exist between two nodes. A line connecting two nodes in a road network is defined as a road section (Figure 5), which is taken as the basic unit to assess the trafficability of a road hit by the EL. The nodes at both ends of a road section may be cities, towns, villages, ramp entrances and exits, highway intersections (including crossings), roundabouts, stations, or other highway beginning and endpoints (Figure 6). A road section is taken as the basic unit in the assessment since an interruption at any position of the section makes it impossible to transport people and goods between two nodes through that section. Under this circumstance, a GIS is employed to partition a road into vector sections, encode these road sections, and process the relevant fields. For this purpose, the field for trafficability of sections is Boolean or logical; that is, the sections of the roads are classified according to the influence of the EL into either trafficable or un-trafficable sections.

3.2 Landslide influence distance and road section buffer zone

A road becomes un-trafficable when it is buried or destroyed by the EL or by the descent of the EL above the road. When a landslide occurs above a road, it may interrupt the road only if its radius goes beyond or reaches the road. As for 5,928 landslides induced in the Wenchuan earthquake (Figure 7), the horizontal projection distance of their movement ranged from 90 to 190 m; the maximum was

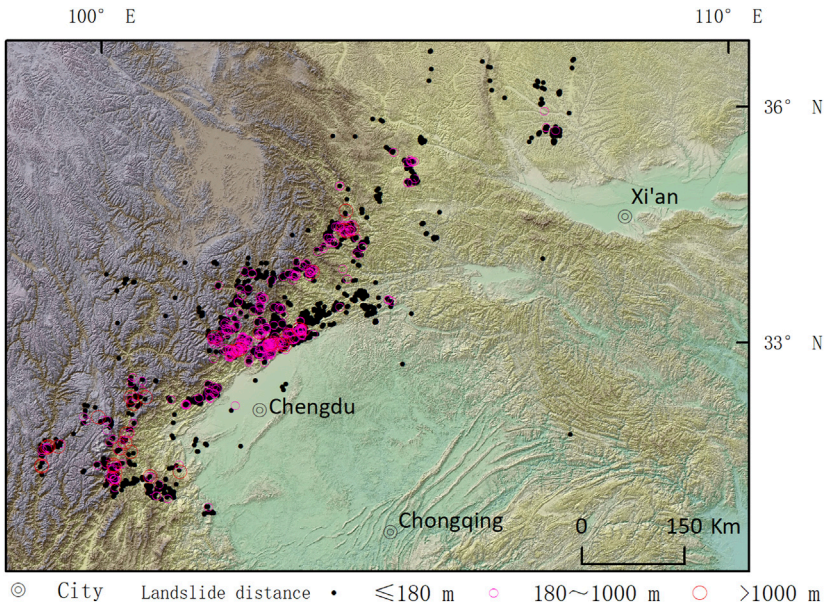

FIGURE 7
Spatial distribution of the landslide distances in the Wenchuan earthquake. To determine the extent of earthquake-induced landslides, we randomly selected 5,928 samples from the landslides triggered by the Wenchuan earthquake. The plotted dots in the figure represent the locations of the selected landslides, while the color of the dots indicates the distance of their movement.

recorded as 1,201 m and the average was 136.6 m. Among them, 386 samples had a distance larger than 180 m, accounting for only 6.51% of total samples. The average turned out to be 168.8 m if the repeated distances were taken out from the sample data. The roads in the mountainous areas of China normally extend along the valleys with higher elevations on both sides. Based on the statistical results of EL distance, a space of 180 m on both sides of a road is defined as the influence of EL on the trafficability of the road. This aims to lower the subsequent statistical redundancy in this study. Therefore, the buffer zone of road sections was made 180 m on both sides of the roads but not provided at the ends of a road section (Figure 8).

3.3 Spatial distribution of earthquake-induced landslide sensitivity levels and assignment of road section landslide attribute

3.3.1 Creation of earthquake-induced landslide sensitivity data for the evaluated regions

Using the module (described in Section 2.3 above), the ELS level for the whole evaluated region area can be created. The process (Figure 9) is as follows: 1) Acquire the disaster areas and the seismic intensity in each area for the current earthquake from the seismic intensity map determined in the rapid assessment (Sometimes it can also be obtained through on-site investigation or other means too). 2) Extract the ELS level distributions in the intensity-specified areas from the ELS dataset for China according to the corresponding seismic intensity. 3) Acquire the ELS distribution for the whole evaluated area affected by the earthquake through the mosaicking of the previously extracted ELS distributions under each seismic intensity.

If the spatial distribution of ELS levels is predicted with the data set, the parameter representing the influence of ground motion in the evaluated region should be seismic intensity or converted into it.

3.3.2 Extraction of the cell information for earthquake-induced landslide sensitivity levels in buffer zones

The cell information of ELS levels in buffer zones is extracted by counting the number of cells at different landslide sensitivity levels in buffer zones based on the data generated in Section 3.3.1. The cells are covered, as indicated in Figure 8. The number of cells is assigned as the earthquake-induced landslide attributes (ELA) of the buffer zone. In the buffer zone attribute table, A_i (i=1, 2, 3, 4, 5) denotes the number of cells at the ELS level i in a buffer zone.

3.3.3 Assignment of earthquake-induced landslide attributes to road sections

After extracting the information as given in Section 3.3.2, the ELA of each buffer zone is assigned to the corresponding road sections based on the data correlation, and these become the ELA for these road sections. After this assignment, the road sections share the same ELA as the buffer zones.

3.4 MDT modeling of the trafficable sections of roads subjected to the earthquake-induced landslides

3.4.1 MDT model

Decision tree modeling is a method commonly used in machine learning. For instance, we may desire to obtain a model from a given

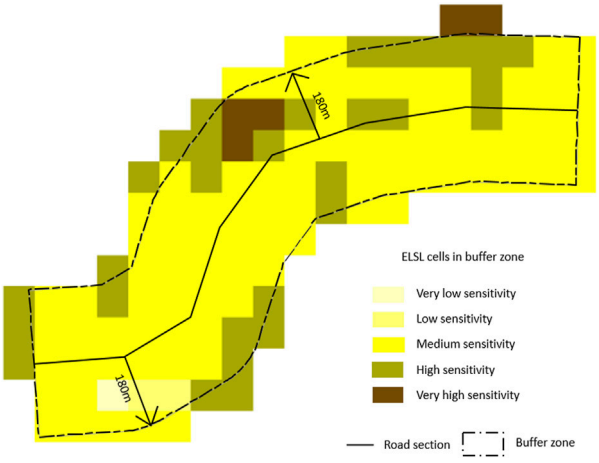

FIGURE 8
The sketch map of the road section buffer zones and cells.

training data set for the classification of new samples in a binary classification task. The task can be regarded as a process of "deciding" or "judging" whether a sample is "positive." As its name suggests, the decision tree has the decision made in a treelike structure. The result of the decision-making process is the judgment we desire. Normally, a decision tree contains a root node, several internal nodes, and several leaf nodes. The leaf nodes reflect the results of the decision, while each of the other nodes represents an attribute test. The sample set for each node is categorized into the child node based on the result of the attribute test. The root node contains the entire set of samples. The path from the root node to each leaf node represents a sequence that is subjected to a judgment test. Decision tree learning generates a decision tree that is highly capable of generalization, i.e., processing new samples. It basically follows the simple and direct strategy of "divide-and-conquer." It is evident that a decision tree is generated in the process of recursion. In the basic algorithm of the decision tree, the return leads to recursion in three circumstances: 1) all the samples contained in a node belong to the same category and are not further classified; 2) the attribute set is empty, or all the samples cannot be classified since their attribute values are identical; 3) the sample set contained in a node is empty, making it impossible to classify. In the second circumstance, the node can be marked as a leaf node, and its category is set as the category containing the most samples of the node. In the third circumstance, the node is also marked as a leaf node, but its category is set as the category containing the most samples of its parent node. There is a substantial difference between them. The posterior distribution of the node is utilized in the second circumstance, while the sample distribution of the parent node is taken as the prior distribution of the node in the third circumstance. A decision tree involves a variety of models and algorithms. Most of the decision tree models require the testing of only one attribute at each node, e.g., CART, ID3, and C4.5. These univariate decision trees assume that the conditional attributes in the information system are immune to the effect of decision attributes. Nevertheless, the correlation between the attributes in various information systems is universal in real life. It is therefore often impossible to reflect such a correlation in a univariate decision tree. Additionally, pruning is costly for a univariate decision tree and causes the loss of some attributes that seem futile but contain important and relevant information. This turns into a bottleneck in improving the classification accuracy of the decision tree. For this reason, Murthy et al. (1994) put forward the Multivariate Decision Tree (MDT) model in 1994. In the MDT model, the nodes that were not leaf nodes, were not used exclusively to decide on a specific attribute but to test the linear combination of attributes. In other words, each node (other than a leaf node) appeared as a line classifier, e.g., $\sum_{i=1}^{d} w_i a_i = t$, where w_i was the weight of the attribute a_i; w_i and t could be learned from the sample set and attribute set contained in the node. The MDT was intended to create a suitable line classifier instead of finding the optimal classification attribute for each node that was not a leaf node as it was conducted in the traditional learning process with a univariate decision tree (Zhou et al., 2016). In this study, the *R* software is utilized to construct the MDT model for the TSR hit by the EL.

3.4.2 Calculation of the trafficable sections of roads subjected to the earthquake-induced landslides

The calculation of the TSR subjected to the EL in a given region is actually the classification of road sections based on MDT in terms of trafficability. The road sections in a region to be evaluated are taken as samples to analyze the correlation between RT and the ELS on both sides of the roads. At the same time, the attributes of these samples are represented by the number of cells at different landslide

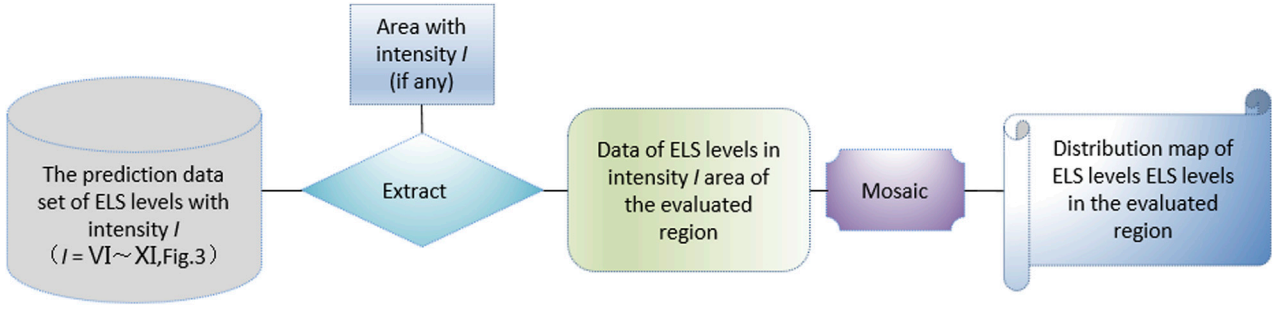

FIGURE 9
Process of the ELS assessment in the evaluated region.

sensitivity levels on both sides of the road sections (i.e., road section landslide attributes). The road sections are classified into trafficable and un-trafficable sections. The RT is obtained in a field survey and then used to determine the actual trafficable sections in these samples. The trafficability of the roads hit by EL T is expressed as:

$$T = \{0, 1\} \tag{1}$$

In Eq. 1, the value of T is 0 when a road section is interrupted by EL, i.e., it is un-trafficable. The value 1 is awarded when the road section is not interrupted by EL, i.e., it is trafficable. The number of cells at the ELS level in the buffer zones on both sides of the road section indicates the possibility of EL. Consequently, each sample has five attributes in correspondence with the five levels of ELS. The five attributes represent the number of cells at each level of ELS in that sample. The value of Eq. 1 is determined by whether the attributes of a road section satisfy Eq. 2:

$$t = \sum_{i=1}^{d} w_i A_i \tag{2}$$

In the linear expression, t represents for the threshold of judgment; A_i stands for the number of cells at the landslide sensitivity level i in the buffer zone; w_i denotes the weight of the landslide sensitivity level i. Normally, w_i varies with nodes in the decision tree. In this study, five ELS levels are used so that the line classifier d=5. The C4.5 model considers the number of cells at only one ELS level for each node, but the MDT model uses the number of cells at all ELS levels for each node. In other words, the products of the number of cells at each ELS level and the weight of the corresponding sensitivity level should be aggregated for this purpose.

3.4.3 The quantification of a node's "purity"

The MDT model was mainly used to find out the optimal linear expression for each node, but a parameter was still needed to judge the linear relationship for the most suitable MDT. Generally, the samples contained in the branch nodes of the tree were desired to be in the same category along with the progress of classification in the decision process. It implied that the purity of nodes became higher and higher. The *Gini* index was the commonest indicator for the purity of the sample set. If the proportion of the samples in the kth category of the sample set D was pk (k=1,2, ... ,$|y|$), the *Gini* index of D was defined as:

$$Gini(D) = \sum_{k=1}^{|y|} \sum_{k \neq 1} pkpk' = 1 - \sum_{k=1}^{|y|} pk^2 \tag{3}$$

The lower the value of the *Gini(D)*, the higher the purity of D. Apart from *Gini* index, information gain, and information entropy was used to measure the purity of nodes. These measures for purity did not exert any significantly different effect on the model. In this study, we evaluated the classification in terms of the *Gini* index. When the value of *Gini(D)* was the smallest, it was believed that the corresponding classifier must be the best.

3.4.4 Accuracy evaluation of the MDT

The MDT model must guarantee the statistical significance of the assessment results and meet the actual needs at work while ensuring that each node has the smallest *Gini* index but the largest purity. The statistical significance of results is a method for estimating the authenticity of results (representing the whole). In the statistical test, the *p-value* (p-value, Probability, Pr) is an indicator of the declining credibility of the results. With greater *p-values*, the correlation of the variables for samples becomes a less reliable indicator for the correlation of variables overall. In many fields, the *p-value* is statistically obtained by virtue of a significance test. However, it is normally believed that 0.05 is the margin of acceptable error for the *p-value*. Under normal circumstances, p<0.05 indicates the existence of a statistical difference, p<0.01 significant statistical difference, and p<0.001 highly significant statistical difference. This means that the probability of sample error caused by the difference between samples is less than 0.05, 0.01, and 0.001. Moreover, the correctness rate of assessment can be considered, or the *kappa* test may be conducted for the model to meet the actual needs. The correctness rate represents the percentage of the assessment results that comply with the actual condition of samples, while the *kappa* coefficient shows the consistency of simulation results with the actual condition. The calculated *kappa* coefficient ranges from −1 to 1, but the *kappa* value normally falls into the range of 0–1. It is common to divide the *kappa* values into five categories for the consistency of different levels. Among them, 0.0–0.20 is the range for slight consistency, 0.21–0.40 for fair consistency, 0.41–0.60 for moderate consistency, 0.61–0.80 for substantial consistency, and 0.8–1 for almost perfect consistency.

4 Results

4.1 Creation of the spatial data for road sections

The data of the roads in the year immediately preceding the occurrence of an earthquake in a region were taken as the basis for creating the spatial data of road sections. The details regarding the spatial distribution of road interruptions caused by EL in these earthquake-stricken regions were obtained from a field survey (Figure 2). By using the above method (Section 3.1), we have divided the roads in the evaluation areas into 29,204 sections, of which 2,254 sections are defined as blocked due to earthquake-induced landslides. The exclusive numbering scheme and fields were designed for each of these road sections. The road sections destroyed or buried by EL were defined as un-trafficable sections, and others as trafficable sections. In this study, we focused only on how EL affected the trafficability of roads and ignored the influence of other disasters. Therefore, some road sections that were inferred to be trafficable may be un-trafficable for other reasons.

4.2 Data extraction of earthquake-induced landslide sensitivity levels

For a better comparison with the actual situation, the data of seismic intensity from the field survey (i.e., spatial vector attribute data) was used to extract the data of ELS levels in the evaluated regions. We followed the ELS assessment process (Figure 9) to extract the data of the corresponding intensity from the prediction data set of ELS level (Figure 3) and prepared a mosaic of the spatial distribution data of ELS levels for the three earthquake-stricken regions (Figure 10). After the data of ELS levels for the evaluated

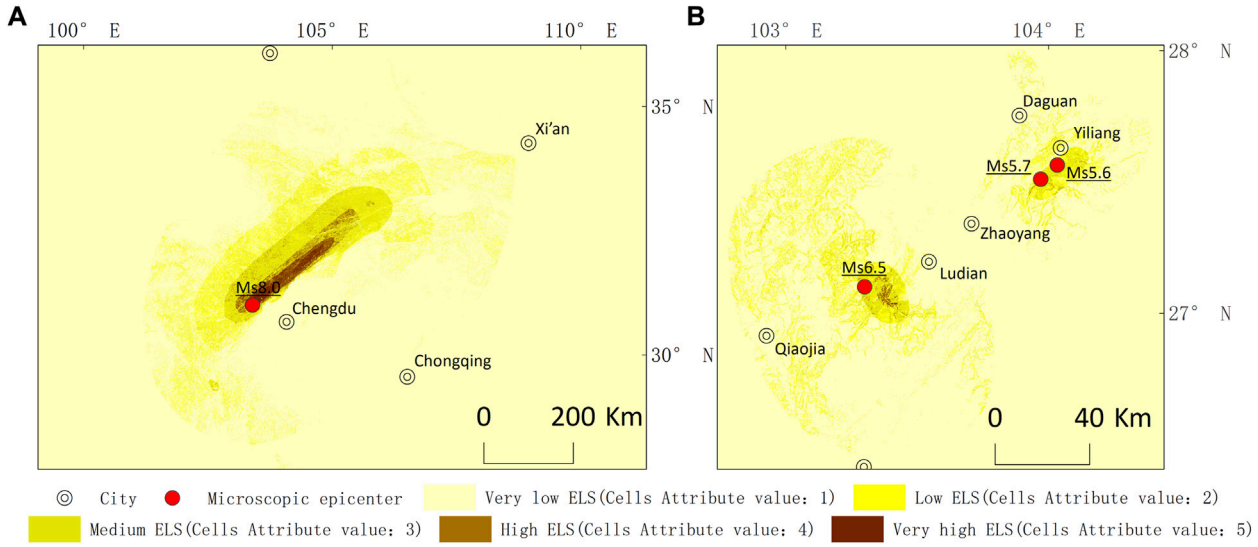

FIGURE 10
Spatial distribution inversion of ELS levels in the evaluated regions. **(A)** Wenchuan evaluated region; **(B)** Ludian-Yiliang evaluated region.

regions were extracted for the spatial distribution data of ELS levels of the evaluated regions, the ELA was assigned to the road sections in the evaluated regions as per the methodology given in Section 3.3.2 and Section 3.3.3. Finally, the data of road sections were obtained for the trafficability of roads hit by EL as well as the ELA.

4.3 Modeling and test in the Wenchuan evaluated region

4.3.1 Factor analysis on the trafficable sections of roads subjected to the earthquake-induced landslides

In this paper, we construct a rapid assessment method for the TSR subjected to the EL and then use it to infer the trafficability of road sections based on their ELA. The road sections in the Wenchuan earthquake-stricken region were classified into two categories. One category contained the road sections interrupted by EL, which were defined as un-trafficable. The other category included the other road sections that were not interrupted by EL, and these were defined as trafficable. The ELA of the road sections interrupted by EL in the Wenchuan evaluated region (i.e., the number of cells at different ELS levels in buffer zones as discussed above) (Figure 11) were compared with the ELA of other road sections (Figure 12). This comparison revealed that the number of cells at the very high or high level of ELS within the 180 m buffer zones on both sides of the road sections that were interrupted by EL was significantly higher than that of other unaffected road sections. Almost all cells were at a very low or low level of ELS within the 180 m buffer zones on both sides of other road sections. The number of cells at a very high or high level of ELS for these roads was very few or even zero. It is evident that roads were more easily interrupted when there were more cells at a high level of ELS on both sides of the roads. On the contrary, there was a greater possibility of roads not being affected by EL if the majority of the cells were at low levels of ELS on both sides of the roads. As shown in Figure 11 and Figure 12, the number of cells at different ELS levels on both sides of road sections could be taken as an important basis for judging the trafficability of roads hit by the EL. This indirectly revealed that the prediction data set of ELS levels was a good indicator for the possible occurrence of EL.

Contingency analysis was carried out to qualitatively identify the correlation between the ELA of road sections and their trafficability. This was intended to infer the correlation between the trafficability of roads subjected to the EL and the number of cells at each ELS level within their buffer zones, i.e., whether they were independent of each other. A contingency table was employed to analyze and infer the correlation between the trafficability of 26,151 road sections hit by the EL and their ELA for the Wenchuan evaluated region (Table 1). In the table, T denotes the trafficability of roads according to EL. The roads are un-trafficable if the value of T is 0 or trafficable if it is 1. Moreover, A_i represents the number of cells at the landslide sensitivity level i in buffer zones. In the contingency analysis, the number of cells at each landslide sensitivity level equaled to or exceeded 0. The number of road sections reflected the number of trafficable road sections for ELA.

In the contingency analysis, we used the null hypothesis H0 that A_1 and T were independent of each other, and the alternative hypothesis H1 that A_1 and T were consistent with each other. The contingency table analysis showed that the *p-value* in the test of each group was much lower than 0.001. It was revealed that the null hypothesis, where the ELA of road sections and their trafficability were independent of each other, was untenable. In other words, the number of cells at different ELS levels within the 180 m buffer zones on both sides of road sections is related to the interruption caused by EL to the road sections. The correlation coefficient indicated a significantly negative consistency between A_1–A_5 and T. When A_3–A_5 were greater than 0, the value of T tended to be 0. In other words, if the number of cells at the medium to very high landslide sensitivity levels in the buffer zones of a road section

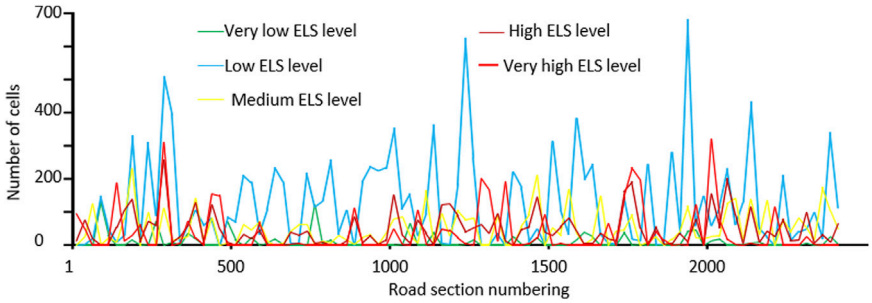

FIGURE 11
Statistical diagram of the landslide attributes of the road sections interrupted by EL in the Wenchuan evaluated region.

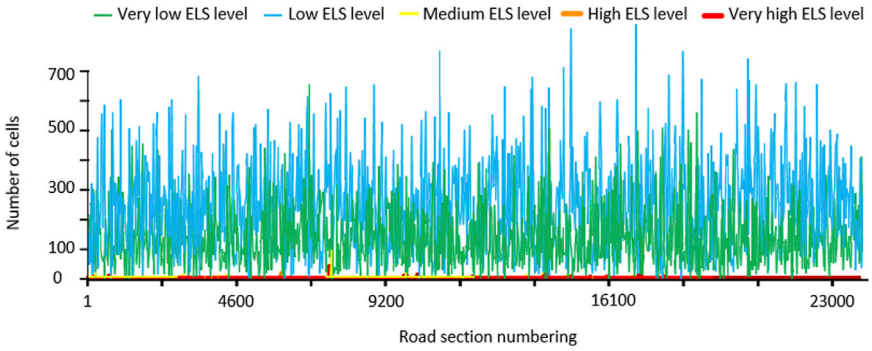

FIGURE 12
Statistical diagram of the landslide attributes of the road sections uninterrupted by the EL in the Wenchuan evaluated region.

was larger, the road section had a stronger tendency to be interrupted by EL. Moreover, there was a significantly positive consistency between A_1–A_2 and T. When the value of A_1–A_2 in the ELA of the road section was greater than 0, the value of T tended to be 1. Therefore, a road section had a stronger tendency of not being interrupted by EL when the numbers of cells at the very low and low landslide sensitivity levels in the buffer zones of the road section were larger. The positive or negative consistency between A_i and T depended on the agreement on the trafficability of road sections but always proved that they were not independent of each other. The number of cells at the very high ELS level was the least consistent with the trafficability of roads. It implies that the cells at the very high ELS level made the highest contribution to the un-trafficable roads hit by the EL. At the same time, the number of cells at the very low ELS level was the most consistent with the trafficability of roads, and its absolute value was the largest. It is revealed that the number of cells at the very low ELS level exerted the highest effect on the trafficability of roads hit by the EL. The *p-value* and consistency coefficient prove that the trafficability of road sections could be inferred by using their ELA.

4.3.2 Node division

The road sections in the Wenchuan evaluated region were classified into two categories. Among them, 8,717 pieces of data for the road sections were taken as the training set to construct the MDT model for the TSR hit by the EL. The remaining 17,434 pieces formed the test set to check the reasonableness of the model. Selecting the optimal classification attribute from the data set was crucial to decision tree learning. Following the above constraints, the statistical software *R* was utilized to build the MDT model. The branching rules of the MDT for the trafficability of the roads hit by the EL were developed according to the output of the *R* software.

The MDT model for the trafficability of the roads hit by the EL started from the root node, which contained 8,717 training samples. The samples included 739 un-trafficable samples and 7,878 trafficable samples. The branching for the root node of the decision tree was conducted in terms of whether the landslide attribute values of road sections satisfied Eq. 4:

$$A_5 + A_4 + (A_3 - 1) \leq 0 \tag{4}$$

Starting from the root node of the decision tree, the samples whose landslide attributes of road sections that satisfied Eq. 4 were deployed to node 1, and other samples went to node 2. The road sections in node 1 of the decision tree were judged to be trafficable. At this time, node 1 had the smallest *Gini* index (0.00561366) but the largest purity so the tree did not grow. In the training set, 7,827 samples satisfied Eq. 4 and were deployed to node 1. Among them, 7,805 road sections were trafficable, so that the fault rate was less than 1%.

The branching was conducted for node 2 of the decision tree based on whether the landslide attributes of road sections satisfied

TABLE 1 Contingency of the ELS and the RT.

			T_i			*p-value* of A_i and T_i	Consistency coefficient of A_i and T_i
			0	1	Total		
A_i	A_5	0	1,127	23,897	25,024	2.42×10^{-116}	−28.9715
		>0	1,104	23	1,127		
		Total	2,231	23,920	26,151		
	A_4	0	207	23,529	23,736	7.52×10^{-185}	−26.1829
		>0	2024	391	2,415		
		Total	2,231	23,920	26,151		
	A_3	0	391	23,368	23,759	2.08×10^{-151}	−22.8983
		>0	1840	552	2,392		
		Total	2,231	23,920	26,151		
	A_2	0	230	23	253	8.884×10^{-23}	21.1148
		>0	2001	23,897	25,898		
		Total	2,231	23,920	26,151		
	A_1	0	1,265	414	1,679	2.91×10^{-99}	96.509
		>0	966	23,506	24,472		
		Total	2,231	23,920	26,151		

Eq. 5. The samples whose landslide attributes of road sections satisfied Eq. 5 were assigned to node 3, and other samples went to node 4. The road sections in node 4 were identified as un-trafficable. At this time, node 3 had the smallest *Gini* index (0.026989308) but the largest purity so the tree stopped growing. In the training set, 368 samples satisfied Eq. 5 and went to node 3. However, 363 road sections were un-trafficable, causing a fault rate of less than 1%.

$$A_5 - 1 \geq 0 \tag{5}$$

The branching was conducted for node 4 of the decision tree based on whether the landslide attributes of road sections satisfied Eq. 6. The samples whose landslide attributes of road sections satisfied Eq. 6 were sent to node 5, and other samples went to node 6. The road sections in node 5 were identified as un-trafficable. At this time, node 5 had the smallest *Gini* index (0.147928994), but the largest purity and branching was halted. In the training set, 247 samples satisfied Eq. 6 and were sent to node 5. Among these samples, 228 road sections were un-trafficable, so that the fault rate was less than 1%.

$$1/(4 - A_3) + 1/(6 - A_4) < 1/4 \tag{6}$$

The branching was conducted for node 6 of the decision tree based on whether the landslide attributes of road sections satisfied Eq. 7. The samples whose landslide attributes of road sections satisfied Eq. 7 were added to node 7 of the decision tree, and other samples went to node 8. The road sections in node 7 were considered un-trafficable. At this time, node 7 had the smallest *Gini* index (0.209876543), but the largest purity and the branching came to an end. In the training set, 63 samples satisfied Eq. 7 and went to node 7. Among these samples, 56 road sections were un-trafficable, causing the correctness rate of 88.89%.

$$1/(A_3 - 13) + 1/(7 - A_4) < 5/104 \tag{7}$$

The branching was conducted for node 8 of the decision tree based on whether the landslide attributes of road sections satisfied Eq. 8. The samples whose landslide attributes of road sections satisfied Eq. 8 were deployed to node 9 of the decision tree, and other samples went to node 10. The road sections in node 9 were judged to be trafficable. In this case, the node had the smallest *Gini* index (0.067776457) but the highest purity. Then, the branching was stopped.

$$1/(A_2 - 102) + 1/(14 - A_3) \leq 15/14 \tag{8}$$

The branching was conducted for node 10 of the decision tree based on whether the landslide attributes of road sections satisfied Eq. 9. The samples whose landslide attributes of road sections satisfied Eq. 9 were deployed to node 11 of the decision tree, and other samples went to node 12. The road sections in node 11 were found to be un-trafficable. At this time, node 11 had the smallest *Gini* index (0.64498791) but the highest purity and the decision tree stopped growing. In the training set, 61 samples satisfied Eq. 9 and were deployed to node 11. Among them, 59 road sections were un-trafficable, so that the fault rate was less than 4%. The road sections in node 12 were judged to be trafficable. Node 12 had the smallest *Gini* index (0.157215802) and the largest purity so the branching of the decision tree was completed. In the training set, 122 samples did not satisfy Eq. 9 and went to node 12. Among them, 112 road sections were trafficable, so the correctness rate was 91.80%.

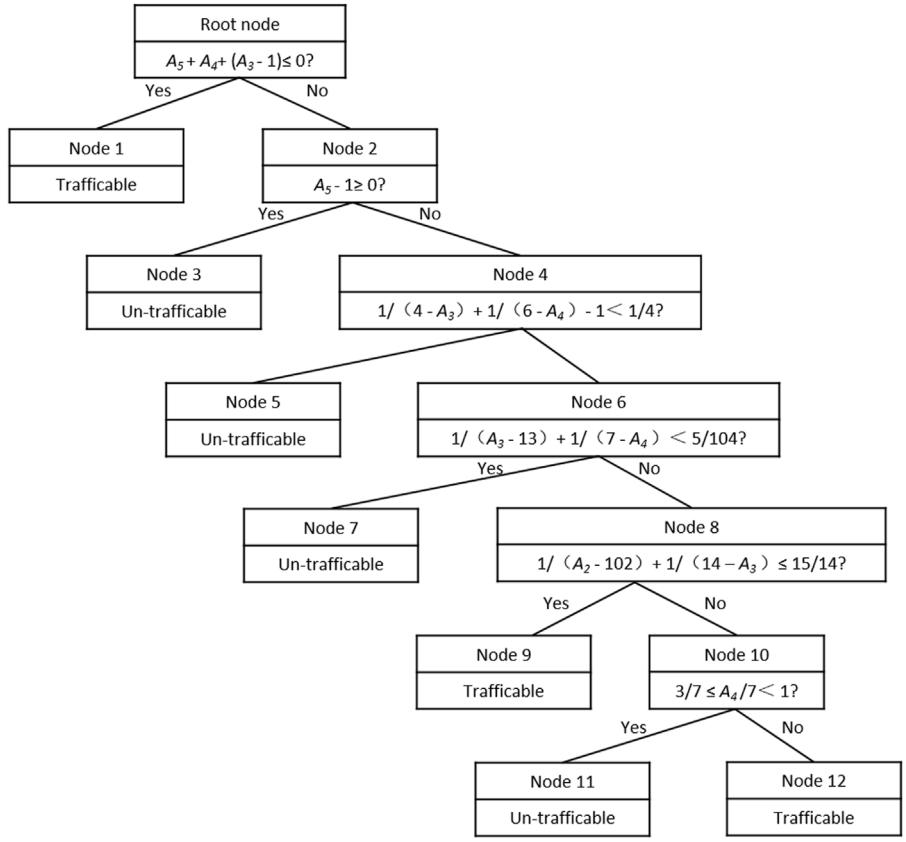

FIGURE 13
MDT model of the TSR hit by the EL in the Wenchuan evaluated region.

$$3/7 \leq A_4/7 < 1 \quad (9)$$

The above MDT rules for judging the trafficability of the roads hit by the EL were drafted into a traditional tree structure, as shown in Figure 13.

The judgment rules given in Figure 13 were used to decide the trafficability of roads hit by the EL for all samples in the Wenchuan evaluated region by virtue of MDT. The results were compared with the actual trafficability of roads. According to the calculation results (Table 2), the *p-value* of the Wenchuan evaluated region was 2.52×10^{-203}, much lower than 0.001, and its overall correctness rate reached 98.50%. Its *kappa* coefficient was 0.91, which falls in the range of 0.81–1 so the assessment results given by the model had almost perfect consistency with the actual condition. Based on the results, the number of interruptions in the trafficable road sections hit by the EL took up only 0.958% of these road sections, while the number of interruptions in the un-trafficable road sections was 12.3 times as high as those in other road sections. Obviously, the MDT model could be taken as a good indicator of the interruption caused by EL in the road sections. Compared with the C4.5 decision tree, the MDT model is applicable in a wider range and shows higher differential significance, that is, higher statistical significance, as well as higher *kappa* coefficient, that is, higher consistency and overall correctness rate.

The above model was utilized in ArcGIS to obtain the spatial distribution of TSR hit by the EL in the evaluated region (Figure 14A) by calculating the trafficability of road sections hit by the EL, based on the seismic intensity from the post-earthquake field survey. The comparison with actual conditions revealed that most of the road sections that were assessed to be un-trafficable but were trafficable belonged to some expressways with high intensity, while most of the road sections that were calculated to be trafficable but were interrupted by landslides existed in some provincial highways with low intensity. The model was not constructed with the classification of roads but assumed that all roads were identically vulnerable to EL. However, provincial highways were more vulnerable to EL than expressways due to design and siting considerations.

4.4 Application of the model to the Ludian-Yiliang evaluation regions

The 2014 Ludian Ms 6.5 earthquake-stricken region and the 2012 Yiliang Ms 5.6 and Ms 5.7 earthquake-stricken region in Yunnan were employed in the study to test the extensibility of the proposed method for the rapid assessment of TSR hit by the EL caused by different earthquake magnitudes in the regions with similar natural and geographical environments. The MDT model constructed for the TSR hit by the EL for the Wenchuan evaluation region was applied to the Yunnan evaluation region without altering the data processing method, model indicators, and parameters. The

TABLE 2 Assessment results based on the MDT model (the Wenchuan evaluated region).

		Actual condition			Overall correctness rate	Kappa coefficient	*p-value*
		Un-trafficable	Trafficable	Total			
Judgment based on the model	Un-trafficable	1978	161	2,139	98.50%	0.91	2.52×10^{-203}
	Trafficable	230	23,782	24,012			
	Total	2,208	23,943	26,151			

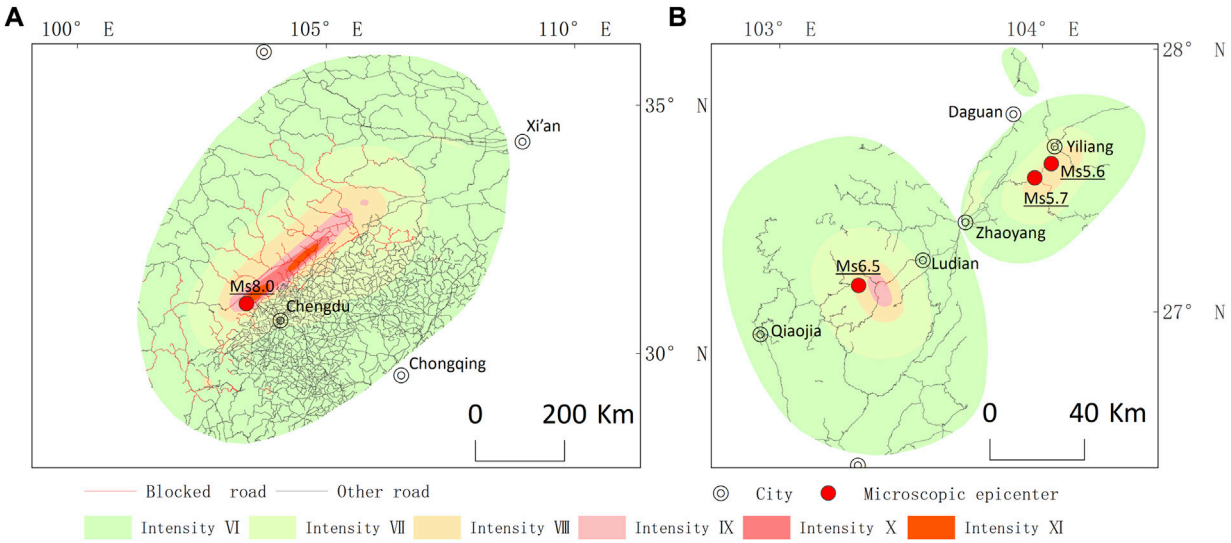

FIGURE 14
Spatial distribution inversion of TSR hit by the EL for the evaluated regions. **(A)** Wenchuan evaluated region; **(B)** Ludian-Yiliang evaluated region.

spatial distribution of TSR that had EL in the Ludian-Yiliang evaluation regions was obtained, as shown in Figure 14B. The Ludian earthquake and the Yiliang earthquake had much lower magnitude and intensity, and the landslides induced were less serious than for the Wenchuan earthquake, but they still triggered different severities of interruption to roads because of EL since they occurred in the mountainous areas. The calculation results (Table 3) showed that the *p-value* in the test of trafficability for the Ludian-Yiliang evaluated regions was closer to 0, and the overall correctness rate reached 99.67%. Moreover, the *kappa* coefficient was 0.81. Its consistency was slightly lower than that of the Wenchuan evaluated region but still fell into the almost perfect range. In the Ludian-Yiliang evaluated regions, the road sections that were interrupted by EL comprised only 1.31% of those with the trafficable attribute. Additionally, the road sections that had the untrafficability attribute and that were interrupted by EL were 5.2 times as high as other road sections. Thus, the calculated trafficability is a good indicator of whether road sections are interrupted by landslides. The constructed model for the Wenchuan evaluated region can be promoted for evaluating the trafficability of other regions with similar natural and geographical environments under conditions of EL damage of their road network. On the premise of acceptable error, the constructed method can be employed to rapidly and more extensively assess the TSR hit by the landslides caused by earthquakes of different magnitudes in Southwest China.

5 Discussion

The strong correlation between the trafficability of road sections and the ELS level is pivotal to the construction method for the rapid assessment of TSR hit by the EL. As discussed above, the model must be constructed under three conditions: 1) The basic unit in the assessment must be a road section. In the assessment process, a road must be divided into sections and should not be simply taken as a unit. 2) The buffer zones on both sides of road sections must be extended by 180 m and not created at both ends of a road. The value of 180 m was determined using the horizontal projection distance of EL in the Wenchuan earthquake. 3) The ELS level uses the 90 m × 90 m raster data. Moreover, the data of landslide sensitivity is obtained by taking intensity as a parameter for the influence of ground motion. The landslide sensitivity is divided into five levels, and the attribute values of the cells for landslides are

TABLE 3 Assessment results based on the MDT model (for the Ludian-Yiliang evaluated regions).

		Actual condition			Overall correctness rate	Kappa coefficient	*p-value*
		Un-trafficable	Trafficable	Total			
Judgment based on the model	Un-trafficable	19	6	25	99.67%	0.81	9.7×10^{-107}
	Trafficable	4	3,047	3,051			
	Total	23	3,053	3,073			

correspondingly 1–5. In the end, the efficacy of this method may vary if any of these conditions are altered, e.g., using a different basic unit for the assessment, changing the distance or way of buffering, or abandoning the 90 m × 90 m raster data of the sensitivity levels.

While developing the rapid assessment method for TSR hit by the EL, road sections are demarcated since they are the basic element connecting two nodes in a road network. Theoretically, a road section fails to serve as a transport medium between two nodes if it is interrupted at any position. However, a problem still needs to be addressed, that is, different lengths of road sections. In other words, the total number of cells at the landslide sensitivity levels in the buffer zones varies with road sections, which inevitably causes the error of the model. In this study, a rapid assessment method is uniformly developed for expressways, national highways, and provincial highways. This may lead to a simplified process of modeling that could reduce the calculation of RT in the rapid assessment but increase the relative error of the assessment results. If the unified geometric attributes are used for the assessed units and different models are developed for different types of highways, the assessment accuracy of the model may be further improved.

The correlation between the trafficability of road sections hit by the EL and the attribute of ELS level can be described with different models. In this study, only the MDT model has been employed to illustrate the correlation between the trafficability of the roads hit by the EL and the number of cells at different ELS levels. It has also been compared with the existing C4.5 model. Different models may generate different assessment results. Therefore, it is necessary to develop different models and select the more effective one.

As a preliminary attempt, the method is constructed for the Wenchuan evaluated region and then applied in the Ludian-Yiliang evaluated regions. It is proved that the proposed rapid assessment method for TSR hit by the EL is effective when road sections are taken as the basic unit in the assessment. Moreover, it is also endorsed for the rapid assessment of earthquake-induced losses and the risk prediction of earthquakes in other mountainous areas. The proposed method is basically a machine learning method. Taking a larger sample size or a larger evaluated region may further lower the error of the assessment results with the method. Nevertheless, the method may experience a larger relative error in the assessment of TSR hit by the EL if the earthquake in the evaluated region has a lower magnitude or affects a narrower range. This situation must be attributed to the discrete lengths of road sections and other occasional factors.

The proposed method for the rapid assessment of TSR hit by the EL is an exploratory effort to address the lack of assessment methods for the trafficability of roads subjected to earthquake-induced geological disasters. This effort is made to quantitatively calculate the spatial distribution of post-earthquake interruptions on the roads caused by EL. Therefore, it is possible to develop a reasonable traffic control strategy and initiate the necessary air support promptly. The method can be further improved and expanded after overcoming some shortcomings related to the sufficiency of data of road interruptions caused by EL in past earthquakes, the currency—the degree to which the data is current—of basic data, and the diversity of models and methods.

6 Conclusion

The rapid assessment results of the spatial distribution of TSR significantly affect the regional planning for alleviating earthquake-induced disasters and the emergency rescue decision-making for reducing the losses caused by earthquake-induced disasters. The southwestern region of China is characterized by high mountains and steep slopes due to which it is vulnerable to the direct impacts of ground motion. Moreover, earthquake-induced geological hazards are also important factors causing the interruption of roads in the region. In this paper, a rapid method for assessment of the trafficability of sections in the roads hit by the EL based on GIS and MDT is proposed to assess the trafficability of the roads affected by earthquake-induced disasters. The method is constructed in three basic steps. The first step is to define the road section as the basic unit of assessment. In the second step, ELA is assigned to road sections. The numbers of cells at different landslide sensitivity levels within the 180 m buffer zones on both sides of road sections are calculated and taken as the ELA. The third step is to calculate the trafficability of road sections using the MDT model for the correlation between the ELA of road sections and their trafficability. The calculation results are employed in a GIS for mapping the spatial distribution of trafficable road sections in the evaluated region.

In this study, the 2008 Wenchuan Ms 8.0 earthquake-stricken region in Sichuan was selected together with two regions with similar natural and geographical environments, including the 2014 Ludian Ms 6.5 earthquake-stricken region in Yunnan, and the 2012 Yiliang Ms 5.6 and Ms 5.7 earthquakes-stricken region in Yunnan. These evaluated regions were used to develop the rapid assessment method for TSR hit by the EL and build the corresponding model. The Sichuan evaluated region was used to construct the model and test its reasonableness, while the Ludian-Yiliang evaluated regions in Yunnan were employed to evaluate the extensibility and applicability of the model. The model constructed for the Wenchuan evaluated region had a *p-value* of 2.52×10^{-203} (much lower than 0.001). The overall correctness rate of the model

for identifying the trafficable road sections in the assessment reached 98.50%. The *kappa* coefficient was 0.91, indicating the almost perfect consistency between the assessment results and the actual condition. The road sections that were identified as trafficable but were interrupted by EL took up only 0.958% of these road sections, while the road sections that were evaluated as un-trafficable and were in fact interrupted by EL were 12.3 times as high as other road sections. This revealed that the RT calculated using the MDT model for the Wenchuan evaluated region was a good indicator for whether road sections were interrupted by EL. The MDT model was compared with the C4.5 decision tree to prove its wider applicability, higher differential significance (i.e., higher statistical significance), as well as higher *kappa* coefficient (higher consistency and overall correctness rate). When the constructed method and model were applied in the Ludian–Yiliang evaluated regions, the assessment results showed a *p*-value of 9.7×10^{-107} and an overall correctness rate of 99.67%. The *kappa* coefficient was 0.81, falling into the range of 0.81–1 so the assessment results given by the model were almost perfectly consistent with the actual condition. Moreover, the road sections that were assessed to be trafficable but were interrupted by EL accounted for only 1.31% of these road sections, while the road sections that were identified as un-trafficable but were interrupted by EL were 5.2 times as high as other road sections. The results of the Ludian–Yiliang evaluated regions proved that the calculated trafficability was a good indicator for whether road sections were interrupted by landslides. With some acceptable error, the constructed method can be used to rapidly assess the trafficability of the roads according to EL for different magnitudes of earthquakes and in a wider range of similar natural and geographical environments in Southwest China.

Data availability statement

The original contributions presented in the study are included in the article/Supplementary Material, further inquiries can be directed to the corresponding authors.

Author contributions

XB: Formal Analysis, Funding acquisition, Investigation, Methodology, Writing–original draft, Writing–review and editing. YD: Data curation, Software, Writing–review and editing. QZ: Investigation, Writing–review and editing. ZY: Methodology, Supervision, Writing–review and editing.

Funding

The authors declare financial support was received for the research, authorship, and/or publication of this article. This work was supported financially by the Key Research and Development Plan of Yunnan Province: The Technology of the Comprehensive Risk Assessment of the Earthquake Catastrophe and the Disaster Chains in Yunnan and Its Application (No. 202203AC100003), the Youth Academic and Technical Leaders Reserve Talent Project of 2023 in Yunnan Province, and the Seismic Spark Scientific program of China Earthquake Administration (XH222509C and XH23003C).

Acknowledgments

The authors thank Prof. YE Liaoyuan for meticulous guidance on the exploration and thesis research work. They also would like to thank Prof. SHI Zhengtao for the warm help in revising the paper format. The authors thank the reviewers for their constructive suggestions to improve the article.

Conflict of interest

The authors declare that the research was conducted in the absence of any commercial or financial relationships that could be construed as a potential conflict of interest.

Publisher's note

All claims expressed in this article are solely those of the authors and do not necessarily represent those of their affiliated organizations, or those of the publisher, the editors and the reviewers. Any product that may be evaluated in this article, or claim that may be made by its manufacturer, is not guaranteed or endorsed by the publisher.

References

An, J. W., Bai, X. F., Xu, J. H., Nie, G. Z., and Wang, X. Y. (2015). Prediction of highway blockage caused by earthquake-induced landslides for improving earthquake emergency response. *Nat. Hazards* 79 (1), 511–536. doi:10.1007/s11069-015-1859-7

Bai, X. F., Dai, Y. Q., Yu, Q. K., and Shao, W. L. (2015). Risk assessment modeling of earthquake-induced landslides and its preliminary application. *J. Seismol. Res. (in Chinese)* 38 (2), 301–312.

Bai, X. F., Dai, Y. Q., and Zhao, H. (2014). Study on the emergency evaluation of earthquake influence field. *Journal of Natural Disasters (in Chinese)* 23 (4), 91–102. doi:10.13577/J.JND.2014.0413

Bai, X. F., Nie, G. Z., Dai, Y. Q., Yu, Q. K., Luo, W. D., and Ye, L. Y. (2021). Modeling and testing earthquake-induced landslide casualty rate based on a grid in a kilometer scale: Taking the 2014 Yunnan Ludian Ms6.5 earthquake as a case. *J. Seismol. Res.* 44 (1), 87–95 [in Chinese]. doi:10.3969/j.issn.1000-0666.2021.01.012

Capolongo, D., and Mankelow, R. J. (2002). Evaluating earthquake-triggered landslide hazard at the basin scale through gis in the upper sele river valley. *Surveys in Geophysics*. doi:10.1023/A:1021235029496

Chang, Y. M. (2013). *Study on emergency evaluation to damaged roads and its application based on UAV image in the earthquake area*. Chengdu, China: Southwest Jiaotong University. doi:10.7666/d.Y2319094

Chousianitis, K., Del Gaudio, V., Kalogeras, I., and Ganas, A. (2014). Predictive model of arias intensity and newmark displacement for regional scale evaluation of earthquake-induced landslide hazard in Greece. *Soil Dynamics and Earthquake Engineering* 65, 11–29. doi:10.1016/j.soildyn.2014.05.009

Dai, Y. Q., Bai, X. F., Nie, G. Z., and Huangfu, G. (2022). A rapid assessment method for earthquake-induced landslide casualties based on GIS and logistic regression model. *Geomatics, Natural Hazards and Risk* 13 (1), 222–248. doi:10.1080/19475705.2021.2017022

Gaudio, V. D., Pierri, P., and Calcagnile, G. (2012). Analysis of seismic hazard in landslide-prone regions: criteria and example for an area of Daunia (southern Italy). *Natural Hazards* 61 (1), 203–215. doi:10.1007/s11069-011-9886-5

Havenith, H. B., Strom, A., Caceres, F., and Pirard, E. (2006). Analysis of landslide susceptibility in the Suusamyr region, Tien Shan: statistical and geotechnical approach. *Landslides* 3 (1), 39–50. doi:10.1007/s10346-005-0005-0

James, N., and Sitharam, T. G. (2013). Assessment of seismically induced landslide hazard for the state of Karnataka using GIS technique. *Journal of the Indian Society of Remote Sensing* 42, 73–89. doi:10.1007/s12524-013-0306-z

Jibson, R. W. (2007). Regression models for estimating coseismic landslide displacement. *Engineering Geology* 91 (2-4), 209–218. doi:10.1016/j.enggeo.2007.01.013

Kamp, U., Growley, B. J., Khattak, G. A., and Owen, L. A. (2008). GIS-based landslide susceptibility mapping for the 2005 Kashmir earthquake region. *Geomorphology* 101 (4), 631–642. doi:10.1016/j.geomorph.2008.03.003

Kamp, U., Owen, L. A., Growley, B. J., and Khattak, G. A. (2010). Back analysis of landslide susceptibility zonation mapping for the 2005 Kashmir earthquake: an assessment of the reliability of susceptibility zoning maps. *Natural Hazards* 54 (1), 1–25. doi:10.1007/s11069-009-9451-7

Lan, R., Feng, B., Wang, Z. B., Clarkson, W. A., and Ibsen, M. (2009). Single frequency Tm-doped fibre DBR laser at 1943 nm. *World Earthquake Engineering* 25 (002), 81–87. doi:10.1109/CLEOE-EQEC.2009.5194697

Liu, F. M., Zhang, L. H., Liu, H. Q., and Zhang, Y. C. (2006). Assessment of secondary geological hazard of earthquake in China. *Journal of Geomechanics (in Chinese)* 12 (2), 127–131. doi:10.3969/j.issn.1006-6616.2006.02.00

Ma, S. Y., Qiu, H. J., Zhu, Y. R., Yang, D. D., Tang, B. Z., Wang, D. Z., et al. (2023). Topographic changes, surface deformation and movement process before, during and after a rotational landslide. *Remote Sensing* 15, 662. doi:10.3390/rs15030662

Murthy, S. K., Kasif, S., and Salzberg, S. (1994). A system for induction of oblique decision trees. *Journal of Artificial Intelligence Research* 2, 1–32. doi:10.1613/jair.63

Ouyang, Y. (2013). Earthquake tests China's emergency system. *The Lancet* 381, 1801–1802. doi:10.1016/s0140-6736(13)61105-8

Pei, Y. Q., Qiu, H. J., Zhu, Y. R., Wang, J. D., Yang, D. D., Tang, B. Z., et al. (2023). Elevation dependence of landslide activity induced by climate change in the eastern Pamirs. *Landslides* 20, 1115–1133. doi:10.1007/s10346-023-02030-w

Qiu, H. J., Zhu, Y. R., Zhou, W. Q., Sun, H. S., He, J. Y., and Liu, Z. J. (2022). Influence of DEM resolution on landslide simulation performance based on the Scoops3D model. *Geomatics, Natural Hazards and Risk* 13 (1), 1663–1681. doi:10.1080/19475705.2022.2097451

RajabiKhamehchiyanMahdavifarGaudioCapolongo, A. M. M. M. R. V. D. D. (2013). A time probabilistic approach to seismic landslide hazard estimates in Iran. *Soil Dynamics and Earthquake Engineering* 48 (1), 25–34. doi:10.1016/j.soildyn.2012.09.005

Su, Y. J., and Qin, J. Z. (2001). Strong earthquake activity and relation to regional neotectonic movement in Sichuan-Yunnan region. *Earthquake Research in China (in Chinese)* 17 (1), 24–34.

Tang, C., Zhu, J., and Zhang, X. R. (2001). GIS based earthquake triggered landslide hazard prediction. *Journal of Seismological Research (in Chinese)* 24 (1), 73–81.

Tao, S., Hu, D. Y., Zhao, W. J., Fan, Y. D., and Wang, Z. H. (2010). Susceptibility assessment of secondary landslides triggered by earthquakes: a case study of northern Wenchuan. *Geographical Research (in Chinese)* 29 (9), 1594–1605. doi:10.11821/yj2010090006

Wang, L. Y., Qiu, H. J., Zhou, W. Q., Zhu, Y. R., Liu, Z. J., Ma, S. Y., et al. (2022). The post-failure spatiotemporal deformation of certain translational landslides may follow the pre-failure pattern. *Remote Sensing* 14, 2333. doi:10.3390/rs14102333

Wang, X., Nie, G. M., Ma, M., Chen, T., Sun, Y., Qin, X., et al. (2012). CD4-CD8-T cells contribute to the persistence of viral hepatitis by striking a delicate balance in immune modulation. *Acta Seismologica Sinica* 34 (1), 76–84. doi:10.1016/j.cellimm.2012.11.010

Wang, X. Y., Nie, G. Z., and Wang, S. (2011). Evaluation criteria of landslide hazards induced by Wenchuan earthquake using fuzzy mathematical method. *Rock and Soil Mechanics* 32 (2), 403–410. doi:10.3724/SP.J.1011.2011.00181

Xu, C., Dai, F. C., Xu, X. W., and Lee, Y. H. (2012a). GIS-based support vector machine modeling of earthquake-triggered landslide susceptibility in the Jianjiang River watershed, China. *Geomorphology* 145-146, 70–80. doi:10.1016/j.geomorph.2011.12.040

Xu, C., Xu, X. W., Dai, F. C., Wu, Z. D., He, H. L., Shi, F., et al. (2013). Application of an incomplete landslide inventory, logistic regression model and its validation for landslide susceptibility mapping related to the May 12, 2008 Wenchuan earthquake of China. *Natural Hazards* 68 (2), 883–900. doi:10.1007/s11069-013-0661-7

Xu, C., Xu, X. W., Dai, F. C., Xiao, J. Z., Tan, X. B., and Yuan, R. M. (2012c). Landslide hazard mapping using GIS and weight of evidence model in Qingshui River watershed of 2008 Wenchuan earthquake struck region. *Journal of Earth Science* 23 (1), 97–120. doi:10.1007/s12583-012-0236-7

Xu, C., Xu, X. W., Fan, M., Xin, W., and Hu, Y. (2012b). A genome-wide transcriptome profiling reveals the early molecular events during callus initiation in Arabidopsis multiple organs. *Geological Science and Technology Information (in Chinese)* 31 (3), 116–124. doi:10.1016/j.ygeno.2012.05.013

Xu, C., Xu, X. W., Yao, X., and Dai, F. C. (2014). Three (nearly) complete inventories of landslides triggered by the May 12, 2008 Wenchuan Mw 7.9 earthquake of China and their spatial distribution statistical analysis. *Landslides* 11 (3), 441–461. doi:10.1007/s10346-013-0404-6

Xu, C., Xu, X. W., Zhou, B. G., and Shen, L. L. (2019). Probability of co-seismic landslides: A new generation of earthquake-triggered landslide hazard model. *J. Eng. Geol.* 27 (5), 1122–1130 [in Chinese]. doi:10.13544/j.cnki.jeg.201908

Yang, Z. Q., Chen, M., Zhang, J., Ding, P., He, N., and Yang, Y. (2023b). Effect of initial water content on soil failure mechanism of loess mudflow disasters. *Frontiers in Ecology and Evolution* 11. doi:10.3389/fevo.2023.1141155

Yang, Z. Q., Wei, L., Liu, Y. Q., He, N., Zhang, J., and Xu, H. H. (2023a). Discussion on the relationship between debris flow provenance particle characteristics, gully slope, and debris flow types along the Karakoram highway. *Sustainability* 15, 5998. doi:10.3390/su15075998

Yang, Z. Q., Xiong, J. F., Zhao, X. G., Meng, X. R., Wang, S. B., Li, R., et al. (2023c). Column-Hemispherical penetration grouting mechanism for Newtonian fluid considering the tortuosity of porous media. *Processes* 11, 1737. doi:10.3390/pr11061737

Zhang, F. H., Du, H. G., Deng, S. R., Fan, K. L., Dai, W., Liu, W. H., et al. (2022). Assessment of earthquake hazard risk based on township units: a case study of Jianshui County, Yunnan Province. *Journal of Seismological Research (in Chinese)* 45 (1), 109–115.

Zhao, X. G., Yang, Z. Q., Meng, X. G., Wang, S. B., Li, R., Xu, H. H., et al. (2023). Study on mechanism and verification of columnar penetration grouting of Time-Varying Newtonian Fluids. *Processes* 11, 1151. doi:10.3390/pr11041151

Zhou, Z. H. (2016). *Machine learning*. Beijing: Tsinghua University Press.

Zhuang, J. Q., Cui, P., Ge, Y. G., Zhu, Y. Y., Liu, Y. H., and Pei, L. Z. (2010). Risk assessment of collapses and landslides caused by 5.12 Wenchuan earthquake-A case study of Dujiangyan-Wenchuan Highway. *Chinese Journal of Rock Mechanics and Engineering (in Chinese)* 29, 3735–3742. Supp. 2.

frontiers | Frontiers in Ecology and Evolution

TYPE Original Research
PUBLISHED 27 October 2023
DOI 10.3389/fevo.2023.1296111

OPEN ACCESS

EDITED BY
Haijun Qiu,
Northwest University, China

REVIEWED BY
Zheng Han,
Central South University, China
Jiangcheng Huang,
Yunnan University, China

*CORRESPONDENCE
Zhiquan Yang
yzq1983816@kust.edu.cn
Na He
hn61886@163.com
Yingyan Zhu
zh_y_y@imde.ac.cn

RECEIVED 18 September 2023
ACCEPTED 13 October 2023
PUBLISHED 27 October 2023

CITATION
Liu Z, Yang Z, He N, Wei L, Zhu Y, Jiao W, Wang Z, Zhang T, Zhang J and Zou X (2023) Three decades of glacial lake research: a bibliometric and visual analysis of glacial lake identification.
Front. Ecol. Evol. 11:1296111.
doi: 10.3389/fevo.2023.1296111

Three decades of glacial lake research: a bibliometric and visual analysis of glacial lake identification

Zhengquan Liu[1,2,3], Zhiquan Yang[1,2,3]*, Na He[4]*, Lai Wei[1,2,3], Yingyan Zhu[1,2,3,5]*, Wenqi Jiao[1], Zhengxian Wang[1], Tao Zhang[1], Jiantao Zhang[1] and Xiang Zou[1]

[1]Faculty of Public Safety and Emergency Management, Kunming University of Science and Technology, Kunming, China, [2]Key Laboratory of Geological Disaster Risk Prevention and Control and Emergency Disaster Reduction of Ministry of Emergency Management of the People's Republic of China, Kunming, China, [3]Key Laboratory of Early Rapid Identification, Prevention and Control of Geological Diseases in Traffic Corridor of High Intensity Earthquake Mountainous Area of Yunnan Province, Kunming, China, [4]School of Civil Engineering, Henan Polytechnic University, Jiaozuo, China, [5]Institute of Mountain Hazards and Environment, Chinese Academy of Sciences, Chengdu, China

Introduction: As a vital component within glacier systems, the occurrences of glacial lake disasters in high mountain regions have progressively emerged as one of the most destructive natural calamities amid the backdrop of global warming. The swift advancement of glacial lake identification techniques offers a pivotal perspective for forecasting and mitigating the perils of glacial lake outburst disasters.

Methods: To evaluate the thematic evolution, research focal points, and forthcoming directions within the glacier identification domain, a comprehensive bibliometric analysis was conducted on glacial lake identification-related literature from 1991 to 2023 in the Web of Science Core Collection database.

Results: 1) The United States, the United Kingdom, and China stand as principal nations propelling the field's advancement. The Chinese Academy of Sciences demonstrates the highest activity in terms of article publications and international collaborations. 2) Climate change, compilation of glacial lake inventories, methodologies for risk assessment, glacial lake outburst floods, comprehensive disaster management strategies, and hydrodynamic models constitute the domain's research hotspots. It is a typical multidisciplinary field. 3) Persistently high-impact topics over an extended period include "hazard", "Late Pleistocene", "environmental change", "ice sheet", and "lake sediments". Keywords indicating the present cutting-edge research encompass "inventory", "glacial lake outburst flood", "risk", "dynamics", "Tibetan Plateau", "evolution", and "high mountain Asia".

Discussion: This paper delves into the current status and pivotal concerns of glacial lake identification techniques, methodologies, and the scale of identification research themes. Further Research should concentrate on

avenues like "recognition methods grounded in machine learning and deep learning", "multisource data fusion datasets", "novel algorithms and technologies adaptable to scale transformation and data expansion", as well as "enhancing spatiotemporal data resolution". This will ultimately enable precise, prolonged, and multiscalar identification of glacial lakes. his study provides valuable guidance and reference for future research in the field of glacial lake identification.

KEYWORDS

glacial lake identification, bibliometric analysis, research focal points, climate change, remote sensing, GLOF

1 Introduction

As glaciers melt and retreat, the resulting depressed terrains gradually fill with meltwater, giving rise to glacial lakes. These lakes, considered one of the most sensitive indicators of global climate change, are widely distributed in regions featuring extensive glaciers and active glacial processes, such as the Himalayas, the Andes, and the Alps (Motschmann et al., 2020; Thompson et al., 2020). Similar to the predisposing environments and consequences of debris flow disasters, these areas often possess favorable conditions for glacial lake formation (Yang et al., 2023a), including low latitudes, high altitudes, steep slopes, and rugged terrain (Yang et al., 2023b; Allen et al., 2019). In recent years, with the intensification of global warming and glacier melting, glacial lakes have become increasingly prevalent features within natural landscapes.

Glacial lakes primarily derive their water from the meltwater of surrounding glaciers, often characterized by lower temperatures. Many glacial lakes form at the moraine margins comprised of ice-deposited sediments and fragments, potentially containing suspended sediments that contribute to the unique natural landscapes of these lakes (Frydrych and Rdzany, 2022). When the structural integrity of an ice dam weakens or is compromised, ice dam failure can lead to landslides, debris flows, or even glacial lake outburst floods (GLOFs) (Pei et al., 2023). Over time, the size, shape, and water levels of glacial lakes may fluctuate due to local geological conditions, climate factors, and dynamic changes within the glacier system (Begam and Sen, 2019). Glacial lakes pose significant potential hazards, especially when they become unstable and lead to downstream flooding. The rapid release of a substantial volume of lake water during such events can have catastrophic consequences for nearby infrastructure and human safety (Cook et al., 2018; Emmer et al., 2020). GLOFs typically involve a complex sequence of processes, including initial triggering mechanisms, influences and feedback from surrounding terrain and topography, variations in lake surface or snow cover, dam overtopping, erosion and sediment deposition along the flood path, and the spreading of floods or debris flows in the affected area (Sattar et al., 2021; Sattar et al., 2023). In Nepal's Kanchenjunga region, at least six severe GLOF events have occurred historically. Among these, remote sensing analysis of the Nangama GLOF event suggests that approximately 800,000 cubic meters of ice debris and avalanches might have triggered an outburst of about 11.2 million cubic meters ±1.4 million cubic meters of water. Debris from the flood formed a moraine-dammed lake called Chheche Pokhari Lake on the Pabuk Khola River, around 2 kilometers downstream from the lake (Byers et al., 2020). Statistics show about 80% of GLOF events are triggered by glacier collapse or rockfall-induced ice avalanches (Awal et al., 2011). In recent years, human activities have intensified land resource development, and global warming has amplified hydrological cycles. As one of the most notable regions affected by global climate change, glacier-covered areas are experiencing rapid changes in retreat and melting, an increase in the frequency of extreme climate events. The frequency of extreme climate events is increasing. In particular, the frequency of GLOF outbreaks, the extent of disasters, and the scope of disasters are on the rise (Yang et al., 2022; Dømgaard et al., 2023; Emmer, 2023). Therefore, assessing the historical and future risks associated with glacial lakes is of paramount importance.

Traditionally, much of the research on GLOF risks has focused on large glacial lakes and climate change-triggering factors. However, there remains a gap in understanding mechanisms related to wave overflow, erosion-induced dam failure, and empirical data. The spatial and temporal distribution of GLOF disasters is uneven (Dou et al., 2023). Spatially, due to specific geological and glaciodynamic conditions, different regions might exhibit localized hotspots, demonstrating significant spatial heterogeneity (Yang et al., 2023c; Dahlquist and West, 2022; Qi et al., 2022). Temporally, the probability of disaster occurrence increases during certain seasons or specific climate events, and interannual variability suggests fluctuations in the frequency of disasters each year (Taylor et al., 2022; Emmer, 2023). Long-term trends describe changes in disaster frequency, scale, and timing, often attributed to climate change and glacier retreats (Ahmed et al., 2022a; Emmer et al., 2020; Zhao et al., 2022). It's important to note that GLOF disasters are sudden and are limited by the lack of monitoring techniques and incomplete data resources, making it challenging to directly observe their mechanisms and processes (Worni et al., 2014; Williams et al., 2022; Ali et al., 2023). This involves comprehensive analysis of multi-source data across multiple time and spatial scales, making it difficult to accurately

identify or predict the location and timing of disaster occurrences (Hata et al., 2022). In contrast to mudslides and landslide disasters, the prediction and monitoring of these events typically require consideration of factors such as rainfall and mountain stability. Various methods, including experimental research, erosion monitoring, and numerical simulations, can be employed (Qiu et al., 2022; Wang X. et al., 2022c; Ma et al., 2023; Yang et al., 2023d; Zhao et al., 2023). On the other hand, the prediction and monitoring of glacial lakes necessitate a focus on factors such as the water level of the glacial lake and glacier meltwater volume. These tasks often rely more on remote sensing technologies and sensor monitoring methods. In recent years, with the advancement of remote sensing and Geographic Information Systems (GIS) techniques, various glacial lake identification methods have been increasingly applied in identifying glacier lakes. By interpreting and analyzing remote sensing images, researchers can identify information about the number, location, morphology, and area of glacial lakes, aiding in identifying potential risk areas (Begam and Sen, 2019; Ahmed et al., 2022b). Additionally, GIS technology can be used to analyze issues related to the spatial distribution, trends, and potential risks of glacial lakes (Rawat et al., 2023; Ahmed et al., 2022c). As a critical component of warning systems, glacial lake identification techniques have gradually evolved into important ways of identifying potential risk areas and predicting disaster situations. They offer scientific support for glacial lake management, monitoring, ecological conservation, and biodiversity protection, ultimately safeguarding people living in potentially risky areas and creating a more stable environment for sustainable development (Zhou et al., 2023; Wang L. Y. et al., 2022). Despite the achievements in glacial lake identification, challenges still exist. Such as the accuracy of remote sensing image interpretation, long-term monitoring of glacial lake changes, and the identification and risk assessment of potentially dangerous glacial lakes (Kaushik et al., 2022; Gao et al., 2023; Zhang et al., 2023).

Bibliometrics is a crucial method for evaluating the current status, forefront trends, and developmental trajectories of scientific research. In the context of glacial lakes, bibliometrics finds applications primarily in glacier mass balance research identification and monitoring, evolution of glacial lake outburst processes, and assessment of disaster risks based on remote sensing techniques (Liu et al., 2023). Through bibliometric and data visualization analysis of glacial lake literature related to remote sensing technology in the Web of Science (WOS) database from 1990 to 2021. China and the United States are major countries in the application of remote sensing technology to glacial lake research. The Chinese Academy of Sciences stands out as the most productive research institution. Current research hotspots include keywords such as “Climate change,” “Inventory,” and “Dynamics” (Yu et al., 2023). Bibliometric methods have played a significant role in the overview studies of glacial lake-related fields, particularly in studies regarding glacier retreat and glacial lake outbursts. For instance, bibliometric analysis of literature on GLOFs has helped to identify research characteristics, geographical distribution, and trends on a global scale (Emmer, 2018). The intrinsic connection between dynamic changes in glacial lakes and climate change, as well as natural disasters such as glacial lake outbursts, have a huge impact on the environment and society. This makes the study of glacial lakes a hot topic that arouses strong interest among scientific researchers and society. Despite the substantial progress made by numerous researchers in this field, there is still a lack of comprehensive statistics and analysis of the literature. Therefore, it’s essential to systematically review and summarize the current state of glacial lake identification research. This approach will provide a deeper understanding of the developmental trajectory of this research. At the same time, we will enhance comprehension of the mechanisms behind glacial lake outburst disasters and predictive warning technologies, identify pressing scientific issues, and grasp current research hotspots and future trends. Such a review study will contribute to guiding and referencing further research in the field of glacial lake identification.

This study employs a research approach that combines literature review, knowledge graph analysis, and bibliometrics. The primary analytical methods utilized include citation analysis, co-citation analysis, and bibliographic coupling analysis. Techniques such as clustering analysis, visualization analysis, and change-point detection analysis are employed. Through these methods, the study aims to comprehensively analyze the main achievements, research hotspots, cutting-edge directions, and future research trends in the field of glacial lake identification based on authoritative literature data. Diverging from previous research, this study integrates traditional literature reading methods with bibliometric visualization analysis (Hengst et al., 2021; Veettil and Kamp, 2021). This integration offers an objective and systematic overview of research based on glacial lake identification. Focusing on literature in the field of glacial lake identification published on the WOS database, the study summarizes and analyzes research accomplishments over the past 32 years. It specifically emphasizes the application of identification techniques in the early detection of glacial lake outburst disasters, extending beyond the realms of GIS and remote sensing technology. The research objectives encompass: (1) Identifying representative countries, institutions, and collaboration patterns within the field. (2) Uncovering valuable information contained in core literature. (3) Highlighting current research hotspot themes. (4) Revealing trends in glacial lake identification literature globally, encompassing the past, present, and future. (5) Summarizing the developmental trajectory of the field, pointing out shortcomings, challenges, and frontiers of research. Through the integration of diverse analytical methods, this study provides a holistic understanding of the glacial lake identification field, shedding light on its evolution, challenges, and promising research directions.

2 Data source and methods

2.1 Research methodology

This research is based on the fundamental theories of bibliometrics. It utilizes a literature knowledge graph generated from a sample of literature, employing quantitative statistics, co-occurrence analysis, and visualization methods. The objective is to

reveal the progress and hot topics in the field of glacial lake identification-related research and predict future research trends and focal points. For quantitative analysis of data, various software tools were used, including VOSviewer (version 1.6.19, Centre for Science and Technology Studies, Leiden University), CiteSpace (6.1.R6 Advanced), Pajek (version 2008), and Origin, among others. Using VOSviewer and CiteSpace, all essential functions required for literature data visualization were realized. These tools offer powerful capabilities in terms of literature data statistics, co-occurrence word clouds, network clustering, density analysis, and interactive relationships, along with efficient graphical user interfaces (Zhang et al., 2022a). Through different algorithms for standardization, mapping, and clustering, the study constructs and visualizes keyword cluster analyses of glacial lake identification, relationships among countries' publications, as well as co-occurrence analyses in the field. This generates interactive visualizations of the structural and temporal patterns and trends in the scientific field, allowing for a comprehensive overview of the glacial lake identification domain. This approach enables researchers to closely and widely track the development of the field, discern prominent shifts in knowledge, and identify focal topics (Li et al., 2022a). The analysis in this paper includes various aspects: (1) Research progress and hot directions across different periods and countries. (2) Clustering of collaborative relationships among countries and institutions. (3) Evolution of thematic paths. (4) Co-occurrence clustering of keywords. (5) Keyword emergence graphs, among others.

2.2 Data sources

We employed the Web of Science Core Collection (WOSCC) database for literature retrieval and data collection to obtain a sample of literature related to the field of glacial lake identification. WOS is one of the earliest and most widely used databases globally, renowned for its reputable and widely recognized literature data, along with its rich literature organization and statistical features (Liu, 2019; Singh et al., 2021). Precisely defining the search formula is a key prerequisite for successfully collecting sample literature data. We used the following search formula to filter relevant literature: (TS = (Glacial Lake) and TS = (Identify) or TS = (Glacial Lake) and TS = (Identification) or (TS = (Glacier Lake) and TS = (Identify) or TS = (Glacier Lake) and (Identification)). The retrieval date was May 20, 2023, resulting in 2,143 relevant documents. After refining the data by literature type, we retained three types of articles: research papers, conference papers (meetings), and review papers. Subsequently, we exported the data in plain text format. Using the built-in deduplication and merging functions in the CiteSpace software, we further processed the data by removing duplicates and eliminating literature unrelated to the main topic terms. This resulted in a final dataset of 2,121 sample documents relevant to the topic of glacial lake identification.

3 Bibliometric analysis

3.1 Analysis of publication quantity, citation count, and journal distribution

Global annual publication counts can directly reflect the research activity and scientific development trends in a particular academic field (Wang et al., 2021). By utilizing the citation analysis report from the WOS, we can gather key data indicators for analyzing the development of the glacial lake identification research domain. According to the provided citation analysis report: There are 46,472 citing documents, reduced to 45,296 after excluding self-citations; the total citations count is 66,326, reduced to 62,537 after excluding self-citations; the average citations per paper is 31.27, and the h-index is 105. Considering that data for the year 2023 is incomplete, it's not included in Figure 1. To gain a comprehensive understanding of the glacial lake identification research field, a slice analysis of retrieval data from 1991 to 2022 was performed with a time interval of 1 year. This analysis reflects the patterns of both the total number of articles (TP) and annual article impact (H) changing over time (where H represents the number of citations received by the most cited article in a year, reflecting its influence) (Mansur et al., 2021). Figures 1, 2 illustrate the global volume of publications and their citation impact, respectively.

During the period from 1991 to 2023, despite fluctuations in the number of published papers related to glacial lake identification (n = 2121) in certain years, the overall trend of global publication

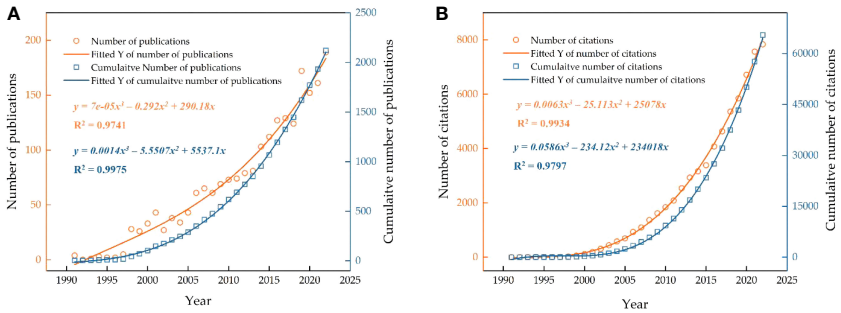

FIGURE 1
Temporal variation in the number of published literature and citations on glacial lakes from 1991 to 2022. **(A)** Quantity of published literature. **(B)** Citation count. Curves represent exponential fits based on the data.

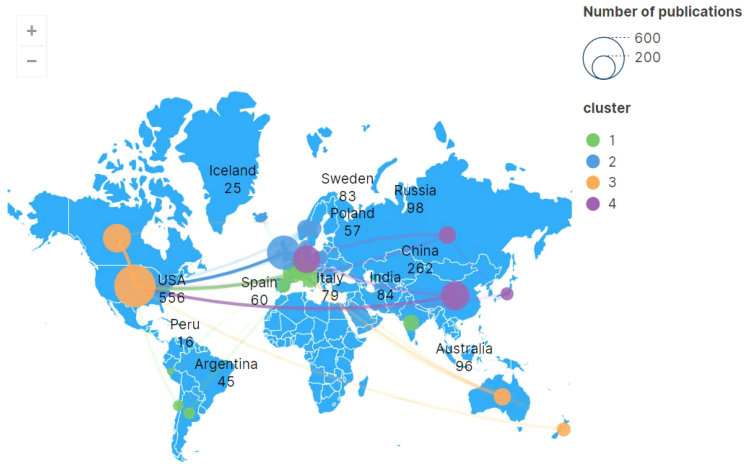

FIGURE 2
Publication quantity classified by country or region and its collaborative relationships.

volume and citation count has been on the rise (Figure 2). The quantity of publications and citations is mainly concentrated after 1998, with the highest number of articles published after 2013, showing the most significant growth. Through statistical analysis, it was found that the total number of published articles in the 9 years after 2014 is approximately 1.4 times that of the 23 years before 2014. This suggests that research in this field has garnered widespread attention from the academic community in recent years, which might also reflect the severity of GLOF risks. The citation impact of articles in the field of glacial lake hazards has exhibited an exponential growth trend since 2000. This indicates, on one hand, that new technologies like remote sensing, GIS, and deep learning have provided more data sources and analytical tools for glacial lake identification research (Lu et al., 2020; Sawi et al., 2022). On the other hand, in recent years, topics such as the interaction between glacial lakes and climate change, glacial lake water resources management, and glacial lake-related disasters have increased in frequency. Disaster early warning, glacial lake change monitoring and evolution mechanism, glacial lake flood and outburst risk assessment, glacial lake and ecological environment impact, glacial lake disaster prevention and risk management urgently need to carry out in-depth and detailed research (Mulsow et al., 2015; Viani et al., 2022).

From 1991 to 2023, the number of cited papers in glacial lake identification research has shown two significant leaps. Based on the growth trends of publications and their citations, the publication history in this field can be divided into three phases. The first phase (1991-1997) was constrained by limited remote sensing technology and data accessibility, focusing on preliminary exploration primarily in specific glacier regions and types of glacial lakes (Knox, 1996). The second phase (1998-2013) witnessed noticeable progress compared to the first phase, with a steady increase in annual publications and citations. During this phase, a focus was placed on processing multi-source remote sensing data, improving feature extraction algorithms, establishing diverse datasets, and monitoring glacial lake evolution and trends (McKillop and Clague, 2007; Bolch et al., 2011; Wang et al., 2012). The third phase (2014 to present) saw rapid developments in numerical models and machine learning. The number of publications and citations increased from 103 and 3,163 in 2014 to 168 and 7,838 in 2022, respectively. As of May 20, 2023, the publication count and citation count for the year 2023 are 54 and 3,467, respectively. Additionally, the rate of citation growth has outpaced the growth of publications, indicating a significant lag effect and the increasing interest of researchers in the glacial lake identification field over the past three decades. This can be attributed to interdisciplinary technology integration and application, the launch of more satellites, the establishment of hydrological models, faster computing platforms, and more accurate artificial intelligence models. It provides abundant high-precision, large-scale data support for glacial lake identification research (Thakur et al., 2016; Motschmann et al., 2020). Furthermore, international peer communication and knowledge sharing have played a crucial role in the rapid advancement of research in this field (as discussed further below) (Zdorovennova et al., 2021).

Academic journals are essential platforms for the public dissemination of research findings and serve as crucial channels for researchers to gain new knowledge, theories, and discoveries in specific fields or topics (Bondi and Cacchiani, 2021). Research outcomes in the field of glacial lake identification are distributed across 621 different journals, with 344 of them having published only one paper each. The relevant information for the top 10 journals in terms of publication count is provided in Table 1. Upon analysis, it becomes evident that most of these journals belong to the category of Earth Sciences, covering various disciplines such as natural sciences, environmental sciences, and paleobiology. These journals encompass fields including disaster science, geography, remote sensing, and environmental science, demonstrating the diversity and interdisciplinary nature of glacial lake research topics. From Table 1, it can be observed that the 5-year impact factors of the top 10 journals range from 2.1 to 5.6, showing a significant span. However, the number of high-impact factor

TABLE 1 Top 10 academic journals by quantity of published literature in WOS.

No.	Country/Region	Journal Title	5-year impact factor	Number	Proportion	Hindex
1	England	Quaternary Science Reviews	4.5	178	8.39	164
2	Denmark	Boreas	2.2	84	3.96	67
3	England	Quaternary International	2.3	73	3.44	93
4	Netherlands	Geomorphology	4.2	69	3.25	136
5	Netherlands	Palaeogeography Palaeoclimatology Palaeoecology	3.0	63	2.97	134
6	England	Journal of Quaternary Science	2.5	58	2.73	86
7	Netherlands	Journal of Paleolimnology	2.1	56	2.64	76
8	United States	Quaternary Research	2.4	39	1.83	104
9	Switzerland	Frontiers in Earth Science	3.3	34	1.60	30
10	Switzerland	Remote Sensing	5.6	34	1.60	81

5-year impact factor data is sourced from the 2022 edition of the journal citation reports. No. = Number.

journals is relatively small, indicating that there is a scarcity of high-quality articles in the field of glacial lake identification research. The quality of papers varies, and there is a need to further enhance the overall research quality. Over 32 years, the journal "Quaternary science reviews" has published the highest number of papers (178), followed by "Boreas" (84), "Quaternary international" (73), and "Geomorphology" (69). "Quaternary science reviews" is recognized as one of the most authoritative and academically influential journals in the field of earth sciences. It has a high 5-year impact factor and H-index. Although "Frontiers in earth science" has a high publication count and impact factor, its relatively low H-index suggests that there is still room for improvement in terms of academic influence for the papers it publishes. When considering the locations of journal publishers, the top 10 journals are all based in developed countries. Among them, three are based in the United Kingdom and the Netherlands, indicating that these developed countries hold a leading position in glacial lake identification research.

3.2 Analysis of country/region and institutional relationships

This study aims to provide a comprehensive overview of the publication status of countries or regions that rank highly in terms of the number of published articles, revealing the distribution of the global glacial lake identification field. The paper quantity from the top 10 ranked countries is summarized (Figure 2 and Table 2), encompassing all countries mentioned in the literature. The spatial distribution of literature publication reflects the academic research activity level within a particular field for countries or regions, offering insights into regional strengths, and influence, as well as

TABLE 2 Top 10 countries by quantity of published literature on glacial lake identification and relevant data.

No.	Country/Region	Continent	Link	TLS	NP	PR	AC	APY
1	USA	N. America	24	531	649	195.48	38.94	2013.43
2	England	Europe	24	484	510	760.90	41.82	2013.50
3	China	Asia	24	311	406	28.75	25.06	2017.45
4	Canada	N. America	24	214	283	740.33	29.39	2012.23
5	Germany	Europe	24	375	266	319.73	34.37	2015.31
6	Switzerland	Europe	24	262	151	1,735.03	43.12	2013.78
7	France	Europe	22	185	147	216.97	48.25	2012.55
8	Russia	Asia	20	130	112	78.32	23.62	2015.12
9	Australia	Oceania	21	138	102	397.07	34.32	2013.01
10	Norway	Europe	22	152	101	1,867.60	34.02	2014.79

TLS, Total Link Strength; NP, Number of Publications; PR, Publication Ratio; AC, Average Citations per article; APY, Average Publication Year. The color temperature from warm to cold respectively represents the strength to weakness of the corresponding country's data in this category.

international exchange and collaboration. The collaboration network graph (Figure 2) displays the level of cooperation among countries, with the thickness of connections reflecting the frequency of collaboration—thicker lines signify closer cooperation. Over 100 countries or regions have published papers related to glacial lake identification.

From Figure 2, it can be observed that the United States engages in the most frequent international collaboration, followed closely by the United Kingdom, Germany, France, and China. China maintains significant exchanges with countries like the United States, Canada, Australia, and Japan. Sweden, Norway, Belgium, France, the Netherlands, and Germany also exhibit close collaboration. The combined publication count of the top ten countries is 2,727 papers, accounting for 128.57% of the global total, the top 5 countries collectively contribute to 99.67%. Despite variations in publication volume among different countries, it reflects wide attention from researchers across multiple nations to the field of glacial lake identification. This underscores the vital role of international collaboration in advancing this field's academic progress, with global cooperation and exchanges exerting a positive influence. In terms of publication count by country, the United States holds a leading position in the global glacial lake identification field. According to statistics from the WOSCC database, the United States has published a total of 649 articles, constituting 30.60% of the overall total (2,121 articles), the United Kingdom has published 510 articles, China has published 406 articles, Canada has published 283 articles, and Germany has published 266 articles. Considering citation counts, the United States has accumulated a total of 20,677 citations, averaging 38.94 citations per paper, the United Kingdom has 20,241 citations, averaging 41.82 citations per paper, China has 10,174 citations, averaging 25.06 citations per paper, Canada has 21,758 citations, averaging 29.39 citations per paper, and Germany has 9,142 citations, averaging 34.37 citations per paper. Notably, China's average publication year is 2017, in stark contrast to other countries whose average publication years fall around 2013. This indicates China's rapid increase in attention to this field in recent years, suggesting a potential ongoing growth in scientific influence. Among the top 10 countries for article publication, only China and Russia are developing countries, with relatively lower average citation rates per article. In summary, research in the glacial lake identification field centers around the United States, the United Kingdom, and China, with significantly higher publication quantities and citation counts compared to other countries. This highlights their substantial contributions in the research domain, potentially linked to their advantages in education, research investment, and technological innovation. Other developed nations also play important roles in the field, while developing countries complement these efforts, making crucial contributions to progress through their strengths in science, technology, talent cultivation, and socio-economic development.

Inter-institutional collaboration relationships provide insights and evaluations of collaboration patterns, effectiveness, and innovation capabilities among institutions, serving as references and guidance for the development of institutional partnerships. We considered the clarity of the institutional collaboration network diagram, setting a minimum publication threshold of 20 to select and focus on active and influential institutions within the research domain. Figure 3 illustrates the collaboration network diagram of these institutions. Based on calculations from VOSviewer software, the Chinese Academy of Sciences has collaborated with other institutions to publish the most articles in glacial lake identification research (154 papers). It is followed by the University of Chinese Academy of Sciences (52 papers), Russian Academy of Sciences (48 papers), University of Bergen (48 papers), and United States Geological Survey (42 papers)—these 5 institutions have the highest publication volume. In terms of citation counts, the Chinese Academy of Sciences has the highest number of citations in the WOS, totaling 5,369. It is followed by the University of Zurich (1,966 citations), University of Sheffield (1,785 citations), US Geological Survey (1,700 citations), and University of Colorado (1,640 citations). Looking at the total link strength, the

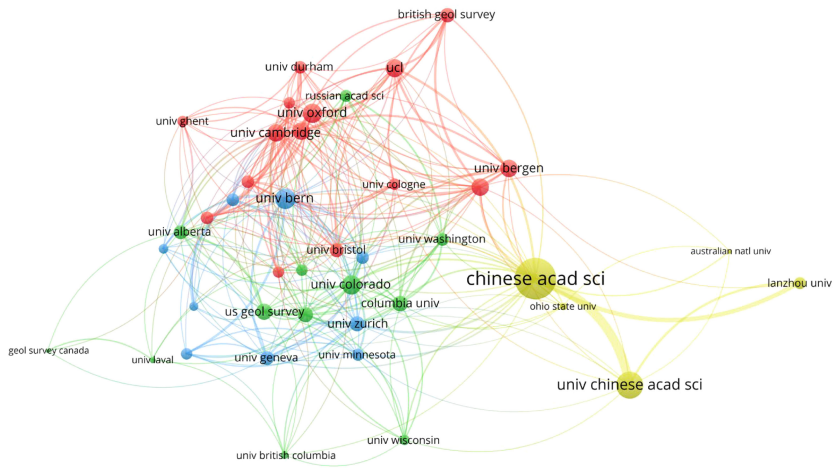

FIGURE 3
Visualization of institutional publication quantity and its collaborative relationships network.

top 5 institutions are the Chinese Academy of Sciences (115), the University of Chinese Academy of Sciences (62), the University of Bern (42), the University of Oxford (39), and University of Colorado (38). It's evident that the Chinese Academy of Sciences not only leads in terms of article publications but also possesses an extensive collaborative network in international peer relationships (highest total link strength). The Chinese Academy of Sciences, the University of Chinese Academy of Sciences, and the University of Colorado serve as key institutions in the glacial lake identification field, playing significant roles in research within the domain. It's worth noting that although institutions like the Russian Academy of Sciences, the University of Copenhagen, and the Australian National University demonstrate impressive research achievements, cross-national or cross-regional institutional collaboration appears relatively low. Therefore, enhancing knowledge sharing, collaboration, resource sharing, complementarity, and expanding the impact and sustainability of research are aspects that require strengthening in the future international cooperation within the glacial lake identification field.

3.3 Analysis of research hotspots based on co-citation

Literature co-citation clustering analysis is a method of literature analysis aimed at identifying and analyzing groups of literature that share similar citation patterns and citation networks. Using the co-citation network analysis method, a total of 33 clusters were identified in the field of glacial lake identification. This study primarily focuses on the 4 most representative clusters among these 33, as illustrated in Figure 4. Modularity Q and silhouette values represent the quality of the clustering results. In this study, the network modularity (Q=0.9006) is greater than 0.3, and the silhouette value (0.9618) is greater than 0.7. This indicates that the co-citation clusters exhibit characteristics of large clusters and that the performance of the network clustering is favorable (Chen, 2006). The study primarily delves into the top 4 major clusters. Tables 3, 4 provide information about these clusters, including silhouette, size, representative terms, and exemplary literature. Based on the clustering analysis, the top 4 clusters are as follows:

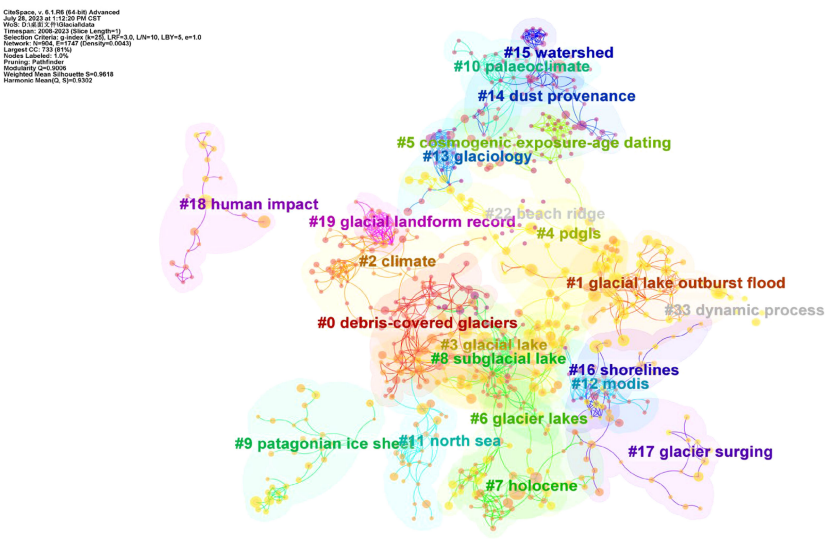

FIGURE 4
Knowledge graph of co-citation network clustering analysis. Here, the Link Retaining Factor (LRF) is 3.0, the maximum Links per Node (L/N) is 10, the Look Back Years (LBY) is 5, the minimum citation number (e) is 1.0, the notes is 904, and the nodal links is 1,747.

TABLE 3 Documentation of co-citation knowledge graph.

Cluster ID	Silhouette	Size	Clusters	Representative Terms	Mean Year	Representative Documents
#0	0.943	68	debris-covered glaciers	surface ponds; hazard assessment; glaciological natural hazards	2011	(Benn et al., 2012)
#1	0.917	56	glacial lake outburst flood	glacier eruption floods; glof hazard; ice thickness glacier velocity	2019	(King et al., 2018)
#2	0.996	52	climate	Last Glacial Maximum; glacial geomorphology; Switzerland	2010	(Barrell et al., 2013)
#3	0.982	49	glacial lake	lake mapping; Eastern Himalayas; hydrodynamic modeling	2014	(Cook and Quincey, 2015)

TABLE 4 Top 5 highly cited references in the top 4 categories.

Cluster ID	Title	Source	Citation	Reference
#0	The State and Fate of Himalayan Glaciers	Science	1,418	(Bolch et al., 2012)
#0	Response of debris-covered glaciers in the Mount Everest region to recent warming, and implications for outburst flood hazards	Earth-Science Reviews	392	(Benn et al., 2012)
#0	Contrasted evolution of glacial lakes along the Hindu Kush Himalaya mountain range between 1990 and 2009	Global and Planetary Change	277	(Gardelle et al., 2011)
#0	Glacial lakes in the Indian Himalayas - From an area-wide glacial lake inventory to on-site and modeling based risk assessment of critical glacial lakes	Science of the Total Environment	161	(Worni et al., 2013)
#0	An integrated socio-environmental framework for glacier hazard management and climate change adaptation: lessons from Lake 513, Cordillera Blanca, Peru	Climatic Change	150	(Carey et al., 2012)
#1	Rapid worldwide growth of glacial lakes since 1990	Nature Climate Change	173	(Shugar et al., 2020)
#1	Glacial lake outburst floods as drivers of fluvial erosion in the Himalaya	Science	165	(Cook et al., 2018)
#1	Unchanged frequency of moraine-dammed glacial lake outburst floods in the Himalaya	Nature Climate Change	103	(Veh et al., 2019)
#1	An inventory of historical glacial lake outburst floods in the Himalayas based on remote sensing observations and geomorphological analysis	Geomorphology	102	(Nie et al., 2018)
#1	Glacial lake inventory of high-mountain Asia in 1990 and 2018 derived from Landsat images	Earth System Science Data	82	(Wang et al., 2020)
#2	The Last Glacial Maximum	Science	2,318	(Clark et al., 2009)
#2	Methods and code for 'classical' age-modeling of radiocarbon sequences	Quaternary Geochronology	1,673	(Blaauw, 2010)
#2	Latest Pleistocene and Holocene glacier variations in the European Alps	Quaternary Science Reviews	344	(Ivy-Ochs et al., 2009)
#2	Synchronisation of palaeoenvironmental records over the last 60,000 years, and an extended INTIMATE(1) event stratigraphy to 48,000 b2k	Quaternary Science Reviews	210	(Blockley et al., 2012)
#2	Rapid climatic changes and resilient vegetation during the Lateglacial and Holocene in a continental region of south-western Europe	Global and Planetary Change	100	(Aranbarri et al., 2014)
#3	A global assessment of the societal impacts of glacier outburst floods	Global and Planetary Change	279	(Carrivick and Tweed, 2016)
#3	An inventory of glacial lakes in the Third Pole region and their changes in response to global warming	Global and Planetary Change	231	(Zhang et al., 2015)
#3	Proglacial lakes: character, behavior and geological importance	Quaternary Science Reviews	226	(Carrivick and Tweed, 2013)
#3	A regional-scale assessment of Himalayan glacial lake changes using satellite observations from 1990 to 2015	Remote Sensing of Environment	210	(Nie et al., 2017)
#3	Inventory and recently increasing GLOF susceptibility of glacial lakes in Sikkim, Eastern Himalaya	Geomorphology	72	(Aggarwal et al., 2017)

Different clusters are distinguished by colors.

Cluster #0 - Debris-Covered Glaciers, Cluster #1 - Glacial Lake Outburst Floods, Cluster #2 - Climate, and Cluster #3 - Glacial Lakes.

As shown in Figure 4, the most prominent cluster topic is #0 "Debris-Covered Glaciers". This cluster comprises 68 articles with an average publication year of 2011 and a Silhouette value of 0.943. The cluster theme is related to the formation of glacial lakes. The most representative article within this cluster is "response of debris-covered glaciers in the Mount Everest region to recent warming and implications for outburst flood hazards". This article highlights that climate warming may intensify the melting of debris-covered glaciers in the Everest region, potentially leading to severe GLOF disasters (Benn et al., 2012). The main thematic terms within this cluster include "surface ponds", "hazard assessment", and "glaciological natural hazards". "Surface ponds" refer to surface water bodies on debris-covered glaciers, playing a critical role in the

field of glacial lake identification. These ponds are a result of accumulated meltwater on the debris-covered ice surface and significantly impact glacier dynamics, such as melt rates and the formation of surface water pools (Miles et al., 2017). "Hazard assessment" and "glaciological natural hazards" emphasize the natural disasters related to glacier dynamics, particularly in cases where the glacier surface is covered with debris. These natural hazards encompass a variety of phenomena, including glacier floods and ice avalanches. In such contexts, conducting hazard assessments is a crucial step in eval-uating the likelihood of global glacier meltwater disasters. Understanding the hazards posed by debris-covered glaciers is essential for assessing risks associated with glacial lakes and implementing disaster mitigation strategies (Ye et al., 2022). Within this cluster, the themes of important articles predominantly cover the impacts of global warming on the current state and prospects of glaciers in the Himalayan region, compiling comprehensive inventories of glacial lakes and risk assessment methods, as well as integrated strategies for managing glacial lake disasters (Bolch et al., 2012; Lesi et al., 2022; Viani et al., 2022; Rinzin et al., 2023; Singh et al., 2023).

The second major cluster topic is #1 "Glacial Lake Outburst Flood" with 56 articles. The average publication year is 2019, and the silhouette value is 0.917. This cluster emphasizes an understanding of GLOF disasters. The key thematic terms within this cluster include "glacier eruption floods", "GLOF hazard", and "ice thickness glacier velocity". This underscores that GLOF disasters are frequently discussed topics in the field of glacial lake identification. In this cluster, considerable attention is given to the frequency and severity of glacial lake outburst events, especially detailed studies concerning factors driving erosion and scouring along their paths. Scholars employ techniques like remote sensing interpretation and historical record analysis to study the frequency and severity of GLOFs (Shan et al., 2021; Dømgaard et al., 2023). This analysis helps identify regions prone to frequent global climate change-induced occurrences, assess potential hazards of GLOFs to human communities, infrastructure, and the environment, and identify environmentally vulnerable areas. This, in turn, prioritizes monitoring, disaster prevention, and mitigation efforts in these regions for decision-makers and stakeholders. Additionally, some researchers explore the significant role of erosion in the formation and evolution of glacier lakes. They study various erosion processes, including glacial erosion, water flow scouring, and sediment transport (Tomczyk and Ewertowski, 2021). Furthermore, certain scholars investigate variables such as glacial lake flow velocity, glacier morphology, and potential topographic conditions to determine how these driving factors impact the formation and expansion of glacial lakes (Wang W. C. et al., 2022). These studies provide crucial insights into understanding the mechanisms and influencing factors of GLOF disasters in greater depth.

The third major cluster topic is #2 "Climate," comprising 52 articles. The average publication year for this cluster is 2010, and its silhouette value is 0.996. The main thematic terms within this cluster include "Last Glacial Maximum", "glacial geomorphology", and "Switzerland." This indicates that climate change as a significant driving factor for glacial lake formation is frequently mentioned in the field of glacial lake identification, particularly when exploring sensitive areas highly influenced by climate. Some scholars conduct research on glacial lakes within their study areas at long-term climate scales, including interannual and decadal scales (Morriss et al., 2013; Harrison et al., 2019). Research findings suggest that rising temperatures and changes in precipitation patterns contribute to glacier retreat and glacier meltwater, providing a water source for glacial lakes and resulting in changes in glacial lake dynamics (Allen et al., 2016; Gao et al., 2023). Certain researchers simulate future climate scenarios to assess potential impacts on glacial lakes (Allen et al., 2022). These studies offer insights into understanding how glacial lakes respond to climate change. Future research will likely focus on quantifying the effects of these interactions on glacial lake formation, development, and outburst. This cluster highlights the importance of investigating how climate change influences glacial lake dynamics and how glacial lakes respond to changing climate conditions. Such research is crucial for understanding the broader implications of climate change on glacial landscapes and associated hazards.

The fourth major cluster topic is #3 "Glacial Lake" encompassing 49 articles. The average publication year for this cluster is 2014, and its silhouette value is 0.982. The key thematic terms within this cluster include "lake mapping", "Eastern Himalayas", and "hydrodynamic modeling". This cluster emphasizes the significance of glacial lake monitoring, remote sensing, and hydrological modeling as crucial technical approaches in the field of glacial lake identification. This is particularly notable for specific regions like the Eastern Himalayas. In terms of lake mapping, some researchers employ techniques such as satellite imagery, aerial photography, and LiDAR scanning to identify and delineate glacial lakes (Dhote et al., 2022). They analyze the spectral and spatial characteristics of these lakes to distinguish their natural features from other bodies of water. Lake mapping studies also focus on detecting and monitoring temporal changes in glacier lakes. By comparing historical imagery with current data, researchers track fluctuations in lake area, volume, and extent (Kellerer-Pirklbauer et al., 2021). This information aids in understanding how glacial lakes respond to climate change, glacier dynamics, and other environmental factors. Furthermore, some scholars have developed comprehensive databases for glacial lakes, including their locations, areas, and other relevant information. These inventories serve as valuable resources for monitoring changes, assessing hazards, and managing glacier lakes (Shugar et al., 2020). In the cluster with the theme "hydrodynamic modeling" mathematical models are primarily applied to simulate and understand the hydrodynamic behavior of glacial lakes. Research in this area includes model development and validation, assessment of lake stability and potential hazards, and predictions of future changes in glacial lake behavior. The focus is on the physical processes and dynamics of glacial lakes, such as water flow, sediment transport, and lake level fluctuations. This cluster underscores the importance of employing advanced techniques like remote sensing and mathematical modeling to comprehensively study glacial lakes' physical characteristics, behavior, and responses to changing environmental conditions (Sattar et al., 2021; Duan et al., 2023).

3.4 Scientific classification

The WOSCC database categorizes papers from various journals precisely and integrates them based on specific scientific fields. This categorization assists researchers in gaining in-depth insights into the unique contributions of various subfields within a specific research area, aiding academic assessment, research orientation, and identifying collaboration opportunities. By mapping these scientific categories onto the comprehensive dataset of glacial lake identification literature, a more targeted and comprehensive research perspective is provided to analyze the subfields and research hotspots involved in this research domain. To reveal the disciplinary characteristics of the research field more visually, this study has created an overlay map of the research domain (Figure 5) based on the Global Science Map, which is derived from the summarized literature data of the WOS database (Leydesdorff et al., 2013; Leydesdorff et al., 2019).

The collection divides all WOS research fields into 5 clusters: #1 Biology & Medicine, #2 Chemistry & Physics, #3 Ecology and Environmental Science & Technology, #4 Engineering & Mathematics, and #5 Psychology & Social Sciences. According to these results, the majority of literature on glacial lake identification research falls under the "Chemistry & Physics" scientific field (cluster #2). Within this, the "spectroscopy" scientific category stands out, indicating the pivotal role spectroscopic techniques play in glacial lake identification and research. Spectroscopic techniques, predominantly employed in remote sensing and satellite image analysis, play a critical role in accurately identifying and monitoring glacial lakes. By studying unique spectral features like glacial lakes and shape and texture features, researchers can differentiate glacial lakes from other substances. This wide application of spectroscopy enables large-scale detection and mapping of glacial lakes, providing valuable data for inventorying and monitoring (He et al., 2021). Spectroscopy is also crucial for assessing the temporal evolution of glacier lakes, including expansion or retreat, causes of GLOFs, climate change impacts, and potential hazards. These pieces of information are vital for an in-depth understanding of dynamic changes within glacial systems (Ahmed et al., 2022b; Kumar et al., 2021). In this scientific field, the second most significant scientific category is "green & sustainable science & technology" which plays a vital role in glacial lake identification through various technological applications. One important application is powering glacial lake monitoring systems using renewable energy sources. By utilizing solar energy and other renewables, researchers can reduce carbon emissions and ensure continuous monitoring of glacial lakes without relying on fossil fuels. Furthermore, green and sustainable technologies aid in comprehending the environmental impacts of GLOFs and the role of climate change. Through sustainable monitoring techniques, researchers have been able to gather data on global warming and its consequences, such as downstream flooding and infrastructure damage, providing support for risk mitigation strategies related to GLOFs (Viani et al., 2022). Moreover, green and sustainable technologies underscore the importance of preserving glacier ecosystems and their biodiversity (Viani et al., 2020). With sustainable methods, researchers can minimize disturbances to these fragile ecosystems, promoting long-term protection and conservation of glacial lakes.

The second most prominent scientific field is "Ecology and Environmental Science & Technology" (cluster #3). Within this field, the most representative scientific categories are "environmental sciences" and "ecology" which have important applications in glacial lake identification. One significant application is the study of the physical and chemical characteristics of glacial lakes. Researchers analyze factors such as water temperature, pH, and sediment composition to understand the characteristics of the glacial lake itself and its surrounding environment. This information aids in identifying and categorizing different types of glacial lakes, allowing for the assessment of their vulnerability to climate change (Qu et al., 2022; Steffen et al., 2022). This understanding of the interaction between glacial lakes and their environment contributes to the scientific basis for protecting and managing these fragile ecosystems. Another application of environmental science in glacial lake identification is the study of

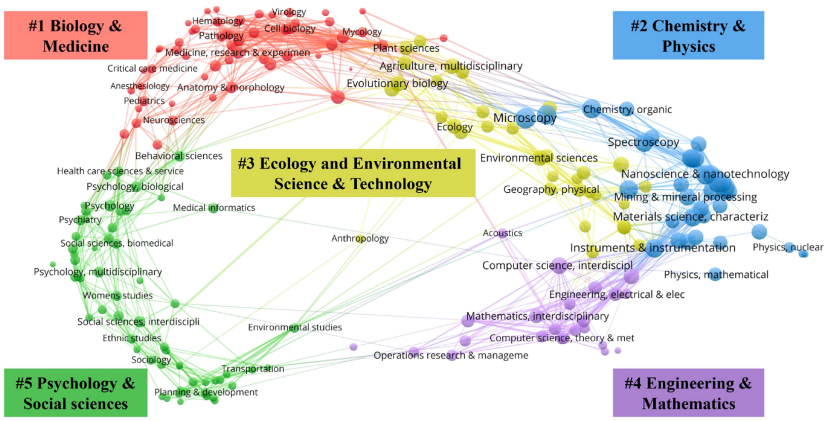

FIGURE 5
Research categories in the field of glacial lake identification on the global science category map.

glacial lake dynamics. Researchers utilize hydrological models and field measurements to explore the processes of glacial lake formation, expansion, and retreat. These applications are crucial for predicting the future changes in glacial lakes and their potential impacts on downstream communities' safety, ecology, and economy (Ogier et al., 2021).

The third most active scientific field is "Engineering & Mathematics" (cluster #4), with the most representative scientific categories being "computer science, interdisciplinary applications" and "engineering, multidisciplinary". Computer science has multiple important applications in glacial lake identification. One primary application is remote sensing and image processing techniques. Computer scientists develop algorithms and models to analyze satellite images and aerial photographs of glacial lakes, determining and mapping features such as their location, size, shape, and depth (Li et al., 2022b). Furthermore, GIS play a crucial role in glacial lake identification within the realm of computer science. Researchers use GIS software to integrate and analyze various spatial data, such as topographic maps, elevation models, and hydrological data (Viani et al., 2016). This helps understand the spatial relationships between glacial lakes and their surrounding environment, as well as predict potential risks of GLOFs. Another important application of computer science in glacial lake identification is the development of automated and efficient recognition methods. Leveraging machine learning and artificial intelligence technologies, researchers have been able to train algorithms to identify and classify glacial lakes from large datasets. This significantly enhances the speed and accuracy of glacial lake identification, thereby improving the monitoring and management of these dynamic environments (Bazilova and Kääb, 2022). Additionally, computer science plays a critical role in the development of decision support systems for glacial lake management. By integrating diverse data sources and utilizing modeling techniques, valuable insights and technical support are provided for glacial lake management decisions, aiming to mitigate risks associated with GLOFs and climate change (Rinzin et al., 2023). Glacial lake identification research exhibits typical interdisciplinary characteristics. Through the integration of various scientific categories such as environmental science, computer science, geology, hydrology, and climatology, researchers can gain a more comprehensive understanding of glacial lakes and their dynamics. This multidisciplinary approach highlights the complex interactions and feedback mechanisms between glacial lakes and their surrounding environment. By considering factors such as climate change, glacier dynamics, hydrological processes, and human activities, researchers can better comprehend the driving factors and impacts of glacial lake formation and changes (Prakash and Nagarajan, 2018). Moreover, interdisciplinary approaches aid in the development of early warning systems for GLOFs and decision support tools, contributing to the improved management and protection of these fragile ecosystems (Gu et al., 2023).

The fourth most active scientific field is "Biology & Medicine" (cluster #1), with a significant and representative scientific category being "mathematical & computational biology". The application of mathematical and computational biology in this field includes: (1) Quantitative modeling of glacial lake dynamics: Mathematical modeling is employed to describe the physical, chemical, and biological processes that control the formation, growth, and decay of glacial lakes. These models integrate various parameters such as glacier melting rates, precipitation, and temperature (Lencioni, 2018; Ogier et al., 2021). (2) Species distribution models: Computational biology techniques are used to establish species distribution models for biological entities within glacial lakes. These models are built based on environmental and ecological data, predicting the spatial distribution and potential habitat suitability for different species within glacial lake ecosystems (Medeiros et al., 2022). By simulating the response of biological communities and habitats to changing environmental conditions, these models help predict the impact of climate change on glacial lake ecosystems. This aids in assessing potential changes in species ranges and ecological disruptions, enabling the development of effective strategies for the protection and management of glacial lake ecosystems. It also facilitates the identification of priority conservation areas within glacial lake ecosystems, allowing targeted conservation efforts to maintain crucial habitats and species. The application of mathematical and computational biology enhances our understanding of the complex interactions between glacial lakes and their biological components, and it contributes to informed decision-making for the conservation and sustainable management of these unique ecosystems.

In our study, we have discovered that the field of "Psychology & Social Sciences" (cluster #5) exhibits the lowest level of activity among scientific domains. All the scientific categories within this field have fewer than 70 documents each, with "social sciences, interdisciplinary" (62 documents), "social issues" (57 documents), and "environmental studies" (53 documents) being the most significant ones.

3.5 Analysis of phased research trends and frontiers

By employing the clustering analysis technique within the CiteSpace software, researchers can visually depict the evolutionary process of various research topics over different periods, thereby unveiling research hotspots and future trends in the field's development (Abbas et al., 2018). In this study, we harnessed CiteSpace's distinctive functionalities, namely Timeline and Burstness, to process the foundational data of the literature. The time range was set from 1991 to 2023, with a time slice length of 1, enabling the detection of burst keywords within each time slice. The research outcomes are presented in Figures 6, 7. Figure 6 illustrates ten timelines, while Figure 7 showcases 25 keywords, with high-frequency keywords predominantly appearing before 2010. The forefront of glacier lake identification research manifests significantly in three distinct research stages, each characterized as follows.

(1) The period from 1991 to 2010 marked the primary stage of research in the field of glacier lake identification. Emerging keywords during this phase include "Canada", "British Columbia", "age", "record", "Younger Dryas", "island",

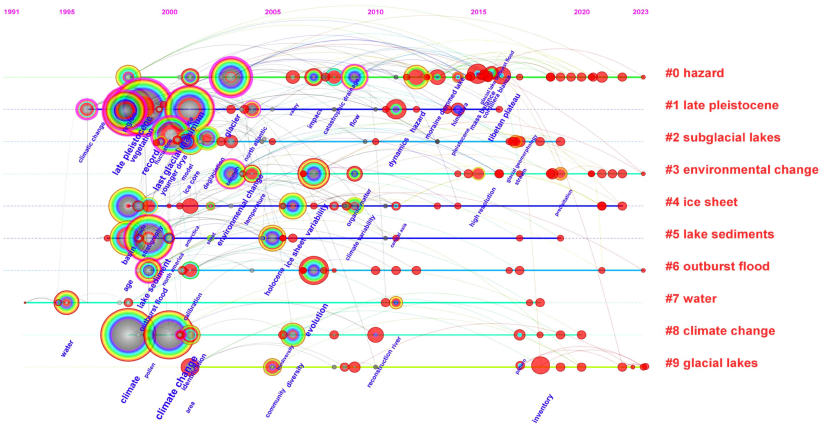

FIGURE 6
Visual timeline clustering of research topic evolution from 1991 to 2023. Curves indicate literature citation relationships, with warmer colors indicating closer research time frames. Larger keyword clusters signify research hotspots for a specific period.

"Antarctica", "vegetation history", "Lake Vostok", and "calibration". Additionally, high-frequency keywords associated with this period encompass "climate change", "Last Glacial Maximum", "lake sediment", "environmental change", and "ice sheet" among others. The timeline chart and burst keywords of this period exhibit a substantial number of terms, indicating a strong academic interest in the glacier lake identification domain and the emergence of numerous new research concepts. The research direction is relatively diverse, encompassing a wide range of scientific inquiries, warranting continuous and profound attention. The primary research themes during this phase pertain to glacial lake formation and evolution, exploration, and research of paleoclimate and paleoenvironment, and lake sediment analysis (Bajracharya and Mool, 2009; Corbett and Munroe, 2010; Sionneau et al., 2010).

(2) The period from 2011 to 2018 witnessed the emergence of keywords such as "catastrophic drainage"; "Pleistocene", "glacial lake", "subglacial lake", "flood", "stream", "volume", and "conservation". High-frequency keywords closely related to this era also encompassed "hazard", "glacial geomorphology", and

Top 25 Keywords with the Strongest Citation Bursts

Keywords	Year	Strength	Begin	End	1991 - 2023
canada	1998	7	1998	2008	
british columbia	1998	5.93	1998	2015	
age	1998	4.89	1998	2003	
record	1996	5.43	1999	2008	
younger drya	2000	6.24	2000	2005	
island	2000	4.7	2000	2009	
antarctica	2001	5.41	2001	2011	
vegetation history	2002	6.85	2002	2005	
lake vostok	2003	6.33	2003	2009	
calibration	1999	5.14	2007	2012	
catastrophic drainage	2008	8.17	2011	2018	
pleistocene	2001	5.59	2014	2016	
glacial lake	2013	6.93	2016	2020	
subglacial lake	2016	5.59	2016	2018	
flood	2011	4.91	2016	2017	
stream	2017	8.36	2017	2020	
volume	2017	4.77	2017	2020	
conservation	2018	4.86	2018	2019	
inventory	2006	11.45	2019	2023	
glacial lake outburst flood	2016	5.41	2020	2023	
risk	2020	4.85	2020	2023	
dynamics	2006	4.77	2020	2023	
tibetan plateau	2014	9.47	2021	2023	
evolution	2007	5.93	2021	2023	
high mountain asia	2021	5.35	2021	2023	

FIGURE 7
Keywords burst analysis from 1991 to 2023.

"mass balance" among others. Building upon the foundation of 1991 to 2010, this stage led to the emergence of several new specific research directions within the GLOF domain, contributing to the enrichment and further development of glacier lake identification research. The primary research themes during this phase encompass glacial lake hazards and risk assessment and glacial lake dynamics. The theme of glacial lake hazards and risk assessment primarily involves the evaluation of potential risks associated with glacial lake disasters, as well as the development of warning systems and disaster management strategies (Petrakov et al., 2012; Aggarwal et al., 2016). On the other hand, the glacial lake dynamics theme focuses on the study of glacier lake volume and dynamics, involving keywords such as "volume", "glacial geomorphology", and "mass balance". This research content encompasses measurements and monitoring of glacier lakes, along with investigations into the mechanisms underlying interactions between glacier lakes and factors such as climate and topography (Li and Sheng, 2012; Emmer et al., 2015).

(3) The period from 2019 to 2023 brought forth keywords such as "inventory", "glacial lake outburst flood", "risk", "dynamics", "Tibetan Plateau", "evolution", and "high mountain Asia". Concurrently, high-frequency keywords included "Himalaya", "moraine dammed lake", "evolution", "permafrost", and "precipitation" among others. During this phase, the glacier lake identification research domain exhibited a rapid increase in annual publications, entering a phase of heightened research activity. Various research branches gradually evolved into more specific directions, yet fewer new research directions emerged. Instead, researchers focused on in-depth investigations building upon the foundation of the preceding phase. Notable research themes in the hotspot literature included the drawing of inventories for lakes in the Qinghai-Tibet Plateau using remote sensing techniques, GLOF risk assessment, precipitation variation and its impact on glacial lake response, and the evolution of glacial lakes in high mountain Asia (Allen et al., 2019; Dwivedi et al., 2022; Zhang et al., 2022b; Compagno et al., 2022).

4 Discussion

4.1 Current research themes and further research

In recent years, the field of glacier lake identification has made significant progress, yet it still faces a range of critical technical challenges. These challenges encompass limitations in spectral resolution, objective factors related to climate change, interference from shadows and ice, as well as constraints on the accuracy of automated algorithms. These factors restrict the depth and breadth of research and also impede the accuracy and applicability of relevant applications (Wangchuk et al., 2019; Hao et al., 2023). In the domain of glacier lake identification, accurate identification of glacier lakes holds extensive academic and practical value in reducing the environmental impact of these lakes. Therefore, this study delves into two research themes—identification techniques and methods, and identification scales—providing insight into the future directions of glacier lake identification research.

(1) In the realm of glacier lake identification techniques and methods, significant strides have been made, giving rise to various remote sensing technologies, GIS, and machine learning approaches (Kaushik et al., 2022; Wangchuk et al., 2022). These include feature extraction and classification methods based on synthetic aperture radar (SAR) and satellite multispectral data, as well as applications of deep learning models. These methods not only accurately identify the spatial distribution of glacier lakes but also distinguish between different types of glacier lakes, allowing researchers to determine the morphology of glacier lakes with unprecedented precision. This offers an effective means for studying glacier lake characteristics. However, despite these advancements, challenges persist. One of the most crucial challenges is the environmental complexity of glacial lakes. Factors like distinct topographic features, spectral differences due to regional water forms, and the transient nature of glacier lakes introduce complexities that existing algorithms struggle to address. This complexity results in potential ambiguities in satellite-derived datasets (Jiang et al., 2023). For instance, small and shallow glacier lakes are often obscured by surrounding vegetation or debris, posing a considerable obstacle. Additionally, while higher-resolution datasets enhance the accuracy of lake identification, they are also susceptible to increased noise, necessitating more intricate processing algorithms to extract accurate information. Existing models and algorithms still simplify the intricate interactions between glacier lakes and their surroundings to a certain extent. To achieve more accurate assessment results, further integration of multidisciplinary data from ecology, meteorology, geology, and more is needed to account for the complex interactions (Emmer and Curin, 2021). Lastly, while many existing models excel in identifying glacier lakes in specific geographical locations or under certain conditions, their applicability across different times and spaces remains a challenge. Investigating the applicability and scalability of these models requires deeper research to ensure their utility across diverse temporal and spatial contexts.

Drawing upon the comprehensive overview presented earlier, we proffer 5 pivotal research topics to steer the trajectory of future glacier lake identification research. To begin, in light of the burgeoning influx and diversification of remote sensing data, researchers must prioritize the advancement of more potent, adaptable, and efficient algorithms. In forthcoming investigations, precedence should be granted to the development of adaptive algorithms capable of dynamic adjustments based on the distinctive characteristics of diverse study areas. Such an approach would markedly enhance the accuracy of models across varying terrains and conditions. Moreover, the exploration of advanced algorithms rooted in machine learning and deep learning offers a propitious avenue to seamlessly identify and further refine glacier lake features within intricate backdrops. Illustratively, Convolutional Neural Networks (CNNs) hold the promise to discern nuanced spectral differentials through meticulous training. Secondly, cognizant of the intricate tapestry characterizing glacier lake regions, it becomes apparent that reliance

on a solitary data source might prove inadequate to satiate the exigencies of accurate identification. Prospective inquiries could envisage the assimilation of data originating from optical, Synthetic Aperture Radar (SAR), and even on-site sensors, coalescing into an amalgamated multi-source data fusion dataset. This dataset, by amalgamating diverse streams of data, engenders a holistic image of the glacier lake landscape. Thirdly, the establishment of a systematic approach to trace the dynamic trajectory of glacier lake's evolution assumes paramount significance. Such a methodological construct facilitates a comprehensive analysis of the evolution of glacier lakes, their latent perils, and the broader repercussions associated with climate fluctuations. Fourthly, the construction of integrative models, harnessing the unique strengths of each constituent model, offers a prudent stratagem to counterbalance the inherent limitations of individual models. Collaborative algorithms across models present the promise of engendering outcomes of heightened applicability, thereby impelling the ubiquity of glacier lake assessment models across a global expanse. Concludingly, notwithstanding the vantage point proffered by remote sensing techniques, the role of field research remains indispensable in the schema of validation and calibration. Future research endeavors should, in particular, be attuned to the exigency of on-site measurements, employing tools such as unmanned aerial vehicles or unmanned boats for the procurement of on-site data. This pivotal validation of remote sensing outcomes bolsters the credence of glacier lake identification.

(2) Concerning the issue of glacier lake identification scales, researchers have explored various scales, encompassing the microscale (such as glacier lake morphology and internal structure), mesoscale (such as geomorphic features of glacier lakes), and macroscale (such as regional distribution of glacier lakes), to delve into the complexity of glacier lake systems (Dahlquist and West, 2022; Li et al., 2022c; Zhang et al., 2022c). Nevertheless, despite headway being made, several outstanding challenges persist. Firstly, the challenge of data matching and fusion across disparate scales remains pivotal. How to organically integrate microscale glacier lake features with the macroscale spatial distribution poses a question that necessitates further inquiry. Secondly, scale conversion and data extrapolation stand as pivotal technical challenges. The translation of microscale data into analyses on a larger scale, as well as effective scale expansion when data is limited, demands comprehensive exploration. Moreover, the potential incongruities across various data sources and interpretations introduce complexity into comparative analyses and global assessments. Factors such as spatial resolution, the diverse geomorphic features of glacial environments, and the manifold physical attributes of glacier lakes themselves, collectively compound the difficulty in interpreting data.

Based on the preceding synthesis, we posit three pivotal research topics for the next phase. Firstly, the development and adoption of a unified standard framework assume paramount significance. Pioneering novel algorithms and techniques applicable to scale conversion and data extrapolation is indispensable to enhancing the precision and reliability of data translation across disparate scales. Such an endeavor would engender a standardized perspective for the observation, analysis, and comparison of glacier lakes, thereby ensuring the congruence of research outcomes. Secondly, concomitant with the escalating demand for heightened glacier lake identification accuracy, the requisition for data of elevated spatial resolution is concurrently mounting. Strategic investment and integration of these monitoring tools will contribute to refining the spectrum of identification scales and bolstering accuracy. Thirdly, cross-scale data fusion constitutes the linchpin in resolving the quandary of multi-scale glacier lake identification. Effectively amalgamating microscale and macroscale data through cross-scale data fusion empowers a more comprehensive apprehension of the complexity underpinning glacier lake systems. Such an approach holds the potential to furnish a more precise depiction and analysis of glacier lake changes by holistically integrating data across scales.

4.2 Limitations of the research

Against the backdrop of accelerated glacier retreat and intensified global warming, the identification and study of glacier lakes geomorphic features characterized by rapid change and pivotal environmental significance have assumed an increasingly urgent tenor. In such a context, bibliometrics emerges as a potent tool to assess the development of literature and research trends, furnishing invaluable insights for the glacier lake identification domain. Admittedly, the bibliometric approach employed in this study is not devoid of limitations. By unveiling these limitations, we can more accurately appraise the current research landscape within glacier lake identification and glean valuable insights to inform the design and methodologies of future research endeavors.

(1) We acknowledge that the utilization of WOSCC in this study, while a widely employed literature repository with abundant scholarly information, may still fall short in comprehensively encompassing all publications within the glacier lake identification domain. This could result in our analysis not fully encapsulating important literature from other databases or non-academic channels, such as CNKI and Scopus databases, thereby raising concerns about data incompleteness. Additionally, specific types of literature like books, doctoral theses, and patents, among others, might not be entirely incorporated in these databases, potentially influencing our grasp of the field's entirety. Such gaps may emanate from the chosen literature search strategies and a subset of studies confined to English-language publications. Furthermore, errors or omissions could potentially arise during data retrieval and indexing processes within the WOS. Despite deploying well-formulated strategies for data retrieval and indexing using the WOS, we cannot guarantee the accurate classification and indexing of all relevant literature. Moreover, it is pertinent to recognize that the WOS primarily encompasses literature in the natural sciences, which could introduce a certain degree of bias in the glacier lake identification field, especially in interdisciplinary studies. This might lead to a partial interpretation of research within the glacier lake identification domain due to the potential omission of research from diverse disciplines.

(2) The analysis of countries and institutions carries inherent limitations. The countries and institutions contributing to the

glacier lake identification field indicate that the United States, the United Kingdom, and China have the highest publication and citation counts, with each producing over 300 papers. From the perspective of the threat posed by glacial lake hazards, scientists from New Zealand and the UK have emphasized the significant challenges that global socio-economics faces due to GLOFs. Notably, in the high mountain Asia region alone, approximately one million people reside within a 10-kilometer radius of glacial lakes. The Himalayan region in Asia (including countries like India, Pakistan, and China) and the Andes region in South America (encompassing Peru and Bolivia) face even greater threats (Taylor et al., 2023). Regarding international collaboration, for instance, collaboration between the United States, the United Kingdom, and China has shown deeper engagement, primarily spanning Europe, North America, and East Asia. However, the level of international collaboration among South American and South Asian nations remains relatively low, exemplified by countries such as India, Pakistan, Peru, and Bolivia. This phenomenon underscores the close connection between research activities in the glacier lake identification field and the economic capabilities of each country. Developed nations, owing to their resource and technological advantages, are more inclined to invest in specialized fields like glacier lake identification within the realm of scientific research. On the other hand, developing countries may allocate resources to more pressing issues. In light of these considerations, it is essential to recognize that the aforementioned analysis, while informative, should be interpreted with the understanding that the distribution of research activities is influenced by complex economic and regional dynamics.

(3) There are certain limitations to the co-citation analysis employed in this study. Co-citation clustering, as a quantitative analytical tool, holds significant advantages in revealing citation relationships and trends in research fields. However, it is important to acknowledge the following challenges: Firstly, co-citation clustering heavily relies on citation relationships between documents, but these relationships may not always accurately reflect the actual knowledge structure within the research field. Citation relationships can be influenced by various factors such as citation practices and the evolution of citation networks. Consequently, this method may suffer from citation bias, potentially affecting the accuracy and reliability of clustering outcomes. Secondly, co-citation clustering primarily utilizes citation data for analysis, often overlooking the semantic content of the documents. This oversight could lead to the erroneous aggregation of documents from different topics or research areas due to citation relationships, resulting in misleading clustering results. Furthermore, the co-citation clustering method typically neglects the temporal factor's impact on citation relationships. Research fields evolve and develop over time, yet this method may not fully account for the dynamic changes in citation relationships across different periods. As a result, the method might provide an incomplete understanding of research trends and evolution. In conclusion, while co-citation analysis offers valuable insights, its limitations highlight the need for a comprehensive approach that integrates multiple analytical methods to obtain a more accurate and nuanced perspective on the development and trends within the glacier lake identification field.

5 Conclusions

This study leveraged the strengths of software tools such as VOSviewer 1.6.19 and CiteSpace 6.1.R6 to employ bibliometric and quantitative analysis methods. Focusing on glacier lake identification as the research theme, an in-depth visual analysis was conducted on 2,121 publications from the WOSCC database spanning the years 1991 to 2023. This analysis encompassed research progress and trends across different periods, national collaboration networks, thematic evolution pathways, and more, providing a comprehensive overview of the field's developmental trajectory, shortcomings, and prospective research directions. Several significant research findings were derived from this investigation.

(1) Regarding the annual distribution of publications and citation counts, both indicators exhibit a clear trend of rapid growth, signaling the increasing scholarly attention toward the field of glacier lake identification. From a national or regional perspective, the involvement of countries, journals, and institutional affiliations in the glacier lake identification domain is predominantly concentrated in Europe and North America. Notably, the United States, the United Kingdom, and China stand at the forefront in terms of publication volume, citation impact, and international collaboration efforts.

(2) Literature co-citation analysis focuses on the citation relationships between documents, serving as a means to assess and analyze the influence, significance, and collaborative networks of research literature within the academic community. Research findings indicate that significant clusters of research topics in the glacier lake identification domain include "debris-covered glaciers", "glacial lake outburst flood", "climate", and "glacial lake". Based on the analysis of the most frequently co-cited documents, research hotspots in the field encompass climate change, compilation of glacier lake inventories, methodologies for risk assessment, GLOFs, strategies for comprehensive disaster management, and hydrodynamic modeling. Notably, Switzerland and the Eastern Himalayas emerged as prominent focal areas in the realm of glacier lake identification.

(3) A detailed analysis of scientific categories and thematic clusters unveils the diversity and interdisciplinary nature of the glacier lake identification domain. Research in this field spans multiple scientific categories, primarily stemming from "Chemistry & Physics" and "Ecology and Environmental Science & Technology." Noteworthy specific disciplines encompassed are "spectroscopy", "environmental sciences", "ecology," "computer science, interdisciplinary applications", "engineering, multidisciplinary", and "mathematical & computational biology".

(4) The analysis of keyword timelines and burst terms has unveiled the developmental trajectory of the glacier lake identification field over the past 32 years. Themes such as "hazard", "Late Pleistocene", "environmental change", "ice sheet", and "lake sediments" have sustained heightened interest over an

extended temporal span. The evolution of research themes can be distinctly categorized into three phases: Firstly, during the period from 1991 to 2010, which marks the nascent stage of glacier lake identification research, numerous novel concepts emerged. Research orientations exhibited a degree of dispersion, accompanied by a prevalence of scientific queries warranting long-term investigation. Key emergent terms encompassed "Canada", "record", "Younger Drya", "vegetation history", "Lake Vostok", and "calibration" among others. Research themes centered on "glacial lake formation and evolution", "exploration and research of paleoclimate and paleoenvironment", and "lake sediment analysis". Secondly, spanning from 2011 to 2018, this phase witnessed a deeper enrichment and expansion of the glacier lake identification domain. Bursting keywords included "catastrophic drainage", "Pleistocene", "glacial lake", "subglacial lake", "flood", "stream", "volume", and "conservation". Research themes predominantly encompassed "glacial lake hazards and risk assessment" as well as "glacial lake dynamics". Thirdly, the phase from 2019 to the present has seen the glacier lake identification field assume a progressively specialized trajectory, with a rapid escalation in annual publications and citations. Eminent keywords during this period comprise "inventory", "glacial lake outburst flood", "risk", "dynamics", "Tibetan Plateau", "evolution", and "high mountain Asia". Noteworthy appearances also include "Himalaya", "moraine dammed lake", "evolution", "permafrost", and "precipitation". The focal literature gravitates toward research avenues such as "utilizing remote sensing techniques for the compilation of Qinghai-Tibet Plateau lake inventories", "glacial lake outburst flood risk", "precipitation variation and glacial lake response", and "evolution of glacial lakes in high mountain Asia".

(5) Building upon the synthesis of preceding research accomplishments, further exploration into the challenges inherent in glacier lake identification methodologies and techniques, as well as the dimensionality of recognition scales, has been undertaken. This endeavor is then complemented by a prospective delineation of forthcoming research trajectories within the glacier lake identification domain. Noteworthy among these trajectories are the "recognition methods based on machine learning and deep learning", the "integration of multi-source data fusion datasets", the "emergence of novel algorithms and techniques tailored for scale transformation and data expansion", alongside the "advancement of remote sensing technologies with elevated spatial resolution".

Data availability statement

The original contributions presented in the study are included in the article/supplementary material. Further inquiries can be directed to the corresponding author.

Author contributions

ZL: Methodology, Software, Visualization, Writing – review & editing. ZY: Funding acquisition, Project administration, Supervision, Writing – original draft. NH: Writing – original draft, Data curation. LW: Writing – original draft. YZ: Writing – original draft. WJ: Writing – original draft. ZW: Writing – original draft. TZ: Writing – original draft. JZ: Writing – original draft. XZ: Writing – original draft.

Funding

The author(s) declare financial support was received for the research, authorship, and/or publication of this article. This research was funded by the National Natural Science Foundation of China (Grant No. 41861134008), the Muhammad Asif Khan academician workstation of Yunnan Province (Grant No. 202105AF150076), the Key R&D Program of Yunnan Province (Grant No. 202003AC100002), and the General Program of basic research plan of Yunnan Province (Grant No. 202001AT070043).

Conflict of interest

The authors declare that the research was conducted in the absence of any commercial or financial relationships that could be construed as a potential conflict of interest.

Publisher's note

References

Abbas, G., Murtaza, B., Bibi, I., Shahid, M., Niazi, N. K., Khan, M. I., et al. (2018). Arsenic uptake, toxicity, detoxification, and speciation in plants: physiological, biochemical, and molecular aspects. *Int. J. Environ. Res. Public Health* 15 (1), 59. doi: 10.3390/ijerph15010059

Aggarwal, A., Jain, S. K., Lohani, A. K., and Jain, N. (2016). Glacial lake outburst flood risk assessment using combined approaches of remote sensing, GIS and dam break modelling. *Geomat. Nat. Haz. Risk.* 7 (1), 18–36. doi: 10.1080/19475705.2013.862573

Aggarwal, S., Rai, S. C., Thakur, P. K., and Emmer, A. (2017). Inventory and recently increasing GLOF susceptibility of glacial lakes in Sikkim, Eastern Himalaya. *Geomorphology.* 295, 39–54. doi: 10.1016/j.geomorph.2017.06.014

Ahmed, R., Ahmad, S. T., Wani, G. F., Mir, R. A., Ahmed, P., and Jain, S. K. (2022c). High resolution inventory and hazard assessment of potentially dangerous glacial lakes in upper Jhelum basin, Kashmir Himalaya, India. *Geocarto Int.* 37, 10681–10712. doi: 10.1080/10106049.2022.2038693

Ahmed, R., Ahmad, S. T., Wani, G. F., Mir, R. A., Almazroui, M., Bansal, J. K., et al. (2022b). Glacial lake changes and the identification of potentially dangerous glacial lakes (PDGLs) under warming climate in the Dibang River Basin, Eastern Himalaya, India. *Geocarto Int.* 37 (27), 17659–17685. doi: 10.1080/10106049.2022.2134461

Ahmed, R., Rawat, M., Wani, G. F., Ahmad, S. T., Ahmed, P., Jain, S. K., et al. (2022a). Glacial lake outburst flood hazard and risk assessment of gangabal lake in the upper jhelum basin of kashmir himalaya using geospatial technology and hydrodynamic modeling. *Remote Sens.* 14, 5957. doi: 10.3390/rs14235957

Ali, S. N., Pandey, P., Singh, P., Mishra, S., Shekhar, M., Misra, K. G., et al. (2023). Intimidating evidences of climate change from the higher himalaya: A case study from lahaul, himachal pradesh, India. *J. Indian Soc Remote Sens.* 51 (5), 1099–1112. doi: 10.1007/s12524-023-01686-0

Allen, S. K., Rastner, P., Arora, M., Huggel, C., and Stoffel, M. (2016). Lake outburst and debris flow disaster at Kedarnath, June 2013: hydrometeorological triggering and topographic predisposition. *Landslides.* 13 (6), 1479–1491. doi: 10.1007/s10346-015-0584-3

Allen, S. K., Sattar, A., King, O., Zhang, G., Bhattacharya, A., Yao, T., et al. (2022). Glacial lake outburst flood hazard under current and future conditions: worst-case scenarios in a transboundary Himalayan basin. *Nat. Hazards Earth Syst. Sci.* 22 (11), 3765–3785. doi: 10.5194/nhess-22-3765-2022

Allen, S. K., Zhang, G., Wang, W., Yao, T., and Bolch, T. (2019). Potentially dangerous glacial lakes across the Tibetan Plateau revealed using a large-scale automated assessment approach. *Sci. Bull.* 64, 435–445. doi: 10.1016/j.scib.2019.03.011

Aranbarri, J. K., Gonzalez-samperiz, P., Valero-garces, B., Moreno, A., Gil-Romera, G., Sevilla-Callejo, M., et al. (2014). Rapid climatic changes and resilient vegetation during the Lateglacial and Holocene in a continental region of south-western Europe. *Global Planet. Change.* 114, 50–65. doi: 10.1016/j.gloplacha.2014.01.003

Awal, R., Nakagawa, H., Kawaike, K., Baba, Y., and Zhang, H. (2011). Study on moraine dam failure and resulting flood/debris flow hydrograph due to waves overtopping and erosion. *Ital. J. Eng. Geol. Env.* 2011, 3–12. doi: 10.4408/IJEGE.2011-03.B-001

Bajracharya, S. R., and Mool, P. (2009). Glaciers, glacial lakes and glacial lake outburst floods in the Mount Everest region, Nepal. *Ann. Glaciol.* 50 (53), 81–86. doi: 10.3189/172756410790595895

Barrell, D. J., Almond, P. C., Vandergoes, M., Lowe, D. J., and Newnham, R. M. (2013). A composite pollen-based stratotype for inter-regional evaluation of climatic events in New Zealand over the past 30,000 years (NZ-INTIMATE project). *Quat. Sci. Rev.* 74, 4–20. doi: 10.1016/j.quascirev.2013.04.002

Bazilova, V., and Kääb, A. (2022). Mapping area changes of glacial lakes using stacks of optical satellite images. *Remote Sens.* 14 (23), 5973–5973. doi: 10.3390/rs14235973

Begam, S., and Sen, D. (2019). Mapping of moraine dammed glacial lakes and assessment of their areal changes in the central and eastern himalayas using satellite data. *J. Mt. Sci.* 16, 77–94. doi: 10.1007/s11629-018-5023-1

Benn, D. I., Bolch, T., Hands, K. A., Gulley, J. D., Luckman, A. J., Nicholson, L. I., et al. (2012). Response of debris-covered glaciers in the Mount Everest region to recent warming, and implications for outburst flood hazards. *Earth Sci. Rev.* 114 (1-2), 156–174. doi: 10.1016/j.earscirev.2012.03.008

Blaauw, M. (2010). Methods and code for 'classical' age-modelling of radiocarbon sequences. *Quat. Geochronol.* 5 (5), 512–518. doi: 10.1016/j.quageo.2010.01.002

Blockley, S. P. E., Lane, C. S., Hardiman, M., Rasmussen, S. O., Seierstad, I. K., Steffensen, J. P., et al. (2012). Synchronisation of palaeoenvironmental records over the last 60,000 years, and an extended INTIMATE(1) event stratigraphy to 48,000 b2k. *Quat. Sci. Rev.* 36, 2–10. doi: 10.1016/j.quascirev.2011.09.017

Bolch, T., Bolch, T., Kulkarni, A. V., Kääb, A., Huggel, C., Huggel, C., et al. (2012). The state and fate of himalayan glaciers. *Science.* 336 (6079), 310–314. doi: 10.1126/science.1215828

Bolch, T., Peters, J., Yegorov, A., Pradhan, B., Buchroithner, M. F., and Blagoveshchensky, V. A. (2011). Identification of potentially dangerous glacial lakes in the northern Tien Shan. *Nat. Hazard.* 59 (3), 1691–1714. doi: 10.1007/s11069-011-9860-2

Bondi, M., and Cacchiani, S. (2021). Knowledge communication and knowledge dissemination in a digital world. *J. Pragmat.* 186, 117–123. doi: 10.1016/j.pragma.2021.10.003

Byers, A. C., Chand, M. B., Lala, J., Shrestha, M., Byers, E. A., and Watanabe, T. (2020). Reconstructing the history of glacial lake outburst floods (GLOF) in the kanchenjunga conservation area, east Nepal: an interdisciplinary approach. *Sustainability.* 12, 5407. doi: 10.3390/su12135407

Carey, M., Huggel, C., Bury, J. T., Portocarrero, C., and Haeberli, W. (2012). An integrated socio-environmental framework for glacier hazard management and climate change adaptation: lessons from Lake 513, Cordillera Blanca, Peru. *Clim. Change.* 112 (3-4), 733–767. doi: 10.1007/s10584-011-0249-8

Carrivick, J. L., and Tweed, F. S. (2013). Proglacial lakes: character, behaviour and geological importance. *Quat. Sci. Rev.* 78, 34–52. doi: 10.1016/j.quascirev.2013.07.028

Carrivick, J. L., and Tweed, F. S. (2016). A global assessment of the societal impacts of glacier outburst floods. *Global Planet. Change.* 144, 1–16. doi: 10.1016/j.gloplacha.2016.07.001

Chen, C. (2006). CiteSpace II: Detecting and visualizing emerging trends and transient patterns in scientific literature. *J. Am. Soc Inf. Sci. Technol.* 57 (3), 359–377. doi: 10.1002/asi.20317

Clark, P. U., Dyke, A. S., Shakun, J. D., Carlson, A. E., Clark, J., Wohlfarth, B., et al. (2009). The last glacial maximum. *Science.* 325 (5941), 710–714. doi: 10.1126/science.1172873

Compagno, L., Huss, M., Zekollari, H., Miles, E. S., and Farinotti, D. (2022). Future growth and decline of high mountain Asia's ice-dammed lakes and associated risk. *Commun. Earth Environ.* 3 (1), 191. doi: 10.1038/s43247-022-00520-8

Cook, K. L., Andermann, C., Gimbert, F., Adhikari, B. R., and Hovius, N. (2018). Glacial lake outburst floods as drivers of fluvial erosion in the Himalaya. *Science.* 362, 53–57. doi: 10.1126/science.aat4981

Cook, S. J., and Quincey, D. J. (2015). Estimating the volume of Alpine glacial lakes. *Earth Surf. Dyn.* 3 (4), 559–575. doi: 10.5194/esurf-3-559-2015

Corbett, L. B., and Munroe, J. S. (2010). Investigating the influence of hydrogeomorphic setting on the response of lake sedimentation to climatic changes in the Uinta Mountains, Utah, USA. *J. Paleolimnol.* 44 (1), 311–325. doi: 10.1007/s10933-009-9405-9

Dahlquist, M. P., and West, A. J. (2022). The imprint of erosion by glacial lake outburst floods in the topography of central Himalayan rivers. *Earth Surf. Dyn.* 10 (4), 705–722. doi: 10.5194/esurf-10-705-2022

Dhote, P. R., Thakur, P. K., Chouksey, A., Srivastav, S. K., Raghvendra, S., Rautela, P., et al. (2022). Synergistic analysis of satellite, unmanned aerial vehicle, terrestrial laser scanner data and process-based modelling for understanding the dynamics and morphological changes around the snout of Gangotri Glacier, India. *Geomorphology.* 396, 108005. doi: 10.1016/j.geomorph.2021.108005

Dømgaard, M., Kjeldsen, K. K., Huiban, F., Carrivick, J. L., Khan, S. A., and Bjørk, A. A. (2023). Recent changes in drainage route and outburst magnitude of the Russell Glacier ice-dammed lake, West Greenland. *Cryosphere.* 17, 1373. doi: 10.5194/tc-17-1373-2023

Dou, X., Fan, X., Wang, X., Yunus, A. P., Xiong, J., Tang, R., et al. (2023). Spatio-temporal evolution of glacial lakes in the tibetan plateau over the past 30 years. *Remote Sens.* 15, 416. doi: 10.3390/rs15020416

Duan, H. Y., Yao, X. J., Zhang, Y., Wang, Q., Du, Z. S., Hu, J. Y., et al. (2023). Lake volume and potential hazards of moraine-dammed glacial lakes-a case study of Bienong Co, southeastern Tibetan Plateau. *Cryosphere.* 17 (2), 591–616. doi: 10.5194/tc-17-591-2023

Dwivedi, S. K., Chandra, N., Bahuguna, S., Pandey, A., Khanduri, S., Lingwal, S., et al. (2022). Hydrometeorological disaster risk assessment in upper Gori-Ramganga catchment, Uttarakhand, India. *Geocarto Int.* 37 (26), 11998–12013. doi: 10.1080/10106049.2022.2063403

Emmer, A. (2018). GLOFs in the WOS: bibliometrics, geographies and global trends of research on glacial lake outburst floods (Web of Science 1979-2016). *Nat. Hazards Earth Syst. Sci.* 18 (3), 813–827. doi: 10.5194/nhess-18-813-2018

Emmer, A. (2023). Vanishing evidence? On the longevity of geomorphic GLOF diagnostic features in the Tropical Andes. *Geomorphology.* 422, 108552. doi: 10.1016/j.geomorph.2022.108552

Emmer, A., and Curin, V. (2021). . Can a dam type of an alpine lake be derived from lake geometry? A negative result. *J. Mountain Sci.* 18 (3), 614–621. doi: 10.1007/s11629-020-6003-9

Emmer, A., Harrison, S., Mergili, M., Allen, S., Frey, H., and Huggel, C. (2020). 70 years of lake evolution and glacial lake outburst floods in the Cordillera Blanca (Peru) and implications for the future. *Geomorphology.* 365, 107178. doi: 10.1016/j.geomorph.2020.107178

Emmer, A., Merkl, S., and Mergili, M. (2015). Spatiotemporal patterns of high-mountain lakes and related hazards in western Austria. *Geomorphology.* 246, 602–616. doi: 10.1016/j.geomorph.2015.06.032

Frydrych, M., and Rdzany, Z. (2022). Glacial outburst flood in the marginal zone of the Wartanian Glaciation: An example from Adamów, central Poland. *Quat. Int.* 617, 21–39. doi: 10.1016/j.quaint.2021.08.014

Gao, Y. P., Yang, W. G., Guo, R., and Jiang, L. M. (2023). Remote sensing monitoring and analysis of jinwuco lateral moraine landslide-glacial lake outburst in southeast tibet. *Remote. Sens.* 15, 1475. doi: 10.3390/rs15061475

Gardelle, J., Arnaud, Y., and Berthier, E. (2011). Contrasted evolution of glacial lakes along the Hindu Kush Himalaya mountain range between 1990 and 2009. *Global Planet. Change.* 75 (1-2), 47–55. doi: 10.1016/j.gloplacha.2010.10.003

Gu, C. J., Li, S. J., Liu, M., Hu, K. L., and Wang, P. (2023). Monitoring glacier lake outburst flood (GLOF) of lake merzbacher using dense chinese high-resolution satellite images. *Remote Sens.* 15 (7), 1941. doi: 10.3390/rs15071941

Hao, T., Jing, L. W., Liu, J. S., Wang, D. L., Feng, T. T., Zhao, A. G., et al. (2023). Automatic detection of subglacial water bodies in the AGAP region, east Antarctica, based on short-time fourier transform. *Remote Sens.* 15 (2), 363. doi: 10.3390/rs15020363

Harrison, S., Smith, D. E., and Glasser, N. F. (2019). Late Quaternary meltwater pulses and sea level change. *J. Quat. Sci.* 34 (1), 1–15. doi: 10.1002/jqs.3070

Hata, S., Sugiyama, S., and Heki, K. (2022). Abrupt drainage of Lago Greve, a large proglacial lake in Chilean Patagonia, observed by satellite in 2020. Commun. *Earth Environ.* 3 (1), 190. doi: 10.1038/s43247-022-00531-5

He, Y., Yao, S., Yang, W., Yan, H. W., Zhang, L. F., Wen, Z. Q., et al. (2021). An extraction method for glacial lakes based on landsat-8 imagery using an improved U-net network. *IEEE J. Sel. Top. Appl. Earth Obs. Remote Sens.* 14, 6544–6558. doi: 10.1109/jstars.2021.3085397

Hengst, A. M., Armstrong, W. H., Rick, B., and McGrath, D. (2021). Short-term variability in alaska ice-marginal lake area: implications for long-term studies. *Remote Sens.* 13 (19), 3955. doi: 10.3390/rs13193955

Ivy-Ochs, S., Kerschner, H., Maisch, M., Christl, M., Kubik, P. W., and Schlüchter, C. (2009). Latest Pleistocene and Holocene glacier variations in the European Alps. *Quat. Sci. Rev.* 28 (21-22), 2137–2149. doi: 10.1016/j.quascirev.2009.03.009

Jiang, L. Y., Fan, X. M., Deng, Y., Zou, C. B., Feng, Z. T., Djukem, D. L. W., et al. (2023). Combining geophysics, remote sensing and numerical simulation to assess GLOFs: Case study of the Namulacuo Lake in the Southeastern Tibetan Plateau. *Sci. Total Environ.* 880, 163262. doi: 10.1016/j.scitotenv.2023.163262

Kaushik, S., Singh, T. S., Joshi, P. K., and Dietz, A. J. (2022). Automated mapping of glacial lakes using multisource remote sensing data and deep convolutional neural network. *Int. J. Appl. Earth Obs. Geoinf.* 115, 103085. doi: 10.1016/j.jag.2022.103085

Kellerer-Pirklbauer, A., Avian, M., Benn, D. I., Bernsteiner, F., Krisch, P., and Ziesler, C. (2021). Buoyant calving and ice-contact lake evolution at Pasterze Glacier (Austria) in the period 1998-2019. *Cryosphere.* 15 (3), 1237–1258. doi: 10.5194/tc-15-1237-2021

King, O., Dehecq, A., Quincey, D. J., and Carrivick, J. L. (2018). Contrasting geometric and dynamic evolution of lake and land-terminating glaciers in the central Himalaya. *Global Planet. Change.* 167, 46–60. doi: 10.1016/j.gloplacha.2018.05.006

Knox, J. C. (1996). Late quaternary Upper Mississippi River alluvial episodes and their significance to the Lower Mississippi River system. *Eng. Geol.* 45 (1-4), 263–285. doi: 10.1016/s0013-7952(96)00017-8

Kumar, M., Al-quraishi, A. M. F., and Mondal, I. (2021). . Glacier changes monitoring in Bhutan High Himalaya using remote sensing technology. *Environ. Eng. Res.* 26 (1), 38–50. doi: 10.4491/eer.2019.255

Lencioni, V. (2018). Glacial influence and stream macroinvertebrate biodiversity under climate change: Lessons from the Southern Alps. *Sci. Total Environ.* 622, 563–575. doi: 10.1016/j.scitotenv.2017.11.266

Lesi, M., Nie, Y., Shugar, D. H., Wang, J. D., Deng, Q. H., and Chen, H. Y. (2022). Landsat- and Sentinel-derived glacial lake dataset in the China-Pakistan Economic Corridor from 1990 to 2020. *Earth Syst. Sci. Data.* 14 (12), 5489–5512. doi: 10.5194/essd-14-5489-2022

Leydesdorff, L., Carley, S., and Rafols, I. (2013). Global maps of science based on the new Web-of-Science categories. *Scientometrics.* 94 (2), 589–593. doi: 10.1007/s11192-012-0784-8

Leydesdorff, L., Wagner, C. S., and Bornmann, L. (2019). Interdisciplinarity as diversity in citation patterns among journals: Rao-Stirling diversity, relative variety, and the Gini coefficient. *J. Informetr.* 13 (1), 255–269. doi: 10.1016/j.joi.2018.12.006

Li, J., Gu, Y. Y., Wu, L. X., Guo, L., Xu, H. D., and Miao, Z. L. (2022b). Changes in Glaciers and Glacial Lakes in the Bosula Mountain Range, Southeast Tibet, over the past Two Decades. *Remote Sens.* 14 (15), 3792. doi: 10.3390/rs14153792

Li, J. J., Mao, Y., Ouyang, J. Y., and Zheng, S. N. (2022a). A review of urban microclimate research based on citeSpace and VOSviewer analysis. *Int. J. Environ. Res. Public Health* 19 (8), 4741. doi: 10.3390/ijerph19084741

Li, J. L., and Sheng, Y. W. (2012). An automated scheme for glacial lake dynamics mapping using Landsat imagery and digital elevation models: a case study in the Himalayas. *Int. J. Remote Sens.* 33 (16), 5194–5213. doi: 10.1080/01431161.2012.657370

Li, W. P., Wang, W., Gao, X., Wang, X. C., and Wang, R. H. (2022c). Inventory and spatiotemporal patterns of glacial lakes in the HKH-TMHA region from 1990 to 2020. *Remote Sens.* 14 (6), 1351. doi: 10.3390/rs14061351

Liu, W. S. (2019). The data source of this study is Web of Science Core Collection? *Not enough. Scientometrics.* 121 (3), 1815–1824. doi: 10.1007/s11192-019-03238-1

Liu, Z. Q., Yang, Z. Q., Chen, M., Xu, H. H., Yang, Y., Zhang, J., et al. (2023). Research hotspots and frontiers of mountain flood disaster: bibliometric and visual analysis. *Water.* 15 (4), 673. doi: 10.3390/w15040673

Lu, H., Zheng, D., Yang, K., and Yang, F. (2020). Last-decade progress in understanding and modeling the land surface processes on the Tibetan Plateau. *Hydrol. Earth Syst. Sci.* 24 (12), 5745–5758. doi: 10.5194/hess-24-5745-2020

Ma, S. Y., Qiu, H. J., Zhu, Y. R., Yang, D. D., Tang, B. Z., Wang, D. Z., et al. (2023). Topographic changes, surface deformation and movement process before, during and after a rotational landslide. *Remote Sens.* 15 (3), 662. doi: 10.3390/rs15030662

Mansur, V., Guimarães, C., Carvalho, M. S., Lima, L. D., and Coeli, C. M. (2021). From academic publication to science dissemination. *Cad. Saude Public.* 37 (7), 140821. doi: 10.1590/0102-311x00140821

McKillop, R. J., and Clague, J. J. (2007). Statistical, remote sensing-based approach for estimating the probability of catastrophic drainage from moraine-dammed lakes in Southwestern British Columbia. *Global Planet. Change.* 56 (1-2), 153–171. doi: 10.1016/j.gloplacha.2006.07.004

Medeiros, A. S., Chipman, M. L., Francis, D. R., Hamerlík, L., Langdon, P., Puleo, P. J. K., et al. (2022). A continental-scale chironomid training set for reconstructing Arctic temperatures. *Quat. Sci. Rev.* 294, 107728. doi: 10.1016/j.quascirev.2022.107728

Miles, E. S., Willis, I. C., Arnold, N. S., Steiner, J. F., and Pellicciotti, F. (2017). Spatial, seasonal and interannual variability of supraglacial ponds in the Langtang Valley of Nepal 1999-2013. *J. Glaciol.* 63 (237), 88–105. doi: 10.1017/jog.2016.120

Morriss, B. F., Hawley, R. L., Chipman, J. W., Andrews, L. C., Catania, G. A., Hoffman, M. J., et al. (2013). A ten-year record of supraglacial lake evolution and rapid drainage in West Greenland using an automated processing algorithm for multispectral imagery. *Cryosphere.* 7 (6), 1869–1877. doi: 10.5194/tc-7-1869-2013

Motschmann, A., Huggel, C., Carey, M., Moulton, H., Walker-Crawford, N., and Muñoz, R. (2020). Losses and damages connected to glacier retreat in the Cordillera Blanca, Peru. *Clim. Change.* 162, 837–858. doi: 10.1007/s10584-020-02770-x

Mulsow, C., Koschitzki, R., and Maas, H. (2015). Photogrammetric monitoring of glacier margin lakes. *Geomatics Nat. Hazards Risk.* 6 (5-7), 600–613. doi: 10.1080/19475705.2014.939232

Nie, Y., Liu, Q., Wang, J., Zhang, Y., Sheng, Y., and Liu, S. (2018). An inventory of historical glacial lake outburst floods in the Himalayas based on remote sensing observations and geomorphological analysis. *Geomorphology.* 308, 91–106. doi: 10.1016/j.geomorph.2018.02.002

Nie, Y., Sheng, Y. W., Liu, Q., Liu, L. S., Liu, S. Y., Zhang, Y. L., et al. (2017). A regional-scale assessment of Himalayan glacial lake changes using satellite observations from 1990 to 2015. *Remote Sens. Environ.* 189, 1–13. doi: 10.1016/j.rse.2016.11.008

Ogier, C., Werder, M. A., Huss, M., Kull, I., Hodel, D., and Farinotti, D. (2021). Drainage of an ice-dammed lake through a supraglacial stream: hydraulics and thermodynamics. *Cryosphere.* 15 (11), 5133–5150. doi: 10.5194/tc-15-5133-2021

Pei, Y. Q., Qiu, H. J., Zhu, Y. R., Wang, J. D., Yang, D. D., Tang, B. Z., et al. (2023). Elevation dependence of landslide activity induced by climate change in the eastern Pamirs. *Landslides.* 20 (6), 1115–1133. doi: 10.1007/s10346-023-02030-w

Petrakov, D. A., Tutubalina, O. V., Aleinikov, A. A., Chernomorets, S. S., Evans, S. G., Kidyaeva, V. M., et al. (2012). . Monitoring of Bashkara Glacier lakes (Central Caucasus, Russia) and modelling of their potential outburst. *Nat. Hazard.* 61 (3), 1293–1316. doi: 10.1007/s11069-011-9983-5

Prakash, C., and Nagarajan, R. (2018). Glacial lake changes and outburst flood hazard in Chandra basin, North-Western Indian Himalaya. *Geomat. Nat. haz. risk.* 9 (1), 337–355. doi: 10.1080/19475705.2018.1445663

Qi, M., Liu, S. Y., Wu, K. P., Zhu, Y., Xie, F., Jin, H., et al. (2022). Improving the accuracy of glacial lake volume estimation: A case study in the Poiqu basin, central Himalayas. *J. Hydrol.* 610, 127973. doi: 10.1016/j.jhydrol.2022.127973

Qiu, H. J., Zhu, Y. R., Zhou, W. Q., Sun, H. S., He, J. Y., and Liu, Z. J. (2022). Influence of DEM resolution on landslide simulation performance based on the Scoops3D model. *Geomat. Nat. Haz. Risk.* 13 (1), 1663–1681. doi: 10.1080/19475705.2022.2097451

Qu, G., Dai, X. A., Cheng, J. Y., Li, W. L., Wang, M. L., Liu, W. X., et al. (2022). Characterization of long-time series variation of glacial lakes in southwestern tibet: A case study in the nyalam county. *Remote Sens.* 14 (19), 4688. doi: 10.3390/rs14194688

Rawat, M., Jain, S. K., Ahmed, R., and Lohani, A. K. (2023). Glacial lake outburst flood risk assessment using remote sensing and hydrodynamic modeling: a case study of Satluj basin, Western Himalayas, India. *Environ. Sci. pollut. Res.* 30, 41591–41608. doi: 10.1007/s11356-023-25134-1

Rinzin, S., Zhang, G. Q., Sattar, A., Wangchuk, S., Allen, S. K., Dunning, S. A., et al. (2023). GLOF hazard, exposure, vulnerability, and risk assessment of potentially dangerous glacial lakes in the Bhutan Himalaya. *J. Hydrol.* 619, 129311. doi: 10.1016/j.jhydrol.2023.129311

Sattar, A., Allen, S. K., Mergili, M., Haeberli, W., Frey, H., Kulkarni, A. V., et al. (2023). Modeling potential glacial lake outburst flood process chains and effects from artificial lake-level lowering at gepang gath lake, Indian himalaya. *J. Geophys. Res. Earth. Surf.* 128, 3. doi: 10.1029/2022jf006826

Sattar, A., Goswami, A., Kulkarni, A. V., Emmer, A., Haritashya, U. K., Allen, S., et al. (2021). Future glacial lake outburst flood (GLOF) hazard of the south lhonak lake, sikkim himalaya. *Geomorphology.* 388, 107783. doi: 10.1016/j.geomorph.2021.107783

Sawi, T., Holtzman, B. K., Walter, F., and Paisley, J. W. (2022). An unsupervised machine-learning approach to understanding seismicity at an alpine glacier. *J. Geophys. Res.: Earth Surf.* 127 (12), e2022JF006909. doi: 10.1029/2022jf006909

Shan, Z., Li, Z. D., and Dong, X. Y. (2021). Impact of glacier changes in the Himalayan Plateau disaster. *Ecol. Inf.* 63, 101316. doi: 10.1016/j.ecoinf.2021.101316

Shugar, D. H., Burr, A., Haritashya, U. K., Kargel, J. S., Watson, C. S., Kennedy, M. C., et al. (2020). Rapid worldwide growth of glacial lakes since 1990. *Nat. Clim. Change.* 10, 939–945. doi: 10.1038/s41558-020-0855-4

Singh, V. K., Singh, P., Karmakar, M., Leta, J., and Mayr, P. (2021). The journal coverage of Web of Science, Scopus and Dimensions: A comparative analysis. *Scientometrics.* 126 (6), 5113–5142. doi: 10.1007/s11192-021-03948-5

Singh, H., Varade, D. M., de Vries, M. V., Adhikari, K., Rawat, M., Awasthi, S., et al. (2023). Assessment of potential present and future glacial lake outburst flood hazard in the Hunza valley: A case study of Shisper and Mochowar glacier. *Sci. Total Environ.* 868, 161717. doi: 10.1016/j.scitotenv.2023.161717

Sionneau, T., Bout-Roumazeilles, V., Flower, B. P., Bory, A., Tribovillard, N., Kissel, C., et al. (2010). Provenance of freshwater pulses in the Gulf of Mexico during the last deglaciation. *Quat. Res.* 74 (2), 235–245. doi: 10.1016/j.yqres.2010.07.002

Steffen, T., Huss, M., Estermann, R., Hodel, E., and Farinotti, D. (2022). Volume, evolution, and sedimentation of future glacier lakes in Switzerland over the 21st century. *Earth Surf. Dyn.* 10 (4), 723–741. doi: 10.5194/asurf-10-723-2022

Taylor, C. J., Carr, J. R., and Rounce, D. R. (2022). Spatiotemporal supraglacial pond and ice cliff changes in the Bhutan–Tibet border region from 2016 to 2018. *J. Glaciol.* 68, 101–113. doi: 10.1017/jog.2021.76

Taylor, C., Robinson, T. R., Dunning, S., Rachel, C. J., and Westoby, M. (2023). Glacial lake outburst floods threaten millions globally. *Nat. Commun.* 14 (1), 487. doi: 10.1038/s41467-023-36033-x

Thakur, P. K., Dixit, A., Chouksey, A., Aggarwal, S. P., and Kumar, A. S. (2016). Ice sheet features identification, glacier velocity estimation and glacier zones classification

using high resolution optical and SAR data. *Asia-Pacific Remote. Sens.* 9877, 19. doi: 10.1117/12.2224027

Thompson, I., Shrestha, M., Chhetri, N., and Agusdinata, D. B. (2020). An institutional analysis of glacial floods and disaster risk management in the Nepal Himalaya. *Int. J. Disaster Risk Reduct.* 47, 101567. doi: 10.1016/j.ijdrr.2020.101567

Tomczyk, A. M., and Ewertowski, M. W. (2021). Baseline data for monitoring geomorphological effects of glacier lake outburst flood: a very-high-resolution image and GIS datasets of the distal part of the Zackenberg River, northeast Greenland. *Earth Syst. Sci. Data.* 13 (11), 5293–5309. doi: 10.5194/essd-13-5293-2021

Veettil, B. K., and Kamp, U. (2021). Glacial lakes in the andes under a changing climate: A review. *J. Earth Sci.* 32, 1–19. doi: 10.1007/s12583-020-1118-z

Veh, G., Korup, O., von Specht, S., Roessner, S., and Walz, A. (2019). Unchanged frequency of moraine-dammed glacial lake outburst floods in the Himalaya. *Nat. Clim. Change.* 9 (5), 379–383. doi: 10.1038/s41558-019-0437-5

Viani, C., Colombo, N., Bollati, I. M., Mortara, G., Perotti, L. E., and Giardino, M. (2022). Socio-environmental value of glacier lakes: assessment in the Aosta Valley (Western Italian Alps). *Reg. Environ. Change.* 22 (1), 1–21. doi: 10.1007/s10113-021-01860-5

Viani, C., Giardino, M., Huggel, C., Perotti, L., and Mortara, G. (2016). An Overview of Glacier Lakes in the Western Italian Alps from 1927 to 2014 Based on Multiple Data Sources (historical maps, orthophotos and reports of the glaciological surveys). *Geogr. Fis. Din. Quat.* 39 (2), 203–214. doi: 10.4461/gfdq2016.39.19

Viani, C., Machguth, H., Huggel, C., Godio, A., Franco, D., Perotti, L., et al. (2020). Potential future lakes from continued glacier shrinkage in the Aosta Valley Region (Western Alps, Italy). *Geomorphology* 355:107068. doi: 10.1016/j.geomorph.2020.107068

Wang, L. Y., Qiu, H. J., Zhou, W. Q., Zhu, Y. R., Liu, Z. J., Ma, S. Y., et al. (2022). The post-failure spatiotemporal deformation of certain translational landslides may follow the pre-failure pattern. *Remote Sens.* 14 (10), 2333. doi: 10.3390/rs14102333

Wang, W., Bai, J. H., Zhang, L., Jia, J., Yu, L., and Zhang, S. Y. (2021). Biochar modulation of the soil nitrogen cycle: a CiteSpace-based bibliometric study. *J. Beijing Norm. Univ. Nat. Sci.* 57 (1), 76–85. doi: 10.12202/j.0476-0301.2020438

Wang, W. C., Yao, T., Yang, W., Joswiak, D. R., and Zhu, M. L. (2012). Methods for assessing regional glacial lake variation and hazard in the southeastern Tibetan Plateau: a case study from the Boshula mountain range, China. *Environ. Earth Sci.* 67 (5), 1441–1450. doi: 10.1007/s12665-012-1589-z

Wang, W. C., Zhang, T. G., Yao, T. D., and An, B. S. (2022). Monitoring and early warning system of Cirenmaco glacial lake in the central Himalayas. *Int. J. Disaster Risk Reduct.* 73, 102914. doi: 10.1016/j.ijdrr.2022.102914

Wang, X., Chen, G., Dai, X. A., Zhao, J. J., Liu, X., Gao, Y., et al. (2022). Improved process management of glacial lake outburst flood hazards by integrating modular monitoring, assessment, and simulation. *Water Resour. Manage.* 36 (7), 2343–2358. doi: 10.1007/s11269-022-03146-9

Wang, X., Guo, X. Y., Yang, C. D., Liu, Q. H., Wei, J. F., Zhang, Y., et al. (2020). Glacial lake inventory of high-mountain Asia in 1990 and 2018 derived from Landsat images. *Earth Syst. Sci. Data.* 12 (3), 2169–2182. doi: 10.5194/essd-12-2169-2020

Wangchuk, S., Bolch, T., and Robson, B. A. (2022). Monitoring glacial lake outburst flood susceptibility using Sentinel-1 SAR data, Google Earth Engine, and persistent scatterer interferometry. *Remote Sens. Environ.* 271, 112910. doi: 10.1016/j.rse.2022.112910

Wangchuk, S., Bolch, T., and Zawadzki, J. (2019). Towards automated mapping and monitoring of potentially dangerous glacial lakes in Bhutan Himalaya using Sentinel-1 Synthetic Aperture Radar data. *Int. J. Remote Sens.* 40 (12), 4642–4667. doi: 10.1080/01431161.2019.1569789

Williams, R. D., Griffiths, H. M., Carr, J. R., Hepburn, A. J., Gibson, M., Williams, J. J., et al. (2022). Integrating historical, geomorphological and sedimentological insights to reconstruct past floods: Insights from Kea Point, Mt. Cook Village, Aotearoa New Zealand. *Geomorphology.* 398, 108028. doi: 10.1016/j.geomorph.2021.108028

Worni, R., Huggel, C., Clague, J. J., Schaub, Y., and Stoffel, M. (2014). Coupling glacial lake impact, dam breach, and flood processes: A modeling perspective. *Geomorphology.* 224, 161–176. doi: 10.1016/j.geomorph.2014.06.031

Worni, R., Huggel, C., and Stoffel, M. (2013). Glacial lakes in the Indian Himalayas-From an area-wide glacial lake inventory to on-site and modeling based risk assessment of critical glacial lakes. *Sci. Total Environ.* 468-469, S71–S84. doi: 10.1016/j.scitotenv.2012.11.043

Yang, L. Y., Lu, Z., Zhao, C. Y., Kim, J., Yang, C. S., Wang, B. H., et al. (2022). Analyzing the triggering factors of glacial lake outburst floods with SAR and optical images: A case study in Jinweng Co, Tibet, China. *Landslides.* 19, 855–864. doi: 10.1007/s10346-021-01831-1

Yang, Z. Q., Chen, M., Zhang, J., Ding, P., He, N., and Yang, Y. (2023a). Effect of initial water content on soil failure mechanism of loess mudflow disasters. *Front. Ecol. Evol.* 11. doi: 10.3389/fevo.2023.1141155

Yang, Z. Q., Wei, L., Liu, Y. Q., He, N., Zhang, J., and Xu, H. H. (2023c). Discussion on the relationship between debris flow provenance particle characteristics, gully slope, and debris flow types along the karakoram highway. *Sustainability.* 15, 5998. doi: 10.3390/su15075998

Yang, Z. Q., Xiong, J. F., Zhao, X. G., Meng, X. R., Wang, S. B., Li, R., et al. (2023d). Column-hemispherical penetration grouting mechanism for newtonian fluid considering the tortuosity of porous media. *Processes.* 11, 1737. doi: 10.3390/pr11061737

Yang, Z. Q., Zhao, X. G., Chen, M., Zhang, J., Yang, Y., Chen, W. T., et al. (2023b). Characteristics, dynamic analyses and hazard assessment of debris flows in Niumiangou Valley of Wenchuan County. *Appl. Sci.* 13, 1161. doi: 10.3390/app13021161

Ye, Q., Zhang, X. Q., Wang, Y. Z., Zhang, Z., Hu, Y. F., and Zhu, L. P. (2022). Monitoring glacier thinning rate in Rongbuk Catchment on the northern slope of Mt. Qomolangma from 1974 to 2021. *Ecol. Indic.* 144, 109418. doi: 10.1016/j.ecolind.2022.109418

Yu, A. J., Shi, H. L., Wang, Y. F., Yang, J., Gao, C. C., and Lu, Y. (2023). A bibliometric and visualized analysis of remote sensing methods for glacier mass balance research. *Remote Sens.* 15 (5), 1425. doi: 10.3390/rs15051425

Zdorovennova, G., Palshin, N., Golosov, S., Efremova, T., Belashev, B. Z., Bogdanov, S., et al. (2021). Dissolved oxygen in a shallow ice-covered lake in winter: effect of changes in light, thermal and ice regimes. *Water.* 13 (17), 2435. doi: 10.3390/w13172435

Zhang, D. H., Zhou, G., Li, W. D., Han, L., Zhang, S. Q., Yao, X., et al. (2023). A robust glacial lake outburst susceptibility assessment approach validated by GLOF event in 2020 in the Nidu Zangbo Basin, Tibetan Plateau. *Catena.* 220, 106734. doi: 10.1016/j.catena.2022.106734

Zhang, G. Q., Yao, T. D., Xie, H. J., Wang, W. C., and Yang, W. (2015). An inventory of glacial lakes in the Third Pole region and their changes in response to global warming. *Global Planet. Change.* 131, 148–157. doi: 10.1016/j.gloplacha.2015.05.013

Zhang, M. M., Chen, F., Guo, H. D., Yi, L., Zeng, J. Y., and Li, B. (2022c). Glacial lake area changes in high mountain asia during 1990-2020 using satellite remote sensing. *Research.* 2022, 9821275. doi: 10.34133/2022/9821275

Zhang, T. G., Wang, W. C., Gao, T. G., An, B. S., and Yao, T. D. (2022b). An integrative method for identifying potentially dangerous glacial lakes in the Himalayas. *Sci. Total Environ.* 806, 150442. doi: 10.1016/j.scitotenv.2021.150442

Zhang, Y. Q., You, X. L., Huang, S., Wang, M. H., and Dong, J. W. (2022a). Knowledge atlas on the relationship between water management and constructed wetlands-A bibliometric analysis based on CiteSpace. *Sustainability.* 14 (14), 8288. doi: 10.3390/su14148288

Zhao, F. Y., Long, D., Li, X. D., Huang, Q., and Han, P. (2022). Rapid glacier mass loss in the Southeastern Tibetan Plateau since the year 2000 from satellite observations. *Remote Sens. Environ.* 270, 112853. doi: 10.1016/j.rse.2021.112853

Zhao, X. G., Yang, Z. Q., Meng, X. R., Wang, S. B., Li, R., Xu, H. H., et al. (2023). Study on mechanism and verification of columnar penetration grouting of time-varying newtonian fluids. *Processes.* 11, 1151. doi: 10.3390/pr11041151

Zhou, Z. Y., Cheng, X. Q., Shangguan, D., Li, W. P., Li, D., He, B. B., et al. (2023). A Comparative Study of a Typical Glacial Lake in the Himalayas before and after Engineering Management. *Remote Sens.* 15, 214. doi: 10.3390/rs15010214

frontiers | Frontiers in Ecology and Evolution

TYPE Original Research
PUBLISHED 03 November 2023
DOI 10.3389/fevo.2023.1279102

OPEN ACCESS

EDITED BY
Haijun Qiu,
Northwest University, China

REVIEWED BY
Guo Liyu,
Xi'an University of Science and Technology, China
Chengwu Wang,
Southwest Petroleum University, China

*CORRESPONDENCE
Junqing Hao
junqinghao@xaufe.edu.cn;
54358526@qq.com

RECEIVED 17 August 2023
ACCEPTED 03 October 2023
PUBLISHED 03 November 2023

CITATION
Hao J, Guo Y, Wu M and Luo Z (2023) How can high-quality development improve the ecotourism efficiency in the region of ecological constraints of China? Empirical evidence from the Yellow River Basin. *Front. Ecol. Evol.* 11:1279102. doi: 10.3389/fevo.2023.1279102

How can high-quality development improve the ecotourism efficiency in the region of ecological constraints of China? Empirical evidence from the Yellow River Basin

Junqing Hao*, Ying Guo, Mengyao Wu and Zhixin Luo

Xi'an University of Finance and Economics, School of Business, Xi'an, China

Despite the massive impacts of ecotourism on regional development, only limited papers empirically examined the responses of the regional development factors to ecotourism in the context of an ecological constraints region. To fill this gap, the primary aim of this paper is to reveal how ecotourism efficiency is affected by quality regional development in the region of ecological constraints. The second aim is to investigate the moderating role of ecological constraints in building relationships of ecotourism efficiency and quality regional development factors. The research was conducted in the Yellow River Basin, a prime area for ecological protection and high-quality regional development in China. Data gathered from 2010 to 2019 were used to analyze ecotourism efficiency by using the super–slacks-based measurement method. Findings indicated that four quality regional development factors—innovative, green, open, and shared factors—have positive impacts on ecotourism efficiency in the Yellow River Basin. Ecological constraints moderate the relationship between ecotourism efficiency and quality regional development. The study makes a significant contribution to the literature in terms of both managing the ecological constraints and improving the sustainability of ecotourism in the region of quality development.

KEYWORDS

efficiency, quality regional development, ecotourism, ecological constraint, the Yellow River Basin

Introduction

In recent decades, the ecology has suffered unprecedented damage (Zou and Shen, 2003; Pei et al., 2023). It is also fairly well understood that, with the rapid development of the global tourism industry, the inherent environmental dependence and resource consumption of this industry aggravate the contradiction between tourism development

and ecological conservation (Peng et al., 2017; Tamario et al., 2019; Wang et al., 2022). This contradiction can have serious adverse effects on the ecology of a tourism area, and the risks of the tourism destination ecosystem are continuously increasing (Ma et al., 2021). Tourism is no longer a "green" industry (Williams and Ponsford, 2009; Briassoulis, 2020); thus, its sustainable development is threatened (Qiu et al., 2017). Developing ecotourism has become some policy note issues by governments concerned for addressing the contradiction between promoting tourism and protecting the ecology (Zhang et al., 2022), and realizing the sustainable development of a regional economy is an urgent practical need.

Previous studies on this subject have concluded that ecotourism provides people with more opportunities to enjoy recreation within the acceptable range of the ecosystem, promotes the sustainable development of ecotourism destinations, and improves the quality of regional development (Shasha et al., 2020; Fuxia and Bizhe, 2022). Ecotourism has a positive effect on the protection of the ecological system and promotes high-quality economic growth (Lundholm, 2015; Chen et al., 2020). That being said, the conclusions of relevant research are relatively vague on whether the quality of regional development affects ecotourism and how it affects the efficiency of ecotourism.

The Yellow River Basin (see Figure 1), located in northern China, is a typical area as far as ecotourism in China is concerned. However, the economic aggregate of the Yellow River Basin has been in a relatively weak position. The development of continuous urbanization and industrial transformation poses a particularly significant threat to ecological and environmental protection, which further leads to ecotourism facing with serious ecological challenges (Zhao and Wu, 2018). The contradiction between the advantages of ecotourism and the disadvantages of regional economics has restricted the quality of regional development in the Yellow River Basin for a long time. The key to solving this contradiction lies in the mechanisms to the quality of regional development on ecotourism (Ma et al., 2023). Therefore, the influence mechanism of regional development quality on ecotourism was examined in this study. Although eco-efficiency is of great significance in the context of ecological protection and regional development, the existing research concerning ecotourism efficiency is insufficient, especially in terms of the relevance of its takeaway lessons to the Yellow River Basin.

Ecotourism, as a form of responsible travel that aims to minimize the negative impacts of tourism on the environment and local communities while promoting conservation and sustainable development, has received attention worldwide (Qiu et al., 2022). In the light of the previous studies, this study mainly contributes innovative suggestions as follows: First, it analyzes the characteristics underlying the efficiency in ecotourism's temporal and spatial evolution in the Yellow River Basin, drawing on the undesirable slacks-based measurement (SBM) model based on undesirable outputs. Second, this study constructed a high-quality development evaluation system and analyzed the regional quality development index. The influence of high-quality development on ecotourism efficiency in the Yellow River Basin was found to be based on the driving factors of innovation (number of college students in school), coordination (urbanization rate), green [energy consumption per unit of Gross Domestic Product (GDP)], openness (amount of foreign capital utilized per capita), and sharing (number of beds per 1,000 people). Finally, it reveals the regional quality development of the Yellow River Basin and the effects of driving factors of high-quality development on the efficiency of ecotourism, thus revealing the much less understood link between high-quality development and ecotourism.

The rest of this paper is organized as follows: Section 2 presents the literature review and theoretical analysis of this study. Section 3

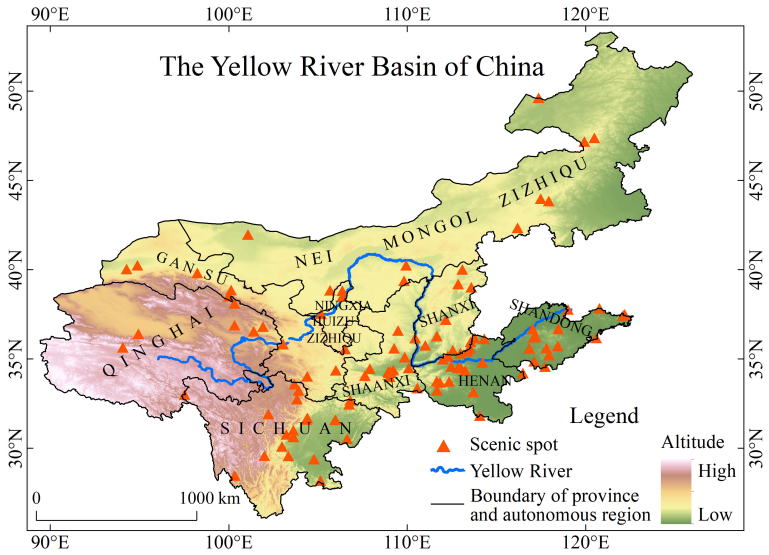

FIGURE 1
Map of the Yellow River Basin.

describes the variables and data sources, and Section 4 analyzes the empirical findings. Finally, the conclusions and recommendations are presented in Section 5.

Literature review and theoretical analysis

Ecotourism efficiency

Ecotourism is a coordinated conservation strategy to link conservation and development, a form of responsible travel that aims to minimize the negative impacts of tourism on the environment and local communities while promoting conservation and sustainable development. However, research into the effectiveness of ecotourism is mixed (Stem et al., 2003).

Eco-efficiency, first proposed by Schaltegger and Sturm (1990), is one of the most widely used indicators regarded as the ratio of economic value to environmental impact. Referring to the previous studies (Fan et al., 2017; Liu et al., 2017), the effectiveness of ecotourism can be assessed by using eco-efficiency indicators and metrics. Therefore, this study considered ecotourism efficiency, as the ratio of comprehensive ecotourism outputs obtained by tourism inputs and ecological inputs refers to the ability of the tourism industry to use resources effectively and efficiently to generate economic benefits while minimizing negative impacts on the environment and local communities.

At present, some tourism studies have examined the measurement and evaluation of ecotourism efficiency (Goessling et al., 2005; Li et al., 2008; Zhang et al., 2010; Peng et al., 2017), but the number of samples and selected indicators is relatively small and, thus, cannot fully reflect ecotourism efficiency (Liu et al., 2017). These studies mainly focus on specific cases without analyzing the factors affecting ecotourism efficiency. The above research objects of ecotourism efficiency include the tourism eco-efficiency of China's coastal cities (Liu et al., 2017), the Yangtze River Delta's ecotourism efficiency (Ma et al., 2021), and rural tourism eco-efficiency (Liang and Shi, 2020). Few scholars have discussed the ecotourism efficiency of the Yellow River Basin from the perspective of research. The research on ecotourism efficiency includes the eco-efficiency of tourism transportation (Reilly et al., 2010), forest ecotourism value (You et al., 2022), ecotourism suitability (Hz et al., 2020), eco-efficiency of tourism products (Kelly et al., 2007), eco-efficiency of tourism destinations (Minoli et al., 2015), and leisure efficiency (Lin, 2017). The research methods include data envelopment analysis (DEA) (Lin, 2017), the spatial Q method (Lee, 2019), the fuzzy analysis hierarchy (Hz et al., 2020), multi-criteria spatial decision-making technology (Feizizadeh et al., 2023), the feedback-loop dynamic system model (Yuan et al., 2018), remote sensing images and social media data (Reilly et al., 2010), and the DEA-tobit model (Liu et al., 2017). However, comprehensive research on ecotourism efficiency is lacking (Liu et al., 2017), and even less research is available on comprehensively measured ecotourism efficiency from the perspective of high-quality development.

The relationship of ecotourism and quality regional development

Quality regional development that is also defined as high-quality development is a major measure for improving total factor productivity and building a modern economic system. This may be done by changing the development mode, optimizing the economic structure, and transforming the growth momentum to achieve better quality and fairer and more efficient and sustainable development (Zeng, 2020). One view is that specific aspects of high-quality regional development include infrastructure (Wong et al., 2013; Wang et al., 2023), community engagement (Khaledi Koure et al., 2023), and policy initiatives (Gibbs et al., 2005; Potts, 2010; Khor et al., 2021). One viewpoint takes "innovation, coordination, green, openness, and sharing" as the overall concept of high-quality development and holds that high-quality development aims at solving the contradiction of unbalanced and insufficient development. It emphasizes both the promotion and realization of regional economic, political, cultural, social, and ecological high efficiency and the promotion and realization of equitable and green sustainable development under the guidance of the five major development factors in the development process (Zhang et al., 2017; Zhu et al., 2019). This research will focus on five factors of high-quality development, namely, "innovation, coordination, green, open, and shared," which are closely related to the eco-efficiency and eco-constrained management that this paper wants to examine.

The existing research studies mainly form the following issues for the relationship of quality regional development and ecotourism, discuss the different model of different area on high-quality development, and provide policy recommendations for achieving high-quality development (Yang et al., 2019). In the field of ecotourism research, there are some studies that carried out the themes of ecotourism and high-quality development, such as rural tourism, red tourism, cultural tourism integration, and large-scale festival tourism (Liu and Han, 2020; Yu et al., 2020; Song et al., 2021). Some studies have examined the response of regional development factors to ecotourism in the context of an ecological constraints region, such as the strategic role of local community participation in ecotourism development (Khaledi Koure et al., 2023), the stimulation of community ecotourism cooperation by large-scale tourism projects (Barkin and Bouchez, 2002), and the support of community tourism decision-makers for ecotourism development (Vincent and Thompson, 2020). However, these studies do not address the impact of the four high-quality regional development factors, namely, innovation, green, open, and shared on ecotourism, let alone explain the process and mechanisms by which high-quality regional development affects the efficiency of ecotourism.

Based on the above analysis, the Super-SBM model evaluation framework was established on the basis of undesirable outputs to make a systematic and complete analysis of ecotourism efficiency. In addition, the SBM model can explain the relationship between tourism and the ecology (Zhang et al., 2022) and further clarify the dynamic synergy between them, thus providing scientific management suggestions for ecological protection and high-quality development in the Yellow River Basin.

The variables, model, and data source

The variables and models of ecotourism efficiency

The variables of ecotourism efficiency

The ecotourism efficiency variables in this study consist of three components: input variables, desirable output variables, and undesirable output variables.

(1) Input variables: According to the most basic factors in classical economics, that is, capital, labor, and land, input factors variables were represented by three indicators: fixed assets investment in tourism industry, the number of employees in tourism industry, and the proportion of natural reserve area. Given that the accommodation industry and the catering industry are the main sectors allied with tourism economics, the indicators of fixed assets investment and the number of employees in tourism are only count enterprises that are above the designated size in accommodation and catering industry. The indicator of proportion of natural reserve area used the ratio of natural reserve area to the total land area. In this study, natural reserve includes national nature reserves, national geological parks, national forest parks, national scenic spots, and world natural and cultural heritage sites, and this may increase the ratio of natural reserve area, but it highlights the developing strategies, i.e., "doing a good job of great protection together," in the Yellow River Basin. Meanwhile, some studies have considered ecotourism resources as an input factor variable to measure the efficiency of ecotourism. Accordingly, this study takes the number of tourism scenic spots as an indicator, including humanistic scenic spots and natural-type scenic spots in the Yellow River Basin.

(2) Desirable output variables: These variables were divided into the scale produces and efficient outputs, which are usually reflected in tourism industry by tourist arrivals and receipts.

(3) Undesirable output variable: This variable was reflected in CO^2 emissions that are calculated by the conversion of energy consumption per 10,000 yuan of GDP in China (Zhu et al., 2018; Zeng, 2020).

The above variables and indicators are further detailed in Table 1.

TABLE 1 Ecotourism efficiency: variables and indicators.

Variables	Indicators	Interpretation of the indicators
Input variables	Fixed asset investment in tourism	Fixed assets of accommodation enterprises + total fixed assets of catering enterprises/ million yuan
	The number of employees in tourism	Year-end number of employees in accommodation enterprises + year-end number of employees in catering enterprises above the designated size/person
	Proportion of natural reserve area	The ratio of the area of nature reserves at or above the national level, forest parks, geological parks, scenic spots, and world cultural and natural heritage sites to the total land area of the province/%
	Tourism resources	The sum of the number of 3A, 4A, and 5A tourist attractions
Desirable output variables	Tourist arrivals	International tourist arrivals + domestic tourist arrivals/million people
	Tourist receipts	International tourism revenue + domestic tourism revenue/billion yuan
Undesirable output variables	CO^2 emissions	Total tourists receipts * energy efficiency consumption per 10,000 yuan of GDP/the million tons of standard coal

The measurement model of ecotourism efficiency

The ecotourism efficiency discussed in this study aims to achieve the maximum output of tourism economic with the help of minimum inputs and ecological impact (Zhu et al., 2018). The impact of ecotourism on the ecological environment runs through the whole process of tourism activities, and tourism's economic benefits are the typically desirable outputs of ecotourism. CO^2 emissions are often considered as the undesirable outputs of ecotourism. Based on this, a production possibility set comprising the desired and undesired outputs was constructed. Furthermore, the possibility of shrinking the desired and undesired outputs under a particular factor input was analyzed, using the directional distance function.

Considering the relaxation problem of variables and the impact of undesired outputs, the non-angle and non-oriented Super-SBM method was adopted to measure ecotourism efficiency (Yu et al., 2015), and the formula is as follows:

$$minp = \frac{\frac{1}{m}\sum_{i=1}^{m}\left(\frac{\bar{x}}{x_{ik}}\right)}{\frac{1}{r_1+r_2}\left[\frac{\sum_{s=1}^{r_1}\overline{y^d}}{y_{sk}^d}+\frac{\sum_{q=1}^{r_2}\overline{y^u}}{y_{qk}^u}\right]}$$

$$\bar{x} \geq \sum_{j=1,\neq k}^{n} x_{ij}\lambda_j; \overline{y^d} \leq \sum_{j=1,\neq k}^{n} y_{sj}^d\lambda_j; \overline{y^d} \geq \sum_{j=1,\neq k}^{n} y_{qj}^d\lambda_j$$

$$\bar{x} \geq x_k; \overline{y^d} \leq y_k^d; \overline{y^u} \geq y_k^u; \lambda_j \geq 0; i = 1, 2, \cdots, m; j = 1, 2, \cdots, n; s = 1, 2, \cdots, r_1; q = 1, 2, \cdots, r_2$$

In the formula, among n Decision Making Units (DMUs), each DMU contains input m, expected output r_1, and unexpected output r_2. x, y^d, and y^u, are the elements in the corresponding input matrix, expected output, and unexpected output matrix, respectively, and p represents the efficiency value.

The variables of high-quality regional development

The concept of high-quality regional development is based on the five development ideas: innovation, coordination, green, open, and shared. This study takes the high-quality development index of the Yellow River Basin as the explanatory variable, which was specifically designed to have five explanatory variables, namely, innovative development, coordinated development, green

development, open development, and shared development. The moderating variable was designed to be an economic variable and an ecological environment variable. The explained variable is ecotourism efficiency. Based on the principles of combining the total index with the per capita index, the efficiency index with the sustainable development index, and the high-quality development index with the economic benefits index (Ren and Du, 2021), the number of college students per 10,000 people, urbanization rate, energy consumption per unit of GDP, per capita utilization of foreign capital, number of beds per 1,000 people, per capita GDP, and types of ecological functional zones were used to reflect the above variables, respectively. The variable indicators and explanations are presented in Table 2.

Data source

In this study, the data on ecotourism efficiency was obtained from the China Statistical Yearbook (2011–2020), the Statistical Yearbooks of the every provinces in the Yellow River Basin (2011–2020), and the Statistical Bulletin of National Economic and Social Development. The data on ecology and environment were obtained from the eco-functional regionalization of each province in the Yellow River Basin. Tourism-related data were acquired from the official websites of the Ministry of Culture and Tourism, People's Republic of China (PRC), and the Department of Culture and Tourism in each of the nine provinces and autonomous regions in the Yellow River Basin. The high-quality development data were sourced from the China Statistical Yearbook for 2011–2020, the Statistical Yearbooks of the nine provinces, and the Statistical Bulletin of the nine provinces in the Yellow River Basin over the years. For all of the collected data, the multiple-imputation method was used to supplement the missing data.

Empirical analysis

Empirical analysis on space-time evolution of ecotourism efficiency in the Yellow River Basin

Temporal evolution of ecotourism efficiency in the Yellow River Basin

The temporal evolution characteristics of ecotourism efficiency in the Yellow River Basin from the perspective of the whole basin are shown in Figure 2. From 2010 to 2019, the ecotourism efficiency in the Yellow River Basin increased steadily from 0.144 to 0.721, with a total growth rate of 400.69% and an average annual growth rate of 40.07%. However, on the whole, the ecotourism efficiency in the Yellow River Basin is low, and the average ecotourism efficiency value in the past 10 years was only 0.356.

From the perspective of different reaches, the ecotourism efficiency in different reaches of the Yellow River Basin showed an increasing trend, but the evolution characteristics were significantly different. (1) In the upper reaches of the Yellow River—Qinghai, Ningxia, Sichuan, Gansu, and Inner Mongolia—ecotourism efficiency showed a fluctuating trend of increase for the period 2010 to 2019. The average ecotourism efficiency increased from 0.126 to 0.542, with an average annual growth rate of 33.02%. Both the average and total growth rates were lower than the whole basin level of 0.303, indicating the lowest ecotourism efficiency. (2) In the middle reaches of the Yellow River, which includes the Shaanxi and Shanxi provinces, the growth of ecotourism efficiency was divided into two stages. From 2010 to 2014, the ecotourism efficiency rose slowly, with the average value ranging from 0.123 to 0.289, lower than the average level of the whole basin. From 2015 to 2019, the ecotourism efficiency increased rapidly from 0.379 to 1.057, with an average annual growth of 17.89%, making it the fastest-growing stretch along the Yellow River Basin in terms of

TABLE 2 High-quality regional development: variable indicators and explanations.

Variables	Variable classification	Variable symbols	Indicators	Explanation of indicators
Explanation variables	Innovative development	*Inova*	Proportion of the number of college students in school	Number of college students in school/total resident population
	Coordinated development	*Green*	Urbanization rate	Urban population/total resident population
	Green development	*Coordi*	Energy consumption per unit of GDP	Total energy consumption/per 10,000 GDP
	Open development	*Open*	Amount of foreign capital utilized per capita	Actual amount of foreign capital utilized/number of employed persons
	Shared development	*Share*	Number of beds per 1,000 people	(Number of beds in health facilities/total resident population) × 1,000
Moderating variables	Ecological constraint	*Environ*	Type of eco-functional region	According to the results of eco-functional regionalization in China, prohibited development area is 4, restricted development area is 3, key development area is 2, and the priority development area is 1
Explained variables	ecotourism	*Toureco*	Ecotourism efficiency	The ecotourism efficiency values are measured above

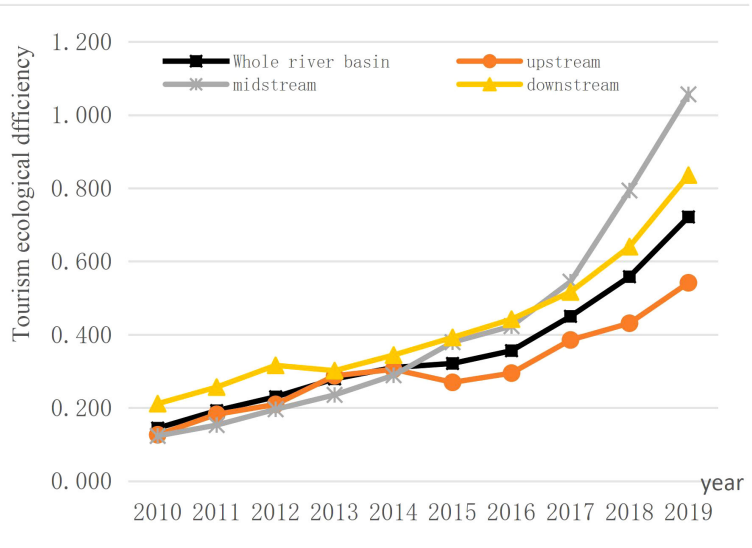

FIGURE 2
Ecotourism efficiency in the Yellow River Basin (2010–2019).

ecotourism efficiency. (3) The lower reaches of the Yellow River Basin are the Henan and Shandong provinces. In the past 10 years, ecotourism efficiency increased steadily in both provinces, with its average ranging from 0.211 to 0.836, which is the highest average rate of ecotourism efficiency in the Yellow River Basin. Notably, in the upper reaches of the Yellow River Basin, it was the lowest, whereas it was the highest in the lower reaches. Furthermore, in the middle reaches, the average growth of this efficiency was the fastest.

Spatial evolution characteristics of ecotourism efficiency in the Yellow River Basin

Taking the average value of ecotourism in the Yellow River Basin in a certain year as the boundary, an area for which the value is higher than the average value has high ecotourism efficiency; otherwise, the area has low ecotourism efficiency (Table 3). From the perspective of the whole river basin, only the Sichuan and Henan provinces had high ecotourism efficiency in 2013. In 2019, these provinces were joined by the Shaanxi and Shanxi provinces. The regions with low ecotourism efficiency changed from seven to five provinces, namely, Qinghai, Ningxia, Gansu, Inner Mongolia, and Shandong. Thus, the spatial scope of the high ecotourism rate areas in the Yellow River Basin gradually expanded, whereas that of the low–ecotourism rate areas gradually shrunk.

TABLE 3 Spatial evolution characteristics of ecotourism efficiency in the Yellow River Basin.

Year	High–ecotourism efficiency areas	Low–ecotourism efficiency areas
2010	Sichuan, Henan, and Shandong	Qinghai, Ningxia, Gansu, Inner Mongolia, Shanxi, and Shaanxi
2013	Sichuan and Henan	Qinghai, Ningxia, Gansu, Inner Mongolia, Shanxi, Shaanxi, and Shandong
2015	Sichuan, Shanxi, Shaanxi, Henan, and Shandong	Qinghai, Ningxia, Gansu, and Inner Mongolia
2017	Sichuan, Shanxi, Shaanxi, and Henan	Qinghai, Ningxia, Gansu, Inner Mongolia, and Shandong
2019	Sichuan, Shanxi, Shaanxi, and Henan	Qinghai, Ningxia, Gansu, Inner Mongolia, and Shandong

From the perspective of the different provinces, Sichuan and Henan have always been areas with high ecotourism efficiency, whereas Qinghai, Ningxia, Gansu, and Inner Mongolia have always had low ecotourism efficiency. The spatial pattern of ecotourism efficiency in the abovementioned six provinces has not changed. The Shandong province was a high-efficiency area that later became a low-efficiency area, but it bounced back to become a high-efficiency area once again, and the spatial evolution obviously fluctuated as a result of these changes. Therefore, except in the case of Sichuan, the spatial pattern of ecotourism efficiency in the upper reaches of the Yellow River Basin hardly changed much and that of the lower reaches of Henan did not change at all. In the middle reaches, though, it changed significantly and played a key role in the spatial evolution of the ecotourism efficiency of the basin on the whole.

Linear regression analysis of high-quality development on ecotourism efficiency

Sample descriptive statistical results

The descriptive statistical results of the main variables of the high-quality development index of the Yellow River Basin are shown in Table 4. The mean value of innovation development is 0.068; the maximum value is 0.512, and the minimum value is 0.0103, indicating a strong difference in the number of college students. The standard deviation of green development was 5.92e-05, indicating significant heterogeneity in unit energy consumption data. The mean values of the coordinated development variables,

TABLE 4 Descriptive statistics of the main variables.

Variable		Observed value	Mean value	Standard deviation	Minimum value	Maximum value
Innovation development	*Inova*	88	0.0680	0.141	0.0103	0.512
Coordinated development	*Coordi*	88	0.000120	5.92e-05	4.11e-05	0.000246
Green development	*Green*	88	0.495	0.0813	0.293	0.634
Open development	*Open*	88	162.3	102.3	1.355	373.2
Shared development	*Share*	88	5.195	0.963	3.483	7.543
Ecotourism efficiency	*Toureco*	88	0.361	0.293	0.0445	1.081
Ecological environment	*Environ*	88	2.295	1.146	1	4

shared development variables, and ecological environment variables were 0.495, 5.195, and 2.295, respectively, and the standard deviations were 0.0813, 0.963, and 1.146, respectively, indicating obvious differences in the indicators. The high standard deviation of the open development variable and the economic variable indicates that the numerical difference between the unit energy consumption index and the per capita GDP index was not obvious, which may affect the reduction of the regression coefficient value in a later period but had little impact on the analysis of the study's results.

The factor analysis method was used to process the relevant data of the high-quality development index evaluation index system of the Yellow River Basin. Thus, the high-quality development index of the nine provinces was calculated for 2010–2019. The SPPS21 software was used for testing and analysis, and the results showed that the sample data passed the Bartlett sphericity test with a value above 0.05 and that the Kaiser-Meyer-Olkin (KMO) value was 0.50. According to the Kaiser metric, the sample data in this study were more suitable for factor analysis. Then, through factor analysis, the comprehensive score values of the high-quality development index were calculated, and these scores were applied to the following empirical test research.

Panel regression results of high-quality development on ecotourism efficiency

Based on the above analysis, we further analyzed the impact mechanism of innovative development, coordinated development, green development, open development, and shared development on ecotourism efficiency. First, the panel regression model was constructed with innovative development (*Inova*), coordinated development (*Coordi*), green development (*Green*), open development (*Open*), shared development (*Share*), and ecotourism efficiency (*Toureco*) as explanatory variables.

According to the characteristics of the panel data, model checking was required to find the optimal model. In this study, the F-test was used to compare the Fixed Effect (FE) and Pooled MLE (POOL) models, the BP test was used to compare the Random Effects (RE) and POOL models, and the Hausman test was used to compare the FE and RE models. As per the results, the F-test showed a significance of 5% [F (8, 74) = 7.627, p = 0.000< 0.05], indicating that the FE model is better than the POOL model. The BP test showed a significance of 5% [χ^2 (1) = 2.099, p = 0.147], indicating that the RE model is better than the POOL model. The Hausman test showed a significance of 5% [χ^2 (5) = 20.630, p = 0.001], indicating that the FE model is better than the RE model. Therefore, the FE model was used as the final regression model in this study.

To consider the role of time factors and regional factors, the fixedeffect test was conducted after the determination of the panel regression model. In general, the FE model considers only individual-fixed effects. However, considering the time dynamic characteristics of the high-quality development and ecotourism efficiency data of the Yellow River Basin, this study tested the time fixed effect as well. The Ordinary Least Squares (OLS) regression was used to include time as a virtual dummy variable in the model for analysis. The results showed that the regression coefficient value of time to ecotourism efficiency was 0.027, showing a 0.05 level significance (t = 2.381, p = 0.020< 0.05). Therefore, this study adopted the double–fixed-effect regression model, considering the individual-fixed and time-fixed effects. Table 5 shows the regression results.

The impact of innovation factors on ecotourism efficiency

Table 5 shows that the index of innovation (*Inova*) is positively correlated with the value of ecotourism efficiency at the significant level of 0.1 (t = 1.684, p = 0.096 > 0.05), indicating that innovation factors have a positive impact on the ecotourism efficiency and improve the ecotourism of Yellow River Basin. Innovation is one of the main drivers for the improvement of the regional economic development level. The innovation-driven economic development, in turn, further stimulates the double growth of ecotourist arrivals and ecotourism revenues. Accordingly, it is argued that innovation factors increase the output of ecotourism, which leads to an increase in the efficiency of ecotourism in Yellow River Basin.

Next, we analyze the moderating effect of ecological constraint variables. Table 5 shows that the degree of influence of innovation factors on tourism efficiency becomes weaker under the moderating effect of ecological constraint factors. The Yellow River Basin specifies the ecological constraints of different zones, which restrict the scope of economic activities in the region and limits the number of ecotourists, and the scale of ecotourism income, which leads to the ecotourism outputs under the ecological constraint requirement that becomes less than that under the non-ecological constraint requirement, so the ecological

constraint factor of the Yellow River basin weakens the degree of influence of the innovation factors on ecotourism efficiency.

The impact of coordinated factors on ecotourism efficiency

The analysis results in Table 5 show that the effect of coordination factors (*Coordi*) on ecotourism efficiency (*Tourceo*) in the Yellow River Basin was not significant ($t = 0.849$, $p = 0.399 > 0.05$). The effect of coordination factor (*Coordi*) on ecotourism efficiency (*Tourceo*) was significant and negatively correlated ($t = -5.671$, $p = 0.000< 0.01$) after adding ecological constraints as a moderating variable.

The coordination factors are the complementary resource advantages and industrial linkage between regions to enhance tourism efficiency through the level of urbanization. The provinces in the Yellow River Basin have low resource complementarity, low industrial linkage, and significant differences in urbanization levels. With different regional functional requirements, the differences in resource complementarity, linkage, and urbanization are more obvious, and the coordination factors in the Yellow River Basin did not positively influence the ecotourism efficiency in the region and did not promote ecotourism development enough.

The impact of green development on ecotourism efficiency

The green development factors (*Green*) and ecotourism efficiency (*Tourceo*) of the Yellow River Basin in Table 5 show a significant difference at the level of 0.1 ($t = 1.670$, $p = 0.099 > 0.1$), indicating that the green development factors have a significant positive impact on the ecotourism efficiency of the Yellow River Basin. Green development is an efficient development mode of low-carbon and low-energy consumption. The tourism industry belongs to the green industry and is also the core of ecotourism efficiency. Therefore, the more significant the low-carbon and low-energy consumption in the Yellow River Basin is, the more significant the positive impact on ecotourism efficiency is. At the same time, the results (Table 5) show that the positive impact of green development in the Yellow River Basin on ecotourism efficiency has been strengthened by the addition of the adjustment variables of ecological constraints, and the two have a significant positive impact relationship at a level of 0.05.

The impact of openness factors on ecotourism efficiency

In Table 5, the significant level is 0.01 ($t = 2.676$, $p = 0.009< 0.01$), and the regression coefficient value is $0.001 > 0$, indicating that openness factors have a significant positive impact on ecotourism efficiency. Moreover, adding the adjustment variable of ecological constraints to the analysis, it was found that the openness factors show a strong relationship between openness factors on ecotourism efficiency.

The tourism industry is a highly open industry. With the flow of tourists between tourist sources and destinations, a strong capital flow, information flow, and material flow have formed, which can promote highly open tourism destinations. Each province in the Yellow River Basin has rich ecotourism resources and is a global and national tourist destination. Therefore, the ecotourism industry plays a strong role in promoting the growth of foreign investment and openness in the Yellow River Basin.

The impact of shared factors on ecotourism efficiency

According to the analysis results in Table 5, the shared factors showed a significant level of 0.1 ($t = 1.888$, $p = 0.063 > 0.05$), indicating that shared factors have a positive impact on ecotourism

TABLE 5 Panel regression results of high-quality development on ecotourism efficiency.

Explanatory variable		Coef	Std. Err	t	p
Intercept	(1)	−0.520	0.332	−1.569	0.121
	(2)	0.958***	0.192	5.003	0.000
Innovation-driven development (*Inova*)	(1)	3.203*	1.903	1.684	0.096
	(2)	−0.685***	0.117	−5.869	0.000
Coordinated development (*Coodi*)	(1)	0.724	0.853	0.849	0.399
	(2)	−1.534***	0.270	−5.671	0.000
Green development (*Green*)	(1)	1693.702*	1014.323	1.670	0.099
	(2)	969.061**	457.135	2.120	0.037
Development for global progress (*Open*)	(1)	0.001**	0.000	2.676	0.009
	(2)	0.001***	0.000	5.853	0.000
Development for the benefit of all (*Share*)	(1)	0.077*	0.041	1.888	0.063
	(2)	−0.002	0.023	−0.080	0.936

Remarks: (1) Adjustment variable is not added. (2) Add regulating variable; $F(5, 74) = 24.543$, $p = 0.000$; $R^2 = 0.624$, adjustment $R^2 = 0.558$; *p< 0.1, **p< 0.05, and ***p< 0.01.

efficiency. However, considering the role of the adjustment variables of ecological constraint, the impact of shared development on ecotourism efficiency was found to have weakened.

Shared factors, including the construction of regional infrastructure and public service capacity, have improved the efficiency of ecotourism in Yellow River Basin. Whereas, the number of infrastructure is lower in the areas with stringent ecological requirements than the areas with loose ecological requirements, and this weakens the impact of shared factors on ecotourism efficiency in Yellow River Basin.

Conclusions

(1) The spatiotemporal evolution characteristics of ecotourism efficiency is significant.

This study used the Super-SBM model of unexpected output to calculate the ecotourism efficiency of the Yellow River Basin in the past decade from 2010 to 2019. From the perspective of time evolution, the ecotourism efficiency value of the Yellow River Basin was generally low—only 0.721 in 2019—but showed a continuous upward trend and an annual growth rate of more than 40%. From the perspective of spatial evolution, significant differences exist in ecotourism efficiency among the upper, middle, and lower reaches of the Yellow River. The ecotourism efficiency value in the upper reaches of the Yellow River was the lowest and its growth rate kept fluctuating. In the middle reaches, the ecotourism efficiency value increased from low to high and its growth rate was the fastest. The ecotourism efficiency in the lower reaches of the Yellow River was the highest, and the development trend was stable. Moreover, significant differences in ecotourism efficiency also exist among different provinces. Sichuan and Henan have always been the areas with high ecotourism efficiency, whereas Qinghai, Ningxia, Gansu, and Inner Mongolia have always been the areas with low ecotourism efficiency. Shanxi and Shaanxi have risen from being low–ecotourism efficiency areas to high–ecotourism efficiency areas, whereas the ecotourism efficiency of Shandong fluctuated.

(2) High-quality regional development factors have a positive impact on ecotourism efficiency in Yellow River Basin.

Based on the five major quality regional development factors, namely, innovation, coordination, green, openness, and sharing, this study constructed a quality-development index system and measured the quality-development index of the Yellow River Basin of the past 10 years from 2010 to 2019. Then, linear regression and panel regression models were employed to analyze the effects of these factors on ecotourism efficiency.

The results showed that the quality-development factors had a significant positive effect on the ecotourism efficiency in the Yellow River Basin, indicating that quality development in the Yellow River Basin is conducive to the improvement of ecotourism efficiency. The innovation factors, green factors, open factors, and shared factors present a positive impact on ecotourism efficiency in the Yellow River Basin. Furthermore, the coordinated factors and ecotourism efficiency did not show a correlation, indicating that no influencing relationship exists between coordinated factors and ecotourism efficiency in the Yellow River Basin.

(3) The moderating effect of ecological constraint is significant.

To further examine the role of ecological constraint on the relationship between the quality development and ecotourism efficiency, this study used ecological constraint as moderating variables for analysis. The results of the study found the following: (1) ecological constraint weakened the positive impact of innovative factors and shared factors on ecotourism efficiency enhancement in the Yellow River Basin and in the context of considering different ecological constraint, the regional innovation capacity, and the public. (2) The ecological constraint strengthened the positive influence of green factors and open factor on the ecotourism efficiency of the Yellow River Basin, considering the influence of different ecological functional zones, the promotional effect of the Yellow River Basin's pursuit of low-carbon and low-energy development methods, and the increase in the amount of foreign capital utilized per capita on the ecotourism efficiency enhancement. (3) Because of the ecological constraint, coordinated factors had a negative influence on ecotourism efficiency in the Yellow River Basin, indicating that insufficient coordinated factors in the Yellow River Basin inhibits ecotourism efficiency improvement. Thus, a negative influence relationship was found between the two.

Discussion

Theoretical implications

First, this study expands the study of the influencing factors of ecotourism. Existing studies point out that ecotourism is affected by economic development level, ecological environment, and natural factors. For example, the findings of Thomas et al. (2021) suggest that universalism value is positively related to ecotourism predisposition; some scholars have explored the relationship between agro-ecotourism and agricultural regional development (Cao, 2018). This study innovatively reveals the influencing factors and mechanisms of ecotourism from the perspective of regional development quality and opens the black box between high-quality development and ecotourism.

Second, this study enriches the research objects of tourism eco-efficiency. Previous research objects on tourism eco-efficiency include the tourism eco-efficiency of China's coastal cities (Liu et al., 2017), the tourism eco-efficiency of Yangtze River Delta (Ma et al., 2021), and rural tourism eco-efficiency (Liang and Shi, 2020). Few scholars have discussed the tourism eco-efficiency of Yellow River Basin. Our study analyzes the temporal and spatial evolution characteristics of ecotourism efficiency in the Yellow River Basin of China and explores the ecotourism efficiency and its driving factors in the nine provinces in the Yellow River Basin from 2010 to 2019.

Third, this study broadens the research perspective of tourism eco-efficiency. Previous scholars have examined the eco-efficiency of tourism transportation (Reilly et al., 2010), forest ecotourism value (You et al., 2022), ecotourism suitability (Hz et al., 2020), eco-efficiency of tourism products (Kelly et al., 2007), eco-efficiency of tourism destinations (Minoli et al., 2015), and leisure efficiency (Lin, 2017). However, comprehensive research on tourism eco-efficiency

is lacking (Liu et al., 2017), and even less research is available on comprehensively measured ecotourism efficiency from the perspective of high-quality development. Based on the tourism efficiency model and high-quality development index, we explore the impact of high-quality development on ecotourism development in the Yellow River Basin from five dimensions: innovation, coordination, green, openness, and sharing, which not only broadens the research perspective of tourism eco-efficiency but also serves as a useful supplement to the research on high-quality development.

Managerial implications

(1) Lead the innovation and open development of ecotourism in the Yellow River Basin with planning

According to the scientific, long-term, strategic, and systematic characteristics and requirements, the "Yellow River Basin ecotourism Special Plan" should be studied and compiled. First, the plan should scientifically analyze the foundation and conditions, advantages and disadvantages, and prospects and risks of ecotourism construction in the upper, middle, and lower reaches of Yellow River Basin. Second, it should scientifically understand the principles, goals, paths, and modes of ecotourism construction in the Yellow River Basin. Third, it should scientifically define the key areas and key regions of ecotourism construction. Fourth, it should scientifically grasp the key links and measures of ecotourism construction and define the status and role of planning

(2) Implement an ecological service–oriented compensation mechanism to promote regional coordinated development and shared development

The ecological value of tourism resources in the upper reaches of Yellow River Basin should be objectively understood, scientifically evaluated, reasonably utilized, and effectively protected. An ecological compensation system for tourism development in the middle and lower reaches of Yellow River Basin should be established and improved to build a bridge for the coordinated development of the region. Using its beautiful, natural, and ecological environment; idyllic scenery; and agricultural cultural heritage, it actively develops green industries, ecotourism, and rural tourism. Moreover, market-oriented ecological compensation brings new income and development opportunities to farmers. Tourism business activities are beneficiaries of ecological service functions and values, but they may also be detrimental to ecological service functions and ecological values. The establishment of ecological compensation mechanisms for tourism development should be explored, and ecological compensation fees (taxes) on tourism development units and individuals should be levied between the upper, middle, and lower reaches of Yellow River Basin.

(3) Create low-carbon and low-energy ecotourism product systems to improve the sustainability of ecotourism in the region of quality development

Our results show that the four high-quality regional development factors, namely, innovation, green, open, and shared, have positive impacts on ecotourism efficiency in the Yellow River Basin, which provide practical enlightenment for improving the sustainability of ecotourism in the region of quality development. Specifically, the goal of the ecotourism product system layout is to control the development intensity and to adjust the spatial structure according to the principle of balanced ecotourism resources and environment as well as unified economic, social, and ecological benefits to promote the space-intensive and efficient ecotourism product and ecological space, mountains, and water. The Shaanxi province that is located in the middle reaches of Yellow River Basin, for example, is focusing on creating a system of nine corridors with three life "blue paths," three health "green paths," and three cultural "purple paths," optimizing the ecotourism product system in the watershed. The product system of ecotourism in water should be optimized, focusing on the Han River ecological experience product; the product system of ecotourism in mountains should also be optimized, focusing on the Qinling National Park product; and, last, the product system of ecotourism in red should be optimized as well, focusing on the geological tourism product in northern Shaanxi.

(4) Take the lead in building industrial access system and optimizing ecological constraint management

The results of this paper show that ecological constraints moderate the relationship between the four quality regional development factors—innovative, green, open, and shared factors—and ecotourism efficiency, respectively, which has important practical significance for optimizing ecological constraint management and promoting regional high-quality development. This should be done according to the requirements of the main functional area planning and nature reserve system of each province in the Yellow River Basin, combined with the key tasks of zoning protection of national land space planning, based on the guiding catalog of industrial structure adjustment, the national negative market access list, the ecological environmental protection access list, the green industry guiding catalog, the negative list of national key ecological function area and county industrial access, and the development of key protected areas and general protected areas' industrial access list. The development of green recycling, energy conservation, environmental protection, organic agriculture, ecotourism, health, and pension industries should be encouraged, especially in the upper reaches of Yellow River Basin. The elimination of backward production capacity in key industries with high energy consumption and high emissions should be increased in the middle reaches of Yellow River Basin. The entry of industries with high pollution and high environmental risks should be prohibited, and the establishment of an ecological economic system with ecological industrialization and industrial ecology as the mainstay should be promoted in the lower reaches of Yellow River Basin. Following the requirements of the industrial access list, construction projects should require strict approval, ecological environmental protection responsibilities should be implemented, and the aftermath should be supervised. Finally, the implementation of the industrial list system should be dynamically monitored, the impact of various industrial development behaviors on changes in the Yellow River ecosystem should be scientifically analyzed, and the industrial access list system should be improved in a timely manner.

Data availability statement

The raw data supporting the conclusions of this article will be made available by the authors, without undue reservation.

Ethics statement

The studies involving human participants were reviewed and approved by The Ethics Committee of Xi'an University of Finance and Economics.

Author contributions

JH: Conceptualization, Formal Analysis, Funding acquisition, Writing – original draft. YG: Formal Analysis, Investigation, Writing – original draft, Writing – review & editing. MW: Investigation, Methodology, Writing – original draft. ZL: Investigation, Software, Writing – review & editing.

Funding

The author(s) declare financial support was received for the research, authorship, and/or publication of this article. This work was funded by the Key project of Natural Science Foundation of Shaanxi Province of China (Grant No. 2022JZ-63), Philosophy and Social Science Foundation of Xi'an (Grant No. 22JX46), and "Support Program for Young and Middle-aged Talent" of Xi'an University of Finance and Economics.

Acknowledgments

We deeply appreciate and warmly thank Professor Huigang Liang and the reviewer and editor, whose constructive and helpful comments substantially improved this manuscript. We express our sincere gratitude for the invaluable assistance and support provided by Yuanyuan Chen and Yanting Ma, our master's student, in the meticulous collection and thorough processing of data.

Conflict of interest

The authors declare that the research was conducted in the absence of any commercial or financial relationships that could be construed as a potential conflict of interest.

Publisher's note

References

Barkin, D., and Bouchez, C. P. (2002). NGO-community collaboration for ecotourism: A strategy for sustainable regional development. *Curr. Issues Tourism* 5 (3-4), 245–253. doi: 10.1080/13683500208667921

Briassoulis, H. (2000). Tourism and the environment. *Springer Netherlands Dordrecht*, 6, 21–37. doi: 10.1007/978-94-015-9584-1

Cao, X. H. (2018). Study on the coordinated development of agricultural eco-tourism and agricultural economy in ethnic regions based on coupling model* — taking Ganzi Tibetan autonomous prefecture in Sichuan province as an example. *Chinese Journal of Agric. Resour. and Reg. Plan.* 39 (8), 205–210. doi: 10.7621/cjarrp.1005-9121.20180828

Chen, H., Dong, K., Wang, F., and Emmanuel, C. A. (2020). The spatial effect of tourism economic development on regional ecological efficiency. *Environ. Sci. pollut. Res.* 27, 38241–38258. doi: 10.1007/s11356-020-09004-8

Fan, Y., Bai, B., Qiao, Q., Kang, P., Zhang, Y., and Guo, J. (2017). Study on eco-efficiency of industrial parks in China based on data envelopment analysis. *J. Environ. Manage.* 192, 107–115. doi: 10.1016/j.jenvman.2017.01.048

Feizizadeh, B., Omrazadeh, D., Ghasemi, M., Bageri, S., Lakes, T., Kitzmann, R., et al. (2023). Urban restaurants and online food delivery during the COVID-19 pandemic: a spatial and socio-demographic analysis. *Int. J. Digit. Earth* 16(1), 1725–1751. doi: 10.1080/17538947.2023.2210313

Fuxia, Z., and Bizhe, W. (2022). Research on allocation efficiency of ecological tourism resources in Hunan Province. *Environment Dev. Sustainability* 1 (24), 12813–12832. doi: 10.1007/s10668-021-01965-1

Gibbs, D., Deutz, P., and Proctor, A. (2005). Industrial ecology and eco-industrial development: A potential paradigm for local and regional development? *Regional Stud.* 39 (2), 171–183. doi: 10.1080/00343400520005995 9

Goessling, S., Peeters, P., Ceron, J. P., Dubois, G., Patterson, T., and Richardson, R. B. (2005). The eco-efficiency of tourism. *Ecol. Economics* 54 (4), 417–434. doi: 10.1016/j.ecolecon.2004.10.006

Hz, A., Ma, A., Idwb, C., Mk, D., Aa, A., and Hs, A. (2020). A gis-based fuzzy-analytic hierarchy process (f-ahp) for ecotourism suitability decision making: a case study of babol in Iran. *Tourism Manage. Perspect.* 36. doi: 10.1016/j.tmp.2020.100726

Kelly, J., Haider, W., Williams, P. W., and Englund, K. (2007). Stated preferences of tourists for eco-efficient destination planning options. *Tourism Manage.* 28 (2), 377–390. doi: 10.1016/j.tourman.2006.04.015

Khaledi Koure, F., Hajjarian, M., Hossein Zadeh, O., Alijanpour, A., and Mosadeghi, R. (2023). Ecotourism development strategies and the importance of local community engagement. *Environment Dev. Sustainability* 25 (7), 6849–6877. doi: 10.1007/s10668-022-02338-y

Khor, H. E., Poonpatpibul, C., and Yong Foo, S. U. A. N. (2021). Belt and road initiative: A framework to address challenges and unlock potential for high-quality and inclusive growth. *Singapore Economic Rev.* 66 (01), 21–58. doi: 10.1142/S0217590819410029

Lee, J. H. (2019). Conflict mapping toward ecotourism facility foundation using spatial q methodology. *Tourism Manage.* 72 (6), 69–77. doi: 10.1016/j.tourman.2018.11.012

Li, P., Yang, G. H., Zheng, B., and Zhang, Y. Q. (2008). GHG emission-based eco-efficiency study on tourism itinerary products in Shangri-La, Yunnan Province, China. *Acta Ecologica Sin.* 27 (7), 2954–2963. doi: 10.10801368350080247594 3

Liang, Y., and Shi, C. (2020). Efficiency evaluation and optimization of rural ecotourism space based on dea model. *Int. J. Low-Carbon Technologies.* 15 (3), 356–360. doi: 10.1093/ijlct/ctz084

Lin, T. Y. (2017). Evaluating the leisure benefits of ecotourism with data envelopment analysis. *Appl. Ecol. Environ. Res.* 15 (2), 33–41. doi: 10.15666/aeer/1502_033041

Liu, Y. J., and Han, Y. J. (2020). Factor structure, institutional environment and high-quality development of the tourism economy in China. *J. Tourism* 35 (3), 28–38. doi: 10.19765/j.cnki.1002-5006.2020.03.008

Liu, J., Zhang, J., and Fu, Z. (2017). Tourism eco-efficiency of chinese coastal cities – analysis based on the dea-tobit model. *Ocean Coast. Manage.* 148 (11), 164–170. doi: 10.1016/j.ocecoaman.2017.08.003

Lundholm, J. T. (2015). The ecology and evolution of constructed ecosystems as green infrastructure. *Front. Ecol. Evol.* 3 (106). doi: 10.3389/fevo.2015.00106

Ma, S., Qiu, H., Zhu, Y., Yang, D., Tang, B., Wang, D., et al. (2023). Topographic changes, surface deformation and movement process before, during and after a rotational landslide. *Remote Sens.* 15 (3), 662. doi: 10.3390/rs15030662

Ma, X., Sun, B., and Hou, G. L. (2021). Evaluation and spatial effects of tourism ecological security in the Yangtze River Delta. *Ecol. Indic.* 131, 108190. doi: 10.1016/j.ecolind.2021.108190

Minoli, D. M., Goode, M., and Smith, M. T. (2015). Are eco labels profitably employed in sustainable tourism? a case study on audubon certified golf resorts. *Tourism Manage. Perspect.* 16, 207–216. doi: 10.1016/j.tmp.2015.07.011

Pei, Y., Qiu, H., Yang, D., Liu, Z., Ma, S., Li, J., et al. (2023). Increasing landslide activity in the Taxkorgan River Basin (eastern Pamirs Plateau, China) driven by climate change. *Catena* 223, 106911. doi: 10.1016/j.catena.2023.106911

Peng, H., Zhang, J., Lu, L., Tang, G., Yan, B., and Xiao, X. (2017). Eco-efficiency and its determinants at a tourism destination: a case study of huangshan national park, China. *Tourism Manage.* 60 (6), 201–211. doi: 10.1016/j.tourman.2016.12.005

Potts, T. (2010). The natural advantage of regions: linking sustainability, innovation, and regional development in Australia. *J. cleaner production* 18 (8), 713–725. doi: 10.1016/j.jclepro.2010.01.008

Qiu, X., Fang, Y., and Yang, X. (2017). Tourism eco-efficiency measurement, characteristics, and its influence factors in China. *Sustainability* 9 (9), 1634. doi: 10.3390/su9091634

Qiu, H., Zhu, Y., Zhou, W., Sun, H., He, J., and Liu, Z. (2022). Influence of DEM resolution on landslide simulation performance based on the Scoops3D model. *Geomatics Natural Hazards Risk* 13 (1), 1663–1681. doi: 10.1080/19475705.2022.2097451

Reilly, J., Williams, P., and Haider, W. (2010). Moving towards more eco-efficient tourist transportation to a resort destination: the case of whistler, british columbia. *Res. Transportation Economics* 26 (1), 66–73. doi: 10.1016/j.retrec.2009.10.009

Ren, B. P., and Du, Y. X. (2021). Coupling coordination of economic growth, industrial development and ecology in the Yellow River Basin. *China Population. Resource Environ.* 31 (02), 119–129. doi: 10.3390/ijerph182010664

Schaltegger, S., and Sturm, A. (1990). Ökologische rationalität: ansatzpunkte zur ausgestaltung von ökologieorientierten managementinstrumenten. *Die Unternehm* 44 (4), 273–290.

Shasha, Z. T., Geng, Y., Sun, H. P., Musakwa, W., and Sun, L. (2020). Past, current, and future perspectives on eco-tourism: a bibliometric review between 2001 and 2018. *Environ. Sci. pollut. Res. Int.* 27 (19), 23514–23528. doi: 10.1007/s11356-020-08584-9

Song, C. Y., Li, X. J., and Zhang, Q. (2021). High-quality development of red tourism. *J. Tourism* 36 (6), 3–5. doi: 10.19765/j.cnki.1002-5006.2021.06.002

Stem, C. J., Lassoie, J. P., Lee, D. R., Deshler, D. D., and Schelhas, J. W. (2003). Community participation in ecotourism benefits: the link to conservation practices and perspectives. *Soc. Natural Resour.* 5), 16. doi: 10.1080/08941920309177

Tamario, C., Sunde, J., Petersson, E., and Forsman, A. (2019). Ecological and evolutionary consequences of environmental change and management actions for migrating fish. *Front. Ecol. Evol.* doi: 10.3389/fevo.2019.00271

Thomas, S. K., Mark, T. S., Azilah, K., Dewa, G. S., and Lexi, P. B. (2021). Millennials' predisposition toward ecotourism: the influence of universalism value, horizontal collectivism and user generated content. *J. Ecotourism* 20 (2), 145–164. doi: 10.1080/14724049,2020.1795183

Vincent, V. C., and Thompson, W. (2020). Assessing community support and sustainability for ecotourism development. *J. Travel Res.* 41 (2), 153–160. doi: 10.1177/004728702237415

Wang, L., Qiu, H., Zhou, W., Zhu, Y., Liu, Z., Ma, S., et al. (2022). The post-failure spatiotemporal deformation of certain translational landslides may follow the pre-failure pattern. *Remote Sens.* 14 (10), 2333. doi: 10.3390/rs14102333

Wang, S., Sun, X., Cong, X., and Gao, Y. (2023). Input efficiency measurement and improvement strategies of new infrastructure under high-quality development. *Systems* 11 (5), 243. doi: 10.3390/systems11050243

Williams, P. W., and Ponsford, I. F. (2009). Confronting tourism's environmental paradox: Transitioning for sustainable tourism. *Futures* 41 (6), 396–404. doi: 10.1016/j.futures.2008.11.019

Wong, H. L., Luo, R., Zhang, L., and Rozelle, S. (2013). Providing quality infrastructure in rural villages: The case of rural roads in China. *J. Dev. Economics* 103, 262–274. doi: 10.1016/j.jdeveco.2013.03.002

Yang, X. Z., Zhang, Z. F., Luo, W., Tang, Z., Gao, X., Wan, Z. C., et al. (2019). The impact of government role on high-quality innovation development in mainland China. *Sustainability* 11 (20). doi: 10.3390/su11205780

You, S., Zheng, Q., Chen, B., Xu, Z., Lin, Y., Gan, M., et al. (2022). Identifying the spatiotemporal dynamics of forest ecotourism values with remotely sensed images and social media data: a perspective of public preferences. *J. Cleaner Production* 341 (3), 130715. doi: 10.1016/j.jclepro.2022.130715

Yu, F. W., Huang, X., and Yue, H. (2020). The high-quality development of rural tourism: Connotative features, key issues and countermeasures. *China's Rural Economy* 428 (08), 27–39.

Yu, H., Lu, L., and Li, Y. J. (2015). Tourism efficiency evaluation, classification and ascension path of lake-type chinese national scenic area. *Scientia Geographica* 35 (10), 1247–1255. doi: 10.1631/jzus.B1000185

Yuan, H., Ping, H., and Hong, X. (2018). Simulation of a dynamical ecotourism system with low carbon activity: A case from western China. *J. Environ. Manage.* 206, 1243–1252. doi: 10.1016/j.jenvman.2017.09.008

Zeng, B. (2020). Spacial structure and spillover effect of China's provincial tourism economic efficiency under environmental constraints. *Techno-economic* 39 (06), 141–146, 174. doi: 1002980X(2020)6/014107

Zhang, H., Duan, Y., and Wang, H. (2022). An empirical analysis of tourism eco-efficiency in ecological protection priority areas based on the DPSIR-SBM model: A case study of the Yellow River Basin, China. *Ecol. Inf.* 70, 101720. doi: 10.1016/j.ecoinf.2022.101720

Zhang, L., Gao, X., Cai, W. M., Chen, X. Q., Wang, L. J., and Huang, Q. (2017). Eco-efficiency evaluation of tourism lands in Qilihai Wetlands, Tianjin. *Wetland Sci.* 15 (04), 489–496.

Zhang, Y. H., Zhang, P. Y., and Zhang, Z. X. (2010). Disquisition of touristic ecological footprint and sustainable development of LHASA. *China Population. Resource Environ.* 20 (7), 154–159. doi: 10.1007/978-90-481-3779-4_12

Zhao, L., and Wu, Y. (2018). Tourism and rural poverty alleviation in China: facts and interpretations. *Nankai Manage. Rev.* 21 (06), 142–155.

Zhu, S. S., Zhang, J. H., Hu, H., and Chen, C. H. (2019). Study on the value-added effect of ecosystem serive values in tourism development. *Resour. Environ. Yangtze River Basin* 28 (03), 603–613. doi: 10.11870/cjlyzyyhj201903011

Zhu, Y., Zhang, B., Ni, H. W., and Lv, J. H. (2018). Study on output efficiency of forest ecological products based on supply theory of public goods. *Economic Problems Forestry* 38 (02), 25–32. doi: 10.16832/j.cnki.1005-9709.2018.02.005

Zou, C. X., and Shen, W. S. (2003). Advances in ecological security. *J. Ecol. Rural Environ.* 19 (1), 56–59. doi: 10.3969/j.issn.1673-4831.2003.01.014

frontiers | Frontiers in Ecology and Evolution

TYPE Original Research
PUBLISHED 22 November 2023
DOI 10.3389/fevo.2023.1324932

OPEN ACCESS

EDITED BY
Haijun Qiu,
Northwest University, China

REVIEWED BY
Gao Yang,
Guizhou Normal University, China
Chuan Li,
Nanjing Forestry University, China

*CORRESPONDENCE
Yuxiao He
heyuxiao@hpu.edu.cn
Weiguo Li
wgli@hpu.edu.cn
Tongqian Zhao
zhaotq@hpu.edu.cn

RECEIVED 20 October 2023
ACCEPTED 06 November 2023
PUBLISHED 22 November 2023

CITATION
Mai S, He Y, Li W and Zhao T (2023) Effects of environmental factors on vertical distribution of the eukaryotic plankton community in early summer in Danjiangkou Reservoir, China.
Front. Ecol. Evol. 11:1324932.
doi: 10.3389/fevo.2023.1324932

Effects of environmental factors on vertical distribution of the eukaryotic plankton community in early summer in Danjiangkou Reservoir, China

Sijie Mai, Yuxiao He*, Weiguo Li* and Tongqian Zhao*

Institute of Resources and Environment, Henan Polytechnic University, Jiaozuo, Henan, China

Introduction: Eukaryotic plankton plays crucial roles in ecosystem processes, impacting aquatic ecosystem stability. This study focuses on Danjiangkou Reservoir, a canyon lake in central China, that acts as the water source of the Mid-route of the South-to-North Water Diversion Project.

Methods: In this study, high-throughput 18S rDNA gene sequencing was employed to investigate eukaryotic plankton community at four water depths (0.5 m, 5 m, 10 m, and 20 m). The environmental factors including pH, water temperature (WT), nitrate nitrogen (NO_3^--N), ammonia nitrogen (NH_4^+-N), total nitrogen (TN), conductivity (Cond), and dissolved oxygen (DO) in reservoir areas were measured, and their correlations with abundance and diversity of eukaryotic plankton were analyzed.

Results: The results showed the presence of 122 genera of eukaryotic plankton from 38 phyla. Eukaryotic plankton communities were mainly composed of *Eurytemora*, *Thermocyclops*, *Sinocalanus*, *Mesocyclops*, and *Cryptomonas*. In particular, significant differences in the diversity of eukaryotic plankton communities were found in vertical distribution. The diversity and abundance of eukaryotic plankton communities in 7 sampling sites decreased with the increase of depth from 0.5 to 10 m, while the diversity and abundance of plankton communities increased at 20 m. RDA analysis indicated that pH, depth, WT, NH_4^+-N, DO, Cond, and NO_3^--N could influence the vertical distribution of the eukaryotic plankton community in the Danjiangkou Reservoir. Among these eukaryotic plankton, *Eurytemora*, *Thermocyclops*, and *Volvox* were negatively correlated with pH and WT and positively correlated with depth.

Discussion: This study revealed a novel perspective on the distribution of the eukaryotic plankton community in Danjiangkou Reservoir, particularly in terms of vertical variation, which will be helpful to comprehensively understand ecological processes and to further ensure the water quality safety in this canyon-style reservoir.

KEYWORDS

Danjiangkou Reservoir, eukaryotic plankton, community structure, environmental factor, high-throughput sequencing

1 Introduction

Eukaryotic plankton is important in aquatic communities and plays crucial roles in material cycling and energy flow in aquatic ecosystems (Zubkov and Tarran, 2008; Jiang et al., 2012; Filker et al., 2016). Based on niche theory, environmental variables such as resource availability and abiotic factors could determine species composition in eukaryotic plankton communities. Variations of the eukaryotic plankton community are related to the physicochemical characteristics and biological conditions of the water bodies at space and time scales (Ishida, 2008; MaChado et al., 2019). The study of eukaryotic plankton diversity and community characteristics can indirectly reflect the water quality of the ecological environment. Therefore, studying the distribution characteristics of eukaryotic plankton communities is vital for understanding the characteristics of water ecosystem processes, formulation of scientific and conservation management measures.

In the past decades, studies on the planktonic eukaryotes community mainly depended on microscopy observation. However, this method is not only influenced by sampling conditions and preservation techniques but also there is great variation and disagreement in the identification of these organisms. With the development of biotechniques (Marianne et al., 2015), the diversity of plankton can be assessed by high-throughput sequencing. For eukaryotic plankton high-throughput sequencing of specific PCR products (e.g., eukaryotic 18S rDNA genes) on such platforms can be used to obtain information on eukaryotic community structure, evolutionary relationships, and correlations between eukaryotic plankton and the environment (Sun et al., 2014; Gao et al., 2018; McInnes et al., 2019; Keck et al., 2020). Currently, high-throughput sequencing has been widely used to study plankton community structure in aquatic ecosystems (Zhao et al., 2019; Liu et al., 2020a; Zhong et al., 2021; Wu et al., 2022). Many studies have focused on the community, distribution, and function of phytoplankton, archaea, plant, bacteria, and animal taxa, and their relationship with water quality (Wurzbacher et al., 2010; Nagano and Nagahama, 2012; Sun et al., 2014; Piwosz et al., 2020). High-throughput sequencing technology provides efficient and rapid assessment with specific DNA fragments and provides a more comprehensive profiling of community composition than other methods (Dijk et al., 2014). Its application in water quality monitoring has attracted increasing attention (BoonFei et al., 2015).

Danjiangkou Reservoir, located in Danjiangkou City, Hubei Province and Xichuan County, Henan Province, is the water source of the Mid-route of the South-to-North Water Diversion Project in central China. Benefit from this project, more than 20 cities along the route are supplied with abundant water resources for agriculture, industry, and human consumption. It is important to ensure the safety of water quality in Danjiangkou Reservoir. According to the data provided by the Ecological Environment Department of Henan Province in 2018–2022, the water quality of Danjiangkou Reservoir has reached the standard of class I or II water. Danjiangkou Reservoir is a canyon-style reservoir with a maximum storage capacity of 29.05 billion m^3 and a maximum depth of 80 m. As an important water source, many studies have investigated the eukaryotic plankton community structure in surface water and its influencing factors in Danjiangkou Reservoir at temporal and spatial scales (Shen et al., 2011; Tan et al., 2011; Wang et al., 2016; Zheng et al., 2018). Wang et al. (2016) detected a total of 66 phytoplankton species belonging to 7 phyla and 38 species in the reservoir area and found that diatoms were the dominant phyla in spring, autumn, and winter. Furthermore, the results of their study showed that dissolved oxygen, pH, and phosphorus concentration were the main environmental factors affecting the composition of phytoplankton communities. Through six continuous monitoring of periphytic algae in Danjiangkou Reservoir, Zheng et al. (2018) found the community was assigned to 6 phyla and 46 genera, and observed significant spatial and temporal differences of them. He et al. (2021) detected 6 phyla and 57 genera of phytoplankton from the samples collected at 1.5 m, 5 m and 10 m in the reservoir area, and diatoms and green algae were the dominant phyla. Recently, Cui et al. (2023) analyzed the spatial and temporal variations of physicochemical indicators and phytoplankton at seven different water depths in four seasons in Danjiangkou Reservoir to reveal the main factors affecting the vertical distribution of phytoplankton. Additionally, the characteristics of phytoplankton community change in Danjiangkou Reservoir in different seasons and spaces were analyzed, as well as the main environmental factors affecting the distribution of phytoplankton community structure (Zhang et al., 2022; Xiao et al., 2023). However, these studies mainly focused on the eukaryotic plankton community in shallow water column, and the patterns in deep water of this canyon-style reservoir are still limited.

In this study, high-throughput sequencing of 18S rDNA V4 regions was used to investigate eukaryotic plankton community structure in four layers (0.5 m, 5 m, 10 m, and 20 m) of water in Danjiangkou Reservoir. Especially, stratified sampling provided a more comprehensive understanding of eukaryotic plankton distribution in Danjiangkou Reservoir. Our main goals were to analyze the vertical structure of the eukaryotic plankton community in deep water at the Danjiangkou Reservoir, and to reveal the relationship between the eukaryotic plankton community and environmental factors.

2 Materials and methods

2.1 Samples collection and physicochemical factors determination

According to the overall structural characteristics of the reservoir area, and the basis of previous research methods (Wang et al., 2017; Ferrera et al., 2020; Lee et al., 2018; Song et al., 2019; Liu et al., 2020b), seven sampling sites including Songgang (SG), Tumen (TM), Heijizui (HJZ), Kuxin (KX), Dangzikou (DZK), Wulongquan (WLQ), and Qushou (QS) were set up in the Danjiangkou Reservoir (Figure 1). In June 2021, the samples at 0.5 m, 5 m, 10 m, and 20 m depth of each sampling site were collected respectively for investigating the vertical distribution patterns of the eukaryotic plankton community. A total of 18 L water samples were collected using a Plexiglas water collector, passed through a 0.22 μm filter membrane, and transferred to a 1.5 mL sterile centrifuge tube to be stored in liquid nitrogen for DNA extraction.

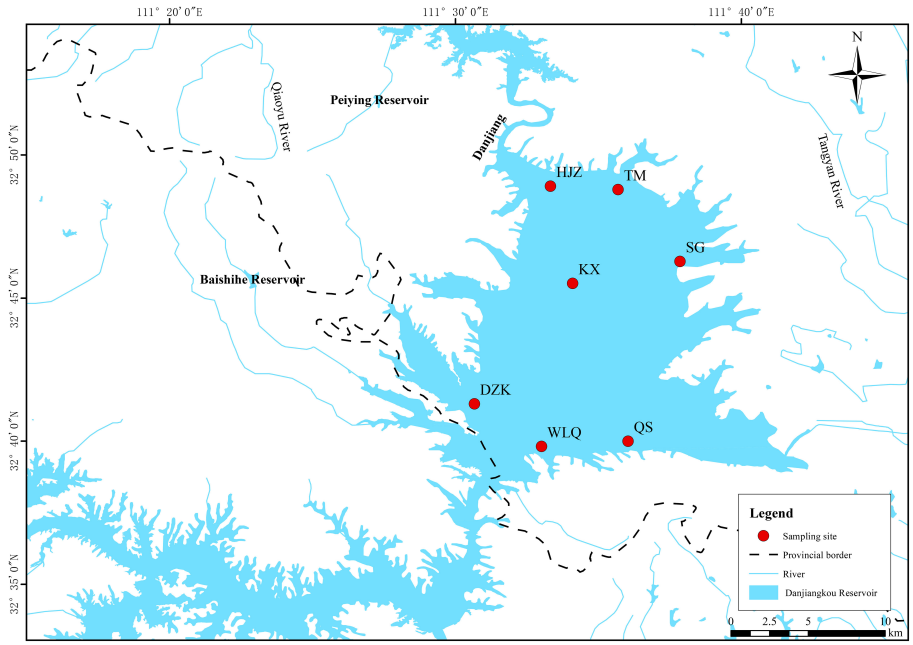

FIGURE 1
Location map of sampling sites in Danjiangkou Reservoir.

The water temperature (WT), pH, dissolved oxygen (DO), and conductivity (Cond) were measured on-site using a portable multifunctional water quality parameter meter. 0.5 L of water samples were taken from each layer and put into polyethylene bottles to be brought back to the laboratory. The physicochemical properties of total nitrogen (TN), ammonia nitrogen (NH_4^+-N), and nitrate nitrogen (NO_3^--N) in the water were determined according to previously described methods (Jin, 1990).

2.2 DNA extraction, PCR amplification and sequencing

DNA was extracted from the samples using the DNeasy Power Water Kit (Mo Bio/QIAGEN) according to the manufacturer's instructions. The extracted DNA was analyzed with a fluorescence spectrophotometer (QuantifluorST fluorometer, Promega, E6090; QuantiT PicoGreen dsDNA Assay Kit, Invitrogen, P7589) and 1% agarose gel electrophoresis to determine concentration and purity. V4 hypervariable region of 18S rDNA was amplified using the specific primers, namely 547F (FCCAGCASCYGCGGTAATTCC) and V4R (ACTTTCGT TCTTGATYRA) (Salmaso et al., 2020). Amplification was carried out in 20 μL reactions with 5×reaction buffer 5 μL, 5×GC buffer 5 μL, dNTP (2.5mM) 2 μL, forward primer (10μM) 1 μL, reverse primer (10uM) 1 μL, DNA Template 2 μL, ddH_2O 8.75 μL, Q5 DNA Polymerase 0.25 μL as the template. Thermal cycling consisted of an initial of 98°C pre-denaturation for 2 min, 30 cycles (denaturation at 98°C for 15 s, annealing at 55°C for 30 s, extension at 72°C for 30 s), and a final extension at 72°C for 10 min. (PCR instrument: ABI Model 2720) The PCR products were isolated and purified using AxyPrep DNA Gel Extraction Kit, Axygen, AP-GX-500. Paired-end sequencing of the amplicon was performed with the Illumina Novaseq platform. The raw sequences were deposited in NCBI under the Bio Project PRJNA (No.782248).

2.3 High-throughput data analysis

After quality control, denoising, splicing, and chimera removal with QIIME2 (Quantitative Insights Into Microbial Ecology) software, the best taxonomic unit (Operational Taxonomic Unit) was classified for high-quality sequences at a classification criterion of ≥97% similarity (default is a species-level similarity). The sequenced OTUs results were compared with the Silva 132 rRNA database using the Classify sklearn algorithm of QIIME2 (Chao, 1984; Bokulich et al., 2013) (https://github.com/QIIME2/q2-feature-classifier) for OTUs representative sequence in the QIIME2 software with default parameters, using a pre-trained Naive Bayes classifier for species annotation.

2.4 Diversity analysis and environmental data analysis

Alpha diversity analysis was performed using QIIME2 software to construct rarefaction curves, the Chao index, Shannon's index and so on. The Chao (Chao, 1984) and Observed-Species indices were used to characterize richness, the Shannon-Winer (Shannon, 1948) and Simpson (Simpson, 1997) indices to characterize diversity, the Pielou-evenness (Pielou, 1966) index for evenness, and Good's coverage (Good, 2010) index for cover. Beta diversity

was calculated using BrayCurtis and unweighted UniFrac distance matrices. PCoA was used to analyze the similarity at the taxonomic level of the eukaryotic plankton phylum in the vertical direction at each sampling. The relevant data were plotted in Excel and Origin 9.0. Redundancy analysis (RDA) and correlation analysis of the main eukaryotic plankton with environmental factors were performed using genescloud. (https://www.genescloud.cn).

3 Results

3.1 Sequencing data of 18S rDNA

A total of 1,972,914 original sequences were obtained, with an average length of 420 bp. After removal of nontargets and the singletons, a total of 1,645,985 high-quality sequences were obtained in all samples, accounting for 83.4% of original sequences. The rarefaction curve gradually became stable when the sequencing reads reached 25000, which indicated that the number of sequencings was sufficient, and the taxon richness was high enough to cover all taxa for further analysis (Figure 2). All sequences were clustered at the 97% similarity level and 2392 OTUs were obtained from all the samples.

3.2 Eukaryotic plankton community composition and relative abundance in Danjiangkou Reservoir

A total of 38 phyla of eukaryotic plankton were identified. The main eukaryotic plankton taxa at the level of phylum in the seven sites were Arthropoda (85.3%), Chordata (4.0%), Chlorophyta (1.6%), while other plankton such as Haptophyceae, Rotifera and Dinophyceae were less than 1% (Figure 3). Obviously, Arthropoda is the dominant species in the reservoir area.

A total of 122 genera of eukaryotic plankton were detected in the 28 samples, all of which contained taxa that could not be identified at the genus level. The eukaryotic plankton community at different depths (0.5 m, 5 m, 10 m, 20 m) comprised 10 higher-level taxon groups (Figure 4). Notably, the relative abundance of major taxa exhibited significant variation across these depth levels. *Eurytemora* dominated at depths from 0.5 to 10 m, while *Thermocyclops* was the dominant species at 20 m. Interestingly, the abundance and species richness of eukaryotic plankton were higher at the 20 m depth, while the other depths showed lower abundance and species richness of eukaryotic plankton. Overall, there were distinct differences in the relative abundance and diversity of eukaryotic plankton at various depths.

3.3 Structural characteristics on vertical distribution of eukaryotic plankton community

There was over 99% coverage of sequences at each sample site, fully reflecting the species and structure of the eukaryotic plankton community in the reservoir region. The average number of OTUs (393) at the 20 m depth water was the largest, and the average number of OTUs (265) at the 5 m depth water was the smallest. The eukaryotic plankton α-diversity of the sampling sites with different depths varied greatly (Table 1). The Observed-Species index and Chao index ranged from 86 to 673 and 89 to 708, respectively, the QS4 (Observed-Species 676 and Chao 713) had the highest richness indices, which were much higher compared to other samples. The Simpson index and Shannon-Wiener index have maximum values in SG1, which had the greatest species diversity, and the minimum

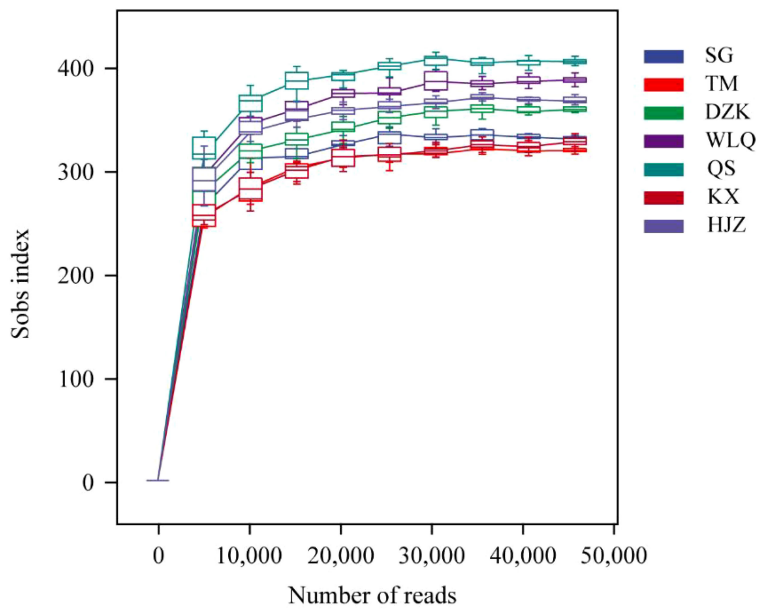

FIGURE 2
Rarefaction curve.

10.3389/fevo.2023.1324932

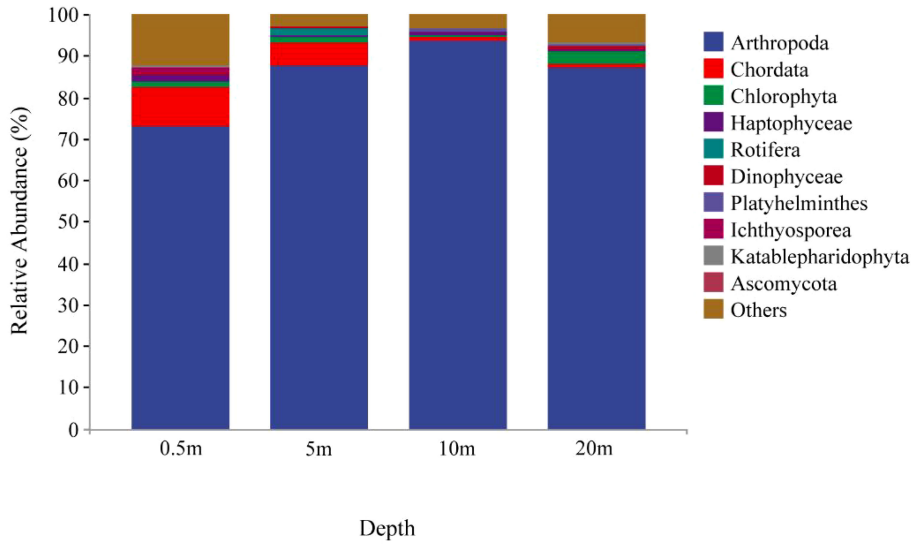

FIGURE 3
Relative abundance of eukaryotic plankton at different depths at the level of phylum.

values of the Simpson index and Shannon-Wiener index were at HJZ2. Pielou-evenness in this study was 0.07–0.68, indicating that the distribution of the number of OUTs varied widely among the samples.

3.4 Changes in richness and diversity on vertical distribution of the eukaryotic plankton

β-diversity analysis showed that different eukaryotic plankton species have unique vertical distribution patterns in Danjiangkou Reservoir (Figure 5). The result showed that the community composition of KX, WLQ and QS at 0.5 m depth water was relatively consistent, and SG, TM, HJZ, DZK each formed a group. At 5 m depth water, HJZ, KX and DZK formed a group with higher similarity, and the remaining four sampling sites each formed a group. At 10 m depth water, KX, DZK and HJZ were more similar as a group, TM and WLQ formed a group, and SG had the same eukaryotic plankton community structure as QS. At 20 m depth water, KX, WLQ, TM and QS formed a group, DZK and HJZ were more similar as a group, and SG formed its own group. The results indicated that the community composition of all sampling sites varied greatly at 0.5–20 m depth water.

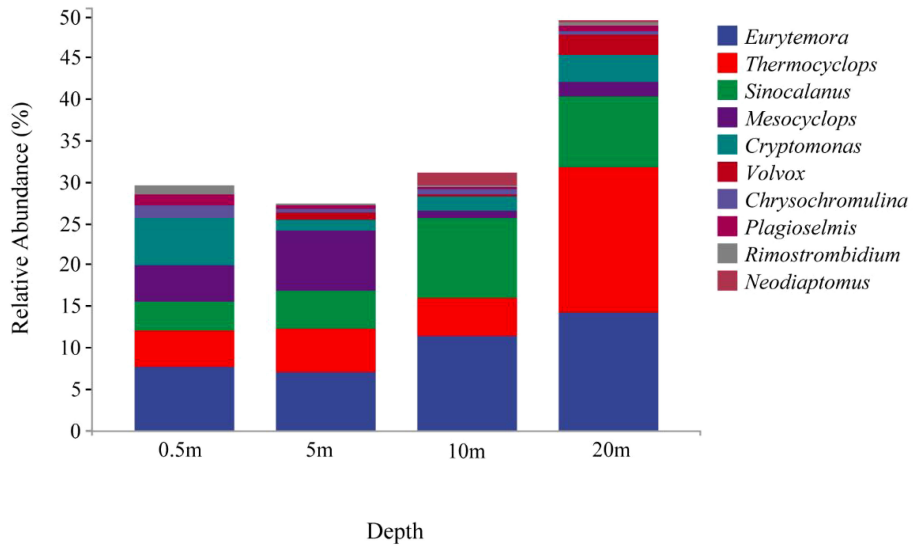

FIGURE 4
Classification of main groups of eukaryotic plankton at the genus level.

10.3389/fevo.2023.1324932

TABLE 1 Diversity indices of eukaryotic plankton in different sampling sites.

Depth	Sample	OTUs	Coverage	Chao	Observed-Species	Pielou-evenness	Shannon-Wiener	Simpson
0.5 m	SG1	604	0.9989	622	606	0.68	6.33	0.96
	TM1	357	0.9992	376	359	0.48	4.09	0.84
	DZK1	361	0.9994	369	360	0.52	4.39	0.85
	WLQ1	253	0.9995	263	252	0.18	1.43	0.25
	QS1	392	0.9994	406	393	0.36	3.09	0.55
	KX1	311	0.9993	316	303	0.26	2.16	0.40
	HJZ1	343	0.9993	357	340	0.48	4.04	0.81
Average		374	0.9993	387	373	0.42	3.65	0.67
5 m	SG2	281	0.9996	283	277	0.32	2.59	0.65
	TM2	233	0.9994	246	234	0.43	3.40	0.70
	DZK2	230	0.9994	249	234	0.30	2.35	0.46
	WLQ2	561	0.9987	595	560	0.61	5.57	0.93
	QS2	266	0.9994	272	264	0.54	4.36	0.88
	KX2	196	0.9996	204	196	0.27	2.09	0.41
	HJZ2	88	0.9998	89	86	0.07	0.48	0.09
Average		265	0.9994	277	264	0.36	2.98	0.59
10 m	SG3	155	0.9996	162	155	0.43	3.15	0.65
	TM3	208	0.9998	210	207	0.55	4.22	0.86
	DZK3	380	0.9991	406	383	0.41	3.48	0.59
	WLQ3	228	0.9994	243	227	0.57	4.43	0.87
	QS3	233	0.9997	236	232	0.58	4.58	0.84
	KX3	328	0.9991	359	332	0.35	2.96	0.53
	HJZ3	546	0.9990	564	549	0.55	5.03	0.83
Average		297	0.9994	311	298	0.49	3.98	0.74
20 m	SG4	244	0.9994	258	247	0.46	3.63	0.78
	TM4	430	0.9991	447	430	0.58	5.10	0.88
	DZK4	385	0.9988	414	385	0.33	2.83	0.53
	WLQ4	432	0.9991	449	428	0.54	4.76	0.84
	QS4	399	0.9984	708	673	0.66	6.21	0.95
	KX4	411	0.9991	431	410	0.47	4.10	0.70
	HJZ4	449	0.9991	461	446	0.59	5.15	0.91
Average		393	0.9990	453	431	0.52	4.54	0.80

To further compare differences in species composition between samples, and to achieve a demonstration of trends in species abundance distribution across samples, species composition analysis of all sites could be performed using a heat map (Figure 6). The cross-sectional comparison showed the differences between samples, taking *Eurytemora* as an example, at the 0.5 m depth water, *Eurytemora* was the most abundant in DZK, at the 5 m depth water, *Eurytemora* was the most abundant in QS, at the 10 m depth water, *Eurytemora* was the most abundant in WLQ, followed by QS and TM, at the 20 m depth water, *Eurytemora* was the most abundant in SG, followed by QS and TM. The vertical comparison showed the distribution of species within the same sample and the degree of similarity between samples, for example, SG species diversity was the most abundant at 0.5 m depth water, containing *Phacotus*, *Chlamydomonas*, *Rimostrombidium*, *Dinobryon*, etc.

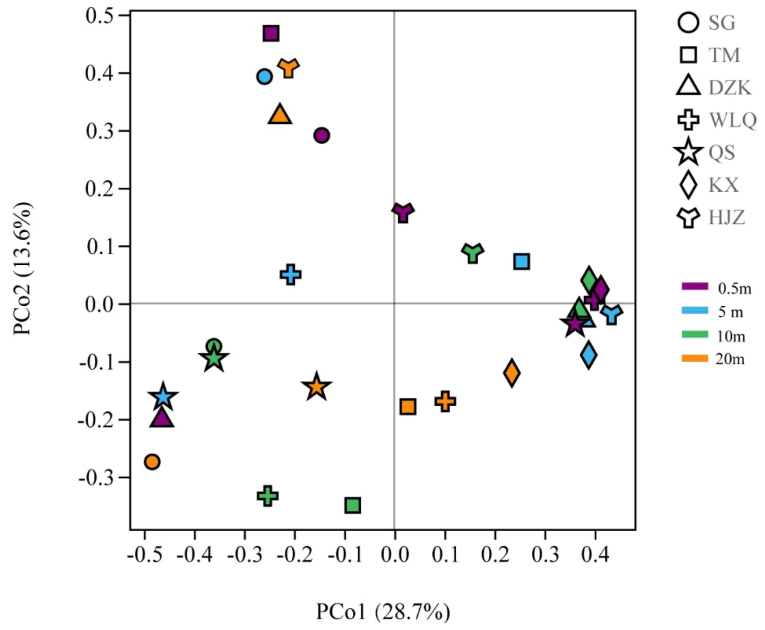

FIGURE 5
PCoA analysis of eukaryotic plankton community diversity. The percentage in the horizontal and vertical coordinate brackets indicates the proportion of sample difference data that can be explained by the corresponding coordinate axis. The closer the two points are on the coordinate axis, the more similar the community composition of the two samples is.

3.5 Environmental factor data analysis

TN, NH_4^+-N, DO and pH were measured at the seven sampling sites of Danjiangkou Reservoir (Table 2). The result showed that all sites met the requirement of class I water standards, except for TN (0.68~1.15 mg·L^{-1}). NH_4^+-N (0.08~0.15 mg·L^{-1}), DO (7.19~8.57 mg·L^{-1}), pH (8.66~8.96) and Cond (274~308 μs·cm^{-1}) had no significant change at all sampling sites. WT at QS (mean value 24.5°C) was higher than other sites (mean value 22.3~24°C). And it was obvious that WT decreased with increasing depth. Remarkably, NO_3^--N concentration at depth water was conspicuously higher than those at the surface sample sites. For example, NO_3^--N concentration was 0.53 mg·L^{-1} at SG1, 0.79 mg·L^{-1} at SG2, 0.93 mg·L^{-1} at SG3 and 0.98 mg·L^{-1} at SG4. NO_3^--N concentration at TM increased from 0.41 mg·L^{-1} (0.5 m) to 0.98 mg·L^{-1} (20 m). Overall, NO_3^--N concentration increased with depth at all sampling sites.

3.6 Relationships between spatial eukaryotic plankton community and environmental factors

The effects of environmental factors in different samples on the eukaryotic plankton communities were analyzed by RDA (Figure 7). The results showed that the percentage of variance explained by the first and second axes were 25.84% and 7.16%, respectively. According to P-values, pH (0.035) was the most important environmental variation factor for the eukaryotic

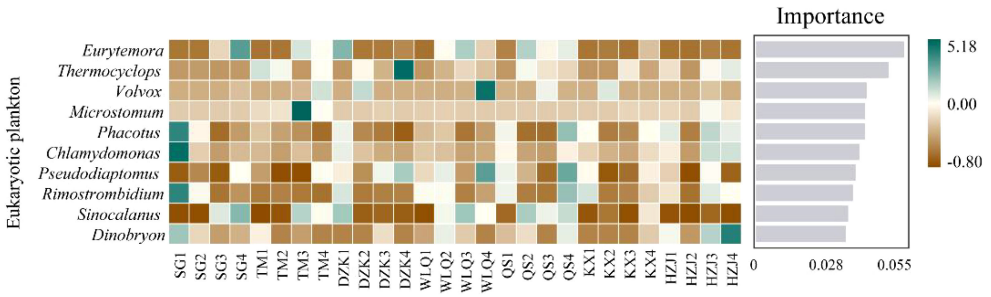

FIGURE 6
Heatmap of eukaryotic plankton. The figure represents a heatmap of eukaryotic plankton at 0.5 m, 5 m, 10 m, and 20 m depth water. The high and low-abundance species were clustered in blocks, and the color gradient was used to reflect similarities and differences in community composition among the 28 samples at the genus levels. The length of the gray bar indicates the importance of the species to the sample, decreasing from top to bottom.

10.3389/fevo.2023.1324932

TABLE 2 Physical and chemical properties in different sampling sites.

Sample	WT/ °C	DO/ $mg·L^{-1}$	pH	Cond/ $\mu S·cm^{-1}$	ρ(TN)/ $mg·L^{-1}$	ρ(NH_4^+-N)/ $mg·L^{-1}$	ρ(NO_3^--N)/ $mg·L^{-1}$
SG1	24.1	8.57	8.89	290	0.93	0.10	0.53
SG2	24.0	8.49	8.90	285	0.93	0.09	0.79
SG3	21.1	8.41	8.80	287	0.97	0.13	0.93
SG4	20.0	7.89	8.66	286	0.96	0.11	0.98
TM1	24.2	8.28	8.93	288	1.06	0.13	0.41
TM2	24.1	8.11	8.94	287	1.09	0.14	0.57
TM3	24.0	7.99	8.90	289	1.08	0.09	0.73
TM4	22.9	7.25	8.83	294	1.06	0.14	0.95
HJZ1	24.3	7.99	8.81	284	1.09	0.08	0.44
HJZ2	24.1	7.77	8.92	289	1.08	0.09	0.54
HJZ3	23.0	7.67	8.87	308	1.15	0.15	0.73
HJZ4	22.1	7.36	8.76	294	1.06	0.11	0.98
KX1	24.7	8.11	8.91	274	0.71	0.13	0.40
KX2	24.5	8.03	8.90	274	0.68	0.09	0.49
KX3	24.1	7.74	8.91	275	0.81	0.09	0.59
KX4	22.3	7.54	8.74	280	0.71	0.14	0.61
DZK1	24.8	7.69	8.90	278	0.90	0.11	0.54
DZK2	24.7	7.57	8.94	282	0.93	0.08	0.55
DZK3	23.5	7.51	8.89	282	0.91	0.09	0.59
DZK4	23.0	7.34	8.88	280	0.94	0.10	0.82
WLQ1	25.1	7.74	9.02	280	0.99	0.09	0.46
WLQ2	24.9	7.51	8.94	288	0.96	0.11	0.63
WLQ3	23.4	7.45	8.85	295	0.94	0.08	0.95
WLQ4	22.1	7.25	8.78	288	0.99	0.08	1.00
QS1	25.6	7.7	8.93	283	1.01	0.12	0.49
QS2	25.0	7.52	8.97	289	1.04	0.12	0.58
QS3	24.4	7.27	8.89	291	1.06	0.11	0.88
QS4	23.0	7.19	8.87	289	1.01	0.11	0.94

plankton community, followed by depth (0.064), WT (0.097), NH_4^+-N (0.163), DO (0.195), Cond (0.231), NO_3^--N (0.283). *Eurytemora*, *Thermocyclops*, and *Volvox* were negatively correlated with pH and WT and positively correlated with depth.

4 Discussions

Microeukaryotes play many roles as primary producers, secondary producers, and decomposers in aquatic ecosystems, affecting the structure of aquatic food webs in terms of taxonomic composition, abundance, biomass, and biodiversity (Tan et al., 2010). However, there are relatively few studies on the composition, distribution characteristics, functions of eukaryotic plankton and their relationship with water quality (Voronin, 2010; Nagano and Nagahama, 2012; Taylor and Cunliffe, 2016). In this study, we used high-throughput sequencing technology to amplify the 18S rDNA V4 region DNA to investigate the community structure of plankton in Danjiangkou Reservoir. As a result, a total of 2392 OTUs belong to 38 phyla and 122 genera of eukaryotic plankton were identified. Based on sequence data, many differences in the diversity of eukaryotic plankton communities were found at a spatial scale, and the environmental factors including pH, depth and WT could influence the vertical distribution of eukaryotic plankton communities. This study would provide a better understanding dynamics of eukaryotic plankton communities in this important water source.

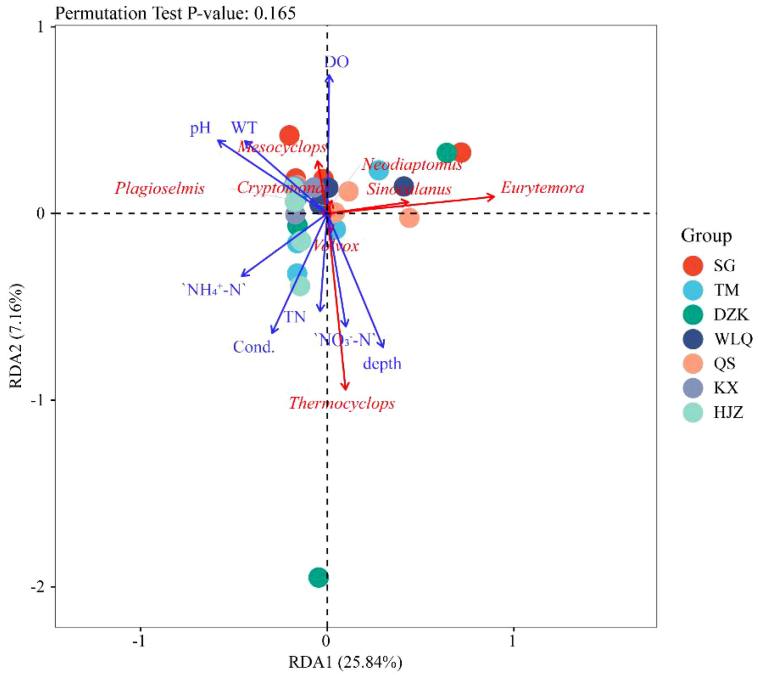

FIGURE 7
RDA ordination biplot of planktonic taxa and environmental factors.

In this study, we found that several taxa including *Eurytemora*, *Thermocyclops*, *Sinocalanus*, *Mesocyclops*, *Cryptomonas*, *Volvox*, *Chrysochromulina* play an important role in the genus level of eukaryotic plankton in Danjiangkou Reservoir (Figure 4). Among them, *Eurytemora*, *Thermocyclops*, *Sinocalanus*, and *Mesocyclops* were reported as common species in still-water bodies (Hu et al., 2021). Water quality, water temperature, and hydrological factors affected the phytoplankton community structure (Yan et al., 2021). Some studies have pointed out that Chrysophyta was more suitable for growing in oligotrophic water bodies. Cryptophyta were the dominant species in mesotrophic water bodies, while Cholorophyta were the dominant species in eutrophic water bodies (Jia et al., 2019). In this study, the relative abundance of *Cryptomonas*, *Volvox*, *Chrysochromulina*, and *Plagioselmis* was ranked in decreasing order. It can be inferred that the degree of eutrophication in the reservoir area was between mesotrophic and oligotrophic water bodies, which was similar to the research conclusions of previous studies on Danjiangkou Reservoir (Wang et al., 2012; Jia et al., 2019). The excellent water quality in the reservoir area allowed *Cryptomonas* to be one of the dominant species. As an important environmental factor, water temperature could affect the composition of plankton community structure in most water bodies (Yang et al., 2014; Zhang et al., 2019; Wang et al., 2020). For example, Trombetta et al. (2019) reported that the growth temperature of Cholorophyta is higher than that of Cryptophyta. In this study, our results indicated that the reservoir water temperature (Table 2) was favorable for the growth and reproduction of Cryptophyta, which was consistent with the previous study. In addition, Cryptophyta were positively correlated with flow, and Cholorophyta were not significantly correlated with hydrological factors. During the investigation, the water level, flow rate, and flow velocity in the reservoir area were low. The excellent water quality, suitable water temperature, and suitable hydrological conditions probably resulted in a planktonic community composition dominated by *Eurytemora*, *Thermocyclops*, *Sinocalanus Mesocyclops Cryptomonas Volvox*, etc in the reservoir area.

The clustering results of the plankton community structure in each layer of each sampling site in the reservoir area were different (Figure 5). It was found that ecological factors such as season, environmental factors, and sampling sites in the Danjiangkou Reservoir area together explained 39% of the variation in phytoplankton structure, with geographical location accounting for 12% (Yan et al., 2021). Different geographical conditions cause changes in the characteristics of the aquatic environment, leading to spatial differences in the major taxa of plankton. Similar to our results, previous studies reported differences in eukaryotic microbial community structure among sampling sites in Xiamen, Qingdao (Zhang et al., 2018), and Yellowstone Park in the United States (Meadow and Zabinski, 2012). Moreover, there are also quite differences in the diversity of planktonic eukaryotes at different temporal and spatial scales in Danjiangkou Reservoir. KX is located in the center of the Reservoir, with fewer human interference factors and closer to the natural state. QS, KX and WLQ are located near the hilly area in the south of the reservoir, which is upstream of the reservoir area. HJZ is near the downstream tributary. TM is close to the northern dry land. DZK is near the Hanjiang River outlet. SG is closer to the paddy fields and human activities are more frequent. The differences in environmental factors and hydrological conditions were responsible for the differences in eukaryotic

plankton community composition among the sampling sites in the reservoir area.

The diversity and abundance of eukaryotic plankton communities in 7 sampling sites decreased with the increase of depth ranging from 0.5 to 10 m, while the diversity and abundance of plankton communities increased at 20 m (Table 1). Notably, our results showed that NO_3^--N concentration was positively correlated with the depth of water. As a main nitrogen resource in ecosystems, NO_3^--N had a strong effect on the abundance of eukaryotic plankton was reported by investigating eukaryotic plankton communities in the South Yellow Sea (Sun et al., 2021). Relevant studies have found that the nitrate concentration increases with depth due to the sinking of nutrient substances (De Queiroz et al., 2015). Furthermore, the nitrate was absorbed and utilized by primary producers in the surface water (Wei et al., 2018), leading to the low NO_3^--N concentration in the surface layer and the high NO_3^--N concentration in the deep layer. In deep water, nutrient concentrations change with depth, resulting in a corresponding change in phytoplankton community structure (Tavernini et al., 2005). In this study, the abundance and diversity of eukaryotic plankton communities at 20 m (mean value of OTUs is 393) are higher than those at 0.5–10 m (mean value of OTUs is 265–374) (Table 1). As nitrate increased with depth, the maximum biomass of eukaryotic plankton in deep water was expected (Leal et al., 2009).In deep water bodies, with the gradient of environmental factors such as light, temperature, and nutrient salinity, the peak biomass of the phytoplankton community appeared at different depths (Huovinen, 1999; Ptacnik et al., 2003). In August 2008, it was found that the abundance of phytoplankton in most stations of Danjiangkou Reservoir decreased with the increase of depth, but there was no obvious regularity in other sampling months (Yin et al., 2011). There is no obvious distribution trend of phytoplankton richness and diversity in the range of 0–50 m in the Three Gorges Reservoir. It has been reported that environmental variability explained only 30% of the seasonal succession of microbiota in the eastern English Channel (Logares et al., 2014). The differences in plankton communities at different depths were attributed to the synergistic effects of different environmental factors (Nabout et al., 2009; Zheng et al., 2020). Because of the stratification phenomenon, the upper layers of water had the advantage of nutrient concentrations and temperature. In contrast, the deeper layer of water had extreme environmental conditions such as higher nutrient concentrations, low light, and low temperature, resulting in significant differences in species diversity (Sun et al., 2021). Based on the variation of Chao, Pielou-evenness, Shannon-Wiener, and Simpson index at all sampling sites (Table 1), changes in eukaryotic plankton abundance and diversity in different water samples (Figure 6) indicated that there were large differences in the vertical distribution of eukaryotic plankton communities in Danjiangkou Reservoir. Previous studies have found that there is no significant difference in the abundance of phytoplankton communities in the vertical direction of Danjiangkou Reservoir (Yin et al., 2011). The results of this study are different from the results of previous studies. The first reason is the expansion of the reservoir area. The previous studies were performed time was from 2007 to 2008, and the reservoir area was expanded in 2012. The hydrological conditions and physical and chemical parameters of the reservoir area changed after the expansion, resulting in a corresponding change in the composition of the plankton community in the reservoir area (Hoyer et al., 2009). The second reason is the identification method. The results of plankton characteristics obtained by high-throughput sequencing technology are more comprehensive than those derived from microscopic observations in previous studies (Dijk et al., 2014; Wang et al., 2017).

There is a certain spatial heterogeneity in the ecological environment of the Danjiangkou Reservoir. It is widely accepted that there is a close relationship between plankton composition and environmental factors (Chalar, 2009; Cudowski et al., 2015; Reich et al., 2017). In this study, the RDA showed that pH was the most important environmental factor affecting the community distribution of eukaryotic plankton in the Danjiangkou Reservoir, followed by depth, WT, NH_4^+-N, DO, Cond and NO_3^--N (Figure 7). It can be indicated from RDA that most of the eukaryotic plankton were negatively correlated with pH, which may result from rotifer species increased and decreased in acidic water bodies, in contrast, the opposite situations occurred in alkaline water bodies. Acidic, neutral, and weakly alkaline water bodies are suitable for the survival of Cladocera, and alkaline water bodies are favorable for the survival of Copepods (He et al., 2022). In the water with low pH, the growth of phytoplankton will be limited, and the number of individuals will decrease. The alkaline water with high pH is more conducive to the photosynthesis of phytoplankton to form organic matter, and the number of phytoplankton reproduction will increase (Liu et al., 2010). If the pH value is in the range of 7.5 to 9.0, it is more favorable for the growth of diatoms and cyanobacteria. When the temperature is higher in summer, the suitable pH range is most conducive to the reproduction of algae and the formation of large-scale blooms (Lu, 1987). On the other hand, phytoplankton photosynthesis absorbs carbon dioxide in the water body, changes the pH value of the water body, and the activities of algae themselves will also change the pH value of the water body, thus affecting the pH value of the water environment (Xu et al., 2009). Overall, pH is the main factor affecting the spatial and temporal variation pattern of phytoplankton, and the interaction between water body pH and phytoplankton is bidirectional (Wang et al., 2016).

Water temperature is considered to be an important factor affecting the growth, development, and species composition of plankton, and it is also the main driving factor affecting the seasonal succession of the plankton community (Marques et al., 2006; Chen et al., 2021). Temperature directly affects the growth state of phytoplankton by controlling the intensity of enzymatic reaction during phytoplankton respiration and photoreaction (Blinn, 1993) and is closely related to the relative abundance of phytoplankton (Lu et al., 2013). WT is one of the main environmental factors affecting the distribution of the eukaryotic plankton community in the reservoir area. WT at 0.5m is significantly higher than that at 20 m at each sampling site. Given that positive correlation with WT,

Mesocyclops and *Cryptomonas* were dominant in the surface layer. Correspondingly, *Eurytemora* and *Thermocyclops* were negatively correlated with WT, and they were abundant in the deep layer. This study suggested that the change of WT is an important factor leading to the difference in the relative abundance of plankton from 0.5 to 20 m depth in Danjiangkou Reservoir.

The rapid increase in the levels of organic pollutants, suspended solids, and other related oxygen-consuming factors in the water could lead to an imbalance in the production of DO in its water column, which has an impact on zooplankton (He et al., 2022). In addition, oxygen production by phytoplankton photosynthesis is the main source of DO, and phytoplankton respiration and mortality are the largest pathways of DO consumption (Ouyang et al., 2013). It should be noted that the interaction between phytoplankton biomass and the physicochemical indicators of the water column is reciprocal, and changes in phytoplankton biomass can also cause changes in DO concentration, pH, and other indicators in the water column (Wang et al., 2016). As an important index for measuring water quality, DO concentration can reflect the concentration can reflect the degree of water pollution, and the pollution is related to the content of organic compounds (Diaz and Rosenberg, 2008). In this study, *Mesocyclops*, *Cryptomonas*, *Plagiosemis*, and *Neodiaptomus* are positively correlated with DO, so these taxa can be used as potential biological reference indicators to monitor the water quality in the Danjiangkou Reservoir in the future.

Due to the limited sampling in this study, additional samples from different seasons are needed to provide comprehensive insights into the eukaryotic plankton communities in Danjiangkou Reservoir. It's worth noting that ArcMap, DEM, and SAR have already found extensive application in ecological environment research (Liu et al., 2022; Qiu et al., 2022; Wang et al., 2022; Ma et al., 2023; Pei et al., 2023). In the future, the integration of sequencing data with ArcMap, DEM, and SAR holds immense promise for portraying the spatial and temporal distribution of eukaryotic plankton within the reservoir area.

5 Conclusions

Our results provide a novel perspective on the distribution of the eukaryotic plankton community in Danjiangkou Reservoir, particularly in terms of vertical variation. This insight holds significant potential for understanding ecological processes and ensuring the water quality safety of this canyon-style reservoir.

(1) A total of 38 phyla and 122 genera of eukaryotic plankton were identified in Danjiangkou Reservoir. Notably, we observed substantial variations in both the diversity and abundance of the eukaryotic plankton community across different depths. Specifically, diversity and abundance exhibited a decreasing trend from depths of 0.5 to 10 m, while an increase was noted at a depth of 20m.

(2) Environmental factors, including pH, depth, WT, NH_4^+-N, DO, Cond, and NO_3^--N, play crucial roles in influencing the vertical distribution of eukaryotic plankton within the reservoir. It's important to note that these environmental factors have distinct effects on the eukaryotic plankton community. For instance, *Eurytemora*, *Thermocyclops*, and *Volvox* were found to be negatively correlated with pH and WT, while they showed a positive correlation with depth.

Data availability statement

The original contributions presented in the study are included in the article/supplementary material. Further inquiries can be directed to the corresponding authors.

Author contributions

SM: Conceptualization, Methodology, Writing – original draft. YH: Formal Analysis, Supervision, Writing – original draft. WL: Resources, Supervision, Visualization, Writing – review & editing. TZ: Funding acquisition, Investigation, Supervision, Writing – review & editing.

Funding

The author(s) declare financial support was received for the research, authorship, and/or publication of this article. This work was financially supported by the National Natural Science Foundation of China (Grant No. U1704241) and the Henan Technological and Innovative Leading Talent Program (Grant No. 194200510010).

Conflict of interest

The authors declare that the research was conducted in the absence of any commercial or financial relationships that could be construed as a potential conflict of interest.

Publisher's note

References

Blinn, D. W. (1993). Diatom community structure along physicochemical gradients in saline lakes. *Ecology* 74 (4), 1246–1263. doi: 10.2307/1940494

Bokulich, N. A., Subramanian, S., Faith, J. J., Gevers, D., Gordon, J. I., Knight, R., et al. (2013). Quality-filtering vastly improves diversity estimates from Illumina amplicon sequencing. *Nat. Methods: Techniques Life scientists Chem.* 10 (1), 57–59. doi: 10.1038/nmeth.2276

BoonFei, T., Charmaine, N., Pierre, N. J., Leng, L. L., G., K. Y. H., and T., J. R. (2015). Next-generation sequencing (NGS) for assessment of microbial water quality: current progress, challenges, and future opportunities. *Front. Microbiol.* 6, 1027. doi: 10.3389/fmicb.2015.01027

Chalar, G. (2009). The use of phytoplankton patterns of diversity for algal bloom management. *Limnologica* 39 (3), 200–208. doi: 10.1016/j.limno.2008.04.001

Chao, A. (1984). Nonparametric estimation of the number of classes in a population. *Scandinavian J. Stat* 11 (4), 265–270. doi: 10.2307/4615964

Chen, Y., Peng, K., Zhang, Q., Cai, Y., Zhang, Y., Gong, Z., et al. (2021). Spatio-temporal distribution characteristics and driving factors of zooplankton in Hongze Lake. *Environ. Sci.* 42 (8), 3753–3762. doi: 10.13227/j.hjkx.202010195

Cudowski, A., Pietryczuk, A., and Hauschild, T. (2015). Aquatic fungi in relation to the physical and chemical parameters of water quality in the Augustow Canal. *Fungal Ecol.* 13, 193–204. doi: 10.1016/j.funeco.2014.10.002

Cui, Z., Gao, W., Li, Y., Wang, W., Wang, H., Liu, H., et al. (2023). Dissolved oxygen and water temperature drive vertical spatiotemporal variation of phytoplankton community: evidence from the largest diversion water source area. *Int. J. Environ. Res. Public Health* 20 (5), 4307. doi: 10.3390/ijerph20054307

De Queiroz, A. R., Flores Montes, M., de Castro Melo, P. A. M., da Silva, R. A., and Koening, M. L. (2015). Vertical and horizontal distribution of phytoplankton around an oceanic archipelago of the Equatorial Atlantic. *Mar. Biodiversity Records* 8, E155. doi: 10.1017/S175526721500130X

Diaz, R. J., and Rosenberg, R. (2008). Spreading dead zones and consequences for marine ecosystems. *Science* 321 (5891), 926–929. doi: 10.1126/science.1156401

Dijk, E. V., Auger, H., Jaszczyszyn, Y., and Thermes, C. (2014). Ten years of next-generation sequencing technology. *Trends Genet.* 30 (9), 418–426. doi: 10.1016/j.tig.2014.07.001

Ferrera, I., Rene, A., Funosas, D., Camp, J., Massana, R., Gasol, J. M., et al. (2020). Assessment of microbial plankton diversity as an ecological indicator in the NW Mediterranean coast. *Mar. pollut. Bull.* 160, 111691. doi: 10.1016/j.marpolbul.2020.111691

Filker, S., Sommaruga, R., Vila, I., and Stoeck, T. (2016). Microbial eukaryote plankton communities of high-mountain lakes from three continents exhibit strong biogeographic patterns. *Mol. Ecol.* 25 (10), 2286–2301. doi: 10.1111/mec.13633

Gao, W. L., Chen, Z. J., Li, Y. Y., Pan, Y. D., Zhu, J. Y., Guo, S. J., et al. (2018). Bioassessment of a drinking water reservoir using plankton: high throughput sequencing vs. *Traditional Morphological Method. Water* 10 (1), 82. doi: 10.3390/w10010082

Good, I. (2010). The population frequency of species and the estimation of the population parameters. *Biometrika* 40 (1953), 237–246. doi: 10.2307/2333344

He, S., Gou, J., Yin, J., Qiu, X., and Zhao, R. (2022). Community structure of zooplankton and its relationship with water environmental factors in ningxia section of the main stream of the YellowRiver. *Water Resour. Power* 40 (10), 66–69+18. doi: 10.20040/j.cnki.1000-7709.2022.20212768

He, Y., Zheng, Y., Li, W., Zhang, Z., Ma, Y., Zhao, T., et al. (2021). Characteristics of eukaryotic phytoplankton community structure in early spring and its relationship with environmental factors in Danjiangkou Rservoir. *Acta Scientiae Circumstantiae* 41 (6), 2912–2200. doi: 10.13671/j.hjkxxb.2020.0550

Hoyer, B. A., Blanco, M. J., Moreno-Ostos, E., Vidal, J., Rueda, J. F., and Palomino, T. (2009). The influence of external perturbations on the functional composition of phytoplankton in a Mediterranean reservoir. *Hydrobiologia* 636, 49–64. doi: 10.1007/s10750-009-9934-2

Hu, Y., Peng, Y., Li, R., Huang, J., Zhou, Z., Hu, S., et al. (2021). Plankton diversity and community charecteristics in Danjiangkou Reservoir based on environmental DNA metabarcoding. *J. Lake Sci.* 33 (6), 1650–1659. doi: 10.18307/2021.0604

Huovinen, (1999). Temporal and vertical dynamics of phytoplankton net growth in Castle Lake, California. *J. Plankton Res.* 2, 373–385. doi: 10.1093/plankt/21.2.373

Ishida, K. N. (2008). Seasonal distribution of photosynthetically active phytoplankton using pulse amplitude modulated fluorometry in the large monomictic Lake Biwa, Japan. *J. Plankton Res.* 30 (10), 1169–1177. doi: 10.1093/plankt/fbn073

Jia, H., Xu, J., and Lei, J. (2019). Relationship of community structure of phytoplankton and environmental factors in Danjiangkou Reservior bay. *Yangtze River* 50 (5), 52–58. doi: 10.16232/j.cnki.1001-4179.2019.05.011

Jiang, Y., Xu, H., and Zhu, M. Z. (2012). Use of planktonic protists for assessing water quality in Jiaozhou Bay, northern China. *Protistology* 7 (1), 34–41.

Jin, X. (1990). *Handbook of eutrophication investigation of Lake. 2nd ed* (Beijing: China Environmental Sciences Press).

Keck, F., Millet, L., Debroas, D., Etienne, D., Galop, D., Rius, D., et al. (2020). Assessing the response of micro-eukaryotic diversity to the Great Acceleration using lake sedimentary DNA. *Nat. Commun.* 11 (1), 3831. doi: 10.1038/s41467-020-17682-8

Leal, M. C., Sá, C., Nordez, S., Brotas, V., and Paula, J. (2009). Distribution and vertical dynamics of planktonic communities at Sofala Bank, Mozambique. *Estuarine Coast. Shelf Sci.* 84 (4), 605–616. doi: 10.1016/j.ecss.2009.07.028

Lee, S.-R., Song, E. H., and Lee, T. (2018). Eukaryotic Plankton Species Diversity in the Western Channel of the Korea Strait using 18S rDNA Sequences and its Implications for Water Masses. *Ocean Sci. J.* 53 (1), 119–132. doi: 10.1007/s12601-018-0005-3

Liu, S., Gibson, K., Cui, Z., Chen, Y., Sun, X., and Chen, N. (2020a). Metabarcoding analysis of harmful algal species in Jiaozhou Bay. *Harmful Algae* 92, 101772. doi: 10.1016/j.hal.2020.101772

Liu, Z., Qiu, H., Zhu, Y., Liu, Y., Yang, D., Ma, S., et al. (2022). Efficient identification and monitoring of landslides by time-series InSAR combining single- and multi-look phases. *Remote Sens.* 14, 1026. doi: 10.3390/rs14041026

Liu, X., Shi, X., Qi, G., Liu, G., Zhao, Y., and Wu, S. (2010). Appliction of freshwater alage in monitoring water quality and sewage purification. *J. Biol.* 27 (6), 76–78+86. doi: 10.3969/j.issn.1008-9632.2010.06.076

Liu, L., Wang, S., Ji, J., Xie, Y., Shi, X., and Chen, J. (2020b). Characteristics of microbial eukaryotic community recovery in eutrophic water by using ecological floating beds. *Sci. Total Environ.* 711, 134551. doi: 10.1016/j.scitotenv.2019.134551

Logares, R., Audic, S., Bass, D., Bittner, L., Boutte, C., Christen, R., et al. (2014). Patterns of rare and abundant marine microbial eukaryotes. *Curr. Biol.* 24 (8), 813–821. doi: 10.1016/j.cub.2014.02.050

Lu, Q. (1987). *The ecological society panel on environmental issues ed. Environmental and biological indicator (water volume)* (Beijing: China Environmental Science Press (in Chinese).

Lu, Q., Chen, H., Shao, X., Wang, Y., Tao, M., He, J., et al. (2013). Ecological characteristics of macrobenthic communities and its relationships with environmental factors in Hangzhou Xixi Wetland. *Acta Ecologica Sin.* 33 (9), 2803–2815. doi: 10.5846/stxb201203080316

Ma, S., Qiu, H., Zhu, Y., Yang, D., Tang, B., Wang, D., et al. (2023). Topographic Changes, Surface Deformation and Movement Process before, during and after a Rotational Landslide. *Remote Sens.* 15 (3), 662. doi: 10.3390/rs15030662

MaChado, K. B., Targueta, C. P., Antunes, A. M., Soares, T. N., d. C. Telles, M. P., Logares, R., et al. (2019). Diversity patterns of planktonic microeukaryote communities in tropical floodplain lakes based on 18S rDNA gene sequences. *J. Plankton Res.* 41 (3), 241–256. doi: 10.1093/plankt/fbz019

Marianne, S., Purificación, L.-G., Philippe, D., David, M., Gwendal, R., Paola, B., et al. (2015). Marked seasonality and high spatial variability of protist communities in shallow freshwater systems. *ISME J.* 9 (9), 1941–1953 doi: 10.1038/ismej.2015.6

Marques, S. C., Azeiteiro, U. M., Marques, J. C., Neto, J. M., and Pardal, M. A. (2006). Zooplankton and ichthyoplankton communities in a temperate estuary: spatial and temporal patterns. *J. Plankton Res.* 28 (3), 297–312. doi: 10.1093/plankt/fbi126

McInnes, A. S., Laczka, O. F., Baker, K. G., Larsson, M. E., Robinson, C. M., Clark, J. S., et al. (2019). Live cell analysis at sea reveals divergent thermal performance between photosynthetic ocean microbial eukaryote populations. *Isme J.* 13 (5), 1374–1378. doi: 10.1038/s41396-019-0355-6

Meadow, J. F., and Zabinski, C. A. (2012). Spatial heterogeneity of eukaryotic microbial communities in an unstudied geothermal diatomaceous biological soil crust: Yellowstone National Park, WY, USA. *FEMS Microbiol. Ecol.* 82 (1), 182–191. doi: 10.1111/j.1574-6941.2012.01416.x

Nabout, J. C., Siqueira, T., Bini, L. M., and Nogueira, I. (2009). No evidence for environmental and spatial processes in structuring phytoplankton communities. *Acta Oecologica* 35 (5), 720–726. doi: 10.1016/j.actao.2009.07.002

Nagano, Y., and Nagahama, T. (2012). Fungal diversity in deep-sea extreme environments. *Fungal Ecol.* 5 (4), 463–471. doi: 10.1016/j.funeco.2012.01.004

Ouyang, X., Zhao, Q., and Wei, Y. (2013). A preliminary exploration of dissolved oxygen based on FVCOM in Meiliang Bay, Lake Taihu and its influence mechanism. *Lake Sci.* 25 (4), 478–488. doi: 10.18307/2013.0404

Pei, Y., Qiu, H., Zhu, Y., Wang, J., Yang, D., Tang, B., et al. (2023). Elevation dependence of landslide activity induced by climate change in the eastern Pamirs. *Landslides* 20, 1115–1133. doi: 10.1007/s10346-023-02030-w

Pielou, E. C. (1966). The measurement of diversity in different types of biological collections. *J. Theor. Biol.* 13, 131–144. doi: 10.1016/0022-5193(66)90013-0

Piwosz, K., Shabarova, T., Pernthaler, J., Posch, T., Simek, K., Porcal, P., et al. (2020). Bacterial and eukaryotic small-subunit amplicon data do not provide a quantitative picture of microbial communities, but they are reliable in the context of ecological interpretations. *mSphere* 5, 2, e00052–e00020. doi: 10.1128/mSphere.00052-20

Ptacnik, R., Diehl, S., and Berger, S. (2003). Performance of sinking and nonsinking phytoplankton taxa in a gradient of mixing depths. *Limnology Oceanography* 48 (5), 1903–1912. doi: 10.4319/lo.2003.48.5.1903

Qiu, H., Zhu, Y., Zhou, W., Sun, H., He, J., and Liu, Z. (2022). Influence of DEM resolution on landslide simulation performance based on the Scoops3D model, Geomatics. *Natural Hazards Risk* 13 (1), 1663–1681. doi: 10.1080/19475705.2022.2097451

Reich, M., Wichels, A., Panzer, K., Krause, E., Gimenez, L., and Gerdts, G. (2017). Impacts of a reduction of seawater pH mimicking ocean acidification impacts on assemblage, structure and diversity of marine fungal communities. *Aquat. Microbial Ecol.* 79 (3), 221–233. doi: 10.3354/ame01831

Salmaso, N., Boscaini, A., and Pindo, M. J. F. i. M. (2020). Unraveling the diversity of eukaryotic microplankton in a large and deep perialpine lake using a high throughput sequencing approach. *Front. Microbiol.* 11, 789. doi: 10.3389/fmicb.2020.00789

Shannon, C. E. (1948). A mathematical theory of communication. *Bell Syst. Tech. J.* 27, 623–656.

Shen, H., Xu, Y., Wang, L., Zhang, M., Kong, L., and Cai, Q. (2011). Spatial and temporal variations of phytoplankton in Danjiangkou Reservoir and its affecting factor. *Plant Sci. J.* 29, 683–790. doi: 10.3724/SP.J.1142.2011.60683

Simpson, E. H. (1997). Measurement of diversity. *J. Cardiothoracic Vasc. Anesth.* 11 (6), 812–812. doi: 10.1136/thx.27.2.261

Song, L., Wu, J., Du, J., Li, N., Song, G., Wang, K., et al. (2019). The characteristics and distribution of eukaryotic phytoplankton community in Liaodong bay, China. *Ocean Sci. J.* 54 (2), 183–203. doi: 10.1007/s12601-019-0007-9

Sun, Z., Li, G., Wang, C., Jing, Y., Zhu, Y., Zhang, S., et al. (2014). Community dynamics of prokaryotic and eukaryotic microbes in an estuary reservoir. *Sci. Rep.* 4 (1), 6966. doi: 10.1038/srep06966

Sun, Y., Liu, Y., Wu, C., Fu, X., Guo, C., Li, L., et al. (2021). Characteristics of eukaryotic plankton communities in the cold water masses and nearshore waters of the South Yellow Sea. *Diversity* 13 (1), 21. doi: 10.3390/d13010021

Tan, X., Shi, X., Liu, G., Xu, H., and Nie, P. (2010). An approach to analyzing taxonomic patterns of protozoan communities for monitoring water quality in Songhua River, northeast China. *Hydrobiologia* 638 (1), 193–201. doi: 10.1007/s10750-009-0040-2

Tan, X., Xia, X., and Zhang, Q. (2011). Temporal and spatial pattern of Phytoplankton community and its biodiversity indices in the Danjiangkou Reservoir. *Environ. Sci.* 32 (10), 2875–2882. doi: 10.13227/j.hjkx.2011.10.008

Tavernini, S., Mura, G., and Rossetti, G. (2005). Factors influencing the seasonal phenology and composition of zooplankton communities in mountain temporary pools. *Int. Rev. Hydrobiology* 90 (4), 358–375. doi: 10.1002/iroh.200510801

Taylor, J. D., and Cunliffe, M. (2016). Multi-year assessment of coastal planktonic fungi reveals environmental drivers of diversity and abundance. *Isme J.* 10 (9), 2118–2128. doi: 10.1038/ismej.2016.24

Trombetta, T., Vidussi, F., Mas, S., Parin, D., Simier, M., and Mostajir, B. (2019). Water temperature drives phytoplankton blooms in coastal waters. *PLoS One* 14 (4), e0214933. doi: 10.1371/journal.pone.0214933

Voronin, L. V. (2010). The fungi of small acid lakes. *Inland Water Biol.* 3 (3), 254–259. doi: 10.1134/S1995082910030089

Wang, Y., Chen, L., Niu, Y., Yu, H., and Luo, M. (2016). Spatio-temporal variation in phytoplankton community and its influencing factors in Danjiangkou Reservoir. *J. Lake Sci.* 28 (5), 1057–1065. doi: 10.18307/2016.0516

Wang, Q., Huang, W., Chen, K., Yi, Q., and Li, H. (2020). Phytoplankton community structure and trophic status evaluation in Reservior Daxi. *Acta Scientiae Circumstantia* 40 (4), 1286–1297. doi: 10.13671/j.hjkxxb.2019.0497

Wang, L., Qiu, H., Zhou, W., Zhu, Y., Liu, Z., Ma, S., et al. (2022). The post-failure spatiotemporal deformation of certain translational landslides may follow the pre-failure pattern. *Remote Sens.* 14, 2333. doi: 10.3390/rs14102333

Wang, Z., Tan, Y., Li, Z., and Xiao, X. (2012). Assessment on eutrophication in typical bays and tributaries of Danjiangkou Reservoir. *Yangtze River* 43 (8), 61–64+75. doi: 10.16232/j.cnki.1001-4179.2012.08.016

Wang, J., Wang, S., Zhang, Y., Lin, J., Gao, X., Zang, X., et al. (2017). Community structure characteristics of eukaryotic planktonic algae in Liaohe River through high-throughput Sequencing. *Environ. Sci.* 38 (4), 1403–1413. doi: 10.13227/j.hjkx.201609133

Wei, N., Satheeswaran, T., Jenkinson, I. R., Xue, B., Wei, Y., Liu, H., et al. (2018). Factors driving the spatiotemporal variability in phytoplankton in the Northern South China Sea. *Continental Shelf Res.* 162, 48–55. doi: 10.1016/j.csr.2018.04.009

Wu, J.-Y., Hua, Z.-L., Gu, L., Li, X.-Q., Gao, C., and Liu, Y.-Y. (2022). Perfluorinated compounds (PFCs) in regional industrial rivers: Interactions between pollution flux and eukaryotic community phylosymbiosis. *Environ. Res.* 203, 111876. doi: 10.1016/j.envres.2021.111876

Wurzbacher, C. M., Baerlocher, F., and Grossart, H.-P. (2010). Fungi in lake ecosystems. *Aquat. Microbial Ecol.* 59 (2), 125–149. doi: 10.3354/ame01385

Xiao, Y., Cheng, J., Mo, X., Li, Y., Liu, X., and Bi, S. (2023). Spatio-temporal variation of phytoplankton community and its relationship with environmental factors in Danjiangkou Reservoir. *Lake Sci.* 35 (3), 821–832. doi: 10.18307/2023.0306

Xu, H., Liu, Z., Yuan, L., and Yang, L. (2009). Effect of pH on growth of several freshwater algae. *Environ. Sci. Technol.* 32 (1), 27–30. doi: 10.3969/j.issn.1003-6504.2009.01.007

Yan, X., Zhang, Y., Li, Y., Jiang, Y., Cui, Z., Gao, X., et al. (2021). Hydrologic and physicochemical factors codrive seasonal changes of phytoplankton during dynamic water diversion processes in the Danjiangkou Reservoir. *J. Lake Sci.* 33 (5), 1350–1363. doi: 10.18307/2021.0505

Yang, L., Yu, P., Zhu, J., Xu, Z., Lü, G., and Jin, C. (2014). Community structure characteristics of phytoplankton and related affecting factors in Heng-shan Reservoir, Zhejiang, China. *Chin. J. Appl. Ecol.* 25 (2), 569–576. doi: 10.13287/j.1001-9332.2014.0060

Yin, D., Zheng, L., and Song, L. (2011). Spatio-temporal distribution of phytoplankton in the Danjiangkou Reservoir, a water source area for the South-to-North Water Diversion Project (Middle Route), China. *Chin. J. Oceanology Limnology* 29 (3), 531–540. doi: 10.1007/s00343-011-0120-9

Zhang, C., He, Y., Li, W., Guo, X., Xiao, C., and Zhao, T. (2022). High-throughput sequencing of diatom community, its spatial and temporal variation and interrelationships with physicochemical factors in Danjiangkou Reservoir, China. *Water* 14 (10), 1609. doi: 10.3390/w14101609

Zhang, W., Pan, Y., Yang, J., Chen, H., Holohan, B., Vaudrey, J., et al. (2018). The diversity and biogeography of abundant and rare intertidal marine microeukaryotes explained by environment and dispersal limitation. *Environ. Microbiol.* 20 (2), 462–476. doi: 10.1111/1462-2920.13916

Zhang, Q., Song, L., Ji, D., Fang, H., He, J., Huo, J., et al. (2019). Relationship between water quality of Xiangxi River Reservoir and the algal blooms in non-return area in the Three Gorges Reservoir Area. *China Environ. Sci.* 39 (7), 3018–3026. doi: 10.19674/j.cnki.issn1000-6923.2019.0356

Zhao, Y. J., Sato, Y., Inaba, T., Aoyagi, T., Hori, T., and Habe, H. (2019). Activated sludge microbial communities of a chemical plant wastewater treatment facility with high-strength bromide ions and aromatic substances. *J. Gen. Appl. Microbiol.* 65 (2), 106–110. doi: 10.2323/jgam.2018.05.002

Zheng, B. H., Chen, Z. J., Li, Y. Y., Fohrer, N., Zhang, Y., Wu, D. Y., et al. (2020). Structural characteristics and driving factors of the planktonic eukaryotic community in the Danjiangkou reservoir, China. *Water* 12 (12), 3499. doi: 10.3390/w12123499

Zheng, B., Zhu, J., Xu, X., Xin, Y., Song, J., Shi, Y., et al. (2018). Community structure of periphyton algae and water quality in the Danjiangkou Reservoir. *J. Henan Normal Univ. (Natural Sci. Edition)* 46 (4), 95–101. doi: 10.16366/j.cnki.1000-2367.2018.04.015

Zhong, K. X., Cho, A., Deeg, C. M., Chan, A. M., and Suttle, C. A. (2021). Revealing the composition of the eukaryotic microbiome of oyster spat by CRISPR-Cas Selective Amplicon Sequencing (CCSAS). *Microbiome* 9 (1), 230. doi: 10.1186/s40168-021-01180-0

Zubkov, M. V., and Tarran, G. A. (2008). High bacterivory by the smallest phytoplankton in the North Atlantic Ocean. *Nature: Int. weekly J. Sci.* 455, 224–226. doi: 10.1038/nature07236

frontiers | Frontiers in Environmental Science

TYPE Original Research
PUBLISHED 22 November 2023
DOI 10.3389/fenvs.2023.1287128

OPEN ACCESS

EDITED BY
Wen Nie,
Jiangxi University of Science and Technology, China

REVIEWED BY
Bochen Zhang,
Shenzhen University, China
Xing Peng,
China University of Geosciences Wuhan, China
Ruya Xiao,
Hohai University, China

*CORRESPONDENCE
Ziyuan Li,
li_ziyuan@csu.edu.cn

RECEIVED 01 September 2023
ACCEPTED 02 November 2023
PUBLISHED 22 November 2023

CITATION
Jiang Z, Wu Z, Li Z, Hu J, Wu Y, Ou L and Zhang T (2023), Investigating the behavior of an expansive soil slope in critical linear infrastructure in China using multi-temporal InSAR.
Front. Environ. Sci. 11:1287128.
doi: 10.3389/fenvs.2023.1287128

Investigating the behavior of an expansive soil slope in critical linear infrastructure in China using multi-temporal InSAR

Zhen Jiang[1], Zigui Wu[2], Ziyuan Li[3]*, Jun Hu[3], Yuwei Wu[1], Liye Ou[1] and Tongyuan Zhang[2]

[1]Jiangxi Institute of Land Space Survey and Planning, Nanchang, China, [2]State Grid Ji'an Electric Power Supply Company, Ji'an, China, [3]School of Geosciences and Info-Physics, Central South University, Changsha, China

One of the most significant pieces of linear infrastructure in China is the Middle Route of the South-to-North Water Diversion Project (MR-SNWDP), a large section of which consists of an expansive soil slope (ESS) that threatens the safety of the canal. Here, we prepared 144 Sentinel-1 data from May 2017 to July 2022 to study the behavior of the ESS in the canal section in Huixian City in the MR-SNWDP. Then, the Elastoplastic Deformation model under Wetting and Heating Effects (EDWHE) was employed to accurately characterize the displacement of the ESS. The InSAR results illustrate that the unstable zones tend to be small and are distributed along the canal slope, with the magnitude of deformations generally no more than 20 mm/year. Additionally, their deformation time series generally accumulate exponentially and evolve in a significant pattern of seasonal swelling and shrinkage. We observed that the slope movements significantly accelerated during the period when extreme rainfall occurred around 22 July 2021. Affected by satellite imagery and the geometric structure of the slope, the magnitudes and evolving trends of LOS deformation vary with different aspects of the slope sections. Then, the elastic swelling-shrinkage deformations were derived through the EDWHE model, of which the uplift or settlement was mainly dependent on geological and meteorological conditions. Moreover, the active zone depths of the ESS were retrieved using an InSAR-based lag-time approach and clearly reflected their distribution pattern. In this investigation, the behavior of the ESS in the study area was quantitatively analyzed using InSAR, and the results provide support for designing protective slope treatments and keeping the canal safe in the MR-SNWDP.

KEYWORDS

InSAR, expansive soil slope, elastoplastic deformation, geohazard, landslide, SNWDP, linear infrastructure

1 Introduction

The Middle Route of the South-to-North Water Diversion Project (MR-SNWDP) is an extremely significant infrastructure project in China and is effective at alleviating the imbalance in water distribution between South and North China (Office of the South-to-North Water Diversion Project Construction Committee et al., 2016; Dong et al., 2021). It has a total length of 1,432 km from Danjiangkou Reservoir, Henan, to Beijing and largely consists of excavated and filled slopes. However, 387 km of the MR-SNWDP is well

distributed with destructive expansive soil, posing a significant threat to the safety of the channel slopes (Dai et al., 2021; Dong et al., 2021).

The damage to infrastructure by expansive soil is mainly attributed to its elastic volume swelling/shrinking in response to soil moisture gain/loss (Mitchell, 1980; Ng et al., 2003; Zhan et al., 2007). The soil swells and shrinks repeatedly with wetting-drying cycles, which conforms to elastic behavior (Wang and Wei, 2014; Qi and Vanapalli, 2016; Li et al., 2023), facilitating soil mass softening and then accumulating plasticity. An expansive soil slope (ESS) acts as the down-slope shallow displacement and probably ends up inducing a progressive failure (Ng et al., 2003; Dai et al., 2021). Especially for the MR-SNWDP, which is subject to a monsoon season, expansive soil undergoes coupled swelling and shrinkage in summer that accelerates the process of wetting-drying cycles and thus faces more severe geohazard problems (Yang et al., 2006; Li et al., 2023). Therefore, for the safety of the MR-SNWDP, the characterization of the elastoplastic displacements of an ESS plays a significant role in preventing geohazards. In addition, a better understanding of the swelling and shrinkage dynamics of an ESS can help the design of more effective treatments for unstable slopes (Ting et al., 2018; Cohen-Waeber et al., 2023; Li et al., 2023).

The ground displacements of expansive soil receive contributions from the volume change of soil mass within a certain depth that is generally referred to as the active zone depth (AZD) (Aubeny and Long, 2007; Yue and Veenstra, 2018; Huang et al., 2022). It essentially defines the zone where moisture beneath the ground moves and soil deforms. AZD is a fundamental parameter for foundation design and protective treatment (Zongjun et al., 2006; Yue and Veenstra, 2018; Huang et al., 2022). Given the active zone, we can effectively protect against unstable slopes in the MR-SNWDP.

The Interferometric Synthetic Aperture Radar (InSAR) technique provides us with the ability to approach the demands mentioned previously. InSAR allows the remote imaging of vast earth surfaces at one time with high spatial resolution, after which multitemporal InSAR (MT-InSAR) can observe ground displacements in a magnitude of millimeters. Nowadays, huge archives of SAR data (e.g., Sentinel-1 data or NISAR in the future) make it convenient to characterize more detailed deformation patterns (Zheng et al., 2023). There have been many instances in which MT-InSAR has been successfully used to study the pattern of ground displacements caused by groundwater exploitation, active slow-moving landslides, and some special soil issues (Chaussard et al., 2014; Zhao et al., 2016; Miller et al., 2017; Hu et al., 2020; Lan et al., 2021; Cohen-Waeber et al., 2023; Dong et al., 2023). Furthermore, some publications have investigated the deformation distribution on a section of the MR-SNWDP and studied the destructive behavior of expansive soil––the swelling and shrinkage responsible for wetting and drying (Vallone et al., 2008; Bonì et al., 2018; Özer et al., 2019; Cook, 2023; Xiong et al., 2023).

InSAR time series have demonstrated the advantages of characterizing the downslope displacements of the ESS with seasonal variation (Zhang et al., 2022; Cook, 2023). Some methods, such as using a specific deformation model or independent component analysis, have been employed to investigate the characteristics of ESS movement, and its lagging effect on soil wetting (and drying) has been further studied (Özer et al., 2019; Cohen-Waeber et al., 2023). Owing to the monsoon season, the expansive soil's expansion and contraction are coupled, resulting in a more complex deformation pattern that has a higher risk of inducing geohazards in the MR-SNWDP. Then, an Elastoplastic Deformation model under Wetting and Heating Effects (EDWHE) is proposed to characterize this deformation pattern of the ESS in the channel head of the MR-SNWDP, and an InSAR-based time-lag approach is developed to retrieve the corresponding slope's AZD (Li et al., 2023). Here, considering the heterogeneity of expansive soil and the different engineering geological setting, we intend to employ the EDWHE model and time-lag approach to explore its spatiotemporal pattern on a larger scale and study the behavior of the ESS further in another section of the MR-SNWDP, i.e., the canal sections in Huixian City, Henan. In addition, with the knowledge that an unusually heavy rainstorm occurred there on 22 July 2021, we try to investigate how the extreme precipitation impacts the ESS displacements.

In this paper, a Sentinel-1 SAR dataset covering the study area, the canal section in Huixian City, is collected, spanning from July 2017 to May 2022, with a total of 144 scenes. The EDWHE model is applied to investigate the deformation pattern of ESS in the study area, in which the by-products, the expansive soil's time delays corresponding to rainfall and temperature, are obtained for analysis and subsequent work. Then, the elastoplastic displacement of the ESS is discussed in detail, and the elastic component is derived from the EDWHE model to explore its characteristics in response to rainfall events and temperature changes. In addition, we employ the time-lag approach to derive the AZD along the canal slope. Our study on the behavior of the ESS in multiple aspects provides support for the prevention of the expansive soil geohazard in the MR-SNWDP.

2 Materials

2.1 Geological setting of the study area

The canal section is located in Huixian City, northern Henan Province, China. It flows through the northeast boundary of the urban area and extends eastward, covering part of the ESS in this section. The canal section in Huixian City is hereafter called CSHC for simplicity. The geographical location and spatial distribution of the canal are shown in Figure 1. The expansive soils in Huixian City are mainly Upper Tertiary littoral lake facies, fluvial lacustrine sedimentary strata, and Quaternary Middle Pleistocene alluvial and diluvial strata (Q2al + pl), including heavy silty loam, silty clay, marl, and clay rock, with weak expansibility (Xu et al., 2019; Zhang et al., 2021). Owing to the specific expansion and contraction of the ESS in the channel, the cracks in the upper zone are fully developed, and the level of soil saturation is high, which seriously weakens the shear strength and causes severe damage to the safety of the ESS (Xu et al., 2019).

Under the influence of expansive soil, there is a high risk of geohazards occurring on the ESS, which would affect the safe operation of the water diversion channel (Li et al., 2023). Therefore, the EDWHE InSAR model is applied in this study to investigate the potential hazards of the expansive soil slope in the

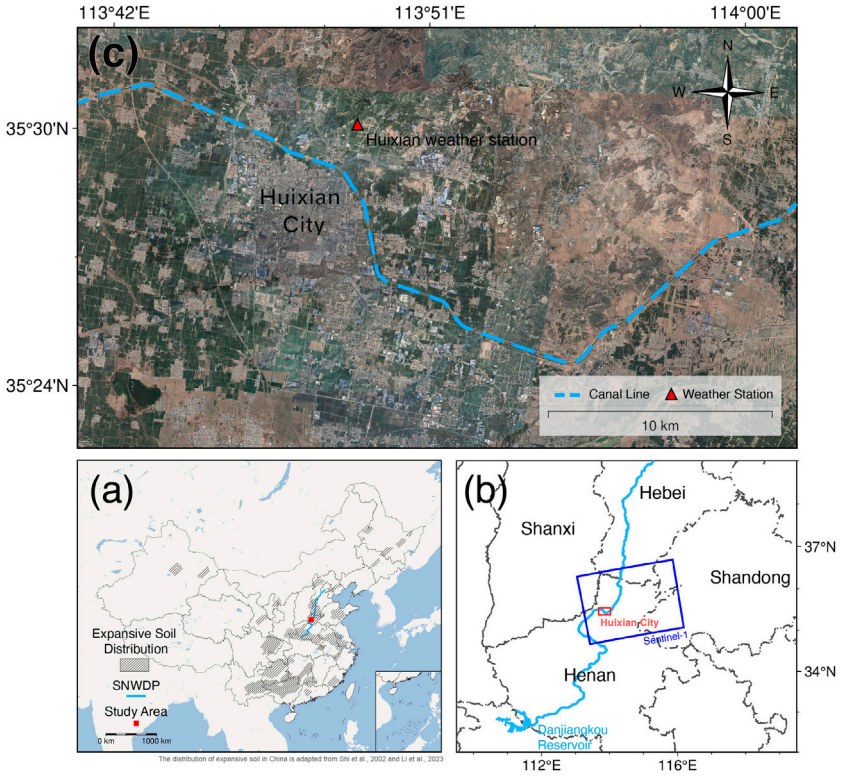

FIGURE 1
Geographical location and spatial distribution of the canal section in Huixian City, Henan, China. **(A)** The location of the study area and the distribution of expansive soil in China (Shi et al., 2002; Li et al., 2023). **(B)** More detailed information about the geographical location of the study area and the footprint of the Sentinel-1 SAR data in path 40 and frame 112. **(C)** Optical image obtained by Google Earth. The dashed blue line delineates the channel.

TABLE 1 Parameters of the Sentinel-1 SAR data used in this study.

Parameters	Description
SAR satellite	Sentinel-1A
Orbit direction	Ascending
Path	42
Frame	112
Number of scenes	144
Time span	July 2017–May 2022

Huixian City channel in the MR-SNWDP and study the dynamics of expansive-soil deformation, providing a better understanding of expansive soil geohazards. Furthermore, the method of retrieving the AZD is used to obtain the active layer of expansive soil in this channel section, providing support for an effective protective measure.

2.2 The dataset

In this study, the Sentinel-1 SAR data of ascending orbit in path 42 and frame 112 were obtained, spanning from July 2017 to May 2022, with 144 scenes, as shown in Figure 1B. The specific parameters of the SAR data used are listed in Table 1. The thresholds of the perpendicular and temporal baselines were set to 200 m and 96 days, respectively, for the construction of the multi-baseline interferometric pairs. To avoid the influence of severe atmospheric and decoherent noise, the interferograms with significantly noisy fringes in the objective region were excluded as much as possible, and finally, a total of 387 high-quality interferometric pairs were obtained. The resulting spatiotemporal baseline network is shown in Figure 2. In addition, to more accurately remove the contribution of the height phase, 30 m Copernicus DEM, derived during the MR-SNWDP construction, was used for differential interferometry.

Before the InSAR analysis using the EDWHE model, it is necessary to collect enough meteorological data, i.e., precipitation and temperature records, as the inputs of the EDWHE model, which can also support the subsequent analysis of the behavior of the ESS. For this reason, the daily rainfall and temperature data from recent years from the weather station in Huixian City were collected, as shown in Figure 3. It should be noted that there was abnormally high rainfall on 22 July 2021, much higher than the daily rainfall peak in previous years (corresponding to the peak in Figure 3).

3 Methodology

In this study, the EDWHE model was applied to investigate the deformation pattern of the ESS in the Huixian City section of the

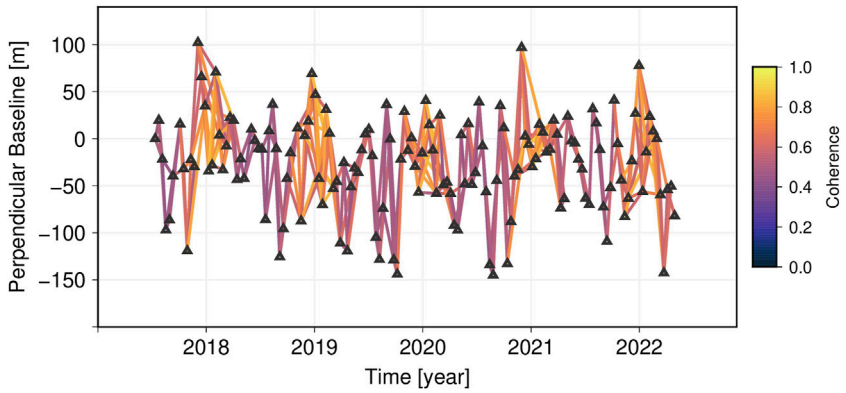

FIGURE 2
Spatiotemporal baseline network, with 200-m and 96-day perpendicular and temporal baseline thresholds, respectively.

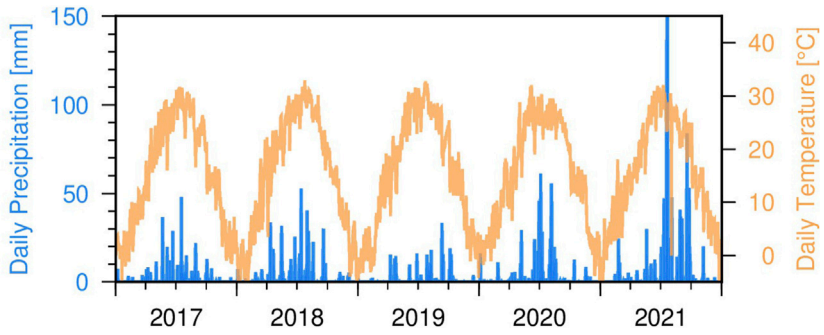

FIGURE 3
Meteorological data from the weather station in Huixian City, which were used to construct the deformation model and for subsequent analysis. The blue bars denote the daily precipitation records and the solid yellow lines indicate the daily temperature records.

MR-SNWDP. The time-lag approach was used to determine the active zone of the expansive soil (Li et al., 2023). The overall flowchart of the study is shown in Figure 4.

3.1 SAR data preprocessing

SAR data preprocessing, including co-registration, multi-look (4 × 1 in range and azimuth), and interferometry, was first completed using GAMMA software. Then, the adaptive filter and minimum-cost flow (MCF) were separately implemented to suppress the noisy signal and unwrap the phase (Goldstein and Werner, 1998; Costantini and Rosen, 1999). The filtering window should be relatively small to retain the spatial detail as much as possible. After that, phase ramps were removed by fitting the polynomial function before the time-series analysis, and a topographic power-law exponential model was exploited to mitigate the tropospheric disturbance (Bekaert et al., 2015; Li et al., 2019; Liang et al., 2019).

Considering that the research object (the expansive soil slope) is distributed in a pattern of long and narrow strips, which only occupies a small part of the whole image and the coverage area of the SAR data, there are various ground objects and complicated ground activities possibly affecting deformation interpretation. Therefore, to focus more on the spatial deformation pattern and analysis of the ESS along the channel of the MR-SNWDP, we created a 1 km buffer along both sides of the canal line with the InSAR data to isolate the main region of the channel, as shown in Figure 5.

Here, the strategy of multiple quality measures to select reliable pixels was employed (Yunjun et al., 2019; Li et al., 2023), in which the measures included average coherence γ, temporal coherence γ_{temp}, and average intensity m_A, separately shown in Supplementary Figures S1B–D. When selecting reliable points, the average coherence $\gamma_0 = 0.65$ was initially applied to mask out low-coherence pixels, after which the pixels with low phase closure and faint decoherence were further picked out by $\gamma_{temp,0} = 0.7$ (Yunjun et al., 2019; Li et al., 2023). Then, the average intensity (of the threshold set as 0.02) wass used as a complement to separate the pixels in the water body from the selected pixel subset. The final result is shown in Supplementary Figure S1A. As InSAR is a well-developed technique and has been qualified by a great deal of advanced research, the numerous practices demonstrate that we could calculate a theoretical accuracy of InSAR deformation through the given coherence and the Cramer–Rao bounds (Rodriguez and Martin, 1992; Delbridge et al., 2016; Zheng et al., 2023). The theoretical accuracy of InSAR deformation can be derived

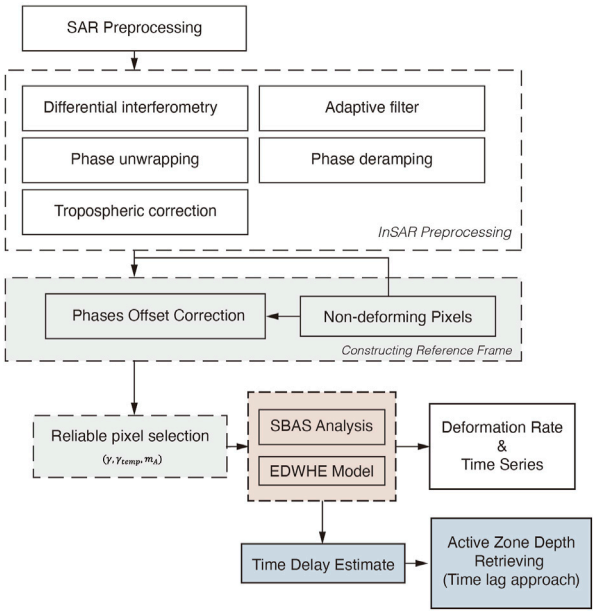

FIGURE 4
Workflow for investigating the expansive soil's behavior using the elastoplastic deformation under wetting and heating effects (EDWHE) model and time-lag approach, which are highlighted by the gray, light-red, and light-blue boxes. γ, γ_{temp}, and m_A denote average coherence, temporal coherence, and average intensity, respectively.

through the given parameters above (multi-look ratio, wavelength, and average coherence) and was 1.8*mm*.

Owing to the widespread existence of expansive soil in the study area, its unique expansion and contraction characteristics can increase the difficulty of selecting reference points in constant phase correction, which in turn will offset the derived time series of ESSs (Murray and Lohman, 2018; Jiang and Lohman, 2021; Zebker, 2021; Li et al., 2023). Here, we employed a multi-reference frame to mitigate the influence of the inaccurate selection of a local (single) reference, in the same way as Li et al. (2023). Therefore, we calculated the standard deviation (SD) of the time-series deformation of routine SBAS solution (Supplementary Figure S1A) and identified the reference frame by selecting pixels with an SD of less than 6 mm (Supplementary Figure S1B). Finally, the median phase value of the pixels under the reference frame was calculated and subtracted from each unwrapped interferogram.

3.2 Constructing the EDWHE model

Owing to the expansive soil's characteristics and weather activities, the ESS deforms in a seasonal way that forms a specific elastoplastic behavior. Here, to characterize the deformation of the ESS in the CSHC of the MR-SNWDP, we employed an Elastoplastic Deformation model under Wetting and Heating Effects, referred to as the EDWHE model (Li et al., 2023). In this way, capturing the variations of elastic swelling-shrinkage deformation and the plastic accumulation of the ESS is possible. The EDWHE model is defined as:

$$\begin{aligned} \boldsymbol{d_{EDWHE}} &= \boldsymbol{d_{pla}}(\boldsymbol{t}) + \boldsymbol{d_{ela}}(\boldsymbol{t}) \\ &= \underbrace{\sum_{k=1}^{n} \boldsymbol{\alpha_k t^k}}_{\boldsymbol{d_{pla}}} + \underbrace{\boldsymbol{\beta_1 P_e}(\boldsymbol{t}-\boldsymbol{\tau_1}) + \boldsymbol{\beta_2 T_m}(\boldsymbol{t}-\boldsymbol{\tau_2}) + \boldsymbol{c_e}}_{\boldsymbol{d_{ela}}} \end{aligned} \quad (1)$$

where the first term $d_{pla}(t)$ denotes the plastic deformation of the ESS that is the approximated polynomial function of time t, in which α_k indicates a time-related coefficient; k represents the order of the polynomial function. In this study, we employed k= 4 to better characterize the non-linear plastic evolution of the ESS. The second term $\boldsymbol{d_{ela}}(\boldsymbol{t})$ corresponds to elastic deformation relating to efficient rainfall and mean temperature, in which the efficient rainfall $P_e(t-\tau_1) = \sum_{k=1}^{m} \omega^k p(t-\tau_1-k+1)$ can take the persisting effect of previous rainfall infiltration into consideration, where m is taken as 15 days as in Li et al. (2023), $p(t)$ is the rainfall record at time t, and τ_1 is time delays for a deeper layer influence of precipitation infiltration. $T_m(t-\tau_2)$ is the average temperature between two sequential SAR acquisitions, where τ_1 will shift the temperature data to characterize its delay effect. β_i, i= 1, 2 can represent the magnitudes of swelling and shrinkage; c_e is the constant offset caused by the first two terms. Afterward, the EDWHE model can be integrated with the phase term of the residual height, $\varphi^i_{topo} = \frac{4\pi B_\perp \Delta h}{\lambda r \sin\theta}$, into the frame of SBAS analysis.

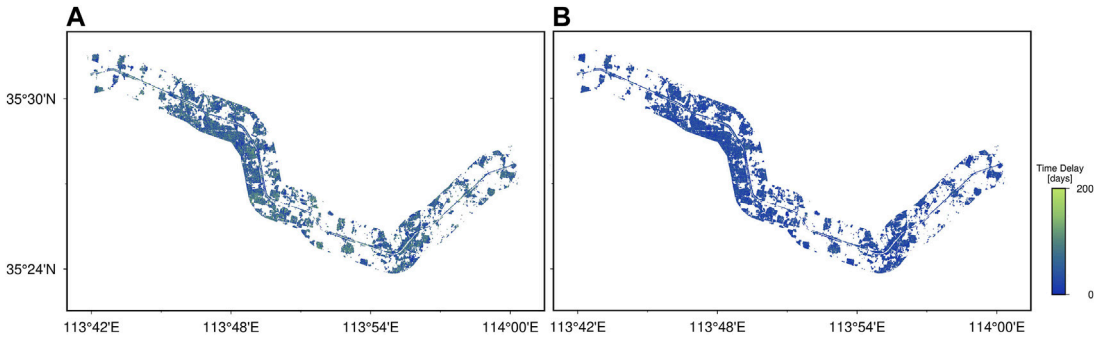

FIGURE 5
Estimated parameters of time delays responding to rainfall infiltrations and temperature changes. **(A)** Rainfall-related and **(B)** temperature-related time delays.

Here, the pattern-matching method developed by Li et al. (2023) was used to simultaneously estimate the time delays of precipitation and temperature from the coupled elastic swelling and shrinking. The method employed sum square error as the pattern-matching function to find the best similarities between the estimated elastic deformation $\hat{d}_{ela}(t, \hat{\tau}_1, \hat{\tau}_2)$ and the observable one $d_{ela}(t)$:

$$\boldsymbol{argmin\ SSE}\left(\boldsymbol{d_{ela}}, \hat{\boldsymbol{d}}_{\boldsymbol{ela}}\right) = \boldsymbol{argmin}\sum_{t}^{M}\left(\boldsymbol{d_{ela}}(\boldsymbol{t}) - \hat{\boldsymbol{d}}_{\boldsymbol{ela}}(\boldsymbol{t}, \hat{\boldsymbol{\tau}}_{\boldsymbol{1}}, \hat{\boldsymbol{\tau}}_{\boldsymbol{2}})\right)^2 \quad (2)$$

where $d_{ela}(t)$ is first derived by initially assuming zero-value time delays and solving the EDWHE model. Then, an iterative procedure is performed 2–3 times to acquire more accurate estimates.

3.3 Retrieval of the active zone depth

To estimate the AZD of the ESS on the CSHC, we employed an InSAR-based time-lag approach developed by Li et al. (2023). The inversion of the AZD utilizes the derivation of a one-dimension diffusion equation (Mitchell, 1980), as follows:

$$\boldsymbol{z} = \boldsymbol{2\Delta t\sqrt{\alpha \pi n}} \quad (3)$$

where z is the depth of the active zone, Δt can be represented by the time delay of rainfall $\hat{\tau}_1$, α is the moisture diffusion coefficient, which is usually determined from field measurements or laboratory data, and n is the frequency of the suction cycle. The last two parameters are unknown.

Given the lack of any accessible ground-based data, we empirically used the upper value $\hat{\alpha} = \frac{10^{-7}m^2}{s}$ in a general range 10^{-9} to $10^{-7}m^2$ to be conservative, as suggested by Tu and Vanapalli (2016). Considering the same climatic zone as in Li et al. (2023), the frequency of the suction cycle n= 2 was determined. Hereafter, the AZD of the ESS along the channel could be retrieved.

4 Results and discussion

By solving the EDWHE model and employing the time-lag approach, a series of products within the boundaries of the canal buffer have been derived and are shown in this section. Except for general descriptions of the results, we further investigate the underlying behavior of expansive soil with external meteorological conditions in the CSHC.

4.1 Estimated parameters of the EDWHE model

The time delay parameters are crucial in the EDWHE model, accounting for the delayed swelling and shrinkage caused by rainfall infiltration and temperature changes. First, they are estimated through the pattern-matching method; hence, the EDWHE model can be solved in the linear least-square sense. The estimated time delays after three iterations are shown in Figure 5, which shows that the time delays caused by rainfall infiltration, which are generally greater than 100 days (Figure 5A), are considerably greater than the temperature-related ones, which are generally close to zero (Figure 5B). In addition, the time delays of rainfall seem to spatially distribute in clusters; therefore, the size may be large or small depending on the ground setting (ground types, geological conditions, etc.). Temperature-induced time delays are spatially uniform due to all their lower values. From the results, we can see that the ESS takes longer to respond to rainfall infiltration but, conversely, responds rapidly to temperature changes.

After obtaining two parameters of the time delays, the EDWHE model can be inverted through the linear least-square solution, thereby obtaining each estimate of the model coefficients, as shown in Figure 6. The first four estimated coefficients in Figures 6A–D are time-dependent terms representing the long-term plastic evolution. We know that plastic deformations accumulate gradually to significant magnitudes in a decaying way. Figures 6E, F indicates the magnitudes of the elastic expansion and contraction deformation of expansive soil. Figure 6E shows the deformations responding to rainfall infiltration, which are basically positive values, and have maximum values up to 0.12 mm/mm on some sections of the channel slopes. Figure 6F shows the temperature-related deformation coefficient, which illustrates a negative correlation with temperature in the channel slope and a significant positive correlation outside the channel in the urban area. Figure 6G shows the topographic discrepancies relative to the Copernicus DEM. The positive values mainly appear in urban areas, mostly caused by urban construction; there are also positive residual heights on the channel slope, which may also be caused by slope construction.

4.2 Deformation analysis

4.2.1 Spatial pattern of the InSAR deformation

Owing to the lack of knowledge about the study area's canal structure, we also collected 30 m resolution SRTM DEM of the corresponding area. We subtracted it from the sum of the Copernicus DEM and residual height (Figure 6G) to obtain the quasi-ground heights (Figure 7). Given the quasi-ground height results, we divided the channel in the study area into four main sections, as shown in Figure 7, delineated by the light gray dashed boxes "a-d".

The CSHC consists of completely excavated/filled or half-excavated and half-filled slopes, and a clear building distribution surrounding the channel can also be observed (Figure 7). Afterward, combined with the InSAR deformation results, the causes of specific deformation generation are discussed and analyzed. There are several clusters with positive coefficients of temperature-dependent deformation in urban regions (Figure 6F), corresponding to the significant positive height region in Figure 7. It is easy to infer that it is the result of the building's thermal expansion.

Subsequently, the InSAR products––the annual LOS displacement velocity and InSAR time series––could be derived. Here, we first describe the spatial characteristics of LOS displacement rates (Figure 8) and then discuss the InSAR time series. In these canal sections, the slope deformation does not distribute continuously or extensively but occurs in scattered small pieces, and the deformation rates are positive and negative, mainly fluctuating in the range of magnitude of 6.0–20 mm/year.

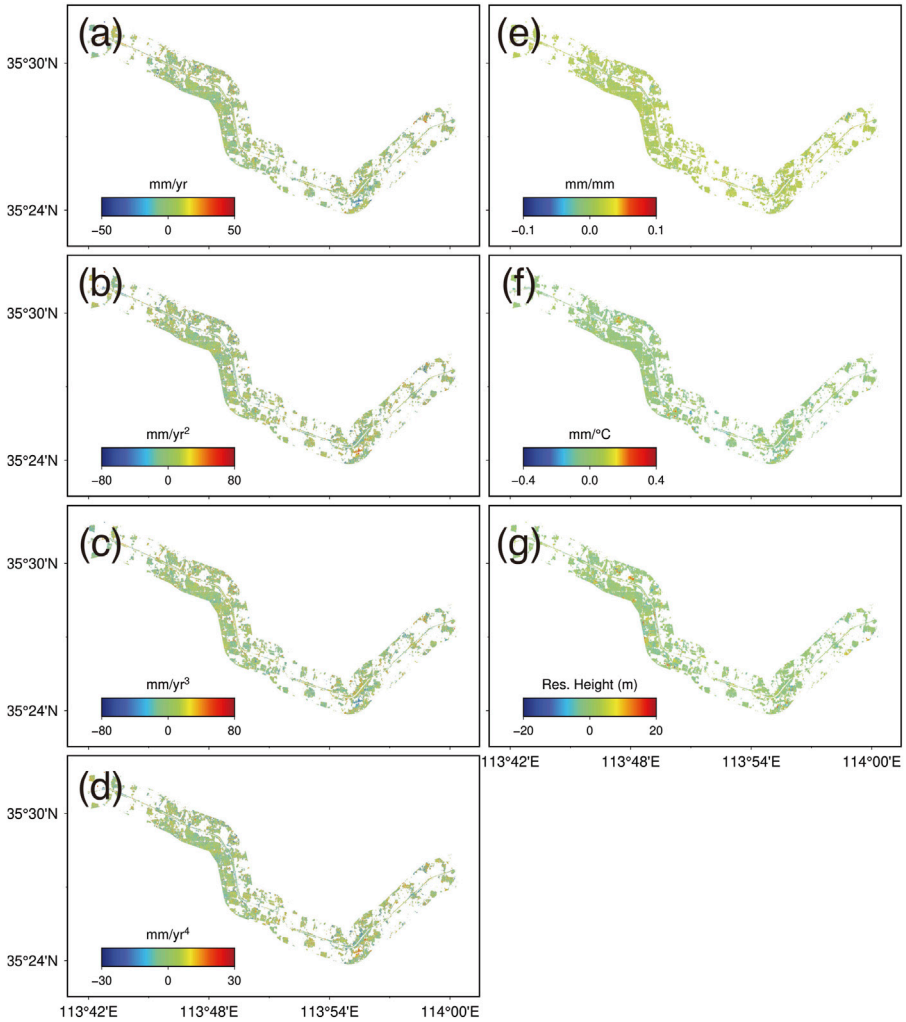

FIGURE 6
Estimated coefficients in the EDWHE model. Each subplot indicates the values of **(A)** α_1; **(B)** α_2; **(C)** α_3; **(D)** α_4; **(E)** β_1; **(F)** β_2; and **(G)** Δh.

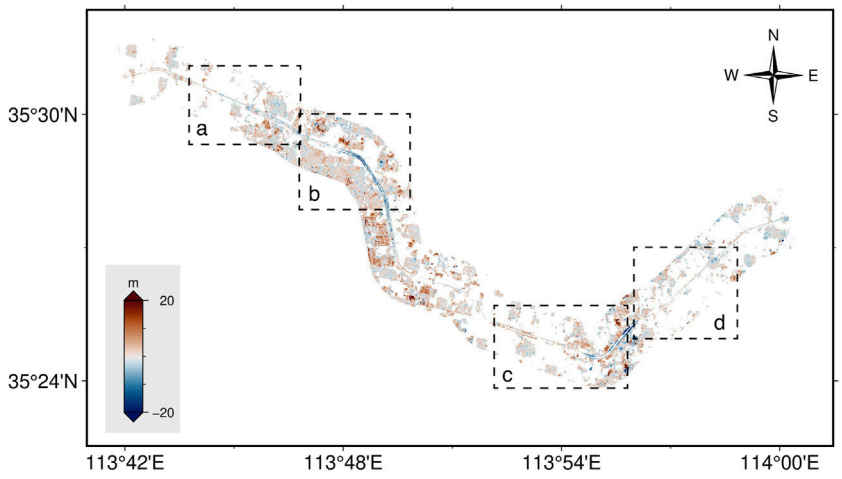

FIGURE 7
The difference between the 30 m SRTM dem and the sum of Copernicus dem and the estimated dem error Δh.

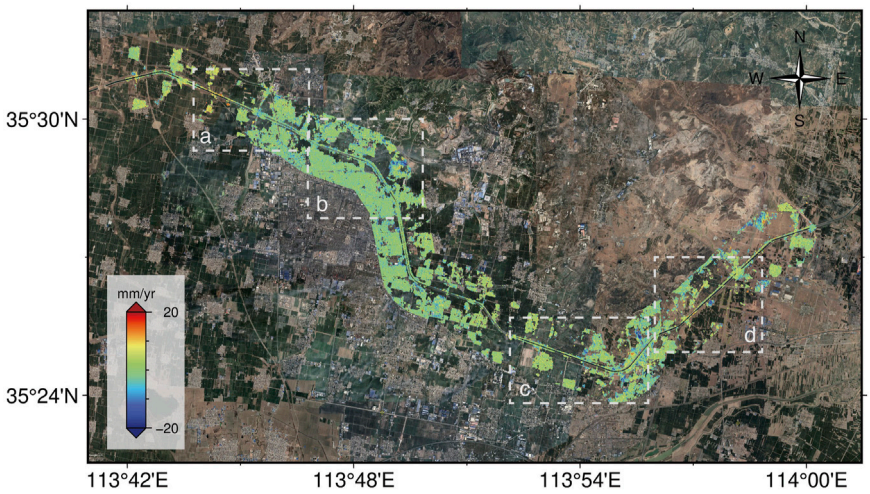

FIGURE 8
Annual LOS deformation rates. The dashed white boxes a-d indicate the local sections where the slopes with significant deformation are. The dashed black boxes a-d in Figure 7 delineate the same local regions.

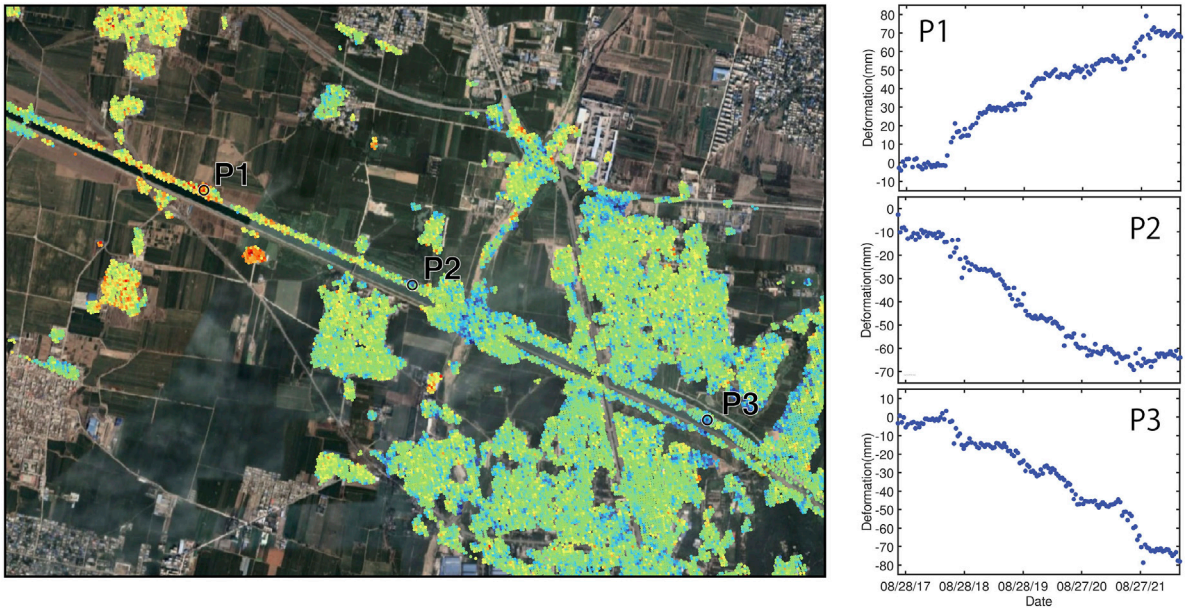

FIGURE 9
The magnified local region "a" denoted in Figure 7 and Figure 8, with the same colormap and scale as Figure 8.

The deformation magnitudes may result from heterogeneity in the ESSs of different formations and geological conditions. In addition, some of the causes of the observed deformation in the slope are possibly contributed to by slope maintenance or construction.

Furthermore, the four local regions "a-d" marked in Figure 8 are magnified separately to display where the time-series deformations on several feature points are plotted (Figures 9–12). According to the LOS deformation rates, we observed that the unstable slopes are small and distributed sparsely along the channel. Then, we could understand that slope instability does not occur continuously or on a massive scale but rather in small and scattered areas, which significantly increases the challenge of slope monitoring and treating the unstable zones. The deformation time series of the unstable regions generally evolved exponentially and were accompanied by significant swelling and shrinkage (the featured points in Figures 9–12). We can note that there was a significant acceleration of the ESS displacements around 22 July 2021. It demonstrates that torrential rain on these days severely

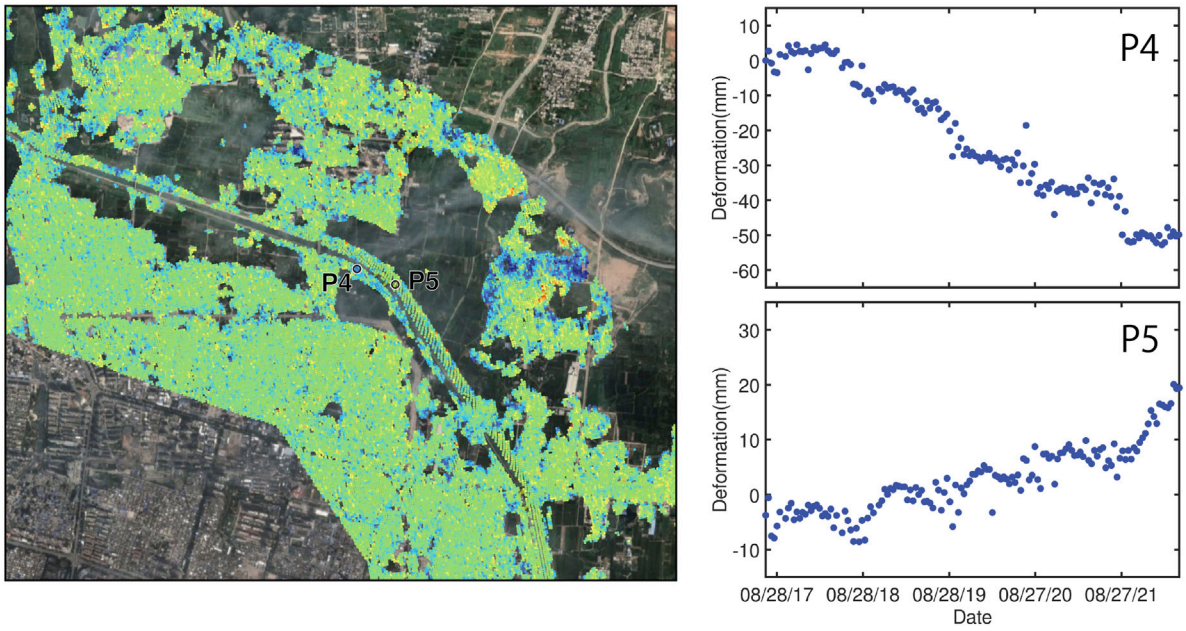

FIGURE 10
The magnified local region 'b" denoted in Figure 7 and Figure 8, with the same colormap and scale as Figure 8.

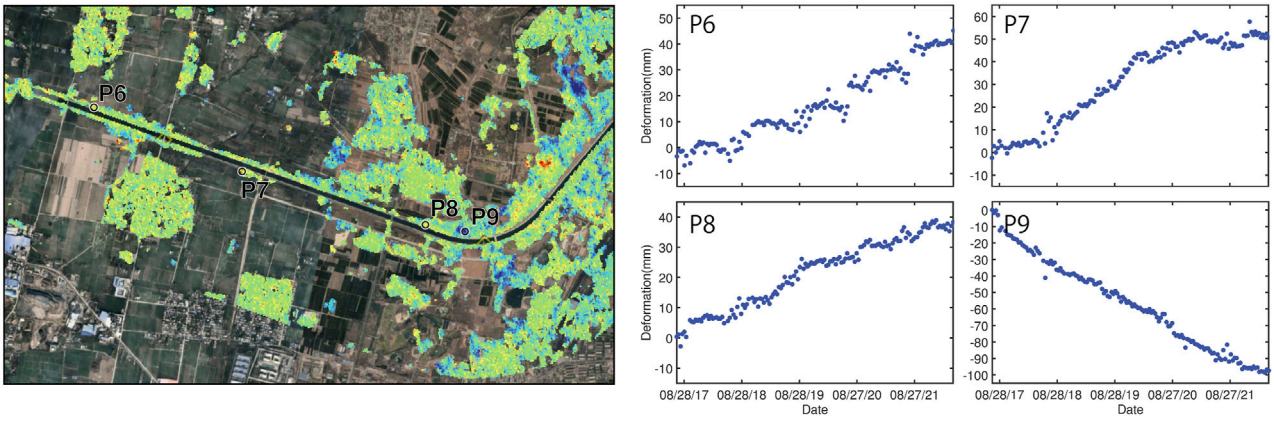

FIGURE 11
The magnified local region "c" denoted in Figure 7 and Figure 8, with the same colormap and scale as Figure 8.

impacted the stability of the ESS and facilitated their down-slope movements.

It is also intriguing that different locations on the channel slope exhibit diverse accumulation trends. Taking points P1 and P2 as an example, they are located at the canal section with the same slope direction, but their deformation trends are inverse, possibly because of the geometric structure of the slopes and the limitation of satellite SAR imagery. According to Figure 9, P2 is located at the filling part of a half-cut and half-fill slope, where settlement may occur at a significant magnitude, which turns out to be negative LOS deformation, and its temporally exponential evolution shown in Figure 9 proves this process. For other sub-regions, the feature points basically exhibit the elastoplastic characteristics as described above. Except for P9 and P12, they (Figures 11, 12) are the points outside the canal slope, of which the displacements were caused by engineering construction.

Although the evolutions of time series with the deformation pattern specific to ESS were captured, the magnitudes of displacements seem to differ among sub-regions "a-d" of Figures 9–12. Specifically, the final accumulated LOS displacements of those featured points in sub-region "b, c" (except for P9) were generally less than those of others, i.e., sub-region "a, d", approximately 20 mm. It is presumable that the direction of the canal slope extending and the viewing mode of the SAR satellite causes this phenomenon, as a result of the deformation pattern of the downslope slide in the ESS; the LOS displacements in this case

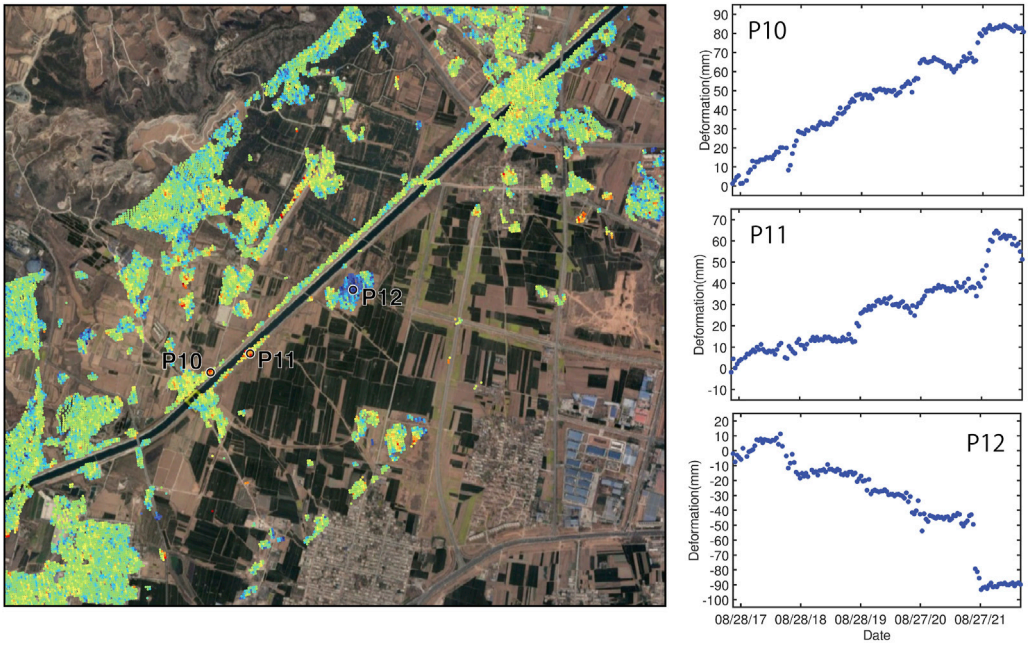

FIGURE 12
The magnified local region "d" denoted in Figure 7 and Figure 8, with the same colormap and scale as Figure 8.

will become larger at a slope that extends non-west-east than at one along "west-east" where the slope movements are approximately in a south-north direction, i.e., sub-region "b, c" (Ng et al., 2003; Li et al., 2023). It is a pity that only a single source of SAR data was available, and therefore, we could not view the deformation pattern of the ESS from a two-dimensional or even three-dimensional perspective (Zheng et al., 2023).

4.2.2 Dynamic of the elastic deformation

Elastic swelling and shrinkage are the main incentives for the progressive landslide of the ESS (Ng et al., 2003; Dai et al., 2021; Li et al., 2023); therefore, further analysis of its evolving characteristics is necessary. Therefore, in this section, we decouple the ESS's deformation through the EDWHE model and then derive the elastic-plastic component. Here, the time series of elastic deformation corresponding to P2, P5, and P7 are analyzed as examples (Figure 13). Among them, the delay times of points P2, P5, and P7 corresponding to rainfall infiltration are 18, 2, and 153 days, respectively; the temperature-induced ones are 49, 3, and 6 days, respectively.

The elastic deformation is prone to obvious shrinkage deformation under the influence of high temperature every summer, corresponding to the green fitting lines in Figure 13 significantly evolving downward during that period. Under the temperature change, the elastic contraction presented periodic changes on a long-term scale. However, summer also corresponds with a rainy season; therefore, it can be observed that the elastic deformation appears to uplift mid-year in some years with heavy rainfall. In the extraordinary rainstorm that occurred in July 2021, significant swelling can be observed as a result of a large amount of rainfall infiltration, which is also the reason for the significant acceleration of plastic deformation during this period. In addition, we find that, for P7, the response of the soil shrinkage to temperature is not obvious; by contrast, it responds greatly to rainfall events and therefore it mainly shows expansion deformation in summer. This may be attributed to the different geological properties of P7.

The elastic deformation mentioned above is the process of swelling and shrinkage coupling, which results in uplift or settlement, as analyzed previously, mainly depending on geological and meteorological conditions. Under monsoon effects, the frequent swelling and shrinkage provide more chances to weaken slope strength and accelerate slope instability (Ng et al., 2003; Bao, 2004).

4.3 Active zone depth

Owing to the lack of ground measurement data in the study area, the necessary parameters in Equation (8) were determined empirically by the moisture diffusion coefficient $\hat{\alpha} = 10^{-7} m^2/s$ and suction cycle frequency n= 2. Here, to focus on the AZD distribution pattern of the ESS in the CSHC, the region outside the channel was cut out, and the retrieval of the AZD was then completed, which is shown in Figure 14. The most active zones are in shallow layers of expansive soil, and the other part of them extends to greater depths, up to 4 m. It does reflect the spatial distribution of the AZD at different locations. Additionally, we could see that the AZDs on the bridges across the channel are generally close to zero, which means there is no active zone under the bridges. Furthermore, most of the AZDs are uniform and continuous along the canal sections (e.g., downstream of the channel in Figures 14C, D). In fact, in the shallow active zone in the canal slope, those AZDs close to 0 demonstrate the effectiveness of the waterproof measure on the ESS

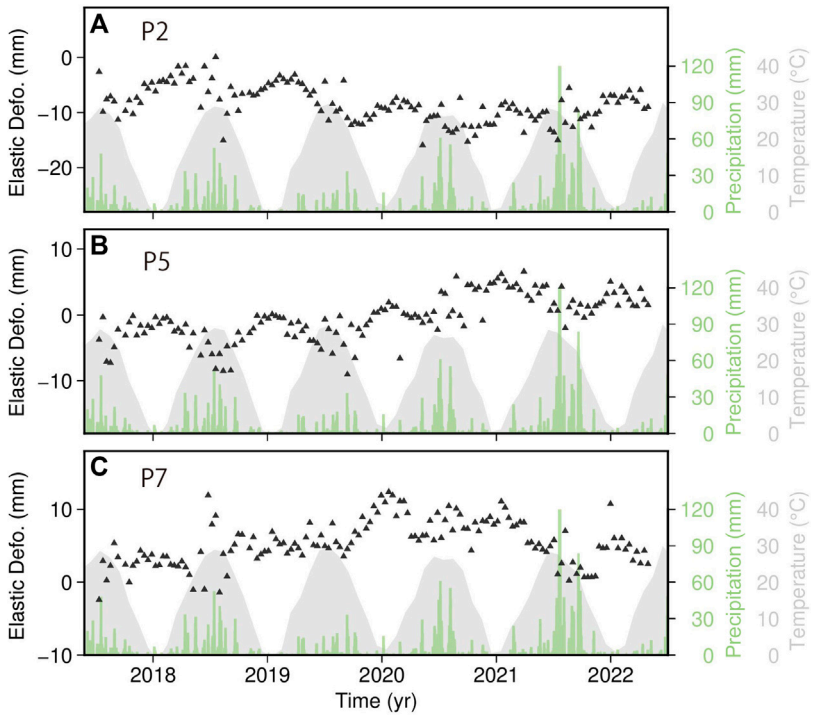

FIGURE 13
Evolutions of the elastic swelling-shrinkage deformations. Three elastic deformation time series are located at feature points **(A)** P2, **(B)** P5, and **(C)** P7. The black triangles indicate the elastic deformation of the expansive soil, which is then fitted by the solid green lines. The light green and gray shadows are the daily precipitation and monthly temperature.

that prevents moisture or rainwater from permeating deeper. However, there are discrete and abnormal values among the uniform AZDs in some sections (e.g., Figures 14A, B). It may be the reason that the construction and maintenance of the ESS during the monitoring period brought in a different deformation pattern unrecognizable to the EDWHE model, which can probably lead to the overestimated time lag and then the abnormally high value of the AZD in some locations.

Although using the time-lag approach to calculate AZD has been evaluated in the geotechnical field and has demonstrated its effectiveness, the lack of ground data makes it the only choice for determining the diffusion coefficient α empirically by Tu and Vanapalli (2016) and stops further quantitative analysis of AZD retrieval based on the InSAR results. Therefore, in the future, it will be necessary to use *in situ*-measured AZD to verify the efficiency of the InSAR-based method of retrieving AZD.

5 Conclusion

In this study, we collected 144 Sentinel SAR data between July 2017 to May 2022 to study the behavior of expansive soil in the Huixian section of the MR-SNWDP to provide a further understanding of ESS displacement and investigate the impact of torrential rainstorms on the stability of the ESS, consequently supporting the protective measure for geohazards in expansive soil in the MR-SNWDP. To this end, the EDWHE model was applied to interpret the expansive soil's elastoplastic deformation. Except for deriving the deformation results by solving the model, the time delays responsible for rainfall and temperature were estimated simultaneously, and the rainfall-induced delay was used for subsequent AZD retrieval using the time-lag approach.

According to the estimated time delays, the expansive soil deformation responses are longer for rainfall infiltration than for temperature change. As revealed by the InSAR results, the unstable zones are small and distributed on the channel slope in the study area, where the LOS deformation rates are generally no more than the absolute values of 20 mm/year. The displacement time series on some feature points temporally accumulate with significant seasonal swelling and shrinkage. The extreme torrential rains on 22 July 2021, in Huixian City led to the significant displacement acceleration of the ESS. Owing to the slope aspects and geometric structure in different locations, the magnitudes and evolving trends of the ESS's LOS displacements may be different. Additionally, the elastic deformations are derived through the model. We find there is significant coupled swelling and shrinkage in the rainy/hot season, and the elastic deformation presenting uplift or settlement mainly depends on geological and meteorological conditions.

The depths of the active zone in the study area were obtained through the InSAR-based lag-time approach, which illustrated their spatial distribution pattern with high resolution. Even though we

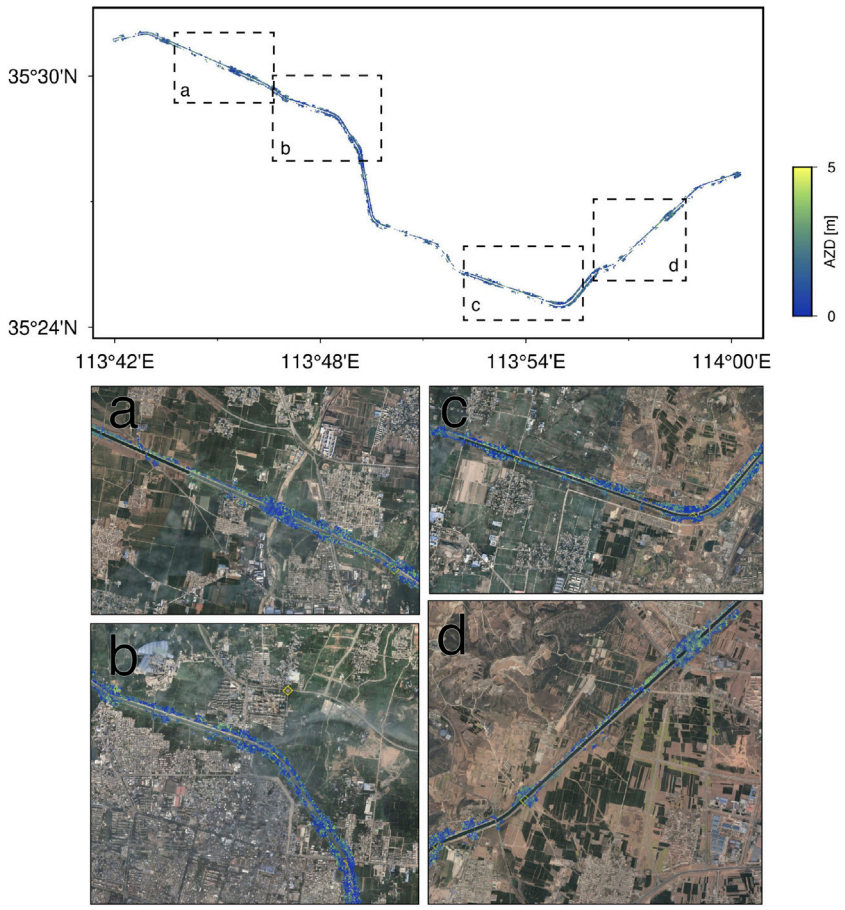

FIGURE 14
The Active Zone Depth (AZD) results along the channel.

could not further quantify the accuracy of the retrieved AZD because of the limited available ground data, it does provide the potential to support the protective measures for the unstable ESS in the MR-SNWDP.

Nevertheless, the studies carried out in this paper investigated the behavior of the ESS from a macroscopic perspective using InSAR and can offer a better understanding of the prevention of expansive soil geohazards, which is significant for the safety of the MR-SNWDP.

Data availability statement

The original contributions presented in the study are included in the article/Supplementary Material, further inquiries can be directed to the corresponding author.

Author contributions

ZJ: Validation, Writing–original draft, Writing–review and editing. ZW: Funding acquisition, Resources, Validation, Writing–review and editing. ZL, Conceptualization, Formal analysis, Investigation, Methodology, Software, Validation, Visualization, Writing–original draft, Writing–review and editing. JH: Conceptualization, Funding acquisition, Investigation, Project administration, Supervision, Validation, Writing–original draft, Writing–review and editing. YW: Data curation, Investigation, Resources, Validation, Writing–review and editing. LO: Data curation, Investigation, Validation, Writing–review and editing. TZ: Resources, Validation, Writing–review and editing.

Funding

The author(s) declare financial support was received for the research, authorship, and/or publication of this article. This study was supported by the State Grid Corporation of China Science and Technology Project (SGJXJA00YJJS2200480, the National Natural Science Foundation of China (42030112), and the Science and Technology Innovation Program of Hunan Province (2022RC3042).

Acknowledgments

The Sentinel-1 data are freely available from the European Space Agency and distributed and archived by the Alaska Satellite Facility

(https://www.asf.alaska.edu/sentinel/accessed on 24 March 2023). The Copernicus DEM used in this study can be downloaded from the Nevada Geodetic Laboratory (https://www.opentopography.org accessed on 24 March 2023).

Conflict of interest

Authors ZW and TZ were employed by State Grid Ji'an Electric Power Supply Company.

The remaining authors declare that the research was conducted in the absence of any commercial or financial relationships that could be construed as a potential conflict of interest.

Publisher's note

Supplementary material

The Supplementary Material for this article can be found online at: https://www.frontiersin.org/articles/10.3389/fenvs.2023.1287128/full#supplementary-material

References

Aubeny, C., and Long, X. (2007). Moisture diffusion in shallow clay masses. *J. Geotechnical Geoenvironmental Eng.* 133, 1241–1248. doi:10.1061/(asce)1090-0241(2007)133:10(1241)

Bao, C. (2004). Behavior of unsaturated soil and stability of expansive soil slope. *Chin. J. Geotechnical Eng.*, 1–15. doi:10.3321/j.issn:1000-4548.2004.01.001

Bekaert, D. P. S., Hooper, A., and Wright, T. J. (2015). A spatially variable power law tropospheric correction technique for InSAR data. *J. Geophys. Res. Solid Earth* 120, 1345–1356. doi:10.1002/2014JB011558

Bonì, R., Bosino, A., Meisina, C., Novellino, A., Bateson, L., and McCormack, H. (2018). A methodology to detect and characterize uplift phenomena in urban areas using sentinel-1 data. *Remote Sens.* 10, 607. doi:10.3390/rs10040607

Chaussard, E., Wdowinski, S., Cabral-Cano, E., and Amelung, F. (2014). Land subsidence in central Mexico detected by ALOS InSAR time-series. *Remote Sens. Environ.* 140, 94–106. doi:10.1016/j.rse.2013.08.038

Cohen-Waeber, J., Bürgmann, R., Chaussard, E., Giannico, C., and Ferretti, A. (2023). Spatiotemporal patterns of precipitation-modulated landslide deformation from independent component analysis of InSAR time series. *Geophys. Res. Lett.* 45, 1878–1887. doi:10.1002/2017gl075950

Cook, M. E., Brook, M. S., Hamling, I. J., Cave, M., Tunnicliffe, J. F., and Holley, R. (2023). Investigating slow-moving shallow soil landslides using Sentinel-1 InSAR data in Gisborne, New Zealand. *Landslides* 20, 427–446. doi:10.1007/s10346-022-01982-9

Costantini, M., and Rosen, P. A. (1999). "A generalized phase unwrapping approach for sparse data," in IEEE 1999 International Geoscience and Remote Sensing Symposium. IGARSS'99 (Cat. No.99CH36293), Hamburg, Germany, June, 1999, 267–269. doi:10.1109/IGARSS.1999.773467

Dai, Z., Zhang, C., Wang, L., Fu, Y., and Zhang, Y. (2021). Interpreting the influence of rainfall and reservoir water level on a large-scale expansive soil landslide in the Danjiangkou Reservoir region, China. *Eng. Geol.* 288, 106110. doi:10.1016/j.enggeo.2021.106110

Delbridge, B. G., Bürgmann, R., Fielding, E., Hensley, S., and Schulz, W. H. (2016). Three-dimensional surface deformation derived from airborne interferometric UAVSAR: application to the Slumgullion Landslide. *J. Geophys. Res. Solid Earth* 121, 3951–3977. doi:10.1002/2015JB012559

Dong, J., Guo, S., Wang, N., Zhang, L., Ge, D., Liao, M., et al. (2023). Tri-decadal evolution of land subsidence in the Beijing Plain revealed by multi-epoch satellite InSAR observations. *Remote Sens. Environ.* 286, 113446. doi:10.1016/j.rse.2022.113446

Dong, J., Lai, S., Wang, N., Wang, Y., Zhang, L., and Liao, M. (2021). Multi-scale deformation monitoring with sentinel-1 InSAR analyses along the middle route of the Southsouth-north water diversion project in China. *Int. J. Appl. Earth Observation Geoinformation* 100, 102324. doi:10.1016/j.jag.2021.102324

Goldstein, R. M., and Werner, C. L. (1998). Radar interferogram filtering for geophysical applications. *Geophys. Res. Lett.* 25, 4035–4038. doi:10.1029/1998GL900033

Hu, X., Bürgmann, R., Schulz, W. H., and Fielding, E. J. (2020). Four-dimensional surface motions of the Slumgullion landslide and quantification of hydrometeorological forcing. *Nat. Commun.* 11, 2792–2799. doi:10.1038/s41467-020-16617-7

Huang, Z., Shi, H., Zhang, W., Ma, S., Gao, F., and Ma, M. (2022). Expansive soil embankment filling and cutting treatment Technology: a systematic review. *Adv. Mater. Sci. Eng.* 2022, 1–20. doi:10.1155/2022/4045620

Jiang, J., and Lohman, R. B. (2021). Coherence-guided InSAR deformation analysis in the presence of ongoing land surface changes in the Imperial Valley, California. *Remote Sens. Environ.* 253, 112160. doi:10.1016/j.rse.2020.112160

Lan, H., Zhao, X., Macciotta, R., Peng, J., Li, L., Wu, Y., et al. (2021). The cyclic expansion and contraction characteristics of a loess slope and implications for slope stability. *Sci. Rep.* 11, 2250. doi:10.1038/s41598-021-81821-4

Li, Z., Cao, Y., Wei, J., Duan, M., Wu, L., Hou, J., et al. (2019). Time-series InSAR ground deformation monitoring: atmospheric delay modeling and estimating. *Earth-Science Rev.* 192, 258–284. doi:10.1016/j.earscirev.2019.03.008

Li, Z., Hu, J., Zhang, X., Zheng, W., Wu, W., Chen, Y., et al. (2023). Characterization of elastoplastic behavior and retrieval of active zone depth for expansive soil slopes in the middle-route channel head of the South-to-North Water Diversion Project, China, using InSAR time series. *Remote Sens. Environ.* 295, 113666. doi:10.1016/j.rse.2023.113666

Liang, H., Zhang, L., Ding, X., Lu, Z., and Li, X. (2019). Toward mitigating stratified tropospheric delays in multitemporal InSAR: a quadtree aided joint model. *IEEE Trans. Geoscience Remote Sens.* 57, 291–303. doi:10.1109/TGRS.2018.2853706

Miller, M. M., Shirzaei, M., and Argus, D. (2017). Aquifer mechanical properties and decelerated compaction in tucson, Arizona: tucson subsidence and aquifer properties. *J. Geophys. Res. Solid Earth* 122, 8402–8416. doi:10.1002/2017JB014531

Mitchell, P. W. (1980). The structural analysis of footings on expansive soil. In (ASCE). Available at: https://cedb.asce.org/CEDBsearch/record.jsp?dockey=0031270 (Accessed June 23, 2022).

Murray, K. D., and Lohman, R. B. (2018). Short-lived pause in Central California subsidence after heavy winter precipitation of 2017. *Sci. Adv.* 4, eaar8144. doi:10.1126/sciadv.aar8144

Ng, C. W. W., Zhan, L. T., Bao, C. G., Fredlund, D. G., and Gong, B. W. (2003). Performance of an unsaturated expansive soil slope subjected to artificial rainfall infiltration. *Géotechnique* 53, 143–157. doi:10.1680/geot.2003.53.2.143

Office of the South-to-North Water Diversion Project Construction Committee, State Council, and PRC (2016). The South-to-North Water diversion project. *Engineering* 2, 265–267. doi:10.1016/J.ENG.2016.03.022

Özer, I. E., Rikkert, S. J. H., van Leijen, F. J., Jonkman, S. N., and Hanssen, R. F. (2019). Sub-seasonal levee deformation observed using satellite radar interferometry to enhance flood protection. *Sci. Rep.* 9, 2646–2710. doi:10.1038/s41598-019-39474-x

Qi, S., and Vanapalli, S. K. (2016). Influence of swelling behavior on the stability of an infinite unsaturated expansive soil slope. *Comput. Geotechnics* 76, 154–169. doi:10.1016/j.compgeo.2016.02.018

Rodriguez, E., and Martin, J. M. (1992). Theory and design of interferometric synthetic aperture radars. *IEE Proc. F (Radar Signal Process.* 139, 147–159. doi:10.1049/ip-f-2.1992.0018

Shi, B., Jiang, H., Liu, Z., and Fang, H. Y. (2002). Engineering geological characteristics of expansive soils in China. *Eng. Geol.* 67, 63–71. doi:10.1016/S0013-7952(02)00145-X

Ting, L., Chaosheng, T., Dan, X. U., Yunsheng, L. I., Yan, Z., Kan, W., et al. (2018). Advance on the engineering geological characteristics of expansive soil. *gcdzxb* 26, 112–128. doi:10.13544/j.cnki.jeg.2018.01.013

Tu, H., and Vanapalli, S. K. (2016). Prediction of the variation of swelling pressure and one-dimensional heave of expansive soils with respect to suction using the soil-water retention curve as a tool. *Can. Geotech. J.* 53, 1213–1234. doi:10.1139/cgj-2015-0222

Vallone, P., Giammarinaro, M. S., Crosetto, M., Agudo, M., and Biescas, E. (2008). Ground motion phenomena in Caltanissetta (Italy) investigated by InSAR and geological data integration. *Eng. Geol.* 98, 144–155. doi:10.1016/j.enggeo.2008.02.004

Wang, G., and Wei, X. (2014). Modeling swelling–shrinkage behavior of compacted expansive soils during wetting–drying cycles. *Can. Geotechnical J.* 52, 783–794. doi:10.1139/cgj-2014-0059

Xiong, S., Deng, Z., Zhang, B., Wang, C., Qin, X., and Li, Q. (2023). Deformation evaluation of the SouthSouth-to-North water diversion project (SNWDP) central route over handan in hebei, China, based on sentinel-1A, radarsat-2, and TerraSAR-X datasets. *Remote Sens.* 15, 3516. doi:10.3390/rs15143516

Xu, D., Liu, H., Zhang, Y., Li, Y., and Chen, Y. (2019). Study on application of PS-InSAR technique in safety monitoring of expansive soil zone in South-to-North water diversion middle route project in huixian, henan Province. *Geomatics Spatial Inf. Technol.* 42, 31–34.

Yang, H.-P., Zhang, R., and Zheng, J.-L. (2006). Variation of deformation and strength of expansive soil during cyclic wetting and drying under loading condition. 28, 1936–1941.

Yue, Er, and Veenstra, J. N. (2018). Prediction of active zone depth in Oklahoma using soil matric suction. *J. Geoengin.* 13. doi:10.6310/jog.201803_13(1).3

Yunjun, Z., Fattahi, H., and Amelung, F. (2019). Small baseline InSAR time series analysis: unwrapping error correction and noise reduction. *Comput. Geosciences* 133, 104331. doi:10.1016/j.cageo.2019.104331

Zebker, H. (2021). Accuracy of a model-free algorithm for temporal InSAR tropospheric correction. *Remote Sens.* 13, 409. doi:10.3390/rs13030409

Zhan, L., Chen, P., and Ng, C. W. W. (2007). Effect of suction change on water content and total volume of an expansive clay. *J. Zhejiang Univ. - Sci. A* 8, 699–706. doi:10.1631/jzus.2007.A0699

Zhang, S., Si, J., Niu, Y., Zhu, W., Fan, Q., Hu, X., et al. (2022). Surface deformation of expansive soil at ankang airport, China, revealed by InSAR observations. *Remote Sens.* 14, 2217. doi:10.3390/rs14092217

Zhang, Y., Tian, F., Li, Y., and Liu, H. (2021). Application of time series InSAR to deformation monitoring in central line project of South-to-North water transfer. *J. Yangtze River Sci. Res. Inst.* 38, 72–77.

Zhao, R., Li, Z., Feng, G., Wang, Q., and Hu, J. (2016). Monitoring surface deformation over permafrost with an improved SBAS-InSAR algorithm: with emphasis on climatic factors modeling. *Remote Sens. Environ.* 184, 276–287. doi:10.1016/j.rse.2016.07.019

Zheng, W., Hu, J., Lu, Z., Hu, X., Sun, Q., Liu, J., et al. (2023). Enhanced kinematic inversion of 3-D displacements, geometry, and hydraulic properties of a north-south slow-moving landslide in three gorges reservoir. *J. Geophys. Research-Solid Earth* 128, e2022JB026232. doi:10.1029/2022JB026232

Zongjun, P. a. N., Yongli, X. I. E., Xiaohua, Y., and Zhifeng, L. I. (2006). Depth identification of the active and cracking zones in expansive soils from *in-situ* suction measurement. *gcdzxb* 14, 206–211.

frontiers | Frontiers in Ecology and Evolution

TYPE Original Research
PUBLISHED 29 November 2023
DOI 10.3389/fevo.2023.1326980

OPEN ACCESS

EDITED BY
Haijun Qiu,
Northwest University, China

REVIEWED BY
Bingwei Tian,
Sichuan University, China
Yu Liu,
Chinese Academy of Sciences (CAS), China

*CORRESPONDENCE
Hui Yu
yuhui@imde.ac.cn
Pengshang Li
targetlps@163.com

†These authors have contributed equally to this work and share co-first authorship

RECEIVED 24 October 2023
ACCEPTED 13 November 2023
PUBLISHED 29 November 2023

CITATION
He H, Yu H, Rong Z, Yang Y and Li P (2023) Estimation of grassland aboveground biomass and its response to climate changes based on remote sensing inversion in Three-River-Source National Park, Tibet Plateau, China.
Front. Ecol. Evol. 11:1326980.
doi: 10.3389/fevo.2023.1326980

Estimation of grassland aboveground biomass and its response to climate changes based on remote sensing inversion in Three-River-Source National Park, Tibet Plateau, China

Hui He[1,2†], Hui Yu[1,3*], Ziwei Rong[4], Yan Yang[1†] and Pengshang Li[5*]

[1]Institute of Mountain Hazards and Environment, Chinese Academy of Sciences, Chengdu, China, [2]Chongqing Jiaotong University, Chongqing, China, [3]Technology Innovation Center for Southwest Land Space Ecological Restoration and Comprehensive Renovation, Ministry of Natural Resources, Chengdu, China, [4]Shandong Jianzhu University, Jinan, China, [5]Chengdu Land Consolidation and Ecological Rehabilitation Center, Chengdu, China

Three-River-Source (TRS) National Park stands as one of China's earliest established national parks, dedicated to significant ecological responsibilities that include conserving soil and water resources in the Tibetan Plateau region. Research on climate change's influence on the TRS region's grasslands is of great significance in our efforts to comprehend and conserve the grassland ecosystem. The most effective random forest (RF) model was chosen to invert the aboveground biomass (AGB) of grassland in the previous 6 years (2015–2020) and predict the grassland AGB in the following 20 years (2021–2040) by comparing linear regression and multivariate nonlinear regression models such as RF, support vector machine, decision tree, and artificial neural network. A Theil–Sen median trend analysis and a Mann–Kendal test were then used to examine the trends of grassland AGB. The results showed that (1) RF outperformed other models in estimating grassland AGB, with a test set decision coefficient of multiple determination (R^2) of 0.722, a root mean square error of 42.596 g/m^2, and a mean absolute error of 35.619 g/m^2; (2) over 6 years, the grassland AGB in TRS National Park had a spatial trend of a steady rise from the northwest to the southeast. The average annual grassland AGB was 247.333 g/m^2, with averages of 44.836 g/m^2, 92.601 g/m^2, and 120.217 g/m^2 in the Yangtze River, Yellow River, and Lancang River source parks respectively. The trend of the grassland AGB was primarily stabilized and slightly recovered, with a small portion of the slightly deteriorated areas; (3) climate change significantly affected grassland AGB, and when temperature

and precipitation conditions were adequate, grassland AGB values increased with temperature and precipitation. In the scenarios of ssp119, ssp245, and ssp585, grassland AGB is projected to exhibit a dynamic upward trend over the next 20 years. Global warming is expected to boost grassland AGB. Comprehensive measures are essential to maintain grassland health and ensure a positive impact on global carbon and ecological balance. The study's findings hold great importance for the ecological security of the TRS region and contribute to our global understanding of sustainable grassland development.

KEYWORDS

climate change, grassland AGB, machine learning, model evaluation, remote sensing inversion, Three-River-Source National Park

1 Introduction

Grassland ecosystems, recognized as the most important ecosystem types globally, encompass over 40% of the Earth's land area. They have a vital role in the global carbon cycle, climate regulation, and carbon storage (Chapin et al., 2013). As the largest nature reserve in China and a critical grassland ecological function area, Three-River-Source (TRS) National Park is essential to maintaining water conservation and ecological security on the Tibetan Plateau and inland Asia (Yu et al., 2020b; Jiang F. et al., 2022). However, TRS National Park is located in the hinterland of the Qinghai–Tibetan Plateau, where the high altitude and harsh natural conditions make the region's ecological environment very fragile (Ma et al., 2022). Furthermore, the TRS region is confronting a pressing ecological challenge—grassland degradation. This predicament has arisen due to global warming, escalating environmental deterioration, and overgrazing (Li C. et al., 2019; Shu et al., 2022). Therefore, assessing the status and trends of the grassland biomass in TRS National Park and monitoring and analyzing critical parameters of grassland ecosystems can provide a scientific basis for the sustainable use of grassland resources and ecological restoration in the region (Yu et al., 2020a).

Grassland aboveground biomass (AGB) is an important indicator reflecting grassland ecosystems' productivities and carbon cycles. It is also a critical factor in assessing the degree of grassland degradation and the effect of restoration (Jia et al., 2016; Zhou et al., 2023). Due to the vast scope, complex terrain, and inconvenient transportation of TRS National Park, it is difficult and costly to obtain grassland AGB data with the use of traditional field survey methods, and the spatial and temporal coverage is low (Zhang F. et al., 2022). Despite significant progress in the estimation of grassland AGB, several challenges persist. The unique environmental conditions, extreme weather variations, and specific vegetation types found in high-altitude and high-latitude regions pose distinct challenges for accurate AGB estimation (Gao et al., 2020). Remote sensing technology can provide high spatial- and temporal-resolution remote sensing image data, and by establishing a quantitative relation model between remote sensing images and grassland AGB, rapid, accurate, and large-scale inversion and prediction of grassland AGB can be achieved (Jiang L. et al., 2022; Liu et al., 2022). Fan et al. (2022) used Sentinel-2 images to estimate the grassland AGB of the Qinghai–Tibetan Plateau, and Chapungu et al. (2020) assessed grassland biomass in northeastern Zimbabwe by hyperspectral remote sensing data using the relation between vegetation indices and grassland organisms. In addition to remote sensing imagery, uncrewed aerial vehicle (UAV) imagery is often a favored tool for analyzing grassland AGB (Alvarez-Mendoza et al., 2022). Zhang H. et al. (2022) used UAV technology to obtain large-area grassland AGB with an R^2 of 0.78, which is good evaluation accuracy. New technologies like the 3D-laser point cloud technology are essential in estimating grassland biomass (Wijesingha et al., 2019). In future scenarios, sky–ground integration for estimating grassland AGB will help to understand the changing characteristics of grassland ecosystems and achieve the scientific use of grassland resources and sustainable development (Yu et al., 2021a).

To establish inversion models, most studies use empirical statistical models, such as linear and nonlinear regression. Although those models can describe the mathematical relation between grassland AGB and remote sensing indices, they lack the explanatory value of physical mechanisms. They are also limited by the number of sample data, making it difficult to achieve a generalized application across regions and time (Zhang Y. et al., 2022). In recent years, machine learning models have provided new methods for the inversion of grassland AGB (Morais et al., 2021). Ge et al. (2022) constructed grassland AGB data from 2000 to 2019 in North China by comparing 4 machine learning algorithms and selecting the optimal random forest (RF) model. Liu et al. (2023) also constructed a model of grassland biomass in the western part of Southwest China with the use of RF and analyzed the relation between its response to climatic factors. Although machine learning algorithms are widely used in various fields for their advantages and accuracy, they differ markedly in sample requirements, parameter adjustment, and computational efficiency (Wang Y. et al., 2022; Ma et al., 2023). Also, overfitting during the machine learning fitting process remains a critical problem that continues to be addressed (Yu et al., 2021b). Therefore, it is essential to compare and evaluate the accuracy, performance, and applicability of various machine learning algorithms and emerging algorithms in remote sensing inversion to promote the application of machine learning in this field.

For grassland AGB inversion in TRS National Park, the current method still has some problems in data selection, modeling, and result validation (Xu et al., 2021). More in-depth studies are urgently required to improve the accuracy and reliability of grassland AGB inversion. Also, because TRS National Park is located in an area sensitive to global warming, the past and future spatial and temporal distribution and changes of its grassland AGB are significantly affected by climatic factors (Xu et al., 2022; Zhang L. et al., 2022). Therefore, exploring how the AGB in TRS National Park will respond to future climate change is important for determining the health and sustainability of grassland ecosystems. This study aimed to (1) assess the suitability and limitations of various regression models for estimating grassland AGB in TRS National Park through remote sensing and determine the best inversion models, (2) analyze the spatial and temporal distribution patterns of AGB and its trends in the park and offer a reference for addressing degradation in specific regions, and (3) explore the impacts of climate change on the AGB in TRS National Park to better understand the ecological influences on grasslands and to provide strategic information on grassland management in the TRS region.

2 Data and research methods

2.1 Study area

The TRS National Park encompasses the headwaters of 3 major rivers in southern Qinghai Province and is accordingly divided into 3 zones: the sources of the Yangtze Yellow, and Lancang rivers (Figure 1). The park covers an expansive area of 123,100 km^2, extending from approximately long 89°50'57"E to long 99°14'57"E and from lat 32°22'36"N to lat 36°47'53"N. This area constitutes 31.16% of the entire TRS region. It spans 4 counties: Zhiduo, Maduo, Qumalai, and Zaoduo, and encompasses the Cococli Nature Reserve (Zhang et al., 2019). The park is in the heart of the Qinghai–Tibetan Plateau, with an average altitude exceeding 4,500 m. The climate is characterized by extreme cold and aridity, featuring an average annual temperature of 1.9°C and an average annual precipitation of 498.5 mm (Zheng et al., 2020). The park has various grassland ecosystems, including alpine meadows, alpine steppes, alpine swamps, and alpine scrub meadows. Among those, the alpine steppes and meadows are the most pivotal ecosystems, significantly contributing to water conservation and biodiversity preservation.

2.2 Data collection

2.2.1 Sampling data

In this study, ground sample data from grasslands were collected primarily during the peak months of July and August between 2018 and 2020. The sample area for grass collection was standardized to 1 m by 1 m, with a minimum separation distance of more than 20 m between each sampling square. The key recorded information included ground cover, species names, vegetation height, biomass measurements, and latitude and longitude coordinates of each sample square. All grass samples were carefully harvested during sampling, subsequently dried at 85°C within a laboratory setting, and weighed. The AGBs of the sample squares were determined by averaging the data obtained from 3 sample squares. One hundred sixty sampling points were established, concentrated primarily within the TRS area.

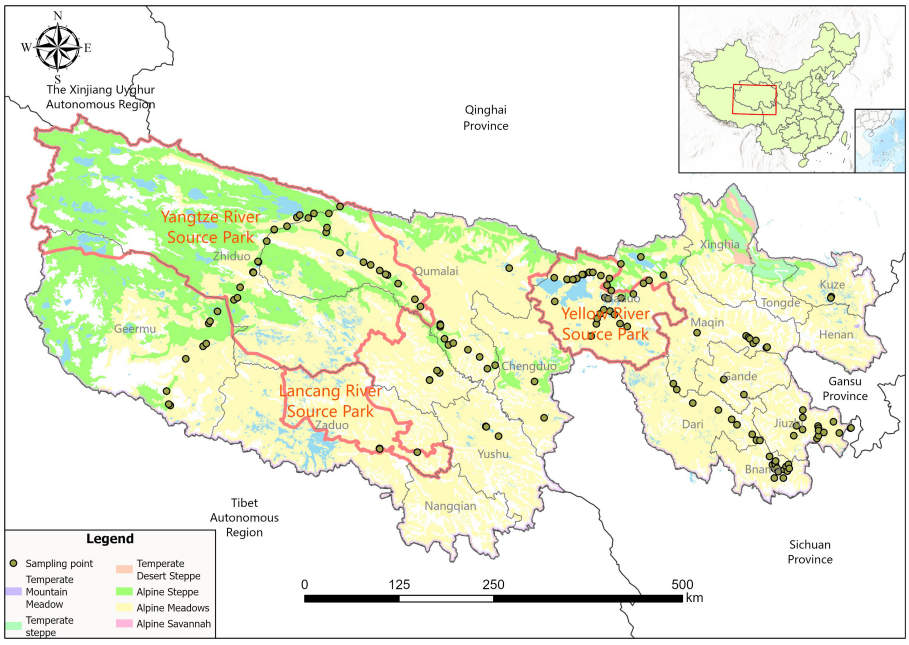

FIGURE 1
Distribution of grassland types and sampling points in the study area.

2.2.2 Remote sensing data

Remote sensing data were acquired using MOD13Q1/Global 250 m resolution with 16 d composite data, accessible at https://search.earthdata.nasa.gov/search. That dataset included 2 images, h25v05 and h26v05, covering the designated study area. MODIS Reprojection Tool software was used for data processing tasks such as format conversion, projection adjustment, and image mosaicking. Subsequently, relevant vegetation indices were extracted from the data with the use of ENVI software.

2.2.3 Climate and other data

Climate data for 2015 to 2020 were sourced from the National Science and Technology Basic Conditions Platform-National Earth System Science Data Center (http://www.geodata.cn). Those data primarily included monthly average temperature and precipitation data. Future climate data from 2021 to 2040 were obtained from CMIP6 (cmip6–Home | ESGF-CoG [llnl.gov]), comprising monthly average temperature and precipitation data. That dataset featured data from EC-Earth3, encompassing 3 future climate scenarios: ssp119, ssp245, and ssp585. Those scenarios correspond to various socio-economic development pathways and greenhouse gas emission levels. The numerical suffix in the ssp scenarios indicates the projected radiative forcing level for the year 2100, with higher radiative forcing values indicating more substantial global warming (Hurtt et al., 2020). Specifically, ssp119 represents a low-emission and low-forcing scenario aimed at limiting global warming to approximately 1.5°C above pre-industrial temperatures, ultimately stabilizing at approximately 1.4°C by the end of the century. ssp245 signifies a medium-emission and medium-forcing scenario, where temperatures are projected to rise by 2.7°C by the end of the century. ssp585 denotes a high-emission and high-forcing scenario, anticipating global average temperatures to increase by 4.4°C by 2100 (Popp et al., 2017). The climate data used in the text were average monthly temperatures and precipitation for August. Three-River-Source grassland-type data were acquired from the National Tibetan Plateau Data Center (https://data.tpdc.ac.cn/zh-hans/). Digital elevation model (DEM) data were derived from the Geospatial Data Cloud (http://www.gscloud.cn/) SRTMTPI 90 m resolution data product, and the slope data were generated from the DEM data.

2.3 Modeling and data analysis

2.3.1 Inversion model construction and accuracy assessment

(1) Vegetation index: This study used IBM's SPSS Statistics software to establish correlations between the extracted vegetation indices and the collected sample grassland biological data (Table 1). The primary objective was to assess the potential of the selected vegetation indices and actual grassland AGB as influential factors in estimating overall biomass within the study area (Li M. et al., 2019). This validation process facilitated determining the correlation strength between these factors, laying the groundwork for constructing the inversion model and identifying the most strongly correlated vegetation index for the model's development.

TABLE 1 Vegetation index information.

Type	Equation	
Difference vegetation index (DVI)	$DVI = \rho_{NIR} - \rho_R$	(1)
Ratio vegetation index (RVI)	$RVI = \frac{\rho_{NIR}}{\rho_R}$	(2)
Normalized difference vegetation index (NDVI)	$NDVI = \frac{\rho_{NIR}-\rho_R}{\rho_{NIR}+\rho_R}$	(3)
Enhanced vegetation index (EVI)	$EVI = 2.5\frac{\rho_{NIR}-\rho_R}{\rho_{NIR}+6\rho_R-7.5\rho_B+L}$	(4)
Soil adjustment vegetation index (SAVI)	$SAVI = \frac{(\rho_{NIR}-\rho_R)(1+L)}{\rho_{NIR}+\rho_R+L}$	(5)
Fractional vegetation cover (FVC)	$FVC = \frac{NDVI-NDVI_{soil}}{NDVI_{veg}-NDVI_{soil}}$	(6)

Where:

ρ_{NIR} is the reflectance in the near-infrared band.

ρ_R is the reflectance in the red band.

ρ_B is the reflectance in the blue band.

L is the soil conditioning coefficient, which assumes a value of 1 in the *EVI* and 0.5 in the *SAVI* (Ren et al., 2018). $NDVI_{soil}$ is the *NDVI* value of an area that is completely bare soil or has no vegetation cover, while $NDVI_{veg}$ is the *NDVI* value of an image element that is completely covered by vegetation.

(2) Model construction: This study used various modeling approaches for remote sensing inversion, including traditional simple linear regression, multivariate linear models, and machine learning models such as RF, decision tree (DT), support vector machine (SVM), and artificial neural network (ANN).

In the simple linear regression, the normalized difference vegetation index (NDVI), the vegetation index with the highest correlation, was selected as the independent variable, and measured grassland AGB in grams per square meter (g/m^2) as the dependent variable y. The model is represented as

$$y = kx + b \tag{7}$$

where k and b are the model parameters representing the slope and intercept respectively.

A multiple linear regression model used several independent variables to describe the linear relation between those variables and the dependent variable. Let the dependent variable be denoted as y and the respective independent variables as x_1, x_2, x_3, and so forth up to x_n. The linear relation between the dependent and independent variables can be represented as

$$y = a_1x_1 + a_2x_2 + \cdots + a_nx_n + \varepsilon \tag{8}$$

where y is the dependent variable; x_1, x_2, x_3 and x_n are the independent variables; a_1, a_2, a_3, and a_n are the regression coefficients; and ε is the error coefficient. This error coefficient accounts for the difference between the actual true value and the predicted value.

Machine learning methods contain mainly RFs, decision trees, SVMs, and ANNs.

An RF is an algorithm that combines the strengths of multiple decision trees. Each tree is independently trained on randomly selected data subsamples, reducing the risk of overfitting (Zeng et al., 2019). Moreover, RFs are known for their high predictive accuracy and exceptional performance in handling complex data and high-dimensional features.

Decision trees divide the input space into regions, each corresponding to an output value. Predictions of the output variable are made based on the value of the input variable (Zhang J. et al., 2022).

Support vector machines map the input data to a high-dimensional feature space with the use of nonlinear mapping. They then construct an optimal hyperplane in the feature space to minimize the distance from all data points to the hyperplane for predicting the output variable (Amarsaikhan et al., 2023).

Artificial neural networks are composed of interconnected neurons, with layers for input, hidden, and output nodes. The network architecture, including the number of nodes in each layer and their connections, is defined. Those networks are trained using optimization algorithms to handle linear and nonlinear regression problems (Yang et al., 2018).

(3) Accuracy assessment: During the model construction process, 80% of the samples were designated as the training set, and 20% the test set. Our goal was to ensure that the inversion model accurately reflected the conditions within the study area. To evaluate model accuracy, several metrics were used, including the root mean square error (RMSE), R^2, and mean absolute error (MAE) between the actual grassland AGB and the simulated grassland AGB. Those metrics were crucial for assessing the model's performance. In accuracy evaluation, the R^2 value ranged from 0 to 1, where the closer the value 1, the higher the accuracy of the constructed inversion model. Additionally, the RMSE and the MAE measured the deviation between actual and simulated grassland AGB values. Smaller values for the RMSE and MAE signified a smaller difference between the actual and simulated values, thereby indicating higher accuracy in the constructed inversion model (Zhang et al., 2023).

The accuracy of the validation inversion model was determined using the following equations:

$$RMSE = \sqrt{\frac{\sum_{i=1}^{N}(y_i - y_i')^2}{N}} \tag{9}$$

$$R^2 = 1 - \frac{\sum_{i=1}^{n}(y_i - y_i')^2}{\sum_{i=1}^{n}(y_i - \bar{y}_i)^2} \tag{10}$$

$$MAE = \frac{1}{n}\sum_{i=1}^{n}|y_i - y_i'|, \tag{11}$$

where y_i is the actual grassland AGB of the sample, y_i' is the corresponding calculated simulated grassland AGB, $\bar{y}_i$ is the mean of the simulated grassland AGB across all samples, and N is the total number of samples.

2.3.2 The Theil–Sen median slope estimation and Mann–Kendall nonparametric test

The Theil–Sen median slope estimation and Mann–Kendall nonparametric test are combined methods for analyzing time-series data trends (Wu N. et al., 2023).

The Theil–Sen median slope estimation is a robust nonparametric statistical approach used to calculate the average rate of change, or slope, in time-series data. This method determines the direction and magnitude of trends within a time series.

$$\beta = \text{median}\left(\frac{x_j - x_i}{j - i}\right), \forall\, j > i \tag{12}$$

A calculated value of β greater than 0 signifies an upward trend in the time series, whereas a value of less than 0 indicates a downward trend in the time series. If β equals 0, it suggests a stable or flat trend within the time series.

The Mann–Kendall nonparametric test is a method used to assess the presence of marked trend changes in time-series data. What sets this test apart is that it does not assume that the data follow a specific distribution, making it versatile for various applications. Furthermore, it is robust at handling missing values and outliers and is particularly well suited for conducting trend-significance testing on lengthy time-series data.

$$Z = \begin{cases} \frac{S-1}{\sqrt{V}}, & \text{if } S > 0 \\ 0, & \text{if } S = 0, \\ \frac{S+1}{\sqrt{V}}, & \text{if } S < 0 \end{cases} \tag{13}$$

where

$$S = \sum_{i=1}^{}\sum_{j=i+1}^{} sign(x_j - x_i) \tag{14}$$

$$V = \frac{n(n-1)(2n+5)}{18} \tag{15}$$

where x_i and x_j are the AGB values in years i and j respectively, while n is the total number of data points in the time series. The *sign* function refers to the mathematical signum function. The statistic Z is a measure that can take a range of values from negative infinity to positive infinity. At a given significance level α, when $|Z| > \mu_{1-\alpha/2,}$ it indicates a significant change in the time series at the α level. Typically, α is set to 0.05, leading to a value of $\mu_{1-\alpha/2,}$ approximately ±1.96. In this study, the significance of trend changes in the AGB time series was determined with a confidence level of 0.05 (Table 2).

TABLE 2 Distribution of trend scenarios under various β and Z values.

β	Z	Scenario
$\beta < 0$	$Z > 1.96$	Significant deterioration
$\beta < 0$	$Z \leq 1.96$	Slight deterioration
$\beta = 0$	Z	Stabilized
$\beta > 0$	$Z \leq 1.96$	Slightly recovered
$\beta > 0$	$Z > 1.96$	Significant recovery

3 Results

3.1 Correlation between vegetation index and grassland aboveground biomass

Among the vegetation indices, the highest correlation coefficient was observed between grassland AGB and the NDVI, which stood at 0.61. Following closely, the correlation coefficients for the enhanced vegetation index, the ratio vegetation index, and the fractional vegetation cover were 0.60, indicating a high degree of similarity among these 3 vegetation indices, and their correlation coefficients ranked second only to that of the NDVI. The soil adjustment vegetation index and the difference vegetation index had slightly lower correlation coefficients, with values of 0.58 and 0.56 respectively. All vegetation indices had a positive correlation with AGB. The higher the vegetation index, the higher the AGB value. This suggests that vegetation indices effectively characterize grassland AGB. In the realm of climatic factors, the correlation coefficients between grassland AGB and monthly average air temperature and precipitation were 0.38 and 0.46 respectively. Notably, precipitation influenced grassland AGB significantly more than air temperature did. Within certain bounds, precipitation and air temperature increases lead to higher grassland AGB values. Geographic factors also affect grassland AGB. The correlation coefficient between AGB and the DEM was −0.48, indicating that grassland AGB decreases with rising altitude. Because the study area was in a plateau region, there was also a positive correlation between grassland AGB and slope, albeit with a relatively small correlation coefficient of 0.28 (Figure 2).

3.2 Model accuracy

Six distinct models were used to analyze and predict grassland AGB within the TRS National Park area (Table 3). In the simple linear regression, the independent variable chosen was solely the vegetation index NDVI, because it showed the highest correlation coefficient with AGB. For the multivariate linear model and the machine learning model, 5 influential factors were integrated: NDVI, average monthly precipitation, average monthly temperature, elevation, and slope, because those factors collectively contributed to the construction of the regression model.

In the training set constructed by the 6 grassland AGB models, the DT model yielded the highest R^2 at 0.893. Furthermore, it showed the lowest RMSE and MAE at 29.382 g/m^2 and 20.500 g/m^2 respectively. Notably, the RF model closely followed with an R^2 of 0.876 and relatively low RMSE and MAE values. On the other hand, simple linear regression achieved the lowest R^2 at 0.560 in the training set, resulting in higher RMSE and MAE compared to the other models. In the test set, the RF model had the highest R^2 at 0.722, along with corresponding RMSE and MAE values of 42.596 g/m^2 and 35.619 g/m^2 respectively. The multivariate linear model achieved the second-highest R^2 in the test set at 0.690, demonstrating its effectiveness. In general, all 4 machine learning models attained R^2 values exceeding 0.63 in the test set, indicating a strong fit. In contrast, simple linear regression had the lowest R^2 in the test set at 0.624, resulting in comparatively higher RMSEs and MAEs. Due to its limitation of relying on only one factor to predict grassland AGB, that model had a poorer fit. Overall, the RF approach demonstrated advantages in predicting grassland AGB in both the training and test sets.

Through the comparison of 6 different models and their actual versus predicted values, the RF approach stood out for its superior performance (Figure 3). As shown in Figure 3D, the predictions obtained through the RF model closely aligned with the actual values. The fitting line in those figures closely approximates a 1:1 relation, with only a few predictions deviating markedly from the observed AGB. Multivariate linear regression, DT regression, and ANN models also demonstrated relatively minor differences between their predicted values and actual values. However, the SVM model was more accurate when AGB values were below 150 g/m^2. Conversely, when the AGB value was relatively high, the gap between the actual and predicted values of the SVM became more pronounced. Simple linear regression showed the lowest correlation with measured AGB values, with a more dispersed distribution of sample points, indicating the least effective modeling.

Building upon the preceding context, RF was used to estimate the grassland biomass within TRS National Park.

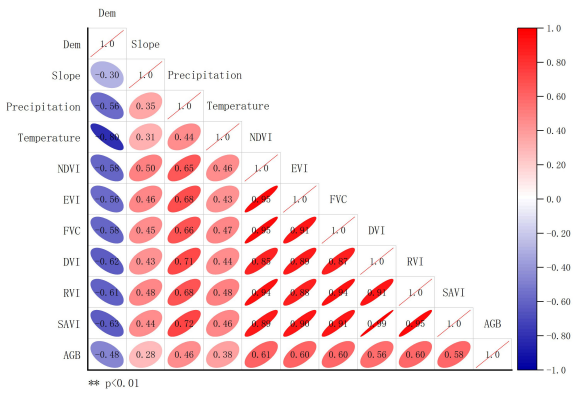

FIGURE 2
AGB correlation with indicators.

3.3 Temporal dynamic and spatial pattern of grassland aboveground biomass distribution in each park

3.3.1 Temporal dynamic of grassland aboveground biomass

From the inversion of the grassland AGB in TRS National Park from 2015 to 2020 with the use of RF modeling, the average AGB values in the Yellow River, Yangtze River, and Lancang River source parks showed a consistent and dynamic increasing trend (Figure 4). The most substantial increase in grassland AGB occurred in the Yellow River source park from 2016 to 2017, with an average AGB rise of 19.224 g/m^2. The Yangtze River source park, influenced by its geographic location and climatic factors, had lower average

TABLE 3 Evaluation of the accuracy of each model.

Model	Training accuracy			Test accuracy		
	R^2	RMSE (g/m^2)	MAE (g/m^2)	R^2	RMSE (g/m^2)	MAE (g/m^2)
Simple linear regression	0.560	61.165	50.721	0.624	49.691	58.777
Multivariate linear regression	0.641	55.237	45.225	0.690	52.684	46.060
RF	0.876	32.826	25.432	0.722	42.596	35.619
SVG	0.758	46.193	31.140	0.639	53.026	41.027
DT	0.893	29.382	20.500	0.647	61.261	43.730
ANN	0.626	56.227	44.224	0.686	54.262	44.798

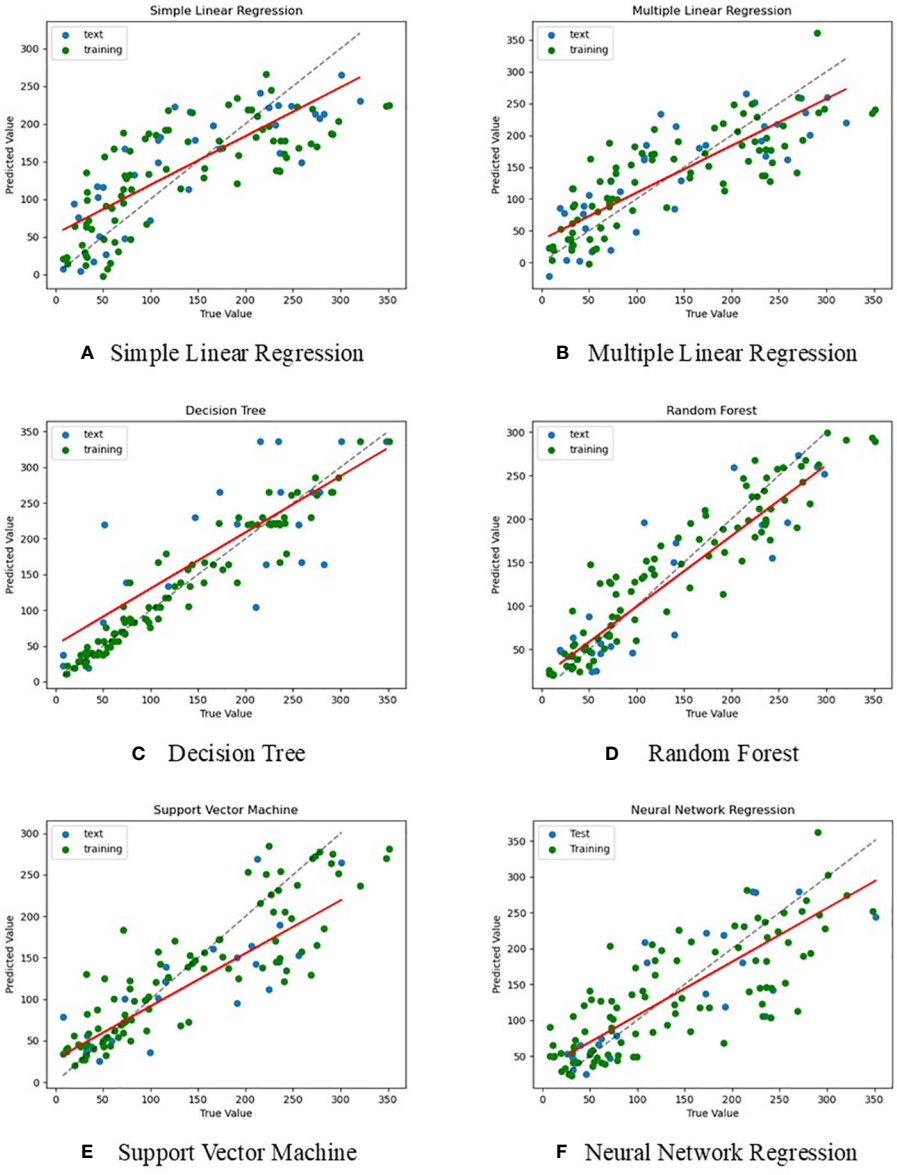

FIGURE 3
Comparison of the actual value of each model with the predicted value (unit: g/m^2). **(A)** Simple Linear Regression, **(B)** Multiple Linear Regression, **(C)** Decision Tree, **(D)** Random Forest, **(E)** Support Vector Machine, **(F)** Neural Network Regression.

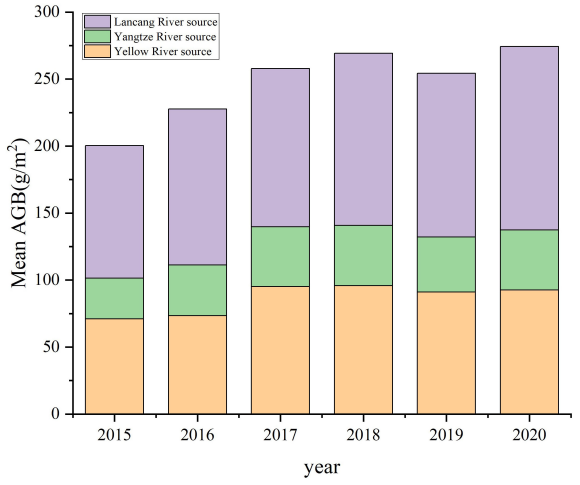

FIGURE 4
Average grassland AGB of Three-River-Source National Park by park from 2015 to 2020.

grassland AGB values than the other 2 parks. The maximum AGB value within the 6 years did not surpass 50 g/m^2. Notably, the AGB in that park showed a linear increase from 2015 to 2017, with a growth rate of 24.73%, suggesting an enhancement in the ecological health of the Yangtze River source park grassland. Conversely, the Lancang River source park showed a relatively consistent growth trend during the same 6-year period, with annual average values ranging from 98.966 g/m^2 to 136.892 g/m^2. TRS National Park had a growth trend similar to those of the individual parks over the 6 years, consistently showing a dynamic increase. The average AGB rose from 200.371 g/m^2 in 2015 to 274.330 g/m^2 in 2020, marking a total increase of 73.958 g/m^2. All 3 parks experienced a reduction in grassland AGB during 2018–2019, with a decrease of 5.54%. The primary reason for that was insufficient precipitation in the TRS region during that period, leading to limited grass growth.

3.3.2 Spatial pattern of grassland AGB

The overall spatial distribution of TRS National Park from 2015 to 2020 had relatively minor changes, and all areas demonstrated a gradual increase in AGB from the northwest to the southeast (Figure 5). That pattern showed noticeable heterogeneity, aligning closely with the distribution of actual sampling data. The average grassland AGB for TRS National Park as a whole was 247.333 g/m^2. When considering the region's individual parks, the Yangtze River source park had the lowest average AGB at 44.836 g/m^2. That can be attributed to its elevated average altitude and less favorable water and heat conditions. In contrast, the Yellow River and Lancang River source parks boasted higher average grassland AGB values, standing at 92.601 g/m^2 and 120.217 g/m^2 respectively. The Lancang River source park enjoyed a more suitable climate and altitude, resulting in a higher grass biomass.

3.3.3 Trends of changes in grassland aboveground biomass

By overlaying the results of grassland AGB changes with their significance, we delineated the trends in grassland AGB changes across TRS National Park during the 6-year period. As shown in Figure 6, the 3 parks predominantly slightly recovered and stabilized in their AGB trends. A few areas showed slight deterioration, with minimal signs of either significant recovery or significant deterioration. The areas showing slight recovery are the most extensive and are situated primarily in the southeast of the Yangtze River source park, a substantial portion of the Lancang River source

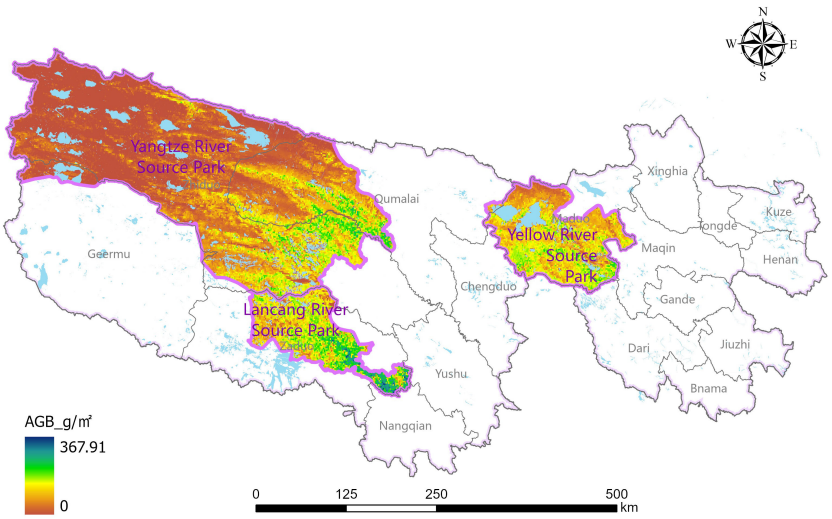

FIGURE 5
Spatial distribution of average grassland aboveground biomass in Three-River-Source National Park.

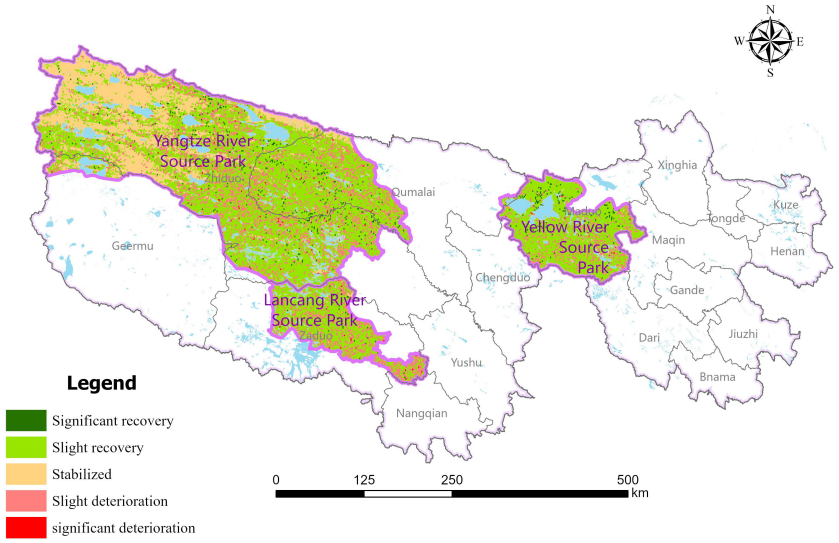

FIGURE 6
Trend analysis of grassland aboveground biomass changes in national parks.

park, and the south-central area of the Yellow River source park. Stabilized areas are concentrated in the northwestern region of the Yangtze River source park, while scenarios of slight deterioration were observed primarily in the southeastern part of all 3 parks.

The most extensive category was slight recovery, encompassing an area of 69,780.53 km², which accounts for 56.99% of TRS National Park's total area. This suggests that the overall grassland recovery in the TRS region has been relatively positive in recent years. The stabilized category encompassed a total area of 28,148.06 km², distributed primarily in the Yangtze River source park area. That region is relatively undisturbed, resulting in a more stable grassland condition. Notably, the Yangtze River source park comprises 25,654.65 km², representing 91.14% of the total stabilized area, while the Yellow River and Lancang River source parks had smaller stabilized areas. Areas of slight deterioration were dispersed across the 3 parks, totaling 22,003.87 km². Within this category, the Yellow River, Yangtze River, and Lancang River source parks occupied 13.54%, 69.27%, and 17.19% of the total area respectively. Moreover, the combined areas of significantly deteriorated and significantly restored regions measured 2,535.63 km², constituting 2.07% of TRS National Park's total area. These results suggest that from 2015 to 2020, the TRS area experienced an overall trend of grassland recovery, stability in the eastern part of the Yangtze River source park, and localized deterioration trends (Table 4).

3.4 Distribution of grassland aboveground biomass in future scenarios

Using the RF approach, the future changes in grassland AGB in TRS National Park were modeled for the period 2021–2040 under 3 scenarios: ssp119, ssp245, and ssp585 (Figure 7). All scenarios had a dynamic upward trend in grassland AGB, with trend lines showing slopes greater than 0. Notably, the ssp119 scenario showcased the most rapid upward trend in grassland AGB for TRS National Park, with a slope of 7.618. That slope exceeded those observed in the ssp245 and ssp585 scenarios. The fluctuations in overall grassland AGB remained relatively consistent across the 3 parks, with the Lancang River source park displaying the highest values, followed by the Yellow River and Yangtze River source parks. Under the ssp585 scenario, the mean grassland AGB in TRS National Park averaged 320.92 g/m² over the 20-year period. This figure surpassed the mean values of ssp119 and ssp245, which stood at 288.80 g/m² and 311.53 g/m² respectively. This suggests that higher radiative forcing corresponds to increased global warming, resulting in elevated temperatures and, consequently, higher grassland AGB values.

In the ssp119 scenario, the average grass biomass in Changjiang Yuan Park increased to 54.77 g/m² from 2020 to 2035, surpassing the average value from 2015 to 2020. Notably, in 2035, the AGB of

TABLE 4 Area of different trend changes in each park (km²).

Source park	Significant recovery	Slight recovery	Stabilized	Slight deterioration	Significant deterioration
Yellow River	555.19	13394.31	1877.05	2979.18	32.95
Yangtze River	1544.76	47368.61	25654.65	15242.44	220.33
Lancang River	117.15	9017.61	616.36	3782.25	65.25
Total	2217.1	69780.53	28148.06	22003.87	318.53

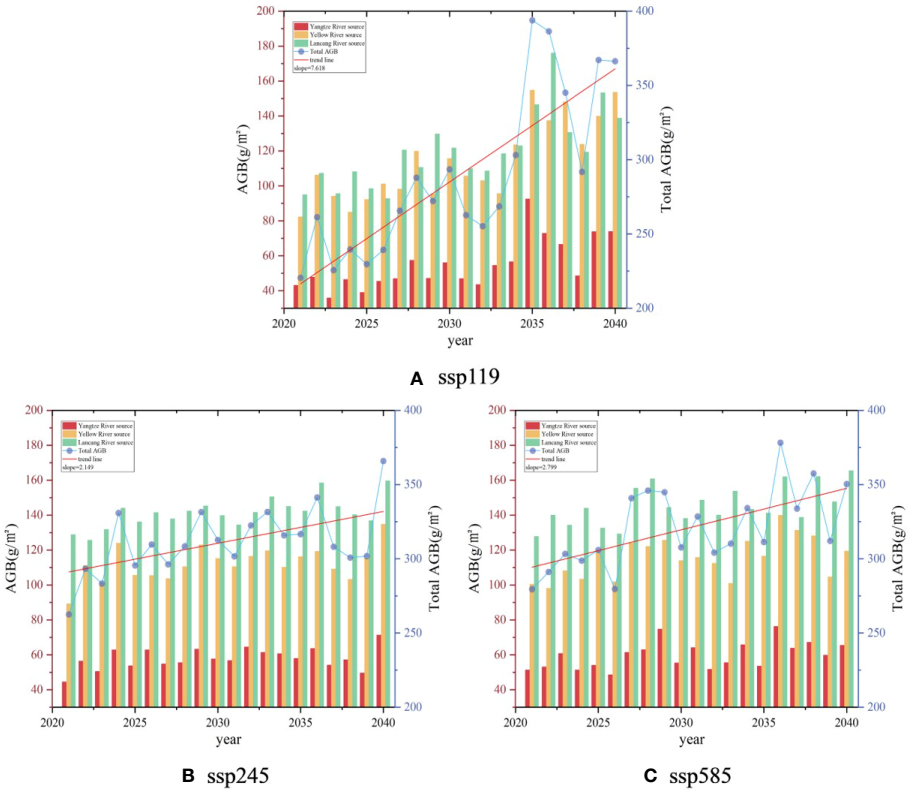

FIGURE 7
Changes in grassland aboveground biomass under various scenarios. **(A)** ssp119 scenarios, **(B)** ssp245 scenarios, **(C)** ssp585 scenarios.

grassland in the Yangtze River source park peaked at 92.55 g/m². In the subsequent years, an average AGB of approximately 60 g/m² was maintained, which was markedly higher than the period from 2020 to 2034. The Yellow River source park showed an average grass biomass of 113.79 g/m² over 20 years, with 101.29 g/m² from 2020 to 2035 and a peak of 142.93 g/m² from 2035 to 2040. The Lancang River source park had the highest average grassland AGB of 120.24 g/m² over the 20-year period, displaying a dynamic upward trend, with a peak of 92.55 g/m² in the subsequent years. That was a 33.19% increase from 2031 to 2035.

Under the ssp245 scenario, the mean grassland AGB in TRS National Park increased at a lower rate than in ssp119, showing a fluctuating upward trend. In this scenario, the Yangtze River source park peaked at 71.37 g/m² in 2040, with a mean value of 57.29 g/m² from 2020 to 2039, showing a steep increase between 2039 and 2040. The mean value of grass biomass in the Yellow River source park remained relatively stable at 112.17 g/m² over the 20 years, ranging from 89.20 g/m² to 134.83 g/m². In that scenario, the mean value of grassland AGB in the Lancang River source park exceeded that of the other 2 parks, with a mean value of 141.36 g/m², marking a 21.25 g/m² increase compared to the period from 2015 to 2020, accounting for 17.59% of the total.

Under the ssp585 scenario, the mean grassland AGB in the Yangtze River source park averaged 59.87 g/m² over 20 years, reaching a peak of 76.30 g/m² in 2036. The Yellow River source park showed an average grassland AGB of 115.60 g/m² over 20 years, with occasional lower values in 2021, 2022, and 2033, whereas the remaining years consistently exceeded 100 g/m². In the Lancang River source park, the ssp585 scenario showed an increase in the mean grassland AGB, with a minimum value of 129.26 g/m² and an average of 145.49 g/m². That indicated that temperature increases had a more pronounced effect on grassland AGB in the Lancang River source park than in the Yellow River and Yangtze River source parks.

4 Discussion

4.1 Factors affecting the accuracy of grassland aboveground biomass inversion models

Machine learning algorithms offer clear advantages over traditional simple and multivariate linear regression models, because they excel in capturing and characterizing the relation between grassland AGB and its influencing factors. When constructing models, it became evident that relying solely on a single variable like NDVI could not encompass the full spectrum of characteristics within grassland biomass. The complexity of measured grassland AGB data and the presence of multicollinearity among influencing factors further hinder the accurate estimation of grassland AGB through multiple linear regression models, as noted by Zhou et al. (2021).

Among the 4 machine learning algorithms considered, RF was the top performer when assessed using training set accuracy analysis. Following RF, the ranking continued with ANN, DT, and SVM respectively. Its effectiveness in estimating grassland biomass in the TRS region was further substantiated by the findings of Zeng et al. (2021), who found that the RF model outperformed other machine learning models, achieving an impressive correlation coefficient (r) of 0.84 and RMSE of 76.99 g/m^2. Moreover, Zhang J. et al. (2022) also successfully applied the RF model to estimate alpine grassland AGB from 2001 to 2019 in the Tibetan Plateau, which encompasses the TRS region, thereby emphasizing the strong regional representation offered by the RF fitting method.

The machine learning approach effectively captures the nonlinear relation between independent and dependent variables and often yields higher accuracy relative to traditional regression models. However, is not without its challenges, notably the problem of overfitting in practical applications due to noise interference. This concern is further exacerbated when pertaining to studies that use smaller sample sizes and a greater number of variables for fitting, as observed in many contemporary research works (Yu et al., 2021b). To mitigate overfitting, it is crucial to increase the number of samples during the fitting process while simultaneously exercising control over the number of variables. Furthermore, note that the accuracy of machine learning models can also be affected by problems related to the model's physical parameters, as highlighted by Liang et al. (2016). Therefore, optimizing model parameters is another critical and challenging aspect that merits continued exploration and refinement in future research endeavors.

It is essential to recognize that model inversion accuracy is subject to various influencing factors (Qiu et al., 2022). Because the actual sampling data years were 2018 to 2020, and the inversion grass biomass years were 2015 to 2020, the model inversion results were subject to errors caused by the mismatch in the numbers of sampling years. The TRS region, situated on the Tibetan Plateau, has substantial variations in elevation, with different areas being affected by varying elevations and slopes (Liang et al., 2016; Wang L. et al., 2022). The remote sensing estimation method for grassland AGB represents a transition from statistical analysis to growth-process simulation. It involves simulating the grass's growth and development by analyzing the statistical relations among various influencing factors, including environmental, anthropogenic, topographic, and climatic factors. In this intricate process, irregular fluctuations in external factors can significantly affect the precision of grass biomass model construction.

4.2 Impacts of climate change on grassland aboveground biomass

Temperature and precipitation fluctuations directly influence the supply and demand of water and heat crucial for grass growth. Moreover, climate factors can induce alterations in the attributes of grassland vegetation by affecting the transformation of biological conditions like soil (Chi et al., 2021; Shi et al., 2023).

Future global warming will alter soil temperature and moisture levels (Pei et al., 2023). Research indicates that temperature determines grassland growth, with higher temperatures promoting vegetation growth and development (Xu and Li, 2021). Precipitation also has a broad spectrum of effects on grass vegetation characteristics. It influences the interaction between plants and soil microorganisms, leading to changes in vegetation biomass distribution (Zhang and Xi, 2021). Moreover, there is an asynchronous relation between grassland biomass and changes in precipitation. Zhang et al. (2023) researched moisture conditions affecting both the aboveground and belowground biomasses of grasslands during different stages of vegetation flowering and fruiting. Wang Q. et al. (2022) found that increased temperatures have a significant effect on the biomass and species diversity of degraded grasslands in their natural recovery state, although they have little effect on natural grasslands. Therefore, restoring degraded grasslands might become more challenging under future warming scenarios. To address the degradation trend observed in the grasslands of the TRS National Park, sustainable grazing management practices should be implemented, grassland restoration projects advanced, and proactive measures taken to protect and enhance biodiversity to ensure the health and sustainability of the grasslands.

This study explored the relation between grass biomass and temperature and precipitation within the TRS National Park area. The relations among average monthly temperature, monthly precipitation, and grassland AGB were constructed based on sample data (Figure 8). It was observed that when precipitation was below 90 mm, the average grassland AGB remained below 136.6 g/m2 regardless of temperature changes. In the range of 90–120 mm of precipitation and temperatures ranging from 9°C to 12°C, the grassland AGB increased with rising temperatures. The peak grassland AGB was reached when precipitation was approximately 95 mm, and the temperature was approximately 11°C. This suggests that grassland AGB increases with both precipitation and temperature under favorable climatic conditions. In the ssp585 scenario, grassland AGB increased more substantially with rising temperature and precipitation compared to the ssp119 and ssp245 scenarios. Precipitation appeared to have a greater influence than

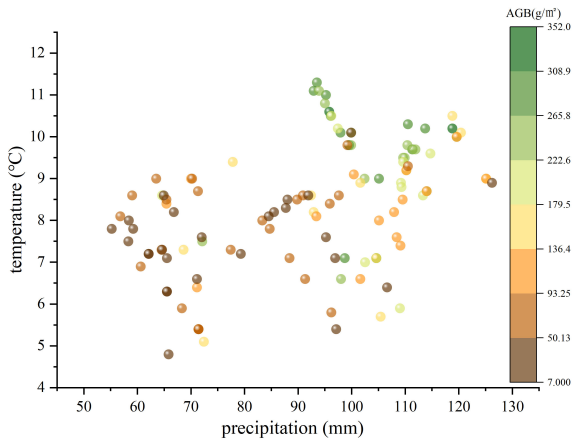

FIGURE 8
Relation between mean monthly temperature, mean monthly precipitation, and grassland aboveground biomass.

temperature change, mainly because, at lower temperatures, increasing precipitation led to more grassland AGB. However, the relation between temperature change and grassland AGB was weaker under lower precipitation conditions. Wu W. et al. (2023) also demonstrated that climate factors have varying effects in Inner Mongolia and the Tibetan Plateau, with increased precipitation positively affecting grassland material production, while increased temperature has varying effects in different regions, both promoting and suppressing scenarios. In the context of global warming, most of the extreme climate indicators have risen in the TRS region, the frequency of extreme heat events has increased, and the frequency of extreme precipitation is higher than in other regions of the globe (Jin et al., 2020). To address the challenge of climate warming in the TRS region, key measures to improve the sustainability of agriculture and animal husbandry, strengthen water resource management, and raise awareness of ecological protection are required to ensure the health and balance of grassland ecosystems.

5 Conclusion

This paper delves into the practicality of various remote sensing inversion models for estimating grassland AGB, using actual sampling points and remote sensing data. The analysis covers changes in grassland AGB within the TRS National Grassland from 2015 to 2020, forecasts future biomass trends, and examines the potential influence of climate change on grassland AGB. The key findings can be summarized as follows:

(1) Grassland AGB strongly correlates with vegetation indices, with the highest correlation coefficient observed with the NDVI. Machine learning models proved more accurate in estimating grassland AGB in the TRS region than traditional linear regression models. Among the machine learning methods, the RF fitting approach yielded the highest accuracy, with a test set coefficient of determination reaching 0.722, making it well suited for grassland AGB analysis in TRS.

(2) From 2015 to 2020, the mean grassland AGB in TRS National Park showed a continuous upward trajectory characterized by a gradual increase from northwest to southeast. The analysis of grassland AGB trend changes revealed a predominant pattern of slight recovery and stabilization, with some areas experiencing slight deterioration. Notably, the areas displaying significant recovery or deterioration were limited. For degraded grassland areas, measures such as vegetation restoration, improved grazing management, and soil protection should be taken to restore and maintain the ecological health of grasslands.

(3) The grassland AGB in TRS National Park consistently displayed fluctuating and increasing trends across three future climate change scenarios (ssp119, ssp245, and ssp585). Apart from geographic factors, the effects of temperature and precipitation on grassland AGB proved to be more pronounced. Within specific ranges, grassland AGB values also increased as temperatures continued to increase and precipitation grew. Notably, the growth rate was particularly evident under conditions of 100–120 mm of precipitation and temperatures ranging from 9°C to 12°C. Global warming is expected to further drive the rise in grassland AGB values. Proactive measures must be taken to protect grasslands in the context of global warming. Those measures include implementing sustainable grassland management methods and enacting policies focused on preserving grasslands to mitigate the effect of climate change on these ecosystems.

Data availability statement

The original contributions presented in the study are included in the article/supplementary material. Further inquiries can be directed to the corresponding authors.

Author contributions

HH: Data curation, Writing – original draft. HY: Methodology, Writing – review & editing. ZR: Data curation, Writing – original draft. YY: Conceptualization, Methodology, Writing – original draft. PL: Writing – review & editing.

Funding

The author(s) declare financial support was received for the research, authorship, and/or publication of this article. The research was funded by the Strategic Priority Research Program of the Chinese Academy of Sciences (Grant No. XDA23060601), National Natural Science Foundation of China (U20A2088), Sichuan Science and Technology Program (Grant Nos. 2022YFS0494 and 2019YFS0467), Sichuan Natural Resources Scientific Research Project (Kj-2021-12).

Acknowledgments

The authors thank the Northwest Institute of Plateau Biology, Chinese Academy of Sciences and the Three-River-Source National Park Administration for providing grass sampling data.

Conflict of interest

The authors declare that the research was conducted in the absence of any commercial or financial relationships that could be construed as a potential conflict of interest.

Publisher's note

References

Alvarez-Mendoza, C. I., Guzman, D., Casas, J., Bastidas, M., Polanco, J., Valencia-Ortiz, M., et al. (2022). Predictive modeling of above-ground biomass in brachiaria pastures from satellite and UAV imagery using machine learning approaches. *Remote Sens.* 14 (22), 5870. doi: 10.3390/rs14225870

Amarsaikhan, E., Erdenebaatar, N., Amarsaikhan, D., Otgonbayar, M., and Bayaraa, B. (2023). Estimation and mapping of pasture biomass in Mongolia using machine learning methods. *Geocarto Int.* 38 (1), 1-19. doi: 10.1080/10106049.2023.2195824

Chapin, F. S., Sala, O. E., and Huber-Sannwald, E. (2013). *Global biodiversity in a changing environment: scenarios for the 21st century* (German: Springer Science & Business Media).

Chapungu, L., Nhamo, L., and Gatti, R. C. (2020). Estimating biomass of savanna grasslands as a proxy of carbon stock using multispectral remote sensing. *Remote Sens. Applications: Soc. Environ.* 17, 100275. doi: 10.1016/j.rsase.2019.100275

Chi, Q. D., Wang, J., Liu, Y. Q., Zhao, J., Cheng, Y., Cai, Z. C., et al. (2021). Varying interactive effects of climate, soil properties, and gross nitrogen dynamics on biomass production between the topsoil and the subsoil in natural grassland ecosystems. *Eur. J. Soil Biol.* 104, 103299. doi: 10.1016/j.ejsobi.2021.103299

Fan, X., He, G., Zhang, W., Long, T., Zhang, X., Wang, G., et al. (2022). Sentinel-2 images based modeling of grassland above-ground biomass using random forest algorithm: A case study on the Tibetan Plateau. *Remote Sens.* 14 (21), 5321. doi: 10.3390/rs14215321

Gao, X., Dong, S., Li, S., Xu, Y., Liu, S., Zhao, H., et al. (2020). Using the random forest model and validated MODIS with the field spectrometer measurement promote the accuracy of estimating aboveground biomass and coverage of alpine grasslands on the Qinghai-Tibetan Plateau. *Ecol. Indic.* 112, 106114. doi: 10.1016/j.ecolind.2020.106114

Ge, J., Hou, M., Liang, T., Feng, Q., Meng, X., Liu, J., et al. (2022). Spatiotemporal dynamics of grassland aboveground biomass and its driving factors in North China over the past 20 years. *Sci. Total Environ.* 826, 154226. doi: 10.1016/j.scitotenv.2022.154226

Hurtt, G. C., Chini, L., Sahajpal, R., Frolking, S., Bodirsky, B. L., Calvin, K., et al. (2020). Harmonization of global land use change and management for the period 850–2100 (LUH2) for CMIP6. *Geosci. Model. Dev.* 13 (11), 5425–5464. doi: 10.5194/gmd-13-5425-2020

Jia, W., Liu, M., Yang, Y., He, H., Zhu, X., Yang, F., et al. (2016). Estimation and uncertainty analyses of grassland biomass in Northern China: Comparison of multiple remote sensing data sources and modeling approaches. *Ecol. Indic.* 60, 1031–1040. doi: 10.1016/j.ecolind.2015.09.001

Jiang, F., Zhang, J. J., Song, P. F., Qin, W., Wang, H. J., Cai, Z. Y., et al. (2022). Identifying priority reserves favors the sustainable development of wild ungulates and the construction of Sanjiangyuan National Park. *Ecol. And Evol.* 12 (11), e9464. doi: 10.1002/ece3.9464

Jiang, L., Cui, T., Liu, H., and Xue, Y. (2022). Remote sensing monitoring and analytical evaluation of grasslands in the muli region of Qinghai, China from 2000 to 2021. *Land* 11 (10), 1733. doi: 10.3390/land11101733

Jin, Z., You, Q., Wu, F., Sun, B., and Cai, Z. (2020). Changes of climate and climate extremes in the Three-Rivers Headwaters' Region over the Tibetan Plateau during the past 60 years. *Trans. Atmospheric Sci.* 43 (6), 1042–1055. doi: 10.13878/j.cnki.dqkxxb.20201008001

Li, C., De Jong, R., Schmid, B., Wulf, H., and Schaepman, M. E. (2019). Spatial variation of human influences on grassland biomass on the Qinghai-Tibetan plateau. *Sci. Total Environ.* 665, 678–689. doi: 10.1016/j.scitotenv.2019.01.321

Li, M., Wu, J., Song, C., He, Y., Niu, B., Fu, G., et al. (2019). Temporal variability of precipitation and biomass of alpine grasslands on the Northern Tibetan Plateau. *Remote Sens.* 11 (3), 360. doi: 10.3390/rs11030360

Liang, T., Yang, S., Feng, Q., Liu, B., Zhang, R., Huang, X., et al. (2016). Multi-factor modeling of above-ground biomass in alpine grassland: A case study in the Three-River Headwaters Region, China. *Remote Sens. Environ.* 186, 164–172. doi: 10.1016/j.rse.2016.08.014

Liu, W., Xu, C., Zhang, Z., De Boeck, H., Wang, Y., Zhang, L., et al. (2023). Machine learning-based grassland aboveground biomass estimation and its response to climate variation in Southwest China. *Front. Ecol. Evol.* 11. doi: 10.3389/fevo.2023.1146850

Liu, Z., Qiu, H., Zhu, Y., Liu, Y., Yang, D., Ma, S., et al. (2022). Efficient identification and monitoring of landslides by time-series InSAR combining single- and multi-look phases. *Remote Sens.* 14 (4), 1026. doi: 10.3390/rs14041026

Ma, S., Qiu, H., Zhu, Y., Yang, D., Tang, B., Wang, D., et al. (2023). Topographic Changes, Surface Deformation and Movement Process before, during and after a Rotational Landslide. *Remote Sens.* 15 (3), 662. doi: 10.3390/rs15030662

Ma, B. R., Zeng, W. H., Xie, Y. X., Wang, Z. Z., Hu, G. Z., Li, Q., et al. (2022). Boundary delineation and grading functional zoning of Sanjiangyuan National Park based on biodiversity importance evaluations. *Sci. Total Environ.* 825, 154068. doi: 10.1016/j.scitotenv.2022.154068

Morais, T. G., Teixeira, R. F. M., Figueiredo, M., and Domingos, T. (2021). The use of machine learning methods to estimate aboveground biomass of grasslands: A review. *Ecol. Indic.* 130, 108081. doi: 10.1016/j.ecolind.2021.108081

Pei, Y., Qiu, H., Zhu, Y., Wang, J., Yang, D., Tang, B., et al. (2023). Elevation dependence of landslide activity induced by climate change in the eastern Pamirs. *Landslides* 20 (6), 1115–1133. doi: 10.1007/s10346-023-02030-w

Popp, A., Calvin, K., Fujimori, S., Havlik, P., Humpenöder, F., Stehfest, E., et al. (2017). Land-use futures in the shared socio-economic pathways. *Global Environ. Change* 42, 331–345. doi: 10.1016/j.gloenvcha.2016.10.002

Qiu, H., Zhu, Y., Zhou, W., Sun, H., He, J., and Liu, Z. (2022). Influence of DEM resolution on landslide simulation performance based on the Scoops3D model. *Geomatics Natural Hazards Risk* 13 (1), 1663–1681. doi: 10.1080/19475705.2022.2097451

Ren, H., Zhou, G., and Zhang, F. (2018). Using negative soil adjustment factor in soil-adjusted vegetation index (SAVI) for aboveground living biomass estimation in arid grasslands. *Remote Sens. Environ.* 209, 439–445. doi: 10.1016/j.rse.2018.02.068

Shi, Y., Gao, J., Li, X., Brierley, G., Lin, C., and Ma, X. (2023). Spatiotemporal variability of alpine meadow aboveground biomass and sustainable grazing in light of climate warming. *Rangeland Ecol. Manage.* 90, 64–77. doi: 10.1016/j.rama.2023.05.009

Shu, K., Gao, X., Qian, D., Zhao, L., Li, Q., and Dai, L. (2022). Relationship between biomass and biodiversity of degraded grassland in the sanjiangyuan region of Qinghai–Tibet Plateau. *Diversity* 14 (11), 1002. doi: 10.3390/d14111002

Wang, Y., Qin, R., Cheng, H., Liang, T., Zhang, K., Chai, N., et al. (2022). Can machine learning algorithms successfully predict grassland aboveground biomass? *Remote Sens.* 14 (16), 3843. doi: 10.3390/rs14163843

Wang, L., Qiu, H., Zhou, W., Zhu, Y., Liu, Z., Ma, S., et al. (2022). The post-failure spatiotemporal deformation of certain translational landslides may follow the pre-failure pattern. *Remote Sens.* 14 (10), 2333. doi: 10.3390/rs14102333

Wang, Q., Zheng, J., Zhao, M., and Zhang, J. (2022). Effects of warming on early restoration of degraded grassland in desert steppe. *Acta Agrestia Sin.* 30 (5), 1077–1085. doi: 10.11733/j.issn.1007-0435.2022.05.007

Wijesingha, J., Moeckel, T., Hensgen, F., and Wachendorf, M. (2019). Evaluation of 3D point cloud-based models for the prediction of grassland biomass. *Int. J. Appl. Earth Observation Geoinformation* 78, 352–359. doi: 10.1016/j.jag.2018.10.006

Wu, N., Liu, G., Wuyun, D., Yi, B., Du, W., and Han, G. (2023). Spatial-temporal characteristics and driving forces of aboveground biomass in desert steppes of inner Mongolia, China in the past 20 years. *Remote Sens.* 15 (12), 3097. doi: 10.3390/rs15123097

Wu, W., Sun, R., Liu, L., Liu, X., Yu, H., Ma, Q., et al. (2023). Precipitation consistently promotes, but temperature inversely drives, biomass production in temperate vs. *alpine grasslands. Agric. For. Meteorology* 329, 109277. doi: 10.1016/j.agrformet.2022.109277

Xu, M., and Li, X. (2021). Review of response of grassland community stability to global warming based on correlation between species biodiversity and biomass. *Acta Botanica Boreali-Occidentalia Sin.* 41 (2), 348–358. doi: 10.7606/j.issn.1000-4025.2021.02.0348

Xu, C., Liu, W., Zhao, D., Hao, Y., Xia, A., Yan, N., et al. (2022). Remote sensing-based spatiotemporal distribution of grassland aboveground biomass and its response to climate change in the Hindu Kush Himalayan region. *Chin. Geographical Sci.* 32 (5), 759–775. doi: 10.1007/s11769-022-1299-8

Xu, D., Wang, C., Chen, J., Shen, M., Shen, B., Yan, R., et al. (2021). The superiority of the normalized difference phenology index (NDPI) for estimating grassland aboveground fresh biomass. *Remote Sens. Environ.* 264, 112578. doi: 10.1016/j.rse.2021.112578

Yang, S., Feng, Q., Liang, T., Liu, B., Zhang, W., and Xie, H. (2018). Modeling grassland above-ground biomass based on artificial neural network and remote sensing in the Three-River Headwaters Region. *Remote Sens. Environ.* 204, 448–455. doi: 10.1016/j.rse.2017.10.011

Yu, H., Liu, B.-T., Wang, G.-X., Zhang, T.-Z., Yang, Y., Lu, Y.-Q., et al. (2021a). Grass-livestock balance based grassland ecological carrying capability and sustainable strategy in the Yellow River Source National Park, Tibet Plateau, China. *J. Mountain Sci.* 18 (8), 2201–2211. doi: 10.1007/s11629-020-6087-2

Yu, H., Wang, G., Yang, Y., Bai, Z., Liu, B., Zhang, T., et al. (2020a). Enhancing ecological value through sustainable food supply of grasslands in the Three-River-Source National Park, Tibet Plateau, China. *Ecosystem Serv.* 46, 101218. doi: 10.1016/j.ecoser.2020.101218

Yu, H., Wang, G., Yang, Y., and Lu, Y. (2020b). Concept of grassland green carrying capacity and its application framework in national park. *Acta Ecologica Sin.* 40 (20), 7248–7254. doi: 10.5846/stxb201906171276

Yu, H., Wu, Y., Niu, L., Chai, Y., Feng, Q., Wang, W., et al. (2021b). A method to avoid spatial overfitting in estimation of grassland above-ground biomass on the Tibetan Plateau. *Ecol. Indic.* 125, 107450. doi: 10.1016/j.ecolind.2021.107450

Zeng, N., Ren, X., He, H., Zhang, L., Li, P., and Niu, Z. (2021). Estimating the grassland aboveground biomass in the Three-River Headwater Region of China using machine learning and Bayesian model averaging. *Environ. Res. Lett.* 16 (11), 114020. doi: 10.1088/1748-9326/ac2e85

Zeng, N., Ren, X., He, H., Zhang, L., Zhao, D., Ge, R., et al. (2019). Estimating grassland aboveground biomass on the Tibetan Plateau using a random forest algorithm. *Ecol. Indic.* 102, 479–487. doi: 10.1016/j.ecolind.2019.02.023

Zhang, J., Fang, S., and Liu, H. (2022). Estimation of alpine grassland above-ground biomass and its response to climate on the Qinghai-Tibet Plateau during 2001 to 2019. *Global Ecol. Conserv.* 35, e02065. doi: 10.1016/j.gecco.2022.e02065

Zhang, Y., Huang, J., Jin, Y., Wang, J., Zhao, Y., Feng, Q., et al. (2022). Estimation of grasslands aboveground biomass: A review. *Acta Agrestia Sin.* 30 (4), 850–858. doi: 10.11733/j.issn.1007-0435.2022.04.010

Zhang, F., Li, H., Yi, L., Luo, F., Zhang, G., Wang, C., et al. (2022). Spatial response of topsoil organic carbon, total nitrogen, and total phosphor content of alpine meadows to grassland degradation in the Sanjiangyuan National Park. *Acta Ecologica Sin.* 42 (14), 5586–5592. doi: 10.5846/stxb202106111566

Zhang, B., Min, Q., Jiao, W., Liu, M., He, S., Liu, X., et al. (2019). Comparative study between Three-River-Source National Park of China and Jiri national park of Korea. *Acta Ecologica Sin.* 39 (22), 8271–8285. doi: 10.5846/stxb201903190511

Zhang, H., Tang, Z., Wang, B., Meng, B., Qin, Y., Sun, Y., et al. (2022). A non-destructive method for rapid acquisition of grassland aboveground biomass for satellite ground verification using UAV RGB images. *Global Ecol. Conserv.* 33, e01999. doi: 10.1016/j.gecco.2022.e01999

Zhang, C. H., and Xi, N. X. (2021). Precipitation changes regulate plant and soil microbial biomass via plasticity in plant biomass allocation in grasslands: A meta-analysis. *Front. Plant Sci.* 12. doi: 10.3389/fpls.2021.614968

Zhang, L., Xiao, P., Yu, H., Zhao, T., Liu, S., Yang, L., et al. (2022). Effects of climate changes on the pasture productivity from 1961 to 2016 in sichuan yellow river source, Qinghai-Tibet Plateau, China. *Front. Ecol. Evol.* 10. doi: 10.3389/fevo.2022.908924

Zhang, Y., Zhou, T., Liu, X., Zhang, J., Xu, Y., Zeng, J., et al. (2023). Crucial roles of the optimal time-scale of water condition on grassland biomass estimation on Qinghai–Tibet Plateau. *Sci. Total Environ.* 905, 167210. doi: 10.1016/j.scitotenv.2023.167210

Zheng, D., Hao, S., Lv, L., Xu, W., Wang, Y., and Wang, H. (2020). Spatial-temporal change and trade-off/synergy relationships among multiple ecosystem services in Three-River-Source National Park. *Geographical Res.* 39 (1), 64–78. doi: 10.11821/dlyj020180898

Zhou, W., Li, H., Xie, L., Nie, X., Wang, Z., Du, Z., et al. (2021). Remote sensing inversion of grassland aboveground biomass based on high accuracy surface modeling. *Ecol. Indic.* 121, 107215. doi: 10.1016/j.ecolind.2020.107215

Zhou, Y., Liu, T., Batelaan, O., Duan, L., Wang, Y., Li, X., et al. (2023). Spatiotemporal fusion of multi-source remote sensing data for estimating aboveground biomass of grassland. *Ecol. Indic.* 146, 109892. doi: 10.1016/j.ecolind.2023.109892

frontiers | Frontiers in Ecology and Evolution

TYPE Original Research
PUBLISHED 13 December 2023
DOI 10.3389/fevo.2023.1330749

OPEN ACCESS

EDITED BY
Haijun Qiu,
Northwest University, China

REVIEWED BY
Lei Huang,
Tsinghua University, China
Jie Tao,
Zhengzhou University, China

*CORRESPONDENCE
Junhua Li
ljhyym@126.com

RECEIVED 31 October 2023
ACCEPTED 21 November 2023
PUBLISHED 13 December 2023

CITATION
Xu L, Li J, Xu H, Zhang X, Lai R, Zhang X and Gao X (2023) Evolution and drivers of secondary suspended rivers in typical wandering sections of the lower Yellow River from 1960–2021.
Front. Ecol. Evol. 11:1330749.
doi: 10.3389/fevo.2023.1330749

Evolution and drivers of secondary suspended rivers in typical wandering sections of the lower Yellow River from 1960–2021

Linjuan Xu[1], Junhua Li[1]*, Haifan Xu[1,2], Xiangping Zhang[1], Ruixun Lai[1], Xiang Zhang[1] and Xiangyu Gao[1,3]

[1]Key Laboratory of Lower Yellow River Channel and Estuary Regulation, Ministry of Water Resources (MWR), Yellow River Institute of Hydraulic Research, Yellow River Conservancy Commission (YRCC), Zhengzhou, China, [2]North China University of Water Resources and Electric Power, School of Water Conservancy, Zhengzhou, China, [3]School of Water Resources and Transportation, Zhengzhou University, Zhengzhou, China

The secondary suspended river increases the probability of the occurrence of "Heng river", "Xie river" and "Gun river" in the lower Yellow River, and is the main factor threatening the safety of human life and property in the Yellow River levee and beach area. Here, the Dongbatou–Gaocun section of the severe secondary suspended river in the lower Yellow River was taken as the research object. The trend and periodicity of the evolution characteristics of the secondary suspended river in the study area from 1960–2021 were systematically analyzed using the Theil-Sen estimator and wavelet analysis, and the factors influencing its development were quantitatively explored. Over the past 62 years, development of secondary suspended rivers can be divided into four stages: initial formation (1960–1973), slow development (1974–1986), rapid development (1987–1999) and stable (2000–2021) periods. The evolution period of the beach transverse gradient differed significantly before and after operation of Xiaolangdi Reservoir commenced, prior to which there was a first main period of 31 years followed by a second main period of 21 years. Development of secondary suspended rivers was primarily related to floodplain flooding and human activity. When the inflow sediment coefficient of a floodplain flood (ζ) was < 0.04 and the floodplain coefficient was < 1.29, the secondary suspended river was relieved; when ζ > 0.04 or ζ < 0.04 and the floodplain coefficient was > 1.29, the secondary suspended river was intensified. The production levees have exacerbated development of secondary suspended rivers to some extent.

KEYWORDS

secondary suspended rivers, evolution trend, beach transverse slope, wavelet analysis, driver analysis, lower Yellow River, wandering section

1 Introduction

The Yellow River has characteristics such as a small amount of water and a large amount of sediment", various sources of water and sediment, and inconsistent water-sediment relationships (Liao, 2003). The lower Yellow River is in a strong siltation state because of the large amount of sediment (Hu and Zhang, 2006), and with annual average elevation of 0.05–0.10 m, the current riverbed is generally 4–6 m higher than the ground on both sides of the back river. Hence, the lower Yellow River has become a world-renowned "suspended river" (Jiang et al., 2003; Sun et al., 2008). Since the 1960s, with construction and operation of Sanmenxia Reservoir and construction of production levees (Gao et al., 2004; Yan et al., 2006), the water-sediment relationship in the lower Yellow River has become extremely disharmonious, and the downstream riverbed has continued to reduce in size. The main river channel gradually rises above the beach near the levee, forming a secondary suspended river with a high channel, low beach, and low levee root (Figure 1). Since the middle to late 1980s, the Yellow River has been in a relatively dry season. Downstream runoff has decreased, industrial and agricultural water use has increased significantly, the probability of deluge has decreased, the flood floodplain has reduced beach siltation, and the process of low flow has greatly increased. This changed the horizontal siltation distribution of the sediment that occurs under natural conditions, and the elevation difference between the beaches and channels further reduced; thus, the secondary suspended river is extremely severe.

Since operation of Xiaolangdi Reservoir commenced in 2000, significant changes have occurred in the process of water and sediment entering the downstream area. Sedimentation of the downstream has been reduced; however, the situation of high channel, low beach, and low levee root remains. The most severely affected river section extends from Dongbatou–Taochengpu (Shan and Wang, 2021). The entire river water and sediment regulation with Xiaolangdi Reservoir as the core has slowed development of the secondary suspended river to a certain extent. However, there are problems such as insufficient subsequent momentum in the water and sediment regulation of Xiaolangdi Reservoir (Zhang et al., 2021). After the sediment retention capacity of Xiaolangdi Reservoir is reached, without the use of other backbone projects, the lower Yellow River will once again be severely silted and raised (YRCC, 2013) and the secondary suspended river will develop rapidly. In the event of a deluge, when the horizontal slope of the river beach is much greater than the vertical slope, the overflow ratio in the beach area will increase, which will directly threaten the safety of the Yellow River levee and human lives and property in the beach area. Therefore, there is an urgent need to study the evolution mechanism of secondary suspended rivers.

Since the early 1970s, secondary suspended rivers have formed in the lower Yellow River, and extensive research has been conducted on the causes, which are believed to be closely related to changes in the inflow, sediment, and boundary conditions of the river (Hu and Zhang, 2006). In terms of incoming water and sediment conditions, the amount of water and sediment entering the downstream has decreased due to human activities (Duanmu and Zhang, 2003; Liu, 2020), particularly with reductions in peak flow and flood frequency, which greatly reduces the probability of floodplain floods with a siltation beach and scouring channel. Furthermore, long-term low flow causes sedimentation and a reduction in size of the riverbed and accelerates development of secondary suspended rivers (Yan et al., 2006; Yang et al., 2006). Hyper-concentrated floods promote development of secondary suspended rivers (Jiang et al., 2003). Excessive use of Yellow River water has caused the total amount of water diverted from the Yellow River to exceed its carrying capacity, and production and social water use have long been occupying a large amount of sediment flushing water, which has also promoted development of secondary suspended rivers (Pang, 2005). In terms of channel boundary conditions, although production levees have alleviated inundation losses in the beach area to some extent, they have hindered water and sediment exchange in the beach and channel, accelerating development of secondary suspended rivers (Zhang, 2004; Pang, 2005; Yang et al., 2006; Zhang et al., 2018). To eliminate secondary suspended rivers, it is necessary to break down production levees (Zhang, 2004; Pang, 2005). Jiang et al. (1999) conducted extensive research on the adjustment laws of the vertical and horizontal sections, water and sediment transport, and exchange characteristics of the lower Yellow River, and highlighted that the lateral imbalance of sediment transport in the channel gradually formed secondary suspended rivers. Sun et al. (2008) established a

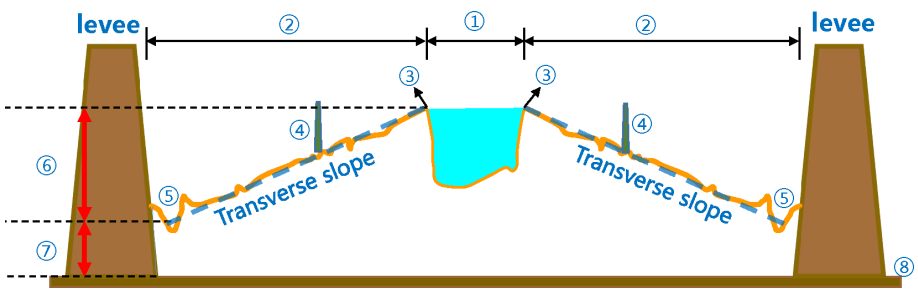

FIGURE 1
Schematic diagram of the secondary suspended river in the lower Yellow River: ① Main channel; ② beach area; ③ beach lip; ④ production levee; ⑤ channel at the root of the levee; ⑥ secondary suspended river; ⑦ primary suspended river; ⑧ ground behind levee.

planar two-dimensional water and sediment mathematical model for development of the secondary suspended river in the lower Yellow River and studied the impacts of the suspended difference in the secondary suspended river on flood routing, beach and channel flow structures, and flood discharge along the levee. The frequent occurrence of extreme weather worldwide (Pei et al., 2023) has also led to some geological disasters (Wang et al., 2022; Ma et al., 2023). Time series analysis is conducive to disaster identification and monitoring (Liu et al., 2022), and many experts have established corresponding prediction models (Qiu et al., 2022). However, there are still shortcomings in time series analysis of secondary suspended rivers.

Although the water and sediment regulations of Xiaolangdi have alleviated the secondary suspended river situation in the lower Yellow River to some extent, the threat of secondary suspended rivers to flood control remains significant, and secondary suspended rivers are receiving increasing attention. The 2021 Yellow River Basin Ecological Protection and High-Quality Development Plan Outline mentions that carrying out secondary suspended river management in the lower Yellow River to reduce the safety risks of the Yellow River levees, and which has put forward higher requirements for secondary suspended river management at the national level. Research on the causes and mechanisms of secondary suspended river formation has mostly been qualitative. However, research on the evolution characteristics of long-term secondary suspended rivers, their development and evolution after operation of Xiaolangdi Reservoir commenced, and the quantitative impact of various factors on secondary suspended rivers, remains relatively weak. Therefore, in the context of increasingly intensified human activities, there is an urgent need to comprehensively study the development and evolution of secondary suspended rivers from a long-term perspective, as well as the quantitative impact of various influencing factors on their formation. In this study, the most severe secondary suspended river section from Dongbatou–Gaocun in the wandering section of the lower Yellow River was selected to analyze the basic parameter evolution characteristics and periodicity of secondary suspended rivers under long-term time-series conditions, determine their severity, and quantitatively analyze and calculate the various factors that caused their development. The research results will have significant implications for managing wandering river channels and downstream flood control and provide theoretical and technical support for scientific management of secondary suspended rivers.

2 Materials and methods

2.1 Study areas

The wandering section of the lower Yellow River starts in Baihe in Mengjin, Henan, and ends in Gaocun in Dongming, Shandong. The river has a total length of 299 km, a wide and shallow channel, and significant erosion and sedimentation. The main stream oscillates frequently; the distance between the main levees on both sides is generally 5–10 km, with the widest levee distance exceeding 20 km. The Dongbatou–Gaocun section is 70 km long (Figure 2) and has a beach area of 402 km. The flood discharge width decreased from 10.5 km before construction of the production levee to 4.2 km after its construction. In the late 1990s, the bank-full discharge in this section of the river decreased to 2000 m^3/s on one occasions, and the river was heavily silted up. Under the influence of various factors, the entire Dongbatou–Gaocun section forms a secondary suspended river, which is one of the most severe secondary suspended river situations (Jiang et al., 2006).

2.2 Study methods

2.2.1 Data sources

Based on the large-section topography data of the Dongbatou–Gaocun section from 1960–2021, the elevations and starting distances of the beach lip and beach surface near the levees were determined, and the elevation difference and beach width between the beach lip and beach surface near the levees were calculated, followed by calculation of the beach transverse slope. The transverse slope of the beach is the ratio of the elevation difference between the beach lip and beach surface adjacent to the levee to the beach width. Taking the Gaocun section (1996) as an example, the calculation process of lateral slope is shown in Figure 3. Due to the fact that the lowest point elevation at the levee root cannot reflect the true transverse slope of the beach, the average elevation of the levee root within a certain range (300m) is used as the levee root elevation for this study. The main channel of the observation section set up in the research river section is mostly located on the right bank, which leads to the width of the right bank beach being too small and abnormal values in the transverse slope. To avoid this problem, we take the left bank as the research object. The system sorted and calculated the annual water volume and sediment volume of Huayuankou station in the lower Yellow River from 1960–2021, as well as the water volume, sediment volume, peak discharge, and other floodplain flood data. Large-section data were measured by professional departments of the Yellow River Conservancy Commission (YRCC). The water and sediment data of the series of years and floods were obtained from the sediment bulletin of the YRCC and hydrological data of the Yellow River basin. All data were official and of high authority.

2.2.2 Data processing methods

(1) Theil-Sen estimator

The Theil-Sen estimator is a stable non-parametric statistical trend calculation method. Using this method to estimate the linear slope has advantages of high calculation efficiency and insensitivity to measurement errors and discrete group data, and it is widely used in trend analysis of long time-series data (Kong et al., 2022). The formula is as follows:

$$k = Median\left(\frac{x_j - x_i}{j - i}\right), \forall j > i \quad (1)$$

where *Median* represents the median; x_j and x_i are the sample data corresponding to time j and time i ($j > i$), respectively; and k is the degree

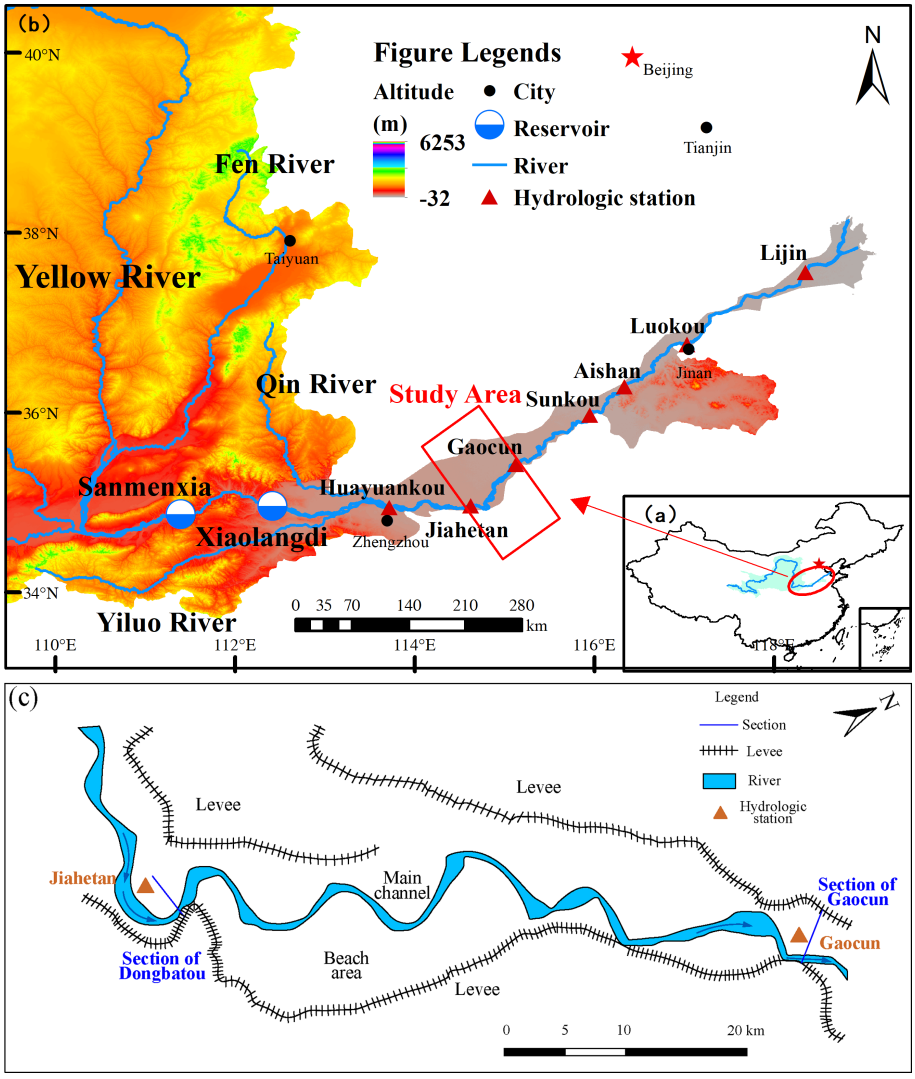

FIGURE 2
Study area location: **(A)** location of the lower Yellow River in China; **(B)** magnified lower Yellow River and location of the study area; **(C)** magnified study area.

of the trend of the time series. When $k > 0$, the time series shows an upward trend, and when $k< 0$, the time series shows a downward trend.

(2) Wavelet analysis

Wavelet analysis is a signal analysis method based on the Fourier transform and developed in the early 1980s. The key to wavelet analysis is selection of the wavelet functions. A complex Morlet (Cmor) wavelet with good resolution in both the time and frequency domains was selected for this study.

Before using the wavelet analysis, the data of each sequence were subjected to anomaly processing, i.e., taking the mean difference between each element in the sequence and the sequence as the anomaly sequence. The amplitude of the wavelet coefficients calculated after leveling is smaller, which better reflects the fluctuation details of the wavelet coefficients (Wang et al., 2006). Because the measured sequence is a finite time series, boundary effects may occur at both ends. To eliminate the boundary effects generated at both ends of the sequence during wavelet transform, the two ends of the anomalous sequence were symmetrically extended (Sun and Luo, 2008). After the calculations were completed, the corresponding added data were deleted.

For wavelet functions that satisfy certain conditions, $\Psi(t)$, the wavelet transform of the time series $f(t) \in L^2$ (R) is:

$$W_f(a,b)=|a|^{-\frac{1}{2}}\int_{-\infty}^{+\infty} f(t)\,\bar{\Psi}\left(\frac{t-b}{a}\right)dt \quad (2)$$

where W_f (a, b) is the wavelet transform coefficient; $f(t)$ is a signal or a flat integrable function; a is the scaling factor; b is the time factor, i.e., the translation of the reaction in time; $\bar{\Psi}$ is the complex conjugate function of Ψ. $W_f(a, b)$ is a binary function that varies with parameters a and b, with b as the abscissa and a as the

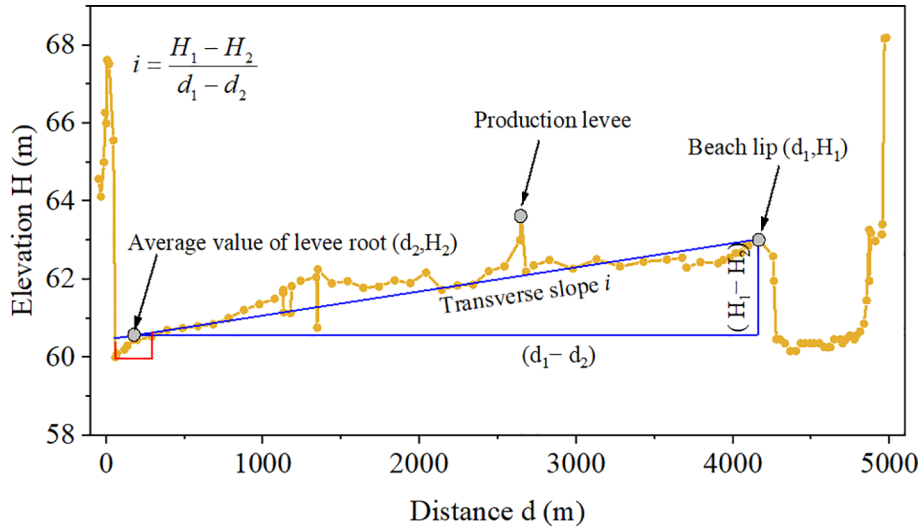

FIGURE 3
Schematic diagram for calculating transverse slope.

ordinate, drawing a three-dimensional surface map W_f, and its projection on the plane is a two-dimensional contour map. The wavelet transform three-dimensional surface map and contour map reflect the time-frequency variation characteristics of the time series. When the scale of a was the same, the wavelet coefficient changed with time, reflecting the variation characteristics of the time series at that scale. By analyzing the wavelet coefficients, the periodic evolution characteristics of a long time series at multiple timescales can be identified (Sang et al., 2013).

The real parts of the Cmor wavelet coefficients reflected periodic changes in the transverse slope time series of the beach at different timescales. The modulus of the wavelet coefficients reflected the distribution of the energy density corresponding to different timescale periods in the time domain. The larger the modulus of the wavelet coefficients, the stronger the periodicity of their corresponding timescale during that time period, and the color mapping in the 3D surface and contour maps is warm. The square of the wavelet coefficient modulus is equivalent to the wavelet energy spectrum, which was used to analyze the oscillation energy of different periods and obtain the limitations of the periods in the time domain at different timescales.

To determine the main timescale of the time series, the square value of the wavelet coefficient modulus was integrated into the time domain to obtain the wavelet variance, as follows:

$$\boldsymbol{Var(a,b)} = \int_{-\infty}^{+\infty} \left| \boldsymbol{W_f(a,b)} \right|^2 \mathbf{d}\boldsymbol{b} \quad (3)$$

where $Var(a,b)$ is the wavelet variance, and the meaning of $W_f(a,b)$ is as described previously.

The process of changing the wavelet variance with the timescale a is called the wavelet variance map. Each peak in the wavelet variance map corresponded to a significant period. When the wavelet variance reaches its maximum value, the scale of the wavelet function most accurately matches the period of the time series, indicating that the periodic oscillation is the strongest at that scale and is referred to as the main period.

3 Results

3.1 Evolution characteristics of secondary suspended rivers

The main characteristics of secondary suspended rivers are the high beach lip elevation and low depression of the levee root. The average elevation of the levee root and average transverse slope of the beach were selected to characterize the development of the secondary suspended river.

3.1.1 Evolution process of average elevation of left-bank beach lip and levee root

Severe sedimentation of the beach lip of the main channel was the direct cause of the formation of the secondary suspended river, and changes in its elevation reflected its evolution characteristics. Figure 4 shows the changes in the average elevations of the levee root and beach lip on the left bank in the Dongbatou–Gaocun section from 1960–2021. Owing to the inconsistent years of layout along the cross sections, the number of cross sections varied in different years. Figure 4 shows that an increase in the number of sections impacted the average levee root and beach lip elevations, which may have increased (e.g., from 1963–1965) or decreased (from 1999–2003). When the impact caused by the unstable period of the cross section was not considered, analyses of the data from other long-term series showed that the average elevations of the left-bank beach lip and levee root had both increased over time, and that the trend of their changes was relatively consistent. Although there was a slight increase in the

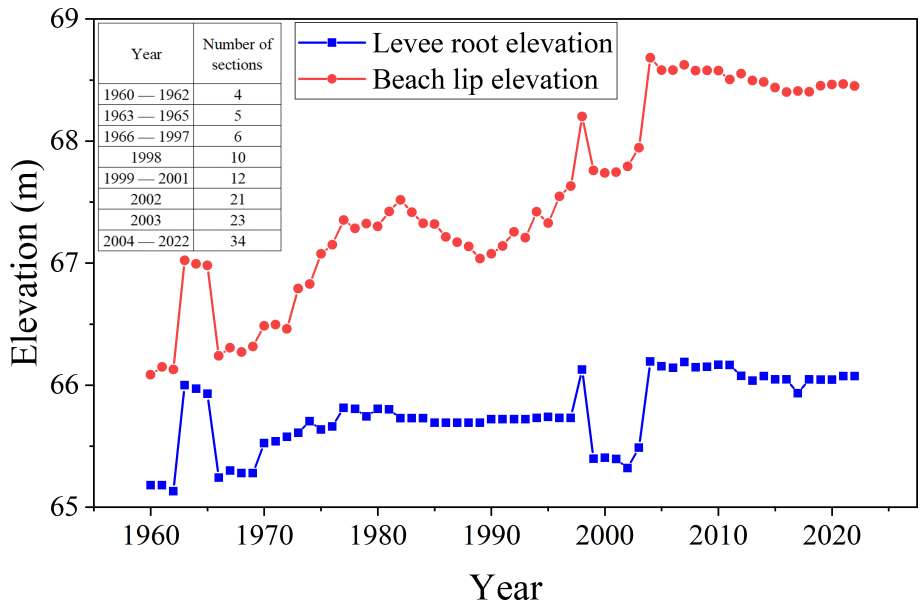

FIGURE 4
Changes in levee root elevation and beach lip elevation.

average elevation of the levee root from 1970–1997, this change was extremely gentle. During this period, the average beach lip elevation changed significantly and increased annually; it decreased after 1983, and increased gradually after 1989. This indicated that the floodplain floods during this period only caused sedimentation at the beach lip with minimal impact on the levee roots. After 2004, the cross-sectional data remained stable, with both the average beach lip elevations and levee root being relatively high and the changes being relatively stable.

3.1.2 Evolution process of average transverse slope on the left-bank beach

The transverse slope of a beach is an important parameter that reflects the development level of secondary suspended rivers and an important indicator of the degree of flood risk in river channels. Therefore, variation in the transverse slope was an important manifestation of the evolution of the riverbed in the lower Yellow River.

Figure 5 shows the evolution of the average transverse slope of the left-bank beach in the Dongbatou–Gaocun section from 1960–

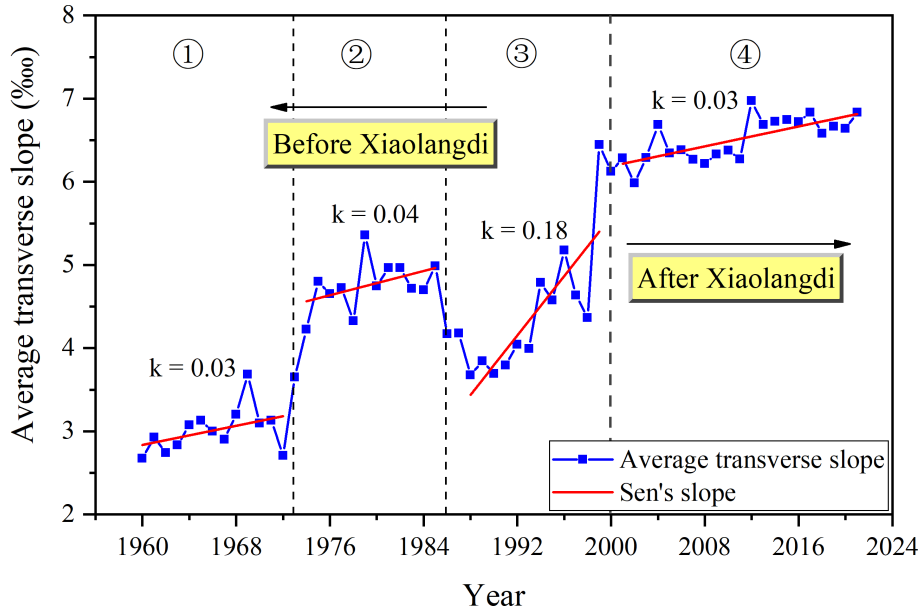

FIGURE 5
Trend of transverse slope change.

10.3389/fevo.2023.1330749

2021. Overall, prior to commencement of operation of Xiaolangdi Reservoir in 2000, the evolution trend of the average transverse slope of the beach underwent multiple fluctuations, and the overall trend gradually increased. In the analyses of its trend using the Theil–Sen estimator, the trend degree is expressed in k, which could be divided into four stages: ① 1960–1973, the transverse slope of the beach had a trend degree of k = 0.03, which belongs to the initial formation period of secondary suspended rivers; ② 1974–1986, k = 0.04, which belongs to the period of slow development of secondary suspended rivers; ③ 1987–1999, k = 0.18, which belongs to the rapid development period of secondary suspended rivers; and ④ 2000–2021, k = 0.03, which belongs to the stable period of secondary suspended rivers. The first three periods were before commencement of operation of Xiaolangdi Reservoir and the fourth period was after operation commenced.

Figure 6 and Table 1 present the transverse slope of the left-bank beach for each section from Dongbatou–Gaocun in 2021. As of 2021, the transverse slope of 88% of the cross section was within 10% and 12% of the cross section was > 10%. The secondary suspended rivers in the Shuangjing and Qingzhuang sections were the most severe, with a transverse slope of > 20% on the beach. The transverse slope from Xiezhaizha–Hedao was relatively small, i.e., basically within 5%. The current secondary suspended river situation in the lower Yellow River remains serious.

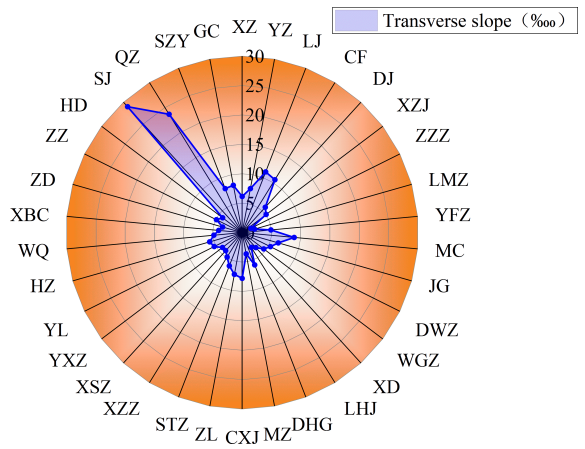

FIGURE 6
Trend of transverse slope change with channel section (numbers represent the transverse slope)(starting from XZ, clockwise direction is Xinzhuang, Yangzhuang, Leiji, Chanfang, Dianji, Xizhangji, Zuozhaizha, Limenzhuang, Youfangzhai, Machang, Jinggang, Dawangzhai, Wanggaozhai, Xindian, Liuheji, Dongheigang, Mazhai, Changxingji, Zhulin, Shitouzhuang, Xiezhaizha, Xiaosuzhuang, Yangxiaozhai, Yulin, Huangzhai, Wuqiu, Xibaocheng, Zhaodi, Zhangzhai, Hedao, Shuangjing, Qingzhuang, Shiziyuan and Gaocun respectively).

3.2 Periodicity of secondary suspended river evolution

The time-series changes in the transverse slope of the left bank beach from Dongbatou–Gaocun showed that the evolution law of the transverse slope had nonlinear characteristics and had been in a fluctuating state. The following presents a periodic analysis of the transverse slope using the Cmor wavelet analysis method.

Figure 7 shows the wavelet coefficients of the transverse slope of the left-bank beach from Dongbatou–Gaocun, China. Figures 7A, B show the wavelet real part three-dimensional surface maps and real-part contour maps, respectively, which reflect the distribution of the transverse slope in the timescale and the periodic changes in different time domains. Figure 7 shows that the wavelet coefficients fluctuate on timescales of 25–32, 15–25, 10–15, and 5–9 years, indicating multiple timescale characteristics in the transverse slope. There were three quasi-oscillations with alternating rises and falls on the 25–32-year timescale, and four and a half oscillations on the 15–25-year timescale. The wavelet coefficients exhibited the most drastic changes at these two timescales and most accurately represented the fluctuation pattern of the transverse slope.

Figures 7C, D show the three-dimensional surface and contour maps of the wavelet coefficients of the transverse slope, respectively, reflecting the periodicity intensity of the corresponding timescales during this period. Warm colors indicated strong periodicities, and cold colors indicated weak periodicities. Figure 7 shows that during the evolution of the transverse slope, the modulus values on the 15–25 and 25–32-year timescales were the highest, indicating that the transverse slope period of the beach was the strongest within these two timescales; whereas, the modulus values of periodic changes on other timescales were small, indicating that the transverse slope period of the beach was not significant at other timescales.

Figures 7E, F show the three-dimensional surface and contour maps of the modulus of the wavelet coefficients of the transverse slope, which were used to analyze the oscillation energy of different periods. Unlike Figures 7C, D, Figures 7E, F clearly reflects the timescale of the strongest period. It can be seen that the energy on the 15–25-year timescale was the strongest, with a time domain distribution after 2000. The energy on the 25–32-year timescale was the second strongest, with a time-domain distribution from 1975–2000.

Figure 8 shows the variance and main period trend charts of the wavelet coefficient of the transverse slope of the beach, which reflect the main period and evolution trends of the transverse slope of the beach, respectively. Figure 8A shows two clear peaks in the wavelet variance map of the beach transverse slope: the first and second main periods. The first main period corresponded to a 31-year timescale, and the second main period corresponded to a 21-year timescale. Figure 8B shows that on the 31-year timescale of the first

TABLE 1 Transverse slope distribution of the left-bank beach from Dongbatou–Gaocun in 2021.

Transverse slope	0~5‰	5~10‰	10~15‰	15~20‰	20~30‰
Number of sections	15	15	2	0	2
Proportion	44%	44%	6%	0	6%

10.3389/fevo.2023.1330749

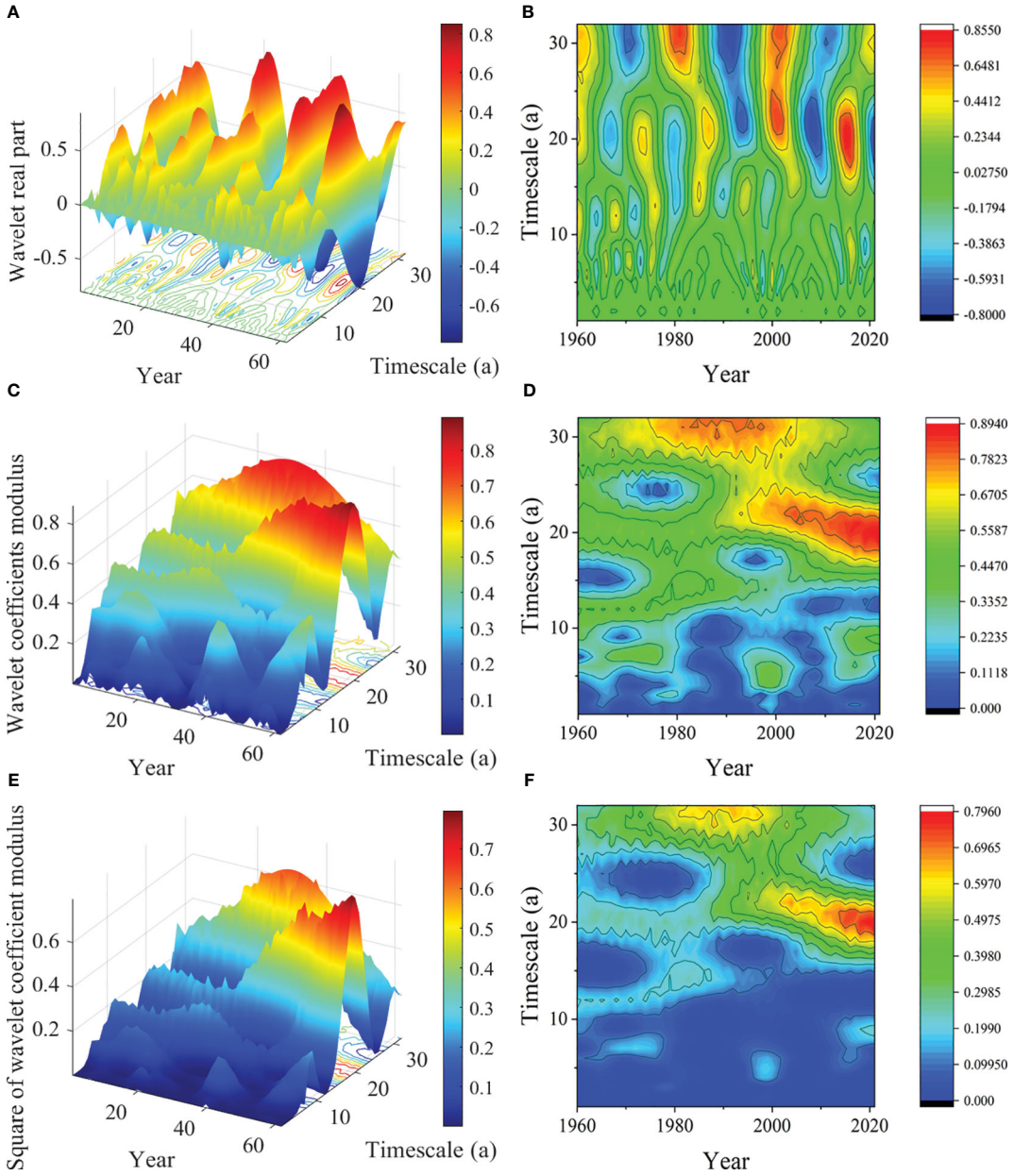

FIGURE 7
Wavelet coefficient map of the time series of the beach transverse slope: **(A)** wavelet real part 3D surface map, **(B)** wavelet real part contour map, **(C)** wavelet coefficient modulus 3D surface map, **(D)** wavelet coefficient modulus contour map, **(E)** 3D surface map of wavelet coefficient modulus square, **(F)** contour map of wavelet coefficient modulus square.

main period, the transverse slope experienced three quasi-oscillations with an evolution period of 20 years. On the 21-year timescale of the second main period, the transverse slope experienced four and a half oscillations, with an evolution period of 13–14 years.

Figures 7 and 8 show that the first and second main periods corresponded to two different timescales. Using 2000 as the boundary, it was divided into two stages. The first main period was before 2000 and the second was after 2000. After 2000, the construction and operation of Xiaolangdi Reservoir changed the original periodic evolution of the beach transverse slope.

4 Discussion

According to previous studies, the formation and development of the secondary suspended river in the lower Yellow River result from the combined effects of incoming water, sediment, and river boundary conditions. The impact of human activities has also promoted development of secondary suspended rivers. This study focused on quantitative research on the various factors that affect development of secondary suspended rivers and explored the evolutionary characteristics of secondary suspended river development under the influence of various factors.

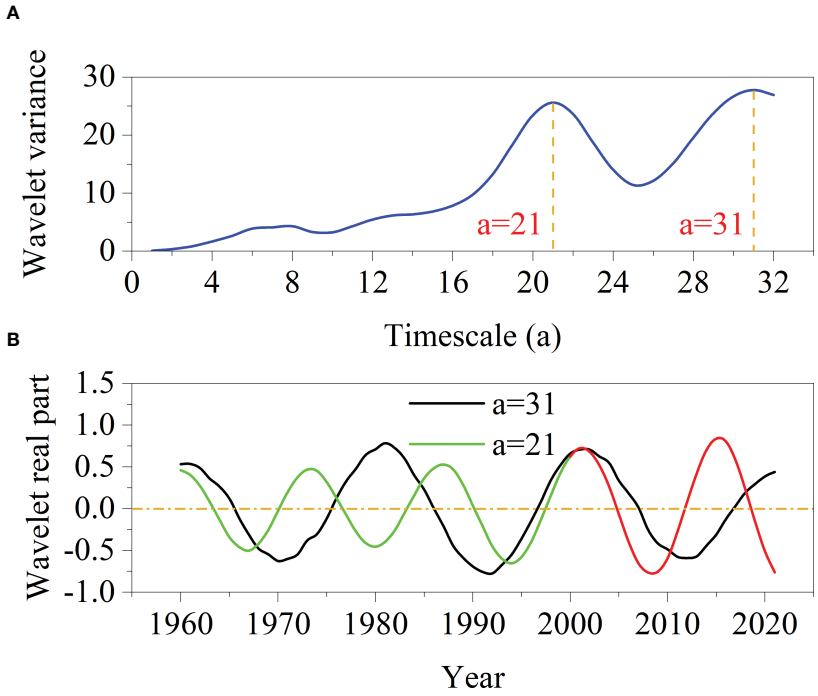

FIGURE 8
Wavelet map of the beach transverse slope: **(A)** wavelet variance map, **(B)** main period trend map of the beach transverse slope.

4.1 Annual water and sediment impact on secondary suspended rivers

Figure 9 shows the impacts of annual runoff, annual sediment transport, incoming sediment coefficient, and bank-full discharge on the transverse slope at Huayuankou station in the lower Yellow River from 1960–2021. From a long-term perspective, annual runoff and sediment transport in the lower Yellow River decreased; whereas, the transverse slope showed an overall increasing trend (Figures 9A, B). Specifically, the overall trends of annual runoff and sediment transport at Huayuankou station gradually decreased from 1960–2000. Although overall annual runoff was relatively low after 2000, there was a steady increasing trend. The overall change in annual sediment transport was not significant, with an increase over the past 5 years (2017–2021). The incoming sediment coefficient at Huayuankou station (Figure 9C) fluctuated between 0–0.06 kg·s/m^6 before 2000, with an average of 0.024 kg·s/m^6. After 2000, the incoming sediment coefficients fluctuated between 0–0.01 kg·s/m^6 overall, with an average of 0.005 kg·s/m^6. Changes in annual runoff and sediment transport in the lower Yellow River only reflected the overall impact on the transverse slope. Before 2000, the high sediment coefficient and repeated fluctuations significantly impacted the morphology of river sections, resulting in an overall increase in the transverse slope. After 2000, no floodplain flood shaped the previously formed floodplain; the transverse slope was still relatively large, and the threat of secondary suspended rivers remained. However, the overall incoming sediment coefficient was relatively small, and the riverbed had a certain degree of erosion, resulting in a clear trend of stability and slowing down development of secondary suspended rivers.

When the incoming sediment coefficient was large, it caused sedimentation and shrinkage of the main channel, resulting in a decrease in the bank-full discharge and an increase in the probability of water flooding. On one hand, the lateral sedimentation of floodplain sediment was mainly distributed near the beach lip; on the other hand, river regulations and production levees limited floodplain floods to a certain range, exacerbating the sedimentation of the beach lip. Figure 9D shows the relationship between the transverse slope and full bank discharge. Overall, the transverse slope also increased with a decrease in bank-full discharge, particularly at the two turning points. One of these turning points was around 1972, during the early stage of the rapid development of the transverse slope, when the bank-full discharge decreased to its minimum value. The other was around 1999, when the transverse slope tended to a higher value and the bank-full discharge decreased to its historically minimum value.

Figure 5 shows that development of the secondary suspended river was divided into four stages. Table 2 shows the relationship between the average annual runoff, average annual sediment transport, average annual incoming sediment coefficient, and the development trend k value of the secondary suspended river in these four stages at Huayuankou station in the lower Yellow River. From 1960–1973, the average annual sediment coefficient was relatively high, at 0.0224 kg·s/m^6. This is because from September, 1960 to March, 1962, Sanmenxia Reservoir was used for water storage and sediment retention, resulting in severe sedimentation in the reservoir. From March, 1962 to October, 1973, Sanmenxia Reservoir was used for flood detention and sediment discharge, resulting in a high incoming sediment coefficient and serious sedimentation in the downstream channel,

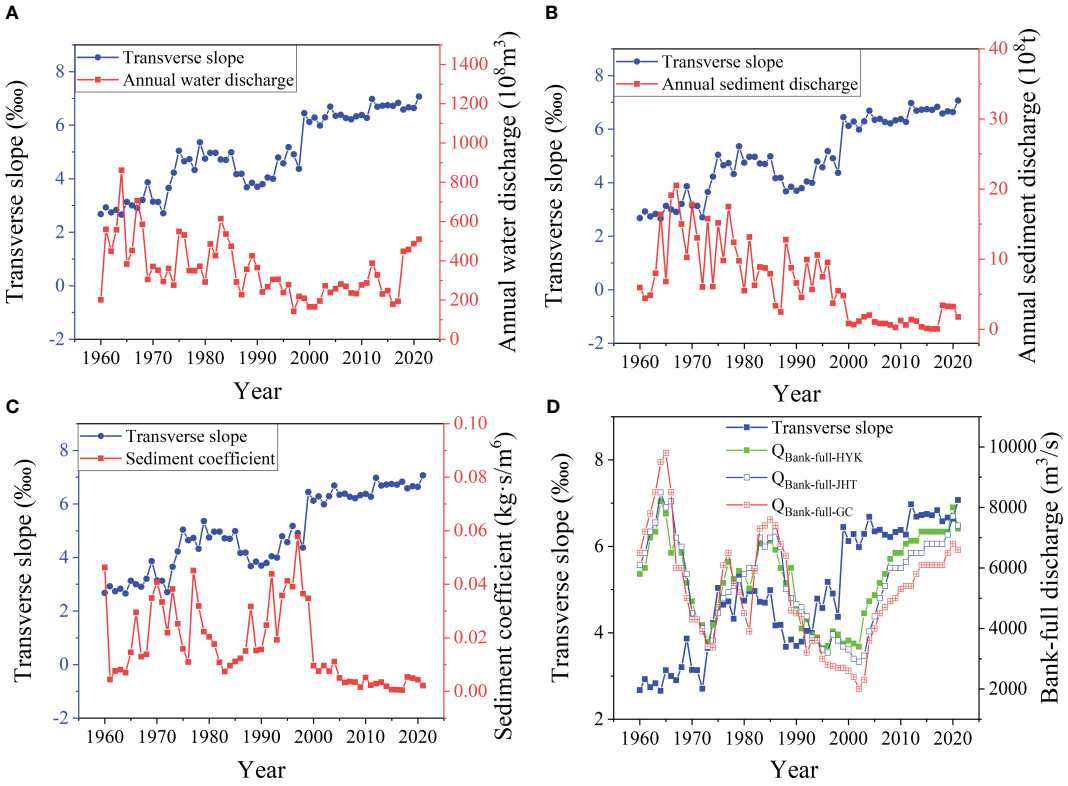

FIGURE 9
Incoming water and sediment from Huayuankou station in the lower Yellow River (1960–2021): **(A)** annual water volume; **(B)** annual sediment volume; **(C)** incoming sediment coefficient; **(D)** bank-full discharge.

causing the rapid development of secondary suspended rivers. From November, 1974 to 1985, Sanmenxia Reservoir implemented a storage and sediment discharge operation method of non-flood season water storage and sediment retention, and flood season flood and sediment discharges. Although the flood season was still silted, the rate of increase in the transverse slope slowed, and the secondary suspended river developed slowly. From 1986–1999, under the influence of the completion of and joint regulation with Longyangxia Reservoir, development and utilization of water resources of the Yellow River, comprehensive management of the middle and upper reaches, and low precipitation, the inflow of water and sediment in the lower reaches underwent tremendous changes. The water inflow in the flood season decreased and that in the non-flood season increased, the peak flow decreased, the dry water duration lengthened, and the sediment-carrying capacity of the water flow decreased, leading to a sharp decrease in the size of the main channel and a reduction in the bank-full discharge. The transverse slope was rapidly increasing, and development of secondary suspended rivers was accelerating. From 2000–2021, after completion and commencement of operation of Xiaolangdi Reservoir, the amount of water and sediment entering the lower Yellow River was effectively controlled. Through water and sediment regulations, the main channel was scoured and cut down and the bank-full discharge gradually increased. The water flow did not flood the beach, and the rapid upward trend of the transverse slope was restrained and became relatively gentle.

TABLE 2 Relationship between water and sediment and the development trend of secondary suspended rivers in the lower Yellow River.

Number	Time	Annual average runoff (10^8m^3)	Annual average sediment transport (10^8t)	Annual average sediment inflow coefficient (kg·s/m^6)	k
1	1960–1973	459.8	11.71	0.0224	0.03
2	1974–1985	438.0	10.10	0.0190	0.04
3	1986–1999	276.5	6.84	0.0302	0.18
4	2000–2021	288.4	1.22	0.0044	0.03

However, the transverse slope remains large, and the secondary suspended river situation remains severe.

Notably, after 2000, the water flow in the lower Yellow River did not flood the floodplain. In this case, the driving force for the change in the transverse slope mainly came from changes in the shape of the river section, such as the widening of the main channel, which led to changes in the beach lip elevation (decreasing) and beach width (narrowing). Changes in river section shape are generally caused by an abnormal river regime and bank collapse; however, this situation accounts for a very small proportion of the entire lower Yellow River. At the time of the present study, the overall river section morphology in the lower Yellow River was relatively stable; therefore, development of secondary suspended rivers caused by changes in the morphology of river sections was relatively rare. Therefore, we did not focus on this issue.

4.2 Impact of floodplain floods on secondary suspended rivers

The bed formation pattern of the floodplain floods differed from that of the non-floodplain floods. After flooding, the cross section suddenly increased, the average velocity of the cross section decreased, the sediment-carrying capacity of the water flow decreased, and a large amount of sediment was deposited, forming new beach lips at the beach edge and increasing the transverse slope of the beach. Figure 10 shows the relationship between flood peak discharge, bank-full discharge, and beach transverse slope of Huayuankou station floodplain in the lower Yellow River from 1960–2021. From 1973–1985, the floodplain frequency during this period was relatively high (up to 61%) and the sediment coefficient was relatively small (Table 3), the transverse slope was in a slow development stage. From 1986–1999, the frequency of floodplains was also high (up to 43%), moreover, the terrain was affected by the previous floodplain floods, the transverse slope decreases first during this period. Subsequently, due to the occurrence of two Hyper-concentrated floods in 1992 and 1994, the river siltation was severe, and the bank-full discharge continued to decrease, resulting in rapid development of the transverse slope. The shapes of the river channels were completely different because of the different sediment concentrations in the floodplain floods. For floodplain floods with a high sediment content, after the floodplain, the cross-section increased and the average flow velocity decreased, resulting in a decrease in the sediment-carrying capacity of the water flow. A large amount of sediment accumulated in the river channel and beach lip, resulting in a decrease in the bank-full discharge and an increase in the transverse slope of the beach, which promoted development of secondary suspended rivers.

Table 3 presents the flood situation in the floodplain from 1960–2021 and shows the characteristic values of floodplain floods in different years, such as peak flow, water volume, sediment volume, and bank-full discharge. The average sediment concentration, sediment inflow coefficient, floodplain coefficient, and height difference changes of each floodplain flood were calculated. The floodplain flood category was determined based on whether the production levees overflowed and was combined with the floodplain coefficient. The floodplain coefficient was calculated as the ratio of the peak discharge to the bank-full discharge of the current year, which represented the degree of floodplain in this flood (Hu and Zhang, 2015; Shen et al., 2017). The height difference refers to the difference between the elevation of the beach lip and the levee root, and the change in height difference refers to the difference between the height of the previous year that of the current year. If the change in height difference was positive, it indicated that the current secondary suspended river had developed. A negative change in height difference indicated that the current secondary suspended river had eased. When the floodplain coefficient was >1.5 (Zhang et al., 2016) and the floodplain flood overflowed the production levee, it was determined that the flood was a large floodplain flood; otherwise, it was a general floodplain flood (Table 3).

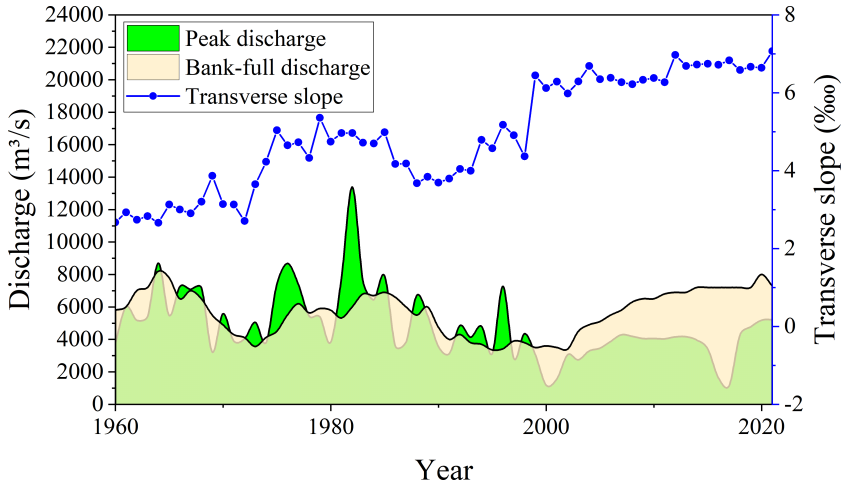

FIGURE 10
Relationship between peak discharge and bank-full discharge.

TABLE 3 Statistics of characteristic values of floodplain floods in different years.

Number	Time	Peak discharge (m^3/s)	Bank-full discharge (m^3/s)	Water amount (10^8m^3)	Sediment amount (10^8t)	Average sediment concentration (kg/m^3)	Incoming sediment coefficient ($kg·s/m^6$)	Height difference change (m)	Floodplain coefficient*	Has it overflowed the production levee	Floodplain category
1	1966-07-20/11-27	8480	6500	81.17	7.71	94.98	0.0253	-0.052	1.30	no	general
2	1968-09-14/09-26	7340	6500	64.70	2.47	38.23	0.0066	-0.017	1.13	no	general
3	1970-07-24/10-10	5830	4900	38.99	4.16	106.78	0.0331	-0.043	1.19	no	general
4	1971-07-25/07-31	5040	4300	9.30	1.32	141.75	0.0659	-0.005	1.17	no	general
5	1972-08-26/09-23	4170	4110	17.51	0.70	40.02	0.0158	-0.072	1.01	no	general
6	1973-08-20/11-23	5890	3560	31.80	6.98	219.42	0.0656	0.295	1.65	no	general
7	1975-07-08/11-30	7580	4500	37.65	1.48	39.35	0.0063	0.310	1.68	Yes	huge
8	1976-07-08/11-30	9210	5510	80.82	2.86	35.44	0.0049	0.057	1.67	no	general
9	1977-08-04/08-12	10800	6200	30.02	6.51	216.92	0.0562	0.050	1.74	Yes	huge
10	1981-09-24/10-12	8060	5320	94.63	2.20	23.30	0.0040	0.125	1.52	no	general
11	1982-07-30/08-28	15300	6000	61.09	1.99	32.64	0.0051	0.168	2.55	Yes	huge

(Continued)

10.3389/fevo.2023.1330749

TABLE 3 Continued

Number	Time	Peak discharge (m^3/s)	Bank-full discharge (m^3/s)	Water amount (10^8m^3)	Sediment amount (10^8t)	Average sediment concentration (kg/m^3)	Incoming sediment coefficient ($kg·s/m^6$)	Height difference change (m)	Floodplain coefficient*	Has it overflowed the production levee	Floodplain category
12	1983-06-25/11-19	8180	6800	55.43	1.33	24.07	0.0049	-0.100	1.20	no	general
13	1985-08-25/11-06	8260	6900	43.06	1.77	41.12	0.0074	0.032	1.20	no	general
14	1988-07-07/09-21	7000	5500	73.23	6.30	85.97	0.0172	-0.035	1.27	no	general
15	1989-07-02/10-21	6100	6000	32.59	1.17	35.96	0.0105	-0.100	1.02	no	general
16	1992-07-27/10-24	6430	4300	24.87	4.54	182.63	0.0634	0.115	1.50	no	general
17	1994-08-06/08-19	6300	3700	30.47	4.64	152.37	0.0605	0.200	1.70	no	general
18	1996-07-17/08-26	7860	3420	58.92	5.29	89.82	0.0277	0.228	2.30	Yes	huge

*Floodplain coefficient = Peak discharge/Bank-full discharge.

10.3389/fevo.2023.1330749

Figure 11 shows the relationship between floodplain floods and changes in the elevation difference of the secondary suspended rivers. When incoming sediment coefficient (ζ) was >0.04, the changes in elevation difference were basically positive, and the suspension difference of the secondary suspended river increased. When ζ < 0.04, the changes in elevation difference were basically negative (Figure 11A) and the difference in height of the secondary suspended river decreased. However, there are situations in which the elevation difference increased within the sediment coefficient range. Floodplain floods with ζ < 0.04 were selected, and a relationship was established between the elevation difference and the floodplain coefficient to analyze the factors affecting the elevation difference (Figure 11B). As the degree of the floodplain increased, the elevation difference changed from negative to positive and gradually increased. When the change in the elevation difference was zero, the floodplain coefficient was approximately 1.29; i.e., when the flood coefficient of the floodplain was <1.29 and the sediment coefficient was <0.04, the suspension difference of the secondary suspended river was negative, and the secondary suspended river situation could be alleviated to some extent.

Figure 12 shows the shaping effect of different floodplain floods on the river cross-section, and the impact on the development of secondary suspended rivers was analyzed. Figures 12A, B show the changes in erosion and sedimentation of the Youfangzhai section in 1989 and Mazhai section in 1970, respectively, before and after the flood season. The sediment coefficient and floodplain degree of the 1989 flood were relatively low, and changes in erosion and sedimentation mainly occurred within the production levee. After the flood, the main channel was scoured and the left-bank beach lip elevation decreased. The elevation of the left bank levee root remained unchanged, and the height difference between the beach lip and levee root decreased. Although the 1970 flood did not overflow the production levee, the sediment coefficient was higher than that in in 1989, and the bank-full discharge in the river channel was lower than that in 1989. The degree of flooding increased, causing the river to be in a silted state with the beach lip raised and the elevation difference increased. Figures 12A, B show the general floodplain floods, in which it can be seen that general floodplain floods may have promoted (1970 floodplain floods) or slowed (1989 floodplain floods) the development of secondary suspended rivers, which mainly related to the incoming sediment coefficient.

Figures 12C, D show the cross-sectional erosion and sedimentation changes in the Gaocun section in 1982 and Yangxiaozhai section in 1996 before and after the flood season. The floods in 1982 and 1996 were both large floodplain floods, and the main channel eroded to a certain extent. The floodplain overflowed the production levee and silted up along the beach; however, lateral siltation gradually decreased to the outside, and erosion occurred near the levee root, leading to a further increase in the height difference. The causes of the flooding in 1982 and 1996 differed. In 1982, the peak discharge of Huayuankou station reached 15300 m^3/s, the bank-full discharge was 6000 m^3/s, and the sediment coefficient was 0.0051, which was a typical case of high water and low sediment flow. In 1996, the peak discharge of Huayuankou station reached 7860 m^3/s, and its main channel was affected by previous sedimentation and shrinkage, resulting in bank-full discharge of only 3420 m^3/s. The sediment coefficient was as high as 0.0277, causing all floodplains in the lower Yellow River. This showed that floods in the floodplain were beneficial for erosion of the river channel, which had a positive effect on shaping the subsequent form of the river channel. This could improve the sediment transport capacity of the river channel, increase the bank-full discharge, and slow the development of the secondary suspended river to some extent.

4.3 Impact of human activities on secondary suspended rivers

Human activities have changed the boundary conditions of the riverbed, and their impact on the secondary suspended river was the same as that of the riverbed boundary conditions. Human activities mainly include construction of river regulation works and production levees. Since the 1960s, the construction and gradual

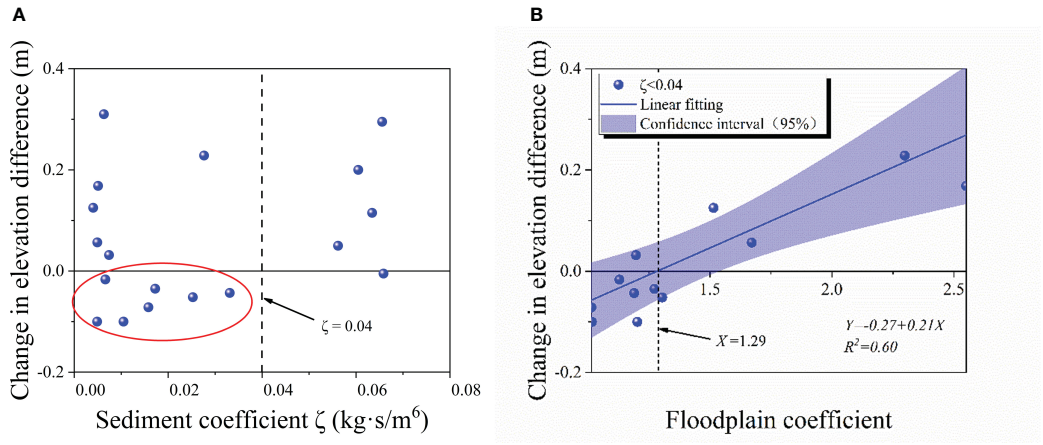

FIGURE 11
Relationship between characteristic values of floodplain floods and changes in elevation difference. Relationships between **(A)** sediment coefficient and changes in elevation difference and **(B)** floodplain coefficients and changes in elevation differences (ζ < 0.4).

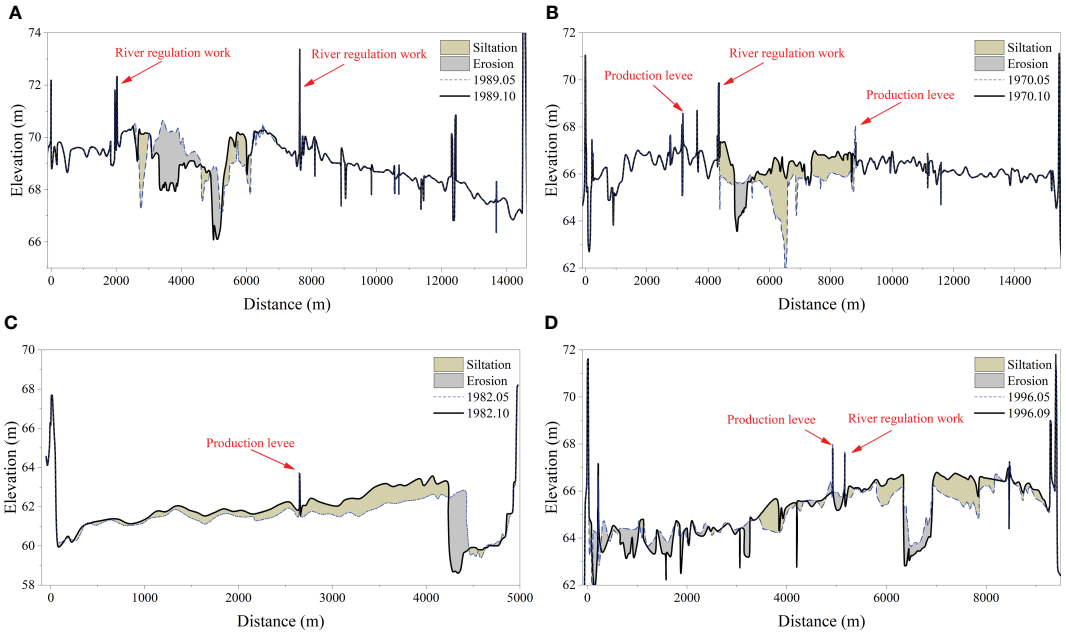

FIGURE 12
Cross-section changes in erosion and sedimentation in a typical flood year: **(A)** Youfangzhai station (1989); **(B)** Mazhai station (1970); **(C)** Gaocun station (1982); **(D)** Yangxiaozhai station (1996).

improvement of river regulations in the lower Yellow River have played a dual role in controlling the river regime and protecting levees. River regulations have controlled the river regime in the curved section of the lower Yellow River. The transitional section is basically controlled, and the majority of the wandering section is controlled. The relatively stable main channel is an excellent container for sediment deposition. Once the main channel accumulates, a secondary suspended river develops in it. However, the river regulations are mainly used to control water flow, stabilize river regimes, and protect levees. Moreover, after water and sediment regulation in Xiaolangdi Reservoir, the downstream river channel underwent a certain degree of erosion, and the effect of river regulation on stabilizing the river regime became increasingly obvious without directly affecting development of secondary suspended rivers.

The production levees in the lower Yellow River were built based on the historical Minnian (People spontaneously build earth embankments to protect farmland and villages for blocking water). Historically, people living on beaches spontaneously built Minnian to defend themselves against certain levels of flooding. Due to war and floods, Minnian has dilapidated and can no longer function effectively. Since the people's governance of the Yellow River in 1946, Minnian has been repaired and production levees have been added to the building. By the 1970s, production levees had already reached a certain scale; therefore, the overall effect of floodplain floods after the 1970s continued to be affected by production levees.

After construction of the production levee in the Dongbatou–Gaocun section, the flood width of the general floodplain has been reduced from >10.5 km to 4.2 km (Jiang et al., 2019). Generally, it is difficult for floodplain floods to cross production levees, resulting in changes in river erosion and siltation occurring only in the middle of the production levees on both banks. Although large floodplains can cross production levees, and beaches outside the production levees also exchange water and sediment, production levees limit the lateral distribution of sediment deposition. Figure 12 shows that there was a significant difference in the amount of erosion and sedimentation on both sides of the production levee, and that the sedimentation depth on the side near the main channel was significantly greater than that on the side far from the main channel. Table 4 shows the erosion and sedimentation conditions of the erosion and sedimentation situation near the main channel and far from the main channel at each section of the Dongbatou–Gaocun section under the action of flooding in 1982 (taking the left bank as an example). It is evident from Table 4 that owing to the production levees, the amount of sedimentation on the beach near the main channel was significantly greater than that on the beach far from the main channel.

These results showed that although production levees can block the inundation loss of local beach areas caused by floodplain floods, they seriously hinder normal water and sediment exchange in the beach channel, which causes most of the sediment in the flood not to overflow the production levees to settle at the beach lip. However, because of the inability of the flood to reach the root of the levee, there was no sediment deposition, which caused the beach lip to increase and the levee root to decrease, accelerating development of the secondary suspended river.

5 Conclusions

Considering the Dongbatou–Gaocun section as the research object, the evolution process of the secondary suspended river on the left-bank beach from 1960–2021 was analyzed. The trend and

TABLE 4 Changes in erosion and sedimentation before and after the flood in 1982.

Section	Left bank			
	the beach away from the main channel		the beach near the main channel	
	Area of erosion and sedimentation (m^2)	Thickness of erosion and sedimentation (m)	Area of erosion and sedimentation (m^2)	Thickness of erosion and sedimentation (m)
Dongbatou1	−69.74	−0.09	346.75	0.09
Chanfang	3.06	0.02	119.07	0.11
Youfangzhai	25.14	0.01	186.41	0.14
Yangxiaozhai	184.1	0.03	198.92	0.10
Hedao	−206.46	−0.06	27.32	0.02
Gaocun	575.88	0.22	1220.82	0.77

periodicity of the transverse slope change on the left-bank beach were studied, and the evolution law of the secondary suspended river in the wandering river channels was explored. Factors influencing the development of secondary suspended rivers were quantitatively analyzed. The main conclusions are as follows.

(1) The evolution process of the transverse slope from 1960–2021 can be divided into five stages: ① The period from 1960–1973 belongs to the initial formation period of secondary suspended rivers, with a transverse slope trend of k = 0.03; ② the period from 1974–1986 belongs to the slow development period of secondary suspended rivers, with a transverse slope trend of k = 0.04; ③ the period from 1987–1999 belongs to the rapid development of secondary suspended rivers, with a transverse slope trend of k = 0.18; ④ the period from 2000–2021 belongs to the stable period of secondary suspended rivers, with a transverse slope trend of k = 0.03.

The first three periods were before commencement of operation of Xiaolangdi Reservoir and the fourth period was after operation commenced. This showed that in the early stages of operation of Xiaolangdi Reservoir, a secondary suspended river developed to a very serious extent. Through water and sediment regulation in Xiaolangdi Reservoir, the sedimentation of the downstream river channel was reduced, which effectively alleviated the development trend of the secondary suspended river.

(2) The evolution period of the transverse slope on the beach differed significantly before and after commencement of operation of Xiaolangdi Reservoir. Prior to commencement of operation of Xiaolangdi Reservoir in 2000, incoming water and sediment from the lower Yellow River were mainly affected by Sanmenxia Reservoir. The transverse slope of the beach had a primary period of 31 years (period of 20 years). After commencement of operation of Xiaolangdi Reservoir, owing to its influence on water and sediment regulation, the overall downstream river channel continued to erode, the transverse slope of the beach changed, and there was a second main period of 21 years (period of 13–14 years).

(3) Incoming water and sediment affected development of secondary suspended rivers. When the incoming sediment coefficient of floodplain flood (ζ) was >0.04 or <0.04 and floodplain coefficient was >1.29, the change in height difference of the secondary suspended river increased, and the secondary suspended river intensified. When ζ < 0.04 and the floodplain coefficient was <1.29, the change in height difference of the secondary suspended river decreased, and the secondary suspended river was alleviated. The production levee blocked the water and sediment exchange between the general floodplain flood and the floodplain outside the production levee, which affected the lateral sedimentation distribution of sediment in a large floodplain flood and promoted development of secondary suspended rivers.

Data availability statement

The original contributions presented in the study are included in the article/supplementary material. Further inquiries can be directed to the corresponding author.

Author contributions

LX: Conceptualization, Funding acquisition, Methodology, Writing – original draft. JL: Conceptualization, Methodology, Project administration, Writing – original draft, Writing – review & editing. HX: Formal analysis, Methodology, Writing – original draft. XPZ: Methodology, Validation, Writing – original draft. RL: Validation, Visualization, Writing – original draft. XZ: Methodology, Writing – original draft. XG: Investigation, Resources, Writing – original draft.

Funding

The author(s) declare financial support was received for the research, authorship, and/or publication of this article. This research was financially supported by the National Natural Science Foundation of China (No. 42041006, U2243219), the Major Science and Technology Project of Henan Province (No. 231100320100), the Excellent Youth Foundation of He'nan Scientific Committee (No. 222300420013), the Significant Science and Technology Project of the Ministry of Water Resources (No. SKS-2022011), the Excellent Young Talents Project of the Yellow River Conservancy Commission (No. HQK-202309), the Water

Conservancy Cadres Education and Talent Cultivation (No. 102126222015800019041).

Conflict of interest

The authors declare that the research was conducted in the absence of any commercial or financial relationships that could be construed as a potential conflict of interest.

Publisher's note

References

Duanmu, L., and Zhang, S. (2003). Forming, Present Condition and Control measures of secondary rivers of the Yellow River in Henan province. *China Water.* 12), 58–59. doi: 10.3969/j.issn.1000-1123.2003.12.025

Gao, J., Hu, C., and Chen, X. (2004). A preliminary study on alteration of watercourse and improvement of the "secondary perched river" in the lower Yellow River. *J. China Institute Water Resour. Hydropower Res.* 01), 12–22. doi: 10.13244/j.cnki.jiwhr.2004.01.002

Hu, Y., and Zhang, X. (2006). Brief discussion on the secondary perched river. *J. Sediment Res.* 5), 1–9. doi: 10.16239/j.cnki.0468-155x.2006.05.001

Hu, C., and Zhang, Z. (2015). The research of mechanism of constructing riverbed and index of flow and sediment of floodwater in the Lower Yellow River. *Scientia Sinica (Technologica).* 45 (10), 1043–1051. doi: 10.1360/N092015-00012

Jiang, E., Cao, Y., and Zhang, Q. (2003). "Causes and control measures of the "Secondary suspended river," in *Lower yellow river* (Zhengzhou: The Yellow River Water Conservancy Press), 334–349.

Jiang, E., Cao, Y., Zhang, L., Zhao,, and Zhang, Q. (2006). *Study on the evolution law and mechanism of river regime in the wandering reach of the lower yellow river* (Beijing: China Water & Power Press).

Jiang, E., Li, J., Chen, J., Wang, Y., and Cao, Y. (2019). *Research on the function of flood detention and sedimentation in the wide beach area of the lower yellow river and the disaster reduction technology in the beach area* (Beijing: China Water & Power Press).

Jiang, E., Zhang, H., Zhao, L., and Zhang, L. (1999). Study of bed building law of hyper-concentrated flood and river facies relation. *Yellow River.* 21 (1), 14–16.

Kong, D., Miao, C., Duan, Q., Li, J., Zheng, H., and Gou, J. (2022). Xiaolangdi Dam: A valve for streamflow extremes on the lower Yellow River. *J. Hydrology.* 606, 127426. doi: 10.1016/j.jhydrol.2022.127426

Liao, Y. (2003). *Causes and control measures of the "Secondary suspended river" in the lower yellow river* (Zhengzhou: The Yellow River Water Conservancy Press).

Liu, X. (2020). The water and sediment situation and countermeasure. *Yellow River.* 42 (09), 34–40. doi: 10.3969/j.issn.1000-1379.2020.09.007

Liu, Z., Qiu, H., Zhu, Y., Liu, Y., Yang, D., Ma, S., et al. (2022). Efficient identification and monitoring of landslides by time-series inSAR combining single- and multi-look phases. *Remote Sensing.* 14, 1026. doi: 10.3390/rs14041026

Ma, S., Qiu, H., Zhu, Y., Yang, D., Tang, B., Wang, D., et al. (2023). Topographic Changes, Surface Deformation and Movement Process before, during and after a Rotational Landslide. *Remote Sensing.* 15, 662. doi: 10.3390/rs15030662

Pang, J. (2005). Pondering over issues of a general plan of the lower yellow river harnessing. *Yellow River.* 27 (1), 3–4. doi: 10.3969/j.issn.1000-1379.2005.01.002

Pei, Y., Qiu, H., Zhu, Y., Wang, J., Yang, D., Tang, B., et al. (2023). Elevation dependence of landslide activity induced by climate change in the eastern Pamirs. *Landslides.* 20, 1115–1133. doi: 10.1007/s10346-023-02030-w

Qiu, H., Zhu, Y., Zhou, W., Sun, H., He, J., and Liu, Z. (2022). Influence of DEM resolution on landslide simulation performance based on the Scoops3D model, *Geomatics. Natural Hazards Risk* 13 (1), 1663–1681. doi: 10.1080/19475705.2022.2097451

Sang, Y., Wang, Z., and Liu, C. (2013). Applications of wavelet analysis to hydrology: Status and prospects. *Prog. Geography.* 32 (09), 1413–1422. doi: 10.11820/dlkxjz.2013.09.011

Shan, L., and Wang, F. (2021). Some scientific issues in the cooperative management of the yellow river basin. *Yellow River.* 43 (10), 7–10. doi: 10.3969/j.issn.1000-1379.2021.10.002

Shen, G., Zhang, Y., and Zhang, M. (2017). Definition of channel and floodplain and spatio-temporal sedimentation characteristics for overbank hyper-concentrated flood in the lower Yellow River. *Adv. Water Science.* 28 (05), 641–651. doi: 10.14042/j.cnki.32.1309.2017.05.001

Sun, D., Liu, X., Xue, H., Wang, P., and Liao, X. (2008). Numerical simulation of fluvial process in the Lower Yellow River with "secondary perched river. *J. Hydroelectric Engineering.* 27 (06), 136–141.

Sun, L., and Luo, J. (2008). Research of point-symmetric boundary extension in wavelet transform. *J. Comput. Applications.* 28 (2), 443–445, 468. doi: 10.3724/SP.J.1087.2008.00443

Wang, L., Qiu, H., Zhou, W., Zhu, Y., Liu, Z., Ma, S., et al. (2022). The post-failure spatiotemporal deformation of certain translational landslides may follow the pre-failure pattern. *Remote Sensing.* 14, 2333. doi: 10.3390/rs14102333

Wang, H., Ye, L., Liu, M., and Liu, L. (2006). Problems and improvement methods in wavelet periodic analysis of hydrological sequences. *Prog. Natural Science.* 16 (8), 1002–1008. doi: 10.3321/j.issn:1002-008X.2006.08.013

Yan, Y., Zhang, H., and Fu, B. (2006). "Discussion on the causes and control measures of the "Secondary suspended river," in *Lower yellow river*, vol. 02). (Yellow River: China Flood & Drought Management), 57–59.

Yang, J., Xu, J., and Liao, J. (2006). The process of secondary suspended channel in the lower yellow river under different conditions of runoff and sediment load. *Acta Geographica Sinica.* 01), 66–76. doi: 10.3321/j.issn:0375-5444.2006.01.007

YRCC (2013). *Comprehensive planning of the yellow river basin: 2012-2030* (Zhengzhou: The Yellow River Water Conservancy Press).

Zhang, R. (2004). Suggestions on a general plan for lower yellow river management. *Yellow River.* 05), 1-2, 46. doi: 10.3969/j.issn.1000-1379.2004.05.001

Zhang, M., Huang, H., and Zhang, X. (2016). A study of the characteristics of sedimentation in the Lower Yellow River during overbank floods. *Adv. Water Science.* 27 (02), 165–175. doi: 10.14042/j.cnki.32.1309.2016.02.001

Zhang, J., Liu, Y., and Li, C. (2018). Discussion on effect of ecological security barrier of the lower yellow river. *Yellow River.* 40 (02), 21–24. doi: 10.3969/j.issn.1000-1379.2018.02.005

Zhang, J., Lu, J., Wei, S., Luo, Q., and Wan, Z. (2021). Causes and countermeasures of insufficient follow-up power for water and sediment regulation in xiaolangdi reservoir. *Yellow River.* 43 (1), 5–9. doi: 10.3969/j.issn.1000-1379.2021.01.002

frontiers | Frontiers in Ecology and Evolution

TYPE Original Research
PUBLISHED 22 December 2023
DOI 10.3389/fevo.2023.1344664

OPEN ACCESS

EDITED BY
Haijun Qiu,
Northwest University, China

REVIEWED BY
Jinping Liu,
North China University of Water Resources and Electric Power, China
Pei Liu,
Hainan Academy of Ocean and Fisheries Sciences, China

*CORRESPONDENCE
Zhichao Chen
czc@hpu.edu.cn

RECEIVED 26 November 2023
ACCEPTED 11 December 2023
PUBLISHED 22 December 2023

CITATION
Chen Z, Zhang X, Jiao Y, Cheng Y, Zhu Z, Wang S and Zhang H (2023) Investigating the spatio-temporal pattern evolution characteristics of vegetation change in Shendong coal mining area based on *kNDVI* and intensity analysis.
Front. Ecol. Evol. 11:1344664.
doi: 10.3389/fevo.2023.1344664

Investigating the spatio-temporal pattern evolution characteristics of vegetation change in Shendong coal mining area based on *kNDVI* and intensity analysis

Zhichao Chen*, Xufei Zhang, Yiheng Jiao, Yiqiang Cheng, Zhenyao Zhu, Shidong Wang and Hebing Zhang

School of Surveying and Land Information Engineering, Henan Polytechnic University, Jiaozuo, China

Alterations in vegetation cover serve as a significant indicator of land ecology. The Shendong Coal Mining Area, being the largest coal base globally, holds significant importance for national energy security. Moreover, it has gained recognition for its environmentally conscious approach to coal mining, characterized by the simultaneous implementation of mining activities and effective governance measures. In order to assess the ongoing vegetation recovery and the temporal changes in vegetation within the Shendong Coal Mining Area, we initially utilized Landsat TM/ETM+/OLI remote sensing data. Using the Google Earth Engine (GEE), we developed a novel kernel-normalized vegetation index (*kNDVI*) and subsequently generated a comprehensive *kNDVI* dataset spanning the years 2000 to 2020. In addition, the Sen (Theil-Sen median) trend analysis method and MK (Mann-Kendall) test were utilized to examine the temporal trends over a span of 21 years. Furthermore, the Hurst exponent model was employed to forecast the persistent changing patterns of *kNDVI*. The utilization of the intensity analysis model was ultimately employed to unveil the magnitude of vegetation dynamics. The findings indicated a notable positive trend in the overall *kNDVI* of vegetation within the study area. In relation to the analysis of changing trends, the vegetation in the region underwent a slight improvement from 2000 to 2010, followed by a significant improvement from 2010 to 2020. During this transition period, a total of 289.07 km^2, which represents 32.36% of the overall transition area, experienced a shift in vegetation. The predictive findings from the Hurst model indicate that while the majority of areas within the mining region will exhibit an upward trend in vegetation growth, there will be certain areas that will demonstrate a decline. These declining areas account for 39.08% of the total transition area. Furthermore, the intensity analysis results reveal notable disparities in the characteristics of vegetation growth and evolution between the periods of 2000-2010 and 2010-2020. Throughout the entirety of the transformation process, the transition from slight improvement to significant improvement prevails in terms of both relative intensity and absolute intensity, surpassing alternative transformation processes. Various trend transitions display diverse

intensity characteristics that adhere to the overarching principles governing shifts in vegetation growth. Furthermore, the utilization of the intensity analysis framework and intensity spectrum employed in this study demonstrates their efficacy in elucidating the temporal dynamics of vegetation changes. Furthermore, this study plays a pivotal role in the surveillance and assessment of the efficacy of ecological restoration in mining regions. It carries substantial implications for comparable land ecological restoration efforts in mining and reclamation, thereby furnishing a theoretical foundation.

KEYWORDS

kNDVI **(kernel normalized difference vegetation index), vegetation coverage, spatio-temporal changes, Sen's + Mann-Kendall trend analysis, intensity analysis, Shendong coal mine**

1 Introduction

According to Zeng et al. (2023), vegetation serves as a reliable indicator of ecological changes and offers a comprehensive depiction of land and environmental conditions. The investigation of vegetation growth and its dynamic fluctuations in mining regions has consistently been a focal point of scholarly inquiry (Han et al., 2021b). Hence, the assessment of vegetation degradation and analysis of spatiotemporal dynamics in mining regions are of paramount importance in terms of their theoretical and practical implications for ecological restoration and enhancement of environmental quality in such areas (Guo et al., 2019; Jiang et al., 2022).

The Shendong Mining Area, situated in the loess-wind deposit sand mining region within the middle and upper reaches of the Yellow River basin, is characterized by an arid climatic condition (Xu et al., 2021). The area in question holds significant ecological fragility and serves as a crucial monitoring site for soil and water erosion in the context of governance in China (Chi et al., 2022). The ecological environment of the area is significantly impacted by the extensive coal mining activities (Xiao et al., 2020; Yang et al., 2022b). The restoration of vegetation in coal mining areas has gained widespread acceptance among nations (Roy et al., 2022). In addition, the monitoring of the fluctuating patterns of vegetation in mining regions is a fundamental aspect of initiatives aimed at restoring vegetation and holds significant importance in the planning, execution, and supervision of vegetation-related activities in mining areas (Liu et al., 2021a; Wang et al., 2021a; Xu et al., 2023b). Hence, the monitoring of vegetation dynamics and alterations in the Shendong Coal Mine carries significant importance. The research findings provide a theoretical basis for the implementation of vegetation management, soil erosion control, and ecological restoration efforts within the Shendong Coal Mine.

The production of coal has an undeniable impact on the ecological environment. Within the context of coal production, monitoring the ecological environment plays a crucial role in attaining economic sustainability (Burchart-Korol et al., 2016; Li et al., 2021a). At present, the predominant method for ecological monitoring in coal mines involves the utilization of remote sensing methods in conjunction with vegetation indices to evaluate the extent of vegetation coverage and the prevailing growth conditions on the terrain (He et al., 2019; Han et al., 2021a; Shang et al., 2022). The subject of long-term ecological monitoring has gained significant attention in recent times. Long-term ecological monitoring predominantly depends on the utilization of Landsat data, which offers a consistent supply of high-resolution multi-spectral remote sensing data spanning several decades, starting from the 1970s (Shan et al., 2019; Jiang et al., 2021; Pei et al., 2023). The utilization of remote sensing technology enables the temporal monitoring of vegetation, facilitating the investigation of alterations in the ecological environment. The Landsat TM/ETM satellite provides data with a high level of spatial resolution, which has led to its extensive utilization in the monitoring of land cover and land use change (Garioud et al., 2021; Pérez-Cabello et al., 2021; Zhou et al., 2022). The Normalized Difference Vegetation Index (NDVI) has emerged as the predominant vegetation index employed in long-term monitoring studies. Extensive research utilizing NDVI has contributed significantly to the understanding and characterization of spatiotemporal variations in vegetation cover, both at a national level within China and on a global scale (Huang et al., 2020; Jimenez et al., 2022; Martinez and Labib, 2023). Nevertheless, the Normalized Difference Vegetation Index (NDVI) does possess certain limitations. The relationship between the subject and green biomass exhibits a non-linear and saturated pattern (Carlson and Ripley, 1997). Additionally, it is important to consider potential errors that may arise when working with atmospheric noise, soil background, and saturation (Liu and Huete, 1995). Despite efforts made by researchers to address these limitations by integrating data from different spectral bands, the problem of saturation has yet to be resolved (Andualem and Berhan, 2021; Huang et al., 2021). In the year 2021, the kernel-

normalized difference vegetation index (*kNDVI*) was introduced by Camps-Valls et al. (2021). The present vegetation index incorporates the benefits of machine learning principles and employs kernel methods for the extraction and computation of NDVI, with the objective of mitigating the constraints associated with the conventional methodology (Gustavo and Lorenzo 2009; Luis et al., 2018). Camps-Valls et al. (2021) conducted an evaluation and comparison of the performance of three vegetation indices, namely *kNDVI*, NDVI, and NIRv. Based on the outcomes of their research, it was observed that *kNDVI* demonstrated a higher level of effectiveness compared to NDVI and NIRv in diverse applications, biomes, and climatic zones. This study highlighted the distinct benefits of utilizing *kNDVI* in mitigating saturation effects, managing intricate phenological cycles, and accounting for seasonal variations. The suitability of the index for effectively representing the status of vegetation coverage in both natural and agricultural systems has been demonstrated in several studies (Liu et al., 2021b; Forzieri et al., 2022; Gensheimer et al., 2022; Wang et al., 2022b). Furthermore, the suitability of *kNDVI* for evaluating the growth conditions and temporal variations of vegetation in the mining region has been well-recognized (Wang et al., 2023). Therefore, in the present study, we opted for *kNDVI* as the preferred metric for assessing the condition of the vegetation ecosystem.

Nevertheless, previous research in the field of vegetation dynamics has predominantly concentrated on the gradual and uniform alterations within vegetation ecosystems, while investigations into the magnitude of spatiotemporal patterns have been relatively scarce. Presently, the main focus of scholarly inquiry pertaining to vegetation cover in mining regions revolves around the utilization of extensive time-series remote sensing data. This approach entails an examination of the effects of coal mining activities on the surrounding vegetation and broader ecological landscapes. The objective of this study is to analyze the dynamic patterns of vegetation cover in response to coal mining disturbances. The study aims to contribute valuable data and technical assistance for future restoration and management initiatives in mining regions (Wang et al., 2021b; Chen et al., 2022; Qi et al., 2023). Nevertheless, the extent to which vegetation growth is affected in mining areas remains uncertain. Therefore, the present study aims to introduce the intensity analysis method proposed by Pontius et al. (2004) for the purpose of assessing the intensity of vegetation dynamics. The analysis of intensity and vegetation change shows the extent to which vegetation change is influenced by factors such as climate change and human activities. This is accomplished by examining variables such as vegetation cover, vegetation growth rate, and vegetation types (Guesewell et al., 2007; Tong et al., 2016; Guo et al., 2018). In recent years, there has been a significant amount of scholarly research dedicated to the examination of vegetation change intensity (Murwira and Skidmore, 2006; Liu and Liu, 2018). One the one hand, the utilization of remote sensing technology enables the acquisition of vegetation index data, which in turn facilitates the examination of fluctuations in vegetation growth. Consequently, this approach enables the quantitative assessment of the magnitude of changes in vegetation (Siteur et al., 2014). Alternatively, an avenue for further exploration lies in examining the variations in response to climate change across different types of cover, thereby elucidating the connection between intensity analysis and vegetation change (Xu et al., 2013; Sun et al., 2023). This methodology not only examines the relative stability or dynamics of transitioning vegetation growth trend types, but also determines the dominant category during the transition process. Consequently, this enables us to gain understanding and discern the potential ramifications of ecological restoration initiatives on the recuperation of vegetation in the area.

In summary, this research employed Landsat TM/ETM+/OLI data spanning from 2000 to 2020 to construct a *kNDVI* dataset on the Google Earth Engine (GEE) platform. The primary objective is to analyze the spatial and temporal variations in vegetation cover and the magnitude of its alterations within the Shendong Coal Mine area. The research utilized Theil-Sen median slope analysis, Mann-Kendall (MK) test, and Hurst exponent analysis to investigate the spatiotemporal characteristics of vegetation cover and its future development trends in Shendong Coal Mine. Furthermore, the application of the intensity analysis framework is utilized to examine the evolutionary attributes of various types of vegetation growth trends during two distinct time periods: 2000-2010 and 2010-2020. The primary objective is to evaluate the current state of vegetation restoration in the mining region and offer informed suggestions for the long-term sustainability of Shendong Coal Mine.

2 Materials and methods

2.1 Study area

Shendong mining area (38°52′N–39°41′N, 109°51′E–110°46′E) is situated in the southeastern part of the Ordos Plateau and the northern edge of the Loess Plateau. It is situated at the geographical border between Yulin City in Shaanxi Province and Ordos City in Inner Mongolia Autonomous Region (as depicted in Figure 1A). The estimated land area encompasses approximately 900 km^2. The region exhibits an average annual temperature of 6.2 °C, characterized by extreme minimum temperatures of -31.4 °C and extreme maximum temperatures of 36.6 °C. The annual precipitation in the region varies between 300 and 400 mm. Additionally, the rate of evaporation surpasses the amount of rainfall by more than fourfold, suggesting a characteristic arid to semi-arid continental climate. The region exhibits variations in topography, characterized by elevated terrain in the northwestern portion and comparatively lower terrain in the southeastern part (as depicted in Figure 1B). On average, the altitude of the area hovers around 1200 meters. The mining area's eastern and northeastern regions are comprised of loess hills and mountains, which are distinguished by a network of gullies. The region is situated within a transitional ecological zone characterized by a blend of steppe and forest-steppe ecosystems (as depicted in Figure 1C). The dominant vegetation types in this area include grasslands, deciduous broadleaf shrubs, and sand-based vegetation. These areas display three distinct landforms, namely ridges, gullies, and loess tablelands. These regions are prone to erosion and significant soil degradation. The western and southwestern regions are characterized by the presence of mobile, semi-fixed, and fixed sand dunes, which provide a suitable environment for sand-based vegetation communities. These

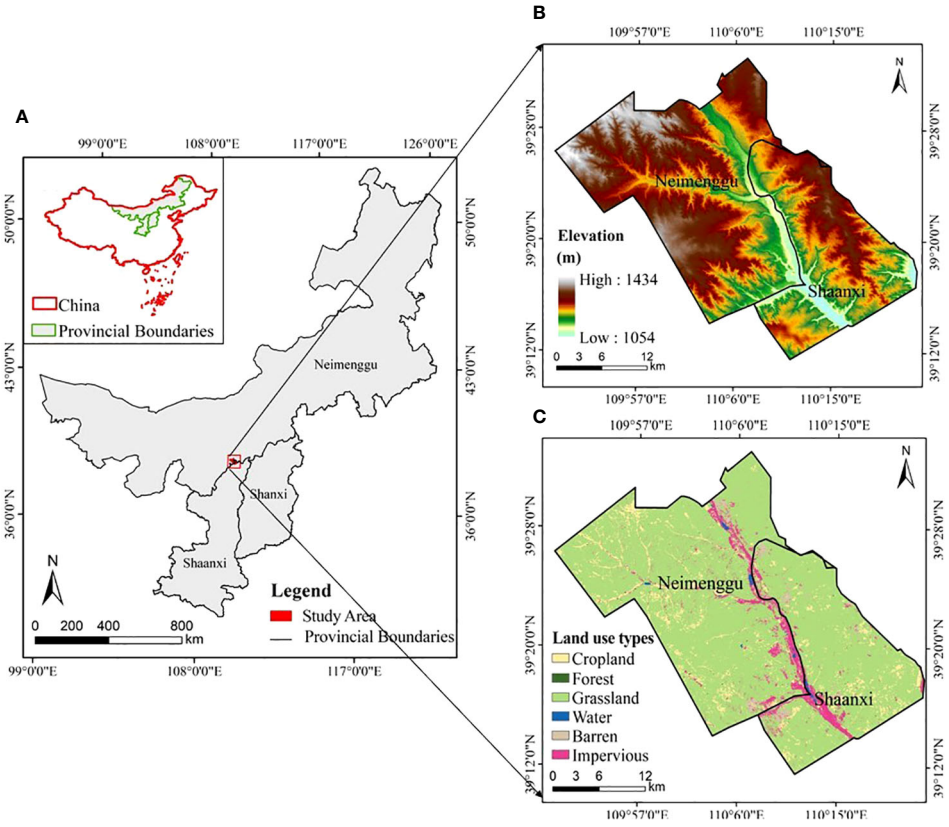

FIGURE 1
The study area in the Shendong Coal Mine **(A)** location in China, **(B)** elevation, and **(C)** land-cover class.

communities include sand-based pioneer plant communities and Artemisia communities. Wetland vegetation is commonly observed in low-lying areas, adjacent to river courses, and encircling bodies of water such as lakes.

2.2 Data collection and preprocessing

The remote sensing image data utilized in this investigation were acquired from the United States Geological Survey (USGS) as Landsat T1_L2 products encompassing the time period from 2000 to 2020. The data were obtained through the utilization of the Google Earth Engine (GEE) platform. The resolution of the images was 30 meters, while the temporal resolution was 16 days. The data underwent preprocessing techniques, such as atmospheric correction, radiometric calibration, and cloud removal, specifically targeting data with cloud cover below 20% within the local vegetation growth season spanning from July to October. Table 1 presents comprehensive details regarding the data utilized in the present study. In order to mitigate the problem of data striping observed in Landsat 7 satellite imagery, a destriping algorithm provided by the Google Earth Engine (GEE) platform was utilized. Following that, the computation of the Normalized Difference Vegetation Index (NDVI) and Kernel Normalized Difference Vegetation Index (*kNDVI*) was carried out on the cloud. The study employed a median composite algorithm to generate composite images. Additionally, the Quality Mosaic algorithm available online was employed for image clipping in order to address the negative impacts of clouds, atmosphere, and satellite sensor angles on the remote sensing data.

TABLE 1 Sources of data used in this study.

Dataset		Type	Image Usability Analysis	Spatial Resolution/m	Time Resolution/Year	Data Source
Image data	Landsat 5 T1	Raster	73 scenes	30	2000-2011	United States Geological Survey https://www.usgs.gov/
	Landsat 7 T1	Raster	129 scenes	30	2000-2020	United States Geological Survey https://www.usgs.gov/
	Landsat 8 T1	Raster	74 scenes	30	2013-2020	United States Geological Survey https://www.usgs.gov/

The present study examines the accessibility of Landsat images within the Shendong mining area, utilizing the GEE cloud platform. A comprehensive analysis yielded a total of 276 images that were deemed suitable for further investigation. Figure 2 illustrates the temporal distribution of satellite images from the years 2000 to 2020, as depicted in Figure 2A, along with the corresponding number of available images, as shown in Figure 2B.

2.3 Research methods

As illustrated in Figure 3, this study acquired a dataset of *kNDVI* spanning 21 years, from 2000 to 2020, specifically from the Shendong Coal Mine. The dataset was partitioned into two distinct periods, namely 2000-2010 and 2010-2020, in order to investigate the patterns of vegetation change. The Theil-Sen Median slope estimation and Mann-Kendall trend test methods were utilized to discern patterns of vegetation change. The Hurst exponent was employed to assess the long-term persistence of vegetation dynamics in the studied area. We employed the intensity analysis framework model to evaluate the intensity of transition trends in vegetation changes during the two periods. This assessment took into account both absolute and relative intensity perspectives.

2.3.1 *kNDVI* vegetation index calculation

The *kNDVI* is a normalized vegetation index that utilizes kernel functions, which are a type of machine learning techniques. The proposed approach represents an advancement of the conventional

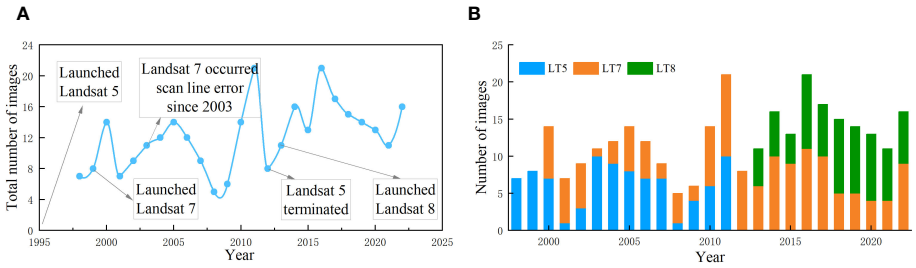

FIGURE 2
Availability of Landsat images of a time series of the reserve from 2000 to 2020, **(A)** Landsat image time distribution, **(B)** total number of sensor image (Landsat5/7/8).

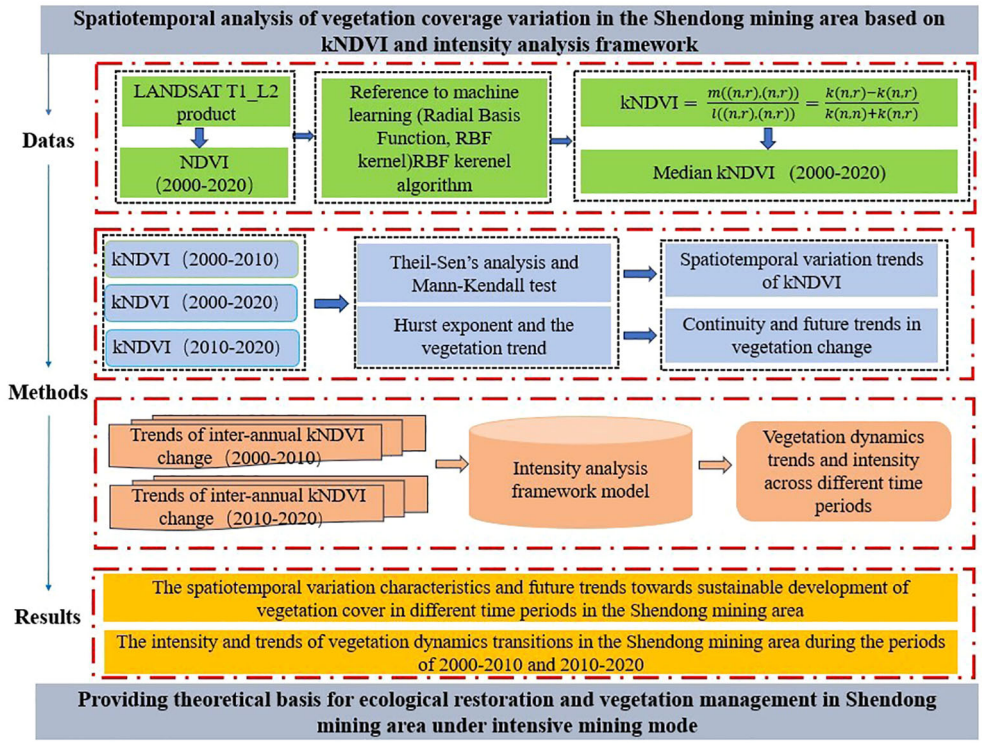

FIGURE 3
Flow chart of the research.

NDVI index, with the primary objective of addressing the challenges related to scale transformation and nonlinearity. According to Camps-Valls et al., 2021), the integration of kernel technology enables *kNDVI* to offer enhanced vegetation information that is both dependable and precise, even in scenarios involving nonlinear variations and across various scales. The calculation formula is as follows (Equation 1):

$$\boldsymbol{kNDVI} = \boldsymbol{tanh}\left(\left(\frac{\boldsymbol{NIR-Red}}{\boldsymbol{2\sigma}}\right)^2\right) = \boldsymbol{tanh}\left(\left(\frac{\boldsymbol{NDVI}}{\boldsymbol{2\tau}}\right)^2\right) \quad (1)$$

Where σ represents a length scale directly proportional to the mean values of near-infrared and red reflectance obtained from the remote sensing image. A τ =0.5 strikes a favorable compromise between accuracy and simplicity (Wang et al., 2023). Using $\sigma = \tau(NIR+Red)$. The calculation formulas are as follows : (Equations 2, 3)

$$\frac{\boldsymbol{dkNDVI}}{\boldsymbol{dNDVI}} = \frac{\boldsymbol{1}}{\boldsymbol{2\tau^2}}\boldsymbol{(1 - kNDVI^2)NDVI} \quad (2)$$

$$\boldsymbol{kNDVI} = \boldsymbol{tanh(NDVI^2)} \quad (3)$$

2.3.2 Sen+Mann-Kendall vegetation trend analysis

The Theil-Sen median trend analysis, also referred to as Sen trend analysis, is a resilient non-parametric statistical technique employed to compute trends. In contrast to linear regression trend analysis, the Sen trend analysis method has the ability to mitigate the influence of missing time series data and the shape of the data distribution. Additionally, it effectively eliminates the interference caused by outliers in the time series data (Gocic and Trajkovic, 2013). The mathematical expression denoted as Equation 4 provides the formula for determining the magnitude of the Sen trend.

$$\boldsymbol{\beta_{kNDVI}} = \boldsymbol{median}\left(\frac{\boldsymbol{kNDVI_j - kNDVI_i}}{\boldsymbol{j-i}}\right), \forall_{\boldsymbol{i}} \quad (4)$$

Where $kNDVI_i$ and $kNDVI_j$ represent *kNDVI* time series. A $\beta_{kNDVI} > 0.0005$ indicates an improved *kNDVI* trend. Conversely, a $\beta_{kNDVI} < 0.0005$ implies a degraded *kNDVI* trend.

The Mann-Kendall test, also known as the MK test, is frequently employed in conjunction with Sen trend analysis. The aforementioned approach is a non-parametric statistical test that exhibits robustness in the presence of missing values and outliers. Additionally, it does not make any assumptions regarding the underlying data distribution (Yue and Wang, 2004). The statistical test procedure is demonstrated in (Equations 5–8).

$$\boldsymbol{Z} = \begin{cases} \frac{\boldsymbol{S-1}}{\sqrt{\boldsymbol{Var(S)}}} & \boldsymbol{(S > 0)} \\ \boldsymbol{0} & \boldsymbol{(S = 0)} \\ \frac{\boldsymbol{S-1}}{\sqrt{\boldsymbol{Var(S)}}} & \boldsymbol{(S < 0)} \end{cases} \quad (5)$$

$$S = \sum_{j=1}^{n=1}\sum_{i=j+1}^{n} \boldsymbol{sign(kNDVI_j - kNDVI_i)} \quad (6)$$

$$\boldsymbol{Var(S)} = \frac{\boldsymbol{n(n-1)(2n+5)}}{\boldsymbol{18}} \quad (7)$$

$$\boldsymbol{sign(\theta)} = \begin{cases} \boldsymbol{1} & \boldsymbol{(\theta > 0)} \\ \boldsymbol{0} & \boldsymbol{(\theta = 0)} \\ \boldsymbol{-1} & \boldsymbol{(\theta < 0)} \end{cases} \quad (8)$$

Where $kNDVI_j$ and $kNDVI_i$ refer to *kNDVI* time series; *sign* represents the sign function; *S* denotes the test statistic; *Z* is the standardized test statistic; *n* is the number of data points. At a given significance level α, if $|Z| > Z_{1-\alpha/2}$, it suggests the presence of a significant trend change. In this study, α is set as to 0.05, implying the evaluation of the significance of *kNDVI* time series changes at a 0.05 significance level.

2.3.3 Analysis of vegetation change sustainability

The calculation of the Hurst exponent is derived from the application of the rescaled range (R/S) analysis method. This exponent is utilized as a metric to discern whether a given set of time series data adheres to a random walk or a biased random walk process. The description of time series patterns is a widely employed approach in the fields of hydrology, geology, and climate studies (Sioris et al., 2016). This study employs the Hurst exponent to characterize the future temporal evolution of pixel values within the study area. The computation method is as follows:

For a given time series { kNDVI (t), 1, 2,..., n }, the mean sequence is defined by Formula (Equation 9):

$$\overline{\boldsymbol{kNDVI}}_{\boldsymbol{(T)}} = \frac{\boldsymbol{1}}{\boldsymbol{T}}\sum_{\boldsymbol{t=1}}^{\boldsymbol{T}}\boldsymbol{kNDVI_{(T)}} \quad \boldsymbol{T = 1, 2, \cdots, n} \quad (9)$$

The cumulative deviation formula is (Equation 10) :

$$\boldsymbol{X_{(t,T)}} = \sum_{\boldsymbol{t=1}}^{\boldsymbol{t}}\boldsymbol{(kNDVI_{(t)} - \overline{kNDVI_{(T)}})} \quad \boldsymbol{1 \le t \le T} \quad (10)$$

The value range formula of and is (Equation 11) :

$$\boldsymbol{R_{(T)}} = \boldsymbol{maxX_{(t,T)} - minX_{(t,T)}} \quad \boldsymbol{T = 1, 2, \cdots, n} \quad (11)$$

The standard deviation formula is (Equation 12) :

$$\boldsymbol{S_{(T)}} = \left[\frac{\boldsymbol{1}}{\boldsymbol{T}}\sum_{\boldsymbol{t}}^{\boldsymbol{T}}\boldsymbol{(kNDVI_{(t)} - kNDVI_{(T)})^2}\right]^{\frac{1}{2}} \quad \boldsymbol{T = 1, 2 \cdots, n} \quad (12)$$

And using the above formula, we can get Formula (Equation 13) :

$$\frac{\boldsymbol{R_{(T)}}}{\boldsymbol{S_{(T)}}} \cong \frac{\boldsymbol{R}}{\boldsymbol{S}} \quad (13)$$

A $R/S \propto T^H$ indicates the presence of the Hurst phenomenon in the analyzed sequence. Here, *H* represents the Hurst exponent, which can be obtained by fitting $log\ (R/S)_n = R/S(\ )_n = \alpha + H*log(n)$, using the least squares method. A $0< H< 0.5$ indicates anti-persistent kNDVI in the time series, implying that the future trend is opposite to the past. As H gets closer to 0, the degree of anti-persistence increases. Similarly, a $0.5 < H < 1$ suggests positive correlation in the *kNDVI* time series, meaning that the future trend is consistent with the past. As H approaches 1, the degree of positive

correlation strengthens. A $H = 0.5$ signifies that the variation trend of *kNDVI* in the time series is a random sequence with no significant correlation.

2.3.4 Intensity analysis framework model

The analysis of intensity focuses on the quantitative assessment of vegetation change trends, which occur at various time intervals. This examination is conducted from two distinct viewpoints: absolute intensity and relative intensity. The concept of absolute intensity pertains to the absolute number of trend conversions occurring within a specific time frame. This measure can be examined from two perspectives: the conversion from a particular trend type to different trend types, and the conversion from other trend types to the specified trend type. The calculation formulas for each intensity pattern are specified as follows:

The absonorlute transition intensity, denoted as AI_{ij}, represents the conversion of the initial vegetation trend level i to a specific final vegetation trend level j within the time interval $[Tn,Tn+_1]$ (where $i \neq j$). Its calculation formula is as follows (Equation 14):

$$AI_{ij} = \frac{\varphi_{ij}/(T_{n+1} - T_n)}{\sum_{i=1}^{I} \varphi_{ij}} \tag{14}$$

The mean absolute transition intensity (MAI_j) for the conversion of all vegetation trend grades except j to grade j within the time interval $[Tn,Tn+_1]$; Its calculation formula is as follows (Equation 15):

$$MAI_j = \frac{\left\{\left[\left(\sum_{i=1}^{I} \varphi_{ij}\right) - \varphi_{jj}\right]/(I-1)\right\}/(T_{n+1} - T_n)}{\sum_{i=1}^{I} \varphi_{ij}} \tag{15}$$

The absolute transition intensity, denoted as AO_{xy}, represents the conversion of the initial vegetation trend grade x to a specific final vegetation trend y within the time interval $[Tn,Tn+_1]$ (where $x \neq y$). Its calculation formula is as follows (Equation 16):

$$AO_{xy} = \frac{\varphi_{xy}/(T_{n+1} - T_n)}{\sum_{y=1}^{Y} \varphi_{xy}} \tag{16}$$

The average absolute transition intensity (MAO_x) is calculated for all vegetation trend grades except x within a specific time interval $[Tn, Tn+_1]$; Its calculation formula is as follows (Equation 17):

$$MAO_x = \frac{\left\{\left[\left(\sum_{y=1}^{Y} \varphi_{xy}\right) - \varphi_{xx}\right]/(Y-1)\right\}/(T_{n+1} - T_n)}{\sum_{y=1}^{Y} \varphi_{xy}} \tag{17}$$

Where i and y represent the initial and final vegetation trend grades, while j and x represent the transition-in and transition-out vegetation trend grades. φ_{ij} and φ_{xy} represent the area of the transition from grade i to grade j and the transition from grade x to grade y, respectively, within the given time interval. φ_{jj} and φ_{xx} represent the area in which the grade remains unchanged within the time interval. I and Y denote the number of initial and final vegetation trend grades, respectively.

The concept of absolute intensity pertains to the absolute number of trend type conversions, encompassing both the process of transitioning into a trend type and the process of transitioning out of it. Relative intensity, in continuation of this foundational analysis, conducts a further examination of the influence of the intensity of land cover conversion on the structure of vegetation change trends in the study area.

The transition intensity, denoted as RI_{ij}, represents the conversion of the initial vegetation trend grade i to a specific final vegetation trend grade j within the time interval $[Tn,Tn+_1]$ (where $i \neq j$), as: Its calculation formula is as follows (Equation 18):

$$RI_{ij} = \frac{\varphi_{ij}/(T_{n+1} - T_n)}{\sum_{y=1}^{Y} \varphi_{iy}} \tag{18}$$

The average relative transition intensity, denoted as MRI_j, is the conversion of all other vegetation trend grades except j to grade j within the time interval $[Tn,Tn+_1]$, as: Its calculation formula is as follows (Equation 19):

$$MRI_j = \frac{\left\{\left[\left(\sum_{i=1}^{I} \varphi_{ij}\right) - \varphi_{jj}\right]/(I-1)\right\}/(T_{n+1} - T_n)}{\sum_{y=1}^{Y}\left[\left(\sum_{i=1}^{I} \varphi_{iy}\right) - \varphi_{jy}\right]} \tag{19}$$

The relative transfer strength RO_{xy} $(x \neq y)$ represents the conversion of the initial vegetation trend level x to a final vegetation trend level y within the time interval $[Tn,Tn+_1]$, as: Its calculation formula is as follows (Equation 20):

$$RO_{xy} = \frac{\varphi_{xy}/(T_{n+1} - T_n)}{\sum_{i=1}^{I} \varphi_{iy}} \tag{20}$$

The average relative transfer strength MRO_x represents the conversion of vegetation trend level x within the time interval $[Tn,Tn+_1]$ to all other vegetation trend levels except x, as: Its calculation formula is as follows (Equation 21):

$$MRO_x = \frac{\left\{\left[\left(\sum_{y=1}^{Y} \varphi_{xy}\right) - \varphi_{xx}\right] \div (Y-1)\right\} \div (T_{n+1} - T_n)}{\sum_{i=1}^{I}\left[\left(\sum_{y=1}^{Y} \varphi_{iy}\right) - \varphi_{ix}\right]} \tag{21}$$

In the equation above, φ_{ix} represents the area where the initial vegetation trend level i transitions to level x, and φ_{iy} represents the area within the time interval $[Tn,Tn+_1]$ where the initial vegetation trend level i transitions to the final levely.

3 Results

3.1 Temporal and spatial variations of vegetation coverage

3.1.1 Temporal dynamics of vegetation coverage

The representative *kNDVI* values for each year between 2000 and 2020 were obtained by utilizing the median value of *kNDVI* pixels in the images from 2000 to 2020, which serves as a comprehensive indicator of vegetation conditions. The annual *kNDVI* values were utilized in order to generate a fitted curve that illustrates the fluctuations in *kNDVI*, as depicted in Figure 4. As depicted in Figure 3, there exists a notable disparity in *kNDVI* values over the course of multiple years. Between the years 2000 and 2020, as depicted by the red line, the normalized difference vegetation index (*kNDVI*) exhibited an upward trajectory from 0.040 to 0.185. This corresponds to an annual growth rate of 0.0065, suggesting a notable and swift enhancement in vegetation coverage.

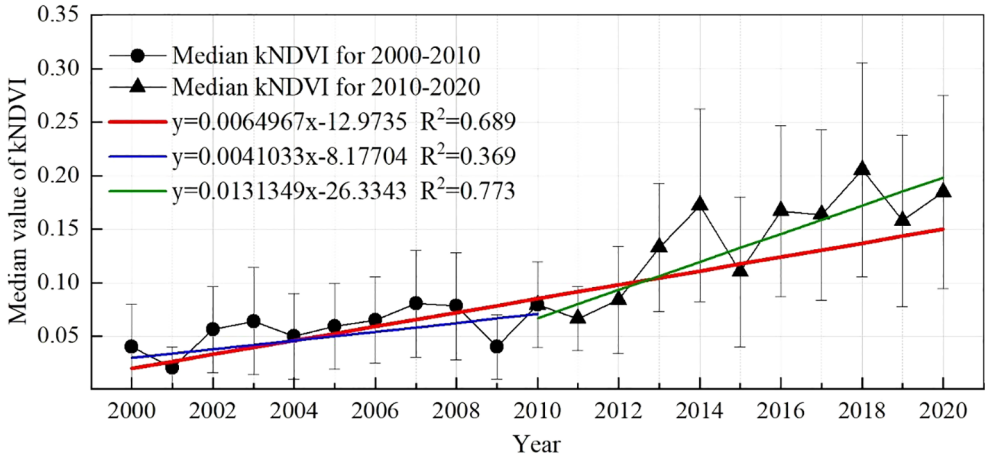

FIGURE 4
Time variation of median kNDVI in the Shendong Coal Mine, 2000—2020.

A model was developed to analyze the spatiotemporal variation of vegetation coverage within the protected area. This model utilized the pixel-based intermediate approach. The findings of the study indicate a statistically significant rise in the mean annual vegetation coverage within the mining region between 2000 and 2020 ($p< 0.05$). The Mann-Kendall mutation test was utilized to construct a map depicting the annual mutation of vegetation coverage in the mining area. The analysis revealed that this mutation occurred in the year 2010, as illustrated in Figure 5. Given the clear presence of discernible mutation points in both the UF and UB curves in the year 2010, the present study opted to partition the time series data pertaining to vegetation coverage within the protected area into two distinct stages: the period spanning from 2000 to 2010, and the subsequent interval from 2010 to 2020. Figure 4 illustrates the *kNDVI* trends from 2000 to 2010, as represented by the blue line. During this time frame, a gradual growth phase is observed, characterized by an increment from 0.04 to 0.079 in *kNDVI* values. The corresponding growth rate is calculated to be 0.0041 per annum. In contrast, the time span from 2010 to 2020 (represented by the green line) exhibited a notable period of expansion, as indicated by the increase in *kNDVI* from 0.079 to 0.185 and a growth rate of 0.013 per annum. During the period from 2000 to 2010, the Shendong Coal Mine undertook extensive afforestation initiatives and implemented diverse ecological and environmental comprehensive management approaches throughout its development and construction endeavors. Nevertheless, the challenging conditions of the mining region posed significant obstacles to the process of vegetation reconstruction and restoration, thereby impeding the rate of growth in comparison to the timeframe spanning from 2010 to 2020. Between the years 2010 and 2020, there was a notable establishment of a foundation for vegetation coverage, accompanied by intensified efforts towards vegetation recovery. Consequently, there was a significant and rapid augmentation in

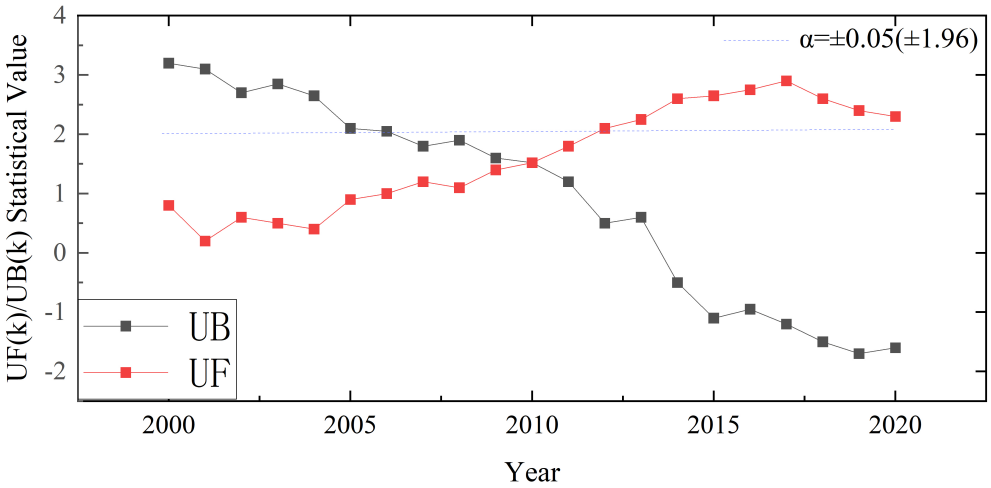

FIGURE 5
Mann-Kendall mutation test.

vegetation coverage. From the year 2000 to 2020, there was a noticeable pattern of substantial vegetation expansion within the mining region.

3.1.2 Spatial distribution characteristics of vegetation coverage

Figure 6 illustrates the distribution characteristics of median values of *kNDVI* during various stages of the 21-year duration of Shendong Coal Mine. The calculation of the overall vegetation for the time periods of 2000-2010, 2010-2020, and 2000-2020 was conducted using the median values of the annual *kNDVI*. The selection of median values was made to serve as a representation of the vegetation coverage across the three stages in question. The findings demonstrated a strong correlation between the extent of vegetation coverage and the corresponding rates of vegetation growth observed at each stage. The vegetation coverage during the time frame of 2010-2020 exhibited the highest value of 0.149, indicating the most favorable conditions. Subsequently, the periods of 2000-2020 and 2000-2010 displayed values of 0.087 and 0.065, respectively, suggesting relatively lower levels of vegetation coverage. Based on the analysis of Figure 6, it is evident that the three stages (Figures 6A–C) exhibit a notable concentration of elevated *kNDVI* values in the eastern and western regions of the Shendong mining area. Additionally, these high values are also observed in the mountainous areas flanking the town, as well as in the southern sections of the Huojitu and Daliuta mining areas. Conversely, the diminished values primarily manifest in the urban regions of the mining vicinity and adjacent areas that experience substantial anthropogenic impact, such as the Ulan Mulun and Shigetai coal mining regions. In general, the spatial distribution of *kNDVI* in the Shendong mining area demonstrates a consistent pattern. The vegetation coverage within the entirety of the Shendong mining area exhibits minimal fluctuations. The vegetation coverage in certain mining regions, such as Da Lita and Ulan Mulun Mine, exhibited a lower extent. In general, the vegetation coverage along the eastern and western boundaries of the Shendong Coal Mine exhibited superior characteristics. Moreover, this geographical area serves as a crucial site for the execution of ecological conservation initiatives in China, including afforestation and reforestation schemes. These endeavors have yielded noteworthy benefits in terms of enhancing vegetation coverage as a result of human interventions.

3.1.3 Spatial variation characteristics of vegetation coverage

In order to accurately capture the patterns of vegetation changes and spatial distribution characteristics in the area, this research integrates Sen's trend analysis with the Mann-Kendall test. The Sen's values can be categorized into three distinct groups. The first group consists of values falling within the range of -0.0005 to 0.0005, which are considered as indicative of a stable condition. The second group includes regions with Sen's values equal to or greater than 0.0005, which are classified as areas showing improvement. Lastly, the third group comprises regions with Sen's values less than -0.0005, which are identified as areas experiencing degradation. The outcomes of the Mann-Kendall test are categorized into two groups: statistically significant changes ($Z > 1.96$ or $Z < -1.96$) and statistically insignificant changes ($-1.96 \leq Z \leq 1.96$), with a confidence level of 0.05. The vegetation change trend map for the entire region is derived by aggregating the results at each pixel scale. Based on the aforementioned classification criteria, the entire region can be categorized into five distinct groups, as illustrated in Table 2.

Based on the analysis of the annual inter-annual variation trend of *kNDVI* in the Shendong Coal Mine spanning from 2000 to 2020 (Figure 7), it is evident that the vegetation growth within the region has exhibited a notable enhancement, encompassing approximately 89.47% of the entire mining area. The proportion of the total area that is classified as degraded is 2.74%. The degraded areas primarily exist within different open-pit mining sites, specifically the northern section of Huojitu Mine and the southern section of Shigetai Mine. The mining region has adopted strategies for concurrent mining and restoration, with each individual mine making efforts to mitigate environmental harm and engage in active restoration of impacted areas. Consequently, the areas exhibiting slight

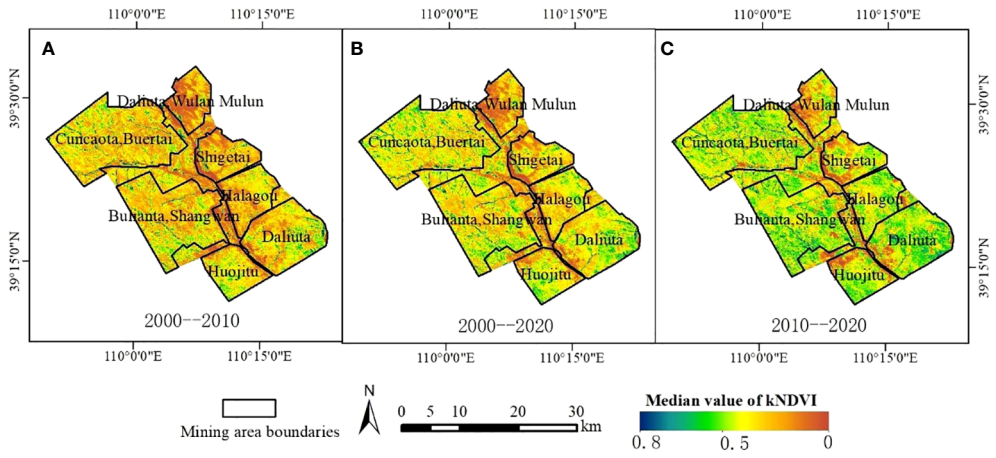

FIGURE 6
Spatial distribution characteristics of vegetation cover **(A)** 2000—2010, **(B)** 2000—2020, **(C)** 2010—2020.

TABLE 2 Statistical analysis results of *kNDVI* trends.

Sen's	*Z* value	Trend of *kNDVI*
≥0.0005	≥1.96	Significantly Improved
≥0.0005	-1.96-1.96	Slightly Improved
-0.0005-0.0005	-1.96-1.96	Stable
≤-0.0005	-1.96-1.96	Slightly Degraded
≤-0.0005	≤-1.96	Severely Degraded

improvements are primarily localized along the perimeters of the open-pit regions of each mine, constituting approximately 4.65% of the overall land area. The Shendong Coal Mine holds significant importance as a focal region for the implementation of ecological conservation initiatives within China. From the year 2000 to 2020, there was a notable increase in vegetation coverage within the mining area.

To provide a comprehensive depiction of vegetation dynamics from 2000 to 2020 and elucidate patterns of vegetation change, the temporal span is partitioned into two distinct stages: 2000-2010 and 2010-2020. This division is predicated on the growth rate of vegetation coverage, as illustrated in Figure 8. The examination of the trend in vegetation growth during two distinct stages provides insight into the intensity of vegetation restoration and the mode of transition observed in the mining area at different points in time. According to the data presented in Figure 8, the period from 2000 to 2010 witnessed a discernible but modest upward trajectory in the Shendong Coal Mine. This particular phase accounted for 54.83% of the overall area. The trend of significant improvement represents the second largest proportion, comprising 31.47% of the total area. In contrast, the period from 2010 to 2020 witnessed a notable upward trend in the dominance of the mining sector, with its share increasing from 31.47% in the 2000-2010 period to 61.16% in the 2010-2020 period. The percentage of the area exhibiting a slight improvement trend decreases from 54.83% to 32.39%. In general, the trajectory of vegetation dynamics progresses from a slight improvement to a significant improvement pattern.

3.2 The spatial distribution and future development trend of the Hurst exponent for vegetation coverage

3.2.1 Spatial distribution of Hurst exponent for vegetation coverage

According to the data presented in Figure 9, the average Hurst exponent for *kNDVI* in the Shendong Coal Mine is 0.521. The regions exhibiting Hurst values below 0.5 are primarily concentrated in the northwestern section of the mining area, encompassing the Cuncaota and Buertai Mines. These regions account for approximately 40.12% of the total area. Conversely, it can be observed that regions exhibiting Hurst values exceeding 0.5 are predominantly situated in the southeastern portion of the mining area, encompassing Bulianta, Shanwan, and Daliuta Mines. These specific regions account for approximately 59.88% of the overall area. The comprehensive examination of the mining region reveals that the *kNDVI* in Shendong Coal Mine demonstrates a spatial pattern characterized by clustering, accompanied by a certain level of variability.

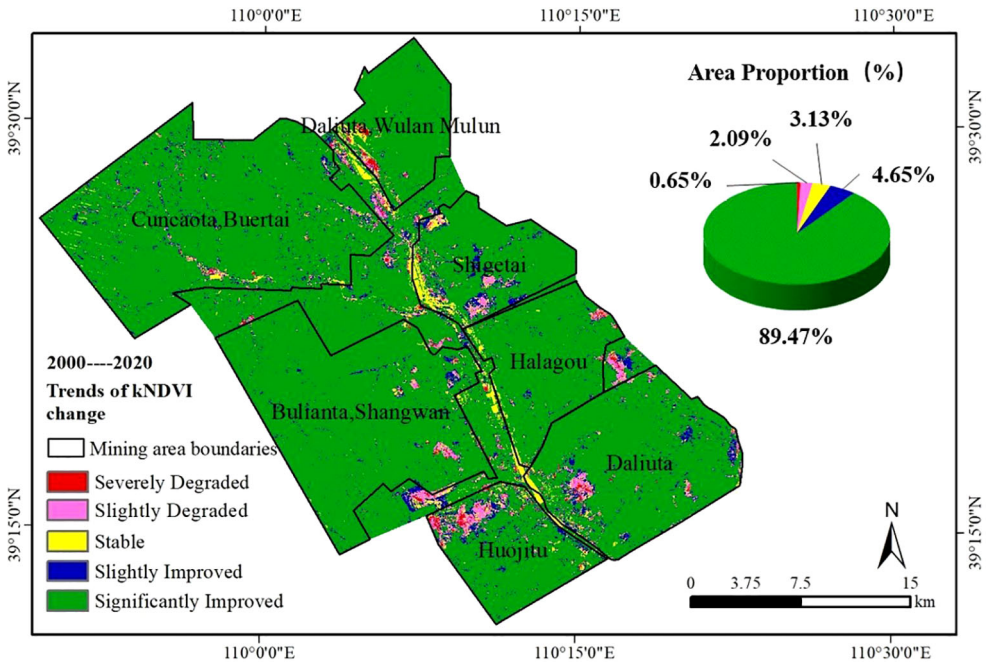

FIGURE 7
Trends of inter-annual kNDVI change in the Shendong Coal Mine from 2000 to 2020.

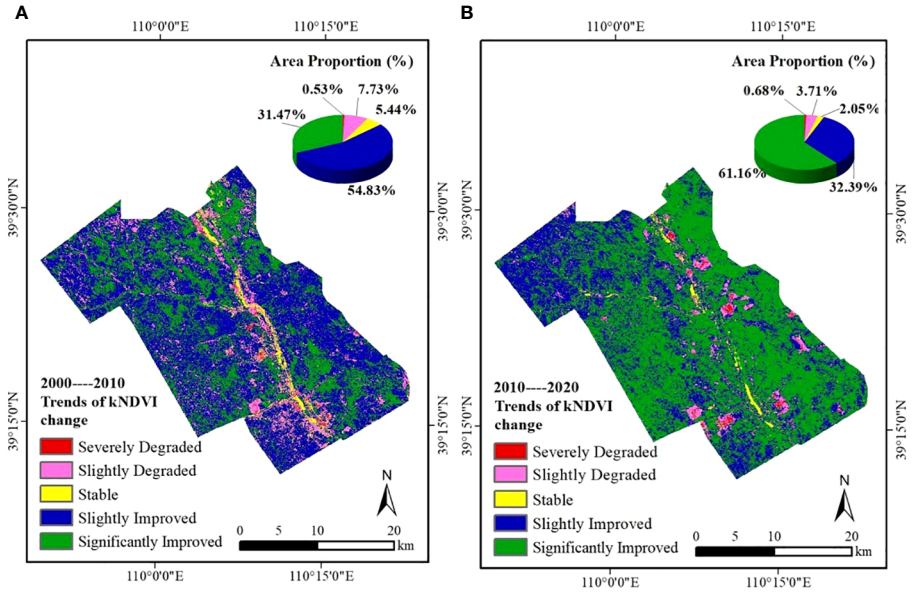

FIGURE 8
Trends of inter-annual kNDVI change in the Shendong coalfield: **(A)** 2000—2010, **(B)** 2010—2020.

3.2.2 Future development trend of vegetation coverage

To enhance comprehension regarding the trajectory and long-term viability of vegetation, an examination is conducted on the *kNDVI* trend, which is subsequently juxtaposed with the Hurst exponent. This integration yields interconnected insights, as depicted in Figure 10. The findings can be categorized into four distinct groups: a consistent downward trend, a consistent upward trend, a decline in the present with an anticipated increase in the future, and an increase in the present with an expected decrease in the future. The persistent decline in vegetation levels within the region signifies a sustained and pronounced downward trajectory. A continuous increase denotes a persistent and consistent upward trajectory in vegetation. The present reduction and forthcoming

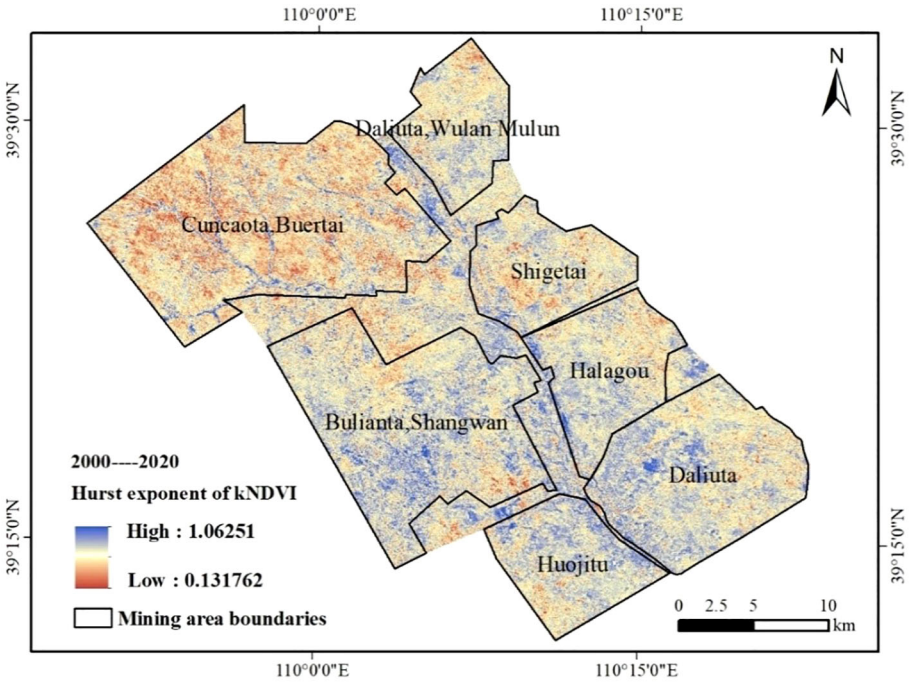

FIGURE 9
Spatial distribution of Hurst exponent in vegetation coverage.

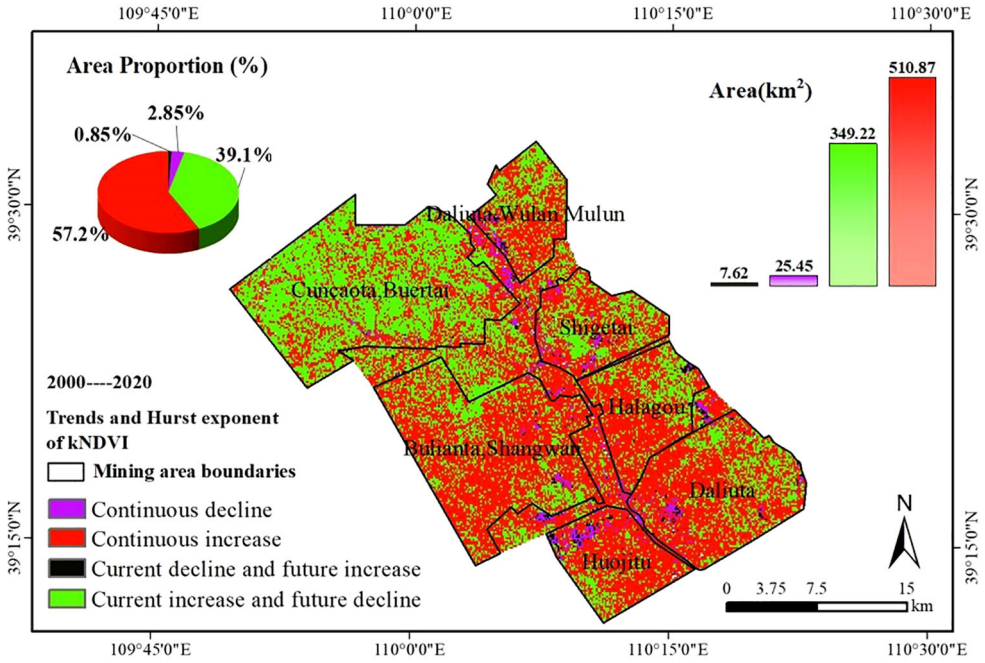

FIGURE 10
Future trends in vegetation coverage.

improvement signify a contemporary pattern of diminishing vegetation, with a prospective shift towards an ascending trajectory. The present improvement and forthcoming diminution signify a prevailing positive trajectory in vegetation, yet a prospective shift towards a negative trajectory.

Based on the data presented in Figure 10, it is evident that the majority of regions exhibit an increasing trend in vegetation, with certain areas projected to undergo a decline in the future. These declining areas encompass a total land area of 349.22 km², constituting approximately 39.10% of the overall region. The aforementioned regions primarily encompass the Cuncaota and Buertai coal mine areas. Nevertheless, it is important to acknowledge that the observed decrease in vegetation in Buertai coal mine and similar regions may not provide an accurate representation of the true state of vegetation on the terrain. Based on field investigations, it has been discovered that the Cuncaota and Buertai coal mines have adopted an "ecological restoration and utilization model" that aligns with the local ecological conditions. This model involves the establishment of ecological restoration bases in areas affected by coal subsidence, as well as the implementation of photovoltaic-assisted planting techniques across a designated land area spanning 42,000 acres. As a result, the utilization of photovoltaic panels has made remote sensing techniques insufficient for accurately monitoring the current state of ground vegetation. The areas in question exhibit a consistent pattern of growth, encompassing a total land area of 510.87 km², which corresponds to 57.20% of the overall territory. These areas hold significant influence within the context of the Shendong Coal Mine. Only a small proportion, specifically 2.85%, of the entire region exhibits a persistent decline, predominantly concentrated within the open-pit areas of diverse mining operations.

3.3 Analysis of the intensity of vegetation change in Shendong coal mine

3.3.1 Analysis of vegetation growth trend changes in Shendong coal mine

The vegetation growth trend observed in Shendong Coal Mine can be divided into two stages: 2000-2010 and 2010-2020. During the first stage, there was a slight improvement in vegetation growth, while during the second stage, there was a significant improvement. The combined area percentage of vegetation growth during the 2000-2010 period was 95%, whereas it was 86.30% during the 2010-2020 period. A transition matrix (Table 3) is utilized to conduct a more comprehensive examination of the change characteristics of various vegetation trend types in Shendong Coal Mine. During the transition from the 2000-2020 period to the 2010-2020 period, the prevailing pattern of vegetation change predominantly exhibits a modest improvement, as evidenced by an area measuring 489.75 km² transitioning away from this particular category. The predominant form of vegetation change that occurs during the transition process is characterized by a substantial improvement, encompassing a total area of 546.29 square kilometers. Among the diverse categories of vegetation trend transitions, the transition from a slight to a significant improvement stands out as the most notable. This transition encompasses an area of 289.07 km², constituting approximately 58.02% of the total area undergoing a transition away from the slight improvement category. In general, the vegetation trends observed in Shendong Coal Mine during the two stages exhibit a consistent and stable pattern of cross-transition. This pattern primarily involves a shift between slight improvement and significant improvement types, indicating the favorable influence of local ecological restoration initiatives on the recovery of vegetation.

TABLE 3 Transition matrix of vegetation growth trends from the period of 2000-2010 to the period of 2010-2020.

2000—2010/km²	2010—2020/km²					Total
	Severely Degraded	Slightly Degraded	Stable	Slightly Improved	Significantly Improved	
Severely Degraded	0.03	0.18	0.81	1.48	2.20	4.70
Slightly Degraded	0.66	2.75	3.24	25.10	37.33	69.08
Stable	0.33	1.80	5.33	15.44	25.72	48.61
Slightly Improved	3.33	17.90	5.59	173.86	289.07	489.75
Significantly Improved	1.77	10.50	3.37	73.42	191.97	281.02
Total	6.11	33.13	18.32	289.30	546.29	893.16

The existing research primarily emphasizes the direct utilization of area change information from the transition matrix, without considering the underlying relationship between the structure of vegetation trend and its transformation. To fully harness the information contained in the transition matrix, this study proposes an intensity analysis model. This model aims to delve into the deeper-level information within the transition matrix and comprehensively analyze the characteristics of vegetation trend transitions in the region.

Figure 11 displays the chart depicting the intensity of change in vegetation growth trends. The chart comprises units that symbolize the reciprocal transformation between the initial vegetation growth trend (i) and the final vegetation growth trend (j) within a specific time interval. The x-axis is indicative of the initial trend in vegetation growth, whereas the y-axis represents the final trend in vegetation growth. The intensity chart comprises four components for each unit: absolute inflow intensity, absolute outflow intensity, relative inflow intensity, and relative outflow intensity. The filling rules can be described as follows: the color light green is used to represent a tendency, while the color orange is used to represent an inhibition. Specifically, when all units in the chart are horizontally filled with light green, it signifies a transformation process from the initial vegetation growth trend i to the final vegetation growth trend j. This transformation is characterized by both the absolute inflow intensity and absolute outflow intensity exhibiting a tendency, which reflects an overall absolute tendency in the transformation. When all units are occupied by the color orange, it signifies a relative inclination within the process of transformation. When a collection of entities is populated exclusively with either light green or orange, it signifies the presence of a systematic tendency or inhibition.

The intensity analysis framework offers a comprehensive examination of the transfer matrix data, thereby enhancing the availability of decision-making information for local ecological restoration efforts. Figure 11 illustrates discernible attributes in the alteration of vegetation growth patterns during two distinct time periods: 2000-2010 and 2010-2020. There exist four primary forms of intensity conversion, with the relative tendency emerging as the prevailing type. Furthermore, there is a relatively balanced distribution of tendencies and inhibitions in general. The shift from significant improvement to slight improvement signifies a complete transformation in trend. This suggests that the vegetation within the mining region exhibits a propensity for degradation in terms of absolute intensity, yet demonstrates an increasing trend in terms of relative intensity. For instance, the transitions observed between

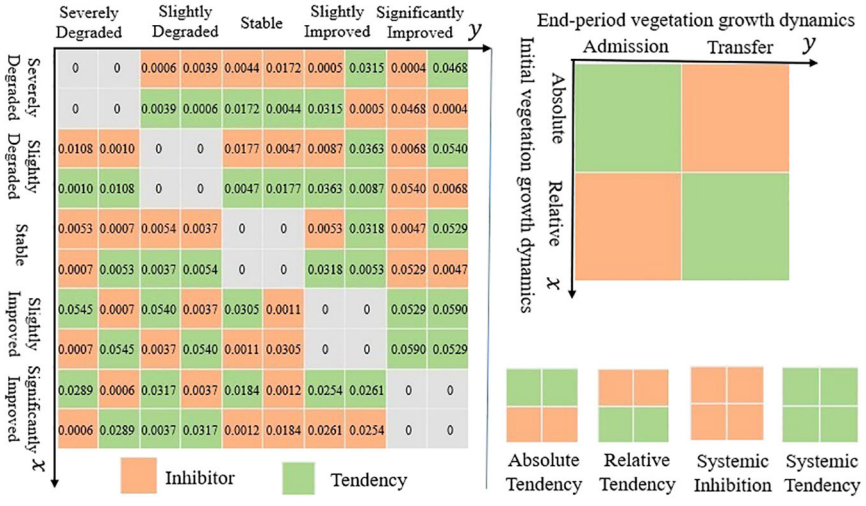

FIGURE 11
Atlas of vegetation change intensity from 2000—2010 to 2010—2020.

significant degradation and slight degradation, significant degradation and stability, and slight degradation and stability demonstrate inherent tendencies that are relative in nature. The observed shift from slight to significant improvement indicates a consistent pattern, providing additional evidence for the positive impact of ecological restoration initiatives on vegetation in the mining region. The observed results are consistent with the patterns of local vegetation evolution. The intensity spectrum encompasses the fundamental principles governing vegetation growth trends as well as the dynamic variations in vegetation growth characteristics. The transition from slight to significant improvement aligns with the overarching principles governing alterations in vegetation growth patterns, thus affirming the viability of the intensity analysis framework and visualization spectrum employed in this research. The forthcoming analysis will concentrate on conducting a comprehensive examination of these patterns of change.

3.3.2 Analysis of the transformation pattern from slight improvement to significant improvement

The primary analysis was centered on examining the transitional region and variations in the intensity of various types of vegetation growth trends. In the examination of the intensity chart pertaining to the transition from slight improvement to significant improvement (Figure 12), the dashed line denotes the uniform transitional intensity expressed as a percentage. When the transitional intensity surpasses the uniform intensity, it signifies a preferential focus on gains and losses within a specific growth trend category. The analysis reveals that the significant improvement trend type demonstrates a notable expansion in its coverage area, exhibiting an intensity that surpasses the average level by a significant margin (0.016%). This is in contrast to the slight improvement trend type, as depicted in Figure 12A. These findings suggest a propensity for transitioning from the slight improvement trend type to the significant improvement trend type. Furthermore, this transition appears to impede the shift from the slight degradation trend type and the remaining four types. In a similar vein, the slight improvement trend type demonstrates a heightened intensity surpassing the average level (0.016%) during the transition to the significant improvement trend type. This suggests a propensity towards transitioning to the significant improvement, while inhibiting transitions to the significant degradation trend type and other types (see Figure 12C). When considering the relative intensity, if each type transitions to the significant improvement trend type in proportion to its initial area, the inflow intensities of each type should be equal. The data reveals that the slight improvement trend type experiences

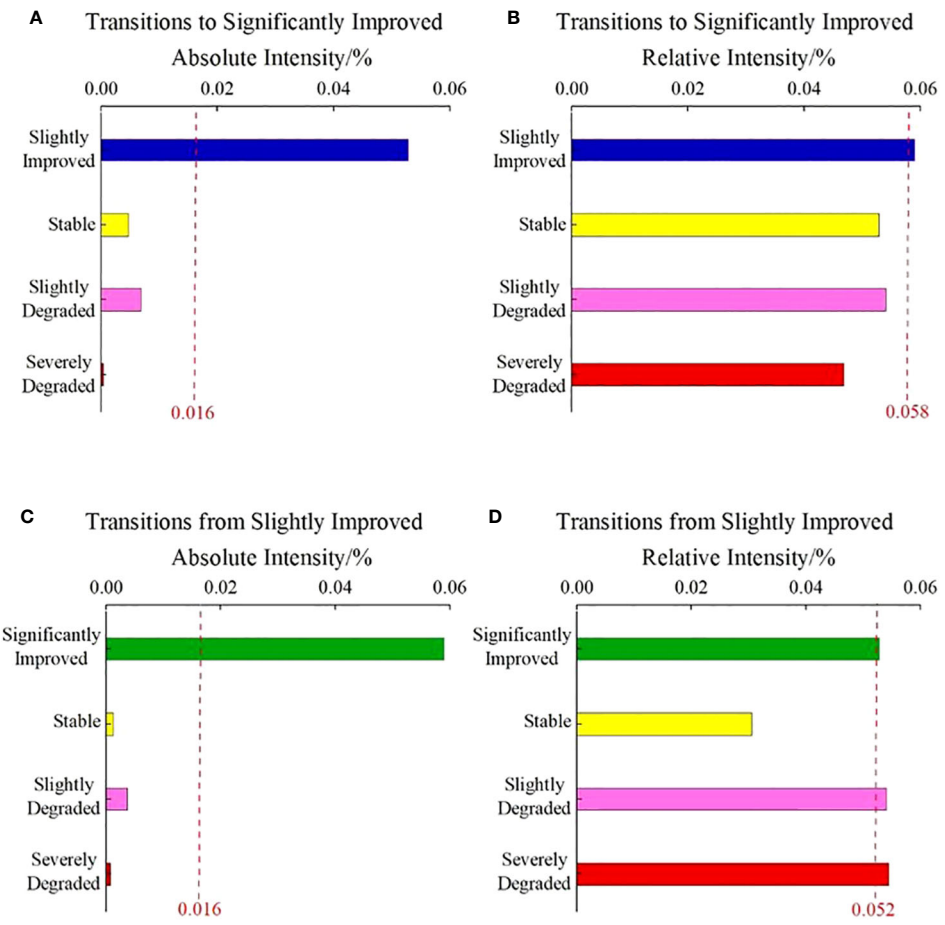

FIGURE 12
Intensity analysis of Slightly Improved to Significantly Improved, **(A)** Transitions to significantly improved absolute intensity, **(B)** Transitions to significantly improved relative intensity, **(C)** Transitions from slightly improved absolute intensity, **(D)** Transitions from slightly improved relative intensity.

a relatively higher inflow intensity (0.058%) towards the significant improvement trend type (Figure 12B). This suggests that there is a tendency for the slight improvement type to transition into the significant improvement type with a larger proportion of its area, resulting in a more substantial impact on the percentage of the significant improvement type in the study area. In a similar vein, the type characterized by a slight improvement trend demonstrates a relatively higher outflow intensity (0.052%) towards the slight degradation and significant improvement types (Figure 12D). This suggests a greater increase in the proportions transitioning to other types, as opposed to the inhibited transition to the stable type. This implies that the process of transformation has a substantial influence on the proportion of the significant improvement category within the study region.

3.3.3 Analysis of the transformation pattern from stable to slight degradation

The examination of the intensity chart depicting the transition from stable to slight degradation (Figure 13) reveals that Shendong Coal Mine exhibits a discernible inclination in the progression from the stable vegetation growth category to the slight degradation category. Regarding absolute intensity, it is observed that both the inflow from stable to slight degradation and the outflow from stable to slight degradation exhibit values that are below the average absolute intensity, specifically 0.023% and 0.022% respectively. This observation suggests that the size of the transition zone between stable and slightly degraded types is relatively limited when compared to other types. This implies that there is an inhibitory effect in terms of the overall quantity, as depicted in Figures 13A, C. However, in terms of relative intensity, the slight degradation type demonstrates a greater inflow from both the stable and significant degradation types compared to the average level (0.0037%). In a similar vein, the stable type demonstrates a greater outflow towards the slight degradation type from both the stable and significant degradation types compared to the average level of 0.005% (as depicted in Figures 13B, D). The aforementioned findings demonstrate a notable inclination towards transitions from the stable category to the slightly degraded category. It is important to acknowledge that the inhibitory behavior observed in absolute intensity does not directly constrain the relative tendency in terms of intensity. Although the transition area between the stable type and the slight degradation type is small, it can still exert a notable influence on the distribution of these types within the region.

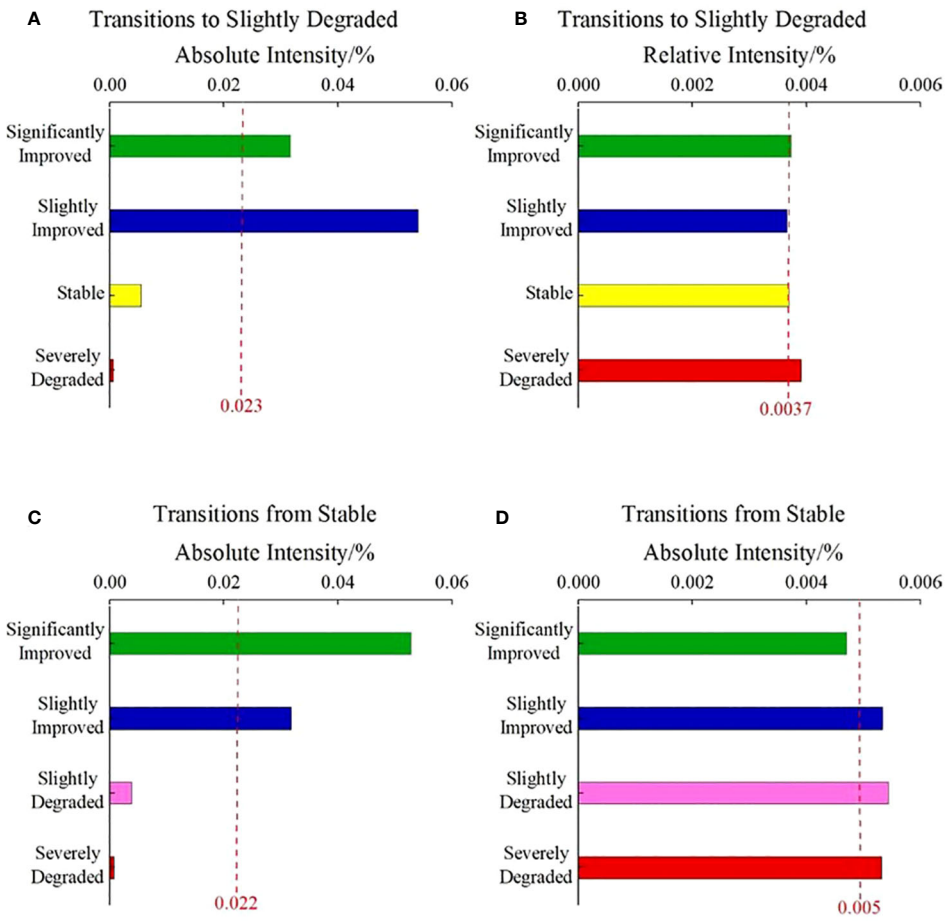

FIGURE 13
Intensity analysis of Stable to Slightly Degraded, **(A)** Transitions to slightly degraded absolute intensity, **(B)** Transitions to slightly degraded relative intensity, **(C)** Transitions from stable absolute intensity, **(D)** Transitions from stable absolute intensity.

4 Discussion

4.1 The *kNDVI* index and spatiotemporal changes

This study provides a comprehensive examination of the spatial distribution, inter-annual variability, and intensity transitions of the *kNDVI* (kernel Normalized Difference Vegetation Index) in the Shendong Coal Mine area from 2000 to 2020. The analysis is conducted using the Google Earth Engine (GEE) platform. In contrast to prior research, the primary emphasis of this paper lies in the enhancement of vegetation indices and the examination of spatiotemporal variations in vegetation. The current body of research primarily relies on NDVI products, primarily derived from MODIS data, which may not provide an accurate representation of vegetation changes in mining areas (Li et al., 2020; Li et al., 2021b; Xu et al., 2022). Nevertheless, the utilization of *kNDVI* in this research significantly deviates from the conventional NDVI approach by effectively addressing the challenge of mixed pixels. Both the *kNDVI* and NIRv indices operate within the near-infrared spectrum. Pixels exhibiting high vegetation coverage demonstrate a robust association between *kNDVI* and variables such as chlorophyll fluorescence. However, this correlation diminishes as vegetation coverage declines (Zhang et al., 2022; Ma et al., 2023b; Wang et al., 2023). Yet, the reduction in correlation observed for *kNDVI* is comparatively less pronounced than that observed for NDVI, suggesting that the *kNDVI* index exhibits a notable capability in distinguishing reflectance across various vegetation levels (Ding et al., 2022; Qiu et al., 2022). Furthermore, the *kNDVI* metric possesses a robust theoretical foundation, rendering it straightforward to compute and implement. Moreover, it holds significant utility in the examination of both natural and agricultural systems. The index demonstrates a strong association with GPP and SIF in grasslands, farmland, mixed forests, and arid areas. This suggests that the index effectively addresses saturation and mixed pixel challenges that are commonly encountered by conventional indices (Deng et al., 2020; Wang et al., 2022a). Moreover, the scope of its application extends beyond the monitoring of vegetation, encompassing change and anomaly detection, phenology, and greening research. Furthermore, this exemplifies the viability and significance of utilizing this index as a means of monitoring alterations in vegetation restoration within the Shendong mining area. A comprehensive analysis of vegetation spatiotemporal changes over a period of 21 years in the Shendong mining area has been conducted, focusing on the utilization of the *kNDVI* index to address saturation effects in vegetation analysis. The current body of literature predominantly centers on the examination of spatiotemporal variations in vegetation within a specific geographic area over an extended duration (Zhang et al., 2021; Guo et al., 2023). However, there is a dearth of research investigating vegetation dynamics across distinct time periods within the same region, as well as the evolving nature of these changes over time. The Shendong Coal Mine is situated in a region that serves as a transitional zone between the Loess Plateau and the Mu Us Desert. This location renders it a representative mining area of significant importance for ecological restoration efforts (Yang et al., 2022a). In order to evaluate the efficacy of vegetation restoration and elucidate the temporal evolution of vegetation recovery in Shendong Coal Mine over a span of 21 years, this study undertakes a comprehensive analysis of the spatial and temporal patterns as well as the magnitude of changes in vegetation. Drawing upon prior research, the objective of this study is to enhance the breadth of knowledge regarding the fluctuations in vegetation within the Shendong Coal Mine. By doing so, it aims to contribute valuable insights that can inform ecological and environmental restoration endeavors in the area.

4.2 Analysis of factors influencing *kNDVI* spatiotemporal changes

The study utilized Sen's and Mann-Kendall trend analysis to examine the spatiotemporal variation trend of vegetation coverage in the research area. The findings of the study revealed a statistically significant alteration in the extent of vegetation coverage when implementing the concurrent mining and restoration approach in the Shendong East mining region. The study area exhibited a consistent upward trajectory in vegetation coverage from 2000 to 2010, followed by a substantial acceleration in growth from 2010 to 2020. Consequently, there was a notable enhancement in the overall vegetation coverage. This discovery is consistent with the research findings of Wu et al. (2023). The recovery of vegetation in the mining area can be attributed to the successful implementation of various strategies such as reforestation, grassland enclosure, and rotational grazing policies in the Shendong East mining area since 2000. These measures have had a positive impact on the restoration of grassland ecology. The Shendong East mining area is characterized by its geographical location within a semi-arid and arid climate zone, which contributes to the presence of a delicate natural environment and challenging climatic conditions. The degradation of the ecological environment in this mining area has been intensified by the large-scale, high-intensity, and multi-layered mining activities that have been repeatedly conducted. The intensive mining activities in the region have initiated a cascade of interconnected consequences, encompassing diverse environmental and societal concerns. Among these, the degradation of soil and vegetation has been identified as the most profoundly affected aspect (Xu et al., 2021). In the Shendong East mining area, the simultaneous mining and remediation model has been implemented, incorporating vegetation restoration practices since the initiation of production in 1985. In light of the recurrent sandstorms and significant soil erosion observed in the mining region, early-stage efforts in vegetation restoration involved the implementation of measures such as grid fixation and sand flow improvement. These measures were aimed at stabilizing the areas characterized by mobile sand. Water storage and soil conservation were accomplished utilizing techniques such as "horizontal ditches" and "fish-scale pits." Following this, various models for vegetation restoration were developed, taking into account the varied ecological conditions found in different regions (Song et al., 2022). Liu et al. (2021a) have classified the vegetation restoration

models in the Shendong East mining area as economic forest, ecological forest, photovoltaic grassland, and sand control models. Subsequently, crops and vegetation have been cultivated in accordance with these models. Following an extensive period of ecological restoration, the Shendong East mining area has witnessed a substantial augmentation in vegetation coverage, surging from a mere 3% to an impressive figure exceeding 64%. The plant community has undergone a transition from an herbaceous community primarily governed by *Artemisia ordosica* to a shrub-grass community predominantly governed by *Hippophae rhamnoides*. The plant species have experienced a substantial increase in their numbers, expanding from the initial count of 16 to approximately 100. This notable growth has had a significant impact on the populations of microorganisms and animals. The enhancement of the existing delicate ecological environment has been observed (Xu et al., 2023a). Nevertheless, the notable augmentation in vegetation coverage within the mining region cannot be exclusively ascribed to artificial ecological restoration initiatives. Temperature and precipitation are significant factors that contribute to the promotion of vegetation growth in mining areas (Yu et al., 2020). In brief, the notable reestablishment of vegetation within the mining region can be attributed to the collaborative endeavors of local afforestation initiatives and climatic influences.

4.3 Limitations and future work

Moreover, this study employs intensity analysis as a means to further investigate the transformation characteristics exhibited by various types of vegetation growth trends within the designated study area. The intensity analysis method was employed to visually represent the transition patterns of vegetation growth trends in the region. This analysis revealed distinct tendencies and inhibitions in the transformation processes of different types of vegetation growth trends. For example, the trend types of significant improvement and slight improvement demonstrate an absolute tendency in their transformations, whereas the trend types of slight and significant improvement exhibit a relative tendency in their transformations. The results of this study further confirm the efficacy of the intensity analysis approach employed, while also offering additional insights into the comprehension of alterations in vegetation growth within the research site. Furthermore, through the integration of the *kNDVI* trend and the Hurst exponent, this investigation unveils the long-term viability of alterations in vegetation. The findings indicate the existence of four distinct sustainability patterns: a consistent decline, a consistent growth, a decline in the present with projected growth in the future, and growth in the present with projected decline in the future. These findings provide additional evidence of the lack of sustainability and the existence of a positive correlation between vegetation changes in the study area. Moreover, they contribute to enhancing our comprehension of the dynamic processes associated with vegetation changes.

Nevertheless, this study exhibits specific constraints and deficiencies. The scope of this study was limited to the Shendong East mining area, which may restrict the generalizability and applicability of the research findings. Furthermore, the present study exclusively utilized remote sensing data for analysis, without taking into account field data and other relevant factors. In addition, there was a lack of investigation into the influence of meteorological factors on the spatial and temporal variations of local vegetation, as well as a failure to explore the underlying mechanisms driving these changes. The specific contributions of human activities and meteorological conditions to the observed substantial increase in vegetation coverage remain uncertain. Furthermore, the long-term dynamics of vegetation coverage are subject to various non-climatic influences, including urban expansion, construction projects, grazing, and land use changes (Ma et al., 2023a). Hence, it is imperative for future studies to integrate field surveys and other pertinent data sources in order to holistically and precisely elucidate the mechanisms by which coal mining activities affect vegetation coverage. In addition, it is imperative to integrate human activities and meteorological factors into the analysis in order to enhance comprehension of the spatial distribution of diverse climatic and non-climatic driving factors. This will ultimately enable a more profound exploration of the correlation between coal mining activities and vegetation ecological environments.

5 Conclusions

The analysis focused on the spatiotemporal pattern of vegetation *kNDVI* in the Shendong mining area from 2000 to 2020, utilizing Landsat *kNDVI* data. This examination provided insights into the sustainability and intensity of evolution in vegetation change trends. The findings indicated a consistent upward trajectory in *kNDVI* values throughout the span of 21 years. The implementation of ecological restoration initiatives resulted in a significant improvement of *kNDVI* throughout the entire region. Specifically, during the period from 2010 to 2020, there was a notable and swift growth rate of 0.013 per annum. The analysis of vegetation coverage in the mining area using the Theil-Sen median trend and Mann-Kendall tests demonstrated a noteworthy enhancement in vegetation growth over the course of the previous two decades. Specifically, the vegetation now encompasses 89.47% of the total area, while only 2.74% of the area has experienced degradation. In general, there was a notable upward trajectory observed in the vegetation coverage within the mining region. The examination of various stages indicated that during the period from 2000 to 2010, there was primarily a marginal enhancement trend, constituting approximately 54.83% of the observed data. Conversely, from 2010 to 2020, a substantial improvement trend emerged as the prevailing pattern, encompassing approximately 61.16% of the analyzed data. In general, there was a transition in the vegetation dynamic trend from a slight improvement to a significant improvement.

Despite observing a general improvement and notable enhancement in vegetation within the mining region, analysis of the Hurst index distribution reveals that approximately 40.12% of the area is projected to experience unsustainable vegetation growth in the coming years. Consequently, the vegetation in these regions

will experience a distinct transformation from its initial state of growth. Upon analyzing the vegetation growth patterns, a majority of the studied regions displayed an upward trajectory. However, certain areas that exhibited an initial increase in vegetation are projected to experience a decline in the future. These areas encompass a landmass of 349.22 km^2, accounting for approximately 39.10% of the overall mining area. Moreover, the transformation characteristics and transition intensities of vegetation growth trends in the Shendong mining area during the periods of 2000-2010 and 2010-2020 were visually depicted within the framework of intensity analysis. As an illustration, the shift from a slight to a significant increase demonstrated a consistent pattern, whereas the shift from a substantial increase to a slight increase displayed an unequivocal pattern. The observed characteristics suggest that the vegetation within the mining site exhibits a degree of adherence to the principles of ecological restoration during the mining process.

Data availability statement

The original contributions presented in the study are included in the article/supplementary material. Further inquiries can be directed to the corresponding author.

Author contributions

ZC: Conceptualization, Writing – original draft. XZ: Investigation, Methodology, Writing – original draft. YJ: Data curation, Validation, Writing – review & editing. YC: Software, Supervision, Writing – original draft. ZZ: Investigation, Resources, Writing – original draft. SW: Project administration, Resources, Writing – original draft. HZ: Funding acquisition, Project administration, Visualization, Writing – review & editing.

Funding

The author(s) declare that financial support was received for the research, authorship, and/or publication of this article. This work supported by the State Key Project of National Natural Science Foundation of China-Key projects of joint fund for regional innovation and development (grant number U22A20620 U21A20108), Doctoral Science Foundation of Henan Polytechnic University (grant number B2021-20), China Shenhua Shendong Science and Technology Innovation Project (grant number E210100573).

Acknowledgments

We appreciate reviewers and their valuable comments. Also, we thank Editors for the editing and comments.

Conflict of interest

The authors declare that the research was conducted in the absence of any commercial or financial relationships that could be construed as a potential conflict of interest.

Publisher's note

References

Andualem, A. T., and Berhan, G. A. (2021). Evaluation of the saturation property of vegetation indices derived from sentinel-2 in mixed crop-forest ecosystem. *Spatial Inf. Res.* 29 (1), 109–121. doi: 10.1007/s41324-020-00339-5

Burchart-Korol, D., Fugiel, A., Czaplicka-Kolarz, K., and Turek, M. (2016). Model of environmental life cycle assessment for coal mining operations. *Sci. Total Environ.* 562, 61–72. doi: 10.1016/j.scitotenv.2016.03.202

Camps-Valls, G., Campos-Taberner, M., Moreno-Martinez, A., Walther, S., Duveiller, G., Cescatti, A., et al. (2021). A unified vegetation index for quantifying the terrestrial biosphere. *Sci. Adv.* 7 (9). doi: 10.1126/sciadv.abc7447

Carlson, T. N., and Ripley, D. A. (1997). On the relation between NDVI, fractional vegetation cover, and leaf area index. *Remote Sens. Environ.* 62 (3), 241–252. doi: 10.1016/S0034-4257(97)00104-1

Chen, L., Zhang, H., Zhang, X., Liu, P., Zhang, W., and Ma, X. (2022). Vegetation changes in coal mining areas: Naturally or anthropogenically Driven? *Catena* 208, 105712. doi: 10.1016/j.catena.2021.105712

Chi, M.-b., Li, Q.-S., Cao, Z.-G., Fang, J., Wu, B.-Y., Zhang, Y., et al. (2022). Evaluation of water resources carrying capacity in ecologically fragile mining areas under the influence of underground reservoirs in coal mines. *J. Clean. Prod.* 379. doi: 10.1016/j.jclepro.2022.134449

Deng, Y., Wang, S., Bai, X., Luo, G., Wu, L., Chen, F., et al. (2020). Vegetation greening intensified soil drying in some semi-arid and arid areas of the world. *Agric. For. Meteorology* 108103, 292–293. doi: 10.1016/j.agrformet.2020.108103

Ding, Y., He, X., Zhou, Z., Hu, J., Cai, H., Wang, X., et al. (2022). Response of vegetation to drought and yield monitoring based on NDVI and SIF. *Catena* 219, 106328. doi: 10.1016/j.catena.2022.106328

Forzieri, G., Dakos, V., McDowell, N. G., Ramdane, A., and Cescatti, A. (2022). Emerging signals of declining forest resilience under climate change. *Nature* 608 (7923), 534–53+. doi: 10.1038/s41586-022-04959-9

Garioud, A., Valero, S., Giordano, S., and Mallet, C. (2021). Recurrent-based regression of Sentinel time series for continuous vegetation monitoring. *Remote Sens. Environ.* 263, 112419. doi: 10.1016/j.rse.2021.112419

Gensheimer, J., Turner, A. J., Kohler, P., Frankenberg, C., and Chen, J. (2022). A convolutional neural network for spatial downscaling of satellite-based solar-induced chlorophyll fluorescence (SIFnet). *Biogeosciences* 19 (6), 1777–1793. doi: 10.5194/bg-19-1777-2022

Gocic, M., and Trajkovic, S. (2013). Analysis of changes in meteorological variables using Mann-Kendall and Sen's slope estimator statistical tests in Serbia. *Glob. Planet. Change* 100, 172–182. doi: 10.1016/j.gloplacha.2012.10.014

Guesewell, S., Pohl, M., Gander, A., and Strehler, C. (2007). Temporal changes in grazing intensity and herbage quality within a Swiss fen meadow. *Botanica Helv.* 117 (1), 57–73. doi: 10.1007/s00035-007-0798-7

Guo, B., Han, F., and Jiang, L. (2018). An improved dimidiated pixel model for vegetation fraction in the yarlung zangbo river basin of qinghai-tibet plateau. *J. Indian Soc. Remote Sens.* 46 (2), 219–231. doi: 10.1007/s12524-017-0692-8

Guo, H., Wang, Y., Yu, J., Yi, L., Shi, Z., and Wang, F. (2023). A novel framework for vegetation change characterization from time series landsat images. *Environ. Res.* 222, 115379. doi: 10.1016/j.envres.2023.115379

Guo, W. B., Guo, M. J., Tan, Y., Bai, E. H., and Zhao, G. B. (2019). Sustainable development of resources and the environment: mining-induced eco-geological environmental damage and mitigation measures-A case study in the henan coal mining area, China. *Sustainability* 11 (16). doi: 10.3390/su11164366

Gustavo, C. V., and Lorenzo, B. (2009). *Kernel methods for remote sensing data analysis* (John Wiley & Sons, Ltd). doi: 10.1002/9780470748992

Han, X. Y., Cao, T. Y., and Yan, X. L. (2021a). Comprehensive evaluation of ecological environment quality of mining area based on sustainable development indicators: a case study of Yanzhou Mining in China. *Environ. Dev. Sustain.* 23 (5), 7581–7605. doi: 10.1007/s10668-020-00935-3

Han, Y., Ke, Y. H., Zhu, L. J., Feng, H., Zhang, Q., Sun, Z., et al. (2021b). Tracking vegetation degradation and recovery in multiple mining areas in Beijing, China, based on time-series Landsat imagery. *GIScience Remote Sens.* 58 (8), 1477–1496. doi: 10.1080/15481603.2021.1996319

He, D. K., Le, B. T., Xiao, D., Mao, Y. C., Shan, F., and Ha, T. T. L. (2019). Coal mine area monitoring method by machine learning and multispectral remote sensing images. *Infrared Phys. Technol.* 103. doi: 10.1016/j.infrared.2019.103070

Huang, S., Tang, L. N., Hupy, J. P., Wang, Y., and Shao, G. F. (2021). A commentary review on the use of normalized difference vegetation index (NDVI) in the era of popular remote sensing. *J. For. Res.* 32 (1), 1–6. doi: 10.1007/s11676-020-01155-1

Huang, C. L., Yang, Q. K., Guo, Y. H., Zhang, Y. Q., and Guo, L. A. (2020). The pattern, change and driven factors of vegetation cover in the Qin Mountains region. *Sci. Rep.* 10 (1). doi: 10.1038/s41598-020-75845-5

Jiang, H., Fan, G. W., Zhang, D. S., Zhang, S. Z., and Fan, Y. B. (2022). Evaluation of eco-environmental quality for the coal-mining region using multi-source data. *Sci. Rep.* 12 (1). doi: 10.1038/s41598-022-09795-5

Jiang, L., Liu, Y., Wu, S., and Yang, C. (2021). Analyzing ecological environment change and associated driving factors in China based on NDVI time series data. *Ecol. Indic.* 129, 107933. doi: 10.1016/j.ecolind.2021.107933

Jimenez, R. B., Lane, K. J., Hutyra, L. R., and Fabian, M. P. (2022). Spatial resolution of Normalized Difference Vegetation Index and greenness exposure misclassification in an urban cohort. *J. Expo. Sci. Environ. Epidemiol.* 32 (2), 213–222. doi: 10.1038/s41370-022-00409-w

Li, J., Garshick, E., Al-Hemoud, A., Huang, S., and Koutrakis, P. (2020). Impacts of meteorology and vegetation on surface dust concentrations in Middle Eastern countries. *Sci. Total Environ.* 712. doi: 10.1016/j.scitotenv.2020.136597

Li, S., Xu, L., Jing, Y., Yin, H., Li, X., and Guan, X. (2021b). High-quality vegetation index product generation: A review of NDVI time series reconstruction techniques. *Int. J. Appl. Earth Obs. Geoinf.* 105. doi: 10.1016/j.jag.2021.102640

Li, P., Yu, H. Y., Zhang, J. S., Du, M. Y., and Xiong, J. (2021a). Coal supply sustainability in China: A new comprehensive evaluation methodology. *Front. Energy Res.* 9. doi: 10.3389/fenrg.2021.701719

Liu, H. Q., and Huete, A. (1995). A feedback based modification of the NDVI to minimize canopy background and atmospheric noise. *IEEE Trans. Geosci. Remote Sens.* 33 (2), 457–465. doi: 10.1109/TGRS.1995.8746027

Liu, Y., Lei, S., Chen, X., Chen, M., Zhang, X., and Long, L. (2021a). Study of plant configuration pattern in guided vegetation restoration: A case study of semiarid underground mining areas in Western China. *Ecol. Eng.* 170, 106334. doi: 10.1016/j.ecoleng.2021.106334

Liu, Z., and Liu, Y. (2018). Does anthropogenic land use change play a role in changes of precipitation frequency and intensity over the loess plateau of China? *Remote Sens.* 10 (11). doi: 10.3390/rs10111818

Liu, Y., Zhao, W., Chen, S., and Ye, T. (2021b). Mapping crop rotation by using deeply synergistic optical and SAR time series. *Remote Sens.* 13 (20). doi: 10.3390/rs13204160

Luis, R. Á. J., Manel, M. R., Jordi, M. M., and Gustau, C. V. (2018). *Digital signal processing with kernel methods* (John Wiley & Sons, Ltd).

Ma, S., Qiu, H., Zhu, Y., Yang, D., Tang, B., Wang, D., et al. (2023b). Topographic Changes, Surface Deformation and Movement Process before, during and after a Rotational Landslide. *Remote Sens.* 15 (3). doi: 10.3390/rs15030662

Ma, M., Wang, Q., Liu, R., Zhao, Y., and Zhang, D. (2023a). Effects of climate change and human activities on vegetation coverage change in northern China considering extreme climate and time-lag and -accumulation effects. *Sci. Total Environ.* 860, 160527. doi: 10.1016/j.scitotenv.2022.160527

Martinez, A. D., and Labib, S. M. (2023). Demystifying normalized difference vegetation index (NDVI) for greenness exposure assessments and policy interventions in urban greening. *Environ. Res.* 220. doi: 10.1016/j.envres.2022.115155

Murwira, A., and Skidmore, A. K. (2006). Monitoring change in the spatial heterogeneity of vegetation cover in an African savanna. *Int. J. Remote Sens.* 27 (11), 2255–2269. doi: 10.1080/01431160500396683

Pei, Y., Qiu, H., Yang, D., Liu, Z., Ma, S., Li, J., et al. (2023). Increasing landslide activity in the Taxkorgan River Basin (eastern Pamirs Plateau, China) driven by climate change. *Catena* 223, 106911. doi: 10.1016/j.catena.2023.106911

Pérez-Cabello, F., Montorio, R., and Alves, D. B. (2021). Remote sensing techniques to assess post-fire vegetation recovery. *Curr. Opin. Environ. Sci. Health* 21, 100251. doi: 10.1016/j.coesh.2021.100251

Pontius, R. G., Shusas, E., and McEachern, M. (2004). Detecting important categorical land changes while accounting for persistence. *Agric. Ecosyst. Environ.* 101 (2-3), 251–268. doi: 10.1016/j.agee.2003.09.008

Qi, J. W., Zhang, Y. C., Zhang, J. Q., Wu, C. Y., Chen, Y. A., and Cheng, Z. S. (2023). Study on the restoration of ecological environments in mining area based on GIS technology. *Sustainability* 15 (7). doi: 10.3390/su15076128

Qiu, H., Zhu, Y., Zhou, W., Sun, H., He, J., and Liu, Z. (2022). Influence of DEM resolution on landslide simulation performance based on the Scoops3D model. *Geomatics Natural Hazards Risk* 13 (1), 1663–1681. doi: 10.1080/19475705.2022.2097451

Roy, R., Sultana, S., Wang, J. X., Mostofa, M. G., Sarker, T., Shah, M. M. R., et al. (2022). Revegetation of coal mine degraded arid areas: The role of a native woody species under optimum water and nutrient resources. *Environ. Res.* 204. doi: 10.1016/j.envres.2021.111921

Shan, W., Jin, X., Ren, J., Wang, Y., Xu, Z., Fan, Y., et al. (2019). Ecological environment quality assessment based on remote sensing data for land consolidation. *J. Clean. Prod.* 239, 118126. doi: 10.1016/j.jclepro.2019.118126

Shang, H., Zhan, H. Z., Ni, W. K., Liu, Y., Gan, Z. H., and Liu, S. H. (2022). Surface environmental evolution monitoring in coal mining subsidence area based on multi-source remote sensing data. *Front. Earth Sci.* 10. doi: 10.3389/feart.2022.790737

Sioris, C. E., Zou, J., McElroy, C. T., Boone, C. D., Sheese, P. E., and Bernath, P. F. (2016). Water vapour variability in the high-latitude upper troposphere - Part 2: Impact of volcanic eruptions. *Atmospheric Chem. Phys.* 16 (4), 2207–2219. doi: 10.5194/acp-16-2207-2016

Siteur, K., Eppinga, M. B., Karssenberg, D., Baudena, M., Bierkens, M. F. P., and Rietkerk, M. (2014). How will increases in rainfall intensity affect semiarid ecosystems? *Water Resour. Res.* 50 (7), 5980–6001. doi: 10.1002/2013WR014955

Song, W., Feng, Y., and Wang, Z. (2022). Ecological restoration programs dominate vegetation greening in China. *Sci. Total Environ.* 848, 157729. doi: 10.1016/j.scitotenv.2022.157729

Sun, L., Li, H., Wang, J., Chen, Y., Xiong, N., Wang, Z., et al. (2023). Impacts of climate change and human activities on NDVI in the qinghai-tibet plateau. *Remote Sens.* 15 (3). doi: 10.3390/rs15030587

Tong, S., Zhang, J., Ha, S., Lai, Q., and Ma, Q. (2016). Dynamics of fractional vegetation coverage and its relationship with climate and human activities in inner Mongolia, China. *Remote Sens.* 8 (9). doi: 10.3390/rs8090776

Wang, X., Biederman, J. A., Knowles, J. F., Scott, R. L., Turner, A. J., Dannenberg, M. P., et al. (2022b). Satellite solar-induced chlorophyll fluorescence and near-infrared reflectance capture complementary aspects of dryland vegetation productivity dynamics. *Remote Sens. Environ.* 270. doi: 10.1016/j.rse.2021.112858

Wang, W., Liu, R. Y., Gan, F. P., Zhou, P., Zhang, X. W., and Ding, L. (2021a). Monitoring and evaluating restoration vegetation status in mine region using remote sensing data: case study in inner Mongolia, China. *Remote Sens.* 13 (7). doi: 10.3390/rs13071350

Wang, Q., Moreno-Martinez, A., Munoz-Mari, J., Campos-Taberner, M., and Camps-Valls, G. (2023). Estimation of vegetation traits with kernel NDVI. *ISPRS J. Photogramm. Remote Sens.* 195, 408–417. doi: 10.1016/j.isprsjprs.2022.12.019

Wang, L., Qiu, H., Zhou, W., Zhu, Y., Liu, Z., Ma, S., et al. (2022a). The post-failure spatiotemporal deformation of certain translational landslides may follow the pre-failure pattern. *Remote Sens.* 14 (10). doi: 10.3390/rs14102333

Wang, Y., Wu, X., He, S., and Niu, R. (2021b). Eco-environmental assessment model of the mining area in Gongyi, China. *Sci. Rep.* 11 (1). doi: 10.1038/s41598-021-96625-9

Wu, Q., Xu, H., Yang, Y., Hou, H., Mi, J., Wang, X., et al. (2023). Identifying structure change of vegetation under long-term disturbance in the Shendong mining area. *Environ. Earth Sci.* 82 (19), 450. doi: 10.1007/s12665-023-11005-y

Xiao, W., Zhang, W. K., Ye, Y. M., Lv, X. J., and Yang, W. F. (2020). Is underground coal mining causing land degradation and significantly damaging ecosystems in semi-arid areas? A study from an Ecological Capital perspective. *Land Degrad. Dev.* 31 (15), 1969–1989. doi: 10.1002/ldr.3570

Xu, Y., Guo, L., Li, J., Zhang, C., Ran, W., Hu, J., et al. (2023b). Automatically identifying the vegetation destruction and restoration of various open-pit mines utilizing remotely sensed images: Auto-VDR. *J. Clean. Prod.* 414, 137490. doi: 10.1016/j.jclepro.2023.137490

Xu, Q.-X., Wang, T.-W., Cai, C.-F., Li, Z.-X., Shi, Z.-H., and Fang, R.-J. (2013). Responses of runoff and soil erosion to vegetation removal and tillage on steep lands. *Pedosphere* 23 (4), 532–541. doi: 10.1016/S1002-0160(13)60046-6

Xu, H., Xu, F., Lin, T., Xu, Q., Yu, P., Wang, C., et al. (2023a). A systematic review and comprehensive analysis on ecological restoration of mining areas in the arid region of China: Challenge, capability and reconsideration. *Ecol. Indic.* 154, 110630. doi: 10.1016/j.ecolind.2023.110630

Xu, Y., Yang, Y., Chen, X., and Liu, Y. (2022). Bibliometric analysis of global NDVI research trends from 1985 to 2021. *Remote Sens.* 14 (16). doi: 10.3390/rs14163967

Xu, J., Zhu, W., Xu, J., Wu, J., and Li, Y. (2021). High-intensity longwall mining-induced ground subsidence in Shendong coalfield, China. *Int. J. Rock Mechanics Min. Sci.* 141, 104730. doi: 10.1016/j.ijrmms.2021.104730

Yang, X., Yao, W., Li, P., Hu, J., Latifi, H., Kang, L., et al. (2022a). Changes of SOC content in China's shendong coal mining area during 1990-2020 investigated using remote sensing techniques. *Sustainability* 14 (12). doi: 10.3390/su14127374

Yang, X. T., Yao, W. Q., Li, P. F., Hu, J. F., Latifi, H., Kang, L., et al. (2022b). Changes of SOC content in China's shendong coal mining area during 1990-2020

investigated using remote sensing techniques. *Sustainability* 14 (12). doi: 10.3390/su14127374

Yu, L., Liu, Y., Liu, T., and Yan, F. (2020). Impact of recent vegetation greening on temperature and precipitation over China. *Agric. For. Meteorology* 295, 108197. doi: 10.1016/j.agrformet.2020.108197

Yue, S., and Wang, C. Y. (2004). The Mann-Kendall test modified by effective sample size to detect trend in serially correlated hydrological series. *Water Resour. Manage.* 18 (3), 201–218. doi: 10.1023/B:WARM.0000043140.61082.60

Zeng, Y., Hao, D., Park, T., Zhu, P., Huete, A., Myneni, R., et al. (2023). Structural complexity biases vegetation greenness measures. *Nat. Ecol. Evol* 7, 1790–1798. doi: 10.1038/s41559-023-02187-6

Zhang, M., Lin, H., Long, X., and Cai, Y. (2021). Analyzing the spatiotemporal pattern and driving factors of wetland vegetation changes using 2000-2019 time-series Landsat data. *Sci. Total Environ.* 780, 146615. doi: 10.1016/j.scitotenv.2021.146615

Zhang, J., Xiao, J., Tong, X., Zhang, J., Meng, P., Li, J., et al. (2022). NIRv and SIF better estimate phenology than NDVI and EVI: Effects of spring and autumn phenology on ecosystem production of planted forests. *Agric. For. Meteorology* 315, 108819. doi: 10.1016/j.agrformet.2022.108819

Zhou, W., Qiu, H., Wang, L., Pei, Y., Tang, B., Ma, S., et al. (2022). Combining rainfall-induced shallow landslides and subsequent debris flows for hazard chain prediction. *Catena* 213, 106199. doi: 10.1016/j.catena.2022.106199

frontiers | Frontiers in Earth Science

TYPE Original Research
PUBLISHED 11 January 2024
DOI 10.3389/feart.2023.1353593

OPEN ACCESS

EDITED BY
Haijun Qiu,
Northwest University, China

REVIEWED BY
Jie Liu,
Henan Polytechnic University, China
Pan Cao,
University of Hertfordshire, United Kingdom

*CORRESPONDENCE
Wenfei Xi,
wenfeixi@ynnu.edu.cn
Zilong Zhao,
364424035@qq.com

RECEIVED 11 December 2023
ACCEPTED 29 December 2023
PUBLISHED 11 January 2024

CITATION
Huang G, Dong J, Xi W, Zhao Z, Li S, Kuang Z, An Q, Wei J and Zhu Y (2024), Study on surface deformation pattern in mine closure area of complex karst mountainous region based on SBAS-InSAR technology.
Front. Earth Sci. 11:1353593.
doi: 10.3389/feart.2023.1353593

Study on surface deformation pattern in mine closure area of complex karst mountainous region based on SBAS-InSAR technology

Guangcai Huang[1,2], Jihong Dong[3], Wenfei Xi[4,5]*, Zilong Zhao[6]*, Sifa Li[1,2], Zhong Kuang[1,2], Quan An[1,2], Jin Wei[1,2] and Yuhua Zhu[1,2,7]

[1]Guizhou Geological Survey, Bureau of Geology and Mineral Exploration and Development Guizhou Province, Guiyang, China, [2]Engineering Technology Innovation Cente of Mineral Resources Explorations in Bedrock Zones Minlsity of Natural Resources, Guiyang, China, [3]Evaluation and Utilization of Strategic Rare Metals and Rare Earth Resource Key Laboratory of Sichuan Province, Sichuan Institute of Comprehensive Geological Survey, Chengdu, China, [4]Faculty of Geography, Yunnan Normal University, Kunming, China, [5]Yunnan Key Laboratory of Plateau Geographic Processes and Environmental Change, Kunming, China, [6]Yunnan Haiju Geographic Information Technology Co., Ltd., Kunming, China, [7]College of Resources and Environmental Engineering, Guizhou University, Guiyang, China

Liupanshui City in Guizhou Province represents a karst mountainous region with a delicate geological environment. The area has a long history of coal mining, and several coal mines have been progressively closed in recent years. However, even after closure of coal mines, the fractured rock mass in the mined-out areas continues to undergo deformation over a specific period. In karst mountainous regions, this deformation is affected by various factors including elevation, slope, precipitation, and vegetation. In this study, we employed SBAS-InSAR technology to construct a time series of surface deformation data from January 2019 to May 2022 within Liupanshui City's LuJiaZhai-DaPingDi Minefield. Subsequently, this data was comprehensively analyzed in conjunction with time series vegetation cover, monthly precipitation, elevation, and slope data from the identical period. The key findings of this research are as follows: 1) After the closure of the mine, the subsidence area gradually stabilized, yet the volume of subsidence continues to increase. The subsidence area primarily occurs near the MaiZiGou Coal Mine air-mining area, which had a relatively short closure time, as well as in higher elevation areas in the southern and eastern parts of the minefield. Specifically, the maximum cumulative subsidence and the subsidence rate during the study period reached −60.3 mm and −21.83 mm/a, respectively. 2) Surface deformation is closely linked to slope, vegetation type, and rainfall, with subsidence rates and amounts noticeably higher during the rainy season than in the dry season. 3) Surface vegetation cover types display varied effects on deformation, with grassland or shrub areas being more sensitive to precipitation than forests. Forests, especially pine and fir, show a delayed subsidence response to rain, typically 2–3 months post-rainy season onset. This inhibitory effect lessens with increasing slope, particularly beyond a 25° threshold, where responsiveness to precipitation and associated subsidence significantly

increase. The findings of this study hold substantial scientific implications for the restoration and management of closed mining areas, as well as the prevention of geological hazards in karst complex mountainous regions.

KEYWORDS

SBAS-InSAR, mine closure, karst collapse, deformation monitoring, slope, precipitation, vegetation cover type

1 Introduction

Karst landscapes are widespread throughout China. Specifically, soluble rocks of Karst landscapes cover over an expansive area of up to 365 × 104 km^2, which accounts for more than one-third of the national territory (Sun et al., 2023). Guizhou Province stands out as the region of Karst landscapes due to its extensive development of carbonate rocks and the thickest exposure, predominantly composed of limestone and dolomite, resulting in the formation of representative karst landforms (Chu et al., 2015). Additionally, Guizhou Province is characterized by significant coal resources, making it one of the southern Chinese regions with abundant coal reserves. The primary coal-producing areas are located within the zone of karst landscape development. The complex terrain and fragile geological environment of this karst mountainous region (Shi and Zhang, 2023), coupled with years of coal mining, have exacerbated surface deformation issues. Furthermore, large-scale landslides and collapses frequently occur, causing severe casualties and property losses (Wang et al., 2020; Chen H. et al., 2022; Zhong et al., 2022; Zhao Q. et al., 2023).

Coal, as a vital energy source (Yu et al., 2021), is extensively utilized in industrial production and electricity generation, remaining a primary source of energy in many countries (Chen et al., 2020). China, with its abundant coal reserves and limited oil resources, heavily relies on coal as a fundamental energy source and essential raw material (Chen B. et al., 2023), accounting for over 60% of primary energy consumption (Deng et al., 2022). However, the exploitation of coal resources has given rise to significant geological environmental challenges, particularly concerning long-term coal mining in the fragile surface environments of karst complex mountainous regions. Prolonged coal mining activities can lead to ground subsidence, damage to surface structures, and the occurrence of geological hazards such as ground fissures, landslides, and surface collapses. These hazards pose severe threats to the productivity and safety of local communities, as well as the construction and operation of critical national infrastructure such as power grids and transportation routes (Zhu Q. et al., 2019; Li et al., 2019; Li et al., 2021). In the 1980s, China experienced a substantial demand for coal resources, resulting in a rapid increase in the number of coal mines in mining cities. Over time, the intensive and large-scale extraction of coal resources has led to resource depletion in certain areas. Furthermore, recent adjustments to China's energy structure and the implementation of supply-side structural reforms have prompted the consolidation and closure of small, scattered, and disorderly coal mines, significantly increasing the number of closed coal mines in the country. The closure of these mines leaves behind a considerable amount of land resources, leading to various issues related to resources, environment, safety, and society, which have gradually become apparent (Hu and Yan, 2018; Chen Z. et al., 2022; Li et al., 2022). The transformation, redevelopment, and management of the ecological environment of these closed mines have become a critical concern for the sustainable economic and social development of resource-based cities. Once a mine is closed, the rock mass of the coal seam undergoes weathering deterioration and a reduction in strength due to factors such as stress and groundwater. Consequently, the stress and bearing capacity of the rock mass, disrupted by mining activities, change, often resulting in secondary subsidence of the air-mined area and the surrounding ground surface (Chen B. et al., 2022). This deformation, particularly in complex karst mountainous regions, tends to exhibit complex, concealed, sudden, and long-term characteristics, posing potential threats to the mining area and its surrounding engineering construction and mining geological environment. Therefore, there is an urgent need for comprehensive, long-term, and high-precision monitoring of subsidence in closed mines. Furthermore, it is crucial to explore the intricate relationship between surface deformation in closed mining areas and variables such as elevation, slope, precipitation, and vegetation cover. This exploration serves as a vital prerequisite for conducting ecological restoration and management of mining areas.

Despite high precision in subsidence monitoring, traditional methods such as precise leveling measurements (Wang, 2013), GPS measurements (Zhao and Zhu, 2020), and crack gauges (Bai et al., 2020) suffer from limitations such as low point density, providing only discrete subsidence data in well-explored deformation areas. Moreover, these methods are characterized by long observation cycles, high costs, lower efficiency, and struggle to meet the increasing demand for regional subsidence monitoring. In contrast, Interferometric Synthetic Aperture Radar (InSAR) technology has gained widespread adoption for surface deformation monitoring due to its advantages such as all-weather capability, extensive coverage, high precision, and cost-effectiveness (Zhu et al., 2017; Yang et al., 2020). Nevertheless, in mining areas, the presence of dense surface vegetation and significant mining-induced deformations often results in decreased coherence of SAR interferograms (Zhu J. et al., 2019). This presence poses a challenge for conventional differential InSAR (D-InSAR) techniques, making it difficult to achieve optimal results in deformation monitoring in mining areas. To address this challenge, mining area InSAR monitoring has transitioned from D-InSAR to time series interferometric synthetic aperture radar (TS-InSAR). TS-InSAR effectively mitigates the challenges associated with D-InSAR, including spatial-temporal decorrelation, DEM errors, and atmospheric delay disturbances, while conforming to the requirements for prolonged dynamic monitoring in mining areas (Du et al., 2017; Tang et al., 2021; Liu et al., 2022). Noteworthily, existing research employed two primary techniques for mining area

deformation monitoring based on TS-InSAR, including the phase stacking method (Zhang et al., 2021) and the small baseline subsets InSAR (SBAS-InSAR) (Berardino et al., 2002). Both of the aforementioned techniques are well-suited for long-term deformation monitoring in mining areas and have gained widespread use in subsidence monitoring. Zhang et al. (2016) utilized the Stacking InSAR method to monitor subsidence in the Pei Bei mining area, such that this method is confirmed to be effective in large-scale deformation monitoring. Based on Sentinel-1 data, Zhang et al. (2018) employed a novel TOPS imaging mode Stacking technique to analyze ground subsidence characteristics in the Huainan mining area, achieving excellent monitoring results. Their work also underscored the advantages of the Sentinel-1 satellite constellation, with its short revisit cycle and wide coverage, making it particularly suitable for subsidence monitoring in mining areas with expansive subsurface regions. Similarly, Xu et al. (2022) applied three InSAR techniques based on Sentinel data to extract mining-induced deformations in the Datong Coalfield from November 2020 to October 2021. The results suggested that both Stacking InSAR and SBAS InSAR outperformed D-InSAR, with SBAS InSAR providing more precise displacement rate results. Notably, Stacking InSAR exhibited superior performance in densely vegetated or low-coherence regions.

The Liupanshui region boasts abundant coal resources and a longstanding mining history. Researchers have successfully utilized InSAR technology to investigate surface deformation in this region. Zhu et al. (2022) employed Stacking InSAR technology, alongside multi-temporal optical remote sensing images, stratigraphy, and geomorphology, to identify 588 active landslides in western Guizhou for the first time. These landslides, primarily mining-induced (91.8%), reservoir bank-induced (4.1%), and reactivated ancient ones (2.4%), underscore the profound impact of coal mining on regional landslides, especially in steep, elevated areas. Wu et al. (2021) applied SBAS InSAR technology using Sentinel-1 radar images for extensive surface deformation monitoring in Liupanshui, Tongren, and Guiyang, Guizhou, identifying 102 hazard areas. Using optical images, they identified 72 deformation areas from mining or construction, along with 16 landslides and 14 suspected landslides. Chen L. et al. (2023) utilized the Intermittent Small Baseline Subset (ISBAS) method with Sentinel-1 images to determine Guizhou's surface deformation rate, mapping 693 active landslides. They noted a significant correlation between landslide distribution and factors such as altitude, slope, and coal-bearing strata. The aforementioned researchers have effectively utilized InSAR technology for a comprehensive surveillance of Guizhou's landslides, providing crucial insights into the macroscopic distribution of surface deformation in the area. Furthermore, researchers have examined and analyzed the destabilization mechanisms behind typical mining-induced landslides in the region (He et al., 2022; Zhao C. et al., 2023; Chen H. et al., 2023; Li et al., 2023). Literature review suggests that research primarily concentrates on extensive landslide monitoring and analyzing deformation and destabilization mechanisms of typical mining-induced landslides in Guizhou's Liupanshui area. Reports on surface deformation of closed mines in this region are scarce. Recent studies on closed mines predominantly focus on long-term monitoring, subsidence trends, and post-closure mechanism analysis in plain areas (Deng et al., 2015; Yu et al., 2021; Liang and Hu, 2022; Qin et al., 2022; Zhang et al., 2023). At present, the majority of researchers have primarily concentrated on long-term monitoring and the analysis of subsidence trends and mechanisms after mine closure. Nevertheless, in the karst mountainous regions of southwestern China, factors (e.g., high altitudes, steep slopes, concentrated precipitation, and diverse vegetation types) complicate the subsidence patterns in closed mines. These mines not only experience the effects of underground goaf areas but are also affected by the mentioned environmental factors. Therefore, investigating the complex relationship between surface deformation within closed mining areas and multiple influencing factors in this region holds significant practical importance.

LiuPanshui City, renowned as the primary "Coal Capital of South China," possesses abundant coal reserves and occupies a significant position as a major coal-producing city in Guizhou Province and even China. The coal mines in this region are predominantly located in high-altitude areas characterized by complex geological formations, including karst mountains. Extensive coal mining activities over the years have exacerbated surface deformations, resulting in the emergence of geological hazards such as ground fissures, landslides, and subsidence (Fang et al., 2016; Wu et al., 2021). In recent times, LiuPanshui City has closed several coal mines, prompting this study to focus on the LuJiaZhai-DaPingDi Minefield as a representative case. Leveraging 100 scenes of Sentinel-1 ascending orbit data spanning from January 2019 to May 2022, the study employs the Small Baseline Subset (SBAS) InSAR technique to continuously monitor surface deformations in four closed mines within the region. Subsequently, the research investigates the intricate relationships among elevation, slope, vegetation coverage, monthly precipitation, and surface deformations. The outcomes of this investigation can serve as a valuable foundation for decision-making pertaining to ecological restoration, judicious land reuse, and the prevention of geological hazards in closed mining areas.

2 Study area and data sources

2.1 Study area overview

The study area encompasses the LuJiaZhai-DaPingDi Minefield (Figure 1), located in the western region of Liupanshui City, Guizhou Province. The mining area's central coordinates are 104°31′37.2″E, 25°59′45.6″N. It falls into the transitional slope zone from the Yunnan Plateau to the central Guizhou mountain area, and is characterized as a typical southwestern karst mountain region. The terrain in this area is intricate, featuring expansive canyons, towering peaks, steep slopes, and deep valleys. It exhibits poor stability and limited resistance to interference. The elevation within the region ranges from 1,501 to 2048 m, with a relative height difference of 547 m. The slopes are notably steep, of which the steepest slope reach 88.27 degrees. The mining area comprises MaiZiGou Coal Mine, LongTouShan Coal Mine, FuGuiZhuang Coal Mine and BaiPing Coal Mine, which have a long history of mining but are currently closed, with the time of mine closure depicted in Figure 1D.

The strata present in the mining area demonstrate a characteristic geological pattern known as "hard on top, soft

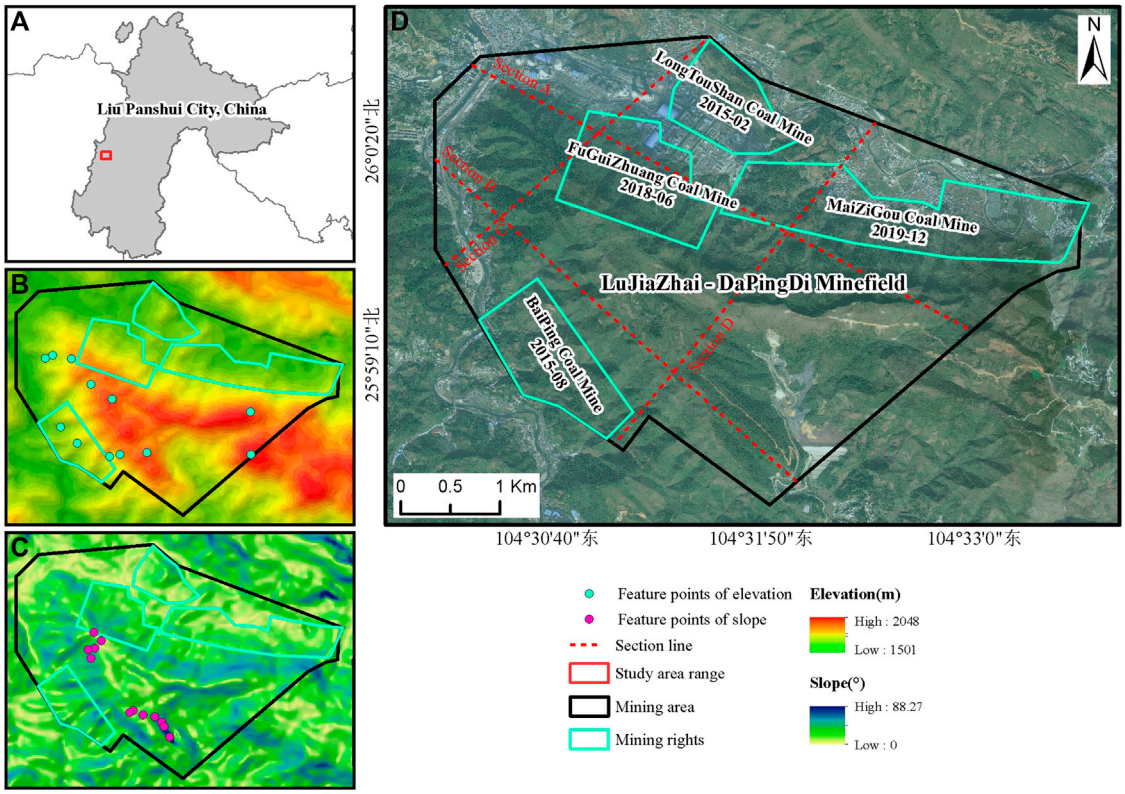

FIGURE 1
Overview of the Study Area and Mine Closure Time. ((**A**) illustrates the study area's schematic location, **(B)** its altitude, **(C)** its slope, and **(D)** the coal mining rights and mine closure times).

below." These formations can be classified into three distinct rock types: hard rock, interbedded hard and soft rock, and soft rock. The hard rock category encompasses the Guanling Formation from the Triassic period and the Emeishan Basalt Formation from the Permian period. These formations consist of limestone, dolomite, and dolomitic limestone, which are characterized by their hardness, brittleness, and high mechanical strength. However, unfavorable slope conditions can lead to deformation and collapse in these rocks. The interbedded hard and soft rock category includes the Yungningzhen Formation from the Triassic period. This formation comprises thin to medium-thickness layers of limestone, dolomite, shale, sandstone, and mudstone. These rocks exhibit variable lithological properties and complex combinations. The presence of karst development, active groundwater flow, high mechanical strength of carbonate rocks, and resistance to weathering contribute to their stability. Nevertheless, the existence of weaker interlayers can result in landslides and other geological hazards under unfavorable slope conditions. The soft rock category consists of the Feixianguan Formation from the Triassic period and the Longtan Formation from the Permian period. These formations consist of thin to medium-thickness layers of mudstone, sandy mudstone, siltstone, sandstone, shale, and coal seams. These rock formations are highly susceptible to disturbances caused by mining activities and exhibit weak resistance to weathering. They tend to soften when exposed to water, leading to poor stability. Under unfavorable slope conditions, these rock formations are prone to landslides, collapses, and other geological hazards.

2.2 Data sources

The study employed Sentinel-1 ascending orbit satellite data to cover the study area. Sentinel-1 is a radar satellite equipped with a C-band radar sensor and is part of the European Space Agency's Copernicus program. The Interferometric Wide (IW) imagery mode and Single Look Complex (SLC) data format were utilized. The data was collected with HH polarization and had a spatial resolution of 5 m × 20 m. The dataset spanned from January 2019 to May 2022, comprising a total of 100 scenes. This dataset was utilized to construct a time-series of deformation information within the study area. To enhance data accuracy, AW3D30 Digital Surface Model (DSM) data was used for terrain phase correction. Geocoding of the data was performed using SAR imagery, following the methodology described by Yang et al. (2021). Systematic errors resulting from orbital inaccuracies were mitigated using Precise Orbit Ephemerides (POD) data. Landsat8 OLI remote sensing images, provided by the USGS, were used to extract Fraction of Vegetation Coverage (FVC) information for the same time period. The extraction of FVC information was conducted on the Google Earth Engine platform. This involved using Landsat OLI remote sensing images from January 2019 to 2022 and calculating the Normalized Difference Vegetation Index (NDVI) based on the image element dichotomous model. The Landsat OLI remote sensing images from January 2019 to May 2022 were utilized to calculate the monthly NDVI for the study area, and subsequently, the time-series FVC of vegetation cover was calculated based on the image element dichotomous model (Adams

TABLE 1 Data details.

Data type	Data track	Date of data	Incident angle/°	Resolution/m	Source
Sentinel-1	Ascending track	2019.01-2022.05	37.03	5 × 20	European Space Agency (https://search.asf.alaska.edu/)
Landsat OLI	—	2019.01-2022.05	—	30	United States Geological Survey (https://glovis.usgs.gov/)
AW3D30 DSM	—	2011	—	30	Japan Aerospace Exploration Agency (https://www.eorc.jaxa.jp/ALOS/en/aw3d30/data/index.htm)
ASTER GDEM	—	2013	—	30	National Aeronautics and Space Administration (https://search.earthdata.nasa.gov/search)
Precise Orbit Ephemerides data	—	2019.01-2022.05	—	—	European Space Agency (https://scihub.copernicus.eu/gnss/)
month average rainfall	—	2019.01-2021.12	—	—	china meteorological data service center (https://data.cma.cn/)

et al., 1986). Furthermore, ASTER Global Digital Elevation Model (GDEM) data from NASA was utilized to obtain elevation and slope information for the study area. Monthly average precipitation data for the study area was obtained from the China Meteorological Data Network. Further details regarding the data sources can be found in Table 1. To synchronize the InSAR cumulative deformation, FVC, and monthly rainfall data for time series analysis, we computed both the monthly cumulative deformation and FVC data, with the month serving as the measurement unit.

3 Research methods and technical principles

3.1 SBAS-InSAR technology principlesw

The small baseline subsets InSAR (SBAS InSAR) technique, initially introduced by Berardino et al. (2002) in 2002.

The fundamental principle of this technique assumes the collection of S Synthetic Aperture Radar (SAR) images, denoted as $(t_1, t_2, \cdots, t_s)$, with the study area covered. Among this collection, one SAR image from the middle of the sequence is selected as the master image. The remaining S − 1 SAR images are then registered and sampled. This process results in the creation of M interferometric pairs, in accordance with the following (Eq. 1):

$$\frac{S}{2} \le M \le \frac{S(S-1)}{2} \tag{1}$$

In general, vertical baseline thresholds and time baseline thresholds are established based on actual conditions to limit the range of M values. This approach can mitigate the adverse effects of excessive vertical and temporal baselines that can induce coherence loss (Li et al., 2013). To calculate the differential interferometric phase, for the j interferogram, which is derived from SAR image interferometry acquired at two distinct times, denoted as t_A and t_B ($t_A < t_B$), the differential interferometric phase of the pixel located at distance coordinate r in the range direction and azimuth coordinate x is given by Xiao et al. (2019) as follows (Eq. 2):

$$\delta\varphi_j(x,r) = \varphi(t_B,x,r) - \varphi(t_A,x,r) \approx \frac{4\pi}{\lambda}(d_{tB} - d_{tA}) + \Delta\varphi_{top,j} + \Delta\varphi_{atm,j} + \Delta\varphi_{noise,j} \tag{2}$$

Where λ denotes the radar wavelength, d_{tB} and d_{tA} represent the cumulative shape variables thought to be the starting value of t_A corresponding to the corresponding moment, $\Delta\varphi_{top,j}$ expresses the residual terrain phase difference, $\Delta\varphi_{atm,j}$ is the atmospheric delay phase difference, and $\Delta\varphi_{noise,j}$ is the noise phase difference. After removing the phases other than the shape variables, the interferometric phase simplifies to:

$$d_{tB} - d_{tA} = V_i(t_B - t_A)$$

Where V_i represents the deformation rate from t_A to t_B time period. The phase of the differential interferogram after the resulting de-entanglement can be expressed by the matrix as:

$$Av = \delta\varphi$$

Where A represents an m × s matrix, which, when subjected to Singular Value Decomposition (SVD), provides the average deformation rate for each time period (Dong et al., 2022).

In this study, the processing of Sentinel-1 data involved multi-view processing with spatial resolutions of 23.8 m × 28.0 m in the range and azimuth directions, respectively, using a 10 × 2 multi-view ratio. The differential interferometric combinations employed a maximum time interval of 48 days and a maximum vertical baseline of ±250 m. This resulted in a total of 416 interferometric pairs acquired from ascending orbit data. The differential interferometric processing was performed on these combinations, leading to the generation of differential interferograms and coherence coefficient maps. To mitigate phase noise, an adaptive filtering method was applied. Subsequently, phase unwrapping was carried out on the filtered interferograms, utilizing the Minimum Cost Flow (MCF) method for this purpose. After error removal, the phase unwrapping results underwent Stacking and Small Baseline Subset (SBAS) processing to obtain deformation rates and time-series results.

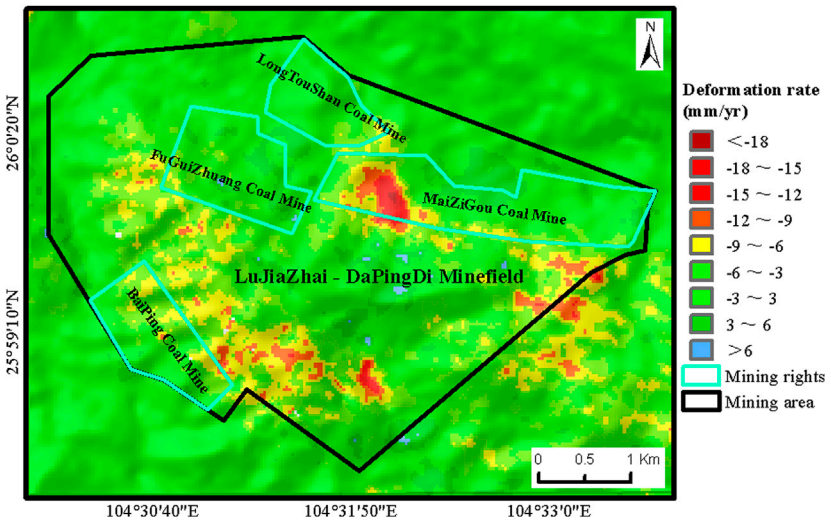

FIGURE 2
Average annual deformation rate of closed mines in LuJiaZhai-DaPingDi Minefield.

3.2 Stacking technology principles

Stacking refers to a technique (Sandwell and Price, 1998) used to perform a weighted average solution on multiple differential interferograms acquired through the Differential Interferometric Synthetic Aperture Radar (D-InSAR) method. This process is aimed at obtaining linear phase deformation rates to mitigate the influence of spatially uncorrelated noise. The solution format can be expressed as follows (Eq. 3):

$$ph\_rate = \frac{\left(\sum_{i=1}^{n} \Delta t_i * ph_i\right)}{\sum_{i=1}^{n} \Delta t_i^2} \quad (3)$$

Where ph_rate represents the linear phase deformation rate, Δt_i stands for the time baseline of the i set of differential interferograms, ph_i represents the unwrapped phase value of the i differential interferogram.

4 Results and analysis

4.1 Subsidence rate results and accuracy analysis

Using SBAS-InSAR technology, we obtained radar line of sight (LOS) deformation rates (Figure 2) and cumulative time-series deformation results (Figure 4) for four closed mines in the LuJiaZhai-DaPingDi Minefield in Liupanshui City from January 2019 to May 2022. In these figures, positive values indicate vertical surface uplift (i.e., along the LOS), while negative values represent vertical subsidence (i.e., along the LOS). As depicted in Figure 2, during the study period, significant deformation was observed in the northeastern and southwestern parts of the mining area. The maximum annual average subsidence rate and the maximum uplift rate within the mining area, located in the western and southern regions of the MaiZiGou Coal Mine, were determined as −21.83 mm/year and 8.13 mm/year, respectively. In the western part of the MaiZiGou Coal Mine, a prominent subsidence center was observed, with subsidence rates irregularly spreading out in an elliptical pattern from the center. This subsidence was notably higher than the other three mines. The overall subsidence within the mine was oriented in an "east-west" direction, primarily affected by the closure time of the mine and the distribution of old goaf areas. The MaiZiGou Coal Mine was closed in December 2019 but was still operational in 2019, resulting in higher and concentrated subsidence rates in the western part of the mine. Furthermore, multiple subsidence centers were observed in the southwestern part of the mining area, which were distributed in a "northwest-southeast" direction, of which the maximum subsidence rate was determined as −15.13 mm/year.

It is imperative to assess the reliability of the monitoring results before the analysis of the results of ground subsidence monitoring. Currently, there are two commonly used accuracy validation methods: internal consistency accuracy validation and external consistency accuracy validation. Due to the lack of concurrent ground-based monitoring data, this study employs the internal consistency accuracy validation method. This method involves cross-validating the subsidence rate results extracted by two different algorithms to investigate the reliability of the surface subsidence monitoring results. Using the SBAS technique to extract Line of Sight (LOS) deformation rates in the study area as the X-axis and the LOS deformation rates extracted by the Stacking technique as the Y-axis, a scatter density plot was created, as presented in Figure 3. The correlation coefficient (R^2) between the LOS deformation rates for corresponding points obtained by the two methods was 0.7017, indicating a high degree of correlation between the deformation rates obtained by the two InSAR techniques in the study area, thus validating the reliability of the subsidence monitoring results in the study area.

To evaluate the extent of ground subsidence development in the study area, this research classifies the ground subsidence rates into four distinct categories, as outlined in Table 2. During the period spanning from January 2019 to May 2022, the LuJiaZhai-DaPingDi Minefield exhibits the following tiers of ground subsidence: Areas experiencing subsidence rates below −15 mm/year are classified as regions with a

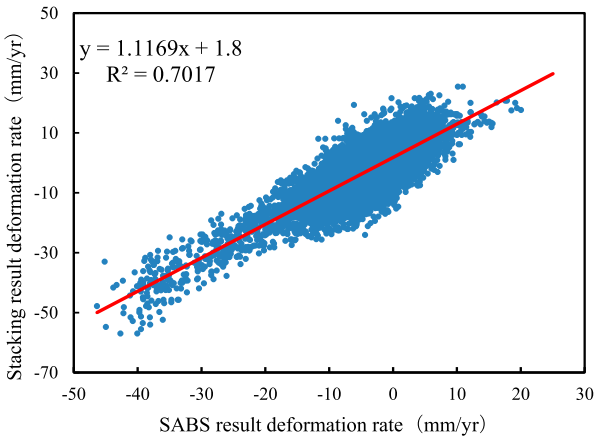

FIGURE 3
Correlation Analysis of Common Points between SBAS and Stacking Techniques.

high degree of ground subsidence development, constituting a mere 0.29% of the overall mining area. Subsidence rates ranging from −15 mm/year to −5 mm/year indicate regions with a moderate level of ground subsidence development, encompassing approximately 19.34% of the total mining area. Regions with subsidence rates falling between −5 mm/year and 5 mm/year denote areas with relatively stable ground subsidence development, representing the largest portion, accounting for 79.55% of the entire mining area. Areas exhibiting subsidence rates exceeding 5 mm/year are categorized as uplifted regions, comprising a mere 0.82% of the total mining area. This classification system serves as a valuable tool for evaluating and characterizing the extent of ground subsidence development in the study area, enabling a comprehensive understanding of the spatial distribution of subsidence and uplift patterns within the mining region.

The results indicate that, following the closure of the mines, the overall proportion of surface deformation areas within the LuJiaZhai-DaPingDi Minefield is relatively high. Except for the relatively stable areas, the combined area of other subsidence development levels accounts for 20.45% of the total mining area.

4.2 Spatial and temporal distribution analysis of surface deformation in the mining area

This study aimed to analyze the spatiotemporal distribution patterns of surface deformation in various closed mines and the mining area. To accomplish this, the study utilized acquired subsidence rates and performed temporal integration to assess the cumulative subsidence over time in the study area (Figure 4). Nine equally spaced time intervals were selected to represent the cumulative subsidence for each period.

Figure 4 demonstrates that the distribution of cumulative subsidence aligned with the subsidence rates. Overall, the region's different mines underwent varying degrees of deformation. The highest cumulative subsidence was observed in the MaiZiGou Coal Mine, measuring −60.3 mm, while the maximum uplift was reported in the southern part of the study area, with a magnitude of 34.17 mm. During the study period, the MaiZiGou Coal Mine was operational in 2019 but closed by the year's end. However, deformation persisted even after closure, expanding from the goaf area to the surrounding regions. The maximum cumulative subsidence and uplift reached −60.3 mm and 21.45 mm, respectively. The FuGuiZhuang Coal Mine ceased operations in June 2018. Within the study period, this mine experienced a maximum cumulative subsidence of −23.48 mm and an uplift of 22.82 mm. Subsidence primarily affected the higher-altitude western area of the mine. Although cumulative subsidence increased over time, deformation in this mine stabilized, with limited diffusion. The LongTouShan Coal Mine closed in February 2015. Its western part remained relatively stable without significant deformation, while the eastern part experienced cumulative subsidence of −24.18 mm and uplift of 19.71 mm, influenced by the MaiZiGou Coal Mine. The BaiPing Coal Mine closed in August 2015. Within its boundaries, the maximum cumulative subsidence and uplift were −21.86 mm and 22.44 mm, respectively. Deformation in this area remained relatively stable, primarily concentrated in the higher-altitude northeastern region of the mine, with ongoing deformation.

Notably, two distinct subsidence clusters were observed near the closed mines. One cluster was located in the southwestern part of the mining area, while the other was found in the eastern region, characterized by higher altitudes and steeper slopes. These clusters experienced cumulative subsidence and uplift of −49.93 mm and 27.95 mm, respectively. Figure 4 indicates that the extent and magnitude of deformation within these areas continued to expand throughout the study period. Although the range of deformation stabilized by May 2022, the deformation values were still increasing, indicating ongoing subsidence beneath the surface with future persistence.

The study also included two profile lines for the LuJiaZhai-DaPingDi Minefield, one in the longitudinal direction and the other in the transverse direction (Figure 1D). These profile lines were strategically positioned to intersect areas with significant subsidence. Subsidence rates and elevation values were then extracted from these profiles. Figure 5 illustrates an overall negative correlation between

TABLE 2 Ground subsidence levels in the LuJiaZhai-DaPingDi minefield.

Subsidence rate/(mm/a)	Subsidence level	Area proportion/(%)
<−15	High Subsidence Area	0.29
−15–−5	Moderate Subsidence Area	19.34
−5–5	Relatively Stable Area	79.55
>5	Uplifted Area	0.82

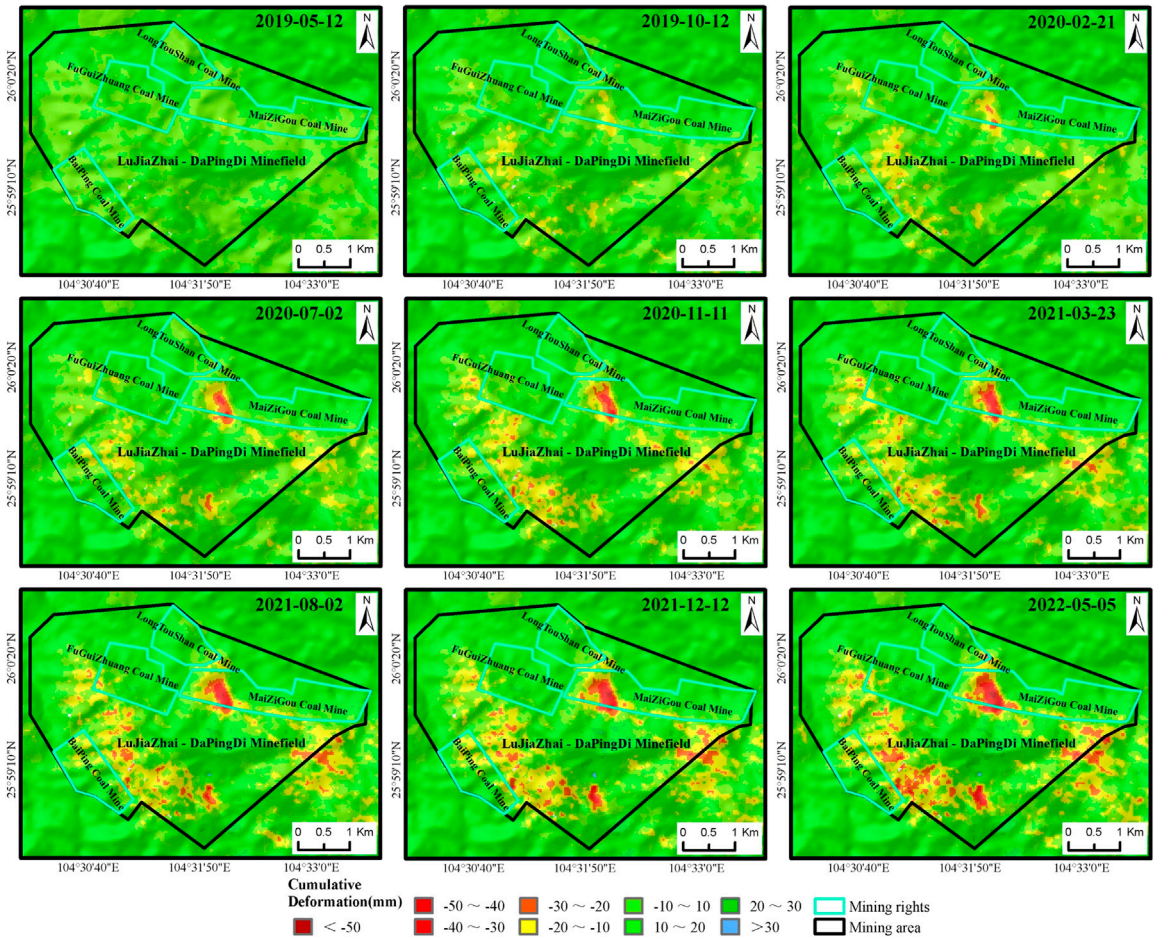

FIGURE 4
Temporal Cumulative Subsidence in the Lu LuJiaZhai-DaPingDi Minefield for Closed Mines (reference time: 2019-01-09).

subsidence rates and elevation. This suggests that as elevation increases, surface deformation becomes more frequent and exhibits a fluctuating decreasing trend. In contrast, as elevation decreases, subsidence rates decrease and tend to stabilize. In the northern section of Profile Line D, influenced by the closure time of the MaiZiGou Coal Mine, a "V"-shaped curve became evident around the profile line points near 100.

The findings of this study indicate that surface deformation within the closed mining area is influenced not only by the timing of mine closures but also by the elevation of the region. This correlation can be attributed to the study area's characteristics as a typical karst mountainous region, where high elevations and significant topographic variations are prevalent. These high-elevation areas are often characterized by steep slopes and deep valleys. Due to external factors such as precipitation, these regions are more susceptible to complex and concealed surface deformation. Additionally, elevation plays a role in determining the types of vegetation covering the surface. Different vegetation types exert diverse effects on slope stability (Asada and Minagawa, 2023). Consequently, this study places particular emphasis on investigating the interconnected relationship between surface deformation, elevation variations, slope characteristics, vegetation distribution, and precipitation patterns following mine closures within karst regions.

4.3 Analysis of surface deformation at different elevation gradients and slope levels

To conduct a comprehensive analysis of surface deformation within a mining area in a complex karst region following mine closures at various elevations and slopes, and to investigate the interplay between surface deformation, precipitation patterns, and vegetation coverage, this study employed two sets of deformation feature points for cross-validation purposes within the designated study area. The selection of these feature points aimed to minimize the influence of anthropogenic activities, such as urban areas and croplands, on surface deformation. Figure 1B illustrates the deformation feature points at different elevations (points a to l), while Figure 1C displays the feature points at various slopes (points m to x). The primary objective of this research is to examine the relationship between surface deformation within a mining area in a typical karst region after mine closures, considering different elevations and slopes, as well as its interaction with precipitation and vegetation coverage.

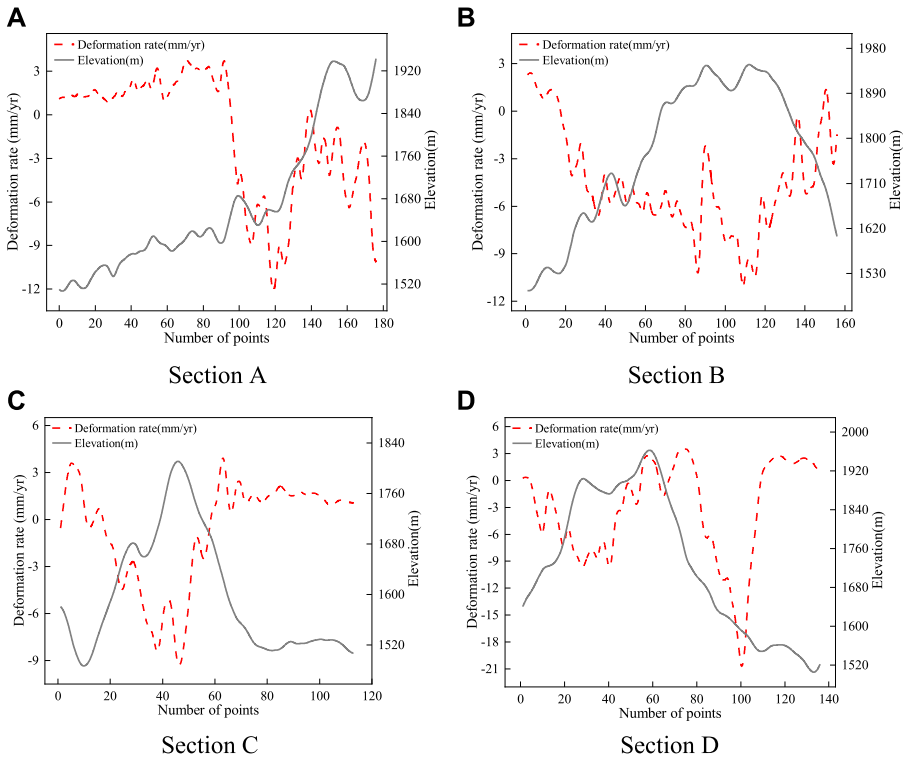

FIGURE 5
Profile of Subsidence Rate and Elevation. [**(A–D)** depict the subsidence rates and elevations for cross-section lines **(A)** through **(D)**, respectively].

Figure 6 presents time series curves depicting the deformation patterns at different elevations, ranging from 1566 m to 2022 m. The subsidence trends for these points consistently exhibit fluctuating downward movement. Among these points, the maximum cumulative subsidence is −31 mm (point c), while the minimum is −16 mm (point f), with the remaining points falling within the −20 mm to −30 mm range. Precipitation in the study area is concentrated between May and October, while vegetation coverage is particularly high from June to September. Generally, the subsidence values at these points display a systematic response to precipitation. During the rainy season, subsidence rates and magnitudes increase significantly, whereas during the dry season, the points tend to experience sliding or uplift. Notably, points a, c, d, and e exhibit a more rapid response to precipitation, showcasing significant subsidence early in the rainy season as precipitation accumulates. In contrast, points b and f demonstrate a delayed response, with noticeable subsidence occurring two to 3 months after the onset of the rainy season.

Precipitation is a significant contributing factor to surface deformation and geological hazards, such as landslides and collapses, particularly when precipitation is prolonged and heavy (Zhang et al., 2020; Wang et al., 2022; Ma et al., 2023; Pei et al., 2023). In the designated study area, precipitation is concentrated within specific periods, with substantial amounts recorded. Monthly average precipitation at the deformation points from May to October can reach as high as 1887 mm, and certain months exhibit maximum monthly precipitation of up to 3,586 mm. The unique geological conditions in this area, characterized by a layered structure of hard rock atop soft rock and the presence of coal seams in the Longtan Formation (P3l) underlying the mountains, have been disrupted by past coal mining activities, resulting in the formation of fractures. Consequently, precipitation plays a significant role in surface deformation and the development of geological hazards in this region. Figure 6 demonstrates that subsidence is more pronounced during the rainy season. This can be attributed to two main factors. Firstly, heavy precipitation leads to surface soil erosion and extensive infiltration through rock fractures, resulting in the softening of rocks and soils, increased water content, and added weight to the slopes. Prolonged precipitation further saturates the soft rock layers, significantly reducing their shear strength and resistance to sliding along contact surfaces. The combination of increased material weight and slope gradient accelerates surface subsidence. Secondly, the study area exhibits typical characteristics of a complex karst mountainous region, with underlying fractured rock bodies and well-developed joint and fracture networks influenced by tectonic movement. Previous coal mining activities have created pathways for atmospheric precipitation to penetrate the rock mass. Prolonged precipitation intensifies dissolution processes, leading to the formation of numerous karst fissures and conduits. These geological features reduce the stability of the mountain mass and trigger surface deformation.

In general, a scarcity of vegetation coverage leads to a relatively exposed surface with limited capacity for retaining soil, rendering it more vulnerable to subsidence during prolonged and heavy precipitation (Jacquemart and Tiampo, 2021). Conversely, high vegetation coverage indicates the presence of well-established surface vegetation, which enhances the soil's ability to retain its

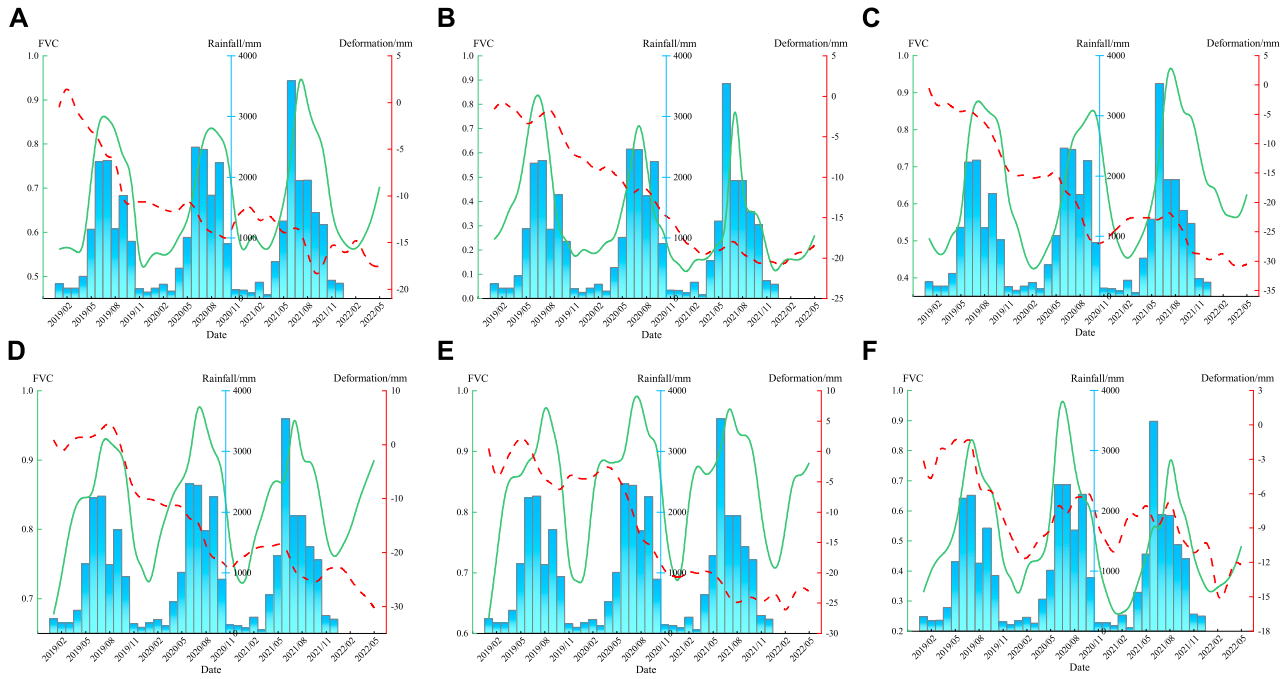

FIGURE 6
Time Series Curves of Deformation Points at Different Elevations. [**(A–F)** have elevations of 1566 m, 1672 m, 1729 m, 1829 m, 1930 m, and 2022 m, respectively].

structure. However, despite the substantial vegetation coverage during the rainy season, significant surface subsidence persists in the study area, indicating a robust response of surface deformation to precipitation. Additionally, it is important to note that vegetation coverage solely reflects the extent of surface vegetation and does not consider the specific types of vegetation present. Different vegetation types have varying impacts on soil retention capacity (Zhang et al., 2020). Among the deformation points presented in Figures 6A–F, with the exception of deformation point d, which has a slope of 33°, the other deformation points exhibit similar slopes ranging from 11° to 19°. Deformation points b and f demonstrate distinct deformation patterns compared to other feature points. These points are predominantly covered by dense coniferous trees, including tall species such as fir and pine. The presence of these tree species, characterized by expansive canopies and deep-rooted systems, plays a crucial role in stabilizing the soil structure, thereby reducing soil loosening and collapse. Furthermore, the dense canopies of fir and pine trees act as effective buffers during precipitation, mitigating the impact of precipitation on the soil. Moreover, the accumulation of fallen branches and leaves on the ground resulting from these trees significantly decelerates water flow and erosion, contributing positively to soil and water conservation efforts.

Although deformation points a, c, d, and e have relatively high vegetation coverage, they exhibit a more rapid response to precipitation. Typically, with the increase in precipitation during the early part of the rainy season, these deformation points experience a significant increase in subsidence. The primary reason for this behavior is that the surface coverage in these deformation points mainly consists of shrubs and grassland. Compared to large trees (such as fir and pine trees), the surfaces with shrubs and grassland are more vulnerable to the impact and erosion of heavy rain, leading to soil loosening and collapse, and consequently accelerating surface deformation.

To establish the correlation between surface deformation at different elevations and precipitation and vegetation coverage, an additional set of deformation points was selected for validation. The selection criteria for these points remained consistent, with efforts made to avoid areas influenced by human activities, such as farmland and urban regions. In Figure 7, deformation points g-l were chosen, exhibiting elevations that incrementally increased by approximately 100 m, ranging from 1591 m to 2011 m. With the exception of deformation points I and j, which possessed a slope of 28°, the slope of the remaining deformation points exhibited minimal variation, falling within the range of 12°–22°. Figure 7 illustrates a comparable pattern among deformation points g-l and deformation points a-f in Figure 6. Overall, all deformation points displayed a fluctuating downward trend, with the subsidence values systematically influenced by precipitation. Notably, the subsidence rate and magnitude of deformation points notably escalated during the rainy season. The diverse types of vegetation coverage observed at the deformation points led to distinct deformation patterns during this period. Deformation points g, k, and l were predominantly characterized by the presence of large trees, such as fir and pine species. These points exhibited a noticeable delay in subsidence, typically occurring 2–3 months after the onset of the rainy season. Conversely, deformation points h and j were primarily covered by shrubs and grasslands, rendering them highly responsive to precipitation. These points often displayed significant subsidence during the initial month of the rainy season. Additionally, deformation point I, despite having tree vegetation, possessed a steep slope of 28.63°. It demonstrated a sensitive response to the rainy season, exhibiting significant subsidence during the early stages

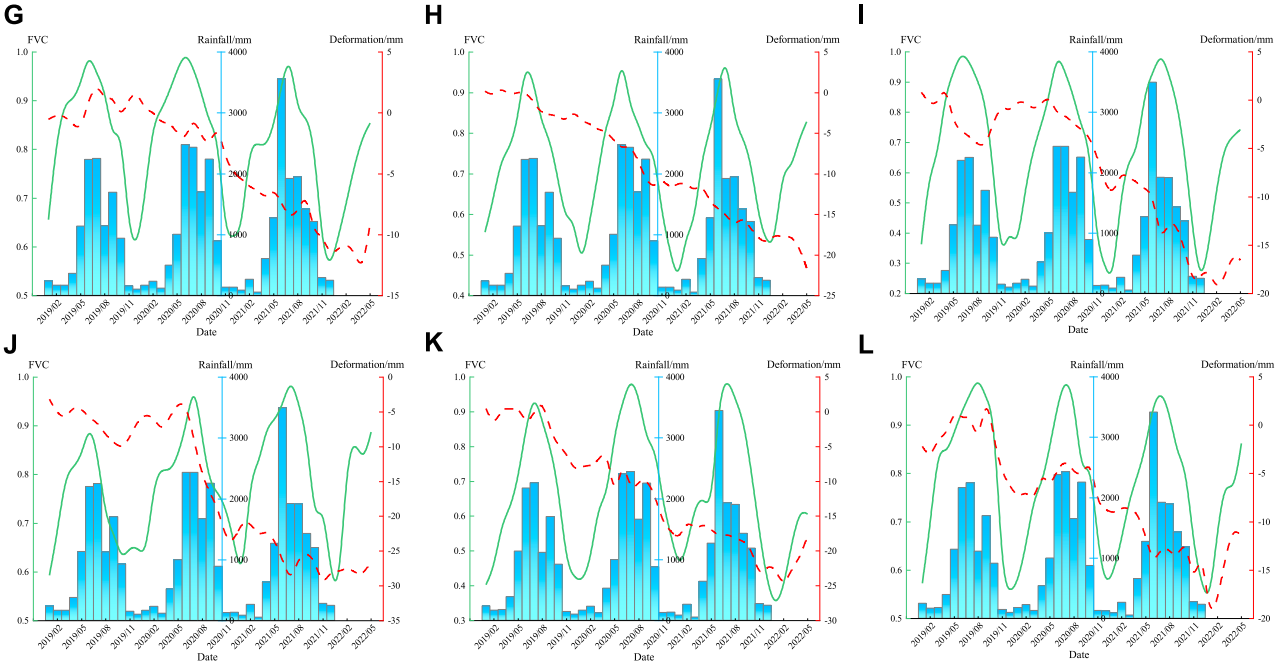

FIGURE 7
Time Series Curves for Deformation Points at Different Elevations. [**(G–L)** have elevations of 1591 m, 1634 m, 1750 m, 1855 m, 1938 m, and 2011 m, respectively].

of precipitation. This suggests that the terrain's slope is a contributing factor to surface deformation, with the steepness of the slope influencing the extent to which precipitation impacts deformation points.

Topography and geomorphology play a significant role in governing slope stability, with slope gradient serving as a crucial parameter for characterizing the terrain (Guo et al., 2008). To examine the deformation patterns of deformation points at different slopes and their response to precipitation, we extracted time series cumulative subsidence data, vegetation cover data, and monthly cumulative precipitation data from two distinct sets of deformation feature points. To reduce the effect of different vegetation types on precipitation data, we selected deformation feature points that all exhibited woody vegetation cover.

As depicted in Figure 8, time series curves were generated for deformation points at different slope levels (<5°, 5°–15°, 15°–25°, 25°–35°, 35°–45°, >45°). The slope angles for points in Figures 8M–R increased progressively, ranging from 4.38° to 57.76°. In general, all deformation points exhibited a fluctuating subsidence trend, demonstrating a distinct response to variations in precipitation. During the rainy season, deformation points are subjected to significant subsidence, while they will remain relatively stable during the dry season. With the increase of the slope gradient, subsidence rates will accelerate. Notably, deformation points in Figures 8M, N, O do not show significant subsidence at the early stages of the rainy season, even under intense precipitation in June 2021. Instead, they exhibit delayed subsidence, typically occurring 2–3 months after the onset of the rainy season. In contrast, deformation points in Figures 8P, Q, R responded rapidly to increased precipitation during the early stages of the rainy season, displaying noticeable subsidence. These results suggested that with the increase of slope gradient, deformation points will become more sensitive to precipitation. Specifically, when the slope gradient was less than 25°, deformation points were less affected by precipitation, and their response time may be delayed, with significant subsidence occurring 2–3 months after the rainy season starts. Nevertheless, when the slope gradient was greater than 25°, deformation points responded more quickly to precipitation, typically showing substantial subsidence at the beginning of the rainy season.

The topographic characteristics of the study area, characterized by elevated mountains and steep slopes, exert a profound influence on slope stability. The gradient of the slope not only impacts the distribution of stress within the slope but also plays a pivotal role in determining crucial factors such as surface water runoff, the distribution of loose deposits across the slope, and the thickness of such deposits. Steeper slopes experience more significant stress distribution across their surfaces and upper sections, rendering them more susceptible to deformation and failure. Furthermore, during the rainy season, steeper slopes tend to accumulate surface runoff, and the steep gradient amplifies the velocity of the runoff. This phenomenon intensifies erosion and scouring of the slope surface, exacerbating soil erosion and facilitating soil loosening and collapse. In such circumstances, surface deformation becomes more probable, thereby increasing the occurrence of geological hazards.

To verify the deformation patterns and their response to precipitation at different slopes, we selected another set of deformation points with varying slopes. The slopes of these points, as presented in Figure 9, were 3.58°, 12.31°, 21.05°, 32.58°, 35.93°, and 49.33°, and all of them had woody vegetation cover. As depicted in Figures 9S–X, these points displayed a similar pattern to those in Figure 8. Overall, with an increase in slope, the deformation points showed an accelerating sinking trend. The response of the deformation points to precipitation was quite apparent, with

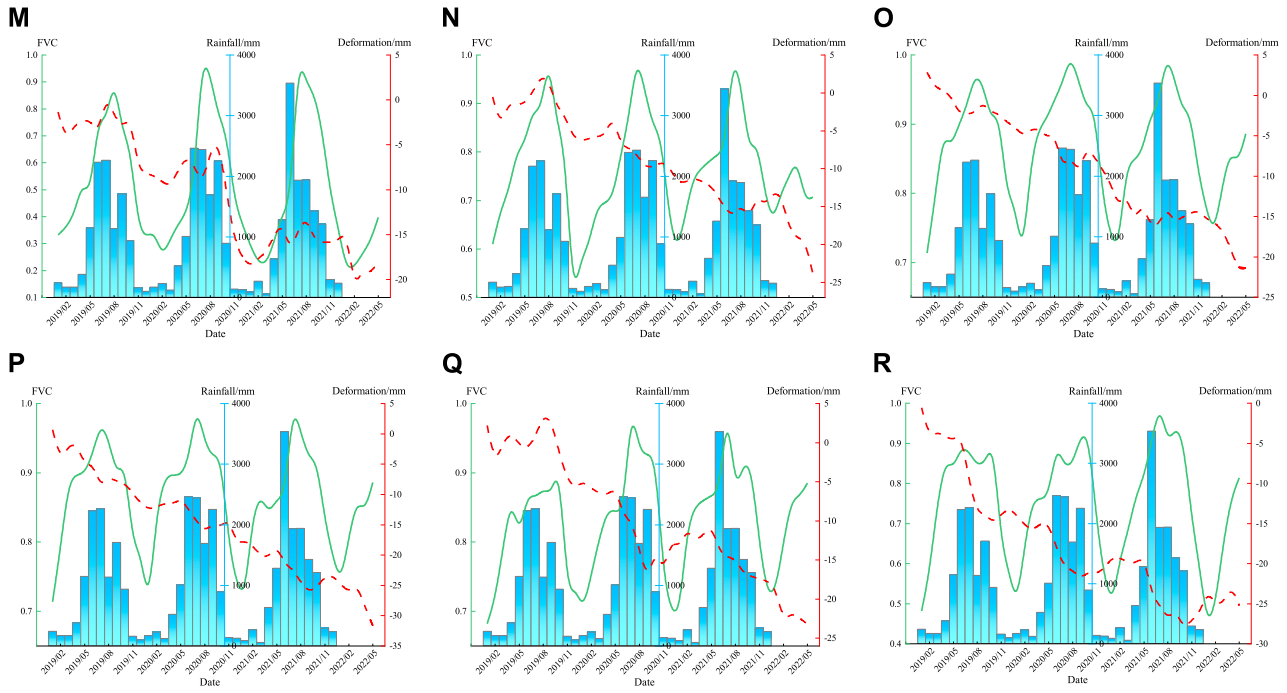

FIGURE 8
Time Series Curves of Deformation Points at Different. [**(M–R)** have slopes of 4.38°, 10.54°, 21.53°, 29.69°, 37.68°, and 57.76°, respectively].

significant sinking occurring during the rainy season. Among these points, a slope of 25° appeared to be a threshold for the speed of response to precipitation. Specifically, when the slope was less than 25°, the deformation points exhibited a delayed response to precipitation, typically showing significant sinking 2–3 months after the rainy season begins. On the other hand, when the slope exceeded 25°, the deformation points responded very rapidly, with significant sinking occurring at the start of the rainy season.

5 Discussion

5.1 Analysis of surface deformation in karstic mountainous regions as affected by subsidence of closed mines

Following the cessation of mining activities, the persistence of ground subsidence, characterized by collapsed rock masses within goaf regions, remains a prominent contributor to land subsidence in the area. Within the study area, which represents a typical karst complex mountainous region, comprehending the implications of subsidence induced by mine closures on surface deformation is of utmost importance. Currently, there exists a dearth of research concerning the distribution patterns and impact models of surface deformation resulting from mine closure within this specific study area. Hence, our discourse is primarily centered around this representative study area.

In their investigation on surface deformation resulting from mine closures, Chen et al. (2020) explored the characteristics of surface deformation in several abandoned goaf areas at Ying'an Coal Mine and Baoshan Coal Mine, situated in the alluvial plains of Jilin, China. Their findings revealed that the subsidence process subsequent to coal mining can be divided into two distinct stages: the initial stage primarily entails subsidence in the central region of the goaf, while the subsequent stage witnesses subsidence predominantly concentrated in the peripheral areas of the goaf. The distribution patterns of surface deformation arising from mine closures in this study exhibit consistency with the observations made by Chen et al. However, it is crucial to recognize that the study area under consideration represents a typical karst complex mountainous region characterized by robust karst processes, thereby rendering the impact of mine closure on ground subsidence more intricate than in plain areas.

Surface deformation in the LuJiaZhai-DaPingDi Minefield extends beyond the confines of the closed mining areas, predominantly impacting high-altitude regions adjacent to the closed mining areas. This phenomenon can be attributed to multiple factors. Coal mining operations typically disrupt the initial stress state of overlying rock layers, resulting in their redistribution and consequent movements and deformations. This process generates various voids, encompassing fractures between rocks, cracks within overlying rock layers, and fissures within loose sedimentary materials (Wang et al., 2016). The study area exhibits significant elevation variation, characterized by a "hard on top and soft underneath" pattern in the rock layers. Coal seams are situated within the Longtan Formation (P3l) at the base of the mountains, while the mining goaf is located at the foothills. During the initial phases of coal mining, the central portion of the goaf, providing the weakest support to the overlying rock layers, experiences substantial early movements and deformations concentrated in its central region. As the overlying rock layers subside, the progressive deformation gradually extends upward, resulting in surface subsidence and the formation of numerous fractures within the mountains. With time, the central part of the mining goaf undergoes compaction first. At this stage, the central portion of the goaf reaches a relatively stable state,

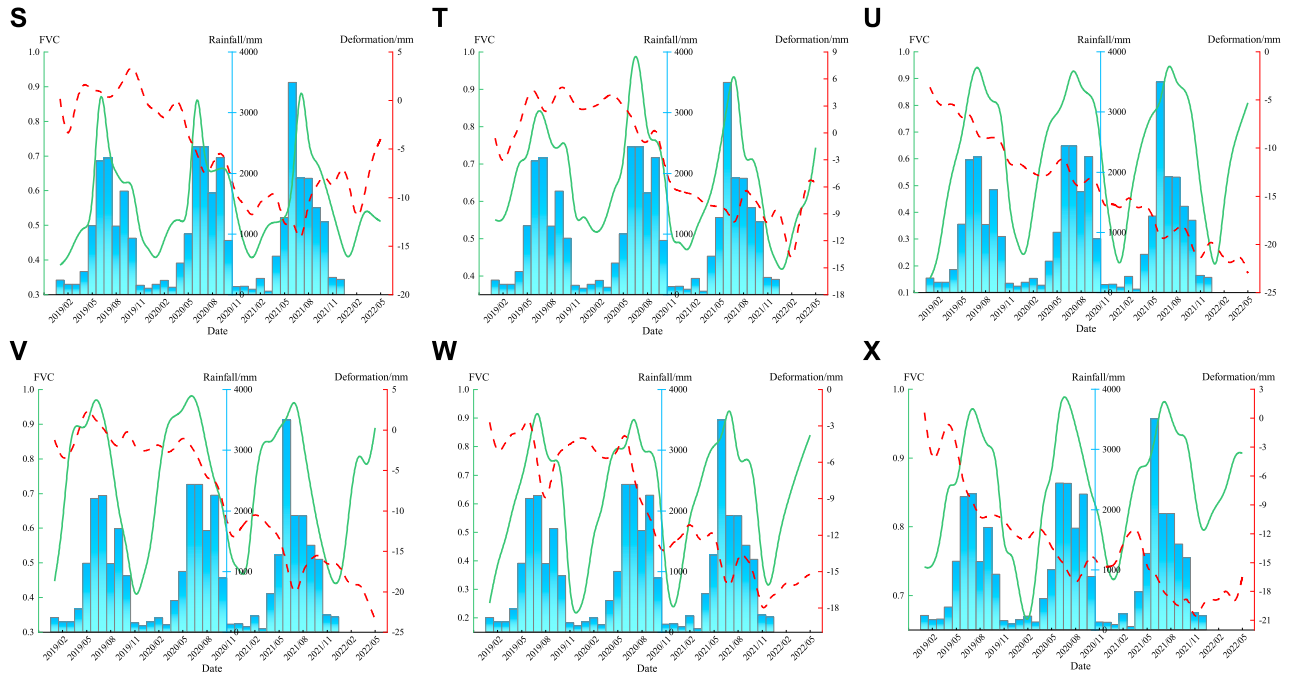

FIGURE 9
Time Series Curves for Deformation Points at Different Slopes. [**(S–X)** have slopes of 3.58°, 12.31°, 21.05°, 32.58°, 35.93°, and 49.33°, respectively].

leading to a decline in surface deformation. However, in the boundary regions of the goaf, there remains space that requires compaction. Consequently, during the later stages following mine closure, subsidence primarily concentrates in the border areas of the goaf.

Preceding the coal mining activities in the karst mountain regions, the area was already influenced by tectonic movements, resulting in fractured rock formations with well-developed joint fissures. Under the influence of precipitation and weathering, the existing cracks had already manifested in the mountainous terrain. As coal mining operations progressed, these initial cracks further widened, and new cracks emerged (Sun et al., 2023). These mountain cracks not only compromised the stability of the terrain but also provided pathways for rainwater infiltration into the rock formations, thereby accelerating the karstification process. Consequently, this gave rise to karst subsidence occurrences within the area.

5.2 Analysis of the coupled relationship between surface deformation of closed mines in karst mountainous areas and factors such as slope, precipitation, and vegetation types

Our experimental results indicate that besides the goaf, slope is the primary factor causing surface deformation in closed mines in karst mountainous areas, with precipitation acting as a triggering factor leading to periodic changes in surface deformation in the study area. When the slope is less than 25°, arboreal coverage (such as pine and fir trees) significantly mitigates surface deformation induced by rainfall. However, this mitigating effect rapidly diminishes when the slope exceeds 25°. To further analyze the impact of slope on surface subsidence in the Karst mountain areas of Liupanshui and its response to precipitation and vegetation coverage, we have compared our findings with previously published similar studies, outlining the complementary aspects of our research and identifying any existing limitations.

Contemporary investigations concerning the impact of slope, precipitation, and vegetation coverage on surface deformation primarily concentrate on landslide causation and susceptibility assessments. For example, Zhang et al. (Zhang et al., 2020) examined the spatial distribution characteristics of landslide-prone regions in Xiangxi Autonomous Prefecture, Hunan Province, China, based on diverse geographical factors. Their study underscored the significance of slope and vegetation coverage in landslide occurrence. Among the 21 geographical factors examined, slope emerged as the most influential contributor to landslides. Furthermore, the distribution of landslide-prone areas exhibited a close association with vegetation coverage. Specifically, regions with higher Normalized Difference Vegetation Index (NDVI) values displayed fewer landslides, indicating that areas with lower NDVI values possessed weaker vegetation stability and were more susceptible to landslides. Bao and You (2010), through field surveys and an analysis of geological hazard-prone locations in the Zhongshan area of Liupanshui, investigated the characteristics and causes of geological disasters. Their findings revealed that landslides predominantly transpired in areas with slopes ranging from 10° to 65°, with the majority falling within the 25°–35° range. Additionally, the peak period for geological disasters was from May to September, corresponding to heightened precipitation and heavy precipitation. Similarly, Qian et al. (2022) conducted a susceptibility analysis of landslides in Liupanshui, employing various geographical factors and a Logistic fuzzy comprehensive coupling model on a Geographic Information System (GIS) platform. Their results

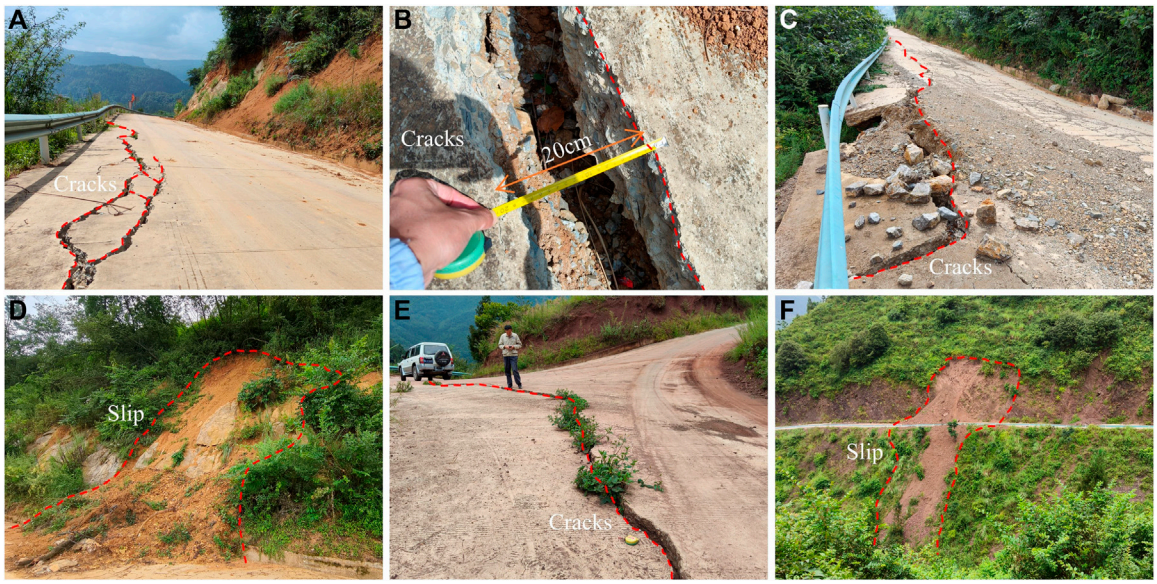

FIGURE 10
Photographs of LuJiaZhai-DaPingDi Minefield survey: **(D)** and **(F)** depict pronounced sliding on steep slopes under bush cover; **(A)**, **(B)**, **(C)** and **(E)** illustrate road damage caused by subsidence.

indicated that areas at extremely high and high risk of landslides were considerably influenced by slope and surface undulation. These researchers generally evaluated the contribution of influencing factors to landslide occurrence at a general level, typically relying on known geological hazard-prone locations and employing statistical or modeling approaches. Our study aligns with these trends in a general sense. However, our research distinguishes itself by utilizing SBAS technique to obtain time series deformation monitoring results, enabling a more detailed assessment of the contributions of different slope levels, vegetation types, and precipitation to surface subsidence in closed mining areas. In recent studies, Asada et al. (2020) emphasized the importance of precipitation as a significant factor compared to vegetation, attributing approximately 40% of the likelihood of shallow landslides to it. Their research also highlighted the effective mitigation of shallow landslides by vegetation under specific conditions. In their more recent study (Asada and Minagawa, 2023), they constructed generalized linear models (GLM) and random forest models (RF) using statistical methods to quantitatively assess the impact of different vegetation conditions on shallow landslide occurrence. The models were developed considering slope and hourly precipitation as critical parameters for evaluating slope stability. The study found that forest-covered slopes exhibited greater stability compared to grass-covered slopes, and secondary grasslands and shrubs were more prone to landslides than coniferous forests. However, it was observed that the slope stability of forested areas had its limitations. Our study exhibits a similar trend to Asada's research. Specifically, under comparable slope conditions, areas with grassland and shrub coverage display heightened sensitivity to precipitation, while areas with forest coverage exhibit a certain degree of delayed response. Moreover, when vegetation primarily consists of trees, slope becomes a pivotal factor influencing the response to precipitation. Specifically, when the slope is less than 25°, tree-covered surfaces exhibit a noticeable delay in response to precipitation. Conversely, when the slope exceeds 25°, the response to precipitation is rapid. Our research provides an analysis of the contributions of slope, vegetation type, and precipitation to surface subsidence in closed mining areas based on time series deformation results. However, numerous factors influence surface deformation in karst mountain areas with closed mines. Consequently, undertaking a quantitative exploration of the contributions of multiple factors to surface deformation in closed mining areas using Interferometric Synthetic Aperture Radar (InSAR) technology represents a crucial focus of our future research.

In addition, in order to further verify the reliability of the deformation extraction results in this study, we went to the LuJiaZhai-DaPingDi Minefield to conduct a field investigation, and the results of the field investigation are shown in Figure 10, from which it can be clearly seen that the slopes with steeper slopes under the cover of shrubs have been sliding obviously (Figures 10D, F) and the sliding surfaces are fresh, and meanwhile, a number of highways in the wellfield have been damaged due to the ground settlement (Figures 10A–C, E), which suggests that surface subsidence has continued to take place in the area even though all the mines in the wellfield are closed to the public so far.

6 Conclusion

In the context of the intricate interplay between surface deformation, precipitation, and vegetation cover in karst mountain regions, this study focuses on the LuJiaZhai-DaPingDi Minefield situated in Liupanshui City. Leveraging remote sensing technology, we investigate the influence of various factors, including altitude, slope, vegetation cover, and precipitation, on surface deformation within closed mining areas. An extensive analysis was performed utilizing time series data of surface deformation, vegetation cover, precipitation, altitude, and slope. The key findings are as follows:

The areas exhibiting surface deformation within the study region are primarily concentrated near the recently closed MaiZiGou Coal Mine

and the higher-altitude eastern and southern regions of the mining field. These deformation areas comprise 20.45% of the total mining area. Over the study period, the maximum cumulative subsidence reaches −60.3 mm, while the maximum uplift is 34.17 mm. The maximum annual average subsidence rate and uplift rate are −21.83 mm/yr and 8.13 mm/yr, respectively. Overall, surface deformation in the closed mining area displays systematic variations with precipitation. During the rainy season, both the subsidence rate and subsidence values in the mining area are significantly higher compared to the dry season. Furthermore, distinct types of vegetation cover exert varying degrees of influence on surface deformation. Surfaces covered by grassland and shrubs exhibit a more rapid response to precipitation compared to areas adorned with deciduous trees such as fir and pine. Typically, substantial subsidence occurs promptly during the initial stages of the rainy season or periods of heavy precipitation on grassland and shrub-covered surfaces. However, when the surface is enveloped by deciduous trees, even in the presence of the rainy season or heavy precipitation, surface subsidence does not manifest immediately. Instead, a delayed response ensues, typically lagging behind precipitation by 2–3 months. In regions characterized by deciduous tree vegetation cover, the response of surface deformation to precipitation is primarily influenced by the terrain slope. When the slope is below 25°, surfaces covered by deciduous trees do not display significant subsidence in the early stages of the rainy season or heavy precipitation, with the response typically lagging behind the rainy season by 2–3 months. Conversely, when the slope exceeds 25°, substantial subsidence occurs early in the rainy season or during heavy precipitation, even if the surface is covered by deciduous trees. This indicates that a slope of 25° represents a critical threshold for surface deformation in response to precipitation within this region. Moreover, deciduous trees such as fir and pine exhibit a certain degree of restraining effect on surface subsidence triggered by precipitation. However, this restraining effect is limited and diminishes as the slope increases.

Data availability statement

The original contributions presented in the study are included in the article/Supplementary Material, further inquiries can be directed to the corresponding authors.

Author contributions

GH: Conceptualization, Methodology, Project administration, Writing–original draft, Writing–review and editing. JD: Software, Writing–review and editing. WX: Conceptualization, Validation, Writing–review and editing. ZZ: Conceptualization, Writing–review and editing. SL: Validation, Writing–review and editing. ZK: Investigation, Validation, Writing–review and editing. QA: Formal Analysis, Writing–review and editing. JW: Investigation, Writing–review and editing. YZ: Software, Writing–review and editing.

Funding

The author(s) declare financial support was received for the research, authorship, and/or publication of this article. This research was funded by Guizhou Scientific and Technology Fund [Grant No. QKHJ-ZK (2023) YB 193], Major scientific and technological projects of Yunnan Province: Research on Key Technologies of ecological environment monitoring and intelligent management of natural resources in Yunnan (Grant No. 202202AD080010), Geological Research Project of Bureau of Geology and Mineral Exploration and Development Guizhou Province [Grant No. QDKKH-(2021)33] and High-resolution Comprehensive Application Demonstration for the Central Yunnan Water Diversion Project (in the Mid-Yunnan Plateau Area) (89-Y50-G31-9001-22/23-05).

Acknowledgments

The authors would like to thank the reviewers for their constructive comments that improved this research.

Conflict of interest

Author ZZ was employed by Yunnan Haiju Geographic Information Technology Co., Ltd.

The remaining authors declare that the research was conducted in the absence of any commercial or financial relationships that could be construed as a potential conflict of interest.

Publisher's note

References

Adams, J. B., Smith, M. O., and Johnson, P. E. (1986). Spectral mixture modeling: a new analysis of rock and soil types at the Viking Lander 1 Site. *J. Geophys. Res. Solid Earth* 91 (B8), 8098–8112. doi:10.1029/JB091iB08p08098

Asada, H., and Minagawa, T. (2023). Impact of vegetation differences on shallow landslides: a case study in Aso, Japan. *Water* 15 (18), 3193. doi:10.3390/w15183193

Asada, H., Minagawa, T., Koyama, A., and Ichiyanagi, H. (2020). Factor analysis of surface collapse on slopes caused by the july 2017 northern kyushu heavy rain. *Ecol. Civ. Eng.* 23 (1), 185–196. doi:10.3825/ece.23.185

Bai, J., Ju, N., Zhang, C., and He, Z. (2020). Characteristics and successful early warning case of Xingyi landslide in Guizhou province. *J. Eng. Geol.* 28 (6), 1246–1258. doi:10.13544/j.cnki.jeg.2019-360

Bao, D., and You, G. (2010). The characteristics of geological hazards and analysis on genesis in zhongshan district of Liupanshui City,Guizhou province. *Mineral. Explor.* 1 (4), 400–406. doi:10.3969/j.issn.1674-7801.2010.04.016

Berardino, P., Fornaro, G., Lanari, R., and Member, S. (2002). A new algorithm for surface deformation monitoring based on small baseline differential SAR

interferograms. *IEEE Trans. Geoscience Remote Sens.* 40 (11), 2375–2383. doi:10.1109/TGRS.2002.803792

Chen, B., Liu, H., Li, Z., and Zheng, M. (2023a). Research progress and prospect of secondary subsidence monitoring, prediction and stability evaluation in closed underground mines. *J. China Coal Soc.* 48 (2), 943–958. doi:10.13225/j.cnki.jccs.2022.1385

Chen, B., Yu, H., Zhang, X., Li, Z., Kang, J., Yu, Y., et al. (2022a). Time-varying surface deformation retrieval and prediction in closed mines through integration of SBAS InSAR measurements and LSTM algorithm. *Remote Sens.* 14(3), 788. doi:10.3390/rs14030788

Chen, D., Chen, H., Zhang, W., Cao, C., Zhu, K., Yuan, X., et al. (2020). Characteristics of the residual surface deformation of multiple abandoned mined-out areas based on a field investigation and SBAS-InSAR: a case study in Jilin, China. *Remote Sens.* 12(22), 3752. doi:10.3390/rs12223752

Chen, H., Zhao, C., Li, B., Gao, Y., Chen, L., and Liu, D. (2023b). Monitoring spatiotemporal evolution of Kaiyang landslides induced by phosphate mining using distributed scatterers InSAR technique. *Landslides* 20 (3), 695–706. doi:10.1007/s10346-022-01986-5

Chen, H., Zhao, C., Sun, R., Chen, L., Wang, B., and Li, B. (2022b). Two-dimensional deformation monitoring of karst landslides in Zongling, China, with multi-platform distributed scatterer InSAR technique. *Landslides* 19 (7), 1767–1777. doi:10.1007/s10346-022-01860-4

Chen, L., Zhao, C., Chen, H., Kang, Y., Li, B., and Liu, X. (2023c). The detection and control factor analysis of active landslides in Guizhou province, China, using sentinel-1 SAR imagery. *Remote Sens.* 15 (23), 5468. doi:10.3390/rs15235468

Chen, Z., Yang, Y., Zhou, L., Hou, H., Zhou, W., Liu, S., et al. (2022c). Ecological restoration of a loess open-cast mining area in China: perspective from an ecological security pattern. *Forests* 13(2), 269. doi:10.3390/f13020269

Chu, X., Dang, S., and Ding, J. (2015). Analysis of karst collapse distribution in Guizhou Province and influential factors. *Yangtze River* 46 (12), 42–44. doi:10.16232/j.cnki.1001-4179.2015.12.010

Deng, K., Wang, L., and Fan, H. (2015). InSAR-based monitoring and analysis of ground subsidence in old goaf. *J. Min. Saf. Eng.* 32 (6), 918–922. doi:10.13545/j.cnki.jmse.2015.06.008

Deng, K., Zheng, M., Zhang, H., Fan, H., and Tan, Z. (2022). Research status and prospect of secondary subsidence in closed mine. *Coal Sci. Technol.* 50 (5), 10–20. doi:10.13199/J.CNKI.CST.2021-1403

Dong, J., Ma, Z., Liang, J., and Liu, B. (2022). A comparative study of the identification of hidden landslide hazards based on time series InSAR techniques. *Remote Sens. Nat. Resour.* 34 (3), 73–81. doi:10.6046/zrzyyg.2021333

Du, Y., Zhang, L., Feng, G., Lu, Z., and Sun, Q. (2017). On the accuracy of topographic residuals retrieved by MTInSAR. *IEEE Trans. Geoscience Remote Sens.* 55 (2), 1053–1065. doi:10.1109/TGRS.2016.2618942

Fang, J., Xie, X., and Liu, J. (2016). Study on causes and countermeasures of geological disasters in panxian Guizhou province. *Coal Technol.* 35 (12), 188–189. doi:10.13301/j.cnki.ct.2016.12.070

Guo, F., Yang, N., Meng, H., and Zhang, Y. (2008). Application of the relief amplitude and slope analysis to regional landslide hazard assessments. *Geol. China* 35 (1), 131–143. doi:10.3969/j.issn.1000-3657.2008.01.014

He, K., Li, J., Li, B., Zhao, Z., Zhao, C., Gao, Y., et al. (2022). The Pingdi landslide in Shuicheng, Guizhou, China: instability process and initiation mechanism. *Bull. Eng. Geol. Environ.* 81 (4), 131. doi:10.1007/s10064-022-02596-0

Hu, B., and Yan, B. (2018). Study on potential geological disasters and prevention technology and resources utility of abandon mine. *Coal Min. Technol.* 23 (3), 1–5. doi:10.13532/j.cnki.cn11-3677/td.2018.03.001

Jacquemart, M., and Tiampo, K. F. (2021). Leveraging time series analysis of radar coherence and normalized difference vegetation index ratios to characterize pre-failure activity of the Mud Creek landslide, California. *Nat. Hazards Earth Syst. Sci.* 21 (2), 629–642. doi:10.5194/nhess-21-629-2021

Li, B., Zhao, C., Li, J., Chen, H., Gao, Y., Cui, F., et al. (2023). Mechanism of mining-induced landslides in the karst mountains of Southwestern China: a case study of the Baiyan landslide in Guizhou. *Landslides* 20 (7), 1481–1495. doi:10.1007/s10346-023-02047-1

Li, J., Gao, F., Lu, J., and Fang, R. (2019). Deformation monitoring and predicton of residential areas based on SBAS-InSAR and GM-SVR. *J. Geodesy Geodyn.* 38 (08), 837–842. doi:10.14075/j.jgg.2019.08.014

Li, T., Wu, M., Duan, C., Li, S., and Liu, C. (2022). The effect of different restoration approaches on vegetation development in metal mines. *Sci. total Environ.* 806 (2), 150626. doi:10.1016/j.scitotenv.2021.150626

Li, X., Zhuo, L., Su, F., and Wu, W. (2021). Application of InSAR technology in landslide hazard: progress and prospects. *Natl. Remote Sens. Bull.* 25 (2), 614–629. 1007-4619(2021) 02-0614-16. doi:10.11834/jrs.20209297

Li, Y., Zhang, J., Li, z., and Luo, Y. (2013). Land subsidence in Beijing city from InSAR time series analysis with small baseline subset. *Geomatics Inf. Sci. Wuhan Univ.* 38 (11), 1374–1377. doi:10.13203/j.whugis2013.11.011

Liang, S., and Hu, H. (2022). Analysis of residual deformation in goaf based on SBAS InSAR technology. *China Min. Mag.* 31 (12), 70–78. doi:10.12075/j.issn.1004-4051.2022.12.002

Liu, Z., Qiu, H., Zhu, Y., Liu, Y., Yang, D., Ma, S., et al. (2022). Efficient identification and monitoring of landslides by time-series InSAR combining Single- and multi-look phases. *Remote Sens.* 14 (4), 1026. doi:10.3390/rs14041026

Ma, S., Qiu, H., Zhu, Y., Yang, D., Tang, B., Wang, D., et al. (2023). Topographic changes, surface deformation and movement process before, during and after a rotational landslide. *Remote Sens.* 15 (3), 662. doi:10.3390/rs15030662

Pei, Y., Qiu, H., Yang, D., Liu, Z., Ma, S., Li, J., et al. (2023). Increasing landslide activity in the Taxkorgan River Basin (eastern Pamirs Plateau, China) driven by climate change. *CATENA* 223, 106911. doi:10.1016/j.catena.2023.106911

Qian, C., Wang, J., and Wu, W. (2022). Analysis of landslide geological hazard susceptibility based on GIS: a case study of Liupanshui City. *J. Tianjin Chengjian Univ.* 28 (5), 336–341. doi:10.19479/j.2095-719x.2205336

Qin, X., Deng, K., Zheng, M., and Wang, L. (2022). Monitoring and analysis of surface secondary subsidence of closed mines in Western Xuzhou. *Sci. Surv. Mapp.* 47 (8). doi:10.16251/j.cnki.1009-2307.2022.08.028

Sandwell, D. T., and Price, E. J. (1998). Phase gradient approach to stacking interferograms. *J. Geophys. Res. Solid Earth* 103 (B12), 30183–30204. doi:10.1029/1998JB900008

Shi, X., and Zhang, W. (2023). Characteristics of an underground stope channel supplied by atmospheric precipitation and its water disaster prevention in the karst mining areas of Guizhou. *Sci. Rep.* 13 (1), 15892. doi:10.1038/s41598-023-43209-4

Sun, R., Zhao, C., Li, B., Chen, H., and Chen, L. (2023). Karst landslides detection and monitoring with multiple SAR data and multi-dimensional SBAS technique in Shuicheng, Guizhou, China. *Front. Earth Sci.* 11, 1121868. doi:10.3389/feart.2023.1121868

Tang, L., Hou, H., Zhang, S., and Guo, S. (2021). Monitoring of short revisited SAR data in rapid deformation field of mining area. *Sci. Surv. Mapp.* 46 (5), 95–103. doi:10.16251/j.cnki.1009-2307.2021.05.014

Wang, J., Wang, C., Xie, C., Zhang, H., Tang, Y., Zhang, Z., et al. (2020). Monitoring of large-scale landslides in Zongling, Guizhou, China, with improved distributed scatterer interferometric SAR time series methods. *Landslides* 17 (8), 1777–1795. doi:10.1007/s10346-020-01407-5

Wang, L. (2013). Application of precision leveling in land subsidence monitoring. *Huabei Land Resour.* (2), 113–116. doi:10.3969/j.issn.1672-7487.2013.02.036

Wang, L., Qiu, H., Zhou, W., Zhu, Y., Liu, Z., Ma, S., et al. (2022). The post-failure spatiotemporal deformation of certain translational landslides may follow the pre-failure pattern. *Remote Sens.* 14 (10), 2333. doi:10.3390/rs14102333

Wang, S., Li, X., and Wang, D. (2016). Void fraction distribution in overburden disturbed by longwall mining of coal. *Environ. Earth Sci.* 75, 151. doi:10.1007/s12665-015-4958-6

Wu, L., Wang, J., and Fu, Y. (2021). Early identifying and monitoring landslides in Guizhou province with InSAR and optical remote sensing. *Bull. Surv. Mapp.* 7, 98–102. doi:10.13474/j.cnki.11-2246.2021.0216

Xiao, L., He, Y., Xin, X., Wen, D., Tong, C., Chen, L., et al. (2019). Time series subsidence analysis of drilling solution miningrock salt mines based on Sentinel-1 data and SBAS-InSAR technique. *J. Remote Sens.* 23 (3), 501–513. doi:10.11834/jrs.20198292

Xu, Y., Li, T., Tang, X., Zhang, X., Fan, H., and Wang, Y. (2022). Research on the applicability of DInSAR, stacking-InSAR and SBAS-InSAR for mining region subsidence detection in the Datong Coalfield. *Remote Sens.* 14(14), 3314. doi:10.3390/rs14143314

Yang, C., Dong, J., Zhu, S., and Xiong, G. (2021). Detection, identification and deformation characteristics of landslide groups by InSAR in Batang section of Jinsha River Convergence Zone, China. *J. Earth Sci. Environ.* 43 (02), 398–408. doi:10.19814/j.jese.2020.12034

Yang, Z., Li, Z., Zhu, J., Wang, Y., and Wu, L. (2020). Use of SAR/InSAR in mining deformation monitoring, parameter inversion, and forward predictions: a review. *IEEE Geoscience Remote Sens. Mag.* 8 (1), 71–90. doi:10.1109/MGRS.2019.2954824

Yu, H., Chen, B., Kang, J., and Han, M. (2021). Research on surface deformation law of closed mines based on SBAS-InSAR. *Industry Mine Automation* 47 (2), 45–51. doi:10.13272/j.issn.1671-251x.2020110044

Zhang, F., Zhu, Y., Zhao, X., and Zhang, Y. (2020). Spatial distribution and identification of hidden danger points of landslides based on geographical factors. *Geomatics Inf. Sci. Wuhan Univ.* 45 (8), 1233–1244. doi:10.13203/j.whugis20200126

Zhang, L., Dai, K., Deng, J., Ge, D., Liang, R., Li, W., et al. (2021). Identifying potential landslides by stacking-InSAR in southwestern China and its performance comparison with SBAS-InSAR. *Remote Sens.* 13 (18), 3662. doi:10.3390/rs13183662

Zhang, L., Liang, L., Chen, B., Hu, J., and Yu, Y. (2023). Spatio-temporal monitoring and analysis method of MIulti-dimensional surface deformation of closed mines based on SBAS-InSAR technique. *Metal. Mine* 1, 83–94. doi:10.13272/j.issn.1671-251x.2020110044

Zhang, X., Zhao, X., Ge, D., and Liu, B. (2018). Subsidence monitoring of Huainan coal mine from Sentinel TOPS images based on Stacking technique. *Remote Sens. Land Resour.* 30 (4), 200–205. doi:10.6046/gtzyyg.2018.04.30

Zhang, Y., Wang, Y., and Yan, S. (2016). Ground subsidence detection of Peibei mining area based on Stacking InSAR technology. *Coal Technol.* 35 (07), 102–105. doi:10.13301/j.cnki.ct.2016.07.042

Zhao, C., Chen, L., Yin, Y., Liu, X., Li, B., Ren, C., et al. (2023a). Failure process and three-dimensional motions of mining-induced Jianshanying landslide in China

observed by optical, LiDAR and SAR datasets. *GIScience Remote Sens.* 60 (1), 2268367. doi:10.1080/15481603.2023.2268367

Zhao, Q., Yang, Z., Jiang, Y., Liu, X., Cui, F., and Li, B. (2023b). Discrete element analysis of deformation features of slope controlled by karst fissures under the mining effect: a case study of Pusa landslide, China. *Geomatics, Nat. Hazards Risk* 14 (1), 1–35. doi:10.1080/19475705.2022.2158376

Zhao, X., and Zhu, Q. (2020). Analysis of the surface subsidence induced by sublevel caving based on GPS monitoring and numerical simulation. *Nat. Hazards* 103 (3), 3063–3083. doi:10.1007/s11069-020-04119-0

Zhong, Z., Xu, Y., Wang, N., Liu, X., and Gao, G. (2022). Environmental characteristics and unified failure mode classification system for mining landslides in the karst mountainous areas of southwestern China. *Carbonates Evaporites* 38 (1), 2. doi:10.1007/s13146-022-00818-w

Zhu, J., Li, Z., and Hu, J. (2017). Research progress and methods of InSAR for deformation monitoring. *Acta Geod. Cartogr. Sinica* 46 (10), 1717–1733. doi:10.11947/j.AGCS.2017.20170350

Zhu, J., Yang, Z., and Li, Z. (2019a). Recent progress in retrieving and predicting mining-induced 3D displacements using InSAR. *Acta Geod. Cartogr. Sinica* 48 (2), 135–144. doi:10.11947/j.AGCS.2019.20180188

Zhu, Q., Zeng, H., Ding, Y., and Xie, X. (2019b). A review of major potential landslide hazards analysis. *Acta Geod. Cartogr. Sinica* 48 (12), 1551–1561. doi:10.11947/j.AGCS.2019.20190452

Zhu, Y., Yao, X., Yao, L., and Yao, C. (2022). Detection and characterization of active landslides with multisource SAR data and remote sensing in western Guizhou, China. *Nat. Hazards* 111 (1), 973–994. doi:10.1007/s11069-021-05087-9

frontiers | Frontiers in Earth Science

TYPE Original Research
PUBLISHED 15 January 2024
DOI 10.3389/feart.2023.1348730

OPEN ACCESS

EDITED BY
Haijun Qiu,
Northwest University, China

REVIEWED BY
Wentao Li,
Hohai University, China
Fei Xu,
Guangdong Academy of Sciences, China

*CORRESPONDENCE
Meihong Ma,
mamh@tjnu.edu.cn

†These authors share first authorship

RECEIVED 03 December 2023
ACCEPTED 21 December 2023
PUBLISHED 15 January 2024

CITATION
Wang D, Zhou Y, Zhang X, Liu Y, Teng Q and Ma M (2024), Simulated research on distributed hydrological models–a case study of the Daxi Water Basin.
Front. Earth Sci. 11:1348730.
doi: 10.3389/feart.2023.1348730

Simulated research on distributed hydrological models–a case study of the Daxi Water Basin

Dacheng Wang[1†], Yue Zhou[2†], Xiaolei Zhang[3], Yalan Liu[1], Qizhi Teng[1] and Meihong Ma[4*]

[1]Aerospace Information Research Institute, Chinese Academy of Sciences, Beijing, China, [2]Faculty of Geographical Science, Beijing Normal University, Beijing, China, [3]China Institute of Water Resources and Hydropower Research, Beijing, China, [4]Geographical and Environmental Science Department Tianjin Normal University, Tianjin, China

Against the backdrop of global climate warming, the issue of flash flood disasters in small watersheds triggered by heavy rainfall is gradually becoming more prominent. Selecting an appropriate hydrological model is crucial for flash flood disaster defense. This article focuses on the Daxi Water Basin in Lianping County, Guangdong Province, as the research area. Firstly, organize the data and subject it to standardization processing. Subsequently, establish the topological relationships within the basin, construct a hydrological model for simulating flood processes in Chinese mountainous regions, and obtain a set of model parameters applicable to the specific basin. The results indicated that: ① the relative errors of flood runoff depth were all less than 7%, with an average of 4.5%; ② the relative errors of peak flow for all events were less than 6%, with an average of 4.2%; ③ peak time errors were all within ±2 h, either earlier or later than the actual peak by 1 h; ④ the Nash-Sutcliffe efficiency coefficient for floods were all greater than 0.8, with an average of 0.86. The research results above will serve as a reference and guidance for flood defense management in the Daxi Water Basin.

KEYWORDS

flash flood, flood simulation, distributed hydrological model, Daxi Water Basin, flood prevention

1 Introduction

Flash flood disaster caused by sudden floods in streams and rivers in hilly areas, which brings losses to humans and the natural environment and constitute one of the most significant natural disasters in China (Zhao, 1995; Liu et al., 2019; Pei et al., 2023). As global climate warming intensifies, the problem of flash floods caused by sudden and localized heavy rainfall in hilly areas has become increasingly prominent, which has had a serious impact on the natural environment and social development, resulting in casualties, property losses, and facility destruction. and environmental damage and other serious consequences (Liu, 2012; Zhou et al., 2022; Ma et al., 2023). For example, in September 2023, floods in Libya caused nearly 13,000 people to die and go missing (Chen and Wei, 2023). Since 2000, the number of deaths due to flash floods in China has accounted for more than 70% of the number of flood deaths every year (Wei et al., 2022); since 2011, the average number of deaths and missing persons caused by flash floods has exceeded 300 per year (Li and Zhao, 2022). China has numerous mountainous areas, dense river networks, and frequent extreme weather, which poses a great threat to flash flood disasters. Among them, the southwest region, South China, and the middle and lower reaches of the Yangtze River have frequent

flash flood disasters, and are all high-risk areas for flash flood disasters (Zhao, 1996; Zhao and Fan, 2006; Qiu et al., 2022; Wang et al., 2022); For example, in the first three-quarters of 2023, natural disasters across the country caused nearly 500 deaths and missing persons, more than 80% of which were caused by flash floods and geological disasters; a flash flood in Jinyang, Sichuan alone at the end of August caused 52 deaths and missing persons (Dong, 2023). Therefore, research on flash flood prevention is a focus issue that has attracted much attention at home and abroad.

In the hilly regions, small watersheds are susceptible to the influences of terrain and vegetation. These areas are prone to short-duration heavy rainfall, and the small watershed areas between mountains and streams, with steep riverbed slopes, accelerate the formation of runoff in the watershed. Moreover, rapid fluctuations in water levels lead to significant impacts and erosive effects, resulting in substantial damage from floods in these small watersheds. Additionally, the occurrence of extreme weather events contributes to frequent flooding and waterlogging disasters, primarily concentrated between April and October. Due to the relatively underdeveloped socio-economic conditions in the hilly regions and issues such as low monitoring station coverage, the defense against flood disasters poses significant challenges. The core hydrological models for flood defense have long been the focus of extensive attention. Improving their simulation accuracy remains a key research priority. Hydrological models can be broadly categorized into distributed hydrological models and lumped hydrological models (Liang et al., 2007). Lumped hydrological models treat watersheds of various scales as a homogeneous entity, typically neglecting spatial variations in natural geographical elements and hydrological processes within the watershed. Consequently, they struggle to describe the internal hydrological processes of the watershed. On the other hand, distributed hydrological models consider differences in rainfall and underlying surface conditions across the watershed, allowing for a more realistic representation of the actual hydrological processes within the watershed. Therefore, selecting a hydrological model that suits the characteristics of the watershed is crucial for effective flood defense in hilly regions.

Based on the dynamic mechanisms of the water cycle, distributed hydrological models can effectively simulate and forecast watershed hydrological processes (Wang et al., 2012). In 1969, Freeze et al. (Rui, 2017) proposed the framework for distributed hydrological physics models and elucidated their theoretical foundations, marking the initiation of research into distributed hydrological models. Researchers from France, the United Kingdom, and Denmark (Rui et al., 2006) collaborated to enhance the System Hydrological European (SHE) model, which could investigate issues such as water quality, runoff, and sediment production in European watersheds, considering human activities. Subsequently, various countries developed hydrological models tailored to their specific characteristics, opening up new possibilities for flood prediction (Liu et al., 2003).

With the development of modern science and technology, especially the application of "3S" information technology (Geographic Information Systems, Remote Sensing, Global Positioning System), important methods and technological support have been provided for watershed flood forecasting. Various hydrological models have undergone iterative optimization, the applicability to watersheds has gradually strengthened, and the forecasting effectiveness has progressively improved. This has further enhanced the importance of hydrological models in flood prediction. Combining geographic information system (GIS) technology, the Hydrologic Engineering Center (HEC) model (Halwatura and Najim, 2013) constructed by the United States federal government, using ARCVIEW as the operating platform, achieved the extraction of watershed characteristic parameters and the generation of river networks and watershed vector boundaries. Shen et al. (Shen et al., 1995) proposed a GIS-based distributed rainfall-runoff model, which simulated characteristic values of slope runoff, convergence, and river channel evolution. Ren (Ren and Liu, 1999), in conjunction with a watershed digital elevation model, encoded the river network and sub-basins within the watershed and established the topological relationships. Cao et al. (Pan et al., 2021) utilized hydrological information extracted from a digital elevation model to construct a distributed hydrological model for rivers in the northeastern part of the Qinghai-Tibet Plateau. They also proposed the potential application of LiDAR data in hydrological modeling for small, high-altitude, and cold regions. Koohi et al. (Koohi et al., 2022) explored the applicability of the Global Water Resources Reanalysis (GWRR) dataset for calibrating the VIC-3L distributed hydrological model in the Sefidroud Basin, Iran, providing insights into the use of GWRR data sources for hydrological modeling in data-scarce regions.

In recent years, the application of distributed hydrological models in multi-scale watersheds has become a research hotspot in flood forecasting. Dong et al. (Dong, 2008), using the LL-II fully distributed hydrological model and the Shaanbei model, investigated their application in flood forecasting in semi-arid areas, taking the Taoqupo Reservoir in Shaanxi Province as an example. Xu et al. (Xu et al., 2021), utilizing the Liuxihe model, designed a flood forecasting scheme for the Bai Penzhu Reservoir in Guangdong Province and verified that the forecasting results exhibited strong accuracy. Marahatta et al. (Marahatta et al., 2021) used the SWAT model to simulate the hydrological processes in the Budhigandaki River Basin (BRB) in Nepal, validating the applicability of the SWAT model in data-scarce and complex mountainous watershed areas.

In summary, scholars both domestically and internationally have achieved rich results in hydrological modeling. However, most of the models mentioned above are applicable to large scales and require high-quality measured data for watershed conditions. In China, there are still challenges in small to medium-sized watershed flood forecasting, including weak non-linear adaptability of models, lack of measured data, and human activities interference. The China Institute of Water Resources and Hydropower Research has independently developed the Chinese Flash Flood Hydrological Model. This model integrates a set of nationwide small watershed basic datasets through investigating and analyzing the natural geographical features and hydrological conditions of the watershed. The model has a limited number of parameters, making it suitable for application in small to medium-sized watersheds. Currently, the model has participated in over ten thousand flood simulation tests in different types of terrain across the country, with over 93% of the simulated flood results meeting forecasting requirements (Zhai et al., 2020). The Daxi Water Basin

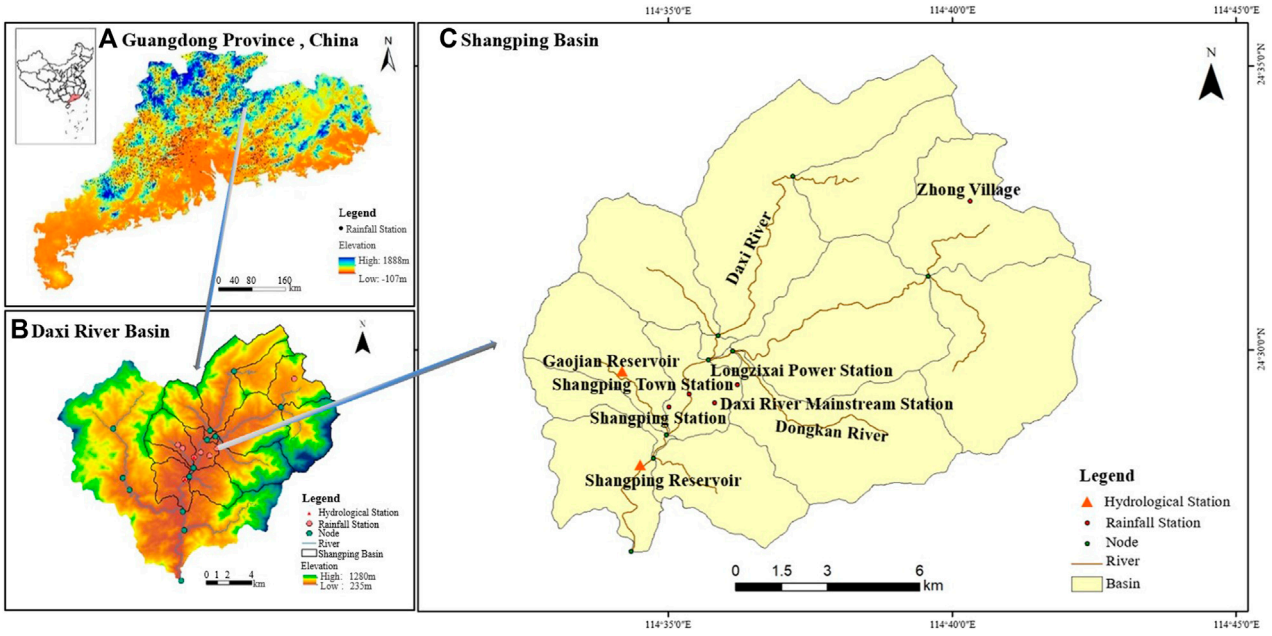

FIGURE 1
Locations of Guangdong Province **(A)**, Daxi Water Basin **(B)**, and Shangping Watershed **(C)**.

in this study is prone to flash floods, and there is currently limited research on flood simulation in this area, with a lack of experience. By introducing the Chinese Flash Flood Hydrological Model, a set of characteristic parameters suitable for this basin was calibrated and validated. Combined with multiple evaluation indicators, the simulation accuracy is analyzed. This research aims to provide reference and guidance for mountainous flood defense and control in the studied watershed.

2 Research area and information

2.1 Research area

The river network system and rainfall-flood monitoring stations in the Daxi Water Basin are concentrated in the eastern Shangping watershed. Therefore, this paper designated the Shangping watershed as the primary study area (Figure 1). The basin is situated in the northeastern part of Lianping County, Guangdong Province. The total area of the basin is 175.95 km^2, with the outlet of the basin located at approximately 114.57°E and 24.44°N. The basin spans from the northeast to the southwest, traversing Lianping County, with the terrain rising in the north and lowering in the south. The northern-central part features undulating mountain ranges, belonging to a segment of the Jiulian Mountain Range in Guangdong Province. The valleys between the mountains are deeply cut by flowing water, developing into narrow and deep "V"-shaped valleys. The main valleys, shaped by river erosion and crustal uplift, give rise to relatively smaller "V"-shaped valleys on their side slopes—hanging valleys. The southwestern part is characterized by low hills, fertile soil, and abundant water resources. The research area experiences a subtropical monsoon climate, characterized by simultaneous high temperatures and rainfall during the rainy season. Summers are hot and rainy, while winters are mild and dry. Rainfall gradually increases from March, with the peak concentrated in May and June. Summer is susceptible to heavy rainfall due to convective thunderstorms and typhoon influences, leading to the occurrence of flash floods. The Daxi Water Basin is one of the six main rivers in Lianping County, with a total of 15 major and minor tributaries. The river originates from the Jiaofeng Ridge (elevation 732.9 m) in Zhongcun, Upper Ping Town, and eventually flows into Xinfeng County. The river has a total length of 75 km, a natural drop of 1,070 m, an average slope of 0.0398, and an average annual runoff of 15.95 m^3/s.

2.2 Data introduction

This study primarily involves two categories of data for the research area: watershed geographic spatial data and rainfall-flood data. The geographic spatial data include a digital elevation model (DEM) of the watershed, as well as spatial distribution maps for the watershed, river channels, nodes, and monitoring stations. The rainfall-flood data consist of observed rainfall data from various rainfall stations and water level-flow data from the outlet hydrological station in the Daxi Water Basin, spanning from March to July 2019. Specific details are provided in Table 1.

2.3 Research methods

(1) Chinese Flash Flood Hydrological Model

The Chinese Flash Flood Hydrological Model is built on the basis of natural small watershed attributes, employing modular and hierarchical architectural concepts. It takes the cluster of watershed

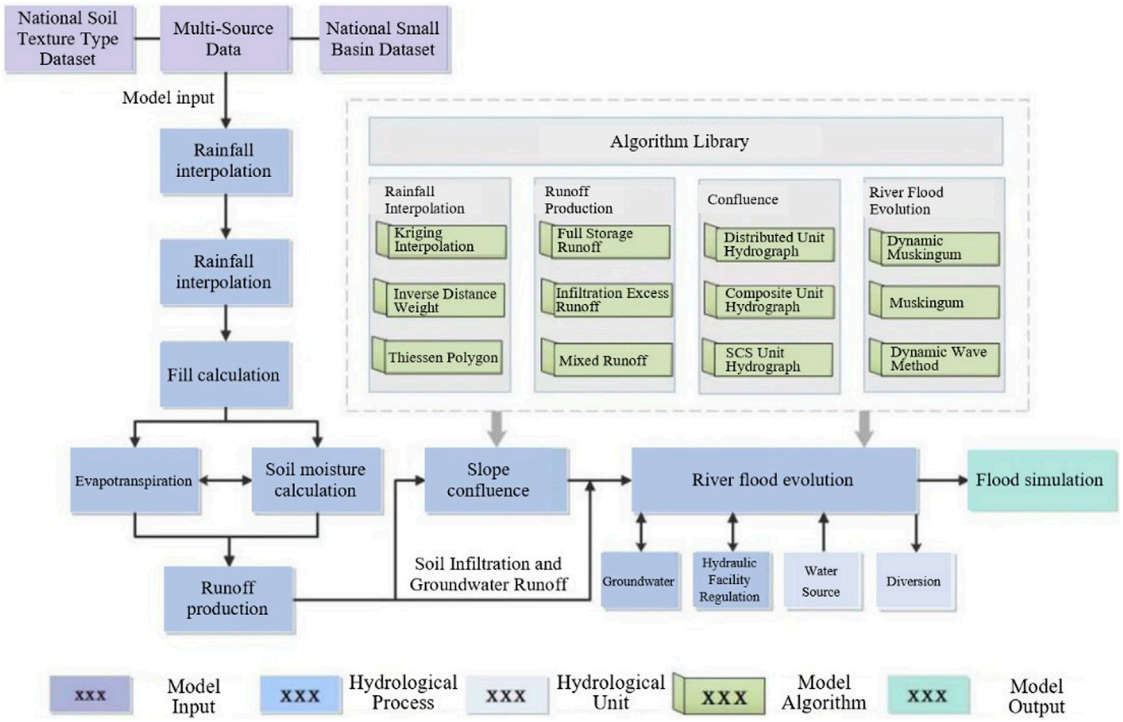

FIGURE 2
China flash flood hydrological model structure diagram.

hydrological relationships, high-precision terrain and topographic data as units, accommodating the characteristics of runoff generation and convergence in different climatic regions. The model establishes a library of multi-process water cycle models, primarily focused on the development of defense against flash floods in small watersheds. It addresses the challenges of nonlinear runoff simulation and computationally efficient modeling under short-duration, intense rainfall conditions. In a certain sense, the Chinese Flash Flood Hydrological Model is a generalized distributed watershed hydrological model. Its hydrological units mainly include watershed, river section, node, water source, watershed divide, reservoir, and depression. The hydrological processes encompass rainfall, runoff generation, hillslope runoff convergence, and flood routing, with runoff generation involving factors such as vegetation interception, evapotranspiration, and soil moisture. The model structure is shown in Figure 2.

The Shangping Watershed comprises 14 sub-watersheds, with sizes ranging from 0.4 km^2 to 29.03 km^2. Within the watershed, there are five rainfall observation stations and two hydrological observation stations. Taking into account the characteristic of the watershed's terrain being higher in the north and lower in the south, the downstream Shangping hydrological station was designated as the outlet node, and the watershed's topological structure was established. Given that the Shangping Watershed is located in a humid region, the runoff module primarily employed the Xin'anjiang three-source storage runoff method. The convergence module utilized distributed unit hydrographs extracted and processed from the "National Mountain Flood Disaster Prevention Project" (1), which effectively reflects the phase-based impact of underlying surface and rainfall intensity on flow velocity in various river sections. The river channel evolution module employed the dynamic Muskingum method (2) suitable for small watersheds with limited data availability.

$$\begin{cases} V = K_s S^{0.5} i^{0.1} \\ T_j = \sum_{m=1}^{M_j} \dfrac{cL_m}{V_m} \end{cases} \tag{1}$$

In the equation: V represents the flood flow velocity, measured in meters per second (m/s); Ks is the coefficient used to calculate water flow velocity, measured in meters per second (m/s); S is the specific drop of the river bed in any grid in the basin; i is the dimensionless rain intensity; T_j is the time required for runoff convergence in the j-th grid of the watershed; M_j is the number of grids passed through by runoff convergence in the j-th grid of the watershed; V_m is the flow velocity in the mth grid of the watershed, measured in meters per second (m/s); $L\ m$ is the length of the river channel passed through by the flood when it traverses the m-th grid; c is the coefficient, taking a value of 1 or $\sqrt{2}$.

$$\begin{cases} K = a \cdot L \cdot N^{0.6} \cdot J^{-0.3} \cdot Q_0^{-0.2} \\ V_w = b \cdot N^{-0.6} \cdot J^{0.3} \cdot Q_0^{0.2} \\ x = 0.5 - 0.11 \dfrac{\sqrt{Q_0}}{J \cdot V_w \cdot L} \end{cases} \tag{2}$$

In the equation: K represents the slope of the reservoir storage curve, in terms of elevation (h); Q_0 is the reference flow rate, measured in cubic meters per second (m^3/s), calculated as $Q0 = Q_b + 0.5(Q_p - Q_b)$, where Q_b is the maximum upstream flood flow rate, and Q_p is the maximum upstream flood flow rate, both measured in cubic meters per

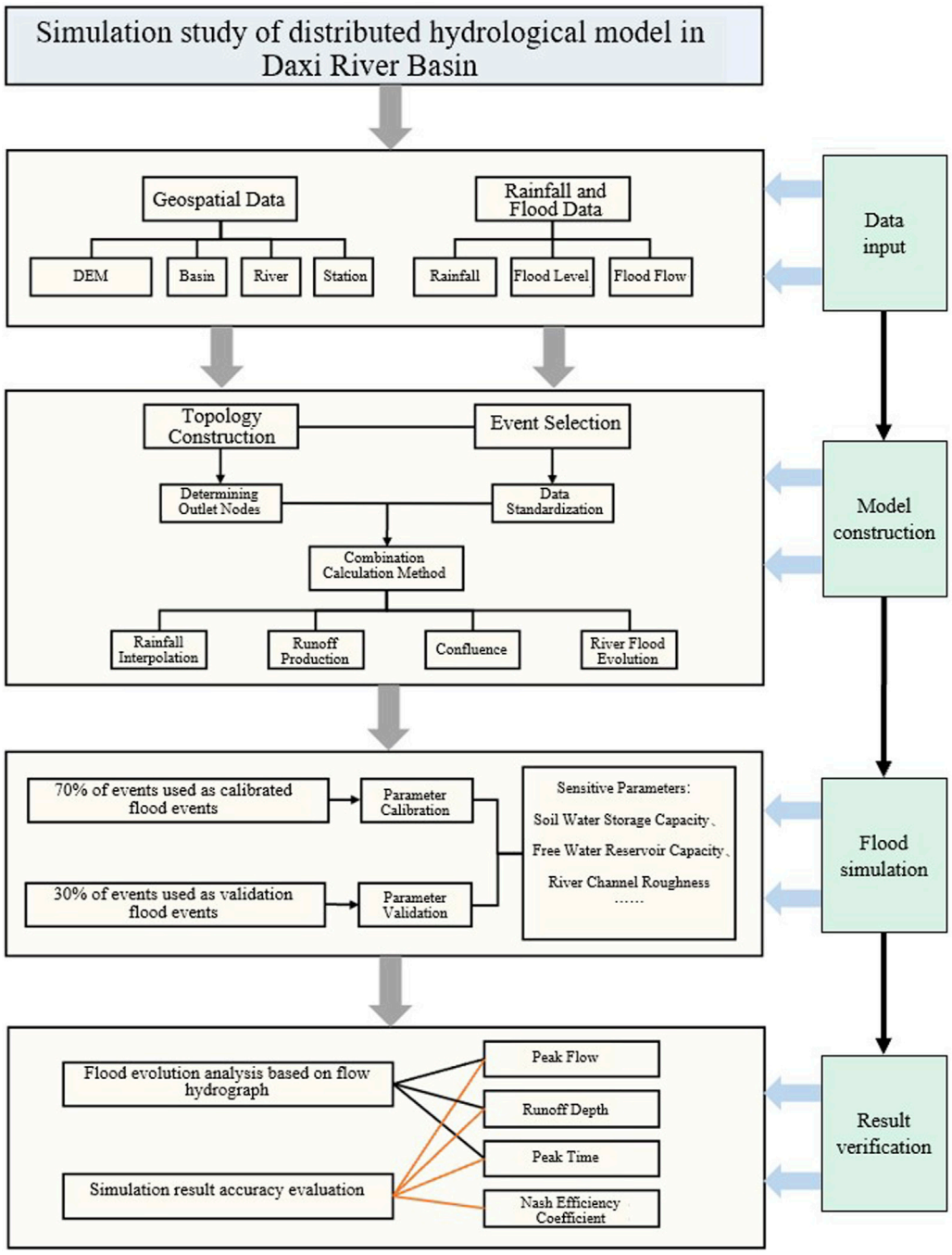

FIGURE 3
Research approach.

second (m^3/s); V_m is the wave velocity, measured in meters per second (m/s); x is the flow ratio coefficient; J is the channel slope; L is the length of the channel, measured in meters (m); N is the Manning's coefficient. Parameters a and b are determined based on the cross-sectional shape.

(2) Simulation Accuracy Evaluation Index

The article employed three indicators, namely, relative error of runoff depth, relative error of peak flow, and peak timing difference, combined with the Nash-Sutcliffe efficiency coefficient to evaluate the accuracy of flood simulations. According to the ⟪Hydrological Information Forecasting Specification⟫, a flood simulation result is considered qualified only if it simultaneously satisfies all error index requirements. The maximum allowable relative errors for runoff depth and peak flow are both 20%, and the permissible error for peak timing difference is ±2 h. The Nash-Sutcliffe efficiency coefficient, approaching 1, indicates better correlation, with the optimal value being 1. If NSE is less than 0, it indicates that the simulation accuracy is worse than the measured average. The formulas for calculating each indicator are shown in Table 2.

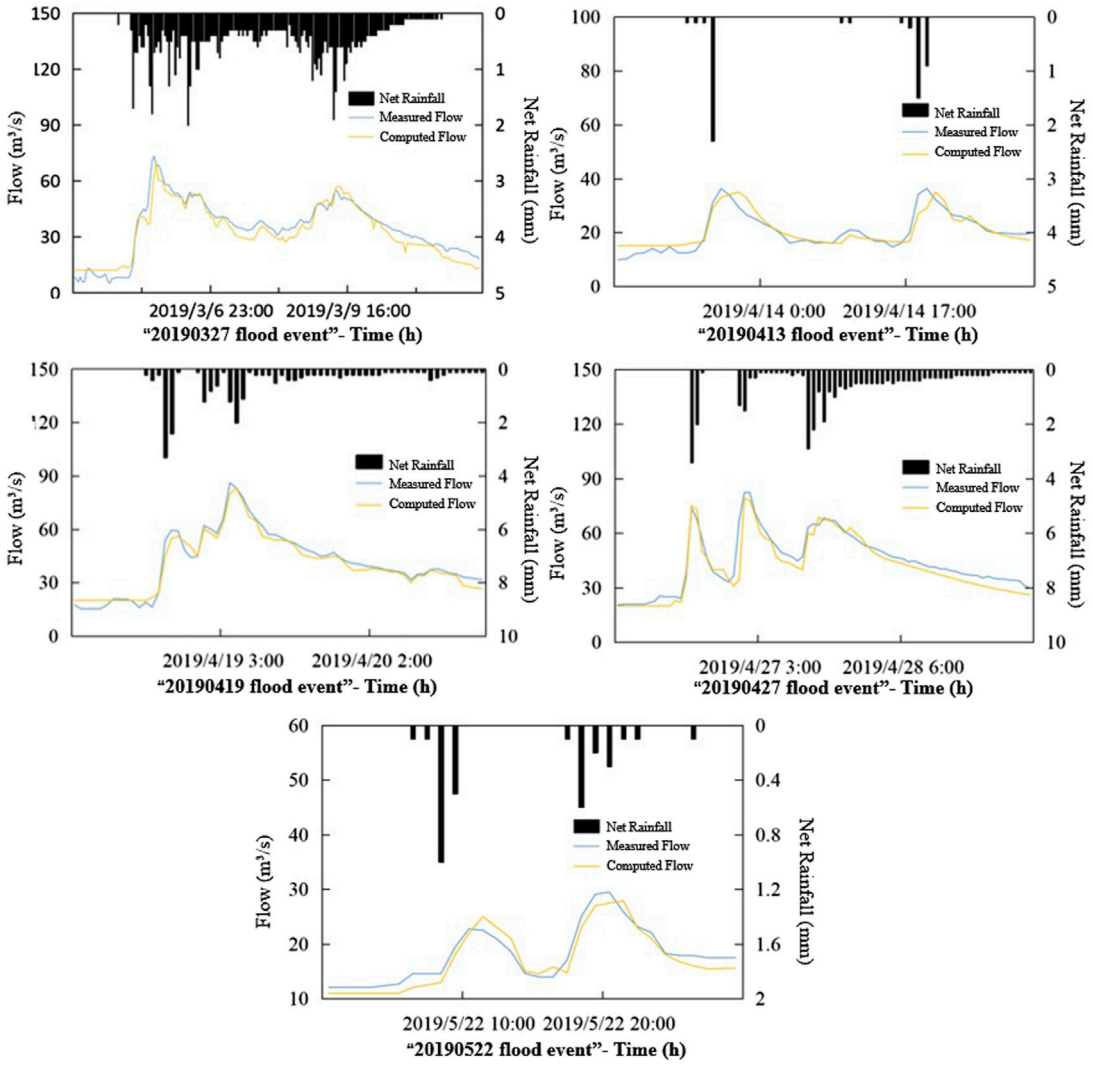

FIGURE 4
Flood simulation results.

In the equation: $\overline{Rs}$, $Q_{s,p}$, $T_{s,p}$ are the simulated average runoff depth (mm), the simulated peak flow (m^3/s), and the simulated peak current (h) respectively; $Q_{s,i}$ is the simulated flow rate at the time i, m^3/s; $\overline{R}_0$, $Q_{0,p}$, $T0,p$ are the measured average runoff depth (mm), the measured peak flow rate (m^3/s), and the actual peak time (h) respectively; $Q_{o,i}$ is the measured flow rate at time i, $\overline{Q}_{0,i}$ is the average measured flow rate, m^3/s.

2.4 Research approach

In this study, the first step involved standardizing data. Subsequently, based on ArcGIS, a digital elevation model of the small watershed was extracted, and the watershed's topological relationships were established by integrating with the Chinese Flash Flood Hydrological Model system. The model was then constructed using data on watershed soil types, soil textures, and the national dataset of small watersheds. Parameters of the model were calibrated and validated. This entailed analyzing the significance of model parameters and the natural geographic features within the watershed, determining the events for calibration and validation of floods, obtaining specific parameter values, and analyzing their feasibility. Subsequently, a set of model parameters suitable for the study area was simulated. Finally, the accuracy of flood simulations was evaluated using relative error and the Nash-Sutcliffe efficiency coefficient. This evaluation was then used to explore the applicability of the Chinese mountain flood hydrological model in the Da Xi River Basin. The specific research approach is illustrated in Figure 3.

3 Results and discussion

3.1 Analysis of flood simulation process

By analyzing rainfall-flood data in the Shangping Watershed, representative flood events are selected. Approximately 70% of these events were defined for model calibration, while the remaining 30%

TABLE 1 Daxi Water Basin information.

Type	Name	Identification	Source	Remark
Geography Space Data	Digital Elevation Model	DEM	Geographical Space Data Cloud	30 m resolution (raster data)
	Basin	WATA	China Water Resources and Hydropower Research Institute	14 sub-watersheds (vector data)
	River	RIVL		22 items (vector data)
	Node	NODE		13 (vector data)
	Station	ZD		11 (vector data)
Rain flood data	Rainfall Value	P	Hydrology of Guangdong Province	INTV=1 h
	Flood Flow	Q	Hydrology of Guangdong Province	INTV=1 h

TABLE 2 Calculation formula of evaluation indicators.

Evaluation index	Calculation formula
Runoff Depth Relative Error	$R_eR = \frac{\lvert \bar{R}_s - \bar{R}_0 \rvert}{\bar{R}_0}$
Relative Error of Peak Flow	$R_eQ = \frac{\lvert Q_{s,p} - Q_{0,p} \rvert}{Q_{0,p}}$
Peak Time Difference	$TP = \lvert T_{s,p} - T_{0,p} \rvert$
Nash-Sutcliffe Efficiency Coefficient	$NSE = 1 - \frac{\sum_{i=1}^{N} (Q_{s,i} - Q_{0,i})^2}{\sum_{i=1}^{N} (Q_{0,i} - \bar{Q}_0)^2}$

were reserved for model validation. Considering the natural geographical features and hydrological conditions of the Shangping watershed, the main model parameters, including upper soil water storage capacity, lower soil water storage capacity, deep soil water storage capacity, and free water storage capacity, were set to 15 mm, 70 mm, 40 mm, and 22 mm, respectively. Figure 4 illustrates the simulation results of the flood events.

The flood event "20190305″ exhibits a double-peak pattern, with an initial flow smaller than other events. The first peak flow occurred at 22:00 on March 5th, reaching 70 m^3/s, differing from the actual peak flow by 3.2 m^3/s. The rise in flow during the second phase was slower, and the relationship between post-peak flow and time became more linear. The period with significantly higher flow concentrations for the entire flood event occurred from 13:00 on March 5th to 08:00 on March 10th, with good fitting between simulated and actual flow processes during this period.

The flood event "20190413″ is a typical double-peak flood. The simulated peak flows occurred at 22:00 on April 13th and 21:00 on April 14th, reaching 35 m^3/s each. The measured peak flows occurred at 21:00 on April 13th and 20:00 on April 14th, both at 36.3 m^3/s. Additionally, the intervals between the simulated and measured peak flows were both 23 h. However, the river channel base flow was relatively high during this flood, and the rainfall continuity was not strong, resulting in a relatively gentle fluctuation of the entire flood.

The flood event "20190419″ is a multi-peak flood. Intense rainfall from 19:00 on April 18th to 10:00 on April 19th caused frequent changes in rainfall intensity, leading to significant fluctuations in flood flow along with the rainfall trend. Three peak flow values occurred during this period: 56 m^3/s at 21:00 on April 18th, 60 m^3/s at 01:00 on April 19th, and the highest flow value of 83 m^3/s at 06:00 on April 19th. After the third peak, rainfall rapidly decreased, followed by a stabilizing trend, and the river flow slowly decreased.

The flood event "20190427″ had a slightly higher base flow than other events. The flood initiated rapidly, with the first peak occurring in the second hour (15:00 on April 26th), reaching 75 m^3/s. However, the short duration of rainfall led to a sudden drop in flood flow. A second round of rainfall occurred at 00:00 on April 27th, resulting in the second peak flow of this event at 79 m^3/s. The third intense rainfall occurred at 13:00 on April 27th, and although the third peak flow was slightly lower than the previous two, the high flow period lasted for 7 h.

The flood event "20190522″ had a shorter duration compared to others, lasting for 1 day. It is a double-peak flood, with the first peak occurring at 12:00 on May 22nd, reaching 25 m^3/s. After 10 h, a second peak flow occurred at 22:00 on the same day, reaching 27.9 m^3/s. Due to the discontinuous nature of rainfall, the fitting degree between the simulated and actual flood processes for this event was smaller than for other events.

Overall, the routing of the five flood events show strong consistency with the changes in rainfall during the study period. Additionally, all five flood events exhibited significant flow fluctuations before the main peak, and the decrease in flow during the declining phase after reaching the maximum value was slow. Comparing the five flood events, the simulated flow results of the three flood events with more continuous rainfall, namely, "20190305," "20190419," and "20190427," were closer to the measured flow values, indicating better overall simulation performance.

3.2 Model error analysis

From the statistical results of flood simulation errors (refer to Table 3), it can be observed that all five simulated flood events are qualified: The relative errors in flood runoff depth for all five events were below the maximum permissible error of 10%; the maximum error was 6.1% for the "20190522″ event, while the minimum was 2.4% for the "20190305″ event, with an average of 4.5%. Relative errors in peak flow were below the maximum permissible error of 20% for all five events, accounting for 100%; the maximum error is

TABLE 3 Simulation error analysis.

Type	Event	Base flow (m^3/s)	Measured runoff depth (mm)	Relative Error of runoff depth (%)	Relative Error of flood Peak (%)	Peak appearance Error (h)	Coefficient of certainty
Calibrate Events	2019 0305	12	136.7	2.4	4.3	1	0.86
	2019 0413	15	20	4.4	3.6	1	0.85
	2019 0419	20	53.7	3.9	3.6	1	0.91
Verify Evens	2019 0427	20	71.4	5.6	4	−1	0.88
	2019 0522	11	10.7	6.1	5.4	1	0.81
Average	–	–	–	4.5	4.2	–	0.86

5.4%, the minimum is 3.6%, and the average is 4.2%. Four events simulated peak times occurring 1 h later than the observed peaks, while for the "20190427″ event, the simulated peak occurred 1 h earlier than the observed peak; the simulated results were within the maximum permissible error of ±2 h. Nash-Sutcliffe efficiency coefficients for all five events were above 0.8; the maximum was 0.91 for the "20190419″ event, the minimum was 0.81 for the "20190522″ flood, and the average was 0.86, indicating a good correlation between the simulated and actual flood processes.

Comparing the analysis of the five flood events, for the "20190522″ event, although all error values were within permissible ranges, the errors were relatively large, and the fitting degree between the simulated and actual flow processes was not high. In contrast, for the "20190419″ flood event, both relative errors in runoff depth and peak flow were the lowest, and the Nash-Sutcliffe efficiency coefficient was closest to 1, making it the event with the best simulation performance. The China Flash Flood Model can accurately simulate the flood processes in the Shangping River basin, and the results are reliable.

4 Discussion

This study, based on the China Flash Flood Model, conducted flood simulations in small watersheds within susceptible mountainous flood areas and evaluated the model's applicability. The main conclusions are as follows: ①small watershed river flood processes exhibit strong spatial heterogeneity, in which distributed unit hydrograph can effectively reflect the impact of different rainfall intensities and underlying surface conditions on flood velocity in various river segments; ②there is a strong consistency between flood flow and rainfall intensity variations, but both lag behind the changes in rainfall; ③the relative errors in simulated runoff depth were all below 7%, peak flow relative errors were below 6%, peak timing differences were within 1 h, and Nash-Sutcliffe efficiency coefficients were all above 0.8, showing simulation results were good, and the accuracy was higher for flood events with continuous rainfall. This research provides reference for flood forecasting and control in the studied region. However, the study also faced numerous challenges, including a limited number of flash flood events and the need for a more in-depth analysis of the mechanisms responsible for heavy rainfall. These issues may affect the operational application of the model and hinder a more comprehensive exploration of flood characteristics. In the future, the researchers plan to incorporate machine learning techniques to reveal the flash flood mechanisms, enhance the model's informatization and intelligence, and provide theoretical and empirical foundations for flash flood simulations in data-scarce regions in China.

Data availability statement

The raw data supporting the conclusion of this article will be made available by the authors, without undue reservation.

Author contributions

DW: Writing–original draft. YZ: Writing–original draft. XZ: Writing–original draft. YL: Writing–original draft. QT: Writing–original draft. MM: Writing–original draft.

Funding

The author(s) declare financial support was received for the research, authorship, and/or publication of this article. This study was supported by National Natural Science Foundation of China (grant number 42101086, 42271095, 42371086), and Study on flash flood risk assessment method based on ensemble learning (grant number IWHR-SKL-KF202310).

Conflict of interest

The authors declare that the research was conducted in the absence of any commercial or financial relationships that could be construed as a potential conflict of interest.

Publisher's note

References

Chen, Z. F., and Wei, Y. (2023). Floods in Libya lead to thousands of deaths-how did all of this happen. *Pengpai News* 2023. Available at: https://www.thepaper.cn/newsDetail_forward_24565310.

Dong, H. (2008). Application of distributed hydrological model to flood prediction in semi-arid areas. *Guangdong Water Resour. Hydropower* (1), 4. doi:10.3969/j.issn.1008-0112.2008.01.007

Dong, X. M. (2023). The Ministry of Emergency Management released the national natural disaster situation in the first three quarters of 2023. *Yangtze River cloud press*, 2023–2110. Available at: https://m.hbtv.com.cn/p/2903053.html.

Halwatura, D., and Najim, M. M. M. (2013). Application of the hec-hms model for runoff simulation in a tropical catchment. *Elsevier Sci. Publ. B. V.* dol: 46, 155, 162. doi:10.1016/j.envsoft.2013.03.006

Koohi, S., Azizian, A., and Brocca, L. (2022). Calibration of a distributed hydrological model (vic-3l) based on global water resources reanalysis datasets. *Water Resour. Manag.* 36 (4), 1287–1306. doi:10.1007/s11269-022-03081-9

Li, Y., and Zhao, S. S. (2022). Floods losses and hazards in China from 2001 to 2020. *Clim. Change Res.* 18(2): 154–165. doi:10.12006/j.issn.1673-1719.2021.196

Liang, Z. Y., Jia, Y. W., Li, K. J., Niu, C. W., and Wang, H. (2007). A review on the application of distributed hydrological model in flood prediction. *Huanghe River* 29 (2), 4. doi:10.3969/j.issn.1000-1379

Liu, C. M., Li, D. F., Tian, Y., Hao, F. H., and Yang, G. L. (2003). Application of distributed hydrological model based on dem in large scale watershed. *Prog. Geogr. Sci.* 22 (5), 437–445. doi:10.11820/DLKXJZ2003.05.001

Liu, Y. S., Yang, Z. S., Huang, Y. H., and Liu, C. J. (2019). Spatial and temporal evolution pattern and driving factors of mountain flood disasters in China since the founding of the People's Republic of China. *Sci. China Earth Sci.* (02), 408–420. doi:10.1360/N072017-00328

Liu, Z. Y. (2012). Research and application of flash flood warning and forecasting technology. *Flood Control Drought Relief China* 22 (2), 6.

Ma, S., Qiu, H., Zhu, Y., Yang, D., Tang, B., Wang, D., et al. (2023). Topographic changes, surface deformation and movement process before, during and after a rotational landslide. *Remote Sens.* 15 (3), 662. doi:10.3390/rs15030662

Marahatta, S., Devkota, L. P., and Aryal, D. (2021). Application of swat in hydrological simulation of complex mountainous river basin (part i: model development). *Water* 13 (11), 1546. doi:10.3390/w13111546

Pan, Z., Wang, X., Cao, H., Zhou, A., and Sun, Z. (2021). Stream network modeling using Remote sensing data in an alpine cold catchment. *Water* 13 (11), 1585. doi:10.3390/w13111585

Pei, Y., Qiu, H., Yang, D., Liu, Z., Ma, S., Li, J., et al. (2023). Increasing landslide activity in the Taxkorgan River Basin (eastern Pamirs Plateau, China) driven by climate change. *Catena* 223, 106911. doi:10.1016/j.catena.2023.106911

Qiu, H., Zhu, Y., Zhou, W., Sun, H., He, J., and Liu, Z. (2022). Influence of DEM resolution on landslide simulation performance based on the Scoops3D model. *Geomat. Nat. Hazards Risk* 13 (1), 1663–1681. doi:10.1080/19475705.2022.2097451

Ren, L. L., and Liu, X. R. (1999). Application of digital elevation model in river basin topology calculation. *Adv. Water Sci.* 10 (2), 6. doi:10.3321/j.issn:1001-6791

Rui, X. F. (2017). On watershed hydrological model. *Adv. Water Resour. hydropower Sci. Technol.* 37 (4), 8. doi:10.3880/j.issn.1006-7647

Rui, X. F., Jiang, C. Y., and Zhang, J. C. (2006). Development of watershed hydrological models. *Chin. J. Hydrology* 26 (3), 5. CNKI: SUN: SWZZ.0.

Shen, X. D., Wang, L. C., and Xie, S. P. (1995). Raster data based rainfall and runoff model in watershed. *Acta Geogr. Sin.* 62 (3). doi:10.11821/xb199503009

Wang, L., Qiu, H., Zhou, W., Zhu, Y., Liu, Z., Ma, S., et al. (2022). The post-failure spatiotemporal deformation of certain translational landslides may follow the pre-failure pattern. *Remote Sens.* 14 (10), 2333. doi:10.3390/rs14102333

Wang, Y., Zhang, B., and Harald, Z. (2012). The European distributed wasim-eth model was applied to simulate the hydrological process of a subtropical agricultural small watershed in southern China. *Acta Pedol. Sin.* 49 (5), 11. CNKI: SUN: TRXB.0.2012-05-004.

Wei, Y. Q., Sheng, D., Dong, L. Y., and Tan, J. Q. (2022). Research status and development trend of mountain flood disaster prevention and control. *China's flood control drought relief* (07), 30–35. doi:10.16867/j.iSSN.1673-9264

Xu, S., Chen, Y., Xing, L., and Li, C. (2021). Baipenzhu reservoir inflow flood forecasting based on a distributed hydrological model. *Water* 13 (3), 272. doi:10.3390/w13030272

Zhai, X. Y., Guo, L., Liu, R. H., Zhang, Y. Y., and Liu, C. J. (2020). Development and application of mountain flood hydrological model in China: a case study of small and medium-sized river basins in Anhui Province. *Chin. J. Basic Appl. Eng. Sci.* 28 (5), 19. doi:10.16058/j.issn.1005-0930.2020.05.002

Zhao, J., and Fan, B. L. (2006). Spatial and temporal distribution characteristics of mountain flood disaster in China. *China Water Resour.* 13, 3. doi:10.3969/j.issn.1000-1123

Zhao, S. P. (1995). Study on system integration method of mountain flood disaster assessment. *Geogr. Res.* 14 (3), 111. doi:10.11821/yj1995030020

Zhao, S. P. (1996). A preliminary study on the overall characteristics of mountain flood disaster system and its risk zoning in China. *J. Nat. Disasters* 5 (3), 7. CNKI: SUN: ZRZH.0.1996-03-014.

Zhou, W., Qiu, H., Wang, L., Pei, Y., Tang, B., Ma, S., et al. (2022). Combining rainfall-induced shallow landslides and subsequent debris flows for hazard chain prediction. *Catena* 213, 106199. doi:10.1016/j.catena.2022.106199

frontiers | Frontiers in Earth Science

TYPE Original Research
PUBLISHED 16 January 2024
DOI 10.3389/feart.2023.1358987

OPEN ACCESS

EDITED BY
Haijun Qiu,
Northwest University, China

REVIEWED BY
Haiming Yan,
Hebei GEO University, China
Ruxin Zhao,
Ministry of Emergency Management, China

*CORRESPONDENCE
Meihong Ma,
201531470011@mail.bnu.edu.cn

RECEIVED 20 December 2023
ACCEPTED 28 December 2023
PUBLISHED 16 January 2024

CITATION
Li Q, Liu Y, Luo L, Wang Y, Wang Q and Ma M (2024), Spatiotemporal drought characteristics during growing seasons of the winter wheat and summer maize in the North China Plain. *Front. Earth Sci.* 11:1358987. doi: 10.3389/feart.2023.1358987

Spatiotemporal drought characteristics during growing seasons of the winter wheat and summer maize in the North China Plain

Qing Li[1], Yun Liu[1], Lanyang Luo[2], Yu Wang[1], Qian Wang[2] and Meihong Ma[2]*

[1]Research Center on Flood and Drought Disaster Reduction, China Institute of Water Resources and Hydropower Research, Beijing, China, [2]Geographical and Environmental Science Department, Tianjin Normal University, Tianjin, China

The North China plain (NCP) is an important production base for winter wheat and summer maize in China. Severe droughts seriously restrict agricultural production in this region, threatening food security. Based on the standardized precipitation evapotranspiration index (SPEI), this study explored the spatial and temporal drought characteristics during the winter wheat and summer maize growing seasons in the region. The study found that: 1) From 1980 to 2013, the drought trend of the winter wheat growing season in the NCP has intensified, with Huang-Huai Plain agricultural area (HH_P) showing the most significant drought trend. However, the summer maize growing season has become wetter, with the Shandong hilly agricultural and forestry area (SD_Q) showing the most significant wetting trend. 2) After the year 2003, the results from Mann-Kendall trend analysis revealed that the drought trend of HH_P during the winter wheat growing season became particularly pronounced, but the wetting trend of SD_Q and HH_P during the summer maize growing season became more evident. 3) The dominant spatial patterns observed in the NCP during the growing seasons of winter wheat and summer maize were marked by a consistent distribution of drought and wetness conditions. For winter wheat, the southern regions of the foothill plain area of Yanshan and Taihang Mountains (YT_P) and the low-lying plain area of Hebei, Shandong, and Henan (JLY_P) were more sensitive to the changes of drought and wet conditions. For summer maize, SD_Q was more sensitive to the changes of the drought and wet conditions. The results of this study could provide references for the formulation of drought relief strategies of winter wheat and summer maize in the NCP.

KEYWORDS

drought, winter wheat, summer maize, the North China Plain, spatial and temporal distribution characteristics

1 Introduction

The North China Plain (NCP) is a key area for grain production in China. Approximately 50% of the country's total winter wheat planting area and yield come from this region (Liu et al., 2006), while the maize planting area in the region accounts for 30% in China, with a yield comprising around 50% of China (Sun et al., 2009). Drought

poses a significant threat to the food security of the area, being the primary meteorological disaster affecting agricultural production. With the backdrop of global climate change, the NCP has experienced a substantial rise in average temperature over the past 50 years, leading to intensified drought (Zhang et al., 2015). Furthermore, drought in this region shows clear cyclic variations and regional differences (Hu, 2014; Li et al., 2023). Studies have shown that droughts, heat waves, and floods can have compound effects (Carvalho and Spataru, 2023). Under extreme climate change, sudden changes between droughts and floods can have lasting and profound effects on soil fertility by altering comprehensive conditions such as water, soil, and temperature, exacerbating threats to food security (Bai et al., 2023). Underground coal mining can cause continuous and long-term surface deformation, triggering landslides, and may also pose a threat to grain-producing areas (Ma et al., 2022).

Fan assessed the impact of El Niño and La Niña phenomena on meteorological drought in the Weihe River Basin in China from 1970 to 2020. They found that on a scale of 3–6 months, attention should be paid to the drought disasters in the summer of the following year caused by La Niña, but the impact of El Niño on the 12-month scale of drought in China cannot be ignored (Fan et al., 2023). Drought is typically classified into meteorological drought, hydrological drought, agricultural drought and socio-economic drought (Jiang et al., 2019). Simultaneous occurrences of multiple droughts can significantly impact the economic development, particularly causing substantial losses in food production. Research on drought in the context of winter wheat and summer corn primarily includes the evolution of drought, drought prediction, spatiotemporal analysis of drought changes, and the drought influences on agricultural production. Some studies have also explored the drought spatiotemporal changes of winter wheat and summer maize from the perspective of solar radiation values (Zheng et al., 2022).

Based on different data sources, the drought indices can be divided into remote sensing-based indices such as Temperature Condition Index (TCI), Vegetation Condition Index (VCI), and Vegetation Health Index (VHI), and meteorological data-based indices such as Standardized Precipitation Index (SPI), Palmer Drought Severity Index (PDSI) and Standardized Precipitation Evapotranspiration Index (SPEI) (Vicente-Serrano and Sergio, 2013). The PDSI is primarily utilized to calculate short-term drought conditions, estimating soil moisture supply and demand through a two-layer model based on precipitation and temperature. It can provide a comprehensive indicator of the overall water condition. However, the PDSI index is mainly used for calculating short-term drought conditions and has a relatively singular time scale (Vicente-Serrano and Sergio, 2013). SPI can monitor drought at different time scales (Pasho et al., 2011). SPI has been widely used in drought monitoring studies due to its simplicity in calculating and ability to measure drought at different time scales. However, its application has limitations in the context of climate change, as it only considers precipitation conditions. The accumulated precipitation, one of the indicators of drought, is not only related to rainfall but also connected to temperature changes (Zhou et al., 2022). In areas lacking rainfall data, it can be used to predict drought, landslides, and debris flow disasters (Zhou et al., 2022). With the development of remote sensing technology, more and more technologies such as unmanned aerial vehicle detection and Synthetic Aperture Radar Interferometry (InSAR) are being applied in the acquisition of drought indices and land instability analysis (Yang et al., 2021; Liu et al., 2022; Wang et al., 2022).

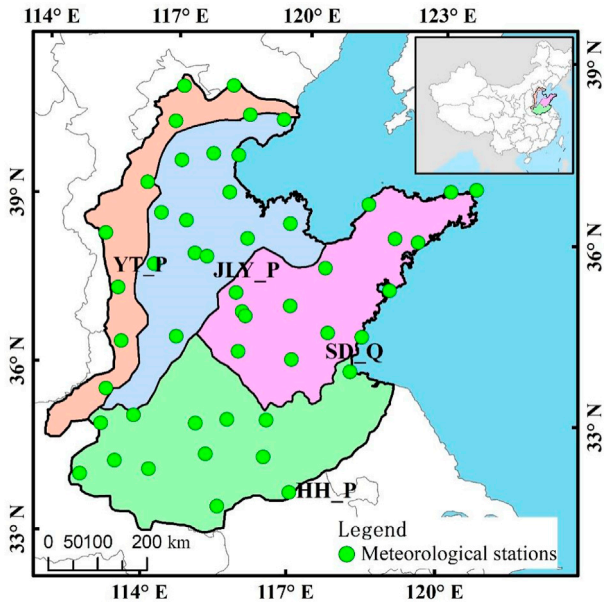

FIGURE 1
Spatial distribution of meteorological stations in the study area.

SPEI combines the advantages of SPI and PDSI, considering the impacts of precipitation and temperature on drought (Vicente-Serrano et al., 2010). It has been widely used in the research for monitoring and assessing the impact of drought (Guo et al., 2017; Cao et al., 2021; Tirivarombo et al., 2018; Wu and Chen, 2019; Yang et al., 2020). The Penman-Monteith (PM) method was used to calculate the national potential evapotranspiration in China from 1961 to 2019. Furthermore, by utilizing the SPEI as a monthly drought indicator, it was determined that there has been an exacerbation of drought in the North China region due to abnormal temperature and wind speed (Wen and Chen, 2023). Therefore, in this study, SPEI was chosen as the drought monitoring index in the NCP. Meteorological data from 50 weather stations in the NCP was selected. And the SPEI could represent the drought conditions during the winter wheat and summer maize growing season were calculated. The study utilized methods such as linear trend analysis, Mann-Kendall trend analysis and Empirical Orthogonal Function (EOF) decomposition to investigate the spatiotemporal characteristics of drought during the winter wheat and summer maize growing seasons in the NCP over the past 33 years. The aim of this study is to provide references for the formulation of drought relief strategies of winter wheat and summer maize in the NCP.

2 Study area and materials

2.1 Study area and data

The North China Plain (NCP) (32°N ~ 40°N, 114°E ~ 121°E) is located in the northern part of China, including all or part of seven

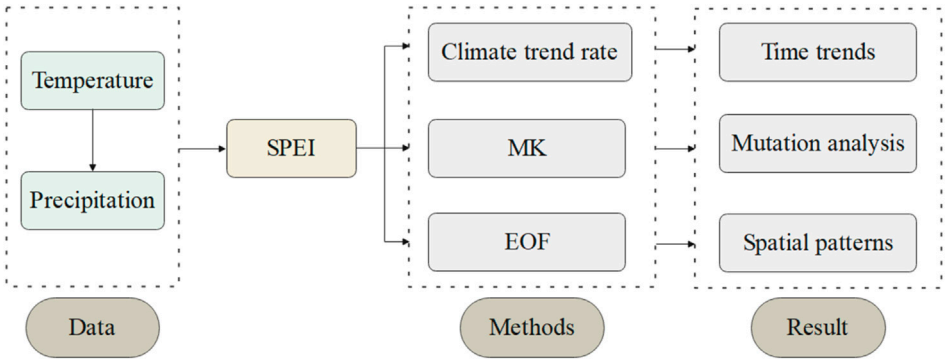

FIGURE 2
Research methodology flowchart.

provinces (municipalities) including Hebei, Henan, Shandong, Jiangsu, Anhui, Beijing, and Tianjin. This region belongs to the Huang-Huai-Hai agricultural region in the comprehensive agricultural zoning of China, including four secondary agricultural regions: the Huang-Huai Plain agricultural area (HH_P), the Shandong hilly agricultural and forestry area (SD_Q), the low-lying plain area of Hebei, Shandong, and Henan (JLY_P), and the foothill plain area of Yanshan and Taihang Mountains (YT_P). It is an important grain production base in China (Figure 1). Winter wheat and summer maize are the main grain crops in this region. The North China Plain is located in the East Asian monsoon climate zone, with uneven spatial and temporal distribution of precipitation. Drought is one of the main factors restricting the growth of winter wheat and summer maize in this region. The meteorological data used in this study are from 50 meteorological stations in North China from 1980 to 2013, obtained from the China Meteorological Data Sharing Service Network.

2.2 Research methods

As shown in Figure 2. By inputting temperature and precipitation data, standardized evapotranspiration index (ETI) can be obtained. The Mann-Kendall test method is used to assess climate and hydrological change trends, while empirical orthogonal function (EOF) analysis is employed to identify abrupt changes and three spatial-temporal distribution patterns.

2.2.1 Standardize precipitation evaporation index (SPEI)

SPEI considers the impact of precipitation, temperature changes, and potential surface evapotranspiration on drought. It can identify the occurrence or end of drought and reflect its actual severity. Here's how it is calculated:

1) This study involves retrieving daily weather data from the selected ground meteorological station and organizing it into monthly climate data. Then, the monthly potential evaporation (Pe) is calculated based on the monthly average temperature recorded at the station. The specific calculation formula is as follows:

$$Pe_i = 16\mathrm{K}\left(\frac{10T_i}{I}\right)^m \quad i = 1, 2 \ldots 12 \tag{1}$$

$$I_i = \left(\frac{T_i}{5}\right)^{1.514} \tag{2}$$

$$I = \sum_{i=1}^{12} I_i \tag{3}$$

where Eqs 1–3, T_i is the monthly average temperature in degrees°C, I_i is the monthly heat index, I is the annual heat index, and K is the correction index, a constant $m = 0.492 + 1.79 \times 10^{-2} I - 7.71 \times 10^{-5} I^2 + 6.75 \times 10^{-7} I^3$

$$\mathrm{K} = \left(\frac{N}{12}\right)\left(\frac{NDM}{30}\right) \tag{4}$$

where Eq. 4, NDM is the total number of days in that month, N is the possible sunshine hours, calculated using Eq. 5:

$$\mathrm{N} = \left(\frac{24}{\pi}\right) w_s \tag{5}$$

Where w_s is the sunrise hour angle, calculated using Eq. 6:

$$w_s = \arccos\left(-\tan\varphi \tan\delta\right) \tag{6}$$

Where φ is the latitude in radians (rad), δ is the solar declination angle, calculated using Eq. 7:

$$\delta = 0.4093 \sin\left(\frac{2\pi J}{365}\right) - 1.405 \tag{7}$$

Where J is the average day number of that month, ranging from 1 to 365 or 366, with 1st January being day 1.

2) Construct the cumulative water deficit X for different time scales. Calculated using Eq. 8:

$$D_i = P_i - Pe_i \tag{8}$$

Where D_i is the monthly water deficit, P_i is the monthly precipitation, and Pe_i is the monthly potential evaporation, all in millimeters (mm).

TABLE 1 Drought classes based on SPEI.

SPEI index	Drought class
−1.0 < SPEI ≤ −0.5	Slight drought
−1.5 < SPEI ≤ −1.0	Moderate drought
−2.0 < SPEI ≤ −1.5	Severe drought
SPEI ≤ −2.0	Extreme drought

Then, calculate the water deficit D_{ij} for the i-th year and j-th month, using Eq. 9 and Eq. 10, depending on different time scales.

$$X_{i,j}^{k} = \sum_{i=13-k+j}^{12} D_{i-1,j} + \sum_{i=1}^{j} D_{i,j} \tag{9}$$

$$X_{i,j}^{k} = \sum_{i=j-k+1}^{j} D_{i,j} \tag{10}$$

3) Calculate the probability distribution of the cumulative water deficit X

Below introduce the probability density function of the three-parameter log-logistic distribution as shown in Eq. 11:

$$f(x) = \frac{\beta}{\alpha}\left(\frac{x-\gamma}{\alpha}\right)^{\beta-1}\left[1+\left(\frac{x-\gamma}{\alpha}\right)^{\beta}\right]^{-2} \tag{11}$$

Where α, β and γ are the scale, shape, and location parameters, $D < \gamma < \infty$. Respectively. α, β, and γ are calculated using Eqs 12–14:

$$\alpha = \frac{(w_0 - 2w_1)\beta}{\Gamma\left(1+\frac{1}{\beta}\right)\Gamma(1-1/\beta)} \tag{12}$$

$$\beta = \frac{2w_1 - w_0}{(6w_1 - w_0 - 6w_2)} \tag{13}$$

$$\gamma = w_0 - \alpha\Gamma(1+1/\beta)\Gamma(1-1/\beta) \tag{14}$$

where Eqs 12, 14, $\Gamma(\beta)$ is the Gamma function, and in Eq. 15, i is the ordinal number of the cumulative water deficit sequence X_i, arranged in ascending order. The probability distribution function of the three-parameter log-logistic distribution is Eq. 16:

$$w_s = \frac{1}{N}\sum_{i=1}^{N}\left(1-\frac{i-0.35}{N}\right)^{s} X_i \tag{15}$$

$$\mathrm{F(x)} = \left[1+\left(\frac{\alpha}{x-\gamma}\right)^{\beta}\right]^{-1} \tag{16}$$

Finally, standardize the probability distributions for each month.

Order P = 1 − F(x), at that time P ≤ 0.5, then $W = \sqrt{-2\ln(P)}$

$$\mathrm{SPEI} = \frac{C_0 + C_1 W + C_2 W^2}{1 - d_1 W + d_2 W^2 + d_3 W^3} \tag{17}$$

Order P > 0.5, at that time $W = \sqrt{-2\ln(1-P)}$

where Eq. 17, $C_0 = 2.515517$, $C_1 = 0.802853$, $C_2 = 0.010328$,

$d_1 = 1.432788$ $d_2 = 0.189269$, $d_3 = 0.001308$ are all involved

The SPEI-based drought classification is given in Table 1.

2.2.2 Climate trend rate

Using the least squares method to calculate the regression coefficient between the sample and time, the change in meteorological elements can be represented by a linear Eq. 18:

$$y = aX + b \tag{18}$$

The climate trend rate is 10a.

2.2.3 M-K trend analysis

The M-K test method is a non-parametric statistical test method. It can not only detect changes in the trend of the sequence but also find mutation points in the sequence. It does not require the sample to follow a certain distribution and is not affected by a few exceptional values. It is suitable for the analysis of type variables and ordinal variables. The calculation process of MK is as follows (Sharma and Goyal, 2020; Alsubih et al., 2021):

For a time series X with a sample size of n, we construct a rank sequence in Eq. 19:

$$S_k = \sum_{i=1}^{k} r_i, \mathrm{k} = 2, 3, \cdots, \mathrm{n} \tag{19}$$

Where $r_i = \begin{cases} +1, x_i > x_j \\ 0, x_i \le x_j \end{cases}, j = 1, 2, 3, \cdots, i$

It can be seen that the rank sequence S_k is the cumulative count of the number of values at time i greater than the values at time j.

Assuming random and independent time series, we define the statistic in Eq. 20:

$$UF_K = \frac{[S_k - E(S_k)]}{\sqrt{var(S_k)}}, k = 1, 2, \cdots, n \tag{20}$$

Where $UF_1 = 0$, $E(S_k)$, $var(S_k)$ are the mean and variance of the cumulative count S_k. When $x_1, x_2, \cdots, x_n$ are mutually independent and have the same continuous distribution, they can be calculated by the following Eq. 21:

$$\begin{cases} E(S_k) = \dfrac{k(k-1)}{4} \\ var(S_k) = \dfrac{k(k-1)(2k+5)}{72} \end{cases} \quad k = 2, 3, \cdots, n \tag{21}$$

Where UF_i is the standard normal distribution. It is a sequence of statistics calculated in the order of the time series X, $x_1, x_2, \cdots, x_n$. Given a significance level α, we check the normal distribution table. If $|UF_1| > U_\alpha$, it indicates a significant trend change in the sequence.

The above process in reverse order of the time series X, $x_n, x_{n-1}, \cdots, x_1$. Simultaneously, we ensure that $UB_k = -UF_k$, k = (n, n − 1, ⋯, 1), $UB_1 = 0$.

Analyze and plot the UF_k and UB_k curves. If the value of UF_k or UB_k is greater than 0, it indicates an upward trend. If it is less than 0, it represents a downward trend. When they exceed the critical line, it indicates a significant upward or downward trend. The range beyond the critical line is determined as the time region of occurrence of the mutation. If the UF_k and UB_k curves intersect, and the intersection is between the critical lines, then the time corresponding to the intersection is the start time of the mutation. If it exceeds the UF_k critical line but the intersection of UF_k and UB_k

is outside the critical line, it cannot be easily determined whether this point is a mutation point.

2.2.4 Empirical orthogonal function (EOF) decomposition

The EOF decomposition was proposed by Pearson in 1902. In the mid-1950s, Lorenz introduced it into the study of atmospheric science (Lorenz and Hartmann, 2003). The advantage of EOF decomposition is that it can decompose meteorological elements into spatial functions that do not change with time (eigenvalues) and time functions that are independent of space. The spatial function part is determined by the main characteristics of the meteorological element field. The convergence speed of EOF decomposition is fast, so as long as a few eigenvectors with large eigenvalues are taken, the spatial characteristics of the climate element field can be fully described. EOF decomposition is to decompose the three-dimensional climate variables into orthogonal spatial typical fields and the corresponding time series, which can represent the main spatial distribution structure of meteorological elements.

The observed data of a certain climate variable field is given in matrix form:

$$\mathrm{X} = \begin{bmatrix} x_{11} & \cdots & x_{1n} \\ \vdots & x_{ij} & \vdots \\ x_{m1} & \cdots & x_{mn} \end{bmatrix} \tag{22}$$

In Eq. 22, m represents spatial points,n represents time points, and x_{ij} represents the j observation at the i station. After removing the anomalies from the variable field, the meteorological significance of the separated eigenvectors is more intuitive.

The above matrix is decomposed into two parts Eq. 23:

$$X = VT \tag{23}$$

The spatial function V and the time function T, where V and T are referred to as the spatial function matrix and the time function matrix, respectively. Each column of V represents a spatial typical field, which is only related to space. According to orthogonality, the spatial typical field and the time weighting coefficient should satisfy the following Eq. 24:

$$\sum_{i=1}^{m} v_{ik} v_{il} = 1, k = l \quad ; \quad \sum_{i=1}^{m} v_{ik} v_{il} = 0, k \neq l \tag{24}$$

According to the theorem of real symmetric decomposition, we have Eq. 25:

$$\mathrm{X}X' = VTX' = VTT'V' = V\Lambda V' \tag{25}$$

where Λ is a diagonal matrix composed of the eigenvalues of the matrix. According to the properties of eigenvectors, (UTU=I). Therefore, the spatial function matrix can be obtained from the eigenvectors of Λ. After obtaining V, the time function matrix T can be obtained. Λ is a diagonal matrix, and the diagonal elements are the eigenvalues of the matrix. Arrange the eigenvalues in descending order as shown in Eq. 26:

$$\lambda_1 \geq \lambda_2 \geq \cdots \geq \lambda_m \tag{26}$$

Calculate the variance contribution of each eigenvalue and the cumulative variance contribution of the first k eigenvectors, based on Eq. 27 and Eq. 28:

$$R_k = \lambda_k \Big/ \sum_{i=1}^{m} \lambda_i, k = 1, 2, \cdots, p\,(p < m) \tag{27}$$

$$G = \sum_{i=1}^{p} \lambda_i \Big/ \sum_{i=1}^{m} \lambda_i \tag{28}$$

3 Results and discussion

3.1 Drought trends during the growing season of winter wheat and summer maize

Between 1981 and 2013, the growth season of winter wheat in the Huang-Huai-Hai Plain area of North China showed an increasing trend of drought, with a decrease rate of SPEI at 0.4/10a ($p < 0.05$). In contrast, the growing season of summer maize in this region overall exhibited a trend towards wetter conditions, with an SPEI growth rate of 0.1/10a (Figure 3A). The changes in SPEI for the crop growing season in the low-lying plains of Hebei, Shandong, and Henan provinces were not significant overall, indicating no significant change in the dryness or wetness conditions during the crop growing season over the past 33 years (Figure 3B). The growing season of summer maize in the hilly and forested area of Shandong showed a trend towards wetter conditions, with a growth rate of approximately 0.27/10a. However, the winter wheat growing season in this region exhibited a slightly drier trend at 0.066/10a (Figure 3C). The foothill plains of the Yanshan and Taihang Mountains showed a trend towards drier conditions for both the winter wheat and summer maize growing seasons, with the summer maize season showing a more pronounced trend towards dryness at 0.158/10a compared to the winter wheat season at 0.072/10a (Figure 3D).

By using climate trend analysis methods to analyze the changes in SPEI at 50 stations in the North China region from 1981 to 2013, it can be observed that during the past 33 years, most stations in North China showed a trend towards drier conditions during the winter wheat growing season, particularly pronounced in the Huang-Huai-Hai Plain area. Only some stations in the northern part of the North China Plain showed a certain trend towards wetter conditions, mainly distributed in the northern parts of the low-lying plains of Hebei, Shandong, and Henan provinces, and the northern foothill plains of the Yanshan and Taihang Mountains (Figure 4). As for the summer maize growing season, apart from some stations in the northern part of North China showing a more pronounced trend towards dryness, most areas in the North China region exhibited a trend towards wetter conditions during the summer maize growing season (Figure 5).

Overall, in the past 30 years, the winter wheat growing season in North China has shown a trend towards drier conditions, while the summer maize growing season has shown a trend towards wetter conditions. This dry-wet trend, in terms of spatial distribution, has manifested as a worsening drought trend at most stations for winter wheat, with a few stations in the north showing a trend towards wetter conditions, such as in cities like Bazhou, Miyun, and Botou (Figure 4). As for summer maize, it has shown a trend towards

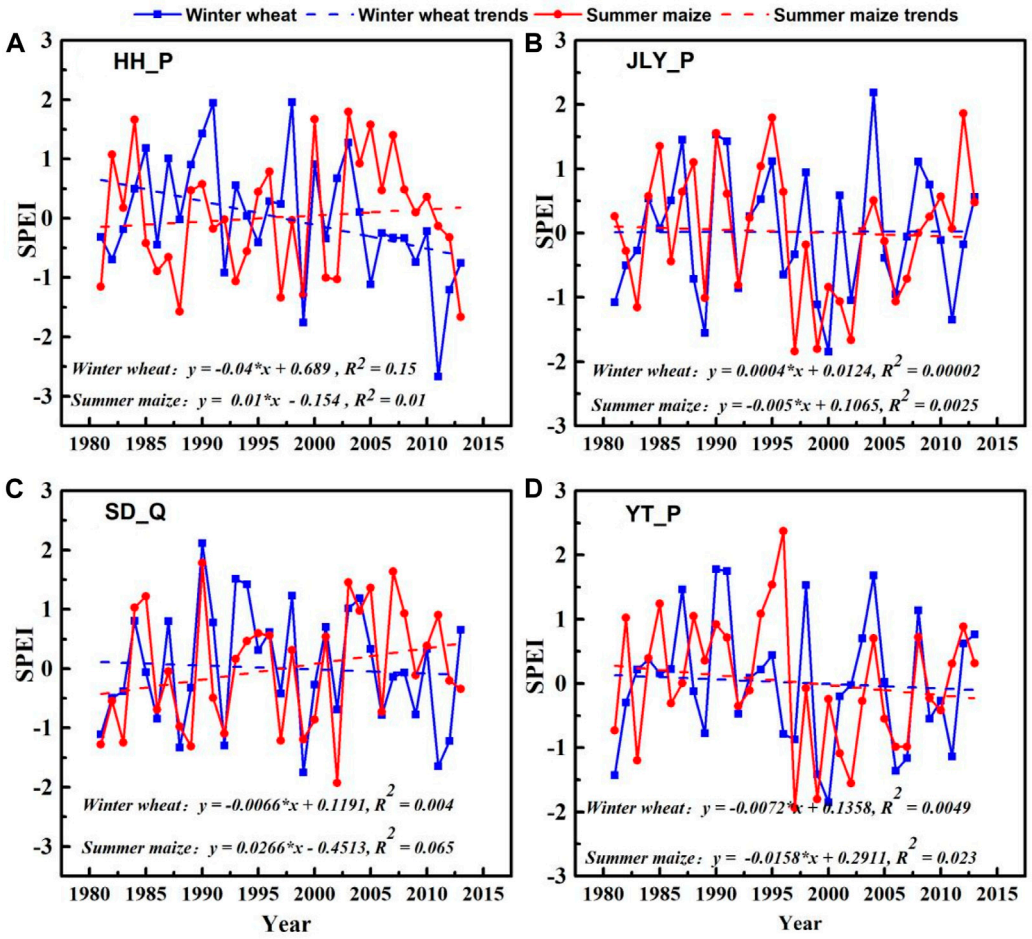

FIGURE 3
Drought trends during the winter wheat and summer maize growing seasons in different agricultural areas of the North China Plain from 1981 to 2013.

wetter conditions at most stations, with a few stations in the north exhibiting a trend towards dryness, such as in cities like Miyun, Beijing, and Tangshan (Figure 5).

3.2 Mann-Kendall trend analysis results of SPEI

The Mann-Kendall method was employed to analyze the variation trends and change patterns of SPEI during the winter wheat and summer maize growing seasons in four secondary agricultural regions in North China. In Figure 6, UF represents the statistics for the upward sequences, while UB represents the statistics for the downward sequences.

In the four secondary agricultural regions of North China, the UF curve of the winter wheat growing season showed an upward trend in the early and mid-1980s, but it exhibited a downward trend after the mid-1980s (Figures 6A, C, E, G). After the mid-1980s, the winter wheat growing season showed a trend towards drier conditions. In the hilly and forested area of Shandong, the UF curve showed a gentle decline after the mid-1980s, suggesting that the trend towards drier conditions was not significant (Figure 6A); in the Huang-Huai Plain area, the UF curve showed a noticeable decline around 2003, indicating an intensified trend towards drier conditions after 2003 (Figure 6C); in the low-lying plains of Hebei, Shandong, and Henan, and the foothill plains of the Yanshan and Taihang Mountains, the UF curve showed a more stable trend after 1998, suggesting relatively unchanged drought conditions in these areas (Figures 6E, G).

In the four major agricultural regions of North China, the UF curve of the summer maize growing season exhibited spatial differences. The UF curve trends in the hilly and forested area of Shandong and the Huang-Huai Plain area were similar (Figures 6B, D). In these two regions, the UF curve changes were relatively stable from around 1980 to 2003, indicating no significant change in drought conditions during this period. After 2003, the UF curves of these two regions showed an upward trend, suggesting a gradual trend towards wetter conditions during the summer maize growing season. In the low-lying plains of Hebei, Shandong, and Henan, and the foothill plains of the Yanshan and Taihang Mountains, the UF curve trends were similar (Figures 6F, H). Before 1997, the UF curve showed some fluctuation trends, but after

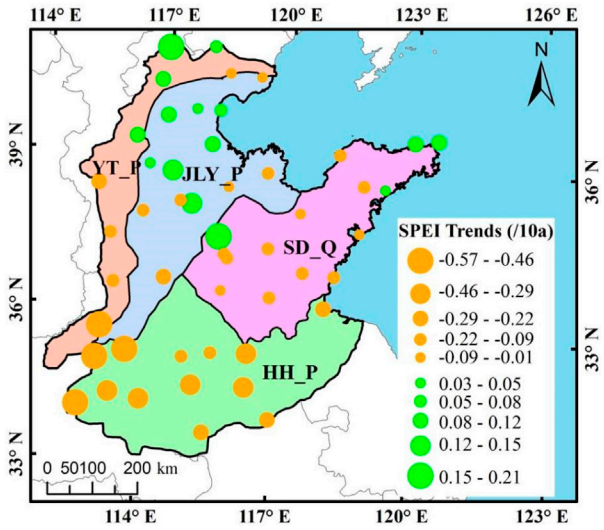

FIGURE 4
SPEI variation trends during the winter wheat growing season in different stations of the North China Plain from 1981 to 2013.

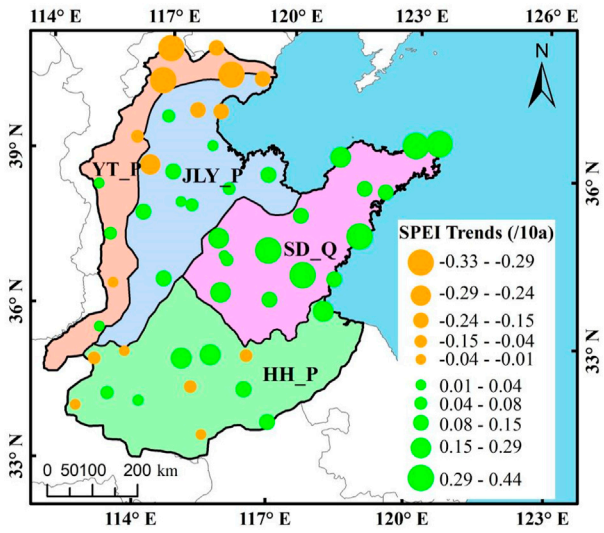

FIGURE 5
SPEI variation trends during the summer maize growing season in different stations of the North China Plain from 1981 to 2013.

1997, the UF curves in both of the mentioned areas exhibited a clear downward trend, indicating that these areas showed a more pronounced drying trend during the summer maize growing season after 1997.

3.3 Drought spatiotemporal characteristics during the growing seasons of winter wheat and summer maize

In order to further analyze the spatiotemporal distribution characteristics of drought during the winter wheat and summer maize growing seasons in North China over the past 30 years, the SPEI for the winter wheat and summer maize growing seasons were separately subjected to EOF decomposition. Through EOF decomposition, mutually orthogonal characteristic vectors can be obtained, which can represent independent drought spatial distribution types in North China. The magnitude of the variance contribution rate after EOF decomposition characterizes the typicality of the corresponding mode's drought spatial distribution form. The larger the variance contribution rate, the more typical the corresponding drought distribution form. The maximum center of each mode is the sensitive center of drought variation. The temporal coefficient can be used as a weight of the spatial coefficient to reflect the contribution rate of a certain year to this drought spatial distribution. The larger the absolute value of the temporary coefficient, the more typical the distribution form of that year.

Based on the magnitude of the variance contribution rate, the first 3 characteristic vectors of the SPEI for the winter wheat and summer maize growing seasons were selected. Table 2 respectively list the variance contribution rates corresponding to the first 3 characteristic vectors of winter wheat and summer maize. It can be seen that the variance contribution rate of the first mode for both crops is much larger than that of the second and third modes, indicating that, whether for winter wheat or summer maize, the first mode corresponds to the main drought spatial distribution type in North China. Below discusses the spatial distribution and temporal coefficients for different modes:

3.3.1 The first mode

The variance contribution rate of the spatial coefficient characteristic vectors of the first mode for the winter wheat and summer maize growing seasons is significantly higher than that of the second and third modes (Table 2), indicating that the spatial distribution type of the first mode is the main spatial distribution type in North China. From Figure 7, it can be seen that the spatial coefficients corresponding to the first mode of the growing seasons for both crops are positive, indicating a good spatial consistency in the drought distribution in North China during the growing seasons of the two crops. For winter wheat, the high-value area of the first mode is mainly distributed in the southern part of the Yanshan and Taihang mountain foothill plains and the low-lying plains of the Hebei, Shandong, and Henan regions, including areas such as Xingtai, Anyang, and Chaoyang. For summer maize, the high-value area of the first mode is mainly distributed in the hilly agricultural and forestry areas of Shandong and the plains of the Huang-Huai region, including areas such as Shangqiu, Dangshan, and Ganyu, indicating that the variability of drought occurrence is more significant and their response to dryness and wetness is more sensitive (Figures 7A, C).

Since the spatial coefficients corresponding to the first mode of the growing seasons for winter wheat and summer maize are both greater than 0 (Figure 7), the positive or negative situation of the temporal coefficients corresponding to the first mode reflects the overall dryness and wetness conditions in North China for that year. The temporal coefficients corresponding to the first mode of the winter wheat growing season show an overall trend of first increasing and then decreasing. Specifically, between 1981 and 1991, the temporal coefficients of the first mode for

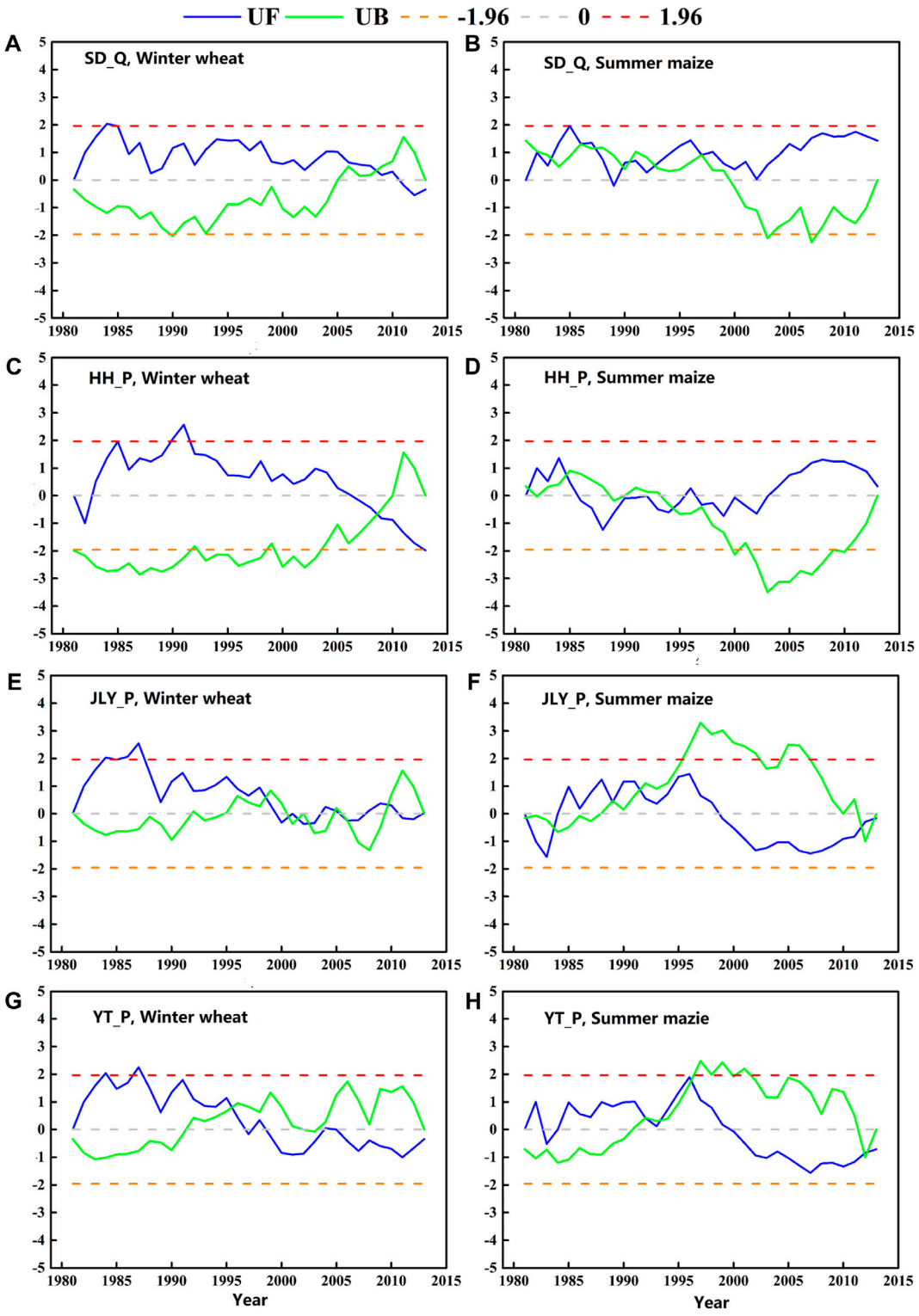

FIGURE 6
Mann-Kendall test figures for winter wheat and summer maize growing seasons in different agricultural areas of North China from 1981 to 2013.

winter wheat show an overall increasing trend, and after 1991, they show an overall decreasing trend, indicating that the main drought spatial distribution type in North China during the winter wheat growing season over the past 34 years has undergone an evolution from wet to dry (Figure 7B). For summer maize, before 2000, its temporal coefficients alternated between positive and negative without a clear trend, indicating that from 1981 to 2000, the overall dryness and wetness conditions during the summer maize growing season in North China did not change significantly. After 2000, there

TABLE 2 Variance contribution rates of the first 3 modes of EOF decomposition of the SPEI index for the winter wheat and the summer maize growing season in the NCP (%).

Winter wheat				Summer maize			
Modal	1	2	3	Modal	1	2	3
Variance	41.29	14.27	8.10	Variance	32.32	17.52	8.37
Cumulative Variance	41.29	55.56	63.66	Cumulative Variance	32.32	49.84	58.21

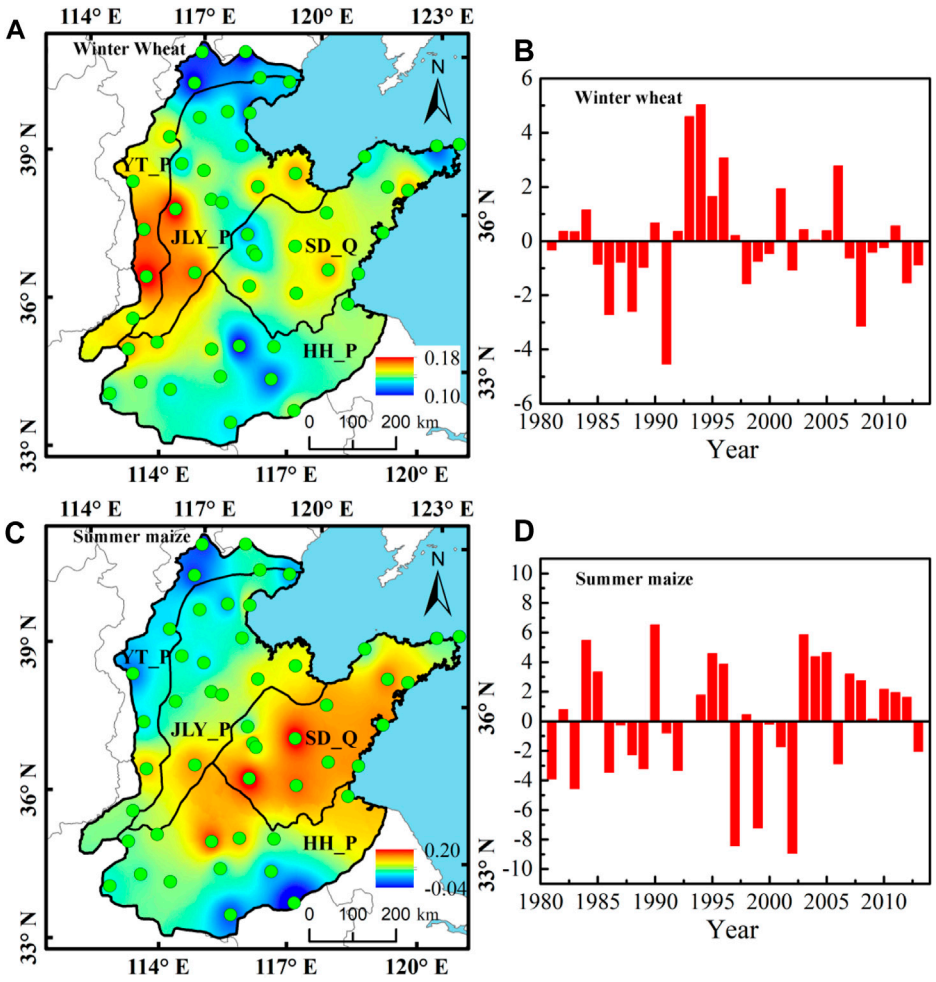

FIGURE 7
Spatial distribution and temporal coefficient changes of the first mode for winter wheat and summer maize growing seasons in the NCP.

were significantly more years with positive temporal coefficients than with negative ones for the winter wheat growing season in North China, showing an overall increasing trend, indicating that after 2000, the summer maize growing season in North China has shown a trend towards wetter conditions (Figure 7D).

3.3.2 The second mode

Both winter wheat and summer maize show significant north-south differences in the spatial distribution of the second mode's SPEI EOF during their growing seasons. Specifically, for the winter wheat growing season, the spatial coefficients of the SPEI EOF exhibit a positive trend in the north and a negative trend in the south (Figure 8A), while for summer maize, it is the opposite, with a negative trend in the north and a positive trend in the south (Figure 8C). This indicates that the second dominant dry-wet spatial distribution pattern during the growing seasons of winter wheat and summer maize in North China exhibits a contrasting spatial pattern from north to south.

After 2000, there is a significant increase in the number of years with positive temporal coefficients corresponding to the second mode of the winter wheat growing season, indicating that the northern drought during the winter wheat growing season in North China has eased, while the southern drought has intensified (Figure 8B). For summer maize, after 2000, the

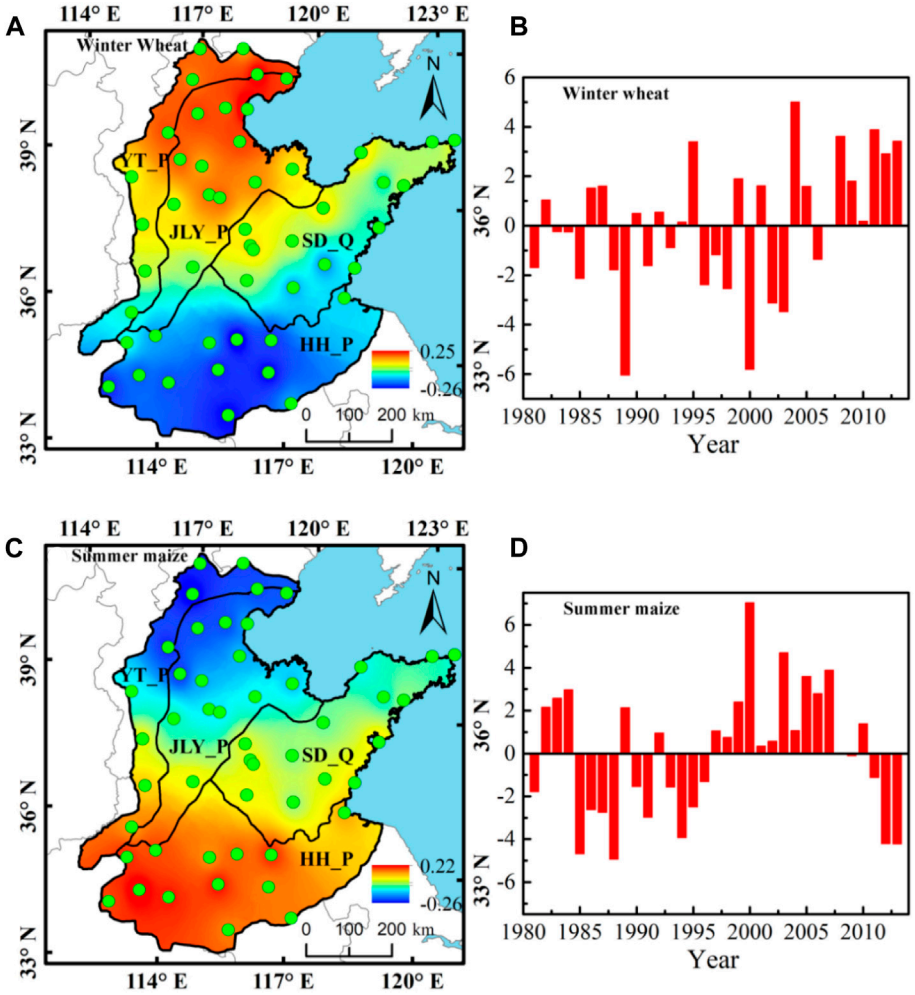

FIGURE 8
Spatial distribution and temporal coefficient changes of the second mode for winter wheat and summer maize growing seasons in the NCP.

temporal coefficients corresponding to the second mode show a decreasing trend, indicating that the northern drought during the summer maize growing season in North China is gradually worsening, while the southern drought is gradually easing. In particular, 2012 and 2013 are typical years of northern drought and southern wetness (Figure 8D).

3.3.2 The third mode

The variance contribution rates of the third mode of the SPEI EOF decomposition for the growing seasons of winter wheat and summer maize are 8.10% and 8.37% respectively (Table 2), to some extent reflecting the drought spatiotemporal distribution characteristics of the two crops' growing seasons in North China. From the spatial distribution maps of the third mode's spatial coefficients for the two crops (Figures 9A, C), it can be observed that for both the winter wheat and summer maize growing seasons' SPEI EOF decomposition, the high-value areas of the third mode are concentrated in the Shandong Peninsula. The difference lies in the fact that for winter wheat, the hilly agricultural and forestry areas of Shandong near Taian and Jinan are also significant high-value areas. Overall, for winter wheat, the third mode exhibits a drought spatial distribution pattern of three northeast-southwest-oriented bands, with the middle band's spatial coefficient higher than the two outer bands, and the northern band having the smallest spatial coefficient. For summer maize, the spatial coefficients of the third mode exhibit a decreasing trend from the eastern coastal areas to the western areas.

The temporal coefficients of the third mode during the winter wheat growing season show an overall trend of first increasing and then decreasing (Figure 9B). In 1986, 1988, 1991, and 2008, the winter wheat growing season in North China exhibited significant dryness in the middle and wetness on the sides; in 1993, 1994, and 2006, it exhibited a spatial distribution pattern of wetness in the middle and dryness on the sides. The temporal coefficients corresponding to the third mode of the summer maize growing season show an overall increasing trend (Figure 9D), indicating that during the summer maize growing season, the eastern part of North China is becoming wetter, while the western part is becoming drier. 1981, 1982, and 2000 were typical years of western wetness and eastern dryness in North China, while 1985, 1986, 1997, 2001, as well as 2005 and 2007, were relatively typical years of eastern wetness and western dryness.

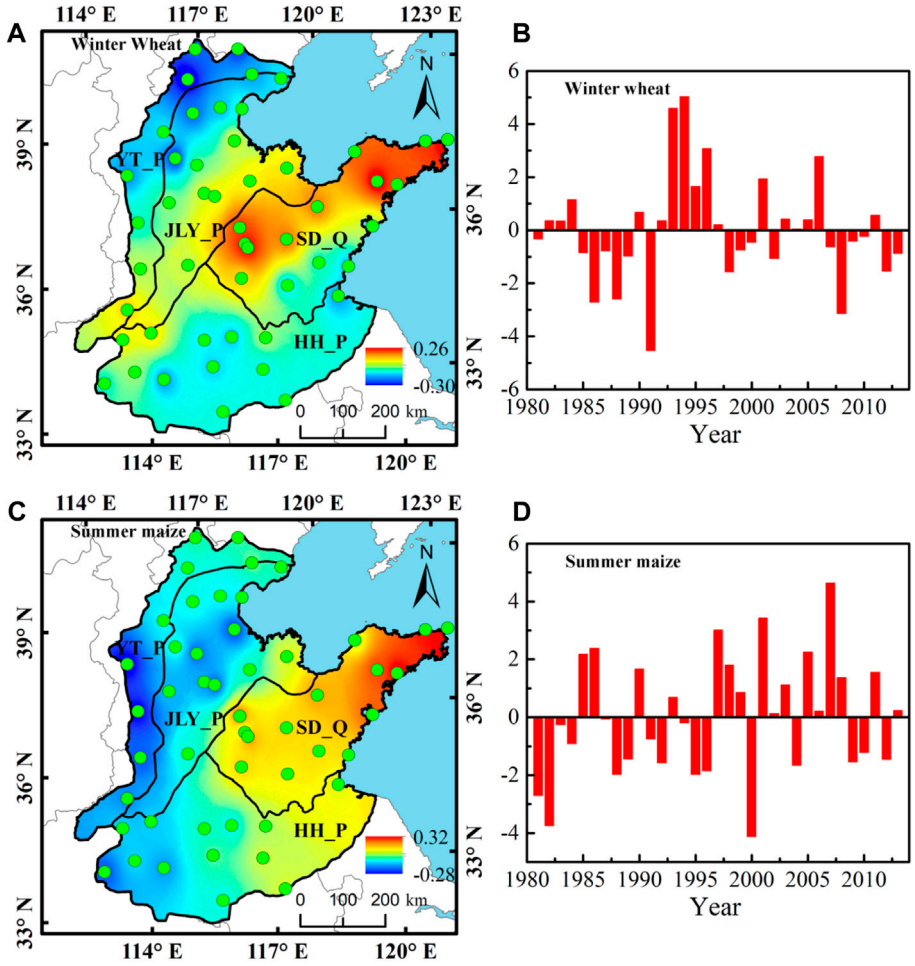

FIGURE 9
Spatial distribution and temporal coefficient changes of the third mode for winter wheat and summer maize growing seasons in the NCP.

4 Conclusion

Based on the SPEI, this study explored the spatiotemporal characteristics of drought during the growing season of the winter wheat and summer maize in the NCP from 1980 to 2013. The main conclusions were as follows:

(1) From 1980 to 2013, except for the northern parts of YT_P and JLY_P, the drought trend during the winter wheat growing season has intensified, with HH_P showing the most significant drought trend. In contrast, the summer maize growing season showed wetting trends generally, with SD_Q showing the most significant wetting trend, only the northern parts of YT_P and JLY_P show a drought trend.

(2) The Mann-Kendall trend analysis results indicate that after the mid-to-late 1980s, the winter wheat growing season in the NCP has shown consistent drought trends, with HH_P showing a particularly pronounced drought trend after 2003. For summer maize, after 2003, the wetting trends in the SD_Q and HH_P was more significant, while the drought trend is evident for JLY_P and YT_P after 1997.

(3) The consistency of the drought-wet spatial distribution is the dominant pattern for the winter wheat and summer maize growing seasons in North China. For winter wheat, the southern parts of YT_P and JLY_P were more sensitive to the changes of drought-wet conditions, while for summer maize, SD_Q were more sensitive to the changes of the drought-wet conditions.

(4) The opposite north-south drought-wet spatial distribution pattern was the second dominant spatial distribution pattern for the winter wheat and summer maize growing seasons in the NCP. The third drought-wet spatial distribution pattern for winter wheat consisted of three northeast-southwest-oriented bands, with the spatial coefficient of the middle band higher than the two outer bands. For summer maize, the third drought-wet spatial distribution pattern overall exhibited opposite characteristics from east to west.

5 Discussion

This study presents a comprehensive analysis of agricultural drought in the North China Plain region, focusing solely on the

Standardized Precipitation Evapotranspiration Index (SPEI) and the Empirical Orthogonal Function (EOF) method. The integration of drone and remote sensing data with SPEI and EOF methods offers a promising approach for monitoring and forecasting agricultural drought, thus contributing to the development of effective strategies for drought management in the North China Plain.

Data availability statement

The original contributions presented in the study are included in the article/supplementary material, further inquiries can be directed to the corresponding author.

Author contributions

QL: Funding acquisition, Writing–review and editing. YL: Project administration, Supervision, Writing–original draft. LL: Validation, Visualization, Writing–review and editing. YW: Formal Analysis, Writing–original draft. QW: Methodology, Writing–original draft. MM: Conceptualization, Project administration, Supervision, Writing–review and editing.

Funding

The authors declare financial support was received for the research, authorship, and/or publication of this article. This research was supported by National Natural Science Foundation of China (42371086, 42101086, 42201387) and the Open Fund of the China Institute of Water Resources and Hydropower Research (IWHR-SKL-KF202310).

Conflict of interest

The authors declare that the research was conducted in the absence of any commercial or financial relationships that could be construed as a potential conflict of interest.

Publisher's note

All claims expressed in this article are solely those of the authors and do not necessarily represent those of their affiliated organizations, or those of the publisher, the editors and the reviewers. Any product that may be evaluated in this article, or claim that may be made by its manufacturer, is not guaranteed or endorsed by the publisher.

References

Alsubih, M., Mallick, J., Talukdar, S., Salam, R., AlQadhi, S., Fattah, M. A., et al. (2021). An investigation of the short-term meteorological drought variability over Asir Region of Saudi Arabia. *Theor. Appl. Climatol.* 145, 597–617. doi:10.1007/s00704-021-03647-4

Bai, X., Zhao, C., Tang, Y., Zhang, Z., Yang, B., and Wang, Z. (2023). Identification,physical mechanisms and impacts ofdrought–flood abrupt alternation: a review. *Front. Earth Sci.* 11, 1203603. doi:10.3389/feart.2023.1203603

Cao, S., Yi, H., Lifeng, Z., Yi, C., Wang, Y., Sheng, Y., et al. (2021). Spatiotemporal characteristics of drought and its impact on vegetation in the vegetation region of Northwest China. *Ecol. Indic.* 133, 108420. doi:10.1016/j.ecolind.2021.108420

Carvalho, P., and Spataru, C. (2023). Gaps in the governance of floods, droughts, and heatwaves in the United Kingdom. *Front. Earth Sci.* 11, 1124166. doi:10.3389/feart.2023.1124166

Fan, J., Wei, S., Liu, D., Qin, T., Xu, F., Wu, C., et al. (2023). Impact of ENSOevents on meteorological drought in theWeihe River basin, China. *Front. Earth Sci.* 11, 1093632. doi:10.3389/feart.2023.1093632

Guo, E., Liu, X., Zhang, J., Wang, Y., Wang, C., Wang, R., et al. (2017). Assessing spatiotemporal variation of drought and its impact on maize yield in Northeast China. *J. Hydrology* 553, 231–247. doi:10.1016/j.jhydrol.2017.07.060

Hu, Y. (2014). *Risk assessment of drought disasters in the North China winter wheat-summer corn rotation area*. Beijing, China: Chinese Academy of Agricultural Sciences.

Jiang, X., Bai, J., and Liu, X. (2019). Progress and prospect of comprehensive drought monitoring based on multi-source information. *Adv. Earth Sci.* 34 (3), 275–287.

Li, S., Ge, W., and Wang, F. (2023). Characteristics of drought events in northern China from 1982 to 2019 and their impact on vegetation. *Res. Soil Water Conservation* 30 (03), 251–259.

Liu, R., Zhu, Z., Fang, W., Wang, Y., Xu, P., and Shi, L. (2006). Risk zoning of drought damage for winter wheat in the North China Plain. *J. Ecol.* (09), 1068–1072.

Liu, Z., Qiu, H., Zhu, Y., Liu, Y., Yang, D., Ma, S., et al. (2022). Efficient identification and monitoring of landslides by time-series InSAR combining single- and multi-look phases. *Remote Sens.* 14, 1026. doi:10.3390/rs14041026

LorenzHartmann, D. J. D. L. (2003). Eddy–zonal flow feedback in the northern hemisphere winter. *J. Clim.* 16 (8), 1212–1227. doi:10.1175/1520-0442(2003)16<1212:effitn>2.0.co;2

Ma, S., Qiu, H., Yang, D., Wang, J., Zhu, Y., Tang, B., et al. (2022). Surface multi-hazard effect of underground coal mining. *Landslides* 20, 39–52. doi:10.1007/s10346-022-01961-0

Pasho, E., Camarero, J. J., de Luis, M., and Vicente-Serrano, S. M. (2011). Impacts of drought at different time scales on forest growth across a wide climatic gradient in north-eastern Spain. *Agric. For. Meteorology* 151 (12), 1800–1811. doi:10.1016/j.agrformet.2011.07.018

Sharma, A., and Goyal, M. K. (2020). Assessment of drought trend and variability in India using wavelet transform. *Hydrological Sci. J.* 65, 1539–1554. doi:10.1080/02626667.2020.1754422

Sun, H., Zhang, X., Chen, S., Wang, Y., Shao, L., and Gao, L. (2009). Impact of meteorological factor changes on summer corn yield in the North China Plain. *Chin. J. Agric. Meteorology* 30 (02), 215–218. doi:10.3969/j.issn.1000-6362.2009.02.019

Tirivarombo, S., Osupile, D., and Eliasson, P. (2018). Drought monitoring and analysis: standardised precipitation evapotranspiration index (SPEI) and standardised precipitation index (SPI). *Phys. Chem. Earth* 106, 1–10. doi:10.1016/j.pce.2018.07.001

Vicente-Serrano, S. M., Beguería, S., and López-Moreno, J. I. (2010). A multiscalar drought index sensitive to global warming: the standardized precipitation evapotranspiration index. *J. Clim.* 23 (7), 1696–1718. doi:10.1175/2009jcli2909.1

Vicente-Serrano, S. M., Sergio, M., Camarero, J. J., Beguería, S., Trigo, R., López-Moreno, J. I., et al. (2013). Response of vegetation to drought time-scales across global land biomes. *Proc. Natl. Acad. Sci. U. S. A.* 110 (1), 52–57. doi:10.1073/pnas.1207068110

Wang, L., Qiu, H., Zhou, W., Zhu, Y., Liu, Z., Ma, S., et al. (2022). The post-failure spatiotemporal deformation of certain translational landslides may follow the pre-failure pattern. *Remote Sens.* 14, 2333. doi:10.3390/rs14102333

Wen, Q. X., and Chen, H. (2023). Changes in drought characteristics over China during 1961–2019. *Front. Earth Sci.* 11. doi:10.3389/feart.2023.1138795

Wu, J. F., and Chen, X. H. (2019). Spatiotemporal trends of dryness/wetness duration and severity: the respective contribution of precipitation and temperature. *Atmos. Res.* 216, 176–185. doi:10.1016/j.atmosres.2018.10.005

Yang, D., Qiu, H., Hu, S., Pei, Y., Wang, X., Du, C., et al. (2021). Influence of successive landslides on topographic changes revealed by multitemporal high-resolution UAS-based DEM. *CATENA* 202, 105229. doi:10.1016/j.catena.2021.105229

Yang, J., Wu, J., Liu, L., Zhou, H., Gong, A., Han, X., et al. (2020). Responses of winter wheat yield to drought in the North China plain: spatial–temporal patterns and climatic drivers. *Water* 12, 3094. doi:10.3390/w12113094

Zhang, Y., Wang, C., and Zhang, J. (2015). Analysis of the spatial and temporal distribution characteristics of drought in the North China winter wheat area based on SPEI index. *Acta Ecol. Sin.* 35 (21), 7097–7107. doi:10.5846/stxb201311272825

Zheng, S., Hu, Q., He, H., Xing, M., Liu, Y., Ma, X., et al. (2022). Spatiotemporal variation characteristics of light energy resources during the winter wheat-summer corn growing season in the North China Plain from 1961 to 2020. *J. China Agric. Univ.* 27 (01), 26–37. doi:10.11841/j.issn.1007-4333.2022.01.03

Zhou, W., Qiu, H., Wang, L., Pei, Y., Tang, B., Ma, S., et al. (2022). Combining rainfall-induced shallow landslides and subsequent debris flows for hazard chain prediction. *CATENA* 213, 106199. doi:10.1016/j.catena.2022.106199

frontiers | Frontiers in Earth Science

TYPE Original Research
PUBLISHED 22 January 2024
DOI 10.3389/feart.2024.1334074

OPEN ACCESS

EDITED BY
Haijun Qiu,
Northwest University, China

REVIEWED BY
Mingtao Ding,
Southwest Jiaotong University, China
Zheng Han,
Central South University, China

*CORRESPONDENCE
Zhiquan Yang,
yzq1983816@kust.edu.cn

RECEIVED 09 November 2023
ACCEPTED 08 January 2024
PUBLISHED 22 January 2024

CITATION
Shen H, Yang Z, Hu G, Tian S, Rahman M, Ren J and Zhang Y (2024), Causal mechanisms and evolution processes of "block-burst" debris flow hazard chains in mountainous urban areas: a case study of Meilong gully in Danba county, Sichuan Province, China.
Front. Earth Sci. 12:1334074.
doi: 10.3389/feart.2024.1334074

Causal mechanisms and evolution processes of "block-burst" debris flow hazard chains in mountainous urban areas: a case study of Meilong gully in Danba county, Sichuan Province, China

Haowen Shen[1,2,3], Zhiquan Yang[1,3,4]*, Guisheng Hu[2,5], Shufeng Tian[2], Mahfuzur Rahman[6], Jincheng Ren[1,3,4] and Yong Zhang[7]

[1]Faculty of Public Safety and Emergency Management, Kunming University of Science and Technology, Kunming, China, [2]Key Lab of Mountain Hazards and Surface Processes, Institute of Mountain Hazards and Environment, Chinese Academy of Sciences, Chengdu, China, [3]Key Laboratory of Geological Disaster Risk Prevention and Control and Emergency Disaster Reduction of Ministry of Emergency Management of the People's Republic of China, Kunming, China, [4]Key Laboratory of Early Rapid Identification, Prevention and Control of Geological Diseases in Traffic Corridor of High Intensity Earthquake Mountainous Area of Yunnan Province, Kunming, China, [5]Academy of Plateau Science and Sustainability, Xining, China, [6]Department of Civil Engineering, International University of Business Agriculture and Technology (IUBAT), Dhaka, Bangladesh, [7]Anyang Institute of Technology, Anyang, China

The research interest in multi-hazard chains lies in the comprehension of how various hazards, such as debris flows, floods, and landslides, can interact and amplify one another, resulting in cascading or interconnected hazards. On 17 June 2020, at approximately 3:20 a.m., a debris flow occurred in Meilong gully (MLG), located in Banshanmen Town, Danba County, in southwest China's Sichuan Province. The debris flow had a discharge volume of approximately 40 × 10^4 m^3 and rushed out to block the Xiaojinchuan (XJC) river, subsequently forming a barrier lake. This event ultimately induced a hazard chain that included heavy rainfall, debris flow, landslides, the formation of a barrier lake, and an outburst flood. The impact of this chain resulted in the displacement of 48 households and affected 175 individuals. Furthermore, it led to the destruction of an 18 km section of National Highway G350, stretching from Xiaojin to Danba County, causing economic losses estimated at 65 million yuan. The objective of this study is to analyze the factors leading to the formation of this hazard chain, elucidate its triggering mechanisms, and provide insights for urban areas in the western mountainous region of Sichuan to prevent similar dam-break type debris flow hazard chains. The research findings, derived from field investigations, remote sensing imagery analysis, and parameter calculations, indicate that prior seismic disturbances and multiple dry-wet cycle events increased the volume of loose solid materials within the MLG watershed. Subsequently, heavy rainfall triggered the initiation of the debris flow in MLG. The cascading dam-break, resulting from three unstable slopes and boulders within the channel, amplified the scale of the hazard chain, leading to a

significant amount of solid material rushing into the XJC river, thus creating a dam that constricted the river channel. With the intensification of river scouring, the reactivation and destabilization of the Aniangzhai (ANZ) paleolandslide occurred, ultimately leading to the breach of the dam and the formation of an outburst flood. The research comprehensively and profoundly reveals the causal mechanism of the MLG hazard chain, and proposes measures to disrupt the chain at various stages, which can aid in enhancing monitoring, early warning, forecasting systems, and identifying key directions for ecological environmental protection in urban areas within the western mountainous region of Sichuan. Additionally, it could also serve as a reference for mountainous urban areas such as the Tianshan, Alps, Rocky Mountains, and Andes, among others.

KEYWORDS

debris flow, hazard chain, slope instability, formation and evolution mechanism, monitoring and early warning, risk assessment

1 Introduction

The study of hazard chains has gained significant attention in recent years, particularly in the context of large-scale debris flow hazards in high mountain and canyon areas. These hazards often trigger a series of interconnected events, including landslides, barrier lakes, and outburst floods. Examples of such hazard chains can be found in various regions, including the Qinghai-Tibet Plateau (CUI et al., 2015; Liu et al., 2023b), the western Sichuan Plateau (Chen et al., 2011), the Italian Alps (Deganutti et al., 2000), the island of Elba (Iotti and Simoni, 1997), Taiwan (Cheng et al., 2000), the SE coast of Australia (Flentje et al., 2000), and Nicaragua (Scott, 2000).

The combination and overlapping impact of multiple hazards create a secondary hazard chain that poses a significantly greater threat than the direct impact of a single debris flow. This phenomenon underscores the complex and interconnected nature of natural disasters, highlighting the need for comprehensive understanding and effective mitigation strategies (Guo et al., 2021; Guo et al., 2022). Mountain hazard chain causes enormous damage to transportation routes, agricultural and forestry economy, ecological environment and the safety of urban residents. For example, in 2018, the Baige landslide in Tibet led to the formation of a dam that blocked the Jinsha River, resulting in severe downstream flooding and devastating economic losses (Zhang et al., 2019; Zhang et al., 2020a; Zhong et al., 2020). Similarly, on 17 October 2018, at approximately 5 a.m., an ice and rock avalanche in Tibet triggered a debris flow, leading to the formation of a barrier lake that posed a significant threat to the lives and property of residents in upstream and downstream towns, as well as the ecological environment and transportation networks in the vicinity (Hu et al., 2019; Liu et al., 2023b; Yang et al., 2023b; Yang et al., 2023d). The devastating impact of hazard chains was exemplified by the extensive floods, landslides, and debris flows that occurred in Venezuela on December 15–16, 1999, causing the worst natural disaster in the country's history, resulting in significant loss of life and widespread destruction of homes and structures. This historical event serves as a poignant reminder of the far-reaching consequences of interconnected hazards and the importance of understanding and mitigating the secondary disaster chain effects (Pérez, 2001).

In the context of studying hazard chains, the Meilong gully (MLG) hazard chain in Danba County, Sichuan Province, China, occurred on 17 June 2020, has emerged as a rare and valuable case for analysis, shedding light on the complexities and implications of such interconnected hazards. The MLG hazard chain in Danba County was triggered by heavy rainfall. However, during the same period, in Zengda gully, Dajin County, Sichuan Province, China, which is located less than 1.2 km away and has a larger watershed area of 125.53 km^2, no debris flow occurred. According to the literature, Zengda gully has experienced six debris flow hazards since the 1990s, with the latest one occurred on 27 June 2019 (Hu et al., 2022). Despite the similarities in topography, geomorphology, and climatic conditions, Zengda gully, with a larger drainage area and more sediment sources, did not experience a debris flow event.

Currently, scholars have conducted research in the MLG watershed. A simulation was conducted to analyze the movement and accumulation process of MLG debris flow (An et al., 2022). Additionally, Ning et al. (2022) analyzedthe implementation of engineering measures aimed at slowing down and reducing the ongoing development of the MLG hazard chain. Liu et al. (2023a) conducted numerical simulations of the XJC river dam failure process and identified that the channel uplift resulting from the dam failure exacerbated the flood hazard of the MLG hazard chain. However, these studies have not revealed the entire process and mechanism of the formation, development, evolution, and hazard-causing of the MLG debris flow hazard chain under the internal and external dynamic coupling. Unlike the simple superposition of single or multiple hazards, the mountain hazard chains often have temporal and spatial continuity and extension, and exhibit cascading and compound effects, often characterized by huge damage, wide impact range, and long duration (Chen and Cui, 2017; Mani et al., 2023). With the acceleration of economic development and population growth, engineering activities in mountainous urban areas in western Sichuan are also increasing rapidly (Wang et al., 2018). At the same time, slope instability, debris flows, and other mountain hazards and their secondary hazard chains are also threatening the safety of mountainous urban areas.

In this context, using the MLG hazard chain that occurred in Danba County, Sichuan Province, China, as a case study, this research investigates the triggering mechanism of debris flow

under the combined influence of earthquakes and multiple dry-wet cycles, in addition to the heavy rainfall factor. This article is pioneering in its utilization of the dry-wet cycle within long-term rainfall sequences to analyze the promotion effect of increased loose source materials on the formation of debris flow in the MLG watershed. It elucidates the whole process of the MLG hazard chain, encompassing formation, occurrence, scale amplification, and disaster. Furthermore, it examined the mechanisms leading to the formation of secondary hazards within the chain. The results shed light on the factors behind the tendency of "block-burst" type debris flow hazard chains in mountainous urban areas in western Sichuan to be large in scale and result in substantial losses. These findings also serve as a reminder that, in future mountainous urban development, it is imperative to accurately identify debris flow gullies and to take into account the impacts of pre-earthquakes, dry-wet cycles, and channel blockages during geological hazard risk assessments.

2 Materials and methods

2.1 Background

2.1.1 Geographic and geomorphic background of the study area

MLG is situated in the high mountain canyon region of western Sichuan Province, specifically in Guanzhou Village, Banshanmen Town, Danba County, within the Ganzi Tibetan Autonomous Prefecture (see Figure 1). Access to MLG is available via the G350 national highway leading to the gully entrance. The geographic coordinates of the MLG debris flow gully entrance are as follows: N30°59′25.11″, E102°1′32.20". The drainage area of MLG spans 62.79 km^2, with the main ditch extending over a length of 12.42 km. The highest point within the watershed reaches an elevation of 4,760 m, while the lowest point is located at the entrance of the XJC river at an elevation of 2,120 m, resulting in a relative height difference of 2,640 m. The average longitudinal drop across the watershed is approximately 212.56 per mille, with the accumulation area near the gully mouth featuring a gentler slope, averaging around 100 per mille. The MLG watershed encompasses ten branch ditches, and the extent of the watershed and its topographic characteristics are illustrated in Figure 1.

2.1.2 Topographic features and earthquakes

The study area is situated within a triangular fault block, enclosed by the Freshwater River Fault, the Longmenshan Fault, and the South Qinling Fault Zone. This region is characterized by high tectonic activity and the presence of well-developed faults. The exposed geological strata in the MLG watershed predominantly consist of clastic rocks from the Devonian Guiguan Group (Dwg), as well as Quaternary avalanche deposits and alluvial soils (refer to Figure 1). Notably, this study area has experienced frequent seismic events in recent history, including significant earthquakes such as the 7.9 magnitude quake in Fuhuo (1973), a 5.0 magnitude event in Tagong (1978), a 6.9 magnitude earthquake in Daofu (1981), an 8.0 magnitude earthquake in Wenchuan (2008), and a 6.3 magnitude earthquake in Kangding (2014), all within the same vicinity (see Figure 1). The most powerful earthquake recorded in this region was the magnitude 8.0 mega-earthquake that struck Yingxiu Township, Wenchuan County, on 12 May 2008.

2.1.3 Meteorological and hydrological characteristics

The study area experiences relatively low average annual rainfall, with a long-term average of 649.34 mm and a maximum annual precipitation of 823.3 mm recorded in 2012. Rainfall is primarily concentrated between May and September, accounting for 82.3% of the annual total, with an average monthly rainfall of about 101 mm during this period, with June having the highest monthly average at 100.5 mm. The average annual temperature is 14.6°C, with the coldest month, January, ranging between 3°C–6°C, and the hottest month, August, typically ranging from 20°C–23°C. The highest recorded temperature in recent years was 39.5°C.

2.2 Methodology

2.2.1 Calculation of debris flow dynamic parameters

The key dynamic parameters for assessing the nature and magnitude of debris flow include density, velocity, and discharge. In this study, field investigations (Figure 2) were conducted, involving the selection of 12 groups for on-site slurry preparation of debris flow samples and the examination of 6 representative sections within the MLG area (Rahman and Konagai, 2017). The parameters characterizing the behavior of debris flow in MLG were determined through a combination of field investigations and laboratory tests. The relevant calculation formulas are as follows (Table 1).

2.2.2 Seismic impact analysis

It has shown that earthquakes can cause landslides and subsequent hazard chains (Fan et al., 2018; Wang et al., 2019). The study combined empirical relationships between earthquakes and landslides, drawing from data provided by the United States Geological Survey seismic database. A total of 720 seismic events with magnitudes exceeding 4, occurring within a 420 km radius centered on MLG, were extracted from the Chinese National Earthquake Science Data Center (http://data.earthquake.cn) and the global seismic database (https://www.usgs.gov/) published by the United States Geological Survey (Keefer, 1984). These data sets were then employed to examine the impact of historical seismic events on the stability of soil formations within the study area.

2.2.3 Drought analysis

The SPI can accomplish the simultaneous assessment of drought because the observed precipitation during each time period is considered a statistical sample from a larger parent population. For computational accuracy, Guttman (1999) recommends a minimum of 50 years of precipitation data. Observational data need not be preprocessed into the desired aggregations; available software codes (such as available from the National Drought Mitigation Center) accept monthly input data [which is usually the minimum

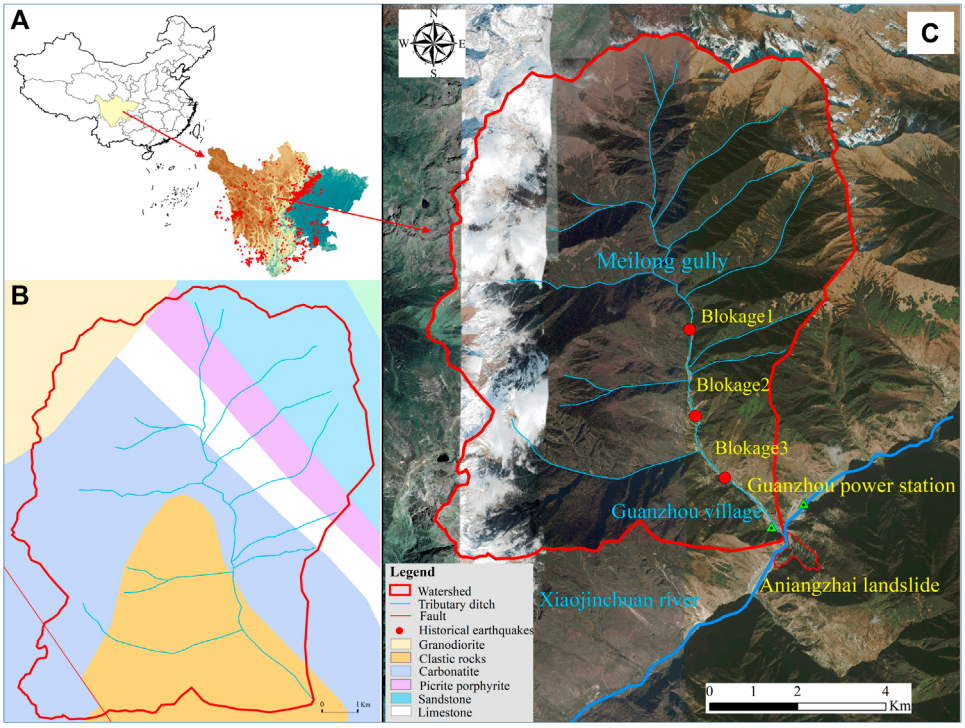

FIGURE 1
Regional setting of the study area. **(A)** The study area is located at the high mountain canyon area of western Sichuan Province and Historical earthquakes with a magnitude greater than 4.0 since 1970 within 420 km centered on MLG. **(B)** Geological background. **(C)** High-resolution remote sensing images of the MLG.

FIGURE 2
On-site soil sampling.

interval frequency used to study drought (i.e., the 1-month SPI)] and aggregate it to desired intervals. Precipitation is known to follow an asymmetric frequency distribution, with the bulk of the occurrences at low values, and a rapidly decreasing likelihood of larger precipitation totals. There are a number of such positively-skewed analytical distributions, six of which were analyzed for SPI computations by Guttman (1999). The distribution for the SPI adopted by McKee et al. (1995), as well as the NDMC, is the incomplete gamma distribution. We first collected historical rainfall data from 1950 to 2020 and then utilized the SPI algorithm in MATLAB to analyze the input data, ultimately obtaining 1-month SPI value.

The 1-month Standardized Precipitation Index (SPI) was employed in this study to evaluate the area's drought and humidity before the disaster (Seiler et al., 2002). The SPI categorizes drought into seven grades based on the values: SPI ≥2 for extremely wet, 1.5 < SPI ≤1.99 for severely wet, 1.0 < SPI ≤1.49 for moderately wet, −0.99 < SPI ≤0.99 for near normal, −1.49 < SPI ≤ −1.0 for moderately dry, −1.99 < SPI ≤ −1.5 for severely dry, and SPI ≤ −2 for extremely dry (McKee et al., 1995). Data were

TABLE 1 Formula tables for debris flow dynamic parameters.

Parameter	Formula	Parameters in the formula
Density	$\gamma_c = G/V$	γ_c is the debris flow density; G is the soil sample weight; V is the soil sample volume
Velocity	$V_c = (M_c/a)H_c^{2/3}I_c^{1/2}$	V_c ais the velocities of the debris flow; I_c is the hydraulic gradient of the debris flow section of the gully obtained by on-site measurement; M_c are the roughness coefficients for debris flows; H_c is the hydraulic radius (m) defined as the mud depth of the debris flow section obtained by on-site measurement. a is the drag coefficient; φ is the increase coefficient; γ_w is the density of water (kg/m^3) determined as 1,000 kg/m^3; γ_s is the density of the solid material (kg/m^3) determined as 2,650 kg/m^3.
	$a = (1+\varphi\gamma_s)^{1/2}$	
	$\varphi = (\gamma_c - \gamma_w)/(\gamma_s - \gamma_c)$	
Discharge	$Q_C = A_{SC} \times V_C$	Q_C is the peak discharge of debris flow (m^3/s), where A_{sc} denotes the area of the cross-section (m^2), and V_C is the average velocity at the cross-section (m/s).

obtained from the National Meteorological Data Center of China (http://data.cma.cn/).

3 Characteristics of MLG hazard chain

3.1 Overview of MLG hazard chain

Based on on-site investigations and related information, MLG experienced a minor mudslide during the flood season of 1952, but it was of a relatively small scale and resulted in no casualties. However, on 17 June 2020, around 3:20 a.m., MLG witnessed a large-scale, infrequent catastrophic mudslide with a recurrence period estimated to be approximately one event in 70 years. This event had significant consequences, including the destruction of an 18 km stretch of National Highway G350 from Xiaojin to Danba (Figures 3A, B). Numerous houses in Guanzhou Village were flooded, resulting in the unfortunate loss of two lives in the area, and it affected 175 villagers from 48 households (as depicted in Figure 3C). Additionally, the substantial material carried by the mudslide in MLG directly obstructed the XJC River, leading to the formation of a barrier lake (Figure 3D). The constriction of the river increased its scouring capacity, destabilizing the ANZ paleolandslide (Figure 3E), and the barrier lake eventually breached, causing an outburst flood that inundated upstream properties and farmland. Simultaneously, this event affected the water discharge of the Guanzhou hydroelectric power station, resulting in a total economic loss estimated at 85 million yuan.

3.2 Calculation results of debris flow motion parameters

3.2.1 Density

As historical monitoring data for debris flow in MLG were lacking, determining the density of the debris flow relied on two methods: on-site preparation of debris flow samples and a table checking method. The weights of the debris flow samples were measured during field investigations, with reference to contemporary debris flows. A total of 12 sets of field experiments were conducted across the upper, middle, and lower reaches of the watershed, as well as in the accumulation area. Additionally, insights from villagers who had witnessed the debris flow events were considered for comparison. This collective data contributed to the calculation of bulk weight parameters for the 12 groups of debris flow samples (as outlined in Table 2). The results revealed an average bulk density of 1.769 g/cm^3 for the MLG debris flow, signifying it as a viscous debris flow.

3.2.2 Velocity and discharge

Discharge serves as a direct indicator of debris flow size and is a pivotal design parameter for prevention and control projects. Calculating debris flow velocity is essential for determining debris flow discharge, which is typically accomplished through morphology investigation methods. Detailed velocity and discharge calculations for six sections within the MLG debris flow are provided in Table 3. The findings reveal that at the mouth of MLG, the debris flow velocity is 4.78 m/s, and the debris flow discharge is 860.40 m^3/s. These results unequivocally classify the MLG debris flow as a large-scale debris flow disaster (as outlined in Table 3).

4 Results

4.1 Causal mechanism and evolution processes of MLG debris flow hazard chain

4.1.1 Rainstorm triggered the initiation of the hazard chain in MLG

Between 23:40 on 16 June 2020, and 02:30 on 17 June 2020, a heavy rainstorm impacted most townships in Danba County, with a particularly intense, short-term heavy rainfall episode occurring in the area of Banshanmen Township. Local interviews with villagers revealed that the debris flow in MLG began at approximately 3:00 p.m. on June 17. While the debris flow initiation was somewhat delayed compared to the onset of rainfall, it was generally consistent with the period of maximum rainfall intensity. According to the contour rainfall map found in the "Small and medium-sized watersheds in Sichuan Province rainstorm and flood calculation manual," the average 24-h maximum rainfall in the Banshanmen area of Danba County is typically around 40 mm. In the mountainous regions of Sichuan, debris flows are often triggered by rainfall amounts of approximately 48–50 mm for a single rainfall event (or 8–12.2 mm for a 10-min rainfall, or 0.8–1.2 mm for a 1-min rainfall). On June 17, the cumulative rainfall in Danba County reached only 16.2 mm (Figure 4). However, data from the county reported a 24-h rainfall of 59.9 mm in the mountainous area of Bawang Township, situated on the rear side of MLG, at 2:00 a.m.

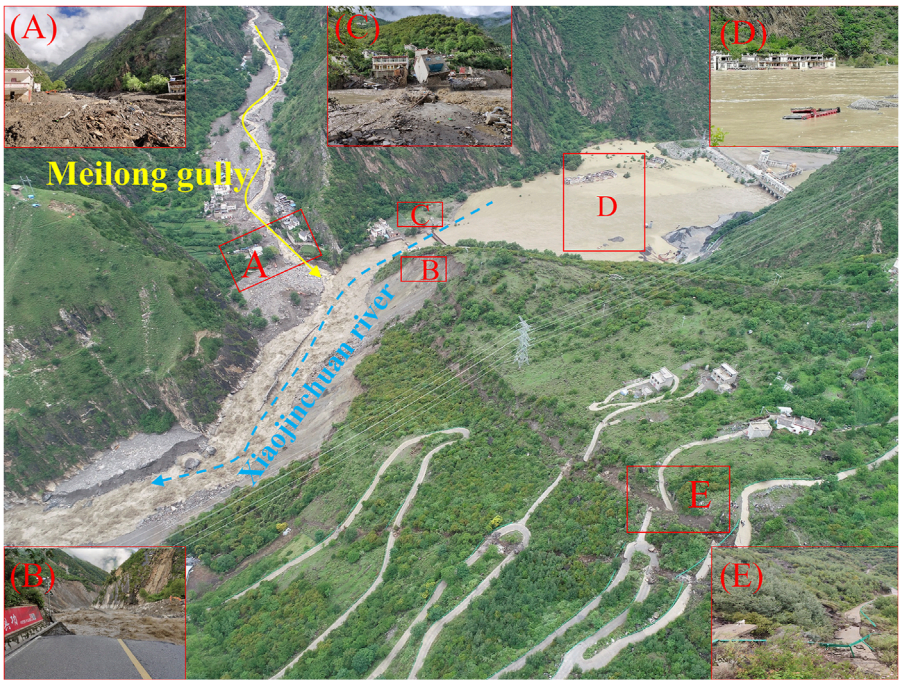

FIGURE 3
MLG debris flow hazard chain. **(A)** MLG debris flow destroyed and buried the houses in the gully mouth **(B)** MLG debris flow destroyed the national highway G350 and The debris flow destroyed the national highway G350 and triggered the resurrection of ANZ landslide on the opposite bank. **(C)** Outburst flood destroyed houses along the coast. **(D)** Barrier lake inundated houses and vehicles. **(E)** Cracks at the back end of landslide ANZ landslide.

on June 17. Based on established rainfall criteria, this amount classifies as a heavy rainstorm. Therefore, it can be inferred that the immediate trigger of the hazard chain was the short-term intense rainfall (Fiorillo and Wilson, 2004; Chen et al., 2006; Ni et al., 2014; Guo et al., 2016).

4.1.2 Earthquakes, landforms, and lithology provided abundant source of materials for the initiation of the hazard chain

The distinctive geomorphology and tectonics of the study area form a favorable foundation for the development of the MLG hazard chain. Situated within a typical alpine canyon landscape, this region lies at the structural heart of the Qinghai-Tibet-Yunnan-Burma-Indonesia tectonic complex. It encompasses north-south trending structures prevalent in the Sichuan-Yunnan region and arc-shaped structures in the Xiaojin-Jintang composite area. The study area is adjacent to the Xianshuihe fault belt, characterized by intense tectonic activity and the development of structural fractures, resulting in frequent regional seismic events. Extensive research has demonstrated that the aftermath of earthquakes significantly amplifies the availability of loose material sources in affected regions (Fan et al., 2019). Earthquakes disrupt the original integrity of rock and soil structures, thereby facilitating the transition of weathered surface rock masses into potential debris flow sources (Keefer, 1984). Moreover, they lower the rainfall threshold required to initiate instability in these material sources. The study area has witnessed several strong earthquakes in its history, with seven earthquakes identified as having significant impacts on soil stability, based on earthquake data acquired from the China Earthquake Data Center (http://data.earthquake.cn) from 1 January 1970, to 17 June 2020. Notably, the most recent three seismic events, including the 8.0 magnitude Wenchuan earthquake in 2008, the

TABLE 2 Calculation table of debris flow density.

Sample	Weight (kg)	Volume (m^3)	Density (g/cm^3)
PJ1	13.04	7.5	1.739
PJ2	14.92	8.46	1.764
PJ3	15.2	8.6	1.767
PJ4	11.13	6.25	1.781
PJ5	13.22	7.32	1.806
PJ6	12.5	6.95	1.799
PJ7	14.23	7.85	1.813
PJ8	14.82	8.25	1.796
PJ9	14.51	8.15	1.780
PJ10	14.35	8.35	1.719
PJ11	14.23	8.1	1.757
PJ12	14.51	8.5	1.707

TABLE 3 Calculation of debris flow velocity and discharge of different cross-sections.

Position	Mud depth H_c (m)	Channel gradient I_c	Roughness coefficient 1/n	Velocity V_c (m/s)	Area (m^2)	Discharge (m^3/s)
S1	4.50	0.229	3.7	4.88	99.00	483.12
S2	12.80	0.220	2.5	6.35	153.60	975.36
S3	5.20	0.214	3.7	5.53	208.00	1150.24
S4	4.80	0.213	3.7	5.62	168.00	944.16
S5	4.60	0.212	3.7	5.45	161.00	877.45
S6	4.55	0.213	3.7	4.78	180.00	860.40

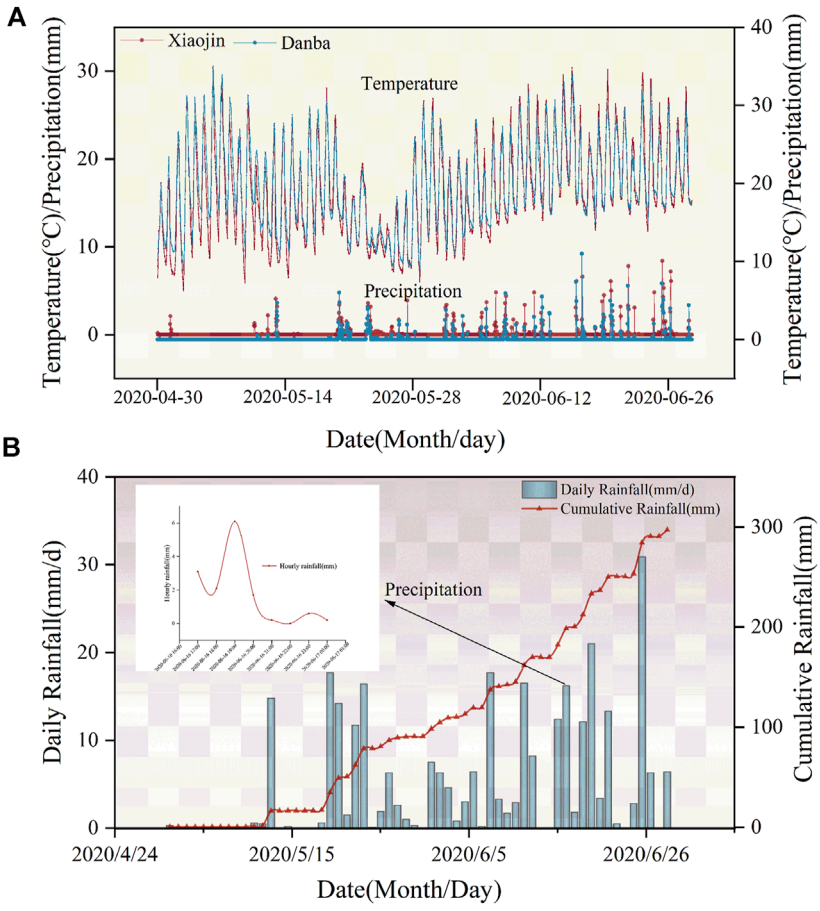

FIGURE 4
Daily rainfall data of two adjacent rainfall stations nearby **(A)** Daily rainfall at Xiaojin and Danba Station **(B)** Daily rainfall at MLG.

7.0 magnitude Lushan earthquake in 2013, and the 6.3 magnitude Kangding earthquake in 2014, all had substantial effects on material source stability within the watershed. These earthquakes have provided the necessary material sources for debris flows and subsequent hazard chains (Figure 5). Past research (Ding et al., 2020; Wang et al., 2022a; Liu et al., 2022; Yan et al., 2023) has indicated that in major tectonic zones, debris flows often concentrate in areas containing metamorphic rock formations like slate, phyllite, gneiss, mixed granite, and quartzite, along with softer rock formations such as mudstone, shale, marl, coal-bearing series, and Quaternary deposits. According to geological maps and field investigations, the exposed strata in the study area predominantly comprise granitic metamorphic rocks, slate, and phyllite from the Weiguan Group of the Devonian System (Dwg), in addition to lose deposits from

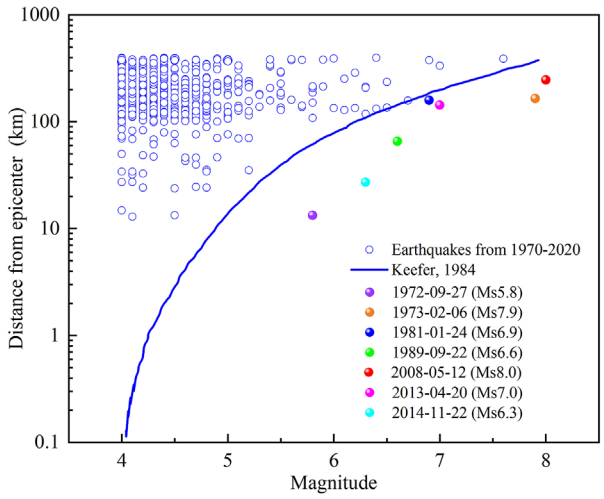

FIGURE 5
Historical earthquake impact map around the MLG.

the Quaternary System. These geological characteristics, coupled with the impact of earthquakes, establish a solid foundation for the initiation of the hazard chain.

Field investigations show that loose solid material sources are very abundant in the MLG watershed, and the main types of material sources in MLG are landslide-type material sources, channel accumulation-type material sources, slope-type material sources and freeze-thaw-type material sources (Figure 6). A total of 212 material sources points were investigated in the study area. Preliminary statistics reveal that there are 112 landslide accumulation solid material source points in the watershed, with a total volume of 7709.73×10^4 m^3 and a potential dynamic storage volume of 1285.48×10^4 m^3 that may contribute to debris flow activities. There are 28 channel accumulation solid material source points, with a total volume of 503.14×10^4 m^3 and a dynamic storage volume of 175.68×10^4 m^3. Additionally, there are 48 slope erosion solid material source points, with a total volume of 101.11×10^4 m^3 and a dynamic storage volume of 10.45×10^4 m^3. There are 22 freeze-thaw material source points, with a total volume of 1731.17×10^4 m^3 and a dynamic storage volume of 141.72×10^4 m^3. Furthermore, there are 2 artificial waste slag disposal points, with a total volume of 0.71×10^4 m^3 and a dynamic storage volume of 0.19×10^4 m^3. In total, the loose solid material sources amount to 10045.86×10^4 m^3, with a potential dynamic storage volume of 1613.52×10^4 m^3 that may contribute to debris flow activities (Table 4).

The material sources found in the MLG watershed exhibit distinct characteristics and distribution patterns, each playing a role in debris flow dynamics under the influence of heavy rainfall and floods. Landslide accumulation material sources are concentrated points of distribution and actively participate in debris flow movement as they are scoured and entrained by heavy rainfall and floods. Channel material sources primarily originate from the accumulation of the original channel, often evolving from landslide material sources and slope erosion material sources. Slope erosion material sources are predominantly located in the surface residual slope deposits on both sides of various tributaries and primarily contribute to debris flow activities through soil erosion. Freeze-thaw material sources, on the other hand, are typically situated near the snowline, representing frozen and thawed collapse material sources located on the thin ridges adjacent to the snowline. The abundance of loose solid materials in the MLG watershed is of paramount importance in understanding the occurrence of large-scale, low-frequency debris flow events, aligning with findings from prior research in this field (Bovis and Jakob, 1999; McGuire et al., 2017).

4.1.3 Multiple cycles of dry-wet cycle in the early stages facilitated the occurrence of the hazard chain in MLG

Multiple dry-wet cycle events in the early stages provided the triggering material source for the outbreak of the MLG debris flow in the hazard chain, promoting the occurrence of the hazard chain. The Standardized Precipitation Index (SPI) can be used to assess drought characteristics and determine the cycle of drought events (Schneider et al., 2013; Keyantash, 2021; Pei et al., 2023). The 1-month SPI results obtained from the analysis of the long-duration rainfall in the study area over a period of 70 years, from 1950 to 2020 (Figure 7), it indicates that at least 27 dry-wet cycle events occurred in MLG watershed prior to the outbreak of the debris flow. Among these 27 dry-wet cycle events, there were 6 moderately dry-moderately wet events, 8 extremely dry-moderately wet events, 1 extremely dry-severely wet event, 8 severely dry-moderately wet events, 3 moderately dry-extremely wet events and 1 severely dry-extremely wet event. A severe drought with an SPI value of −1.69 occurred in March 2020, the year of the MLG debris flow. Subsequently, a short but intense rainfall event on 17 June 2020 triggered the formation of the MLG debris flow. Dry-wet cycle events cause cracking of the soil surface, enhanced physical weathering, and reduced soil strength by altering the structure of the soil mass (Chiarle et al., 2007; Wei et al., 2010; Chen et al., 2014; Yang et al., 2023a), thus making it more susceptible to damage under heavy rainfall conditions. Therefore, the preceding occurrence of 27 moderate or higher intensity dry-wet cycle events significantly facilitated the outbreak of large-scale debris flow in MLG by reducing the strength of the soil mass and increasing the number of potential triggering material sources.

4.1.4 The cascading failure of large-scale landslides and channel-blocking boulders amplified the scale of the hazard chain

In order to analyze the evolution process of the MLG debris flow discharge, six cross-sections were selected (Tables 2, 3) within the MLG watershed, and the density, velocity, and discharge of the debris flow at each cross-section were calculated. Additionally, based on remote sensing images and field investigation, three major landslide dam breach points were identified within the MLG channel, namely, the Dongfengpengzi (DFPZ) landslide, Danyi village (DYV) landslide, and Meilong village (MLV) landslide (Figure 1). The discharge of the debris flow after the breach of these three dam points were as follows: No. 1 discharge was 483.12 m^3/s, No. 2 discharge was 975.36 m^3/s and No. 3 discharge was 1150.24 m^3/s (Figure 8). These three landslide dam breach points represent a sharp increase in the debris flow discharge during the evolution process. DFPZ landslide is located on the left bank slope of the main channel of MLG, approximately 3.43 km away from the outlet. The channel at

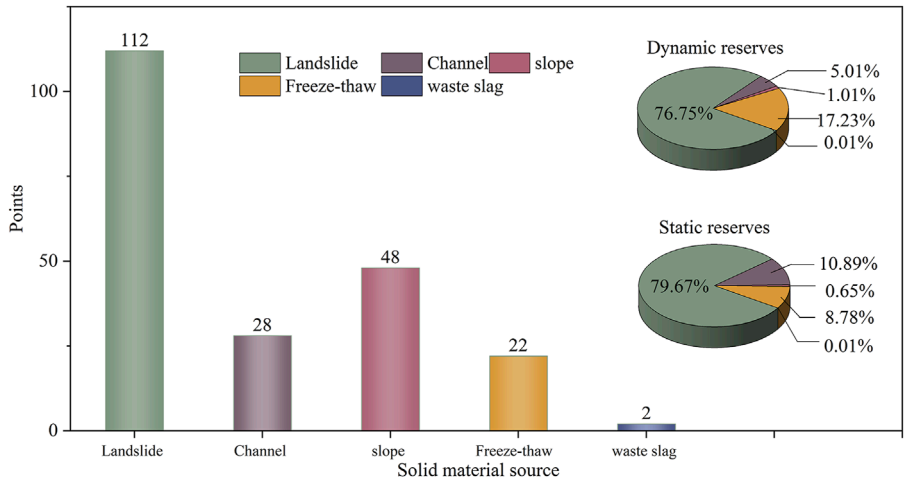

FIGURE 6
Typical material sources in MLG.

TABLE 4 Typical material sources statistics.

Solid material source	Points	Volume (10^4m^3)	Dynamic reserve (10^4m^3)
Landslide	112	7709.74	1285.48
Channel	28	503.14	175.68
slope	48	101.11	10.45
Freeze-thaw	22	1731.17	141.72
waste slag	2	0.71	0.19
Total	212	10045.86	1613.52

the foot of the slope is narrow, with a width of about 3 m–10 m, while its upstream channel has a width of about 40 m–80 m, with an average width of about 60 m. DYV landslide is situated on the right bank slope of the main channel of MLG, approximately 2.78 km away from the outlet. The channel at this location is narrow, with a width of about 3 m–9 m, and exhibits overall meandering with local blockages and clear traces of lateral erosion. MLV landslide is located on the right bank slope of the main channel of MLG, approximately 1.65 km away from the outlet. The channel at the foot of the slope is highly meandering, with a width of about 6 m–10 m, and boulders all over the ditch, and is scattered with boulders ranging from 3 m to 6 m in size. Its upstream channel is slightly wider, with an average width of about 15 m–20 m.

When the debris flow reaches the foot of the DFPZ landslide, the narrow channel and reduced cross-sectional area result in a rapid increase in flow velocity. The high-speed debris flow causes intense lateral erosion at the foot of the landslide. Additionally, continuous rainfall infiltration over a prolonged period weakens the stability of the DFPZ landslide. The intense lateral erosion leads to secondary sliding at the front edge of the landslide (Wang et al., 2022b; Ma et al., 2023), resulting in a blockage that accumulates loose material carried by the debris flow. Simultaneously, the increasing upstream water level and the accumulation of energy lead to the abrupt breaching of the landslide dam. As the debris flow moves towards the DYV landslide, the blockage effect further amplifies the flow velocity and discharge. This intensifies the erosion of the channel bed and banks, resulting in the unloading of the front edge of the DYV landslide to slide. Additionally, the direct impact of the debris flow at the channel diversion points lead to significant sliding at the front edge of the bank slope, causing a secondary blockage (Qiu et al., 2022). When the debris flow continues to move to the foot of MLV landslide, the narrowing of the channel results in a reduction in the cross-section, and an increase in flow velocity, enhancing the erosion process. Furthermore, the debris flow, which has already experienced the secondary blockage at DYV landslide, has its flow velocity and discharge multiplied several times, resulting in more intense erosion of the MLV landslide. This leads to extensive sliding at the front edge of the landslide, with a large number of debris and boulders occupying the channel, forming another blockage. The "6.17"MLG debris flow was significantly enhanced by the large-scale cascading blockage of the DFPZ landslide, DYV landslide, MLV landslide and the boulders in the channel, leading to a large amount of solid material being discharged at the outlet of the channel, triggering subsequent secondary hazard chains.

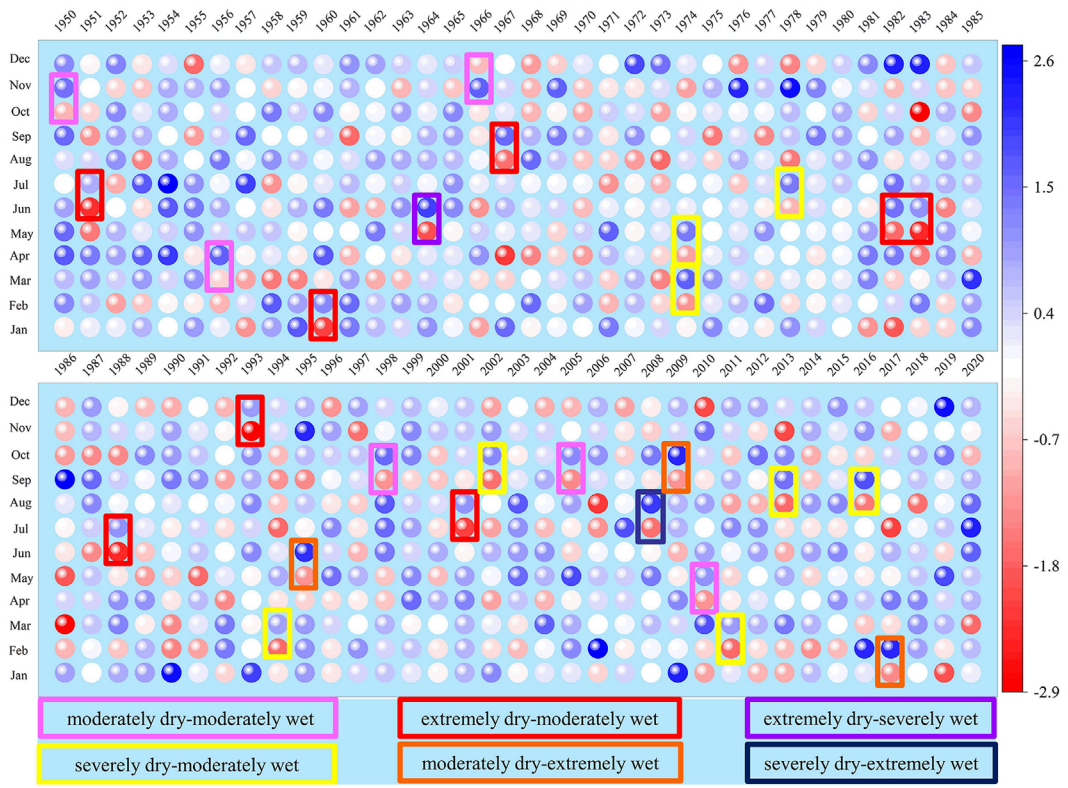

FIGURE 7
1-month SPI values in the study area over the period 1950-2020(Interpretation: SPI≥2, extremely wet; 1.5<SPI≤1.99, severely wet; 1.0<SPI≤1.49, moderately wet; −0.99<SPI≤0.99, near normal; −1.49<SPI≤−1.0, moderately dry; −1.99<SPI≤−1.5, severely dry; SPI≤−2, extremely dry).

4.2 Mitigation measures analysis of chain-breaking

The hazard chain is generally classified into four sections: the hazard pregnancy ring, the triggering ring, the evolution ring, and the damage ring. In the MLG watershed, lithology, geomorphology, pre-seismic activity and dry-wet cycle impacts provide the material and energy basis for the occurrence of the hazard chain, constituting the hazard pregnancy ring. Heavy rainfall as the triggering factor, representing the triggering ring. The amplification process of debris flows and the deformation process of landslides constitute the evolution. The resulting debris flows, landslides, barrier lakes and outburst floods form the damage ring.

Chain breaking refers to interrupting the development of the hazard chain at a certain link of the chain. For the MLG hazard chain, different chain breaking measures should be implemented in different rings (Figure 9). The MLG hazard chain is initiated by heavy rainfall, and the hazardous area is large in scope. It poses a major threat to the reconstructed National Highway G350 and vehicle operations through debris flow impact, siltation, and flood submergence, etc. and at the same time, threatens the lives and property of 99 individuals in 18 households at the gully mouth. So, breaking the hazard chain is necessary. Due to the huge amount of material sources in the MLG watershed, it is impractical to completely remove all debris flow sources. Therefore, engineering measures can be taken at the damage ring, such as constructing sediment retaining dams within debris flow channel, and establishing debris flow drainage canal at the gully mouth. Based on the sediment transport capacity of the XJC River segment, it is recommended to limit the debris flow discharge into the river to within 50,000 cubic meters per event to ensure the flood control and sediment transport capacity of the XJC River.

5 Discussion

The formation and amplification process MLG hazard chain are dominated by the material sources, and the increase in the amount of material sources can be influenced by strong regional tectonic activity and earthquakes (Figure 10). MLG watershed is located in the Sichuan-Yunnan north-south trending tectonic zone and the arc-shaped Xiaojin-Jintang tectonic zone, belonging to Tibetan-Yunnan-Burma-Indonesian tectonics. The tectonic system in the area is complex, with intense metamorphism, which favors the transformation of weathered surface rock masses into debris flow and landslide material sources. In addition, the study area and its neighboring regions experience frequent seismic activities, with multiple strong earthquakes have occurred in history. The latest strong earthquake to the time before the debris flow occurred was the 8.0 magnitude mega-earthquake that occurred on 12 May 2008 in Yingxiu Town, Wenchuan County. This earthquake had a

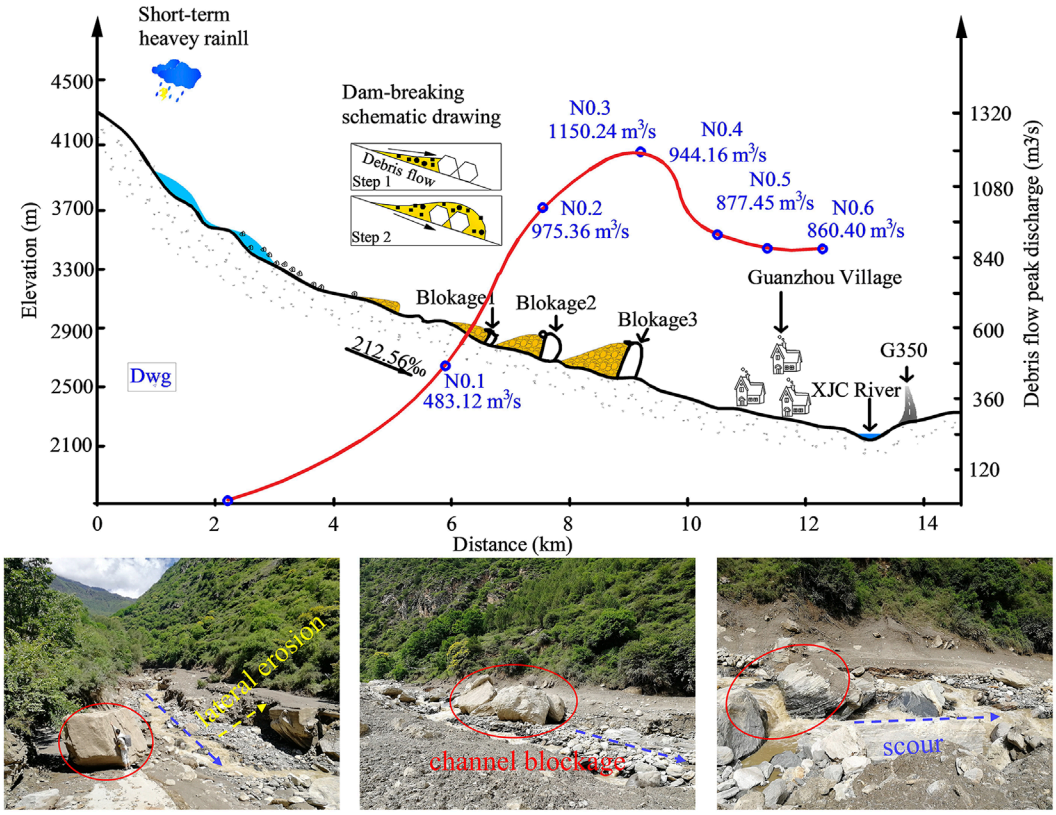

FIGURE 8
The discharge evolution process and photos of blockages of MLG debris flow.

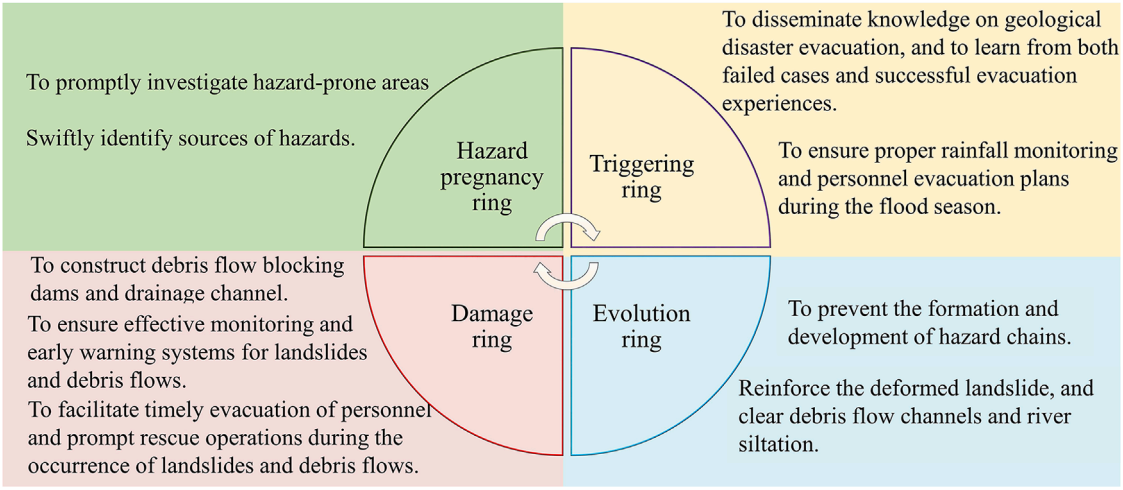

FIGURE 9
Suggestions on chain breaking measures in each link of hazard chain.

certain impact on the formation of material sources in the watershed, as an 8.0 magnitude earthquake can affect landslides up to a distance of 393 km (Delgado et al., 2011), while the study area is approximately 300 km away from the epicenter of the Wenchuan earthquake. Furthermore, previous research has indicated that the 2008 Wenchuan earthquake generated between 5 and 15 billion cubic meters of loose solid material within an area of 13,800 km^2 (Parker et al., 2011).

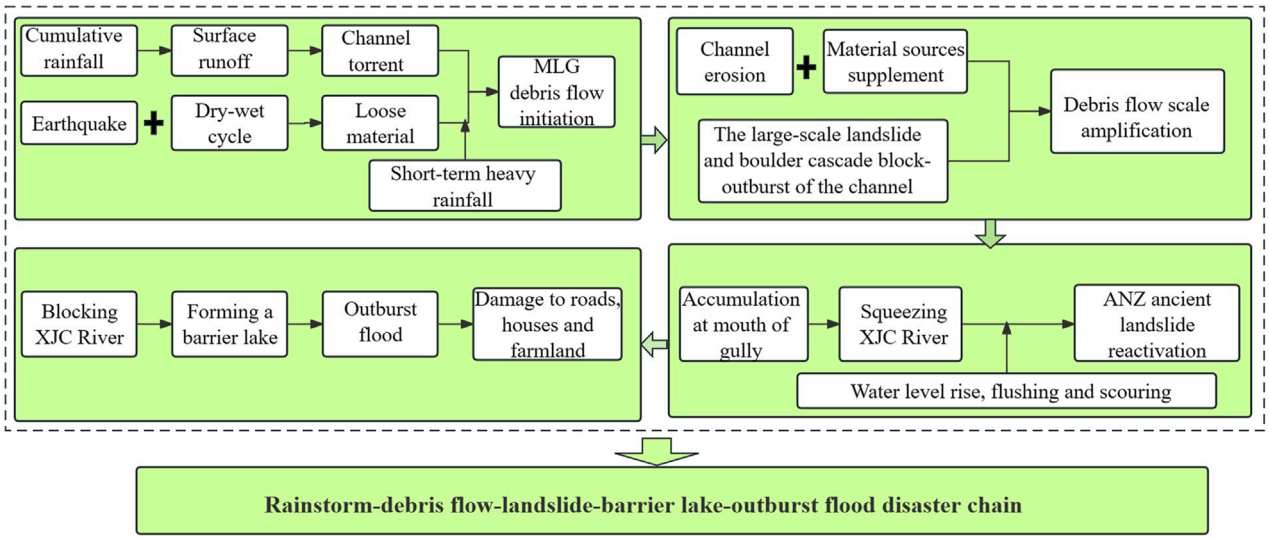

FIGURE 10
The whole process of MLG debris flow hazard chain.

Currently, the amount of loose solid material sources in the MLG watershed that may be involved in debris flow activities are estimated to be 1613.52×10^4 m^3. These sources are distributed in the main channel and various tributaries, but they do not all participate in debris flow activity simultaneously. Furthermore, not all loose solid material sources involved in a single debris flow activity event will be completely washed out of the debris flow channel and enter into the main river. First of all, the MLG watershed has a large area, and rainfall distribution cannot be completely uniform. There may be areas within the watershed where loose solid materials are present but do not meet the conditions for rainfall initiation or there may be no distribution of loose solid materials in areas of heavy rainfall. This rainfall distribution of the unevenness also determines the uneven participation of loose solid materials in debris flow activity. Secondly, not all loose solid materials in tributary channels can participate in debris flow activity in the main channel. With changes in channel slope and width, water-sediment separation can occur in certain sections, resulting in sediment accumulation in the channel. Therefore, the transformation of debris flow sources is a complex process (Yang et al., 2023c; Zhao et al., 2023), and the design of prevention and control engineering is mainly based on the historical records of debris flow disasters and the calculation results of previous debris flow characteristics.

In addition, the on-site investigation has revealed that the sliding of the avalanche deposits at the front edge of the ANZ landslide drove the collapse of the strongly weathered bedrock to form the accumulation at the foot of slope, creating the illusion of bedrock sliding. Salt efflorescence refers to the phenomenon where underground water containing soluble salts flows to the surface and, due to the decrease in atmospheric pressure and increase in temperature, the minerals precipitate and crystallize. Previous studies have shown that the shear strength of the soil decreases continuously after the precipitation of soluble salts, leading to slow deformation of the slope. The cyclic process of leaching and precipitation of soluble salts in groundwater ultimately results in the instability or reactivation of landslides (Zhang et al., 2020b). The boundary between the landslide deposits and the highly weathered bedrock in ANZ landslide is marked by the presence of salt efflorescence. Therefore, it can be inferred that this boundary represents the discharge point of the previous groundwater, and the lower part of the landslide deposit serves as the shear outlet of the landslide. The identification of the salt efflorescence outcrops can help to determine whether the ANZ landslide is characterized by local surface sliding or overall sliding, which is a guide for determining the morphologic characteristics of the blocked barrier dam and the formulation of hazard prevention and mitigation measures. Additionally, it provides new insights and references for understanding the mechanisms of landslide formation, identifying slope instability and the reactivation of paleolandslides in mountainous urban areas.

The MLG hazard chain and the formation of material sources for debris flows and landslides share similarities with other regions around the world that have experienced strong tectonic activity and earthquakes. For example, the 2011 Tohoku earthquake in Japan triggered numerous landslides and debris flows, leading to significant damage and loss of life (Mukunoki et al., 2016). In 2018, the Sulawesi earthquake in Indonesia triggered landslides that buried entire villages, causing widespread devastation (Watkinson and Hall, 2019; Zhao, 2021). In both cases, the formation of material sources for debris flows and landslides was influenced by the seismic activity. The impact of rainfall distribution on the participation of loose solid materials in debris flow activity is also a common factor in other regions. For instance, in the Himalayan region, the uneven distribution of rainfall and the presence of loose solid materials in steep slopes have led to frequent landslides and debris flows (Burtin et al., 2009; Das et al., 2022). In the Andes

Mountains, the combination of steep topography, intense rainfall, and the presence of loose sediments has resulted in frequent debris flows and landslides (Moreiras and Dal Pont, 2017; Angillieri et al., 2020). The role of salt efflorescence in influencing the stability of slopes and the cyclic process of leaching and precipitation of soluble salts leading to slow deformation is also a mechanism that may have relevance in other regions with similar geological and topographical characteristics. For example, in the Ebro Valley (NE Spain), the presence of salt efflorescence on slopes has been linked to the destabilization of slopes and the occurrence of landslides (Gutiérrez et al., 2023).

In conclusion, the MLG hazard chain and the mechanisms of debris flow and landslide formation share similarities with other regions around the world that have experienced strong tectonic activity, earthquakes, and intense rainfall. Studying international cases with similar geological and environmental characteristics could provide valuable insights for understanding and managing hazards related to debris flows, landslides, and slope instability in various parts of the world.

6 Conclusion

In order to investigate the triggering mechanism of landslide-debris flow hazard chain in mountainous urban areas, this study focuses on the hazard chain of MLG debris flow-ANZ landslide-barrier lake -outburst flood that occurred in Danba County, Sichuan Province, on 17 June 2020. Through on-site investigations, model calculations, rainfall analysis, seismic impact analysis, and drought index analysis, the characteristic parameters of the MLG hazard chain were obtained, the hazard pregnancy factors were analyzed, the triggering mechanism of the MLG hazard chain was revealed, and measures to break the hazard chain at different links were proposed. It is helpful to improve the early warning and forecasting system of urban monitoring in western Sichuan mountainous area and grasp the key direction of engineering prevention and control. The conclusions of our research are as follows:

(1) The low-frequency large-scale debris flow disaster in MLG, which occurred on 17 June 2020, has a recurrence interval of approximately 70 years, with an average density of 1.769 g/cm^3. The flow velocity of the debris flow at the outlet of the gully is 4.78 m/s, and the peak flow discharge is 860.40 m^3/s. The tremendous energy of the debris flow forms the basis for the destructive power of the hazard chain.

(2) The unique geomorphology and lithology of the study area provide favorable conditions for the occurrence of the hazard chain in MLG. Seven seismic events, including the Wenchuan 8.0 magnitude earthquake in 2008, have had a significant impact on the stability of the soil mass in the MLG watershed. The occurrence of the large-scale debris flow in MLG was facilitated by the occurrence of 27 moderate and above dry-wet cycle events in the previous period, which reduced the soil strength and increased the availability of material sources. Under the influence of internal and external dynamic forces such as earthquakes, drought, and rainfall, the structure of geotechnical bodies in the MLG watershed was continuously damaged, which accelerated the weathering and erosion of the geotechnical bodies and led to a significant increase in the amount of loose material sources in the watershed. The abundant loose solid material sources in the MLG watershed are the key factors contributing to the outbreak of this large-scale low-frequency debris flow.

(3) The MLG hazard chain is characterized by the presence of three large landslides, namely, DFPZ landslide, DYV landslide, and MLV Village landslide, along with the cascading blockage and breach caused by giant boulders within the channel. This has resulted in a 2.38-fold increase in the debris flow discharge within the 1.78 km-long channel, significantly enhanced the energy of the debris flow and leading to the ejection of a large amount of solid material from the outlet, triggering subsequent secondary disaster chains.

(4) The rainstorm-induced hazard chain in MLG is a complete composite geological hazard chain, forming a hazard chain of rainstorm, debris flow, landslide, barrier lake and outburst flood. For the hazard chain of MLG, chain-breaking measures are proposed at different links. It is recommended to take chain-breaking measures from the damage ring, strengthen the monitoring and early warning during flood season, and construct debris flow blocking dams and drainage canals.

While the specifics of hazard chains may vary across different geographic locations, the principles of hazard chain analysis and the importance of implementing chain-breaking measures are universally applicable. Therefore, our study also provides insights into the triggering mechanisms and characteristics of the MLG hazard chain, offering valuable lessons for similar hazard chains in other regions worldwide. Our findings contribute to the broader understanding of hazard chain dynamics and can inform disaster risk reduction strategies in other settings. The information about the casualties and destruction caused by the hazard chain serves as a reminder of the devastating impact of such disasters and underscores the urgency of proactive measures to mitigate their effects.

Data availability statement

The original contributions presented in the study are included in the article/Supplementary material, further inquiries can be directed to the corresponding author.

Author contributions

HS: Conceptualization, Investigation, Methodology, Software, Writing–original draft, Writing–review and editing. ZY: Conceptualization, Funding acquisition, Project administration, Supervision, Writing–original draft. GH: Investigation, Writing–review and editing. ST: Investigation, Writing–review and editing. MR: Writing–review and editing. JR: Data curation,

Investigation, Writing–original draft. YZ: Data curation, Investigation, Writing–review and editing.

Funding

The author(s) declare financial support was received for the research, authorship, and/or publication of this article. This study was funded by the National Natural Science Foundation of China (Grant No. 41861134008), the Muhammad Asif Khan academician workstation of Yunnan Province (Grant No. 202105AF150076), the Key R&D Program of Yunnan Province (Grant No. 202003AC100002), the General Program of basic research plan of Yunnan Province (Grant No. 202001AT070043). Youth Science Foundation of Henan Province (No. 232300420449).

Conflict of interest

The authors declare that the research was conducted in the absence of any commercial or financial relationships that could be construed as a potential conflict of interest.

Publisher's note

References

An, H. C., Ouyang, C. J., Wang, F. L., Xu, Q. S., Wang, D. P., Yang, W. B., et al. (2022). Comprehensive analysis and numerical simulation of a large debris flow in the Meilong catchment, China. *Eng. Geol.* 298, 106546. doi:10.1016/j.enggeo.2022.106546

Angillieri, M. Y. E., Perucca, L., and Vargas, N. (2020). Spatial and temporal analysis of debris flow occurrence in three adjacent basins of the western margin of Grande River: quebrada de Humahuaca, Jujuy, Argentina. *Geogr. Ann. Ser. a-Physical Geogr.* 102 (2), 83–103. doi:10.1080/04353676.2020.1744075

Bovis, M. J., and Jakob, M. (1999). The role of debris supply conditions in predicting debris flow activity. *Earth Surf. Process. Landforms* 24 (11), 1039–1054. doi:10.1002/(sici)1096-9837(199910)24:11<1039::Aid-esp29>3.0.Co;2-u

Burtin, A., Bollinger, L., Cattin, R., Vergne, J., and Nábelek, J. L. (2009). Spatiotemporal sequence of Himalayan debris flow from analysis of high-frequency seismic noise. *J. Geophys. Research-Earth Surf.* 114, 15. doi:10.1029/2008jf001198

Chen, H., Dadson, S., and Chi, Y. G. (2006). Recent rainfall-induced landslides and debris flow in northern Taiwan. *Geomorphology* 77 (1-2), 112–125. doi:10.1016/j.geomorph.2006.01.002

Chen, N. S., Lu, Y., Zhou, H. B., Deng, M. F., and Han, D. W. (2014). Combined impacts of antecedent earthquakes and droughts on disastrous debris flows. *J. Mt. Sci.* 11 (6), 1507–1520. doi:10.1007/s11629-014-3080-7

Chen, X. Q., Cui, P., Li, Y., and Zhao, W. Y. (2011). Emergency response to the Tangjiashan landslide-dammed lake resulting from the 2008 Wenchuan Earthquake, China. *Landslides* 8 (1), 91–98. doi:10.1007/s10346-010-0236-6

Chen, X.-z., and Cui, Y.-f. (2017). The formation of the Wulipo landslide and the resulting debris flow in Dujiangyan City, China. *J. Mt. Sci.* 14 (6), 1100–1112. doi:10.1007/s11629-017-4392-1

Cheng, J. D., Su, R. R., and Wu, H. L. (2000). "Hydrometeorological and site factors contributing to disastrous debris-flows in Taiwan," in 2nd International Conference on Debris-Flow Hazards Mitigation, LEIDEN (A a Balkema Publishers), 583–592.

Chiarle, M., Iannotti, S., Mortara, G., and Deline, P. (2007). Recent debris flow occurrences associated with glaciers in the Alps. *Glob. Planet. Change* 56 (1-2), 123–136. doi:10.1016/j.gloplacha.2006.07.003

Cui, P., Su, F., Zou, Q., Chen, N., and Zhang, Y. (2015). Risk assessment and disaster reduction strategies for mountainous and meteorological hazards in Tibetan Plateau. *Chin. Sci. Bull.* 60 (32), 3067–3077. doi:10.1360/N972015-00849

Das, R., Phukon, P., and Singh, T. N. (2022). Understanding the cause and effect relationship of debris slides in Papum Pare district, Arunachal Himalaya, India. *Nat. Hazards* 110 (3), 1735–1760. doi:10.1007/s11069-021-05010-2

Deganutti, A. M., Marchi, L., and Arattano, M. (2000). "Rainfall and debris-flow occurrence in the Moscardo basin (Italian Alps)," in 2nd International Conference on Debris-Flow Hazards Mitigation, LEIDEN (A a Balkema Publishers), 67–72.

Delgado, J., Garrido, J., Lopez-Casado, C., Martino, S., and Pelaez, J. A. (2011). On far field occurrence of seismically induced landslides. *Eng. Geol.* 123 (3), 204–213. doi:10.1016/j.enggeo.2011.08.002

Ding, M., Huang, T., Zheng, H., and Yang, G. (2020). Respective influence of vertical mountain differentiation on debris flow occurrence in the Upper Min River, China. *Sci. Rep.* 10 (1), 11689. doi:10.1038/s41598-020-68590-2

Fan, X., Domènech, G., Scaringi, G., Huang, R., Xu, Q., Hales, T. C., et al. (2018). Spatio-temporal evolution of mass wasting after the 2008 Mw 7.9 Wenchuan earthquake revealed by a detailed multi-temporal inventory. *Landslides* 15 (12), 2325–2341. doi:10.1007/s10346-018-1054-5

Fan, X. M., Scaringi, G., Korup, O., West, A. J., van Westen, C. J., Tanyas, H., et al. (2019). Earthquake-induced chains of geologic hazards: patterns, mechanisms, and impacts. *Rev. Geophys.* 57 (2), 421–503. doi:10.1029/2018rg000626

Fiorillo, F., and Wilson, R. C. (2004). Rainfall induced debris flows in pyroclastic deposits, Campania (southern Italy). *Eng. Geol.* 75 (3-4), 263–289. doi:10.1016/j.enggeo.2004.06.014

Flentje, P. N., Chowdhury, R. N., and Tobin, P. (2000). "Management of landslides triggered by a major storm event in Wollongong, Australia," in 2nd International Conference on Debris-Flow Hazards Mitigation, LEIDEN (A a Balkema Publishers), 479–487.

Guo, J., Cui, P., Qin, M., Wang, J., Li, Y., and Wang, C. (2022). Response of ancient landslide stability to a debris flow: a multi-hazard chain in China. *Bull. Eng. Geol. Environ.* 81 (7), 273. doi:10.1007/s10064-022-02745-5

Guo, J., Wang, J., Li, Y., and Yi, S. (2021). Discussions on the transformation conditions of Wangcang landslide-induced debris flow. *Landslides* 18 (5), 1833–1843. doi:10.1007/s10346-021-01650-4

Guo, X., Cui, P., Li, Y., Ma, L., Ge, Y., and Mahoney, W. B. (2016). Intensity–duration threshold of rainfall-triggered debris flows in the Wenchuan Earthquake affected area, China. *Geomorphology* 253, 208–216. doi:10.1016/j.geomorph.2015.10.009

Gutiérrez, F., Sevil, J., and Migon, P. (2023). Landslides in the Remolinos gypsum escarpment (NE Spain): controls imposed by stratigraphy, fluvial erosion, and interstratal salt dissolution. *Landslides* 20 (10), 2075–2093. doi:10.1007/s10346-023-02090-y

Guttman, N. B. (1999). Accepting the standardized precipitation index: a calculation algorithm. *J. Am. Water Resour. Assoc.* 35 (2), 311–322. doi:10.1111/j.1752-1688.1999.tb03592.x

Hu, G. S., Huang, H., Chen, N. S., Somos-Valenzuela, M., Yang, Z. Q., and He, J. (2022). Largest scale successful real-time evacuation after the Wenchuan earthquake in China: lessons learned from the Zengda gully giant debris flow disaster. *Geomatics Nat. Hazards Risk* 13 (1), 19–34. doi:10.1080/19475705.2021.2000045

Hu, K., Zhang, X., You, Y., Hu, X., Liu, W., and Li, Y. (2019). Landslides and dammed lakes triggered by the 2017 Ms6.9 Milin earthquake in the Tsangpo gorge. *Landslides* 16 (5), 993–1001. doi:10.1007/s10346-019-01168-w

Iotti, A., and Simoni, A. (1997). "A debris flow triggered by a soil slip on Elba Island, Italy," in 1st International Conference on Debris-Flow Hazards Mitigation - Mechanics, Prediction, and Assessment, NEW YORK (Amer Soc Civil Engineers), 54–63.

Keefer, D. K. (1984). LANDSLIDES CAUSED BY EARTHQUAKES. *Geol. Soc. Am. Bull.* 95 (4), 406–421. doi:10.1130/0016-7606(1984)95<406:Lcbe>2.0.Co;2

Keyantash, J. (2021). "Indices for meteorological and hydrological drought," in *Hydrological aspects of climate change*. Editors A. Pandey, S. Kumar, and A. Kumar (Singapore: Springer Singapore), 215–235.

Liu, D., Cui, Y., Jin, W., Wang, H., and Tang, H. (2023a). Channel aggradation triggered by dam failure amplifies the damage of outburst flood. *Landslides* 20 (7), 1343–1362. doi:10.1007/s10346-023-02026-6

Liu, Z. J., Qiu, H. J., Zhu, Y. R., Liu, Y., Yang, D. D., Ma, S. Y., et al. (2022). Efficient identification and monitoring of landslides by time-series InSAR combining single- and multi-look phases. *Remote Sens.* 14 (4), 1026. doi:10.3390/rs14041026

Liu, Z. Q., Yang, Z. Q., Chen, M., Xu, H. H., Yang, Y., Zhang, J., et al. (2023b). Research hotspots and Frontiers of mountain flood disaster: bibliometric and visual analysis. *Water* 15 (4), 673. doi:10.3390/w15040673

Ma, S. Y., Qiu, H. J., Zhu, Y. R., Yang, D. D., Tang, B. Z., Wang, D. Z., et al. (2023). Topographic changes, surface deformation and movement process before, during and after a rotational landslide. *Remote Sens.* 15 (3), 662. doi:10.3390/rs15030662

Mani, P., Allen, S., Evans, S. G., Kargel, J. S., Mergili, M., Petrakov, D., et al. (2023). Geomorphic process chains in high-mountain regions-A review and classification approach for natural hazards assessment. *Rev. Geophys.* 61 (4), 51. doi:10.1029/2022rg000791

McGuire, L. A., Rengers, F. K., Kean, J. W., and Staley, D. M. (2017). Debris flow initiation by runoff in a recently burned basin: is grain-by-grain sediment bulking or en masse failure to blame? *Geophys. Res. Lett.* 44 (14), 7310–7319. doi:10.1002/2017gl074243

McKee, T. B., Doesken, N. J., Kleist, J., and Amer Meteorol, S. O. C. (1995). "Drought monitoring with multiple time scales," in 9th Conference on Applied Climatology/75th AMS Annual Meeting, BOSTON (Amer Meteorological Soc), 233–236.

Moreiras, S. M., and Dal Pont, I. P. V. (2017). "Climate change driving greater slope instability in the central Andes," in 4th World Landslide Forum (CHAM: Springer International Publishing Ag), 191–197.

Mukunoki, T., Kasama, K., Murakami, S., Ikemi, H., Ishikura, R., Fujikawa, T., et al. (2016). Reconnaissance report on geotechnical damage caused by an earthquake with JMA seismic intensity 7 twice in 28 h, Kumamoto, Japan. *Soils Found.* 56 (6), 947–964. doi:10.1016/j.sandf.2016.11.001

Ni, H. Y., Zheng, W. M., Song, Z., and Xu, W. (2014). Catastrophic debris flows triggered by a 4 July 2013 rainfall in Shimian, SW China: formation mechanism, disaster characteristics and the lessons learned. *Landslides* 11 (5), 909–921. doi:10.1007/s10346-014-0514-9

Ning, L., Hu, K., Wang, Z., Luo, H., Qin, H., Zhang, X., et al. (2022). Multi-hazard chain reaction initiated by the 2020 Meilong debris flow in the dadu river, southwest China. *Front. Earth Sci.* 10. doi:10.3389/feart.2022.827438

Parker, R. N., Densmore, A. L., Rosser, N. J., de Michele, M., Li, Y., Huang, R., et al. (2011). Mass wasting triggered by the 2008 Wenchuan earthquake is greater than orogenic growth. *Nat. Geosci.* 4 (7), 449–452. doi:10.1038/ngeo1154

Pei, Y. Q., Qiu, H. J., Yang, D. D., Liu, Z. J., Ma, S. Y., Li, J. Y., et al. (2023). Increasing landslide activity in the Taxkorgan River Basin (eastern Pamirs Plateau, China) driven by climate change. *Catena* 223, 106911. doi:10.1016/j.catena.2023.106911

Pérez, F. L. (2001). Matrix granulometry of catastrophic debris flows (December 1999) in central coastal Venezuela. *CATENA* 45 (3), 163–183. doi:10.1016/S0341-8162(01)00149-7

Qiu, H. J., Zhu, Y. R., Zhou, W. Q., Sun, H. S., He, J. Y., and Liu, Z. J. (2022). Influence of DEM resolution on landslide simulation performance based on the Scoops3D model. *Geomatics Nat. Hazards Risk* 13 (1), 1663–1681. doi:10.1080/19475705.2022.2097451

Rahman, M. A., and Konagai, K. (2017). Substantiation of debris flow velocity from super-elevation: a numerical approach. *Landslides* 14 (2), 633–647. doi:10.1007/s10346-016-0725-3

Schneider, D. P., Deser, C., Fasullo, J., and Trenberth, K. E. (2013). Climate data guide spurs discovery and understanding. *Eos, Trans. Am. Geophys. Union* 94 (13), 121–122. doi:10.1002/2013EO130001

Scott, K. M. (2000). "Precipitation-triggered debris-flow at Casita Volcano, Nicaragua: implications for mitigation strategies in volcanic and tectonically active steeplands," in 2nd International Conference on Debris-Flow Hazards Mitigation, LEIDEN (A a Balkema Publishers), 3–13.

Seiler, R. A., Hayes, M., and Bressan, L. (2002). Using the standardized precipitation index for flood risk monitoring. *Int. J. Climatol.* 22 (11), 1365–1376. doi:10.1002/joc.799

Wang, F., Fan, X., Yunus, A. P., Siva Subramanian, S., Alonso-Rodriguez, A., Dai, L., et al. (2019). Coseismic landslides triggered by the 2018 Hokkaido, Japan (Mw 6.6), earthquake: spatial distribution, controlling factors, and possible failure mechanism. *Landslides* 16 (8), 1551–1566. doi:10.1007/s10346-019-01187-7

Wang, J., Cui, Y. F., Choi, C. E., and Ng, C. W. W. (2018). "The effect of climate change on alpine mountain hazards chain: a case study in tianmo ravine, Tibet, China," in 8th International Congress on Environmental Geotechnics (ICEG) (SINGAPORE: Springer-Verlag Singapore Pte Ltd), 461–470.

Wang, L., Chang, M., Le, J., Xiang, L., and Ni, Z. (2022a). Two multi-temporal datasets to track debris flow after the 2008 Wenchuan earthquake. *Sci. Data* 9 (1), 525. doi:10.1038/s41597-022-01658-y

Wang, L. Y., Qiu, H. J., Zhou, W. Q., Zhu, Y. R., Liu, Z. J., Ma, S. Y., et al. (2022b). The post-failure spatiotemporal deformation of certain translational landslides may follow the pre-failure pattern. *Remote Sens.* 14 (10), 2333. doi:10.3390/rs14102333

Watkinson, I. M., and Hall, R. (2019). Impact of communal irrigation on the 2018 Palu earthquake-triggered landslides. *Nat. Geosci.* 12(11), 940–945. doi:10.1038/s41561-019-0448-x

Wei, W., Chen, L. D., Fu, B. J., and Chen, J. (2010). Water erosion response to rainfall and land use in different drought-level years in a loess hilly area of China. *Catena* 81 (1), 24–31. doi:10.1016/j.catena.2010.01.002

Yan, Y., Hu, S., Zhou, K., Jin, W., Ma, N., and Zeng, C. (2023). Hazard characteristics and causes of the "7.22" 2021 debris flow in Shenshuicao gully, Qilian Mountains, NW China. *Landslides* 20 (1), 111–125. doi:10.1007/s10346-022-01992-7

Yang, Z. Q., Chen, M., Zhang, J., Ding, P., He, N., and Yang, Y. (2023a). Effect of initial water content on soil failure mechanism of loess mudflow disasters. *Front. Ecol. Evol.* 11. doi:10.3389/fevo.2023.1141155

Yang, Z. Q., Wei, L., Liu, Y. Q., He, N., Zhang, J., and Xu, H. H. (2023b). Discussion on the relationship between debris flow provenance particle characteristics, gully slope, and debris flow types along the karakoram highway. *Sustainability* 15 (7), 5998. doi:10.3390/su15075998

Yang, Z. Q., Xiong, J. F., Zhao, X. G., Meng, X. R., Wang, S. B., Li, R., et al. (2023c). Column-hemispherical penetration grouting mechanism for Newtonian fluid considering the tortuosity of porous media. *Processes* 11 (6), 1737. doi:10.3390/pr11061737

Yang, Z. Q., Zhao, X. G., Chen, M., Zhang, J., Yang, Y., Chen, W. T., et al. (2023d). Characteristics, dynamic analyses and hazard assessment of debris flows in niumiangou valley of wenchuan county. *Appl. Sciences-Basel* 13 (2), 1161. doi:10.3390/app13021161

Zhang, L., Xiao, T., He, J., and Chen, C. (2019). Erosion-based analysis of breaching of Baige landslide dams on the Jinsha River, China, in 2018. *Landslides* 16 (10), 1965–1979. doi:10.1007/s10346-019-01247-y

Zhang, X., Xue, R., Wang, M., Yu, Z., Li, B., and Wang, B. (2020a). Field investigation and analysis on flood disasters due to Baige landslide dam break in Jinsha River. *Adv. Eng. Sci.* 52 (5), 89–100.

Zhang, Z. L., Zeng, R. Q., Meng, X. M., Zhang, Y., Zhao, S. F., Ma, J. H., et al. (2020b). Effect of soluble salt loss via spring water on irrigation-induced landslide deformation. *Water* 12 (10), 2889. doi:10.3390/w12102889

Zhao, B. (2021). Landslides triggered by the 2018 Mw 7.5 Palu supershear earthquake in Indonesia. *Eng. Geol.* 294, 106406. doi:10.1016/j.enggeo.2021.106406

Zhao, X. G., Yang, Z. Q., Meng, X. R., Wang, S. B., Li, R., Xu, H. H., et al. (2023). Study on mechanism and verification of columnar penetration grouting of time-varying Newtonian fluids. *Processes* 11 (4), 1151. doi:10.3390/pr11041151

Zhong, Q. M., Chen, S. S., Wang, L., and Shan, Y. B. (2020). Back analysis of breaching process of Baige landslide dam. *Landslides* 17 (7), 1681–1692. doi:10.1007/s10346-020-01398-3

frontiers | Frontiers in Earth Science

TYPE Original Research
PUBLISHED 20 June 2024
DOI 10.3389/feart.2024.1355767

OPEN ACCESS

EDITED BY
Wen Nie,
Jiangxi University of Science and Technology, China

REVIEWED BY
Rui Pang,
Dalian University of Technology, China
Mahmood Ahmad,
University of Engineering and Technology, Peshawar, Pakistan

*CORRESPONDENCE
Hui Xu,
xuhui@zstu.edu.cn

RECEIVED 14 December 2023
ACCEPTED 04 June 2024
PUBLISHED 20 June 2024

CITATION
Li Q, Tong Y-Y, Wang J-N and Xu H (2024), Seismically-induced permanent displacements of slopes using 3D Nested Newmark method.
Front. Earth Sci. 12:1355767.
doi: 10.3389/feart.2024.1355767

Seismically-induced permanent displacements of slopes using 3D Nested Newmark method

Qiang Li[1], Yan-Yang Tong[1], Jin-Nan Wang[1,2] and Hui Xu[2]*

[1]School of Civil Engineering and Architecture, Keyi College of Zhejiang Sci-Tech University, Shaoxing, China, [2]School of Civil Engineering and Architecture, Zhejiang Sci-Tech University, Hangzhou, China

The Newmark method is a classic method for evaluating the permanent displacements of a slope under seismic loads. This study aims at proposing a three-dimensional nested Newmark method (3D-NNM) in the framework of the kinematic theorem of limit analysis. The classical three-dimensional rotational failure mechanism is discretized into a series of nested rotating wedges, each of which is subjected to a corresponding yield acceleration determined by employing the work rate balance, and each of which produces relative displacements under seismic excitations when it exceeds the yield acceleration. The total permanent displacement profile is further obtained by integration of the relative displacements from the slope toe to the slope crest. The obtained results show that the proposed 3D-NNM can effectively evaluate the permanent displacement profile of slopes under earthquakes, and the proposed 3D-NNM improves the Leshchinsky's 2D nested Newmark method by 30.7%; the obtained total horizontal displacement at the slope middle height reduces with the number of nested blocks, but increases with the increasing of the slope-width-to-height ratios. Besides, the traditional Newmark method with a single sliding block tends to overestimate the permanent displacements of slope under seismic shakings.

KEYWORDS

seismic slopes, Newmark displacements, kinematic theorem of limit analysis, three-dimensional, nested Newmark method

1 Introduction

Accurate assessment of slope deformations is a classical problem in geotechnical engineering, since it is key to assess the slope stability for resilience design in earthquake-prone regions (Du and Wang, 2013; Zhang et al., 2023; Zhang et al., 2024). The methods used for assessing seismically-induced permanent displacements of slopes include numerical simulations with finite element method and the Newmark-based sliding block approach (Jibson, 2011).

Numerical simulations are able to provide a realistic response regarding stresses and strains of real-world slopes during earthquakes but subjected to large computational burden (Du et al., 2023; Li et al., 2023). Because of its advantage of easy to use and practical rationality, the Newmark-based sliding block approach has been widely used to assess the seismic permanent displacements of a variety of engineering structures (Newmark, 1965; Saygili and Rathje, 2008; Leshchinsky, 2018; Mathews et al., 2019; Song et al., 2019; Zhou et al., 2019; Zheng et al., 2020). The Newmark s approach originally proposed by (Newmark, 1965) is able to give the permanent displacement of a pre-assumed translational rigid block with a linear sliding surface in a slope once the input acceleration of a seismic

wave exceeds the yield acceleration of the slope at the limit equilibrium condition which is determined by the pseudo-static method. The Newmark-based sliding block approach was modified by many researchers by, for example, building empirical formulas that relate the Newmark displacement with the ground motion (e.g., Arias intensity) and the critical acceleration of a slope (Hsieh and Lee, 2011; Chousianitis et al., 2014; Zhu et al., 2024), accounting for the model uncertainty and soil variability in the probabilistic framework (Yegian et al., 1991; Du et al., 2018; Li et al., 2020; Pan et al., 2021), and extending the translational rigid block to a rotational rigid block with a curved sliding surface (Nadukuru and Michalowski, 2013). The rotational failure mechanism with a curved sliding surface of slopes under dynamic loadings was observed in centrifugal model tests (Kutter and James, 1989) and in shake table model tests (Wartman et al., 2005).

However, the traditional single-block Newmark approach suffers from the drawback of neglection of the presence of multiple shear zones or regions of dispersed shear movement inside the slope under dynamic loadings that were observed in physical model tests (Kutter and James, 1989; Wartman et al., 2005). Besides, the traditional Newmark method fails to consider the complex constitutive properties and the time-varying properties of the soil materials under seismic loads (Pang et al., 2018b; Pang et al., 2021; Xu et al., 2023; Lu et al., 2024). The theoretical deficiency may result in bias prediction on seismic slope deformations using the traditional single-block Newmark approach. In order to address this issue, Leshchinsky (Leshchinsky, 2018) proposed a new nested Newmark approach to assess the permanent displacements of slopes subjected to earthquakes, based on the builds upon the well-accepted Newmark sliding block approach. In the proposed nested Newmark approach, the sliding block is discretized by a series of nested critical failure wedges, each yielding a critical yield acceleration. The proposed nested Newmark approach has the benefit of considering multiple shear zones or regions of dispersed shear movements of a slope under seismic loadings. The conceptual nested Newmark approach attract significant attention in the geotechnical community, and many authors published subsequent articles (Song et al., 2019; Zhou et al., 2019; Zheng et al., 2020). Zheng et al. (Zheng et al., 2020) extended the Nested Newmark method from the limit equilibrium framework to the upper-bound limit analysis framework and studied the influences of soil dynamic responses (including slope height, soil shear wave velocity and input ground motion) on the permanent Newmark displacement of slopes. Song et al. (Song et al., 2019) proposed a multi-block sliding approach to calculate the permanent Newmark displacement of slopes by considering a series of rigid blocks and the interactions between two neighbouring sliding blocks. They found that the single-block Newmark method produces unconservative estimates of permanent displacements of a shallow sliding mass when a deep-seated sliding subsequently occurs in a slope subjected to earthquakes. Zhou et al. (Zhou et al., 2019) incorporated the tensile strength cut-off into the Nested Newmark method and studied the seismic slope permanent displacements in the light of the kinematical approach of limit analysis. They found that neglecting the tensile strength of soils may underestimate the permanent displacements of slopes subjected to an earthquake. The aforementioned researches extended the nested Newmark approach and provided valuable academic contribution to seismic displacement assessments of slopes during earthquakes. However, these researches failed to include the three-dimensional (3D) effect of a slope when assessing the permanent displacements using the Newmark approach. In real-word scenario, slope failure often exhibits three-dimensional feature (Michalowski and Drescher, 2009; Gao et al., 2013; Liu Y. et al., 2023). Three-dimensional stability analysis of slopes has attracted great attention in academia (Chen et al., 2023; Dai et al., 2023; Liu W. et al., 2023). This study aims to fill this gap. Three-dimensional displacement analysis of slopes subjected to seismic loads is investigated by using the Nested Newmark method.

This paper aims at proposing a three-dimensional nested Newmark method (3D-NNM) in the framework of the kinematic theorem of limit analysis. The second section presents the nested 3D rotational failure mechanism, together with the formulation of the yield acceleration and the relative displacement of each block. The 3D-NNM is compared with the original Nested Newmark method of Leshchinsky (Leshchinsky, 2018) in the third section, which is followed by performing parametric analysis on checking the influences of the number of nested blocks, the slope-width-to-height ratios, the peak ground acceleration and the slope inclination angle. This paper finally ends up with a conclusion in the last section.

2 Proposed 3D Nested Newmark method

It is practically necessary to assess and monitor geotechnical structure deformations under seismic loadings, which attract great attentions from researchers (Mi et al., 2023; Zhao et al., 2024). The Nested Newmark method, based on the classical Newmark single sliding method, originally proposed by Leshchinsky (Du et al., 2023), considers a two-dimensional translational failure model of a simple homogeneous slope at the ultimate limit state under a seismic excitation. In the Nested Newmark method (Du et al., 2023), the moving body with a linear sliding surface is discretized into multiple nested sliding wedges, each of which is subjected to a constant seismic yield acceleration assessed in the framework of limit equilibrium method. The original Nested Newmark method (Du et al., 2023) provides a prototype to assess post-earthquake slope movements, no matter what kind of failure mechanisms are involved. Generally, the original Nested Newmark method have four main procedures (Du et al., 2023): (1) discretizing the sliding body into a series of nested sub-bodies based on a given failure model; (2) evaluating the seismic yield acceleration of each nested body by using the pseudo-static method; (3) calculating the relative velocity of each nested body by employing the input of a given acceleration time history and the time-dependent exceedance of a yield acceleration at the given time, and obtaining the relative discplacement of each nested body by integrating the relative velocity over time increments; (4) assessing the cumulative displacement profile at the given time t by integrating the relative displacements along the slope height from the slope toe to the slope crest upwards. This paper aims to extend the Nested Newmark method to incorporate the three-dimensional rotational failure mechanism in the framework of the upper-bound limit analysis method. These four basic procedures are introduced below.

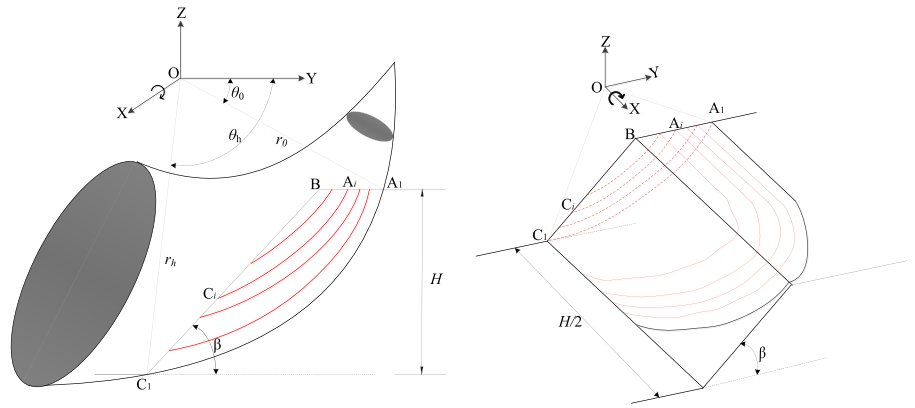

FIGURE 1
Nested 3D rotational failure mechanism.

2.1 Nested 3D rotational failure mechanism

Figure 1 gives a schematic representation of a three-dimensional rotational failure mechanism proposed by Michalowski and Drescher (Xu et al., 2023) in a homogeneous soil slope subjected to the seismic shakings at the ultimate limit state. The slope inclination is represented by the angle β; the slope height and width are denoted respectively by H and B. The sliding soils are presumed to rotate around the horizontal axis OX with an angular velocity ω. The failure of homogeneous soils is characterized by Mohr-Column yield criterion whose shear strength is represented by the internal friction angle φ and the soil cohesion c. The soil unit weight is denoted by γ. The 3D rotational failure mechanism is composed of a 3D curved horn body and a plane-strain insert. The 3D curved horn body is split in half along its longitudinal symmetry plane, between which the plane-strain body is inserted. The plane-strain body is distinguished from the three-dimensional rotation body, when the slope width becomes large, which makes the three-dimensional analysis results reduce to two-dimensional analysis. Readers are referred to Michalowski and Drescher (Xu et al., 2023) for the details of constructing the three-dimensional failure mechanism.

The 3D rotational failure mechanism (Xu et al., 2023) is kinematically admissible on the condition that it obeys the plastic flow rule associated with the Mohr-Column yield criterion of soils. This requires that the geometrical shape of 3D rotational failure mechanism in the longitudinal symmetry plane is defined by two logarithmic spirals, the below one of which represents the sliding surface (see A_1C_1 in Figure 1). The logarithmic spiral of A_1C_1 is formulated as,

$$r = r_0 e^{(\theta-\theta_0)\tan\varphi} \tag{1}$$

where r represents the radius of A_1C_1 to the rotational center O, the angle θ is measured from the horizontal plane, as sketched in Figure 1.

In the proposed 3D nested Newmark method, the sliding body bounded by the critical sliding surface A_1C_1 is discretized into N nested blocks, each of which is bounded by the sliding curved surface A_iC_i in the longitudinal symmetry plane, see Figure 1. For the i-th nested rotating block, the sliding surface A_iC_i in the longitudinal symmetry plane starts at the left hand at the point A_{i-1} on the slope crest and ends above the point C_{i-1} on the slope face, ensuring that nested sliding 3D body does not overlap. The profile in the longitudinal symmetry plane of the sliding curved surface AiCi is a logarithmic spiral whose rotational center may be different from the one of A_1C_1. It should note that the thickness of the sliding body bounded by the sliding curved surface $A_{i-1}C_{i-1}$ and the sliding curved surface A_iC_i tend to become infinitely small as the number of nested blocks become extremely large. This may enhance the predictive accuracy but cause a high computational burden in the proposed 3D nested Newmark method.

2.2 Seismic yield acceleration

Making reference to Nadukuru and Michalowski (Du et al., 2018), the pseudo-static approach is firstly used to evaluate the critical seismic acceleration associated with the critical 3D curved sliding surface (the first nested body) in the framework of the upper-bound limit analysis. Based on the upper-bound limit analysis method, an upper-bound estimation of the seismic acceleration can be obtained by using the work balance equation, for which the external work rates are equal to the internal energy dissipations,

$$W_\gamma^i + kW_s^i = D^i \tag{2}$$

where W_γ^i represents the work rates of gravity with respect to the i-th 3D failure mechanism defined by the sliding curved surface A_iC_i; W_s^i is the work rates of seismic forces with respect to the i-th 3D failure mechanism, and k is the horizontal seismic acceleration coefficient; D^i represents the internal energy dissipations along the curved surface A_iC_i. The details of calculating the three terms in Eq. 1 can be found in Nadukuru and Michalowski (Du et al., 2018). The upper-bound estimation of the seismic acceleration coefficient $k_y{}^i$ can be determined by minimizing k using Eq. 1 in terms of the position of the sliding curved surface A_iC_i.

Once the critical seismic acceleration coefficient of the first nested body is determined, the critical seismic acceleration coefficient $k_y{}^i$ for each nested sliding body defined by the sliding

curved surface A_iC_i can be determined following the same procedure presented above.

2.3 Nested Newmark cumulative displacements

Once the seismic acceleration kt from the acceleration-time history exceeds its critical value $k_y{}^i$ of the i-th nested sliding 3D body, the soil mass tends to rotate around the rotating center of the associated critical failure mechanism. At this moment, the work balance equation does not hold any more. The rotation results in the inertial moment of the nested sliding body with the angular acceleration $\ddot{\Omega}$. The inertial moment M_s^i of the i-th nested body induced by the angular acceleration $\ddot{\Omega}_i$ is expressed in Eq. (3),

$$M_s^i = \left(I_G{}^i + m^i l^i\right)\ddot{\Omega}_i \tag{3}$$

where m^i is the mass of the i-th rotating nested body, and l^i is the distance between the rotation axis and the mass center of the i-th rotating nested body; $I_G{}^i$ is the mass moment of inertia with respect to the axis passing through the mass center. Thus, when the seismic acceleration k_t exceeds its critical value $k_y{}^i$, the moment balance for the i-th nested sliding 3D body can be formulated as,

$$W_\gamma^i + k_t W_s^i = D^i + \left(I_G{}^i + m^i l^i\right)\ddot{\Omega}_i \tag{4}$$

With Eqs 1–4, the angular acceleration $\ddot{\Omega}_i$ can be obtained as,

$$\ddot{\Omega}_i = \frac{W_s^i}{I_G{}^i + m^i l^i}\cdot\left(k_t - k_y{}^i\right) \tag{5}$$

The rotation angle of the i-th rotating nested 3D body, Ω_i, can be obtained by double-integration with respect to time for which the angular velocity is greater than zero. The horizontal displacement $u_y{}^i$ at the ending position C_i on the slope surface can be further formulated in Eq. (6):

$$u_y{}^i = r_0{}^i e^{\left(\theta_h{}^i - \theta_0{}^i\right)\tan\varphi}\sin\theta_h{}^i \iint_t \ddot{\Omega}_i dtdt \tag{6}$$

in which $\theta_0{}^i$, $\theta_h{}^i$, $r_0{}^i$ are geometrical parameters that determine the position of the sliding surface A_iC_i, as sketched in Figure 1. Substitution of Eq. 5 into Eq. 6 leads to,

$$u_y{}^i = \frac{r_0{}^i e^{\left(\theta_h{}^i - \theta_0{}^i\right)\tan\varphi}\sin\theta_h{}^i W_s^i}{\left(I_G{}^i + m^i l^i\right)} \iint_t \left(k_t - k_y{}^i\right)dtdt \tag{7}$$

The horizontal seismic acceleration k_t in Eq. 7 is time-dependent. It is assumed that the critical acceleration $k_y{}^i$ of the i-th nested sliding 3D body is constant during the seismic shaking. In nested Newmark method, the total cumulative horizontal displacement at the given time t of the i-th nested sliding block is obtained by integrating along the slope height form the slope toe to the i-th nested sliding surface upwards. The total horizontal displacement u_y at the given time t of the nested sliding block is given by Eq. (8),

$$u_y = \int_0^H u_y{}^i dt \tag{8}$$

TABLE 1 Model parameters for comparisons.

Slope geometry	Values
Heigh (H)	20.0 m
Inclination angle (β)	45.0°
B/H	2.0–10.0
Soil properties	
Unit weight (γ)	20.0 kN/m3
Cohesion (c)	15.0 kPa
Friction angles (φ)	34.0°

3 Comparisons

In order to validate the proposed Nested Newmark method using 3D rotational failure mechanism, it is compared with the original Nested Newmark method of Leshchinsky (Du et al., 2023). Since that original Nested Newmark method of Leshchinsky (Du et al., 2023) considers a two-dimensional translational failure model, the ratio of slope width to its height is set to change from 2.0 to 10.0 in this study, which is large enough to allow the 3D failure mechanism reduce to 2D analysis. The model parameters regarding slope geometry and soil properties used in this paper are listed in Table 1. In the calculations, the nested blocks, which are evenly-spaced, are set to 150 in this section. The acceleration time history records of 1999 Chi-Chi earthquake, station TCU072-000 are taken for estimating post-earthquake slope deformations, which are also used in Leshchinsky (Du et al., 2023) and plotted in Figure 2.

Figure 3 presents the relative displacement profiles along slope height provided by the proposed 3D nested Newmark method and by Leshchinsky (Du et al., 2023). It is observed both in the proposed 3D-NNM method and in Leshchinsky's 2D model that the relative displacements decrease from the slope base towards the slope crest, and are close to zero above the slope height midpoint. This means that the slope above the slope height midpoint does not produce relative deformations, and its final deformations is purely caused by the sliding of underlying nested blocks. For example, the slope relative displacements, estimated by the proposed 3D-NNM method for the case of B/H being 5.0, increase from 0.05 m at the slope height of 5.0 m–0.22 m at the slope base. Besides, it is interesting to see that the relative horizontal displacements along the slope height of the Leshchinsky's 2D nested Newmark method tends to be bigger than the solutions estimated by the proposed 3D nested Newmark method.

Figure 4 presents the total horizontal permanent displacement profiles along slope height estimated by the proposed 3D-NNM method and given by the Leshchinsky's 2D model (Du et al., 2023). The solution of the classical single-sliding block Newmark method is also plotted in the figure for a comparison. In contrast to the relative displacements, the final permanent displacements estimated both by the proposed method and by Leshchinsky (Du et al., 2023) increase from the slope base towards the slope crest, and

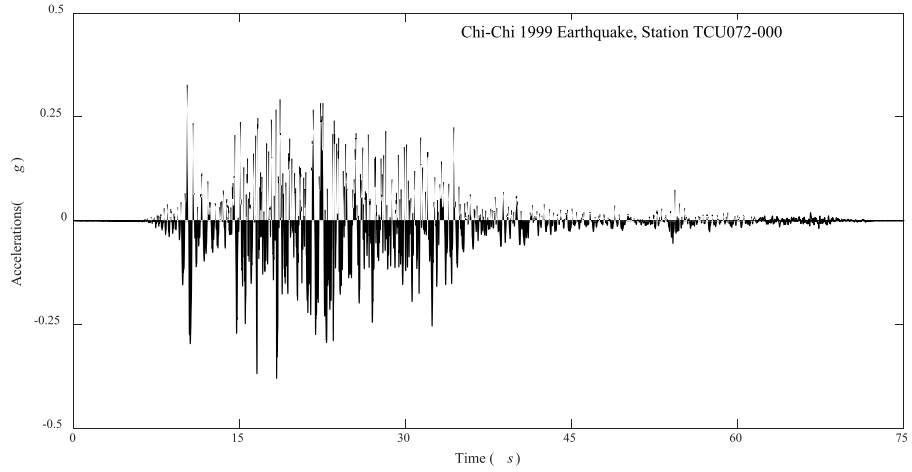

FIGURE 2
Acceleration time history records of 1999 Chi-Chi earthquake, station TCU072-000.

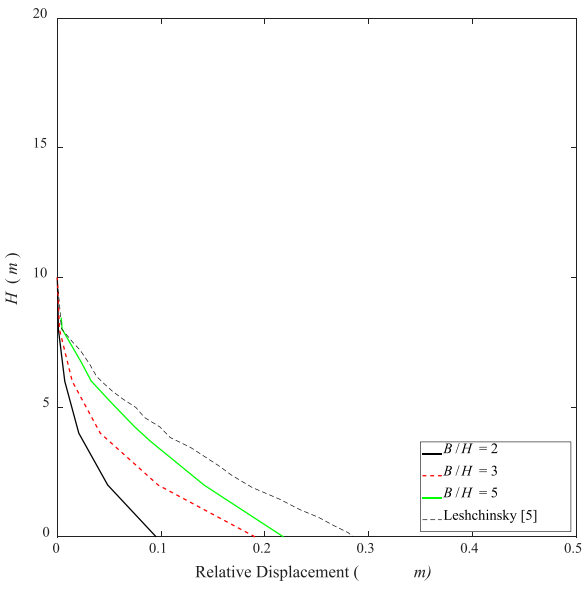

FIGURE 3
Relative horizontal displacement profiles along slope height for the two models.

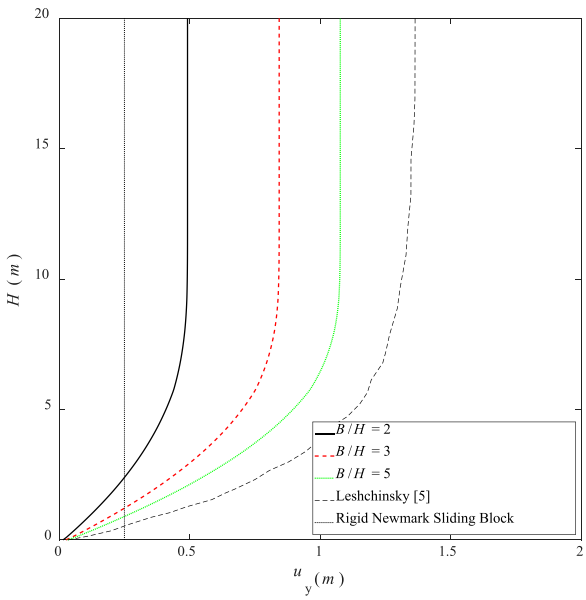

FIGURE 4
The total permanent displacement profiles along slope height for the two models.

tends to remain stable above the slope height midpoint. The maximum total horizontal permanent displacement estimated by the Leshchinsky's 2D nested Newmark method (Du et al., 2023) is around 1.34 m, while it reaches 0.50 m when B/H = 2.0 and 1.08 m when B/H = 5.0 for the proposed 3D nested Newmark method. This indicates that the Leshchinsky's 2D nested Newmark method may overestimate the post-earthquake deformation profile of slopes. The proposed 3D nested Newmark method improves the Leshchinsky's 2D nested Newmark method by 30.7%, due to the fact that the proposed method yields a rigorous upper-bound estimation to the post-earthquake deformations. This divergence is due to the fact that the proposed 3D-NNM assumes a three-dimensional velocity field while Leshchinsky's 2D model (Du et al., 2023) takes a translational velocity field. The finding agrees well with the statement that 2D analysis of slope stability delivers more conservative results compared with 3D analysis, which is well-known in the geotechnical community. Besides, the horizontal permanent displacement estimated by the classical single-sliding block Newmark method is only 0.25 m, which is smaller than the proposed 3D-NNM. This means that the traditional Newmark method with a single sliding block tends to underestimate the permanent displacements of slope under seismic shakings.

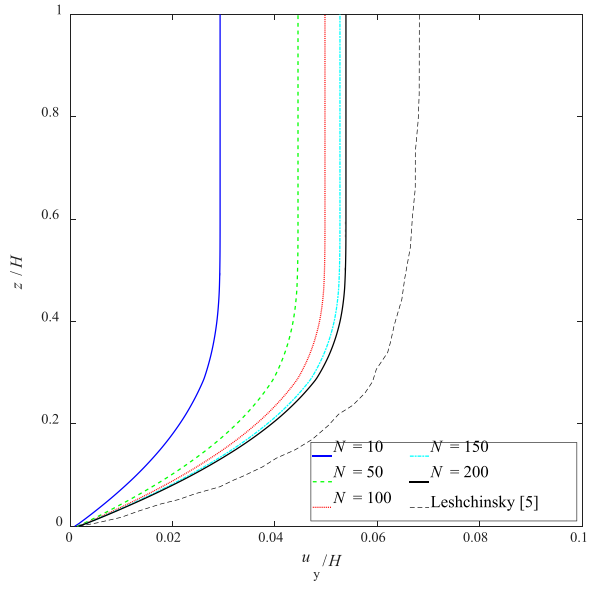

FIGURE 5
Influences of the number of nested blocks on total horizontal permanent displacement profiles.

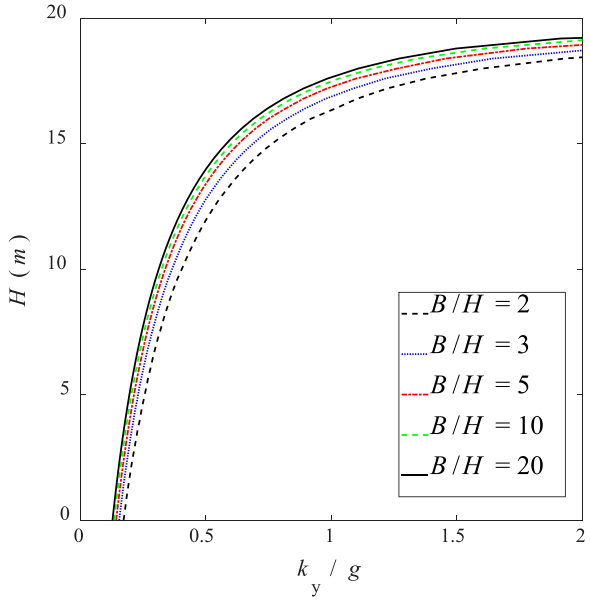

FIGURE 6
Influences of B/H ratio on the seismic yield acceleration profiles.

4 Parametric analysis

4.1 Influence of the number of nested blocks

This section discusses the influence of the number of nested blocks on the total Newmark displacement estimated by the proposed method. Figure 5 shows the profiles of the total horizontal displacements along the slope height for the number of nested blocks ranging between 10 and 200. It is seen that the number of nested blocks has a large influence on the estimated profiles of the total horizontal displacements along the slope height, which increases with the number of nested blocks. For example, the maximum total horizontal displacement at the slope crest is approximately 0.58 m for N = 10, and slowly converges around 1.08 m for N = 200, increasing by 86.2%. However, it should note that the computational burden is positively correlated with the number of nested blocks; the computational cost is around 3 min for the case of N = 10, but increases to around 20 min for the case of N = 200, on a desktop computer with a CPU of Core (TM) i5-12600K, 3.69 GHz. This means that the computational accuracy of the permanent displacements with more nested blocks is at the expense of high computational burden. Thus, in this paper, the number of nested blocks is set to 150 in the subsequent calculations to compromise between the computation burden and the computational accuracy.

4.2 Influence of the slope-width-to-height ratios

This section aims to discuss the influences of the slope-width-to-height ratios, represented by B/H, on the seismic yield acceleration and the total horizontal displacement in the framework of the proposed Nested Newmark method. Figure 6 shows the profiles of seismic yield acceleration along the slope height for the B/H ratio changing from 2.0 to 20.0. For the case of B/H=3, the seismic yield acceleration increases from 0.18 g at the slope base to 0.42 g at the slope middle heigh, and finally raising to 2.0 g at the slope crest. Besides, at the slope middle heigh, the seismic yield acceleration decreases slightly with the increasing of the slope B/H ratio, which declines from 0.42 g at B/H=2 to 0.30 g at B/H=20.

Figure 7 plots the profiles of the total horizontal displacements along the slope height for the B/H ratio changing from 2.0 to 10.0. For the case of B/H=3, the total horizontal displacement increases from 0.0 m at the slope base to 0.84 m at the slope middle heigh, beyond which the total horizontal displacement remains stable. This is because that the peak acceleration on the acceleration time history records of 1999 Chi-Chi earthquake, station TCU072-000, is around 0.375 g, as illustrated in Figure 1, which is smaller than the seismic yield acceleration at the slope middle height. Besides, the total horizontal displacement at the slope middle height increases with the increasing of the slope B/H ratio, which increases from 0.50 m at B/H=2 to 1.2 m at B/H=20. This phenomenon agrees well with what are observed in Nadukuru and Michalowski (Du et al., 2018), who assessed three-dimensional slope displacements under seismic loads using the traditional Newmark displacements.

4.3 Influence of the peak ground accelerations

This section studies the influences of the peak accelerations of ground motions, a_c, on the seismically induced cumulative displacements of slopes by the proposed 3D-NNM. The peak ground acceleration time history records of 1999 Chi-Chi earthquake at station TCU072-000, plotted in Figure 2, are scaled to 0.40 g, 0.45 g,

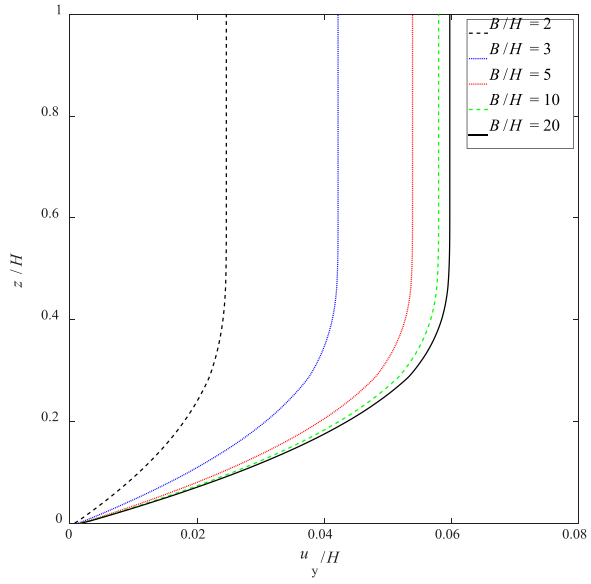

FIGURE 7
Influences of B/H ratio on the total horizontal displacement profiles.

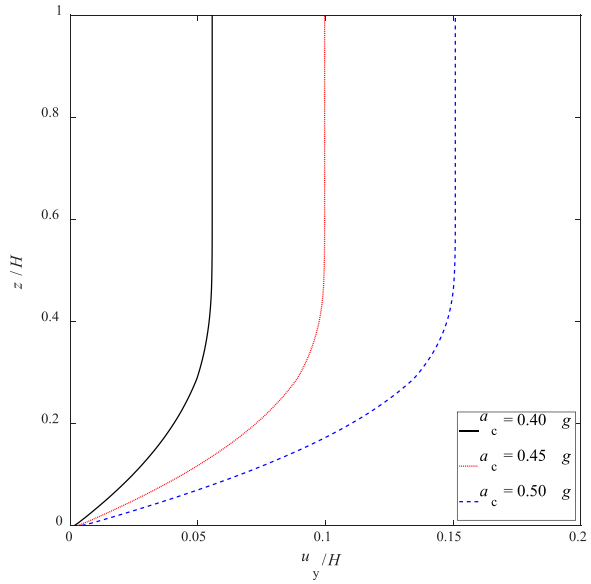

FIGURE 8
Influences of the peak ground accelerations on the total horizontal displacement profiles.

and 0.60 g, without changing the frequency. Figure 8 plots the profiles of the normalized total horizontal displacement profiles along the slope height for the peak accelerations of ground motions being 0.40g, 0.45g and 0.60 g. It is under expectation that the cumulative horizontal displacement profiles increase with the peak ground accelerations. Specially, the maximum cumulative horizontal displacement normalized the slope height is 0.055 for the case of a_c = 4.0 g, and increases to 0.10 at 0.45 g and to 0.15 at 0.60 g. This indicates that the peak ground acceleration poses a great influence on the estimated cumulative horizontal displacements.

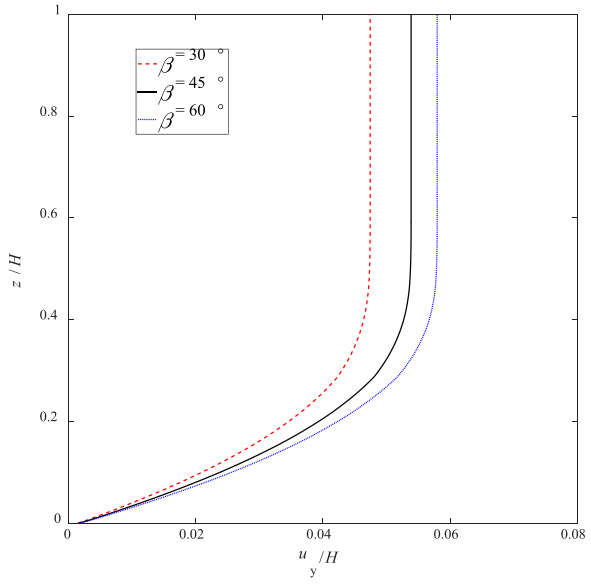

FIGURE 9
Influences of the slope inclination angles on the total horizontal displacement profiles.

4.4 Influence of the slope inclination angles

This section studies the influences of the slope inclination angles, β, on the seismically induced cumulative displacements of slopes by the proposed 3D-NNM. The slope inclination angles are set to change from 30° to 60°, with an increment of 15°. Figure 9 plots the profiles of the normalized total horizontal displacement profiles along the slope height for the slope inclination angles being 30°, 45° and 60°. It is observed that the cumulative horizontal displacement profiles are positively correlated with the slope inclination angles. Particularly, the maximum cumulative horizontal displacement normalized the slope height is 0.047 for the case of β = 30°, and increases to 0.53 at 45° and to 0.58 at 60°.

5 Conclusion

This paper aims at proposing a three-dimensional nested Newmark method (3D-NNM) in the framework of the kinematic theorem of limit analysis. The proposed 3D-NNM is compared with the original Nested Newmark method, which shows that the proposed 3D-NNM can effectively evaluate the permanent displacement profile of slopes under earthquakes. The conclusions of this paper are summarized below:

(1) The proposed 3D-NNM is compared with the original Nested Newmark method of Leshchinsky (Du et al., 2023), whose work inspires this study. The comparisons are made with

respect to the relative displacement profiles along slope height and the total horizontal permanent displacement profiles along slope height. Similar displacement profiles along slope height are observed both in proposed 3D-NNM and in the Nested Newmark method of Leshchinsky. It is interesting to find that the Leshchinsky's 2D nested Newmark method may overestimate the post-earthquake deformation profile of slopes. Specifically, the maximum total horizontal permanent displacement is 1.34 m estimated by the Leshchinsky's 2D nested Newmark method but is 1.08 m by the proposed 3D nested Newmark method with B/H = 5.0. This means that the proposed 3D nested Newmark method improves the Leshchinsky's 2D nested Newmark method by 30.7%, since the proposed method gives a rigorous upper-bound estimation to the post-earthquake deformations.

(2) The performance of the proposed 3D-NNM is highly dependent on the number of nested blocks. It is interesting to find that the estimated total horizontal displacements converge after the number of nested blocks increase to 200. The higher the number of nested blocks, the better estimation of slope permanent displacements by the proposed 3D-NNM. However, the computational burden is positively correlated with the number of nested blocks. In order to balance the computation burden and the computational accuracy, the number of nested blocks is set to 150 in all the calculations in this study. This provides a way to determine the optimal number of nested blocks. The readers should note that the optimal number of nested blocks may be problem-dependent, but it is not difficult to determine the optimal one by following the above procedure. Besides, the traditional Newmark method with a single sliding block tends to underestimate the permanent displacements of slope under seismic shakings.

(3) The total horizontal displacement at the slope middle height increases with the increasing of the slope-width-to-height ratios. This further indicates that the two-dimensional analysis tends to provide conservative results of the proposed Newmark method.

It would be better if the proposed 3D-NNM could be compared with real-data experiments. However, a shaking table test of seismic slope stability is beyond the scope of this study. It will be the topic of future study of doing shaking table tests to check the presence of multiple shear zones or regions of dispersed shear movements of a slope subjected to seismic loads. Besides, two possible future research directions include: (1) the inclusion of reinforcement effect of soil nails in the proposed method, since soil nails are used to stabilize slopes in earthquake-prone zones; (2) considering the uncertainties of soil properties and seismic loadings that poses important influences on slope stability analysis.

Data availability statement

The original contributions presented in the study are included in the article/Supplementary material, further inquiries can be directed to the corresponding author.

Author contributions

QL: Conceptualization, Methodology, Writing–original draft. Y-YT: Conceptualization, Software, Writing–original draft. J-NW: Software, Writing–review and editing. HX: Writing–review and editing.

Funding

The author(s) declare that financial support was received for the research, authorship, and/or publication of this article. The authors are very grateful for the financial support of the National Natural Science Foundation of China (Grant No. 42172309), and the Science Technology Department of Zhejiang Province (Grant No. 2022C03051).

Conflict of interest

The authors declare that the research was conducted in the absence of any commercial or financial relationships that could be construed as a potential conflict of interest.

Publisher's note

References

Chen, G., Zhang, K., Wang, S., Xia, Y., and Chao, L. (2023). iHydroSlide3D v1.0: an advanced hydrological-geotechnical model for hydrological simulation and three-dimensional landslide prediction. *Geosci. Model Dev.* 16, 2915–2937. doi:10.5194/gmd-16-2915-2023

Chousianitis, K., Del Gaudio, V., Kalogeras, I., and Ganas, A. (2014). Predictive model of Arias intensity and Newmark displacement for regional scale evaluation of earthquake-induced landslide hazard in Greece. *Soil Dyn. Earthq. Eng.* 65, 11–29. doi:10.1016/j.soildyn.2014.05.009

Dai, Z., Li, X., and Lan, B. (2023). Three-dimensional modeling of tsunami waves triggered by submarine landslides based on the smoothed particle hydrodynamics method. *J. Mar. Sci. Eng.* 11 (10), 2015. doi:10.3390/jmse11102015

Du, W., Huang, D., and Wang, G. (2018). Quantification of model uncertainty and variability in Newmark displacement analysis. *Soil Dyn. Earthq. Eng.* 109, 286–298. doi:10.1016/j.soildyn.2018.02.037

Du, W., and Wang, G. (2013). Intra-event spatial correlations for cumulative absolute velocity, Arias intensity, and spectral accelerations based on regional site conditions. *Bull. Seismol. Soc. Am.* 103 (2A), 1117–1129. doi:10.1785/0120120185

Du, Y., Xu, W., Han, W., Huang, B., Liu, H., and Du, X. (2023). Dynamic response analysis of wedge-shaped rock slopes under harmonic wave action. *Buildings* 13 (10), 2623. doi:10.3390/buildings13102623

Gao, Y. F., Zhang, F., Lei, G. H., and Li, D. Y. (2013). An extended limit analysis of three-dimensional slope stability. *Géotechnique* 63 (6), 518–524. doi:10.1680/geot.12.t.004

Hsieh, S. Y., and Lee, C. T. (2011). Empirical estimation of the Newmark displacement from the Arias intensity and critical acceleration. *Eng. Geol.* 122 (1-2), 34–42. doi:10.1016/j.enggeo.2010.12.006

Jibson, R. W. (2011). Methods for assessing the stability of slopes during earthquakes-A retrospective. *Eng. Geol.* 122 (1-2), 43–50. doi:10.1016/j.enggeo.2010.09.017

Kutter, B. L., and James, R. G. (1989). Dynamic centrifuge model tests on clay embankments. *Geotechnique* 39 (1), 91–106. doi:10.1680/geot.1989.39.1.91

Leshchinsky, B. A. (2018). Nested Newmark model to calculate the post-earthquake profile of slopes. *Eng. Geol.* 233, 139–145. doi:10.1016/j.enggeo.2017.12.006

Li, D. Q., Wang, M. X., and Du, W. (2020). Influence of spatial variability of soil strength parameters on probabilistic seismic slope displacement hazard analysis. *Eng. Geol.* 276, 105744. doi:10.1016/j.enggeo.2020.105744

Li, Y., Chu, Z., Zhang, L., and He, Y. (2023). Research on the dynamic response of a slope reinforced by a pile-anchor structure under seismic loading. *Buildings* 13 (10), 2500. doi:10.3390/buildings13102500

Liu, W., Zhou, H., Zhang, S., and Zhao, C. (2023b). Variable parameter creep model based on the separation of viscoelastic and viscoplastic deformations. *Rock Mech. Rock Eng.* 56, 4629–4645. doi:10.1007/s00603-023-03266-7

Liu, Y., Gao, Y., Shu, S., Dai, G., and Zhang, F. (2023a). Seismic stability and permanent displacement of 3D slopes with tension cutoff. *Int. J. Geomechanics* 23 (9), 04023158. doi:10.1061/ijgnai.gmeng-8697

Lu, Y., Pang, R., Du, M., and Xu, B. (2024). Simulation of non-stationary ground motions and its applications in high concrete faced rockfill dams via direct probability integral method. *Eng. Struct.* 298, 117034. doi:10.1016/j.engstruct.2023.117034

Mathews, N., Leshchinsky, B. A., Olsen, M. J., and Klar, A. (2019). Spatial distribution of yield accelerations and permanent displacements: a diagnostic tool for assessing seismic slope stability. *Soil Dyn. Earthq. Eng.* 126, 105811. doi:10.1016/j.soildyn.2019.105811

Mi, C., Liu, Y., Zhang, Y., Wang, J., Feng, Y., and Zhang, Z. (2023). A vision-based displacement measurement system for foundation pit. *IEEE Trans. Instrum. Meas.* 72, 1–15. doi:10.1109/TIM.2023.3311069

Michalowski, R. L., and Drescher, A. (2009). Three-dimensional stability of slopes and excavations. *Géotechnique* 59 (10), 839–850. doi:10.1680/geot.8.p.136

Nadukuru, S. S., and Michalowski, R. L. (2013). Three-dimensional displacement analysis of slopes subjected to seismic loads. *Can. geotechnical J.* 50 (6), 650–661. doi:10.1139/cgj-2012-0223

Newmark, N. M. (1965). Effects of earthquakes on dams and embankments. *Geotechnique* 15 (2), 139–160. doi:10.1680/geot.1965.15.2.139

Pan, Q. J., Leung, Y. F., and Hsu, S. C. (2021). Stochastic seismic slope stability assessment using polynomial chaos expansions combined with relevance vector machine. *Geosci. Front.* 12 (1), 405–414. doi:10.1016/j.gsf.2020.03.016

Pang, R., Xu, B., Zhou, Y., and Song, L. (2021). Seismic time-history response and system reliability analysis of slopes considering uncertainty of multi-parameters and earthquake excitations. *Comput. Geotechnics* 136, 104245. doi:10.1016/j.compgeo.2021.104245

Pang, R., Xu, B., Zou, D., and Kong, X. (2018b). Stochastic seismic performance assessment of high CFRDs based on generalized probability density evolution method. *Comput. Geotechnics* 97, 233–245. doi:10.1016/j.compgeo.2018.01.016

Saygili, G., and Rathje, E. M. (2008). Empirical predictive models for earthquake-induced sliding displacements of slopes. *J. geotechnical geoenvironmental Eng.* 134 (6), 790–803. doi:10.1061/(asce)1090-0241(2008)134:6(790)

Song, J., Fan, Q., Feng, T., Chen, Z., Chen, J., and Gao, Y. (2019). A multi-block sliding approach to calculate the permanent seismic displacement of slopes. *Eng. Geol.* 255, 48–58. doi:10.1016/j.enggeo.2019.04.012

Wartman, J., Seed, R. B., and Bray, J. D. (2005). Shaking table modeling of seismically induced deformations in slopes. *J. Geotechnical Geoenvironmental Eng.* 131 (5), 610–622. doi:10.1061/(asce)1090-0241(2005)131:5(610)

Xu, M., Pang, R., Zhou, Y., and Xu, B. (2023). Seepage safety evaluation of high earth-rockfill dams considering spatial variability of hydraulic parameters via subset simulation. *J. Hydrology* 626, 130261. doi:10.1016/j.jhydrol.2023.130261

Yegian, M. K., Marciano, E. A., and Ghahraman, V. G. (1991). Earthquake-induced permanent deformations: probabilistic approach. *J. Geotechnical Eng.* 117 (1), 35–50. doi:10.1061/(asce)0733-9410(1991)117:1(35)

Zhang, H., Xiang, X., Huang, B., Wu, Z., and Chen, H. (2023). Static homotopy response analysis of structure with random variables of arbitrary distributions by minimizing stochastic residual error. *Comput. Struct.* 288, 107153. doi:10.1016/j.compstruc.2023.107153

Zhang, X., Wang, S., Liu, H., Cui, J., Liu, C., and Meng, X. (2024). Assessing the impact of inertial load on the buckling behavior of piles with large slenderness ratios in liquefiable deposits. *Soil Dyn. Earthq. Eng.* 176, 108322. doi:10.1016/j.soildyn.2023.108322

Zhao, N., Li, D. Q., Gu, S. X., and Du, W. (2024). Analytical fragility relation for buried cast iron pipelines with lead-caulked joints based on machine learning algorithms. *Earthq. Spectra* 40 (1), 566–583. doi:10.1177/87552930231209195

Zheng, Z., Yufeng, G., Fei, Z., Jian, S., and Degao, Z. (2020). Effects of soil dynamic response on post-earthquake deformation of slopes based on nested Newmark model. *Earthq. Eng. Eng. Vib.* 19, 573–582. doi:10.1007/s11803-020-0581-y

Zhou, Z., Zhang, F., Gao, Y. F., and Shu, S. (2019). Nested Newmark model to estimate permanent displacement of seismic slopes with tensile strength cut-off. *J. Central South Univ.* 26 (7), 1830–1839. doi:10.1007/s11771-019-4137-0

Zhu, D., Pang, R., Xu, M., Chen, J., and Xu, B. (2024). Seismic safety evaluation of slope with spatially variable soils based on collaborative analysis via optimized subset simulation. *Comput. Geotechnics* 168, 106157. doi:10.1016/j.compgeo.2024.106157

Frontiers in Earth Science

Investigates the processes operating within the major spheres of our planet

Advances our understanding across the earth sciences, providing a theoretical background for better use of our planet's resources and equipping us to face major environmental challenges.

Discover the latest Research Topics

See more →

Frontiers

Avenue du Tribunal-Fédéral 34
1005 Lausanne, Switzerland
frontiersin.org

Contact us

+41 (0)21 510 17 00
frontiersin.org/about/contact